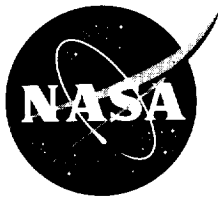# Annual Research Briefs – 1997

Center for Turbulence Research

December 1997

Preface

This report contains the 1997 annual progress reports of the research fellows and students supported by the Center for Turbulence Research. The Annual Research Briefs as well as the proceedings of the summer programs are now available at CTR's site on the world wide web (http://www-fpc.stanford.edu/CTR/welcome.html).

Last year, CTR hosted fourteen resident Postdoctoral Fellows, seven Research Associates, three Senior Research Fellows, and supported four doctoral students and eleven short term visitors. The major portion of Stanford's doctoral research program in turbulence is sponsored by the United States Office of Naval Research and the Air Force Office of Scientific Research. Many students supported by these programs also conduct their research at the CTR, but their works are not included in this report.

In September 1997, the U.S. Department of Energy (DOE) selected Stanford as one of five universities to participate in a long term research program aimed at enhancing numerical simulation capabilities for complex physical systems. DOE has also made its unique supercomputers available to the university participants in this program. It appears that CTR will play an important role in this program because turbulence is a major component in the overarching problems being addressed by all five of the new DOE Centers. Stanford's program, to be carried out in a new Center for Integrated Turbulence Simulations (CITS) co-located with the CTR, involves the simulation of the turbulent flow in a complete gas turbine engine, which is expected to lead to a new paradigm for aircraft engine design. We expect CTR's experience and expertise to contribute greatly to this project, and the engineering challenge provided by the program should induce a number of relevant fundamental investigations at CTR.

The first group of reports in this volume is concerned with fundamental issues in large eddy simulation, LES. These include derivation of the constitutive equations, filtering, and wall modeling. The latter is a pacing item for practical simulation of high Reynolds number turbulent boundary layers. The next group of reports is in Reynolds averaged turbulence modeling, which has always been emphasized at CTR due to its importance to engineering analysis of complex flows. Our major effort continued around extension and application of the V2F model to complex flows and its implementation in general purpose NASA and industrial CFD codes. The next group of reports is in turbulent combustion. We expect to expand CTR's effort in this area to include combustion in realistic geometries and complex chemical reactions. The fourth group of reports is concerned with turbulence physics and control and simulation methodology. The flow control activity at CTR has developed to a point where it is being used in joint research activities with industry. We also expect the CTR's flow control program to have an impact on the problem of combustion instabilities in gas turbine engines, which is an important part of the aforementioned DOE project.

The CTR's roster for 1997 is provided in the Appendix. Also listed are the members of the Advisory Committee, which meets bi-annually to review the Center's program, and the Steering Committee, which acts on fellowship applications.

It is a pleasure to thank Mrs. Debra Spinks for her efforts in the daily management of the Center and her compilation of this report.

Parviz Moin
William C. Reynolds

CONTENTS

Invariant modeling in large-eddy simulation of turbulence

By M. Oberlack

1. Motivation and objectives

Since the derivation of the Smagorinsky model (Smagorinsky 1963), much research has been dedicated to developing more reliable and physically plausible large-eddy models for turbulence. Speziale (1985) made the first attempt to derive realizable large-eddy models. He argued that any subgrid-scale (SGS) model in large-eddy simulation (LES) of turbulence should be Galilean invariant, a fundamental invariance property (also called symmetry) of the Navier-Stokes equations. In his investigation he found that many models violate this symmetry. The most widely used model, the Smagorinsky model, is Galilean invariant.

However, Galilean invariance is only one of several symmetries of the Navier-stokes equations. It will be seen later that several of the symmetries are violated by common SGS models, the bulk of which contain the local grid size of the computation as a length scale. From a theoretical point of view, having an external length scale in the turbulent model which is not related to any turbulent quantity violates certain symmetries of Navier-Stokes equations. This has serious implications for the overall performance of the model, which will be pointed out below. In particular, certain scaling laws cannot be realized by the modeled equations in wall-bounded flows (see Appendix A).

A differential equation admits a symmetry if a transformation can be obtained which leaves the equation unchanged in the new variables. It is said the equation is invariant under the transformation. Symmetries or invariant transformations are properties of the equations and not of the boundary conditions, which are usually not invariant. Symmetries and their consequences form some of the most fundamental properties of partial differential equations and illustrate many important features of the underlying physics. The Navier-Stokes equations admit several symmetries, each of them reflecting axiomatic properties of classical mechanics: time invariance, rotation invariance, reflection invariance, two scaling invariances, pressure invariance, material indifference, and generalized Galilean invariance, which encompasses frame invariance with respect to finite translation and classical Galilean invariance. Each of these symmetries is explained in Section 2.

For example, all known similarity solutions of the Euler and the Navier-Stokes equations for laminar flows can be derived from symmetries (see Pukhnachev 1972). Turbulent flows admit a wide variety of solutions derivable from symmetries. Some of them, like jets and wakes, have global character (see e.g. Townsend 1976; Cantwell 1981) others only apply locally, e.g. in wall-bounded flows. Recently several new scaling laws for turbulent wall-bounded flows were derived in Oberlack (1997a,b) using symmetry methods, and all of these are local self-similar regions. A well

known example, which is also among Oberlack's results, is the logarithmic law of the wall which has a restricted validity near the wall region but can be found in many geometrically different flows. All the known local and global turbulent scaling laws can be derived from symmetries.

In order to reproduce all global and local self-similar turbulent solutions with an SGS model in LES of turbulence, it is a necessary condition that all the above mentioned invariance properties of the Navier-Stokes equations should be built into the SGS model. This implies certain restrictions for the functional form of the model.

In LES of turbulence not only the SGS model is constrained by symmetries, but so also is the filer function. Vreman, Geurts & Kuerten (1994) investigated whether certain filter functions preserve the classical realizability constraint by Schumann (1977). The key result in their analysis is that the filter kernel has to be positive in order to ensure positive turbulent subgrid kinetic energy. They concluded that the spectral cut-off filter is not suitable for LES since the kernel is negative for certain values of its argument. Symmetries of the Navier-Stokes equations imply further constraints for the filter function to be derived below. Moreover, it will be shown that the form of filter function is consistent with the finding of Vreman *et al.*.

The paper is organized as follows: In Section 2. all the known symmetries of the Navier-Stokes equations are discussed. In Section 3 the concept of spatial averaging is reexamined, and its implications for the SGS model and the filter function are derived. In Section 4 several examples of proposed SGS models will be investigated as to whether they obey or violate certain symmetries of the Navier-Stokes equations. Section 5 gives a summary and conclusions of the paper. In Appendix A the effect on near-wall scaling laws will be investigated for the case when the SGS model does not satisfy the proper scaling symmetries.

2. Symmetries of the Navier-Stokes equations

The Navier-Stokes and the continuity equations for an incompressible fluid written in primitive variables in a Cartesian coordinate system are

$$\frac{\partial u_i}{\partial t} + u_k \frac{\partial u_i}{\partial x_k} = -\frac{\partial p}{\partial x_i} + \nu \frac{\partial^2 u_i}{\partial x_k^2} \quad \text{and} \quad \frac{\partial u_k}{\partial x_k} = 0, \tag{1}$$

where x, t, u, p, and ν are, respectively, the spatial coordinate, time, the velocity vector, the pressure normalized by the density and the kinematic viscosity. Equations (1) admit several symmetries, each reflecting fundamental properties of classical mechanics. In the following a list of all known symmetry transformations will be given which preserve the functional form of (1) written in the new variables, subsequently denoted by "*".

I. Time invariance

An arbitrary time shift of the amount a

$$t^* = t + a, \quad x^* = x, \quad u^* = u, \quad p^* = p, \quad \nu^* = \nu \tag{2}$$

has no effect on the functional form of (1).

II. Rotation invariance

Rotating the coordinate system and the velocity vector

$$t^* = t, \quad x_i^* = A_{ij}x_j, \quad u_i^* = A_{ij}u_j, \quad p^* = p, \quad \nu^* = \nu \tag{3}$$

by a finite but arbitrary angle in space, where A is the rotation matrix with $AA^T = A^T A = I$ and $|A| = 1$, preserves the form of Eq. (1) in the new variables after multiplying the momentum equation with A. The superscripts T, I, and $|\cdot|$ denote, respectively, the transpose of a matrix, the unit tensor, and the determinant.

III. Reflection invariance

The reflection symmetry in any direction x_α is given by

$$
\begin{aligned}
t^* &= t, \quad x_\alpha^* = -x_\alpha, \quad u_\alpha^* = -u_\alpha, \\
x_\beta^* &= x_\beta \ , u_\beta^* = u_\beta \ \text{with} \ \beta \neq \alpha, \quad p^* = p, \quad \nu^* = \nu,
\end{aligned}
\tag{4}
$$

where the index α can be any of 1, 2, and 3, and β refers to the remaining two.

IV. Generalized Galilean invariance

Substituting

$$u^* = u + \frac{d\hat{x}}{dt}, \quad p^* = p - x \cdot \frac{d^2\hat{x}}{dt^2} \quad \text{and} \quad \nu^* = \nu \tag{5}$$

into (1), where $\hat{x}(t)$ is any twice differentiable time dependent vector-function, does not alter the functional form of (1). (5) covers two classical symmetries: (i) Invariance with respect to finite translation in space is obtained for $\hat{x}(t) = b$, where b is a constant and (ii) the classical Galilean invariance is recovered if $\hat{x}(t)$ is a linear function in time.

All symmetries (2)-(5) are also admitted by the incompressible Euler equations.

V. Scaling invariance

Considering $\nu = 0$, the two-parameter transformation

$$t^* = \xi t, \quad x^* = \gamma x, \quad u^* = \frac{\gamma}{\xi}u, \quad p^* = \left(\frac{\gamma}{\xi}\right)^2 p \tag{6}$$

is an invariant transformation of Eqs. (1), where ξ and γ are arbitrary positive real numbers. If $\nu \neq 0$ and ν is considered a parameter, then (6) is only a scaling invariance provided $\gamma^2 = \xi$.

Considering ν as an additional independent variable, the full two-parameter scaling invariance (6) for $\nu \neq 0$ is recovered if ν is scaled as

$$\nu^* = \frac{\gamma^2}{\xi}\nu. \tag{7}$$

The two scaling groups corresponding to γ and ζ refer to the fact that in classical mechanics time and space can be measured arbitrarily. Hence, scaling symmetries are equivalent to dimensional analysis.

VI. Pressure invariance

An arbitrary time variation of the background pressure, here denoted by $\varphi(t)$, does not affect an incompressible flow. The corresponding symmetry transformation is given by

$$t^* = t, \quad \boldsymbol{x}^* = \boldsymbol{x}, \quad \boldsymbol{u}^* = \boldsymbol{u}, \quad p^* = p + \varphi(t), \quad \nu^* = \nu. \tag{8}$$

VII. Material indifference

Consider the Navier-Stokes equations in a constantly rotating frame with a rotation rate Ω_3 about the x_3 direction and where all velocities only depend on x_1, x_2, and t. The particular choice of the axis of rotation is not restrictive because of the transformations (3) and (4). The transformation which leaves (1) form-invariant is given by

$$t^* = t, \quad x_i^* = B_{ij}(t)x_j, \quad u_i^* = B_{ij}(t)u_j + \dot{B}_{ik}(t)x_k,$$

$$p^* = p + 2\Omega_3 \int_Q (u_1 dx_2 - u_2 dx_1) - \frac{3}{2}\Omega_3^2(x_1^2 + x_2^2), \quad \nu^* = \nu \tag{9}$$

where $\boldsymbol{B}(t)$ is the rotation matrix with $\boldsymbol{B}\boldsymbol{B}^T = \boldsymbol{B}^T\boldsymbol{B} = \boldsymbol{I}$, $|\boldsymbol{B}| = 1$, $\dot{B}_{ik}B_{jk} = \varepsilon_{3ij}\Omega_3$ and Ω_3 is a constant. The line integral along the arbitrary curve Q in the pressure transformation represents the usual two-dimensional stream-function. The property of material indifference can be reversed if turbulence undergoes rotation-like advection. This can be accomplished either by system rotation or stream-line curvature. In this case turbulence tends to become two-dimensional with the axis of independence aligned with the axis of rotation.

All the symmetry transformations have been obtained by group analysis, except for the reflection symmetry (4), which does not form a continuous group. Pukhnachev (1972) computed the first complete list of all continuous point symmetries (2), (3), (5), (6), and (8) by Lie group methods (see e.g. Ibragimov 1994,1995). Ünal (1994) added the scaling of viscosity (7). The transformation (9) is a well known property of two-dimensional flows (see e.g. Batchelor 1967). From group theoretical methods, it was first derived by Cantwell (1978). He computed it using Lie group analysis applied to the scalar stream-function equation of the two-dimensional Navier-Stokes equations. In this approach the symmetry (9) is a classical point symmetry while in primitive variables it is a non-local symmetry. A corresponding symmetry in three dimensions may not exist. In Oberlack (1997c) it was shown that the three-dimensional Navier-Stokes equations in vector-stream-function formulation admit only those symmetries which can be derived from the Navier-Stokes equations in primitive variables. Recently, additional non-classical symmetries have been obtained by Ludlow & Clarkson (1997). However, these symmetries are not invariant transformations in the classical sense but instead can only be used to obtain self-similar solutions of the Navier-Stokes equations.

3. Invariant modeling and filtering

In contrast to the classical Reynolds averaging, in large-eddy simulation of turbulence the averaging procedure is a spatial filtering defined as

$$\mathcal{L}[\cdot](x) = \int_V G(x, y)[\cdot](y) d^3 y. \tag{10}$$

The kernel G is normalized as

$$\int_V G(x, y) d^3 y = 1 \tag{11}$$

and G is assumed to be sufficiently smooth and decays rapidly enough for large distances y so that the integrals converge.

In the present context f represents the instantaneous variables u and p. f is decomposed as

$$f = \bar{f} + f' \tag{12}$$

where

$$\bar{f} = \mathcal{L}[f](x). \tag{13}$$

Introducing the decomposition (12) for both the velocity and pressure into Eqs. (1) and applying the filter (10) leads to the equation of motion for the large-eddies

$$\frac{\partial \bar{u}_i}{\partial t} + \bar{u}_k \frac{\partial \bar{u}_i}{\partial x_k} = -\frac{\partial \bar{p}}{\partial x_i} + \nu \frac{\partial^2 \bar{u}_i}{\partial x_k^2} - \frac{\partial \tau_{ik}}{\partial x_k} \quad \text{and} \quad \frac{\partial \bar{u}_k}{\partial x_k} = 0. \tag{14}$$

The SGS stress τ_{ik} is given by

$$\tau_{ik} = L_{ik} + C_{ik} + R_{ik}, \tag{15}$$

where

$$L_{ik} = \overline{\bar{u}_i \bar{u}_k} - \bar{u}_i \bar{u}_k, \tag{16}$$

$$C_{ik} = \overline{u'_i \bar{u}_k} + \overline{\bar{u}_i u'_k}, \tag{17}$$

$$R_{ik} = \overline{u'_i u'_k}. \tag{18}$$

L_{ik}, C_{ik}, and R_{ik} are, respectively, referred to as the Leonard stress, the subgrid-scale cross-stress, and the subgrid-scale Reynolds stress. If explicit filtering is employed, the Leonard stress may be computed from the flow field, and closure models only need to be introduced for C_{ik} and R_{ik}. Though the decomposition of τ is arbitrary, (16)-(18) is a very common notation in LES. A different decomposition has been proposed by Germano (1986) because it was found by Speziale (1985) that both L_{ik} and C_{ik} are not Galilean invariant as discussed below.

The principal assertion of this work is given by the following statement: *To derive a physically consistent large-eddy model for turbulence the filtered Navier-Stokes equations (14) with the SGS closure model must admit the same symmetries as the Navier-Stokes equations (as given in section 2).*

This has certain implications for the form of the model for (16)-(18) and puts restrictions on the filter kernel G in (10) to be derived in the next two sub-sections.

3.1 Implications for the subgrid-scale stresses

Suppose the filter (10) preserves the invariance properties of Navier-Stokes equations, then one can deduce from (14) and (15) that

$$\frac{\partial \bar{u}_i^*}{\partial t^*} + \bar{u}_k^* \frac{\partial \bar{u}_i^*}{\partial x_k^*} = -\frac{\partial \bar{p}^*}{\partial x_i^*} + \nu^* \frac{\partial^2 \bar{u}_i^*}{\partial x_k^{*2}} - \frac{\partial \tau_{ik}^*}{\partial x_k^*} \quad \text{and} \quad \frac{\partial \bar{u}_k^*}{\partial x_k^*} = 0 \qquad (19)$$

where

$$\tau_{ik}^* = L_{ik}^* + C_{ik}^* + R_{ik}^*, \qquad (20)$$

and

$$L_{ik}^* = \overline{\bar{u}_i^* \bar{u}_k^*} - \bar{u}_i^* \bar{u}_k^*, \qquad (21)$$

$$C_{ik}^* = \overline{u'_i^* \bar{u}_k^*} + \overline{\bar{u}_i^* u'_k^*}, \qquad (22)$$

$$R_{ik}^* = \overline{u'_i^* u'_k^*}. \qquad (23)$$

and "*" refers to any of the symmetry transformation variables in Section 2. The following is a list of all constraints for the SGS model to properly reproduce all symmetries of the equations of motion.

I. Time invariance

From (2) it can be deduced that the resolved and the unresolved quantities transform as

$$t^* = t + a, \quad \boldsymbol{x}^* = \boldsymbol{x}, \quad \bar{\boldsymbol{u}}^* = \bar{\boldsymbol{u}}, \quad \boldsymbol{u}'^* = \boldsymbol{u}', \quad \bar{p}^* = \bar{p}, \quad p'^* = p', \quad \nu^* = \nu, \qquad (24)$$

which leads to the transformation rule for the stresses

$$\boldsymbol{\tau}^* = \boldsymbol{\tau} \quad \text{or} \quad \boldsymbol{L}^* = \boldsymbol{L}, \quad \boldsymbol{C}^* = \boldsymbol{C} \quad \text{and} \quad \boldsymbol{R}^* = \boldsymbol{R}. \qquad (25)$$

Any model which is autonomous in time complies with this restriction. This is almost always guaranteed since common models are expressed as functionals of $\boldsymbol{x}$ and $\bar{u}$ only.

II. Rotation invariance

From (3) one can conclude that the rotation invariance for the large scale and small scale quantities are given by

$$t^* = t, \quad x_i^* = A_{ij} x_j, \quad \bar{u}_i^* = A_{ij} \bar{u}_j, \quad u'_i^* = A_{ij} u'_j, \quad \bar{p}^* = \bar{p}, \quad p'^* = p', \quad \nu^* = \nu. \qquad (26)$$

As a consequence, the stress tensor (15) and its components (16)-(18) need to transform as

$$\tau_{ik}^* = A_{im} A_{kn} \tau_{mn},$$

$$L_{ik}^* = A_{im} A_{kn} L_{mn}, \quad C_{ik}^* = A_{im} A_{kn} C_{mn} \quad \text{and} \quad R_{ik}^* = A_{im} A_{kn} R_{mn}. \qquad (27)$$

This is always guaranteed if the model is formulated in a "tensorially correct" manner. The author is unaware of any existing model that violates this property.

III. Reflection invariance

Considering reflection in the x_α-direction, one can infer from (4) that the filtered and subgrid quantities transform as

$$t^* = t, \quad x_\alpha^* = -x_\alpha, \quad \bar{u}_\alpha^* = -\bar{u}_\alpha, \quad u_\alpha'^* = -u_\alpha',$$

$$x_\beta^* = x_\beta, \quad \bar{u}_\beta^* = \bar{u}_\beta, \quad u_\beta'^* = u_\beta' \text{ with } \beta \neq \alpha, \quad p^* = p, \quad \nu^* = \nu, \qquad (28)$$

where α and β are defined according to the definitions below (4). Hence, the reflection symmetry is preserved if

$$\tau_{ik}^* = \omega \tau_{ik}, \quad \text{where} \quad \begin{cases} \omega = -1 & \text{for } i = \alpha \ \lor \ k = \alpha \ \land \ i \neq k \\ \omega = 1 & \text{else} \end{cases} . \qquad (29)$$

Similarly, one has the additional restrictions

$$\begin{aligned} L_{ik}^* &= \omega L_{ik}, \\ C_{ik}^* &= \omega C_{ik}, \quad \text{where} \quad \begin{cases} \omega = -1 & \text{for } i = \alpha \ \lor \ k = \alpha \ \land \ i \neq k \\ \omega = 1 & \text{else} \end{cases} . \qquad (30) \\ R_{ik}^* &= \omega R_{ik} \end{aligned}$$

It appears that all common SGS models comply with reflection symmetry.

IV. Generalized Galilean invariance

Generalizing Speziale (1985), (5) and (12) are used to obtain

$$t^* = t, \quad \boldsymbol{x}^* = \boldsymbol{x} + \hat{\boldsymbol{x}}(t), \quad \bar{\boldsymbol{u}}^* = \bar{\boldsymbol{u}} + \frac{d\hat{\boldsymbol{x}}}{dt}, \quad \boldsymbol{u}'^* = \boldsymbol{u}', \quad \bar{p}^* = \bar{p} - \boldsymbol{x} \cdot \frac{d^2\hat{\boldsymbol{x}}}{dt^2}, \quad p'^* = p', \quad \nu^* = \nu. \qquad (31)$$

From the latter result and (20), one can verify that

$$\boldsymbol{\tau}^* = \boldsymbol{\tau}. \qquad (32)$$

As pointed out by Speziale (1985), a corresponding simple transformation does not exist for (16)-(18). Using (31) in (21)-(23), we find

$$L_{ik}^* = L_{ik} - \frac{d\hat{x}_i}{dt}\overline{u_k'} - \overline{u_i'}\frac{d\hat{x}_k}{dt} \qquad (33)$$

$$C_{ik}^* = C_{ik} + \frac{d\hat{x}_i}{dt}\overline{u_k'} + \overline{u_i'}\frac{d\hat{x}_k}{dt} \qquad (34)$$

$$R_{ik}^* = R_{ik}. \qquad (35)$$

Hence, L_{ik} and C_{ik} are not form-invariant, but their sum is. Germano (1986) tackled the latter problem by redefining the turbulent stresses. He introduced modified definitions for the quantities $\boldsymbol{L}$, $\boldsymbol{C}$, and $\boldsymbol{R}$ where each separate term is Galilean

invariant. Since the decomposition is not unique, it appears to be preferable to test the entire SGS model for τ for Galilean invariance.

The requirement of Galilean invariance has nicely been demonstrated by Härtel & Kleiser (1997), who have compared Galilean and non-Galilean invariant models and different filter functions. The most striking result of their computation was a negative dissipation if the model was not Galilean invariant.

V. Scaling invariance

From (6), (7) and (12) one finds

$$t^* = \xi t, \quad x^* = \gamma x, \quad \bar{u}^* = \frac{\gamma}{\xi}\bar{u}, \quad u'^* = \frac{\gamma}{\xi}u',$$

$$\bar{p}^* = \left(\frac{\gamma}{\xi}\right)^2 \bar{p}, \quad p'^* = \left(\frac{\gamma}{\xi}\right)^2 p', \quad \nu^* = \frac{\gamma^2}{\xi}\nu. \tag{36}$$

Applying these results to (20) yields

$$\tau^* = \left(\frac{\gamma}{\xi}\right)^2 \tau. \tag{37}$$

Similarly one can deduce from (21)-(23) that

$$L^* = \left(\frac{\gamma}{\xi}\right)^2 L, \quad C^* = \left(\frac{\gamma}{\xi}\right)^2 C \text{ and } R^* = \left(\frac{\gamma}{\xi}\right)^2 R \tag{38}$$

has to be valid for any SGS model. It will be shown later that (37) is violated by the classical Smagorinsky model. In Appendix A it will be demonstrated by investigating the two-point correlation equations that this symmetry breaking produces incorrect statistical results, particularly in the near-wall region.

VI. Pressure invariance

The pressure invariance (8) should also be observed by the filtered quantities which leads to

$$t^* = t, \quad x^* = x, \quad \bar{u}^* = \bar{u}, \quad u'^* = u', \quad \bar{p}^* = \bar{p} + \varphi(t), \quad p'^* = p', \quad \nu^* = \nu, \tag{39}$$

Since SGS models are usually modeled in terms of velocities, the pressure invariance does not give any restrictions on the stresses L, C, R and τ.

VII. Material indifference

From (9) and (12) one can conclude that

$$t^* = t, \quad x_i^* = B_{ij}(t)x_j, \quad \bar{u}_i^* = B_{ij}(t)\bar{u}_j + \dot{B}_{ij}(t)x_j, \quad u_i'^* = B_{ij}(t)u_j',$$

$$\bar{p}^* = \bar{p} + 2\Omega_3 \int_Q (\bar{u}_1 dx_2 - \bar{u}_2 dx_1) - \tfrac{3}{2}\Omega_3^2(x_1^2 + x_2^2),$$

$$p'^* = p' + 2\Omega_3 \int_Q (u_1' dx_2 - u_2' dx_1), \quad \nu^* = \nu. \tag{40}$$

where $B(t)$ obeys the definitions given below (9). Using the above relations in (20), one finds that an SGS model captures material indifference if

$$\tau_{ik}^* = B_{im}B_{kn}\tau_{mn}. \tag{41}$$

As in (33)-(35), the separated stresses (16)-(18) are not form invariant. Using (40) in (21)-(23) it can be concluded that the separated stresses L_{ik} and C_{ik} are not form invariant under constant rotation rate and hence

$$L_{ik}^* = B_{im}B_{kn}L_{mn} - B_{im}\overline{u'_m}\dot{B}_{kn}x_n - \dot{B}_{im}x_m B_{kn}\overline{u'_n}, \tag{42}$$

$$C_{ik}^* = B_{im}B_{kn}C_{mn} + B_{im}\overline{u'_m}\dot{B}_{kn}x_n + \dot{B}_{im}x_m B_{kn}\overline{u'_n}, \tag{43}$$

$$R_{ik}^* = B_{im}B_{kn}R_{mn}. \tag{44}$$

However, the sum of L_{ik} and C_{ik} is invariant. Employing the modified definition of the stresses as introduced by Germano (1986) leads to form invariant stresses under constant rotation rate in the sense that the last two terms on the right-hand side of (42) and (43) disappear.

3.2 Implications for the filter kernel G

In order to incorporate the symmetries of the Navier-Stokes equations in the large-eddy model, one needs to show that the transformation properties of u and p are preserved for the filtered quantities $\bar{u}$ and $\bar{p}$. This restricts the form of the filter kernel as will be shown subsequently.

Time invariance (2) is always preserved no matter which filter kernel is chosen in (10) because t does not explicitly appear in G.

Generalized Galilean invariance (5) implies a restriction on the form of the filter kernel. Consider the Galilean invariance of the filtered velocities $\bar{u}^* = \bar{u} + d\hat{x}/dt$ given in (31). Employing the definition of the filter (10), one obtains

$$\int_{V^*} G(x^*, y^*)u^*(y^*)d^3y^* = \int_V G(x, y)u(y)d^3y + \frac{d\hat{x}}{dt}. \tag{45}$$

Since the instantaneous unfiltered velocities admit the generalized Galilean invariance, (5) can be substituted into the left-hand side. This yields

$$\int_V G(x + \hat{x}, y + \hat{x})\left[u(y) + \frac{d\hat{x}}{dt}\right]d^3y = \int_V G(x, y)u(y)d^3y + \frac{d\hat{x}}{dt}. \tag{46}$$

Because of (11), $d\hat{x}/dt$ cancels on both sides, and hence for arbitrary u the integrals are equal, provided

$$G(x + \hat{x}, y + \hat{x}) = G(x, y). \tag{47}$$

This functional equation can be transformed by differentiating with respect to $\hat{x}$. The resulting first order partial differential equation has the unique solution

$$G = G(x - y). \tag{48}$$

An additional restriction on G is given due to frame invariance with respect to a fixed rotation. From the rotation invariance of the filtered velocities $\bar{u}_i^* = A_{ij}\bar{u}_j$ given in (26) and the definition of the filter, one can deduce that

$$\int_{V^*} G(\boldsymbol{x}^* - \boldsymbol{y}^*)u_i^*(\boldsymbol{y}^*)d^3y^* = A_{ij}\int_V G(\boldsymbol{x} - \boldsymbol{y})u_j(\boldsymbol{y})d^3y. \tag{49}$$

Employing (3), which results in $d^3y^* = d^3y$, the two integrals are equal except for the filter kernel. Hence, in order for (26) to hold for arbitrary u_i, the condition

$$G(A(\boldsymbol{x} - \boldsymbol{y})) = G(\boldsymbol{x} - \boldsymbol{y}) \tag{50}$$

must be satisfied. For arbitrary A, the latter functional equation has the unique solution

$$G = G(|\boldsymbol{x} - \boldsymbol{y}|). \tag{51}$$

This corresponds to a known result from tensor invariant theory (see e.g. Spencer 1971): a scalar function depending on vectors or tensors can only depend on their scalar invariants. Tensor invariant theory is widely used in Reynolds averaged modeling; e.g. the scalar coefficient in the pressure-strain model depend only on scalar invariants. In (51) G depends only on the magnitude of the separation vector, which is the only invariant of a single vector. An additional consequence of (51) is that the averaging volume V in (10) is restricted to a sphere with center $\boldsymbol{x}$.

The last restriction on G follows from scaling invariance (36). For the present purpose the filter function G is not normalized, denoted by the superscript "u". Using (10) one can conclude from (36) that

$$\frac{\int_{V^*} G^{\mathrm{u}}(|\boldsymbol{x}^* - \boldsymbol{y}^*|)u^*(\boldsymbol{y}^*)d^3y^*}{\int_{V^*} G^{\mathrm{u}}(|\boldsymbol{x}^* - \boldsymbol{y}^*|)d^3y^*} = \frac{\gamma}{\xi}\frac{\int_V G^{\mathrm{u}}(|\boldsymbol{x} - \boldsymbol{y}|)u(\boldsymbol{y})d^3y}{\int_V G^{\mathrm{u}}(|\boldsymbol{x} - \boldsymbol{y}|)d^3y} \tag{52}$$

and a corresponding relation for the pressure, not shown here, needs to hold. Using (6) the spatial scaling factor γ remains in the argument of G^{u} on the left-hand side of (52). As a result, γ can only cancel out for arbitrary u if G^{u} has the following form

$$G^{\mathrm{u}}(|\boldsymbol{x} - \boldsymbol{y}|) = A|\boldsymbol{x} - \boldsymbol{y}|^\alpha \tag{53}$$

where A and α are arbitrary constants. Using (11), the final form of the filter G is obtained

$$\mathcal{L}[\cdot](\boldsymbol{x}) = \frac{\alpha + 3}{4\pi l^{\alpha+3}}\int_{\mathcal{R}_l} |\boldsymbol{x} - \boldsymbol{y}|^\alpha[\cdot](\boldsymbol{y})d^3y, \tag{54}$$

where $\mathcal{R}_l$ refers to a sphere with center $\boldsymbol{x}$ and radius l. (54) preserves all the symmetries in section 2. If the integration argument is sufficiently smooth, the integral converges for all $\alpha > -3$.

The time invariance, the reflection invariance, the pressure invariance, and the material indifference, even though not explicitly considered during the derivation, are consistent with (54).

The constraint for the filter function needs to hold for any filter operation used in LES. However, in practice it is only relevant for schemes that utilize an explicit filter, e.g. in the test filter used in Germano *et al.* (1991). In some LES models the actual form of the filter kernel does not appear explicitly in the computation, and the constraints for the filter derived above are irrelevant.

The restrictions on the filter kernel derived in this sub-section are rarely met by the filtering procedures used in practical applications. For computational convenience, explicit filtering at a given location is often performed by averaging values from adjacent grid points. As a result, in many applications, such as near-wall shear flows, the grid is highly anisotropic, and condition (26) is violated. To investigate this matter of grid dependence in LES, some empirical tests were performed by Scotti *et al.* (1997) to determine whether anisotropic meshes have an effect on isotropic turbulence. They show that on an anisotropic pencil-like grid, isotropic turbulence was severely influenced in an unphysical manner. However, by isotropization of the test-filter many of the features of isotropic turbulence could be restored. This result suggests that the isotropic filter kernel (51) may restore some of the physical properties of turbulence in large-eddy simulations.

4. Invariant properties of proposed large-eddy models

Almost all of the existing SGS models for large-eddy simulation of turbulence which have been proposed have the functional form:

$$\tau_{ik} = \mathcal{F}_{ik}[\bar{u}; x]. \tag{55}$$

In order to capture all of the invariance properties of the Navier-Stokes equations, (55) should reflect the same symmetries. Hence it is a necessary condition to have

$$\tau_{ik}^* = \mathcal{F}_{ik}[\bar{u}^*; x^*] \tag{56}$$

for all the transformations listed in Section 3.1. Nearly all SGS models proposed in the literature conform with time translation, rotation, and reflection invariance. However, as was first investigated by Speziale (1985), several SGS models (Biringen & Reynolds 1981, Moin & Kim 1982, Bardina, Ferziger & Reynolds 1983) are not Galilean invariant and, therefore, are also not invariant under the generalized Galilean transformation (5). In the present investigation it will be shown that several of the proposed SGS models are not scale invariant and not material indifferent. However, it will be demonstrated that a certain class of models, namely the dynamic models, obey all invariance properties derived in Section 3.

One of the most widely-used models in LES, the Smagorinsky model (Smagorinsky 1963), violates scale invariance but captures all other known symmetries. It is given by

$$\tau_{ik} - \frac{1}{3}\delta_{ik}\tau_{mm} = -C\Delta^2|\bar{S}|\bar{S}_{ik} \quad \text{where} \quad \bar{S}_{ik} = \frac{1}{2}\left(\frac{\partial\bar{u}_i}{\partial x_k} + \frac{\partial\bar{u}_k}{\partial x_i}\right). \tag{57}$$

Δ is the filter width which is usually taken to be a function of the local grid spacing. In order to see the shortcoming of (57), Eqs. (36), (37), and (57) are used in (56) to yield

$$\tau_{ik} - \frac{1}{3}\delta_{ik}\tau_{mm} = -C\Delta^2|\bar{S}|\bar{S}_{ik}\gamma^{-2}. \tag{58}$$

The latter expression is not form invariant since it is dependent on the arbitrary scaling parameter γ. The reason for this problem is the explicit external length scale that has been introduced into the model, which is not related to any turbulent length scale. This imposed length scale is particularly damaging in turbulent wall-bounded flows. To overcome this problem empirical wall-damping functions have been adopted to obtain reasonable results in the near-wall region. Wall-damping functions are widely used in conjunction with Reynolds averaged models. There, it has long been known that this approach is not frame invariant, and several new ideas have been put forward to overcome this problem.

Several new near-wall self-similar solutions or scaling laws have been derived in Oberlack (1997a,b) which rely heavily on the scaling symmetry. All near-wall scaling laws may be captured in a large-eddy simulation of turbulence when the symmetry properties of the Navier-Stokes equations are preserved by the model. In Appendix A it is shown by analyzing the two-point correlation equation that the Smagorinsky model is not able to capture important near-wall scaling laws. It can be concluded that any model which contains a fixed external length scale, and which does not account for the proper turbulent length scale, will violate the scaling symmetry. Since the Smagorinsky model is only written in terms of the strain rate $\bar{S}$, material indifference is guaranteed.

A model which violates both scale invariance and material indifference is the structure-function model by Métais & Lesieur (1992). The latter problem has already been reported by Meneveau (1996). The proposed SGS model is of the form

$$\tau_{ik} - \frac{1}{3}\delta_{ik}\tau_{mm} = C^{SF}\Delta\langle(\bar{u}(x+r) - \bar{u}(x))^2\rangle^{1/2}\bar{S}_{ik} \tag{59}$$

where C^{SF}, and $\langle\rangle$ are, respectively, a model constant and a spatial average. Using the condition (56) in conjunction with the transformation (40) and (41) yields

$$\tau_{ik} - \frac{1}{3}\delta_{ik}\tau_{mm} = C^{SF}\Delta\langle(\bar{u}_{(m)}(x+r) - \bar{u}_{(m)}(x) - \varepsilon_{3l(m)}\Omega_3 r_l)^2\rangle^{\frac{1}{2}}\bar{S}_{ik}. \tag{60}$$

The latter expression is not of the form (59) since it contains an additional rotation term. Hence, the structure-function model is not materially indifferent. As for the Smagorinsky model, one can also show that (59) is not scale invariant.

A class of SGS models which have a similar deficiency are those explicitly containing the rotation rate

$$\bar{R}_{ij} = \frac{1}{2}\left(\frac{\partial \bar{u}_i}{\partial x_j} - \frac{\partial \bar{u}_j}{\partial x_i}\right). \tag{61}$$

Lund & Novikov (1992) derived the most general form of SGS model comprising all possible combinations of the strain and the rotation rate tensors. They proposed a model of the form

$$\tau_{ik} - \frac{1}{3}\delta_{ik}\tau_{mm} = \Delta^2 \left[C_1|\bar{S}|\bar{S}_{ik} + C_2 \left(\bar{S}_{im}\bar{S}_{mk} - \frac{\delta_{ik}}{3}\bar{S}_{mn}\bar{S}_{mn} \right) \right.$$
$$+ C_3 \left(\bar{R}_{im}\bar{R}_{mk} - \frac{\delta_{ik}}{3}\bar{R}_{mn}\bar{R}_{mn} \right) + C_4 \left(\bar{S}_{im}\bar{R}_{mk} - \bar{R}_{im}\bar{S}_{mk} \right)$$
$$\left. + \frac{C_5}{|\bar{S}|} \left(\bar{S}_{im}\bar{S}_{mn}\bar{R}_{nk} - \bar{R}_{im}\bar{S}_{mn}\bar{S}_{nk} \right) \right]. \tag{62}$$

For the same reason as the previous two models, (62) is also not scaling invariant. Violation of material indifference can be shown by computing the rotation rate (61) under the transformation (40) which yields

$$\bar{R}_{ij}^* = B_{ik}B_{jl}R_{kl} + \varepsilon_{kij}\Omega_k \tag{63}$$

Using this in (62), the required form of (41) under constant rotation cannot be recovered since the frame rotation term, i.e. the last term of (63), does not cancel out.

An SGS model which captures *all* the invariance requirements derived in Section 3 is the dynamic subgrid-scale model of Germano *et al.* (1991). They proposed a procedure which, used in conjunction with the classical Smagorinsky model, results in the following SGS model

$$\tau_{ik} - \frac{1}{3}\delta_{ik}\tau_{mm} = \frac{(\widetilde{\bar{u}_m\bar{u}_n} - \tilde{\bar{u}}_m\tilde{\bar{u}}_n)\bar{S}_{mn}}{\left(\frac{\tilde{\Delta}}{\Delta}\right)^2 |\tilde{\bar{S}}|\tilde{\bar{S}}_{mn}\bar{S}_{mn} - |\widetilde{\bar{S}|\bar{S}_{pq}}\bar{S}_{pq}}|\bar{S}|\bar{S}_{ik}. \tag{64}$$

Here, all the tilded quantities refer to the "test"-filter

$$\tilde{h}(\boldsymbol{x}) = \int_V \tilde{G}(\boldsymbol{x},\boldsymbol{y})h(\boldsymbol{y})d^3y, \tag{65}$$

which corresponds to the filter length $\tilde{\Delta}$ and $\tilde{\Delta} > \Delta$. The test-filter quantities are explicitly computed from the flow field. The resolved quantities are still denoted by an overbar. The dynamic model contains the ratio of two length scales, which is a dimensionless number, and therefore no external length scale is imposed to break symmetries. Consequently, the scaling invariance (37) is recovered, as can be shown by using (36), provided the proper filter function is utilized. It is straightforward to prove that frame invariance, generalized Galilean invariance, and material indifference are also captured by the dynamic model.

Since its publication by Germano *et al.* (1991), several modified versions of the dynamic model have been proposed. The model by Lilly (1992) keeps the Smagorinsky model as the base model, but the dynamic procedure is modified. Zang *et*

al. (1993) used the mixed model, first introduced by Bardina *et al.* (1983), as a new base model. In addition, they employed Lilly's modification of the dynamic procedure. Yoshizawa *et al.* (1996) developed a new base model and also adopted Lilly's modification of the dynamic procedure. The dynamic mixed model by Zang *et al.* is further extended by Salvetti & Banerjee (1995). This new model contains two parameters which are both computed with a modified dynamic procedure. It can easily be shown that all the latter modified versions of the dynamic model capture the symmetry requirements developed in Section 3. It should be noted that the dynamic procedure only restores scaling invariance, which may be violated by certain base models. Other deficiencies such as the violation of Galilean invariance or material indifference cannot be repaired by the dynamic procedure.

So far, it was tacitly assumed that the symmetries are not broken by the filtering process. However, some of the common filter functions are not consistent with the symmetries of the Navier-Stokes equations. One of these is the Gaussian filter

$$G = \frac{1}{\pi^{3/2}\Delta^3} \exp\left[-\frac{|\boldsymbol{x} - \boldsymbol{y}|^2}{\Delta^2}\right], \tag{66}$$

since it does not match the form (54). The scaling symmetry is violated by (66).

Another common filter function which is not consistent with the form of (54) is the spectral cut-off filter. In physical space it is given by

$$G = \prod_{i=1}^{3} \frac{\sin\left[\dfrac{\pi}{\Delta}(x_i - y_i)\right]}{\pi(x_i - y_i)}. \tag{67}$$

(67) violates both rotation and scaling invariance. It has already been pointed out by Vreman *et al.* (1994) that the latter filter should not be utilized as it may lead to unrealizable results. In Liu *et al.* (1994) it was shown by analyzing experimental results of a turbulent jet that (67) has a very prejudicial influence on the overall statistical behavior of SGS models.

The classical isotropic top-hat filter

$$G = \begin{cases} \dfrac{3}{4\pi\Delta^3} & \text{if } |\boldsymbol{x} - \boldsymbol{y}| < \Delta \\ 0 & \text{otherwise} \end{cases} \tag{68}$$

is of the form (54) with $\alpha = 0$. Hence, it preserves all symmetry requirements of Navier-Stokes equations.

5. Summary and conclusions

The Navier-Stokes equations admit certain symmetries, that is, there are certain form-invariant transformations which preserve the equations. These symmetries are one of the most fundamental properties of the equations of motion. They reflect many features of classical mechanics. It was shown recently that certain statistical properties of turbulent shear flows follow from these symmetries (Oberlack 1997a/b).

To capture those statistical features of the Navier-Stokes equations that are associated with symmetries, the symmetries should be built into the SGS models and the filter functions in LES of turbulence. This leads to necessary conditions on the functional form of the SGS model and the filter kernel.

One particular symmetry, scale invariance, is violated by the most common SGS model, the Smagorinsky model, because it contains the grid size as an explicit length scale. This seriously impairs the ability of the model to describe turbulence. In particular, in near-wall turbulent flows it is known that the Smagorinsky model performs poorly and wall damping functions have to be used. In Appendix A it is shown that the violation of the scaling symmetry excludes important turbulent near-wall scaling laws such as the log law and the algebraic law. Other models such as the structure function model by Métais & Lesieur (1992) violate material indifference.

It appears that the dynamic Smagorinsky model by Germano *et al.* (1991) and its successors (e.g. Lilly 1992, Zang *et al.* 1993, Yoshizawa *et al.* 1996, Salvetti & Banerjee 1995) conserve the symmetries of Navier-Stokes equations. In fact, numerical simulations have shown (see Germano *et al.* 1991) that the dynamic model captures the proper near-wall behavior without introducing any artificial wall treatment such as damping functions.

The symmetry restrictions for the filter function are severe in the sense that only a very confined class of filters is allowed. For example, only a spherical filter function admits finite rotation invariance. The consequences of anisotropic filter functions may be illustrated by a simple example. Consider a simulation of homogeneous turbulent shear flow where explicit filtering is employed. The integration domain of the filter function may have the form of a box whose edges are aligned with the grid, which is chosen to be parallel to the mean flow. In homogeneous shear the dominant turbulent structures have a certain inclination to the mean flow. If the grid and the filter were instead chosen to be parallel to this inclination, averaging would take place over different flow structures. As a consequence, large scale quantities such as the Reynolds stress tensor would exhibit different growth rates. Since a model should be frame independent, the latter result is in contradiction to the basic physics of the problem.

However, the practical implications may be less severe than they appear. Since explicit filtering takes place on very few mesh points, the numerical truncation error may be of the same order of magnitude as the error caused by a non-spherical filter. Numerical tests for different applications need to be performed to determine how closely the filter form given by (54) has to be matched. A first test towards this requirement has been carried out by Scotti *et al.* (1997). An isotropized test-filtering in conjunction with the dynamic model on a highly anisotropic pencil-like mesh considerably improved the LES of isotropic turbulence.

An approach to overcome the very restricted form of the filter function may be to introduce the strain rate into the filter function. Since the strain rate introduces three additional directions corresponding to its principle axes, a more complex geometry for the filter volume may be in order.

Another consequence of the required spherical form of the filter appears to be its use in combination with wall-bounded flows. Close to solid walls the requirement that the filter be spherical filter is always violated, and hence certain symmetries are broken. However, the symmetries listed in Section 2 are only properties of the Navier-Stokes equations. Symmetries are always broken by arbitrary boundary conditions. One can conclude that a non-spherical filter near a solid wall is not a restriction of LES, but a consequence of boundary conditions for turbulence models in general.

It appears that future improvements for LES models should be along the lines of the dynamic model since it mimics fundamental properties of the Navier-Stokes equations. Despite its known superior performance, it has problems with stability since the model coefficient in the SGS model may become negative. If the flow under investigation possesses a homogeneous direction, averaging of the model coefficient in that direction seems to stabilize the simulation. In more complex geometries a clipping procedure is introduced which sets a negative model coefficient to zero. However, the first approach may violate rotation invariance since a preferred direction has been introduced. The clipping approach seems to obey all the symmetry properties of the Navier-Stokes equations but appears to be unrelated to Navier-Stokes equations.

Acknowledgments

Appendix A. Two-point correlation equation of LES models containing an explicit external length scale

To investigate why SGS models containing an explicit length scale are inconsistent with certain near-wall scaling laws, two-point correlation equations derived from LES models are analyzed. The standard Reynolds decomposition is given by

$$\bar{u} = \langle u \rangle + u', \quad \bar{p} = \langle p \rangle + p', \tag{A1}$$

where the instantaneous velocity $\bar{u}$ and the pressure $\bar{p}$ is assumed to be computed by a LES in conjunction with a certain SGS model and $\langle \cdot \rangle$ denotes an ensemble average. Using this, several two-point quantities may be defined

$$R_{ij}(\boldsymbol{x}, \boldsymbol{r}) = \langle u_i'(\boldsymbol{x}) u_j'(\boldsymbol{x}^{(1)}) \rangle, \tag{A2}$$

$$R_{(ik)j}(\boldsymbol{x}, \boldsymbol{r}) = \langle u_i'(\boldsymbol{x}) u_k'(\boldsymbol{x}) u_j'(\boldsymbol{x}^{(1)}) \rangle, R_{i(jk)}(\boldsymbol{x}, \boldsymbol{r}) = \langle u_i'(\boldsymbol{x}) u_j'(\boldsymbol{x}^{(1)}) u_k'(\boldsymbol{x}^{(1)}) \rangle \tag{A3}$$

$$P_j(\boldsymbol{x}, \boldsymbol{r}) = \langle p'(\boldsymbol{x}) u_j'(\boldsymbol{x}^{(1)}) \rangle, \quad Q_j(\boldsymbol{x}, \boldsymbol{r}) = \langle u_j'(\boldsymbol{x}) p'(\boldsymbol{x}^{(1)}) \rangle \tag{A4}$$

$$S_{(ik)j}(\boldsymbol{x}, \boldsymbol{r}) = \langle \tau_{ik}(\boldsymbol{x}) u_j'(\boldsymbol{x}^{(1)}) \rangle, \quad T_{i(jk)}(\boldsymbol{x}, \boldsymbol{r}) = \langle u_i'(\boldsymbol{x}) \tau_{jk}(\boldsymbol{x}^{(1)}) \rangle. \tag{A5}$$

Using the latter definitions the two-point correlation equations are derived from (14)

$$\frac{\mathrm{D}R_{ij}}{\mathrm{D}t} = -R_{kj}\frac{\partial\langle u\rangle_i}{\partial x_k} - R_{ik}\left.\frac{\partial\langle u\rangle_j}{\partial x_k}\right|_{x+r} - [\langle u\rangle_k\,(x+r,t) - \langle u\rangle_k\,(x,t)]\,\frac{\partial R_{ij}}{\partial r_k}$$

$$- \left[\frac{\partial P_j}{\partial x_i} - \frac{\partial P_j}{\partial r_i} + \frac{\partial Q_i}{\partial r_j}\right] - \frac{\partial R_{(ik)j}}{\partial x_k} + \frac{\partial}{\partial r_k}\left[R_{(ik)j} - R_{i(jk)}\right]$$

$$- \frac{\partial S_{(ik)j}}{\partial x_k} + \frac{\partial}{\partial r_k}\left[S_{(ik)j} - T_{i(jk)}\right], \tag{A6}$$

where $\mathrm{D}/\mathrm{D}t = \partial/\partial t + \langle u\rangle_k\partial/\partial x_k$. The tensors in (A2)-(A5) are functions of the physical and correlation space coordinates, x and $r = x^{(1)} - x$ respectively. The vertical line denotes the derivative to be taken with respect to x and evaluated at $x + r$.

In Oberlack (1997a) the 22-component of the two-point correlation equations emerging from the Navier-Stokes equations (A6 with $S_{(ik)j} = T_{i(jk)} = 0$) for parallel mean flows of the form $\langle u\rangle = (\langle u\rangle_1(x_2), 0, 0)^T$ was investigated. The entire system contains one physical and three correlation coordinates and consists of equation (A6) and two Poisson equations for P_j and Q_i (not shown here). It was shown that for four distinct mean velocity profiles similarity variables can be introduced so that the number of independent variables is reduced by one.

The most general self-similar solution, with all group parameters different from zero, is given by

$$\bar{u}_1 = C_1\left(x_2 + \frac{q_4}{q_1}\right)^{1-\frac{q_5}{q_1}} - \frac{q_7}{q_1 - q_5}, \tag{A7}$$

$$\tilde{r}_1 = \frac{r_1 + \frac{q_2}{q_1}}{x_2 + \frac{q_4}{q_1}}, \quad \tilde{r}_2 = \frac{r_2}{x_2 + \frac{q_4}{q_1}}, \quad \tilde{r}_3 = \frac{r_3 + \frac{q_3}{q_1}}{x_2 + \frac{q_4}{q_1}}, \tag{A8}$$

$$R_{22} = \left(x_2 + \frac{q_4}{q_1}\right)^{2\left(1-\frac{q_5}{q_1}\right)}\tilde{R}_{22}, \tag{A9}$$

$$P_2 = \left(x_2 + \frac{q_4}{q_1}\right)^{3\left(1-\frac{q_5}{q_1}\right)}\tilde{P}_2, \quad Q_2 = \left(x_2 + \frac{q_4}{q_1}\right)^{3\left(1-\frac{q_5}{q_1}\right)}\tilde{Q}_2, \tag{A10}$$

$$R_{(2k)2} = \left(x_2 + \frac{q_4}{q_1}\right)^{3\left(1-\frac{q_5}{q_1}\right)}\tilde{R}_{(2k)2}, \quad R_{2(2k)} = \left(x_2 + \frac{q_4}{q_1}\right)^{3\left(1-\frac{q_5}{q_1}\right)}\tilde{R}_{2(2k)}, \tag{A11}$$

where the "~" correlation quantities only depend on (A8). From (A7)-(A11) one can conclude that scaling of the fluctuation velocity is according to

$$u' = \left(x_2 + \frac{q_4}{q_1}\right)^{1-\frac{q_5}{q_1}}\hat{u}'. \tag{A12}$$

The second similarity solution is given by $q_1 = q_5$, which corresponds to the log-law and (A7) changes to

$$\bar{u}_1 = \frac{q_7}{q_1} \ln\left(x_2 + \frac{q_4}{q_1}\right) + C_2, \qquad (A13)$$

while the similarity coordinates (A8) are unaltered and the correlation functions R_{22}, P_2, Q_2, $R_{(2k)2}$, and $R_{2(2k)}$ are un-scaled.

If $q_1 = 0$ and $q_5 \neq 0$, the exponential law holds and the new similarity variables are given by

$$\bar{u}_1 = C_3 \exp\left(-\frac{q_5}{q_4}x_2\right) + \frac{q_7}{q_5}, \qquad (A14)$$

$$\tilde{r}_1 = r_1 + \frac{q_2}{q_4}x_2, \quad \tilde{r}_2 = r_2, \quad \tilde{r}_3 = r_3 + \frac{q_3}{q_4}x_2, \qquad (A15)$$

$$R_{22} = e^{-2\frac{q_5}{q_4}x_2}\tilde{R}_{22}, \qquad (A16)$$

$$P_2 = e^{-3\frac{q_5}{q_4}x_2}\tilde{P}_2, \quad Q_2 = e^{-3\frac{q_5}{q_4}x_2}\tilde{Q}_2, \qquad (A17)$$

$$R_{(2k)2} = e^{-3\frac{q_5}{q_4}x_2}\tilde{R}_{(2k)2}, \quad R_{2(2k)} = e^{-3\frac{q_5}{q_4}x_2}\tilde{R}_{2(2k)}. \qquad (A18)$$

where similar to (A7)-(A11) the "~" correlation quantities only depend on (A15). It can be concluded that the fluctuation velocities scale as

$$\boldsymbol{u}' = e^{-\frac{q_5}{q_4}x_2}\hat{\boldsymbol{u}}'. \qquad (A19)$$

Finally, if $q_1 = q_5 = 0$, the mean velocity is given by

$$\bar{u}_1 = q_7 x_2 + C_4 \qquad (A20)$$

while the similarity variables (A15) are the same as for the exponential case, but the correlations R_{22}, P_2, Q_2, $R_{(2k)2}$, and $R_{2(2k)}$ stay un-scaled.

In order to see that some common SGS models are not consistent with the latter scaling laws if they contain an explicit external length scale, the Smagorinsky model will be investigated. Suppose (57) is substituted for τ in (A2)-(A5), then $S_{(ik)j}$ and $T_{i(jk)}$ will read as follows

$$S_{(ik)j}(\boldsymbol{x}, \boldsymbol{r}) = -C\Delta^2\langle|\bar{S}|(\boldsymbol{x})\bar{S}_{ik}(\boldsymbol{x})u_j'(\boldsymbol{x}^{(1)})\rangle, \qquad (A21)$$

$$T_{i(jk)}(\boldsymbol{x}, \boldsymbol{r}) = -C\Delta^2\langle u_i'(\boldsymbol{x})|\bar{S}|(\boldsymbol{x}^{(1)})\bar{S}_{jk}(\boldsymbol{x}^{(1)})\rangle. \qquad (A22)$$

Here $\bar{S}$ is computed from (57) while for $\bar{u}$ the Reynolds decomposition (A1) is used.

Using (21)-(22) in Eqs. (A6) leads to a reduced set of possible self-similar solutions. From the above-mentioned four scaling laws, only two allow for self-similarity so that the number of independent variables reduces by one. These two scaling laws are the exponential law (A14)-(A18) and the linear law (A20). Both have been derived under the assumption that there is an external symmetry breaking length

scale in the flow and no scaling with respect to the coordinates exists. It is straight-forward to show that the algebraic law (A7) and the logarithmic law (A13) are no longer self-similar solutions of the system (A6) if (21)-(22) is employed.

REFERENCES

BARDINA, J., FERZIGER, J. H. & REYNOLDS, W. C. 1983 Improved turbulence models based on large eddy simulation of homogeneous, incompressible, turbulent flows, Stanford University Tech. Rep. TF-19.

BATCHELOR, G. K. 1967 *An introduction to fluid dynamics*, Cambridge U.P.

BIRINGEN, S. & REYNOLDS, W. C. 1981 Large-eddy simulation of the shear-free turbulent boundary layer. *J. Fluid Mech.* **103**, 53–63.

CANTWELL, B. J. 1978 Similarity transformations for the two-dimensional, un-steady, stream-function equation. *J. Fluid Mech.* **85**, 257–271.

CANTWELL, B. J. 1981 Organized motion in turbulent flow. *Ann. Rev. Fluid Mech.* **13**, 457–515.

GERMANO, M. 1986 A proposal for a redefinition of the turbulent stresses in the filtered Navier-Stokes equations. *Phys. Fluids.* **29**, 2323–2324.

GERMANO, M., PIOMELLI, U., MOIN, P. & CABOT, W. H. 1991 A dynamic subgrid-scale eddy viscosity model. *Phys. Fluids A.* **3**, 1760–1765.

HÄRTEL, C. & KLEISER, L. 1997 Galilean invariance and filtering dependence of near-wall grid-scale/subgrid-scale interactions in large-eddy simulation. *Phys. Fluids.* **9**, 473–475.

IBRAGIMOV, N. H. 1994,1995 (editor) CRC Handbook of Lie Group Analysis of Differential Equations, Vols. 1-3. CRC Press.

LILLY, D. K. 1992 A proposed modification of the Germano subgrid-scale closure method. *Phys. Fluids.* **4**, 633–635.

LIU, S., MENEVEAU, C. & KATZ, J. 1994 On the properties of similarity subgrid-scale models as deduced from measurements in a turbulent jet. *J. Fluid Mech.* **275**, 83–119.

LUDLOW, D. K. & CLARKSON, P. A. 1997 Nonclassical symmetry reductions of the incompressible Navier-Stokes equations. University of Kent at Canterbury, Technical Report No. UKC/IMS/97/21.

LUND, T. S. & NOVIKOV, E. A. 1992 Parameterization of subgrid-scale stress by the velocity gradient tensor. Annual Research Briefs, Center for Turbulence Research, NASA Ames/Stanford Univ. 27–43.

MENEVEAU, C. 1996 Private communication.

MÉTAIS, O. & LESIEUR, M. 1992 Spectral large-eddy simulation of isotropic and stably stratified turbulence. *J. Fluid Mech.* **239**, 157–194.

MOIN, P. & KIM, J. 1982 Numerical investigation of turbulent channel flow. *J. Fluid Mech.* **118**, 341–377.

OBERLACK, M. 1997a Unified theory for symmetries in plane parallel turbulent shear flows. *Under review in J. Fluid Mech.*

OBERLACK, M. 1997b Similarity in non-rotating and rotating turbulent pipe flows. *Under review in J. Fluid Mech.*

OBERLACK, M. 1997c On the non-existence of material indifference in 3D-Navier-Stokes equations. *unpublished.*

PUKHNACHEV, V. V. 1972 Invariant solutions of Navier-Stokes equations describing motions with free boundary. *Dokl. Akad. Nauk.* **202**, 302.

SALVETTI, M. V. & BANERJEE, S. 1995 A priori tests of a new dynamic subgrid-scale model for finite-difference large-eddy simulations. *Phys. Fluids.* **7**, 2831–2847.

SCHUMANN, U. 1977 Realizability of Reynolds–Stress Turbulence Models. *Phys. Fluids.* **20**, 721–725.

SCOTTI, A., MENEVEAU, C. & FATICA, M. 1997 Dynamic Smagorinsky model in anisotropic grids. *Phys. Fluids.* **9**, 1856–1858.

SMAGORINSKY, J. 1963 General circulation experiments with the primitive equations. *Mon. Weath. Rev.* **91**, 99–165.

SPENCER, A. J. M 1971 Theory of Invariants. In: Continuum Physics, (ed. A. C. Eringen)1 239–353.

SPEZIALE, C. G. 1985 Galilean invariance of subgrid-scale stress models in the large-eddy simulation of turbulence. *J. Fluid Mech.* **156**, 55–62.

TOWNSEND, A. A. 1976 Structure of Turbulent Shear Flow. *Cambridge University Press.*

ÜNAL, G. 1994 Application of equivalence transformations to inertial subrange of turbulence. *Lie groups and their applications.* **1**, (1), 232–240.

VREMAN, B., GEURTS, B. & KUERTEN, H. 1994 Realizability conditions for the turbulent stress tensor in large-eddy simulation. *J. Fluid Mech.* **278**, 351–362.

YOSHIZAWA, A., TSUBOKURA, M., KOBAYASHI, T. & TANIGUCHI N. 1996 Modeling of the dynamic subgrid-scale viscosity in large eddy simulation. *Phys. Fluids.* **8**, 2254–2256.

ZANG, Y., STREET, R. L. & KOSEFF J. R. 1993 A dynamic mixed subgrid-scale model and its application to turbulent recirculating flows. *Phys. Fluids.* **8**, 3186–3196.

Validation of large-eddy simulation in a plain asymmetric diffuser

By M. Fatica, H.-J. Kaltenbach[1] AND R. Mittal[2]

Motivation

The main motivation for this study comes from the need to validate wall-resolving LES with the dynamic model in the case of a spatially evolving flow with mild separation.

With the increase in computing power, more complex flow configurations are being investigated by means of three-dimensional, unsteady numerical simulation. The concept of large-eddy simulation (LES), in which resolved and subgrid-scale motions are defined by a spatial filter applied to the Navier Stokes equations, has emerged as a promising tool which complements Reynolds averaged Navier Stokes (RANS) computations. The development of the dynamic SGS-model by Germano *et al.*(1991) was a major advance towards a general model which is applicable to an arbitrary flow and does not need adjustment of model parameters.

An important class of flows which has not been simulated extensively with the LES technique is the pressure driven separation from a smooth surface. Mildly separated flows have always been a challenge for experimentalists as well as modelers.

Experimental research on separated flow physics was hindered by the fact that conventional hot-wire technique is direction insensitive and requires a significant mean flow component to produce reliable measurements. With the increasing use of the LDA technique more data sets of separated flows are becoming available which are suitable for validation purposes. A particularly interesting configuration was investigated recently by Obi *et al.* (1993a, 1993b), using a single-component LDA: a fully developed turbulent flow from a long inlet duct enters a plane, asymmetric diffuser with an opening angle of 10°. The flow separates about half way down the deflected wall, and a separation bubble forms which extends into the straight outlet duct where the flow reattaches.

This flow has several desirable features which make it a good test case for validation of a computational technique such as large-eddy simulation:

a) The flow belongs to the class of 'mild', pressure-driven, separation from a smooth wall. Many technical devices are designed to operate close to these conditions since optimum performance is often achieved when the flow is at the verge of separation.

b) The flow exhibits rich flow physics, such as the combined effect of adverse pressure gradient and curvature near the diffuser inlet and incipient separation and reattachment in the outlet duct.

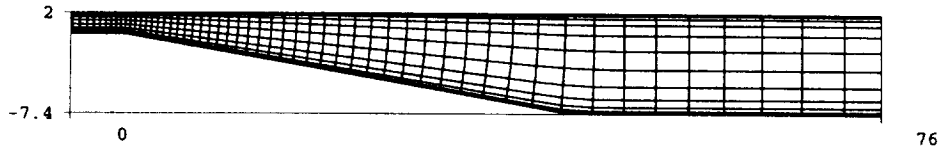1 Technische Universitaet Berlin
2 University of Florida

FIGURE 1.   Computational domain for the plane diffuser. Only a subset of the actual grid lines is plotted.

c) The inflow conditions are unambiguously defined. The inlet duct has a length of more than 100 duct heights, thereby guaranteeing that the flow entering the expansion is a fully developed turbulent channel flow. For validating the computation of a spatially evolving flow, it is crucial to know the upstream conditions with a high degree of accuracy.

d) The wall-shear based Reynolds number of the incoming channel flow is $Re_\tau = 500$. Although a direct simulation of channel flow is feasible at this value, a DNS of the full diffuser is still prohibitively expensive. The Reynolds number is high enough that the flow does not depend much on this parameter. Obi (1994) did not find significant changes of flow physics when doubling the Reynolds number.

During the course of the work, a closer examination of the experimental dataset from Obi et al. (1993a) revealed some inconsistencies. Basic requirements such as mass and momentum balance of the 2D mean flow were not met in the rear part of the expansion (Kaltenbach, 1994). As a result of this, it was felt that an independent confirmation of the experimental data was highly desirable. Therefore, a configuration similar to Obi's rig was built, and great care taken to ensure that the data set satisfied basic requirements for validation purposes (Buice & Eaton, 1996, 1997). For simplicity we refer from now on to the Obi and the Buice experiment, respectively.

Flow configuration

The diffuser geometry as shown in Fig. 1 and Reynolds number $Re_b = U_b\delta/\nu = 9000$ match the experimental configuration of Obi and Buice. Here, the Reynolds number is based on the bulk velocity U_b found in the inlet duct of height $h = 2\delta$. The parallel flow from the inlet duct enters the asymmetric diffuser characterized by an expansion ratio $a = h_{out}/h_{in} = 4.7$ and by an opening angle of 10 degrees. The expanding section extends over 42δ and is followed by a tail-duct of height 9.4δ. With the tail-duct extending over approximately 30δ, the exit plane is located near $x/\delta = 75$. At this location the flow has reattached but is far from being in equilibrium. In the present study we focus on the separation and reattachment and not on the recovery into a canonical channel flow, which occurs over a length of tens of heights of the exit channel.

Simulations were performed on three different meshes and for domain widths of 4δ and 8δ in the spanwise direction. The mesh is stretched in the streamwise and wall-normal direction. Details on the numerical method are given in Fatica & Mittal

(1996).

Computationally, this flow is very challenging because of the large range of timescales encountered. The inertial time scale $\tau = 0.5h(x)/U_b(x)$, based on local diffuser height $h(x)$ and bulk velocity $U_b(x)$, is proportional to the square of the expansion ratio, *i.e.* $\tau_{out} = a^2\tau_{in}$. At the same time, the computational time step is limited by the need to resolve the turbulence in the inlet section. The net effect of the time-scale disparity is that the simulations require very lengthy integration times.

In this brief, we will compare results from two simulations on a domain with a spanwise dimension of 8δ. On the medium mesh ($272 \times 64 \times 96$) the inflow profile has a ratio of centerline to bulk velocity $U_c/U_b = 1.12$, while on the fine mesh ($352 \times 64 \times 128$) the ratio is equal to 1.14, the same value as reported in the experiment of Buice. Before sampling statistics, the simulation is run for an initial period corresponding to approximately one flow-through time in order to flush out the initial transients. Statistics were then sampled over a period of 1080 τ_{in} or 7 flow-through times for the simulation on the medium mesh. The fine simulation is not finished yet and only 3 flow-through times were used. Mean quantities are obtained as averages over both the spanwise direction and time.

Validation of simulation results

The present work aims at exploring the capability of LES for accurate quantitative prediction. For this purpose we compare simulation results with measurements from Obi *et al.* (1993a, 1993b) and Buice & Eaton (1997).

Evaluation of experimental data sets

Meaningful comparison between simulation and experiment hinges on the assumption that the same flow is being studied. Ideally, this requires a match in geometry, inflow and outflow conditions, and Reynolds number. The present state of high-resolution numerical simulations makes it desirable that the computed flows be homogeneous in at least one spatial direction. In a spatially evolving flow such as the diffuser flow, the spanwise direction is considered to be homogeneous. It is hoped that flow physics will become independent of the chosen spanwise domain size once the computational box is wide enough. In this direction periodic boundary conditions can be applied, which is advantageous from a numerical point of view since highly accurate Fourier expansion based methods can be employed. Furthermore, averaging statistics in the homogeneous direction reduces the required sampling time considerably, and this results in significant savings in terms of CPU time.

To set up an experiment of a flow which exhibits spanwise homogeneity remains a challenge. Once the flow separates, the inherent three-dimensionality resulting from side walls of an experimental facility often increases significantly. By choosing configurations with wide aspect ratios, it is hoped that effects from unavoidable secondary flows will be small and will not affect the core region, which should represent a nominally two-dimensional flow.

Assessment of suitability of Obi's data for validation

Obi *et al.* (1993a,b) investigated flow in an asymmetric diffuser using LDA in a wind tunnel. They measured pressure along the flat wall, mean velocity, and Reynolds stresses. The aspect ratio of diffuser inlet and outlet was 1:35 and 1:7.45, respectively. The inlet channel was slightly wider than the diffuser in order to prevent thick sidewall boundary layers from entering the expansion. Buice employed the same technique. In order for the fluid to enter the side slots, the pressure in the slots has to be slightly lower than the ambient pressure. Buice achieved this by obstructing the diffuser exit, thereby raising the average pressure level in the diffuser. Nothing similar is reported for the Obi experiment. Therefore, some doubt remains about the conditions at the diffuser inlet of Obi's setup.

Measurement errors for $\overline{U}$ and Reynolds stresses are estimated to be 0.7% and 2.6% respectively (Maeda *et al.* 1995). Mean flow profiles are two-dimensional within 5% of $\overline{U}$ over 90% of the inlet duct and 60% of the outlet. The mean flow profile measured 22δ upstream of the diffuser throat in the inlet channel is slightly asymmetric. However, the ratio of centerline to bulk velocity at this location is 1.14, which matches closely the prediction by Dean (1978).

The flow-rate per unit width $m = \int \overline{U}(y) \, dy$ computed from profiles measured along the center-plane is plotted in Fig. 2. Up to the end of the expansion near $x/\delta = 40$ the flow-rate is constant within a 2% error band. As the flow leaves the expansion and enters the outlet section the flow-rate increases rapidly. This might indicate that significant secondary flow develops in the outlet section. Obi's data have been made available on ftp-server (Maeda 1995); there, velocity data were scaled in a way such that global mass conservation is guaranteed at every station. We will use the scaled data for comparison with simulation results, keeping in mind that profiles measured downstream of $x/\delta = 40$ should be only used for qualitative comparison.

A special remark is required with respect to proper normalization of pressure measurements which are published in Obi(1993b). There, c_p is given with respect to a reference velocity U_{ref}. Since we choose to present all our data with respect to the bulk velocity of the incoming channel flow, we need to know the ratio U_{ref}/U_{bulk}. Obi *et al.*(1993b) state that the reference velocity corresponds to the centerline velocity of the inlet duct. However, the mean flow profile measured in the inlet duct at $x/\delta = -22$ reaches a peak of $0.975U_{ref}$ (see database of Maeda *et al.* 1995). Thus $U_{ref} = 1.025U_{cent}$, and with $U_{cent}/U_{bulk} = 1.14$, the conversion of c_p given with respect to U_{ref} into c_p with respect to U_{bulk} involves multiplication with the square of $U_{ref}/U_{bulk} = 1.168$. The use of an incorrect reference velocity in Obi (1993b) has been corroborated recently.

Assessment of suitability of Buice's data for validation

The overall dimensions of the experimental facility of Buice (1997) are similar to Obi's setup. The novel feature of this experiment is the fact that the pressure level in the facility was raised through exit blockage, thereby allowing careful control of sidewall boundary layer leakage through slots immediately ahead of the throat. Velocity was measured in air with a hot-wire technique, using single and cross wire
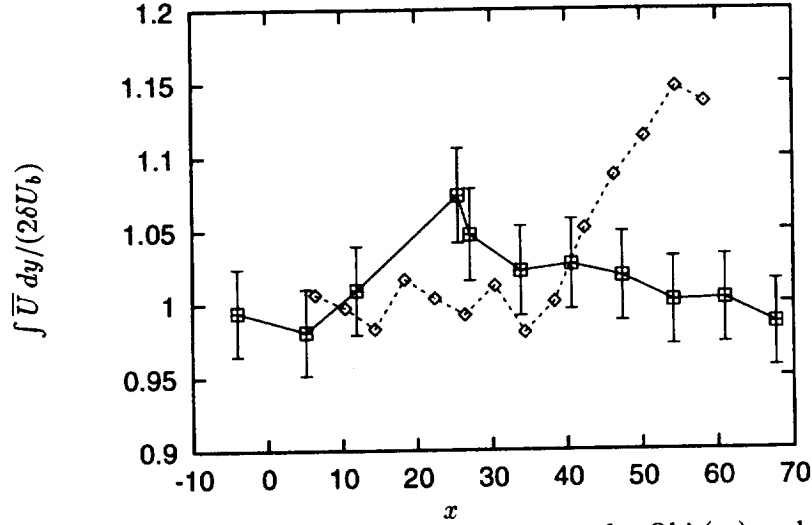
FIGURE 2.   Flow rate $\int \overline{U}\, dy/(2\delta U_b)$ from experiments by Obi ($\diamond$) and Buice ($\square$). U_b is the bulk velocity of the inlet channel. Error bars mark 3% deviation.

in regions with significant forward flow and pulsed wires elsewhere. The maximum error in mean velocity is 3%. Flow rates obtained from integration of velocity profiles measured with single wire upstream of separation and a combination of single and pulsed wire elsewhere are plotted in Fig. 2. An increase in flow rate in the order of 5% occurs in the region downstream of $x/\delta = 20$, i.e. immediately behind the zone of maximum pressure rise. Wool tufts mounted to the side walls did not indicate the presence of secondary flow or sidewall separation. The mass-flow deviation in this region is slightly greater than the confidence level for the measurements. No check of spanwise homogeneity at this location is available. Downstream of $x/\delta = 34$ the mass is globally conserved within 3%, and the flow is uniform in the span within 3%.

Force balance

The integral momentum balance for a fixed control volume for the time- and spanwise averaged force component F_x per unit depth is:

$$\sum F_x = (F_{p,out} - F_{p,in}) + F_{p,ramp} + F_{fric} + (F_{visc,in} - F_{visc,out}) = M_{in} - M_{out} \quad .$$

The corresponding control volume consists of vertical cuts at $x_{in} = -4\delta$ and at a downstream position x_{out} and follows the interior of both walls. With α denoting the local angle between the deflected and the horizontal wall, the individual forces read:

$$F_{p,x} = \int_{bot}^{top}\!\Big(p(x,y) - p_{ref}\Big)dy, \quad F_{p,ramp} = \int_{in}^{out}\!\Big(p(s) - p_{ref}\Big)\sin\alpha(s)ds \quad ,$$

$$F_{fric} = \int_{in}^{out} \tau_w \cos\alpha(s)ds, \quad F_{visc} = \int_{bot}^{top}\frac{1}{Re}\frac{dU}{dx}dy \;, \quad M_x = \int_{bot}^{top}U^2(x,y)dy \quad .$$
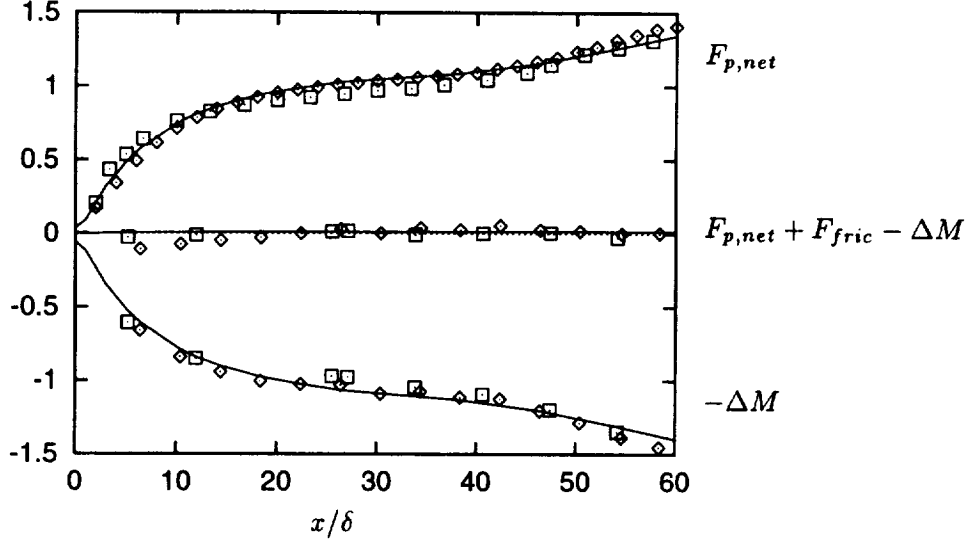
FIGURE 3. Individual terms contributing to the force balance from LES (———),
Obi (◇) and Buice (□). Momentum flux difference $-\Delta M = -(M_{in} - M_{out})$ (lower
curves), residual $F_{p,net} + F_{fric} - \Delta M$ (middle) and net pressure force $F_{p,net}$ (upper
curves) are normalized by δU_b^2.

Here and in the remainder of the brief we set $\rho = 1$. For reference pressure p_{ref} we
use the pressure at the lower end of the downstream control volume face. Pressure
difference force and ramp force can be combined into a net force $F_{p,net} = F_{p,out} -
F_{p,in} + F_{p,ramp}$, which expresses the net effect of pressure acting on all control
volume faces. The force $F_{fric,w}$ is evaluated for both walls. The momentum flux
M consists of the three parts:

$$M = \int \overline{U}^2 dy + \int \overline{u^2} dy + \int \overline{\tau}_{11} dy \quad .$$

Since the deviatoric SGS-stress τ_{11} is smaller than $2 \times 10^{-5} U_b^2$, it can be neglected
in the force balance for LES data. The isotropic part of the SGS stress enters the
balance through the pressure. We neglect F_{visc} since the term scales with $1/Re$ and
$\partial \overline{U}/\partial x \ll \partial \overline{U}/\partial y$.

Computation of the force balance from experimental data requires some minor
modifications such as inserting additional data points near the walls where measure-
ments are scarce and interpolation of c_p-values in x. We assume that the pressure
varies linearly across the duct for the experiment. The c_p-difference between wall
and interior resulting from the variance $\overline{v^2}$ is on average -0.005 and has been ne-
glected for the experiments. Computing the force balance from LES results using
this approximation rather than the real pressure distribution leads to a residual in
the order of $0.04\delta U_b^2$ in the outlet section. The friction force for the experiments is
computed using c_f from the LES. Skin friction from the simulation follows closely
the measurements of Buice (Fig. 5), and the overall contribution to the momentum

balance is less than 5% of the momentum flux difference between two control volume faces. The overall error introduced by these approximations is assumed to be in the order of 5%.

Figure 3 depicts individual terms and residual of the force balance for both experiments and simulation. The residual is below 1% of the momentum flux difference for LES results, thereby validating the internal consistency of the simulation method and the force balance evaluation. Since friction contributes less than 5% to the momentum balance, the flux difference ΔM is mainly balanced by the net effect of pressure, with $F_{p,ramp}$ contributing about one third of the net pressure force.

The maximum residual for Buice's data set is $0.027\delta U_b^2$, which is below 1.5% of the incoming momentum flux. This accuracy is remarkable considering the approximations involved. We found it to be crucial to use raw data, i.e. velocity measurements which were not scaled to satisfy global mass conservation, in order to obtain a small residual for Buice's data. Obi's data develop a higher residual which exhibits a trend from negative to positive values with streamwise location x/δ. The positive values of the residual might come from neglecting the pressure variation across the duct. Another source for the larger force balance residual compared to Buice's data might be the use of scaled velocity data. Raw data were not available for Obi's experiment.

Although the primary purpose of the force balance is a check of the consistency of experimental data, we have included simulation results in Fig. 3. Since LES and experiment have nearly identical incoming momentum flux, the difference ΔM indicates how much outgoing momentum fluxes differ at the downstream control volume face. LES and Obi's data agree well whereas $M_{x,out}$ is slightly higher for Buice in the region $20 < x/\delta < 30$. Lower ΔM in Buice's data corresponds to a smaller net pressure force downstream of $x/\delta = 20$ compared to simulation and Obi. Note that the enhanced momentum flux is consistent with the slight flow-rate increase in Buice's experiment near $x/\delta = 25$. Since LES and Obi have similar c_p-curves (see Fig. 5), the net pressure force should be close.

Overall, both experimental data sets satisfy mass and momentum balance of a nominally two-dimensional flow within acceptable error bounds, which makes them well suited for validation of a computational study.

Consistency check using Bernoulli's Equation

As a consequence of conservation of energy, the total pressure $c_p + U^2$ remains constant along a stream-tube in an inviscid flow. In Fig. 4, this relation has been evaluated for simulation and experimental data using c_p along the upper wall and the peak value of the streamwise velocity $\overline{U}$ at a given station. Included are data from a RANS computation by Durbin (1994).

Figure 4 reveals that the Bernoulli relation holds only approximately in the diffuser with viscous losses accounting for a 30% decrease over the length of the domain. We find that computations and measurements exhibit about the same total pressure with the exception of Obi's data, which fall short by about 5% of the total pressure upstream of $x/\delta = 15$. We attribute this deviation to the fact that raw data had been scaled to satisfy global mass balance.
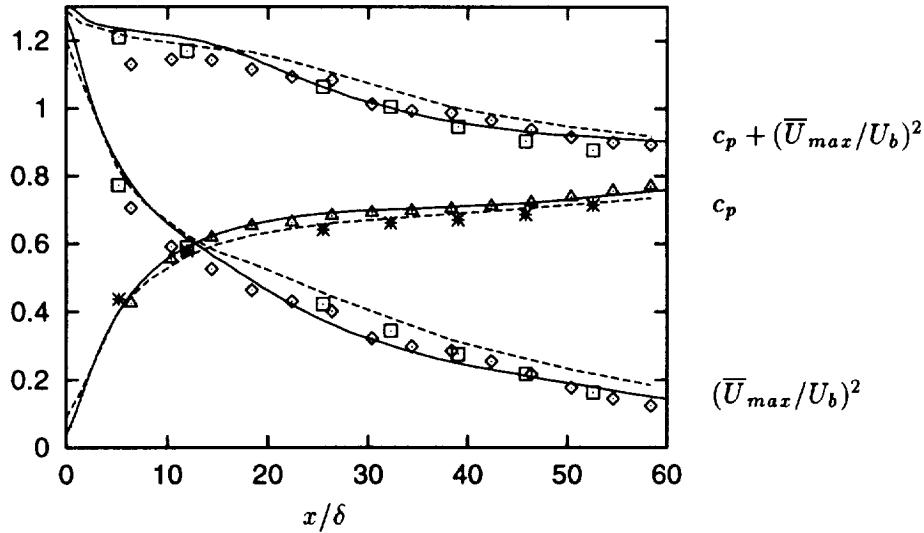
FIGURE 4.   Depicted are c_p (lower curves), $\overline{U}^2_{max}$ (middle), and total pressure $c_p + \overline{U}^2_{max}$ (upper curves) normalized by U_b^2 for LES (———), Durbin's RANS simulation (– – – –), and experiments of Obi ($\diamond$, $\triangle$) and Buice ($\square$, *).

Up to $x/\delta = 15$, LES and Durbin's RANS simulation predict larger $\overline{U}_{max}$ than the experiments. However, both cases differ with respect to c_p as early as $x/\delta = 10$. Here, the limitations of the Bernoulli relation for the present configuration become evident. Conversely, the deviation in c_p between LES and Obi on one side and Buice on the other side is consistent with the larger values of $\overline{U}_{max}$ found near $x/\delta = 25$ in Buice's data. There, the flow rate was about 5% higher than in the inlet duct.

Although the Bernoulli relation is only an approximation, it helps to interpret some of the results which will be shown in the following sections. Since the relation between peak velocity $\overline{U}_{max}$ and pressure is quadratic, a seemingly small mismatch in mean flow profile by e.g. 3% translates into a c_p-difference of 6%. This fact highlights the enormous difficulty involved in accurate quantitative prediction of this flow. If through the presence of secondary flow, for example, additional mass flow is added to a given profile which then accumulates in the region where the profile is peaked, even small fractions of the total flow rate are sufficient to increase $\overline{U}_{max}$ considerably, thereby changing the pressure coefficient strongly. It is also evident that error bounds for measurements of $\overline{U}_{max}$ have to be rather small to make data sets useful for validation purposes.

Comparison of LES with experimental data

Using the LES result as a reference, these plots allow comparison of both experiments against each other. From Buice (1997) we use raw data, i.e. data scaled with U_b measured in the inlet duct. Obi's data have been scaled in order to satisfy the global mass balance. One should keep in mind that the uncertainty in the scaling amounts to 15% downstream of $x/\delta = 40$.

Comparison of mean flow and pressure recovery

In Figs. 6 and 7 we compare profiles of mean streamwise velocity $\overline{U}$, rms of velocity fluctuations, and turbulent shear stress $\overline{uv}$ from simulation and experiments. Results from two simulations obtained on different grids are included in these plots. For the validation we restrict ourself to the data from the finest mesh.

Overall, the agreement of mean flow profiles between simulation and experiments is quite good. Upstream of $x/\delta = 10$ the peak velocity $\overline{U}_{max}$ of the simulation is slightly above the experiments. This deviation is within the experimental error margin. Between $x/\delta = 25$ and $x/\delta = 35$ the situation is reversed, i.e. the experiments exhibit slightly higher peak velocities near the flat wall than the simulation. Note that Buice's profiles have not been scaled to conserve mass, which explains the deviation at $x/\delta = 25$ where the flow-rate was 5% high.

The amount of backflow as well as the location and height of the separation bubble agree well up to $x/\delta = 55$. Reattachment and recovery occur further downstream in the simulation as compared to the experiment. This translates into a mean bubble length of 52δ in the simulation compared to 47δ in Buice's experiment. Skin friction along both walls agrees well with Buice's measurements, see Fig. 5. Near the diffuser throat the mean flow detaches over a very short distance, indicated by c_f dropping to zero near $x/\delta = 2$ on the deflected wall. There, a very thin zone of backflow buried in the viscous layer exists that is completely disconnected from the separation bubble, which begins at $x/\delta = 13$ and extends into the tail-duct. Using a thermal tuft, Buice determined the location of vanishing wall stress to be at $x/\delta = 12$. The location of zero crossing in c_f is reached at a shallow angle. Accurate prediction of the exact location of vanishing shear stress is probably less important than of the overall shape of mean flow profiles and the slope of $c_f(x)$.

Most of the pressure increase occurs within the first third of the expansion with the steepest rise close to $x/\delta = 2$ (Fig. 5).

Comparison of Reynolds stresses

Measurement errors are higher for fluctuations as compared to the mean flow, especially at the early stations where measurement volumes are large compared to the local gradients of rms profiles. Buice's measurements of u' are flawed near walls, and the peak rms values are underpredicted by 10-20%. Measurements of v' are available only for regions where the turbulence level remained below 35%. Therefore, only partial profiles are shown in the rear part. A few profiles from the LES upstream of the first measurement stations are shown. The scatter among the two experiments is larger for rms-values and shear stress than for the mean flow. Still, the agreement of the two datasets is good, as can be seen at stations $x/\delta = 27, 34, 38$ where data from both experiments are available.

Rms profiles from all three velocity components exhibit a characteristic shape with a double peak. The location of the peak value moves away from the wall into the flow interior with increasing distance from the diffuser throat. Locations of peaks of all three rms-values are close to each other and coincide with the locations of extremal values of $\overline{uv}$.
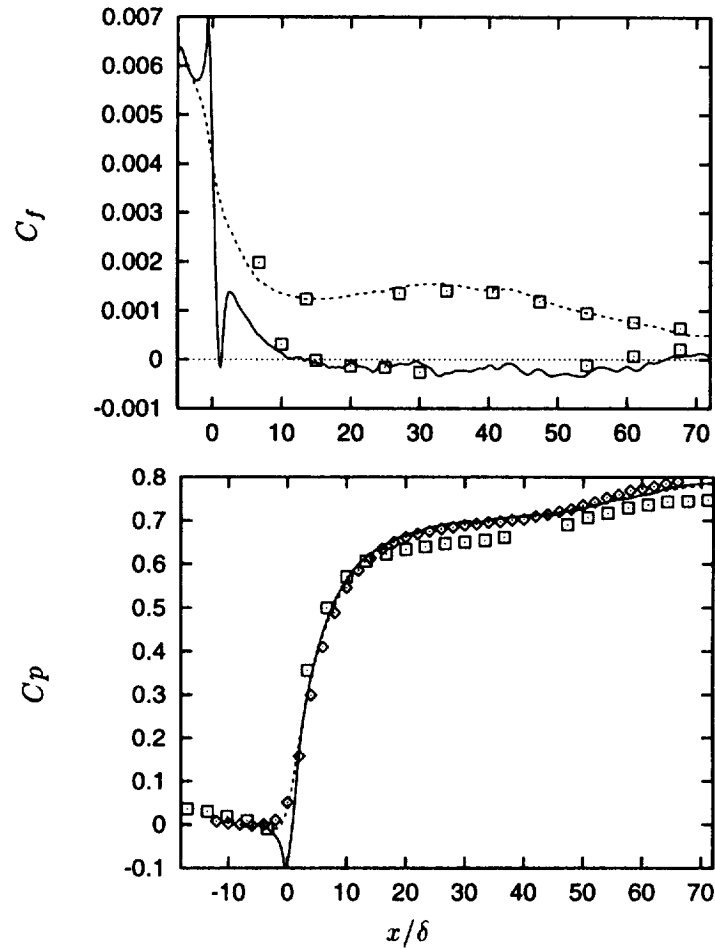
FIGURE 5.   Top: Skin friction coefficient c_f based on U_b along deflected wall
(————) and flat wall (- - - -) from LES and Buice (□). Bottom: Pressure coefficient
c_p based on U_b: LES flat wall (- - - -), LES deflected wall (————), Buice deflected
wall (□) and Obi flat wall (◇).

Profiles of u' from the simulation deviate from measurements upstream of $x/\delta =$ 25. In this region the peak values of u' on the side of the deflected wall are higher by 10-20% than in the experiments. A similar overshoot is observed for $-\overline{uv}$ in the region $10 < x/\delta < 25$. As mentioned earlier, Buice's measurements for fluctuations have rather large error margins. Inside the outlet section, deviations between simulation and measurements become more pronounced near the separation bubble. Near the flat wall, the agreement for u', v', and $\overline{uv}$ is reasonable. Obi's data are less reliable in this region since the flow is no longer two-dimensional in the mean. The vertical velocity fluctuation v' deviates from measurements downstream of $x/\delta = 12$. There, the part of the v'-profile between flat wall and duct centerline is on average 10-20% higher in the LES than in the experiment. Also, $\overline{uv}$ seems to be higher in this profile section.

FIGURE 6. Comparison of the LES result on fine (————) and medium (- - - -)
grid with data from Buice ($\square$) and Obi ($\diamond$), in the first half of the diffuser: *a)* Mean
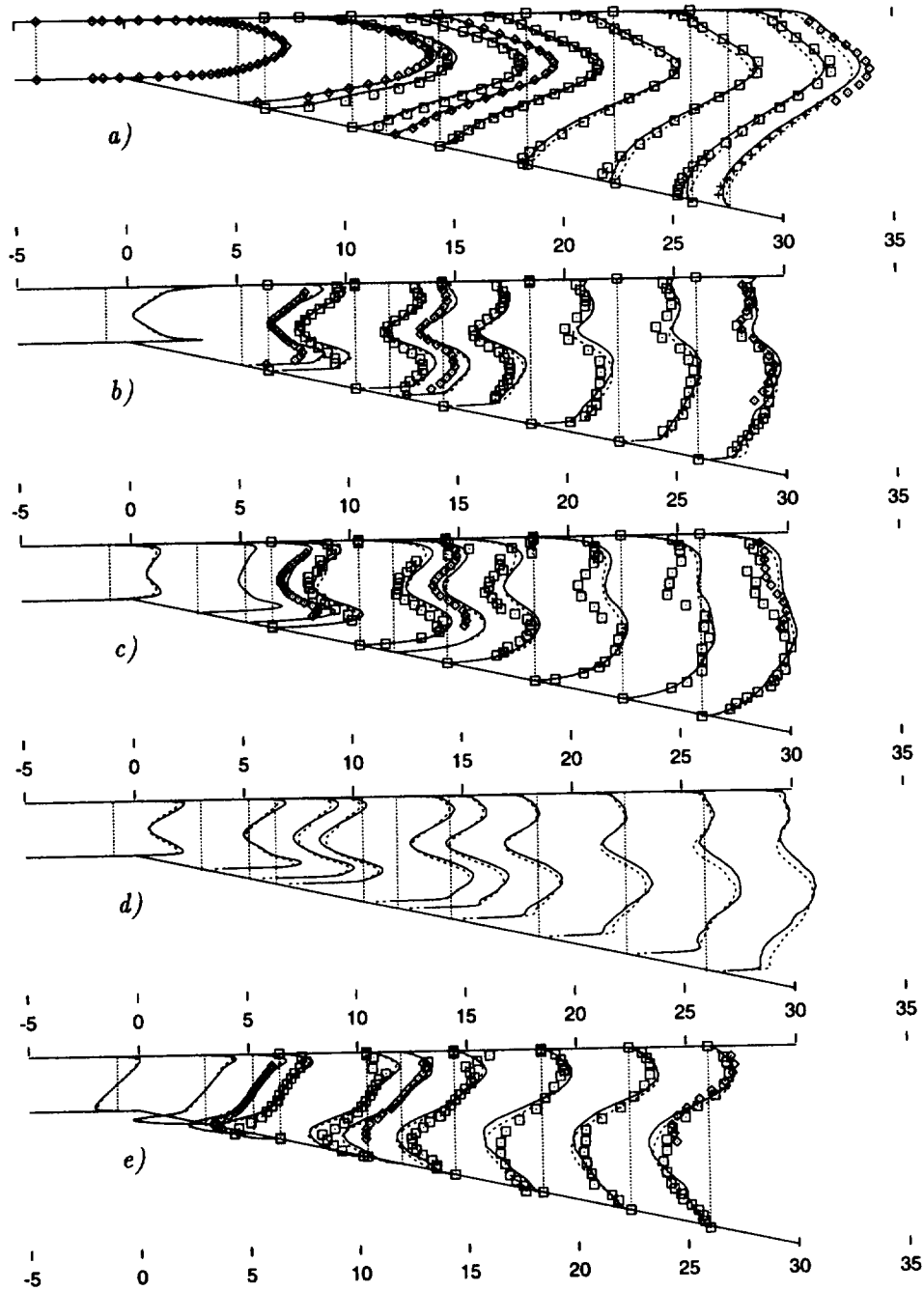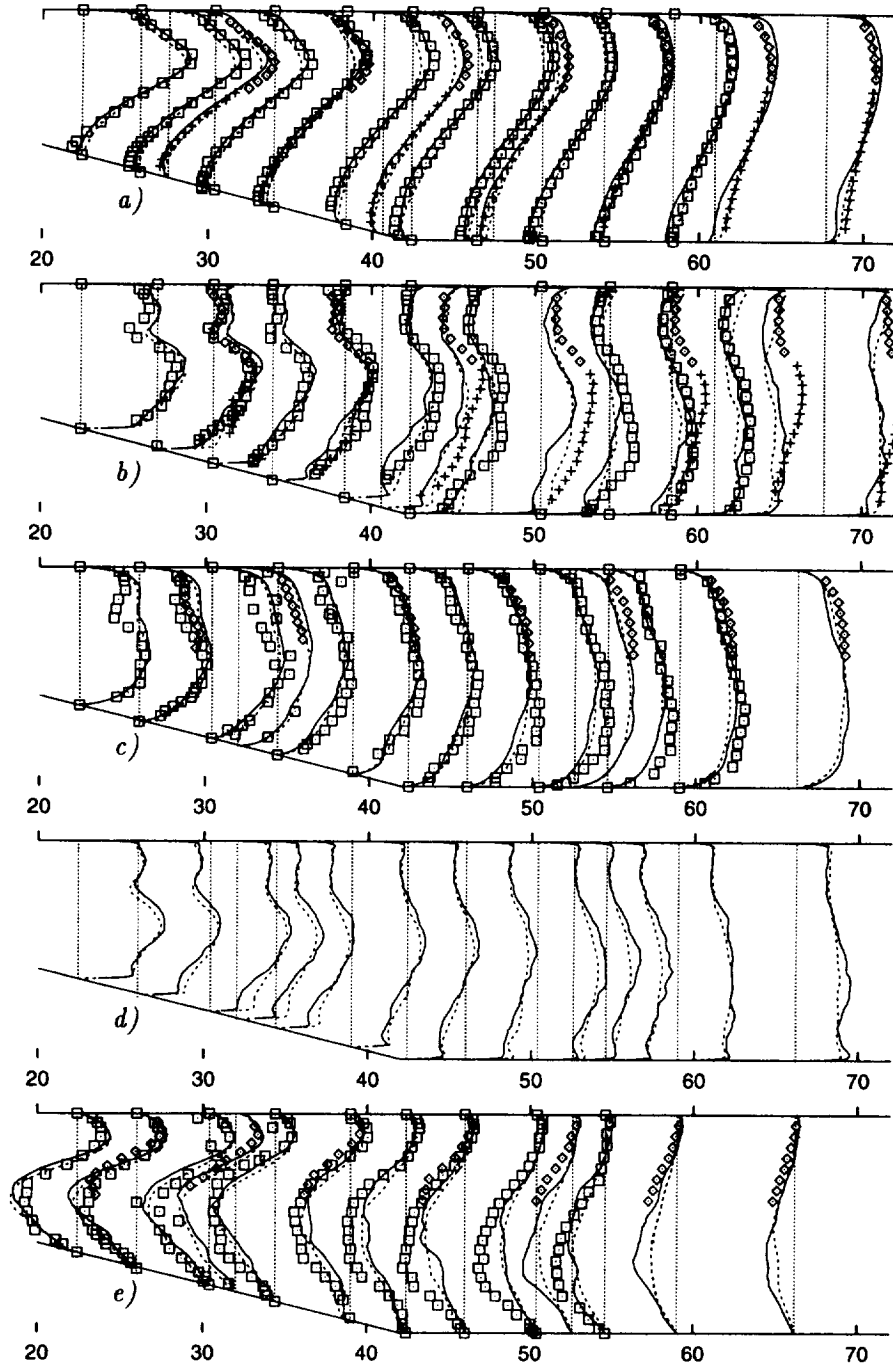velocity $\overline{U}/U_b$; rms velocity fluctuations: *b)* u'/U_b, *c)* v'/U_b, *d)* w'/U_b, *e)* $\overline{uv}/U_b^2$.

FIGURE 7. Comparison of the LES result on fine (———) and medium (----)
grid with data from Buice (□) and Obi (◊), in the rear part of the diffuser: *a)* Mean
velocity $\overline{U}/U_b$; rms velocity fluctuations: *b)* u'/U_b, *c)* v'/U_b, *d)* w'/U_b, *e)* $\overline{uv}/U_b^2$.

Conclusion from the validation

Although mean flow and c_p agree well with the measurements, the agreement in Reynolds stresses is not as good. Part of this discrepancy might be due to measurement errors. However, often the deviation of simulation results is outside the scatter of both experimental data sets. It seems unlikely that both experiments suffer from a similar systematic error since different measurement techniques (LDA versus hotwire) were employed.

We find that the simulation captures many essential features of the flow in this configuration, making it a valuable source for a detailed study of the physical phenomena associated with the separation process. With respect to the ability of LES to make accurate quantitative prediction of this flow, some uncertainties remain. Most importantly, it is not clear to what degree the flow in the experiment might be influenced by the presence of secondary flow. A thorough validation requires additional detailed measurements.

Future plans

The simulation on the fine grid is still running, and it will be continued until the statistic are fully converged. In addition, simulations on coarse grids will be performed with interpolated inflow field used for the fine mesh, to investigate the minimal resolution necessary for LES.

Acknowledgments

REFERENCES

BUICE, C. U. & EATON, J. K. 1996 Experimental investigation of flow through an asymmetric plane diffuser. *CTR Annual Research Briefs-1996*, Center for Turbulence Research, NASA Ames/Stanford Univ. 243-248.

BUICE, C. U. & EATON, J. K. 1997 Experimental investigation of flow through an asymmetric plane diffuser. *Report TSD-107* Dept. of Mech. Eng., Thermosciences Div., Stanford University.

DEAN, R. B. 1978 Reynolds number dependence of skin friction and other bulk flow variables in two-dimensional rectangular duct flow. *Trans. ASME I: J. Fluids Engng.* **100**, 215.

DURBIN, P. 1994 Separated flow computations with the $k - \epsilon - v^2$ model. *AIAA Journal.* **33**, No. 4.

FATICA, M. & MITTAL R. 1996 Progress in the large-eddy simulation of an asymmetric planar diffuser. *CTR Annual Research Briefs 1996*, Center for Turbulence Research, NASA Ames/Stanford Univ. 249-255.

GERMANO, M., PIOMELLI U., MOIN P. & CABOT W. H. 1991 A dynamic subgrid-scale eddy-viscosity model. *Phys. Fluids A .* **3,** 1760-1765.

KALTENBACH, H.-J. 1994 Large-eddy simulation of flow through a plane, asymmetric diffuser. *CTR Annual Research Briefs 1994,* Center for Turbulence Research, NASA Ames/Stanford Univ. 175-184.

MASUDA, S., OBI, S. & AOKI, K. 1994 Control of turbulent separating and reattaching flow by periodic perturbations. *Proceedings of ASME Fluids Engineering Division Summer Meeting Turbulence control, Lake Tahoe, USA.* **FED-Vol. 193,** 55-61.

OBI, S., OHIMUZI, H., AOKI, K. & MASUDA, S. 1993 Turbulent separation control in a plane asymmetric diffuser by periodic perturbation. *Engineering Turbulence Modeling and Experiments 2,* W. Rodi and F. Martelli (Editors), Elsevier Science Publ.

OBI, S., AOKI, K. & MASUDA, S. 1993b Experimental and computational study of turbulent separating flow in an asymmetric plane diffuser. *Ninth Symposium on Turbulent Shear Flows,* Kyoto, Japan, August 16-19, 1993. p.305.

Progress in large-eddy simulation of trailing-edge turbulence and aeroacoustics

By Meng Wang

1. Motivation and objectives

Turbulent boundary layers near the trailing-edge of a lifting surface are known to generate intense, broadband noise through an aeroacoustic scattering mechanism (Ffowcs Williams & Hall 1970; Howe 1978). In addition, the fluctuating surface pressure (pseudo-sound) tends to excite structural vibrations and low frequency noise radiation (Blake 1986).

To numerically predict the trailing-edge noise requires that the noise-generating eddies over a wide range of length scales be adequately represented. This requirement cannot be met by the traditional computational fluid dynamics (CFD) methods based on Reynolds-averaged Navier-Stokes (RANS) equations or Euler equations. Large-eddy simulation (LES) techniques provide a promising tool for obtaining the unsteady surface-pressure fields and the near-field turbulence quantities. LES is best suited for computing the noise source at Reynolds numbers of engineering interest because it resolves only the energy-containing eddies, known to be significant contributors to noise radiation. The effect of small (subgrid) scale eddies on the large (resolved) scale motion is modeled, thus drastically reducing the computational cost as compared with direct numerical simulation (DNS). The latter approach, which attempts to resolve all the physical length scales, is limited to simple, relatively low Reynolds number flows even with today's high performance computing capabilities.

In this project, we aim to develop numerical prediction methods for trailing-edge aeroacoustics using a combination of LES techniques and aeroacoustic theory based on Lighthill's analogy (Lighthill 1952). With this approach, the instantaneous turbulent flow fields near the trailing-edge are obtained by means of LES. The space-time evolution of the surface pressure fluctuations, useful as forcing function for structural vibration models, is also computed directly. The simulation results allow the acoustic source functions, or the fluctuating Reynolds stress, to be evaluated. The radiated noise can then be computed from an integral-form solution to the Lighthill equation, along the line of Ffowcs Williams & Hall (1970). A second objective of the project is to study the physical mechanisms for the generation of sound and pseudosound. Besides the edge scattering effect, we are also interested in the roles played by pressure gradients and boundary-layer separation near a trailing edge.

The general framework and aeroacoustic formulation for the present project are outlined by Wang (1996). During the past year major effort has been devoted to the LES of the near-field, in order to evaluate the acoustic source functions and to assess the predictive capabilities of LES for surface pressure fluctuations.
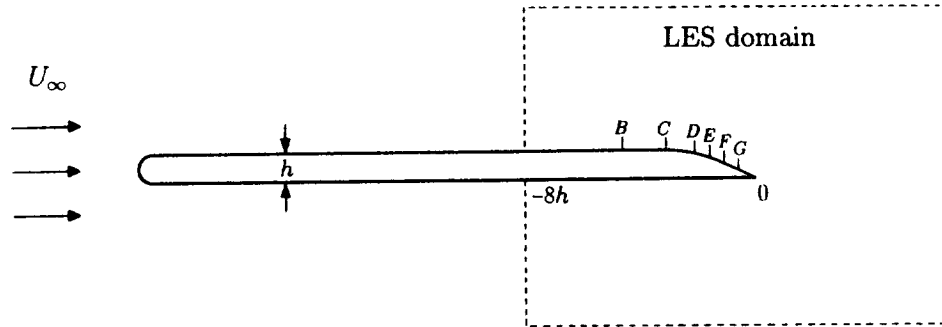
FIGURE 1.   Flow configuration and computational domain. The experimental measurement stations B-G are located at $x/h = -4.625, -3.125, -2.125, -1.625, -1.125$, and -0.625, respectively.

2. Accomplishments

2.1 Flow configuration

The flow being simulated corresponds to the experiment conducted by Blake (1975). As shown in Fig. 1, a two-dimensional flat strut with a circular leading edge and an asymmetric, beveled trailing-edge of 25-degree tip-angle is placed in a uniform stream at zero-degree angle of attack. The strut has a chord to thickness ratio $C/h = 21.125$. The Reynolds number is based on free-stream velocity U_∞, and the chord is 2.15×10^6. This flow is particularly interesting in that the asymmetric edge shape produces a separated flow on the low-pressure side and an attached boundary layer on the high-pressure side, thus creating complex shear-layer interactions in the vicinity of the trailing edge. The experimental data, including the mean and turbulent velocity magnitudes and the fluctuating surface pressure, are available for comparison with computational results.

2.2 Computational methodology

In order to reduce the computational cost while capturing the essential physical processes of interest, numerical simulations are conducted in computational domains that contain the aft section of the strut and the near wake, as illustrated in Fig. 1. Note that only the location of the inlet boundary is depicted exactly; the remaining three sides of the domain have been truncated for plotting clarity (see Table 1 for the actual domain sizes). The letters B, C, D, E, F, and G indicate measurement stations in Blake's experiment. They are located at $x/h = -4.625, -3.125, -2.125, -1.625, -1.125$, and -0.625, respectively, in a Cartesian coordinate system originating from the trailing edge.

The simulations solve the spatially filtered, unsteady, incompressible Navier-Stokes equations in conjunction with the dynamic subgrid-scale model (Germano et al. 1991; Lilly 1992). The numerical code is an adaptation of the C-grid code described by Choi (1993) and Mittal (1996). Spatial discretization is achieved using second-order central differences in the streamwise and wall-normal directions

and using Fourier collocation in the spanwise direction. A significant improvement has been made by implementing a phase-shift dealiasing strategy in the spanwise direction (Lund & Wray, private communication). Compared with the original method of dealiasing by padding, the new method saves 33% CPU time and memory. The time-advancement is of the fractional step type in combination with the Crank-Nicolson method for viscous terms and third order Runge-Kutta scheme for convective terms. The continuity constraint is imposed through a pressure Poisson equation solved at each Runge-Kutta sub-step using a multi-grid iterative procedure.

The boundary conditions at the inlet are obtained by the following procedure. First, an auxiliary RANS calculation is conducted in a C-grid domain enclosing the entire strut. The resulting mean velocities, accounting for the flow acceleration and circulation associated with a lifting surface, are used as the inflow profiles outside the boundary layers on both sides of the strut. Within the turbulent boundary layers the time series of inflow velocities are generated from two separate LES's of flat-plate boundary layers with zero pressure gradient, using the method described by Lund, Wu & Squires (1996). The inflow-generation LES employs an identical mesh resolution as for the trailing-edge flow LES at the inlet and matches the local boundary layer properties, including the momentum thickness and Reynolds number, with those from the RANS simulation.

A no-slip condition is applied on the surface of the strut. The top and bottom boundaries are placed far away ($\sim 20h$ for most simulations) from the strut to minimize the impact of the imposed velocities obtained from RANS calculations. At the downstream boundary the convective outflow condition (Pauley, Moin & Reynolds 1988) is applied to allow the vortical disturbances in the wake to leave the computational domain smoothly.

2.3 Simulations performed

A total of four simulations, summarized in Table 1, have been carried out to date, although only the last two will be described in detail. The first simulation was done on a very coarse grid in the course of code development and testing. More reasonable grid resolutions were employed in simulations 2 and 3, which differ only in the spanwise resolution. The resolution improvement in LES 3 results from a switch to the phase-shift dealiasing method mentioned previously, without increasing the computational cost. The two simulations (LES 2 and LES 3), however, showed insignificant differences in the velocity and mean pressure fields.

The newest simulation, LES 4, differs from LES 3 in two major aspects: the inflow conditions and the spatial resolution. Fig. 2 compares the inlet streamwise velocity profiles (normalized by free-stream velocity U_∞) used in LES 3 and LES 4, obtained from RANS calculations using the v^2-f turbulence model (Durbin 1995) and Menter's (1993) SST k-ω model, respectively. In this figure the strut is located at $0 \leq y/h \leq 1$, and the two boundary layers are represented by the nearly horizontal lines. The two turbulence models produced a noticeable difference in the velocity overshoot (undershoot) outside the upper (lower) boundary layer. The inflow profiles for LES 4 are associated with a smaller mean circulation, which

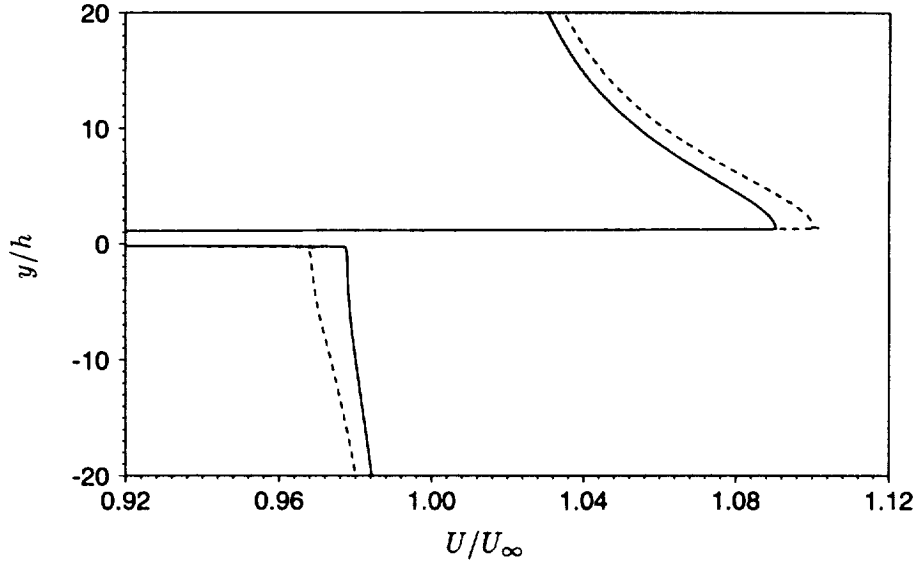| No.	Domain $(l_x \times l_y \times l_z)$	Grid $(n_x \times n_y \times n_z)$	Inlet Re_θ (upper, lower)
1	$20.0h \times 82h \times 0.5h$	$576 \times 80 \times 32$	3660, 2860
2	$16.5h \times 41h \times 0.5h$	$1280 \times 88 \times 32$	3660, 2860
3	$16.5h \times 41h \times 0.5h$	$1280 \times 88 \times 48$	3660, 2860
4	$16.5h \times 41h \times 0.5h$	$1536 \times 96 \times 48$	3380, 2760

Table 1. Domain size, grid size, and inflow Re_θ for simulations performed.

FIGURE 2. Mean streamwise velocity profiles at LES inlets, obtained from RANS calculations. ——— LES 4; - - - - LES 3.

is thought to promote trailing-edge separation (the corresponding RANS solution indeed has larger separation). The different inflow profiles also correspond to different Reynolds numbers Re_θ based on momentum thickness and boundary layer edge velocity U_e, as listed in Table 1.

The streamwise resolution improvement in LES 4 occurs mainly along the upper surface, on which 640 grid points are nonuniformly distributed, compared with 448 points for LES 3. This reduces the maximum grid spacing in wall units at the location of skin-friction peak (cf. Fig. 7) from $\Delta x_{max}^+ \approx 105$ in LES 3 to $\Delta x_{max}^+ \approx 60$. Along the lower surface 512 and 448 points are used in LES 4 and LES 3, with $\Delta x_{max}^+ \approx 74$ and 62, respectively. In both cases, 192 points are distributed along the wake line (branch cut). The wall-normal resolution is increased slightly, although the grid spacing for the first layer of cells adjacent to the surface remains unchanged at $\Delta y^+ \approx 2$. In the spanwise direction, the same number of points with uniform spacing are used in both simulations. Δz_{max}^+ is approximately 55 at the skin friction
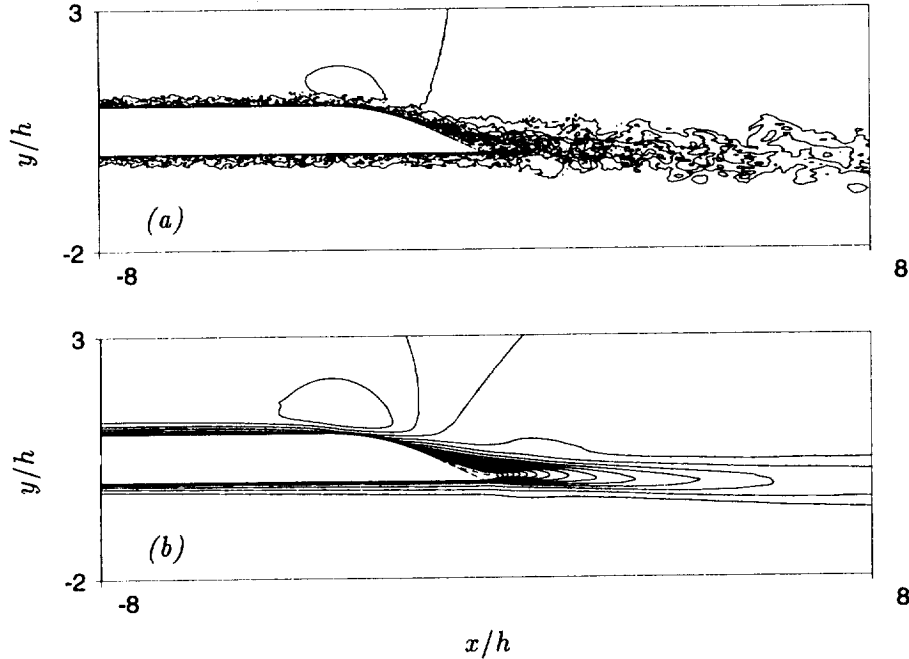
FIGURE 3.   Velocity fields computed from LES 4. (a) Instantaneous streamwise velocity u/U_∞ at a given spanwise cut (contour levels: -0.236 to 1.274, increment 0.116); (b) mean streamwise velocity U/U_∞ (contour levels: -0.081 to 1.207, increment 0.068).

peak and is substantially smaller elsewhere.

The CPU time requirement to advance the simulation one flow-through time, *i.e.*, to follow a fluid element to traverse the streamwise domain length, is approximately 150 single-processor hours on CRAY C90 for LES 3, and 200 hours for LES 4. At least two to three flow-through times are required to eliminate the initial transients and collect converged statistics.

2.4 Results

Figure 3a depicts contours of the instantaneous streamwise velocity u/U_∞ at a given spanwise location. The mean streamwise velocity (U/U_∞) contours, obtained by averaging over the homogeneous spanwise direction and time, are plotted in Fig. 3b. The results of LES 4 are used for both figures. It is observed that the numerically simulated fields exhibit realistic turbulence structures and a small separated zone near the trailing edge. The two shear layers, arising from the separated boundary layer on the upper side and the attached boundary on the lower side, interact in the near wake region to shed unsteady structures downstream.

In Fig. 4, the magnitude of the mean velocity $\tilde{U} = (U^2 + V^2)^{1/2}$, normalized by its value at the boundary-layer edge $\tilde{U}_e$, is plotted as a function of vertical distance from the upper surface at streamwise stations (from left to right) C-G defined in Fig. 1. The solid and dashed lines are based on LES 4 and LES 3,
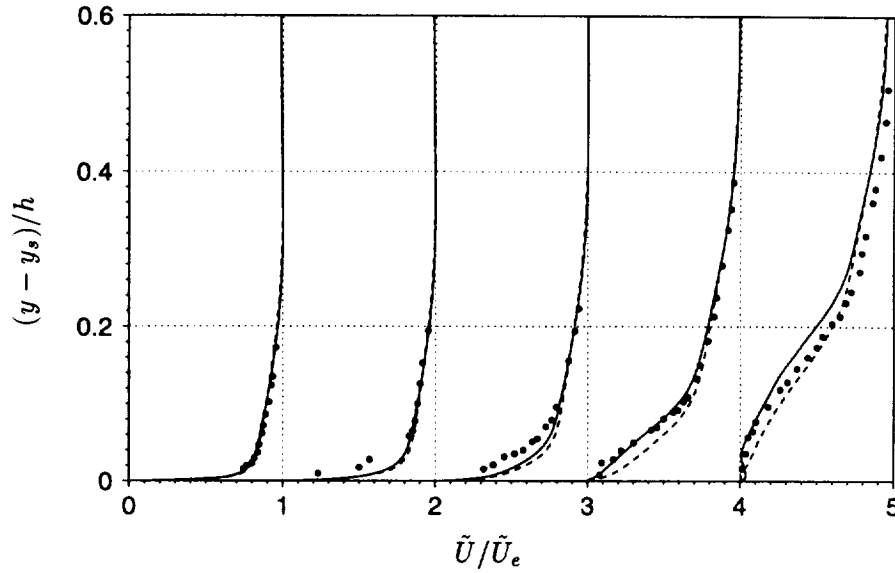
FIGURE 4.   Profiles of the normalized mean velocity magnitude as a function of vertical distance from the upper surface, at streamwise stations (from left to right) C, D, E, F, and G. —— LES 4; - - - - LES 3; ● Blake's experiment. Individual profiles are separated by a horizontal offset of 1 with the corresponding zero lines located at 0, 1, ..., 4.

respectively, and the symbols represent Blake's experimental data. Good agreement with the experimental results is obtained at station C and all the upstream locations. However, significant deviations occur at stations D and E, where the experimental profiles are less full in the near-wall region. Further downstream, at stations F and G, the discrepancy diminishes, and the computed profiles, particularly those from LES 4, compare well again with the experimental results. Between the two simulations, LES 4, which has a smaller mean circulation and better grid resolution, provides better agreement with the experiment.

Figure 5 compares the computational and experimental profiles of the "turbulence intensity", or the normalized rms velocity fluctuations as measured by a single hot-wire thermal anemometer system, at streamwise stations (from left to right) B, D, E, F, and G. In terms of the mean and fluctuating velocity components in the x-y plane, the fluctuating velocity measured by a single wire is approximately

$$\tilde{u}' \approx \frac{U}{(U^2 + V^2)^{\frac{1}{2}}} u' + \frac{V}{(U^2 + V^2)^{\frac{1}{2}}} v'. \tag{1}$$

$\tilde{u}' \approx u'$ in an attached boundary layer where $V \ll U$. The agreement between the LES and the experimental results is fairly good except in the near-wall region and at the last two stations. One notices that the experimental intensity profiles consistently miss the near-wall peaks known to exist in turbulent boundary layers,
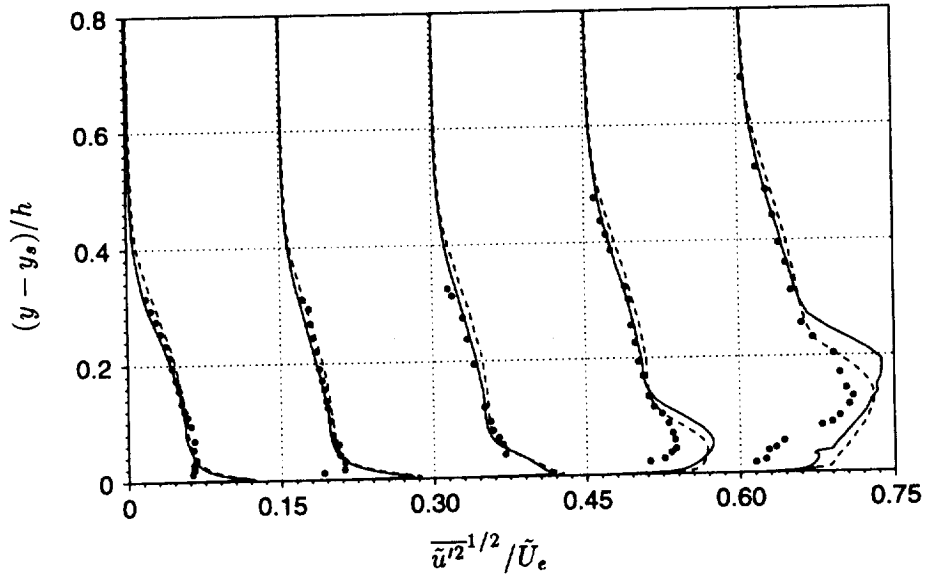
FIGURE 5. Profiles of the rms velocity fluctuations defined in (1) as a function of vertical distance from the upper surface, at streamwise stations (from left to right) B, D, E, F, and G. ——— LES 4; - - - - LES 3; ● Blake's experiment. Individual profiles are separated by a horizontal offset of 0.15 with the corresponding zero lines located at 0, 0.15, ..., 0.60.

suggesting a possible lack of spatial resolution or high-frequency response as the probe approaches the wall. The large discrepancy observed in the separated region (stations F and G) may be caused by both simulation and measurement errors. In general, hot-wire readings become increasingly difficult to interpret if the rms turbulence intensity exceeds 30% of the local mean velocity (Bradshaw 1971). This is seen to be the case in the separation bubble where the mean velocity is very small (cf. Fig. 4). It should also be pointed out that the LES results represent the resolved portion of velocity fluctuations only. No attempt was made to account for the contributions from the subgrid scale stresses.

The dimensionless mean pressure (= $C_p/2$) and the local skin-friction coefficient are depicted in Figs. 6 and 7, respectively, as functions of x. Both simulations show unsatisfactory comparisons with the experimental C_p data, although LES 4 represents a clear improvement over LES 3. The improvement arises from the smaller circulation and the larger separation zone near the trailing edge. The latter can be observed from the C_f curves for the upper surface (cf. Fig. 7), where the solid curve representing LES 4 exhibits a longer portion of negative skin friction.

Comparisons have also been made between the boundary-layer properties predicted numerically and experimentally. Figures 8 and 9 show the streamwise distributions of displacement thickness and momentum thickness, respectively. The experimental values, represented by the solid circles, are given at (from left to right)
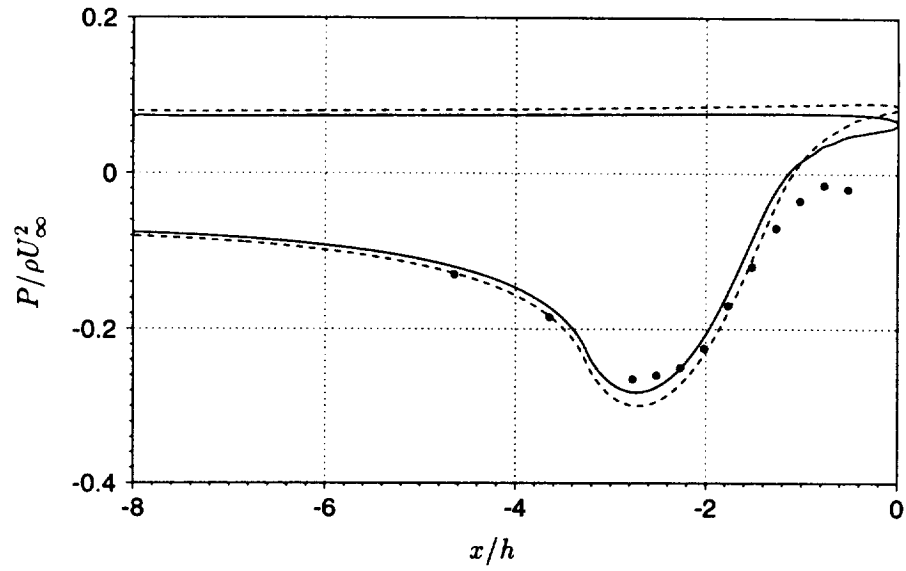
FIGURE 6.   Mean wall pressure distribution near the trailing edge. ——— LES 4;
– – – – LES 3; • Blake's experiment.
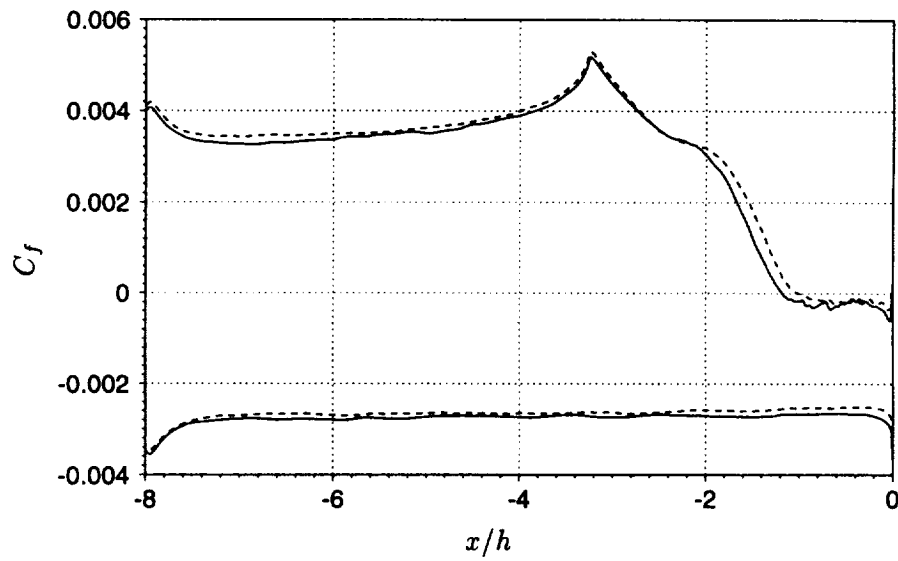
FIGURE 7.   Distribution of the local skin friction coefficient near the trailing edge.
——— LES 4; – – – – LES 3.
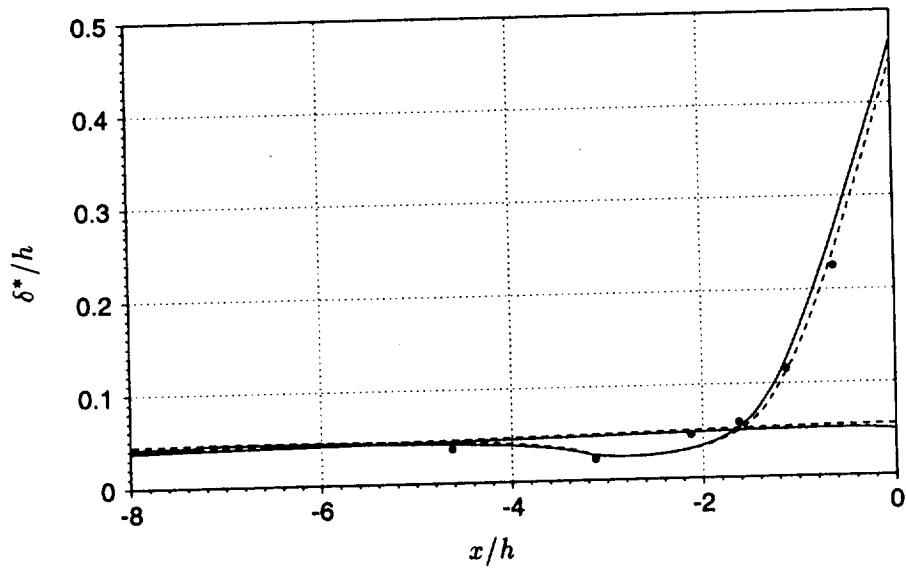
FIGURE 8. Distribution of boundary layer displacement thickness near the trailing edge. ———— LES 4; ———— LES 3; ● Blake's experiment (from left to right: stations *B-G*).
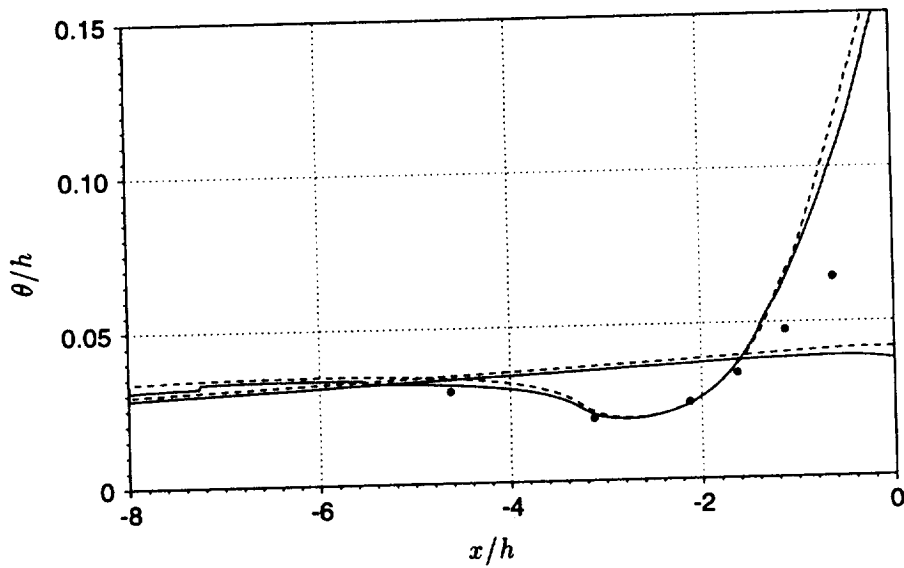
FIGURE 9. Distribution of boundary layer momentum thickness near the trailing edge. ———— LES 4; ———— LES 3; ● Blake's experiment (from left to right: stations *B-G*).
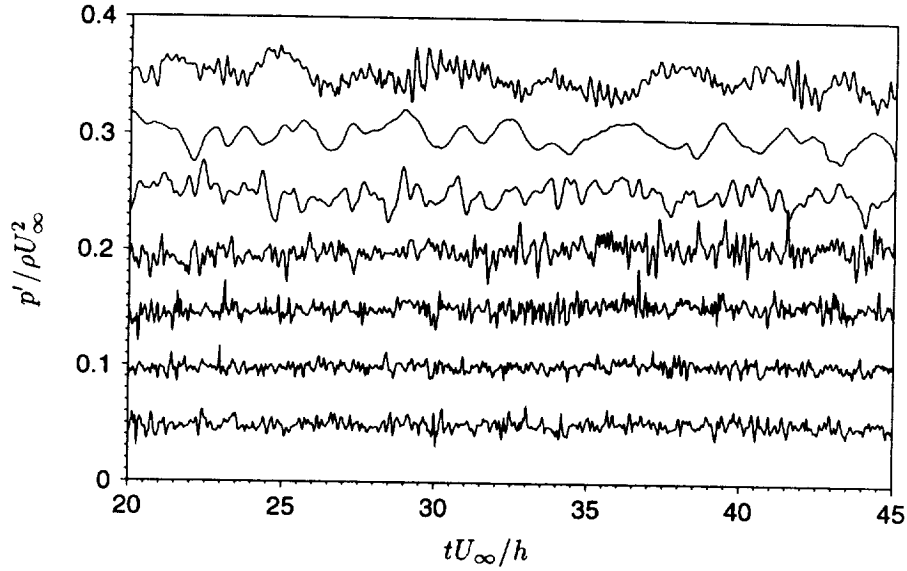
FIGURE 10. Time history of surface pressure fluctuations from LES 4, at stream-wise stations (from bottom to top) B, C, D, E, F, G, and $T.E.$ (trailing edge), at a fixed spanwise coordinate. Individual curves are separated by a vertical offset of 0.05 with the corresponding zero lines located at 0.05, 0.10, ..., 0.35.

stations B-G. The displacement thickness predicted by LES is in general agreement with the experimental data except at station D. The momentum thickness is also predicted well except at the last two stations. The poor agreement at these stations is unexpected, given that the numerical and experimental mean profiles agree well in Fig. 4.

Temporal variations of wall-pressure fluctuations are exemplified in Fig. 10. The signals are obtained from LES 4 for stations (from bottom to top) B-G and the trailing edge, at a fixed spanwise location. At stations B-E the pressure signals consist of predominantly high frequency fluctuations associated with small scale eddies in the attached turbulent boundary layer. The oscillation amplitude is decreased in the favorable pressure gradient region (station C) and increased in the adverse pressure gradient region (stations D and E). After the boundary layer is separated (stations F and G), the high frequency content is diminished, and the surface pressure is characterized by lower-frequency and higher-amplitude oscillations caused by the unsteady separation. The high-frequency content reappears at the trailing edge, owing to the contribution from the attached turbulent boundary layer on the lower side.

Figure 11 depicts the wall-pressure frequency spectra

$$\phi(\omega) = \frac{1}{2\pi} \int_{-\infty}^{\infty} < p'(t)p'(t+\tau) > e^{i\omega\tau} d\tau \tag{2}$$

calculated from LES 4 for stations C, E and G. The ensemble average $< \ >$ is
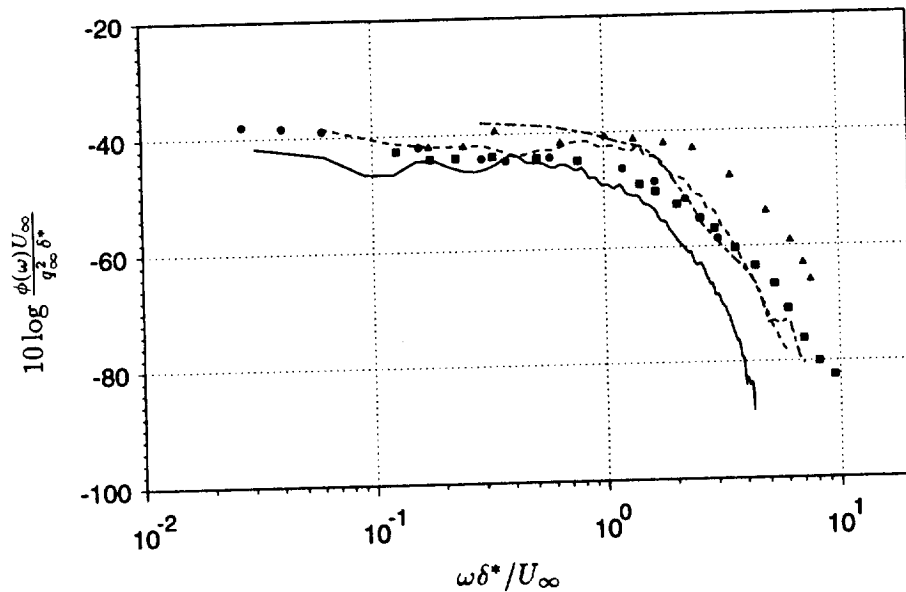
FIGURE 11. Frequency spectra of wall pressure fluctuations compared with Blake's experimental measurements at selected streamwise stations. The lines are from LES 4 (——— station C; ———— station E; ——— station G), and the symbols are from Blake's experiment (● station C; ▲ station E; ■ station G).

replaced by time- and spanwise averages. Outer variables U_∞, δ^*, and the dynamic pressure $q_\infty = \rho U_\infty^2/2$ are used to scale the data for comparison with Blake's experimental measurements. The calculated spectra agree relatively well with the experimental data at stations C and E, although they fall off more quickly at the high frequency end due to limited grid resolution. The high frequency content corresponds to fine spatial structures not resolved on the simulation grid. In the separated region (station G), the LES is seen to significantly overpredict the pressure spectra. The surface pressure frequency-spectra from the coarser grid simulation LES 3, not shown here, show similar agreement with the experiment in a somewhat narrower frequency range. It should be mentioned that the pressure signals plotted here have not completely converged to the statistically stationary state, as suggested by the slight upward drift of some curves in Fig. 10. As a result, the pressure spectra, particularly at the low frequency end, will be subject to small corrections as the simulation continues.

2.5 Discussion and summary

The preliminary LES results described above are encouraging in terms of quantitative predictions of the trailing-edge velocity fields and surface pressure fluctuations. However, significant discrepancies still exist between the computed quantities and those measured experimentally at certain measurement stations. Factors that may have contributed to these discrepancies include the inflow velocity conditions,

spatial resolution, and computational domain size. In addition, experimental errors may have also played a role.

The inflow velocity profiles constitute a major uncertainty for the present LES since they are not available from Blake's experiment. The experimental measurements are limited to the upper-side of the strut, and even there the available data are insufficient for boundary condition specification. As a result, we had to resort to RANS calculations to provide the inflow mean velocities, thus severely compromising the accuracy of the LES. The inflow profiles are directly related to the circulation, which affects the entire flow field including the trailing edge region.

Two major simulations, LES 3 and LES 4, with different inflow profiles and streamwise resolutions were described in this report. The one with smaller mean circulation and better resolution (LES 4) is shown to generate a larger separated region and mean velocity profiles in better agreement with the experimental data. Likewise, the pressure coefficient obtained from LES 4 represents a better approximation to the experimental data although the pressure rise from the suction peak to the trailing edge is still exaggerated significantly. Thus, the circulation associated with the experiment must be smaller than that in either simulation. In principle, one could estimate the circulation based on the lift or the surface integral of the static pressure. This is, however, not feasible because no measurement data were given on the lower surface.

The rms velocity fluctuations from the experiment and both simulations are in general agreement on the flat strut section and the first two stations on the descending ramp, except in the near-wall region where the experiment fails to record the peak. The cause for the large disparity at the last two stations needs to be investigated. Unfortunately, individual components of velocity and Reynolds stress are not available from the experiment, which impedes a more rigorous validation or diagnosis of the computational solutions.

The surface pressure frequency spectra reported here are rather preliminary. We are in the process of validating their statistical convergence as more simulation data become available.

3. Future plans

First, the near-field LES needs to be further validated and the discrepancies with the experimental data reconciled. The effect of inflow conditions and the mean circulation on the edge-flow behavior will be investigated, and more grid refinement studies are to be carried out. Other possible artifacts that may affect the computational solutions such as the computational domain size (particularly in the spanwise direction) should be examined. A careful evaluation of the experimental accuracy is also necessary.

Once a reliable near-field solution is established, we will conduct detailed studies of the structure of wall pressure fluctuations and scattering by the edge. Cross-correlation and spectral analyses will be conducted to investigate the unsteady surface pressure generation and scattering mechanisms. The radiated far-field noise will be calculated following the acoustic analogy formulation with a hard-wall Green's function, as outlined in Wang (1996).

REFERENCES

BLAKE, W. K. 1975 *A Statistical Description of Pressure and Velocity Fields at the Trailing Edge of a Flat Strut*, DTNSRDC Report 4241, David Taylor Naval Ship R & D Center, Bethesda, Maryland.

BLAKE, W. K. 1986 *Mechanics of Flow-Induced Sound and Vibration*, Vol. I and II, Academic Press, London.

BRADSHAW, P. 1971 *An Introduction to Turbulence and Its Measurements*, Pergamon Press, Oxford.

CHOI, H. 1993 Toward large eddy simulation of turbulent flow over an airfoil. *Annual Research Briefs-1993*, Center for Turbulence Research, Stanford Univ./NASA Ames, 145-149.

DURBIN, P. A. 1995 Separated flow computations with the k-ϵ-v^2 model. *AIAA J.* **44**, 659-664.

FFOWCS WILLIAMS, J. E. & HALL, L. H. 1970 Aerodynamic sound generation by turbulent flow in the vicinity of a scattering half plane. *J. Fluid Mech.* **40**, 657-670.

GERMANO, M., PIOMELLI, U., MOIN, P. & CABOT, W. H. 1991 A dynamic subgrid-scale eddy viscosity model. *Phys. Fluids A.* **3**, 1760-1765.

HOWE, M. S. 1978 A review of the theory of trailing edge noise. *J. Sound & Vib.* **61**, 437-465.

LIGHTHILL, M. J. 1952 On sound generated aerodynamically; I. General theory. *Proc. R. Soc. Lond.* A. **211**, 564-587.

LILLY, D. K. 1992 A proposed modification of the Germano subgrid scale closure method. *Phys. Fluids A.* **3**, 2746-2757.

LUND T. S., WU, X. & SQUIRES K. D. 1996 On the generation of turbulent inflow conditions for boundary layer simulations. *Annual Research Briefs-1996*, Center for Turbulence Research, Stanford Univ./NASA Ames, 281-295.

MENTER, F. R. 1993 Zonal two-equation k-ω turbulence models for aerodynamic flows, *AIAA paper* 93-2906.

MITTAL R. 1996 Progress on LES of flow past a circular cylinder. *Annual Research Briefs-1996*, Center for Turbulence Research, Stanford Univ./NASA Ames, 233-241.

PAULEY, L. L., MOIN, P. & REYNOLDS, W. C. 1988 *Numerical Study of Unsteady Laminar Boundary Layer Separation*, Report No. TF-34, Dept. of Mech. Engr., Stanford Univ.

WANG, M. 1996 Towards numerical simulations of trailing-edge aeroacoustics. *Annual Research Briefs-1996*, Center for Turbulence Research, Stanford Univ./NASA Ames, 133-142.

Resolution requirements in large-eddy simulations of shear flows

By J. S. Baggett, J. Jiménez[1] AND A. G. Kravchenko

1. Motivation

Large eddy simulations reproduce faithfully the characteristics of moderately complex turbulent flows (Moin & Jiménez 1993, Moin 1997). This is true even if most of them are, at present, based on variations of the Smagorinsky model, which is known to represent only poorly the subgrid Reynolds stresses (Clark, Ferziger & Reynolds 1979, Bardina, Ferziger & Reynolds 1983). The subgrid stress tensor can be decomposed in isotropic and anisotropic components. The former affects the flow by determining the rate of energy dissipation, but it does not enter directly in the equations for the mean flow. The average value of the latter determines the mean shear stresses and controls directly the mean velocity profiles. In the absence of a mean shear, the rate of energy dissipation fully characterizes isotropic turbulence (Kolmogorov 1941), and it is believed that the dynamic versions of the Smagorinsky model (Germano et al. 1991) work by approximating it correctly (Jiménez 1995). It is, on the other hand, clear that a model which does not well represent the stresses must do a poor job on shear flows unless the resolution of the filter is chosen fine enough that the subgrid stresses are negligible.

While it has long been recognized that adequate resolution is crucial for successful large-eddy simulations, there are few systematic studies that delineate the actual requirements. That is the subject of this note. The issue may actually be of secondary importance in free shear flows, although a clear criterion should also be useful there because it will be shown below that the number of 'anisotropic' degrees of freedom in those flows is independent of the Reynolds number. Large-eddy simulations only have to compute explicitly those anisotropic modes since, as discussed in the previous paragraph, the isotropic ones are handled well by the present models. It follows that large-eddy simulations of free shear flows need only resolve a fixed number of degrees of freedom, depending on the geometry but independent of Reynolds number, and that an overestimation of the resolution requirements would at most result in a fixed penalty factor in computer time.

The situation is different for wall-bounded flows, in which the decrease of the integral scales in the neighborhood of the wall results in a number of anisotropic modes which increases with Reynolds number. The resolution requirements for LES depend, as a consequence, also on the Reynolds number and, although not as large as those of direct simulations, are at present the main limitation for the simulation of those flows (Chapman 1979). It is therefore important in those cases to understand the exact requirements and their causes.

1 Also with the School of Aeronautics, U. Politécnica Madrid.

The present note is organized as follows. In §2 we review the experimental evidence on the anisotropy of the small scales and, in particular, on the dependence of the subgrid off-diagonal stresses with the size of the filter. This section also includes information on the equivalent width to be used for this purpose in anisotropic filters. The predicted stresses are compared in §3 to those obtained by a standard dynamic Smagorinsky model, and a criterion is established for the resolution needed to achieve a given error in the mean flow. The number of computational modes required for large-eddy simulations is estimated from these arguments in §4, and guidelines are offered for further work.

2. The anisotropy of the subgrid stresses

2.1 Spectral information

Although it is generally accepted that the small scales of turbulent flows are isotropic, quantitative measurements are rare (see Saddoughi & Veeravalli, 1994, for a recent experiment and for a review of older results). From the point of view of LES, what is needed is a characterization of the isotropy of the subgrid Reynolds stress tensor. Consider the spectral energy tensor Φ_{ij}, which is a function of the wavenumber vector $\mathbf{k}$. If it is normalized so that $\int \Phi_{ij} \, d\mathbf{k} = \overline{u_i u_j}$, the truncated integral

$$\tau_{ij}(k) = \int_{|\mathbf{k}|>k} \Phi_{ij} \, d\mathbf{k}, \qquad (2.1)$$

represents the subgrid stress tensor corresponding to a sharp filter with cut-off k. For each k it is then possible to define a stress anisotropy tensor,

$$A_{ij} = \frac{\tau_{ij}}{\tau_{kk}} - \frac{1}{3}\delta_{ij}, \qquad (2.2)$$

where repeated indices imply summation, and its L_2 norm, normalized as

$$\alpha = (A_{ij}A_{ij}/3)^{1/2}, \qquad (2.3)$$

measures the anisotropy of the subgrid stresses. It is proportional to the root mean square deviation of the principal stresses with respect to their mean value, normalized with the subgrid energy. It reaches a maximum value of $\alpha \approx 0.47$ for a completely uni-axial stress and is zero for an isotropic tensor.

In practice this quantity is seldom available, and the one-dimensional spectral tensor $\Theta_{ij}(k_1)$, obtained by integrating Φ_{ij} over the two remaining wavenumber components, is used as a surrogate. The subgrid stresses are then estimated by

$$\tau_{ij}(k) = \int_k^\infty \Theta_{ij} \, dk_1, \qquad (2.4)$$

which corresponds to applying a one-dimensional sharp filter with cut-off $k_1 = k$ along the streamwise direction.
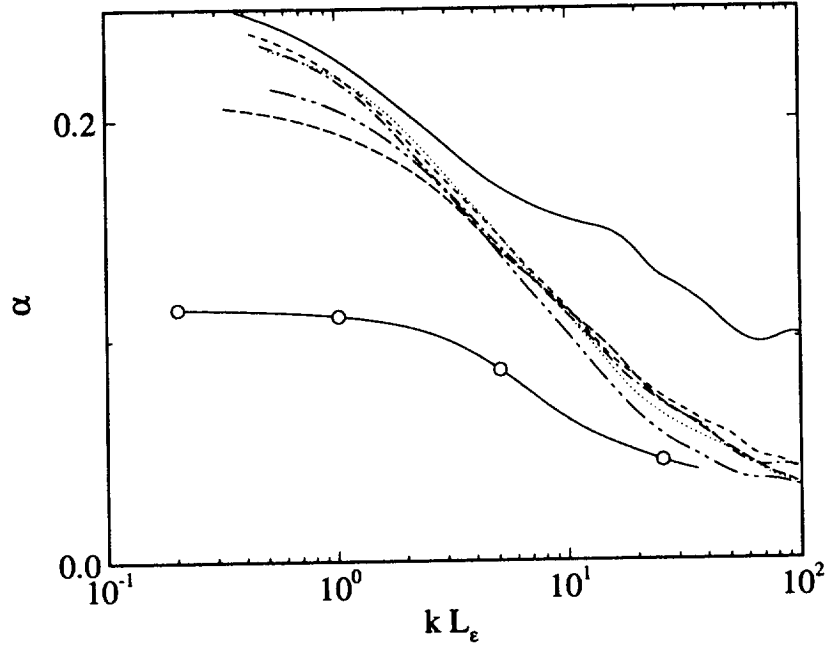
FIGURE 1. Root-mean square subgrid stress anisotropy as a function of the cut-off wavenumber for sharp Fourier filtering. Non-equilibrium boundary layer in an adverse pressure gradient (Marušić & Perry 1995): $Re_\tau = 1253$, $(\delta^*/\tau_w)\,dP/dx = 7.16$. ——— , $y/\delta = 0.049$; ——— , 0.069; ——·—— , 0.095; ········ , 0.168; ——··—— , 0.328; ———— , 0.630. Circular jet from (Bradshaw, Ferris & Johnson 1964): ——o—— . $UR/\nu = 1.7 \times 10^5$, $x/R = 4$, $y/R = 1$.

The issues involved in this substitution are discussed by Batchelor (1953) for the particular case of isotropic turbulence where, within the inertial range, isotropy implies that $\Theta_{22} = \Theta_{33} = \frac{4}{3}\Theta_{11}$. In a more general case the substitution cannot be completely compensated. In the experiments discussed below, it has been taken approximately into account by premultiplying Θ_{11} by 4/3. Even so, the anisotropy becomes uncertain as it approaches the value $\alpha \approx 0.04$, which corresponds to a tensor whose principal stresses are in the ratio (1, 4/3, 4/3).

Two experimental flows are analyzed in this way in Fig. 1: a non-equilibrium boundary layer in a strong adverse pressure gradient (Marušić & Perry 1995), and a circular jet (Bradshaw, Ferris & Johnson 1964). Several wall distances are used in the boundary layer and, in all cases, the streamwise wavenumber is normalized with the integral dissipation length $L_\epsilon = q^3/\epsilon$, where $q^2 = \overline{u_i u_i}$, and ϵ is the energy dissipation rate. The integral dissipation length is always of the same order as the integral scales of the flow and is generally much easier to compute. It can be seen that, although the large scales are fairly different in both flows, they become essentially isotropic for $kL_\epsilon > 50$, corresponding to a filter of width $\Delta x = 2\pi/k \approx L_\epsilon/10$. The exception is the station of the boundary layer very close to the wall, $y^+ \approx 60$, which either does not reach isotropy or does it very slowly. The microscale Reynolds

number is comparable in both cases, $Re_\lambda \approx 150 - 200$, even in the neighborhood of the wall. The differences observed in the behavior of the near-wall spectrum are probably not due to low Reynolds number effects.

Perhaps more relevant to LES is the total, rather than relative, stress anisotropy. Figure 2(a) contains subgrid spectra of the total anisotropic stress, $\tau_A = \alpha^2 \tau_{ii}(k)$, while Fig. 2(b) displays spectra of the $\tau_{12}(k)$, which is the only off-diagonal stress which does not vanish identically in these experiments. All the spectra have been normalized to unity at $k = 0$ and give the fraction of the stresses that would have to be represented by a subgrid model.

The classical scale similarity theory for the cospectrum predicts $\Phi_{12} \sim k^{-7/3}$ (Lumley 1967), which would translate into $\tau_{12} \sim k^{-4/3}$ for the accumulated subgrid cospectrum. A line with this slope has been included in both Fig. 2(a) and (b), but it fits the data only approximately. As in the analysis of the previous figure, it follows from this one that $kL_\epsilon \approx 100$ marks the 'engineering' limit of anisotropic turbulence. The anisotropic subgrid stresses beyond that limit are less than 1% of the total, and even gross errors in their prediction would have a slight effect on the mean flow.

2.2 Triaxial filters

The analysis in the previous section was restricted to one-dimensional filters by the experimental information at hand. A full study of the subgrid stresses under generic triaxial filtering requires knowledge of the full spectral tensor or, equivalently, of the full three-dimensional autocorrelation tensor of the velocities. Both tensors are related by a Fourier transform. The correlation tensor $R_{ij}(\mathbf{x}, \mathbf{x}') = \langle u_i(\mathbf{x}), u_j(\mathbf{x}') \rangle$, where $\langle \rangle$ stands for averaging, is a function of the two points $\mathbf{x}$ and $\mathbf{x}'$ and only becomes a function of the relative displacement $\mathbf{x} - \mathbf{x}'$ along the homogeneous directions of the flow. In the general case it is a six-dimensional object that is seldom compiled in experiments or computations.

If a filter is defined as a convolution

$$\bar{u} = \int g(x, x')u(x')\,\mathrm{d}x',$$ (2.5)

the exact filtered second-order statistics can be obtained from the correlation tensor by a double filtering operation (Jiménez & Moser 1997),

$$R_{\bar{u}\bar{v}}(x, x') = \int\int R_{uv}(\xi, \xi')g(x, \xi)g(x', \xi')\,\mathrm{d}\xi\,\mathrm{d}\xi'.$$ (2.6)

For $x = x'$, we recover the filtered one-point second order statistics $R_{\bar{u}\bar{v}}(x, x) = \langle \bar{u}\,\bar{v} \rangle$, and the subgrid stresses can be obtained by subtracting the filtered from the unfiltered values, $\tau_{uv} = R_{uv} - R_{\bar{u}\bar{v}}$. Besides being applicable to inhomogeneous flows, this procedure has the advantage of requiring only the small-separation correlation tensors (over separation distances less than or equal to the longest desired filter length), thus relaxing somewhat the storage and computational requirements of dealing with such high-dimensional objects.
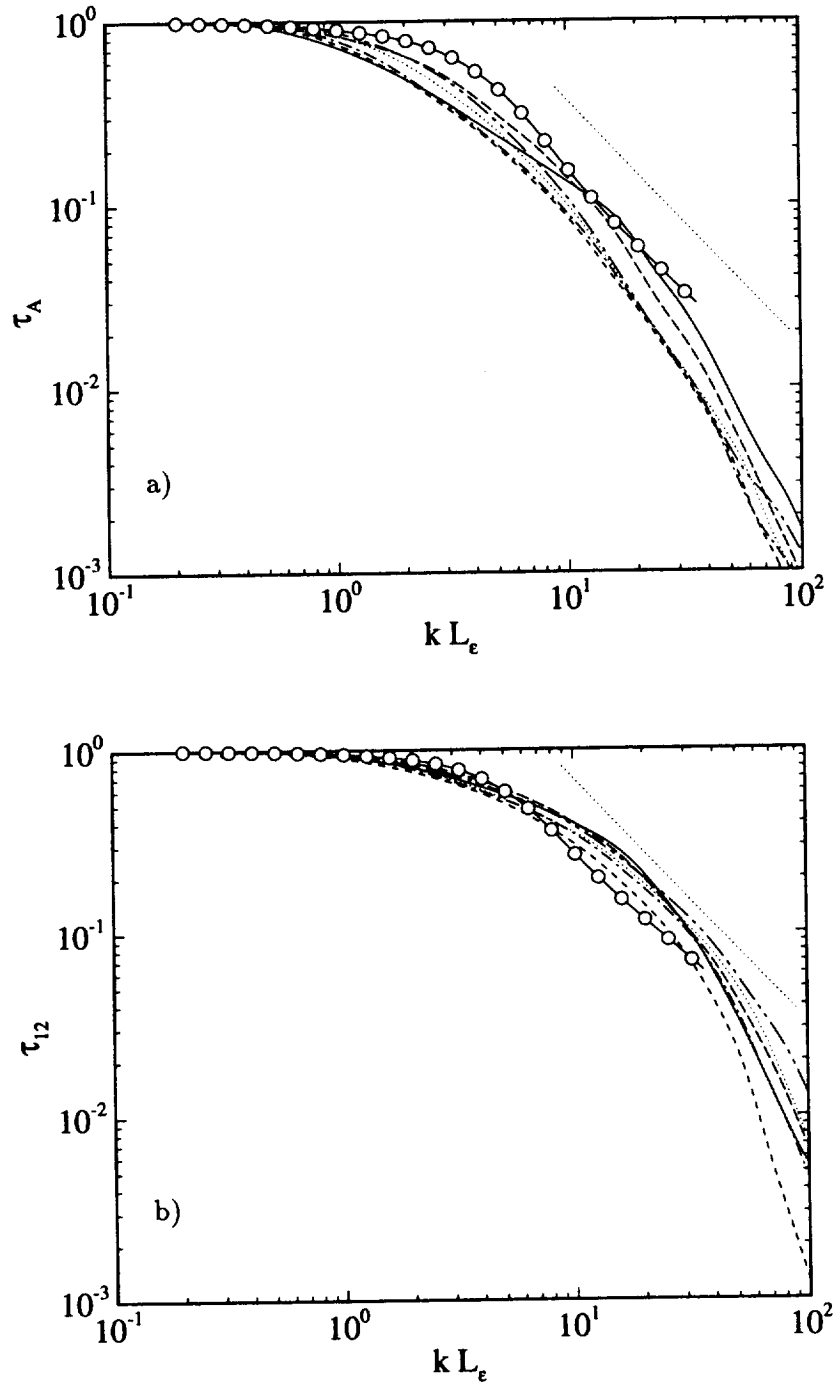
FIGURE 2.   Subgrid stress spectra for the experiments in Fig. 1.   (a) Total anisotropic stress. (b) Off-diagonal component, τ_{12}. Symbols as in Fig. 1. The two dotted straight lines have spectral slope $k^{-4/3}$, as suggested by the inertial theory for the cospectrum.

A compilation of data intended for the validation of LES has recently become available (AGARD 1998), and contains correlation data for several flows. The boundary layer spectra used in the previous section also belong to this collection. Here we use data from a $Re_\tau = 590$ channel computed by Mansour, Moser & Kim (1997) to obtain scaling information for the subgrid stresses under anisotropic filters. The data are compiled at seven locations in the channel, $y^+ = 60 - 500$, and two types of filters are used: a simple box filter

$$g = (\delta_1\delta_2\delta_3)^{-1}, \qquad \text{for} \quad |x_i - x_i'| < \delta_i/2, \qquad i = 1\ldots3, \tag{2.7}$$

which vanishes for $|x_i - x_i'| > \delta_i/2$, and a Gaussian one adjusted so that its variance is the same as that of the box filter in each direction. Each of the δ_i are varied independently in the range from zero (actually the computational grid spacing of a few wall units) to $\delta_i \approx 0.14H$, where H is the half-width of the channel. This generates approximately 700 filter combinations at each location, and the fractional subgrid stresses $\tau_{ij}/\langle u_i u_j \rangle$ are compiled in each case.

The equivalent width to be used for anisotropic filters was first considered by Deardorff (1970) and has been discussed since then by Schuman (1975), Lilly (1988), and Scotti, Meneveau & Fatica (1996). A popular choice is $\Delta = (\delta_1\delta_2\delta_3)^{1/3}$, which was first proposed by Deardorff and which can be approximately justified by considering the integrated dissipation in a Kolmogorov spectrum outside the wavenumber ellipsoid that represents the filter. That scale is, however, not necessarily relevant for the prediction of the subgrid stresses since their spectral tensor is very different from that of the dissipation, and the dominant contributions to the former are due to the anisotropic large scales rather than to the isotropic ones which dominate the latter. In fact, the subgrid stresses from the different filters collapse very poorly when plotted against isotropic combinations of the widths, as seen in Figs. 3A(a)-3B(a). Note that, although we have used in those figures a quadratic combination, the performance of the Deardorff criterion is actually poorer.

It turns out that the optimum collapse of each subgrid stress is obtained for a different combination of δ's. By adjusting the coefficients of the squares to obtain a minimum scatter we find, for example, that the best equivalent width for τ_{11} is (Fig. 3A(b))

$$\Delta_{11} = (\delta_1^2 + 2\delta_2^2 + 2\delta_3^2)^{1/2}. \tag{2.8}$$

This is easily understood by assuming that turbulence is approximately isotropic, even in this shear flow. For small separations we can approximate the correlation function by

$$R_{11}/\langle u_1 u_1 \rangle = 1 - \sum \frac{(x_i' - x_i)^2}{2\lambda_{11,i}^2} + \ldots, \tag{2.9}$$

and it follows from isotropy that the longitudinal and transverse Taylor microscales are related by (Batchelor 1953)

$$\lambda_{11,1}^2 = 2\lambda_{11,2}^2 = 2\lambda_{11,3}^2. \tag{2.10}$$

FIGURE 3A. Subgrid stresses in a channel flow (Mansour, Moser & Kim 1997) using triaxial filters: τ_{11} component. +, box filter. Figure (a) uses $\Delta = (\delta_1^2 + \delta_2^2 + \delta_3^2)$ in the abscissa. Figure (b) uses Δ_{11} given by (2.8). $Re_\tau = 590$, $y^+ = 300$.
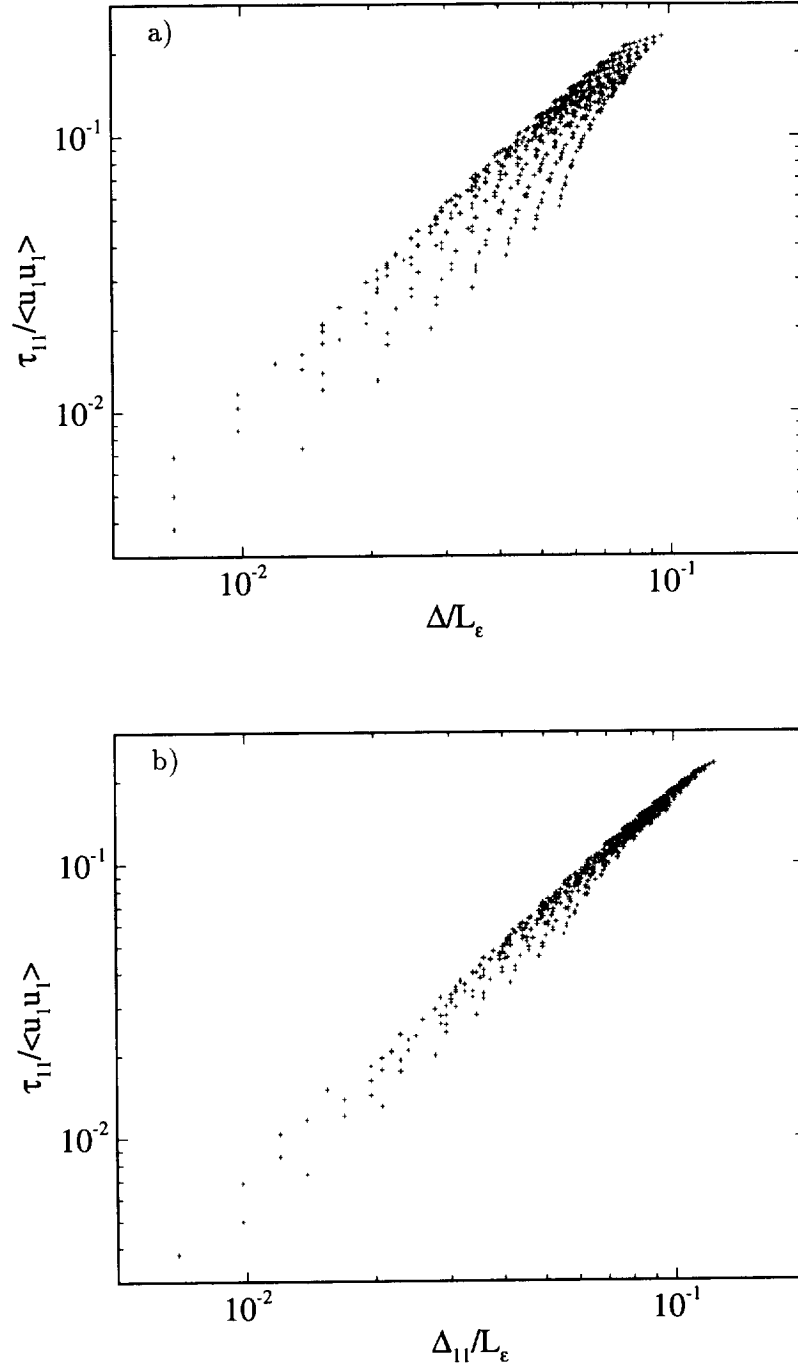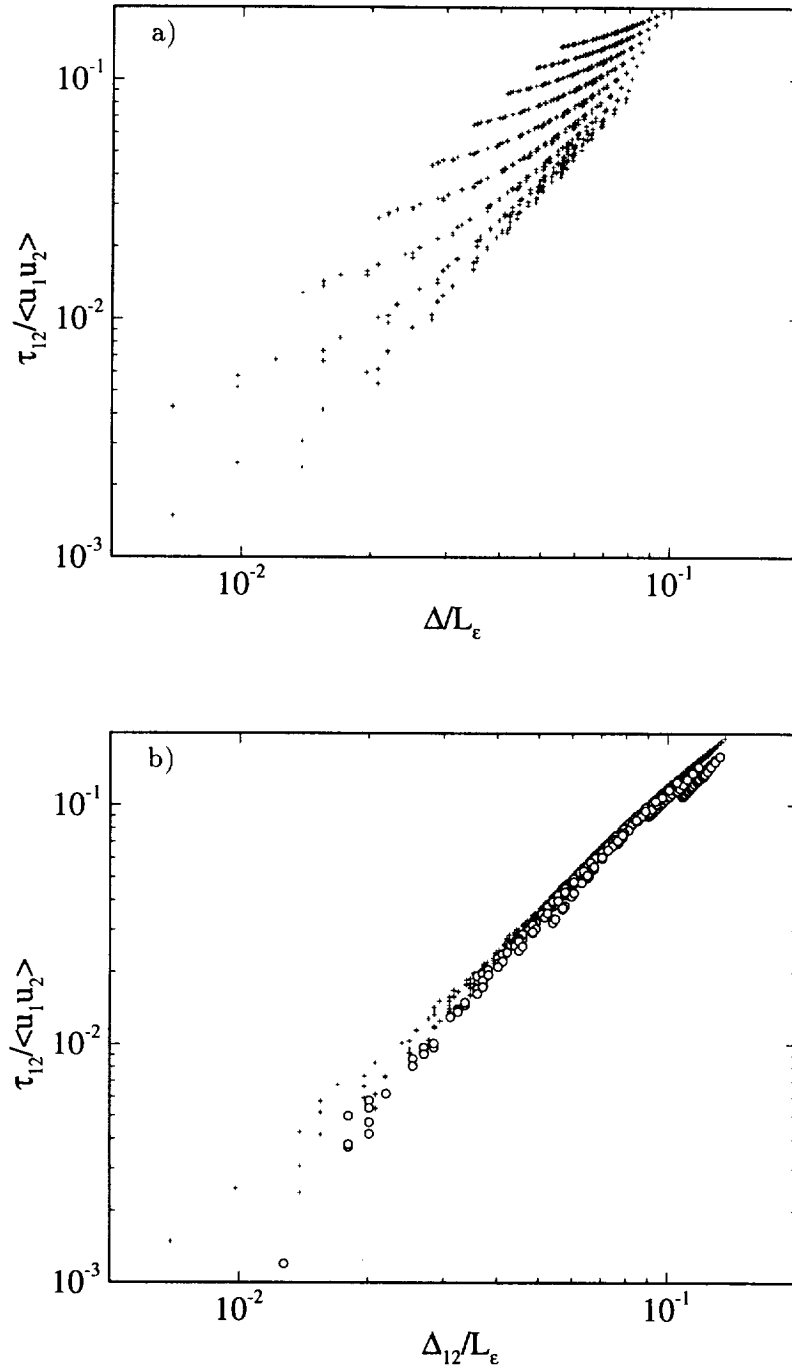
FIGURE 3B.   Subgrid stresses in a channel flow (Mansour, Moser & Kim 1997) using triaxial filters: τ_{12} component. + , box filter; o , Gaussian. Figure (a) uses $\Delta = (\delta_1^2 + \delta_2^2 + \delta_3^2)$ in the abscissa. Figure (b) uses Δ_{12} given by (2.13). $Re_\tau = 590$, $y^+ = 300$.

If we remember that the filtered stresses are essentially the integral of (2.9) within a box defined by the filter, it is reasonable to expect that the relevant scale combination should weigh the different widths with the curvatures of the function along each axis. This, together with (2.10), leads to (2.8). Applying the same argument to R_{22} and R_{33} suggests that the right combinations for τ_{22} and τ_{33} should be

$$\Delta_{22} = (2\delta_1^2 + \delta_2^2 + 2\delta_2^2)^{1/2}, \qquad (2.11)$$

$$\Delta_{33} = (2\delta_1^2 + 2\delta_2^2 + \delta_3^2)^{1/2}. \qquad (2.12)$$

Although they are not shown in the figure, these predictions turn out to be correct.

The isotropic theory does not give information on the scaling of the off-diagonal stresses, which vanish identically in that case. The empirical optimum combination for the present channel is very close to (Fig. 3B(b))

$$\Delta_{12} = (\delta_1^2 + \delta_2^2 + 4\delta_3^2)^{1/2}, \qquad (2.13)$$

which is simple enough to suggest that a theoretical explanation should exist, probably as a perturbation of the isotropic theory including weak shear. Also in this case it is easy to check that the scaling factors correspond to the curvatures of the correlation function in the neighborhood of the origin. It is clear, on the other hand, that these scalings can only be approximations, valid for a particular range of filter scales which are comparable to the Taylor microscale. Much wider filters act on regions of the correlation functions which are not well described by the parabolic approximation (2.9), and they should not scale well with the Taylor microscales. Also, other flows are intrinsically anisotropic, and the isotropic approximation that holds here would not apply to them. Some preliminary tests on homogeneous shear flows (Rogers & Moin 1987, Sarkar 1995) suggest that, although simple quadratic combinations also work well for them, they are different from the ones above. Note that the results of the Gaussian filters have been included in Fig. 3B(b), and that they approximately agree with those of the box filters.

The use of the integral dissipation length to scale the equivalent filters works well here as it did for the spectra in the previous section. In Fig. 4 we have compiled data from several locations in the channel, among which the integral dissipation length varies by up to a factor of two and the collapse of τ_{12} is maintained.

3. Simulations

To compare the subgrid stresses predicted above with those actually provided by standard LES models, we undertook a set of simulations of a plane channel at $Re_\tau \approx 1,000$. They use a multiblock code which allows a high resolution to be maintained near the walls while varying the grid in the center of the channel. This avoids the issues of the representation of the flow near the wall, which are known to be important, while permitting a systematic survey of the effect of the resolution in the central part of the flow. The code itself and its performance across block boundaries are described by Kravchenko, Moin & Moser (1996). It uses a

double Fourier expansion in the periodic streamwise and spanwise directions, and second-order splines normal to the wall. Three computations are analyzed here, all of them using a box of size $2\pi \times 2 \times \pi/2$. The spanwise dimension is narrow for an accurate representation of the central core region, but it should be wide enough for the logarithmic range below $y^+ \approx 500$. The three simulations are comparable to each other except for the resolution. They all use standard dynamic Smagorinsky subgrid modeling with the proportionality constant averaged over planes parallel to the walls.

The first simulation uses a single-block grid $48 \times 64 \times 48$ in the streamwise, normal, and spanwise dimensions. It was checked against a previous simulation on a somewhat larger box ($2\pi \times 2 \times \pi$) at higher resolution, $96 \times 100 \times 96$, and it is considered to be approximately correct. The two other simulations use the same grid near the walls ($48 \times 21 \times 48$), but the horizontal resolution is decreased in a central block, which contains 22 points for the region above $y^+ \approx 250$. The horizontal grids in this region are 24×24, and 16×16. The horizontal resolution of the finer grid is $\Delta x^+ \times \Delta z^+ \approx 130 \times 30$ and becomes respectively two and three times coarser for the other two grids. The wall-normal resolution is identical in all cases and varies from $\Delta y^+ \approx 0.5$ near the wall to $\Delta y^+ \approx 100$ at the center of the channel.

In each case the fraction of the mean subgrid shear stress τ_{12} due to the model was recorded as a function of y. It is given in Fig. 4 in terms of a reduced 'filter' size computed from the local grid spacing using (2.13) and normalized with the local integral dissipation length. Only points in the central block and at least two grid points away from the zonal boundaries are used. Included for comparison are the subgrid fractions of the same quantity obtained in the previous section (Fig. 3d) by explicit filtering of the direct channel simulation.

It is remarkable that both sets of data collapse reasonably well within themselves, taking into account that they represent filters of widely varying aspect ratios at locations in the channel that span from the inner logarithmic region to the central core. They do not, however, agree with each other. The measured subgrid stresses are consistently below those predicted by explicit filtering, by a factor of about 3–4.

Note that the two sets are not strictly comparable since the filtering results are plotted against a known filter width, while the filter width in the simulation is assumed proportional to the grid size with the grid acting as an unknown implicit filter. They should therefore not be expected to agree exactly with each other, but the disagreement is in the wrong direction. Even if the effect of the grid is not well understood, it is clear that it cannot represent features smaller than the grid spacing. This implies that the stresses in the subgrid eddies should correspond to filters at least as wide as the grid, and probably wider, while the only way to collapse the two sets of data in the figure would be to assume that the grid is acting as a filter three times narrower than itself. The only possible conclusion is that the subgrid model is providing at most about 20–30% of the shear stress that it should, in rough agreement with the results obtained by Bardina *et al.* (1983) from *a-priori* testing of the Smagorinsky model.
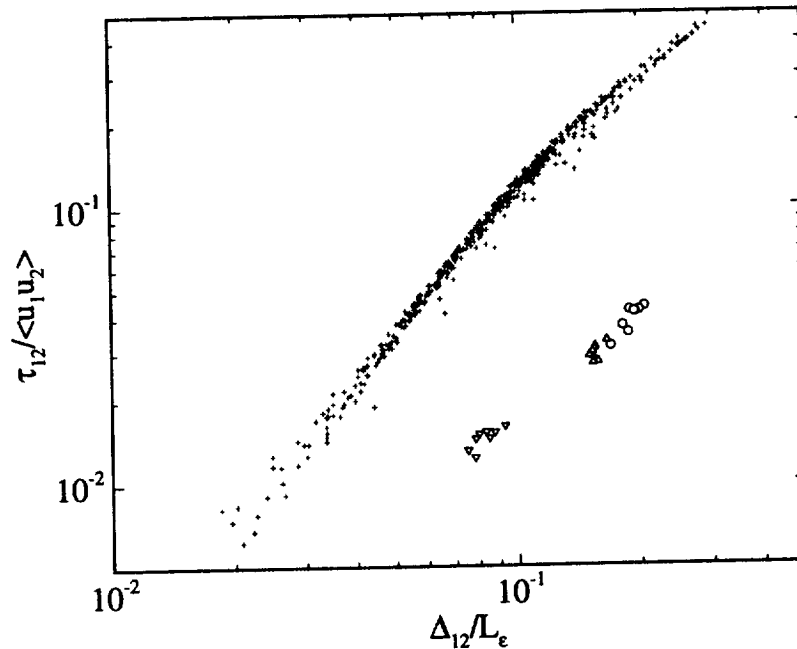
FIGURE 4. Fraction of the subgrid shear stress carried by the dynamic Smagorinsky model, compared with what should be carried at a comparable filtering size. LES simulations of channel at $Re_\tau \approx 1000$, $y^+ > 300$. Resolution in central block: o , 16×16; $\triangle$, 24×24; $\triangledown$: 48×48. Resolution near the wall is always 48×48. + , subgrid τ_{12} obtained by explicit box filtering on a channel at $Re_\tau = 590$, as in Fig. 3. $y^+ > 90$.

It follows that, if the shear stress is underrepresented by the model, the velocity profile should adjust itself until the total stress is that of an equilibrium channel, which varies linearly between the two walls. The errors in the mean velocity profile should then become worse as the resolution is made coarser, making the model responsible for a larger fraction of the total stresses. This can be seen to be true in Fig. 5, which shows the Kármán constant computed from each simulation. It agrees reasonably well with the accepted experimental value $\kappa \approx 0.4$, in the finer grid, where the subgrid stress should be in the range of 5–8% (Fig. 4). Even if in this case the modeled stresses are only about 1%, the total error is 5%, and the effect on the mean flow is slight. In the coarser simulation, it follows from the figure that the subgrid stresses should be of the order of 20%, while those provided by the model are only about 5%. The resulting 15% error translates into an error of the same order of magnitude in the Kármán constant and in the mean profile.

4. Discussion and conclusions

4.1 Degrees of freedom

The analysis in the previous sections suggests that accurate subgrid models for
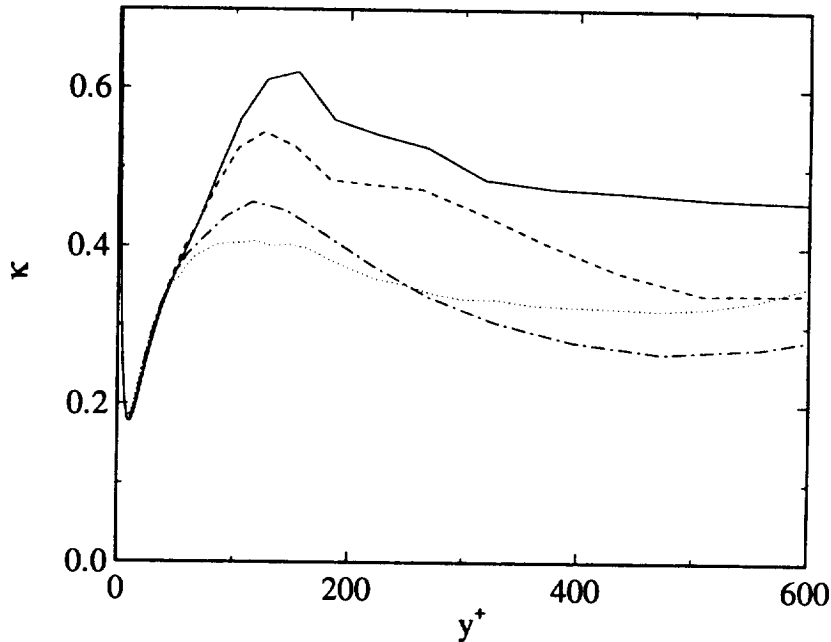
FIGURE 5.   Kármán constant, $\kappa = (y\partial U^+/\partial y)^{-1}$, computed from the large-eddy simulations in Fig. 4. Resolution in central block: ——— , 16 × 16; ---- , 24 × 24; —·— , 48 × 48. ········ , single-block computation on a 96 × 100 × 96 grid, in a larger box, $2\pi \times 2 \times \pi$; included for comparison.

the Reynolds stresses, which are large-scale properties of the flow, may not be strictly necessary in all practical LES. They can be avoided by refining the LES filter until the fraction of the stresses to be modeled becomes negligible, and this happens at a fixed fraction of the integral dissipation length, $\Delta x \approx L_\epsilon/10$. Besides the evidence from the experiments analyzed above, this is a consequence of the form of the spectra of the subgrid stresses, which decay approximately as $k^{-2/3}$ for the isotropic components and as $k^{-4/3}$ for the anisotropic ones. The integral scale is defined by the peak of the energy spectrum, and the decay of the stresses is therefore measured with respect to it. In the cases in which turbulence is driven by large-scale shear, the energy-containing eddies are controlled by the geometry, and the previous argument shows that modeling the stresses correctly requires filters which are a fixed fraction of the geometric scale. This implies that, for situations in which L_ϵ is approximately uniform, as in free shear flows, only a few thousand degrees of freedom need to be computed explicitly, independently of the Reynolds number. All the stresses are contained essentially in them.

Note that the last part of this argument may not be valid if the turbulent forcing is due to factors other than the geometry, in which case the integral scales can be smaller than the geometric ones and may depend on the Reynolds number. Such may be the case, for example, in two phase flows and in turbulent natural convection.

The situation is different for the rate of energy dissipation, which is associated

with eddies of the order of the Kolmogorov scale $\eta \sim L_\epsilon Re^{-3/4}$ and which has to be estimated correctly to avoid the accumulation of energy in the small scales (Jiménez 1993, 1995). In the absence of good subgrid models for the dissipation, this would require the computation of all the eddies down to the level of η and would lead to the well known estimate of the number of degrees of freedom in direct simulations, $N_T \sim Re^{9/4}$. What the previous analysis suggests is that modeling the dissipation and the stresses are different tasks, with different requirements, and could possibly be handled by different models. It also shows that, while modeling the former is an absolute requirement for practical simulations, modeling the latter may not be crucial.

The previous arguments do not apply in the neighborhood of a wall. While the data discussed above shows that the anisotropic modes are confined to eddies larger than a given fraction of the integral scales even in the logarithmic wall layer, the integral scales decrease as we approach the wall. Consider a fluid volume whose size $L_{\epsilon 0}^3$ is determined by the geometric scales, such as the channel half-width. In the neighborhood of the wall the integral length decreases linearly as $L_\epsilon \sim y$, and the eddies remain anisotropic above $\Delta x \sim y$. The number of anisotropic modes in a slab of thickness $\mathrm{d}y$ is then $\mathrm{d}N \sim L_{\epsilon 0}^2 \, \mathrm{d}y / \Delta x^3$, and their total number is given by the integral

$$N_T \sim \int_{y_0}^{\infty} L_{\epsilon 0}^2 \, \mathrm{d}y / y^3 \sim L_{\epsilon 0}^2 / y_0^2, \qquad (4.1)$$

where y_0 is some inner wall distance that determines the number of modes. If, in the absence of a good model for anisotropic turbulence, we choose this limit as a fixed number of viscous wall units, $y_0 = \nu y_0^+ / u_\tau$, the number of anisotropic modes becomes

$$N_T \sim (u_\tau L_{\epsilon 0} / \nu)^2 = Re_\tau^2, \qquad (4.2)$$

which is only slightly lower than the estimation for direct numerical simulation and which increases without limit with the Reynolds number. Note that this estimation is not linked to a particular numerical model, being just a count of the number of 'non-Kolmogorov' modes per unit volume of wall turbulence. These modes depend on more parameters than the rate of energy dissipation, and they are unlikely to be modeled correctly by isotropic approximations of the Smagorinsky type.

Note also that improving the subgrid models so that they represent a higher fraction of the stresses, so that the filter can be chosen as a higher fraction of the integral scale, would only modify the numerical coefficient in (4.2), but not its Reynolds number dependence. The only alternatives to decrease substantially the explicitly computed number of modes would be to improve the subgrid models to represent correctly *all* the Reynolds stresses, even above the integral scale, or to stop the computation at some distance y_0 from the wall, expressed in outer, rather than wall, units.

4.2 Conclusions and future work

We have shown that the anisotropic subgrid stresses are confined in practice to eddies larger than about one tenth of the local integral dissipation scale, and we have

given criteria to compute the equivalent width, for this purpose, of triaxial filters in weakly sheared, quasi-equilibrium, flows. We have also shown that Smagorinsky-type dynamic subgrid models, while representing the energy dissipation correctly, are not able to reproduce the stresses. They only work if the filter widths are chosen so that the subgrid stresses to be modeled are a negligible fraction of the total. The errors due to the model then become unimportant.

For free shear flows this results in a number of degrees of freedom that have to be computed explicitly, which is independent of the Reynolds number, of the order of a few thousands. This would make LES a practical alternative in many applications.

For wall bounded flows the same criterion results in a number of anisotropic, 'non-Kolmogorov', modes which scales like Re_τ^2, most of which are concentrated near the wall. To avoid this Reynolds number dependence, the two alternatives are either to develop better models which are able to describe correctly the full shear stresses, or to find wall representations which can be applied at distances which do not scale in wall units.

Some preliminary tests of mixed Bardina-type models (Vreman, Geurts & Kuerten 1994) disappointingly gave worse results than the Dynamic Smagorinsky model at comparable resolutions, but more work is needed before that line is abandoned. The conclusions of the present work also need to be extended to more general non-equilibrium flows.

Acknowledgments

REFERENCES

AGARD 1998 A selection of test cases for the validation of large-eddy simulations of turbulent flows. *AR-345.*

BARDINA, J., FERZIGER, J. H. & REYNOLDS, W. C. 1983 Improved turbulence models based on large-eddy simulation of homogeneous, incompressible, turbulent flows. *Thermosciences Div. Rep.* **TF-19,** Stanford Univ.

BATCHELOR, G. K. 1953 *The theory of homogeneous turbulence.* Cambridge Univ. Press.

BRADSHAW, P., FERRIS, D. H. & JOHNSON, R. H. 1964 Turbulence in the noise-producing region of a circular jet. *J. Fluid Mech.* **19,** 591-624.

CHAPMAN, D. R. 1979 Computational aerodynamics development and outlook. *AIAA J.* **17,** 1293-1313.

CLARK, R. A., FERZIGER, J. H. & REYNOLDS, W.C. 1979 Evaluation of subgrid-scale models using an accurately simulated turbulent flow. *J. Fluid Mech.* **91,** 1-16.

DEARDORFF, W. 1970 A numerical study of three-dimensional turbulent channel flow at large Reynolds numbers. *J. Fluid Mech.* **41**, 453-480.

GERMANO, M., PIOMELLI, U., MOIN, P. & CABOT, W. H. 1991 A dynamic subgrid scale eddy viscosity model. *Phys. Fluids.* A(3), 1760-1765. Erratum, *Phys. Fluids* A **3**, 3128.

JIMÉNEZ, J. 1993 Energy transfer and constrained simulations in isotropic turbulence. *CTR Res. Briefs*, Center for Turbulence Research, NASA Ames/Stanford Univ., 171-186.

JIMÉNEZ, J. 1995 On why dynamic subgrid-scale models work. *CTR Res. Briefs*, Center for Turbulence Research, NASA Ames/Stanford Univ., 25-34.

JIMÉNEZ, J. & MOSER, R.D. 1997 Data filtering and file formats, §2 of. *AGARD. AR-345*, 5-8.

KOLMOGOROV, A. N. 1941 The local structure of turbulence in incompressible viscous fluids a very large Reynolds numbers. *Dokl. Nauk. SSSR.* **30**, 301-305 (see e.g. L. D. Landau & E. M. Lifshitz, 1959, *Fluid mechanics*, Pergamon, 116-123).

KRAVCHENKO, A. G., MOIN, P. & MOSER, R. D. 1996 Zonal embedded grids for numerical simulations of wall-bounded turbulent flows. *J. Comp. Phys.* **127**, 412-423.

LILLY,D. 1988 The length scale for sub-grid-scale parameterization with anisotropic resolution. *CTR Res. Briefs*, Center for Turbulence Research, NASA Ames/Stanford Univ., 3-9.

LUMLEY, J. L. 1967 Similarity and turbulent energy spectrum. *Phys. Fluids.* **10**, 855-858.

MANSOUR, N. N., MOSER, R. D. & KIM, J. 1996 Reynolds number effects in low Reynolds number turbulent channels. *In preparation.*

MARUŠIĆ, I. & PERRY, A. E. 1995 A wall-wake model for the turbulence structure of boundary layers. Part 2. Further experimental support. *J. Fluid Mech.* **298**, 389-407. Case TBL10 in AGARD (1997).

MOIN, P. 1997 Progress in large eddy simulation of turbulent flows. *AIAA Paper.* **97-0749.**

MOIN, P. & JIMÉNEZ, J. 1993 Large eddy simulation of complex turbulent flows. *AIAA Paper.* **93-3099.**

ROGERS, M. M. & MOIN, P. 1987 The structure of the vorticity field in homogeneous turbulent flows. *J. Fluid Mech.* **176**, 33-66.

SARKAR, S. 1995 The stabilizing effect of compressibility in turbulent shear flow. *J. Fluid Mech.* **282**, 163-186.

SADDOUGHI, S. G. & VEERAVALLI, S. V. 1994 Local isotropy in turbulent boundary layers at high Reynolds number. *J. Fluid Mech.* **268**, 333-372.

SCHUMANN, U. 1975 Subgrid-scale model for the finite-difference simulations of turbulent flows in plane channels and annuli. *J. Comput. Phys.* **18**, 376-404.

SCOTTI, A., MENEVEAU, C. & FATICA, M. 1996 Dynamic Smagorinsky model on anisotropic grids. *Proceedings CTR 1996 Summer Program,* Center for Turbulence Research, NASA Ames/Stanford Univ., 259-274.

VREMAN, B., GEURTS, B. & KUERTEN, H. 1994 On the formulation of the dynamic mixed subgrid-scale model. *Phys. Fluids.* **6**, 4057-4059.

A general theory of discrete filtering
for LES in complex geometry

By Oleg V. Vasilyev AND Thomas S. Lund

1. Motivation and objectives

In large eddy simulation (LES) of turbulent flows, the dynamics of the large scale structures are computed while the effect of the small scale turbulence is modeled using a subgrid scale model. The differential equations describing the space-time evolution of the large scale structures are obtained from the Navier-Stokes equations by applying a low-pass filter. In order for the resulting LES equations to have the same structure as the Navier-Stokes equations, the differentiation and filtering operations must commute. In inhomogeneous turbulent flows, the minimum size of eddies that need to be resolved is different in different regions of the flow. Thus the filtering operation should be performed with a variable filter width. In general, filtering and differentiation do not commute when the filter width is non-uniform in space.

The problem of non-commutation of differentiation and filtering with non-uniform filter widths was studied by Ghosal and Moin (1995), who proposed a new class of filters for which the commutation error could be obtained in closed form. The application of this filter to the Navier-Stokes equations introduces additional terms (due to commutation error) which are of second order in the filter width. Ghosal and Moin suggested that the leading correction term be retained if high order numerical schemes are used to discretize the LES equations. This procedure involves additional numerical complexities which can be avoided by using the filters described in this report. Van der Ven (1995) constructed a family of filters which commute with differentiation up to any given order in the filter width; however, this approach is limited to a specific choice of filters and does not address the issue of additional boundary terms that would arise in finite domains.

Due to the lack of a straightforward and robust filtering procedure for inhomogeneous flows, most large eddy simulations performed to date have not made use of explicit filters. The nearly universal approach for LES in complex geometries is to argue that the finite support of the computational mesh together with the low-pass characteristics of the discrete differencing operators effectively act as a filter. This procedure will be referred to as implicit filtering since an explicit filtering operation never appears in the solution procedure. Although the technique of implicit filtering has been used extensively in the past, there are several compelling reasons to adopt a more systematic approach. Foremost of these is the issue of consistency. While it is true that discrete derivative operators have a low-pass filtering effect, *the associated filter acts only in the one spatial direction in which the derivative is taken.* This fact implies that each term in the Navier-Stokes equations is acted on by a distinct one-dimensional filter, and thus there is no way to derive the discrete

equations through the application of a single three-dimensional filter. Considering this ambiguity in the definition of the filter, it is nearly impossible to make detailed comparisons of LES results with filtered experimental data. In the same vein it is not possible to calculate the Leonard term (Leonard, 1974) that appears as a computable portion in the decomposition of the subgrid-scale stress.

The second significant limitation of the implicit filtering approach is the inability to control numerical error. Without an explicit filter, there is no direct control in the energy in the high frequency portion of the spectrum. Significant energy in this portion of the spectrum coupled with the non-linearities in the Navier-Stokes equations can produce significant aliasing error. Furthermore, all discrete derivative operators become rather inaccurate for high frequency solution components, and this error interferes with the dynamics of the small scale eddies. This error can be particularly harmful (Lund and Kaltenbach, 1995) when the dynamic model (Germano *et al.*, 1991; Ghosal *et al.*, 1995) is used since it relies entirely on information contained in the smallest resolved scales. In addition, it is difficult to define the test to primary filter ratio which is needed as an input to the dynamic procedure.

The difficulties associated with the implicit filtering approach can be alleviated by performing an explicit filtering operation as a part of the solution process. By damping the energy in the high frequency portion of the spectrum, it is possible to reduce or eliminate the various sources of numerical error that dominate this frequency range. Explicit filtering reduces the effective resolution of the simulation but allows the filter size to be chosen independently of the mesh spacing. Furthermore, the various sources of numerical error that would otherwise enter the stresses sampled in the dynamic model can be controlled, which can ultimately result in more accurate estimate for the subgrid scale model coefficient. Finally, the shape of the filter is known exactly, which facilitates comparison with experimental data and the ability to compute the Leonard term.

To realize the benefits of an explicit filter, it is necessary to develop robust and straightforward discrete filtering operators that commute with numerical differentiation. As mentioned above, the earlier works in this area required either adding corrective terms to the filtered Navier-Stokes equations or required the use of a restricted class of filters that could not account properly for non-periodic boundaries. The objective of this work is to develop a general theory of discrete filtering in arbitrary complex geometry and to supply a set of rules for constructing discrete filters that commute with differentiation to the desired order.

This report summarizes the essential results; the details of mathematical derivations and proofs are described by Vasilyev *et al.* (1997), hereafter denoted by VLM.

2. Accomplishments

2.1 Commutation error of filtering and differentiation operations

Consider a one-dimensional field $\psi(x)$ defined in a finite or infinite domain $[a, b]$. Let $f(x)$ be a monotonic differentiable function which defines the mapping from the domain $[a, b]$ into the domain $[\alpha, \beta]$, *i.e.* $\xi = f(x)$. $f(x)$ can be associated with

mapping of the non-uniform computational grid in the domain $[a, b]$ to a uniform grid of spacing Δ, where the non-uniform grid spacing is given by $h(x) = \Delta/f'(x)$.

Let $x = F(\xi)$ be the inverse mapping $(F(f(x)) = x)$. The filtering operation is defined in an analogous way as in (Ghosal and Moin, 1995). Given an arbitrary function $\psi(x)$, we obtain the new function $\phi(\xi) = \psi(F(\xi))$ defined on the interval $[\alpha, \beta]$. The function $\phi(\xi)$ is then filtered using the following definition:

$$\bar{\phi}(\xi) = \frac{1}{\Delta} \int_\alpha^\beta G\left(\frac{\xi - \eta}{\Delta}, \xi\right) \phi(\eta) d\eta, \tag{1}$$

where G is a filter function, which can have different shapes in various regions of the domain. This definition is more general then the one commonly used in the LES literature and, as will be shown later, is crucial for elimination of boundary terms in the commutation error. The introduction of filters of different shapes in different parts of the domain is necessitated by considering inhomogeneous (non-periodic) fields. If we assume that the function $\phi(\xi)$ is homogeneous (periodic) in $[\alpha, \beta]$, then a periodic filter can have the same shape throughout the domain.

The filtering operation in physical space can be written as

$$\bar{\psi}(x) = \frac{1}{\Delta} \int_a^b G\left(\frac{f(x) - f(y)}{\Delta}, f(x)\right) \psi(y) f'(y) dy. \tag{2}$$

Note that definitions (1) and (2) are equivalent. However, the filtering operation (1) in the mapped space is much easier to analyze and implement than (2), and we will use it throughout unless stated otherwise.

Let us consider first the commutation error of filtering and derivative operations in one spatial dimension. We define an operator that measures commutation error by

$$\left[\frac{d\psi}{dx}\right] \equiv \overline{\frac{d\psi}{dx}} - \frac{d\bar{\psi}}{dx}. \tag{3}$$

Introducing the change of variables $\eta = \xi - \Delta\zeta$, Eq. (1) can be rewritten as

$$\bar{\phi}(\xi) = \int_{\frac{\xi-\beta}{\Delta}}^{\frac{\xi-\alpha}{\Delta}} G(\zeta, \xi) \phi(\xi - \Delta\zeta) d\zeta. \tag{4}$$

Performing the formal Taylor series expansion of $\phi(\xi - \Delta\zeta)$ in powers of Δ and changing the order of summation and integration, we obtain

$$\bar{\phi}(\xi) = \sum_{k=0}^{+\infty} \frac{(-1)^k}{k!} \Delta^k M^k(\xi) D_\xi^k \phi(\xi), \tag{5}$$

where $D_\xi^k \equiv \frac{d^k}{d\xi^k}$ is the derivative operator and $M^k(\xi)$ is the k-th filter moment defined by

$$M^k(\xi) = \int_{\frac{\xi-\beta}{\Delta}}^{\frac{\xi-\alpha}{\Delta}} \zeta^k G(\zeta, \xi) d\zeta. \tag{6}$$

The series (5) may have either infinite or finite radius of convergence depending on the filter moments. For the discrete filters, as shown in VLM, the radius of convergence of the series is infinity.

Substituting (5) into (3) and skipping the algebra we obtain

$$\left[\frac{d\psi}{dx}\right] = \sum_{k=1}^{+\infty} A_k M^k(\xi)\Delta^k + \sum_{k=0}^{+\infty} B_k \frac{dM^k}{d\xi}(\xi)\Delta^k, \tag{7}$$

where A_k ($k \geq 1$) and B_k ($k \geq 0$) are, in general, nonzero coefficients. Thus, the commutation error is determined by the filter moments, $M^k(\xi)$, and mapping function, $F(\xi)$.

In this report we consider a general class of filters which satisfy the following properties:

$$M^0(\xi) = 1 \text{ for } \xi \in [\alpha, \beta]; \tag{8a}$$

$$M^k(\xi) = 0 \text{ for } k = 1, \ldots, n - 1 \text{ and } \xi \in [\alpha, \beta]; \tag{8b}$$

$$M^k(\xi) \text{ exist for } k \geq n. \tag{8c}$$

There are many examples of filters which satisfy these properties when the function $\phi(\xi)$ is defined in the domain $(-\infty, +\infty)$. One is the exponentially decaying filter defined in (Van der Ven, 1995). Another example is the correlation function of the Daubechies scaling function used in multi-resolution analysis for constructing orthonormal wavelet bases (Beylkin, 1995; Beylkin and Saito, 1993). Examples of such filters with 5, 9, and 17 vanishing moments and the corresponding Fourier transforms, $\hat{G}(k) = \int_{-\infty}^{+\infty} G(\xi)\exp(-ik\xi)d\xi$, are shown in Fig. 1.

We also note that the definition (8) does not require that the filter kernel be symmetric. This allows us to use a wider class of filters than in (Ghosal and Moin, 1995; Van der Ven, 1995). We do not present continuous filters on an interval, which satisfy definitions (8a-8c), since as it will be shown later, for practical purposes we need discrete filters. For now we only assume that such filters exist and that they can be constructed.

Using properties (8a) and (8b) it follows that

$$\frac{\partial M^k}{\partial \xi}(\xi) = 0 \quad \text{for} \quad k = 0, \ldots, n - 1. \tag{9}$$

Consequently, the commutation error (7) is

$$\left[\frac{d\psi}{dx}\right] = O(\Delta^n). \tag{10}$$

It is easy to show that in the homogeneous (periodic) case, when the shape of the filter does not depend on the location, and the mapping from the physical to the computational domain is linear, A_k is exactly zero for any k and the filter moments are not functions of the location. This results in zero commutation error.
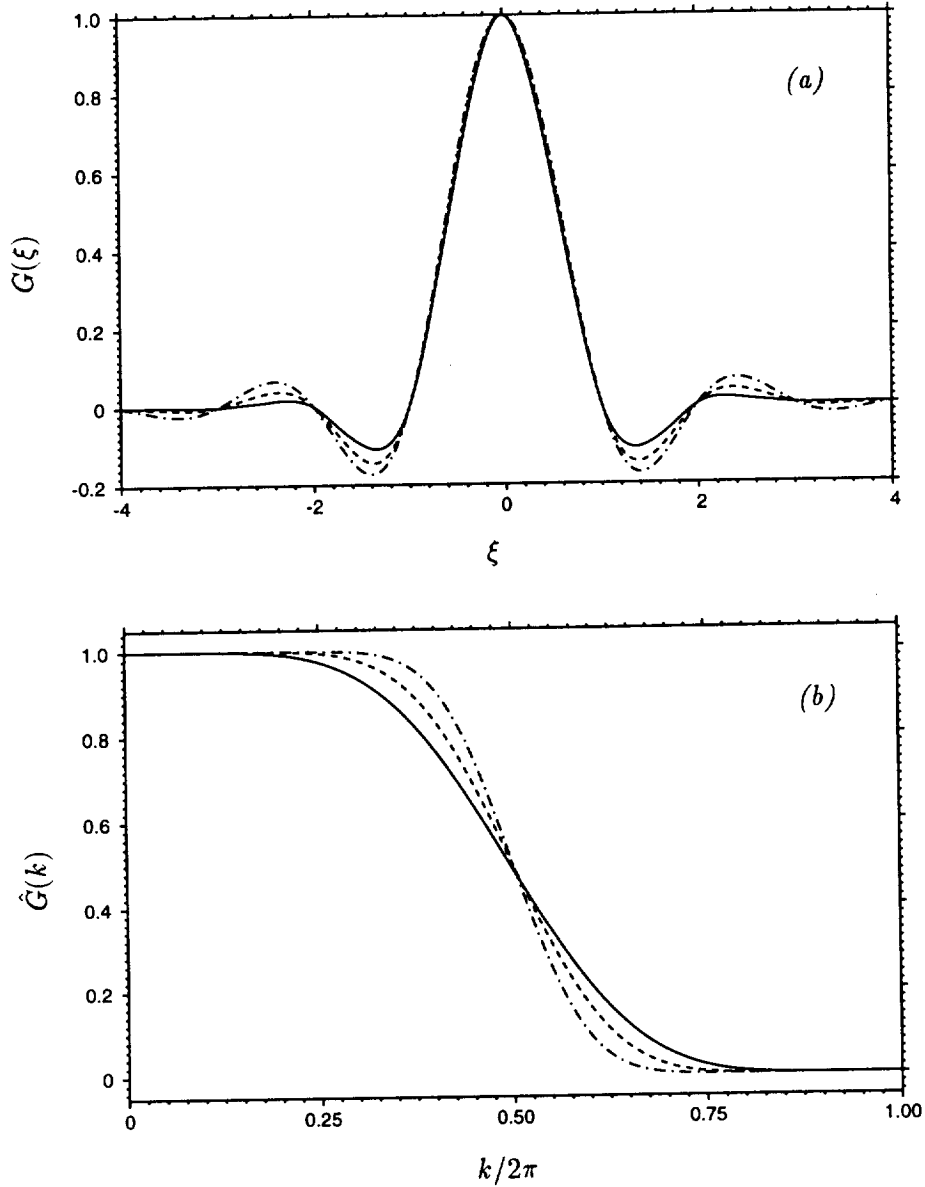
FIGURE 1. Filters $G(\xi)$, (a), with 5 (———), 9 (— — — —), and 17 (— · —) vanishing moments and corresponding Fourier transforms $\hat{G}(k)$, (b).

The non-uniform filtering operation in one spatial dimension can be extended easily to three spatial dimensions (see VLM). As in the one-dimensional case this transformation can be associated with the mapping of spatially non-uniform computational grid to a uniform grid with spacings Δ_1, Δ_2, Δ_3 in the corresponding directions. If one performs the same type of analysis as in one-dimensional case, it is easy to show (see VLM) that the commutation error in three spatial dimensions

is given by

$$\left[\frac{\partial \psi}{\partial x_k} \right] = O(\Delta_1^n, \Delta_2^n, \Delta_3^n). \tag{11}$$

Thus, the commutation error of differentiation and filtering operation is no more than the error introduced by an n-th order finite difference scheme, provided that the filter has $n - 1$ zero moments.

2.2 Discrete filtering in complex geometry

In large eddy simulation of turbulent flows, the solution is available only on a set of discrete grid points, and thus discrete filters are required in various operations. The machinery developed in Section 2.1 can be adapted to discrete filtering. In this section we will limit ourselves to consideration of discrete one-dimensional filtering, since three dimensional filtering can be considered as an application of a sequence of three one-dimensional filters. Also, since the filtering operation is performed in the mapped space, we will consider only the case of uniformly sampled data.

2.2.1 Construction of discrete filters

Let us consider a one-dimensional field $\phi(\xi)$ defined in the domain $[\alpha, \beta]$. $\{\phi_j\}$ corresponds to values of $\phi(\xi_j)$ at locations $\xi_j = \alpha + \Delta j$ $(j = 0, \ldots, N)$, where Δ is the sampling interval. A one-dimensional filter is defined by

$$\frac{1}{\Delta} G\left(\frac{\xi_j - \eta}{\Delta}, \xi_j \right) = \sum_{l=-K_j}^{L_j} \mathrm{w}_l^j \delta(\eta - \xi_{j+l}), \tag{12}$$

where $\delta(\xi)$ is the Dirac δ-function and w_l^j are weight factors. We consider the general class of non-symmetric filters for which $K_j \neq L_j$. One of the important aspects of discrete filters is that all filter moments exist and the radii of convergence of Taylor series (5) and other related series are infinite. Substitution of (12) into (1) gives the following definition for a discrete filter

$$\overline{\phi}_j = \sum_{l=-K_j}^{L_j} \mathrm{w}_l^j \phi_{j+l}. \tag{13}$$

It is the property (12) which allows us to apply results of Section 2.1 to discrete filters.

In light of the filter definition (8), the weight factors should satisfy the following properties

$$\sum_{l=-K_j}^{L_j} \mathrm{w}_l^j = 1, \tag{14a}$$

$$\sum_{l=-K_j}^{L_j} l^m \mathrm{w}_l^j = 0, \quad m = 1, \ldots n - 1. \tag{14b}$$

Equations (14) give us n constraints on w_l^j and are solvable if and only if $L_j + K_j + 1 \geq n$. If $L_j + K_j + 1 > n$ then additional constraints can be applied.

Conditions (14) give the minimum number of degrees of freedoms for a discrete filter in order for the derivative and filtering operations to commute to order n. This condition gives the minimum filter support, which can be increased by adding additional constraints. The additional linear or nonlinear constraints can be altered depending on the desired shape of the Fourier transform $\hat{G}(k)$ associated with the filter (12) given by

$$\hat{G}(k) = \sum_{l=-K_j}^{L_j} w_l^j e^{-i\Delta kl}. \tag{15}$$

case	number of vanishing moments	W_{-3}	W_{-2}	W_{-1}	W_0	W_1	W_2	W_3	W_4	W_5
1	1			$\frac{1}{4}$	$\frac{1}{2}$	$\frac{1}{4}$				
2	2				$\frac{7}{8}$	$\frac{3}{8}$	$-\frac{3}{8}$	$\frac{1}{8}$		
3	2			$\frac{1}{8}$	$\frac{5}{8}$	$\frac{3}{8}$	$-\frac{1}{8}$			
4	3				$\frac{15}{16}$	$\frac{1}{4}$	$-\frac{3}{8}$	$\frac{1}{4}$	$-\frac{1}{16}$	
5	3			$\frac{1}{16}$	$\frac{3}{4}$	$\frac{3}{8}$	$-\frac{1}{4}$	$\frac{1}{16}$		
6	3		$-\frac{1}{16}$	$\frac{1}{4}$	$\frac{5}{8}$	$\frac{1}{4}$	$-\frac{1}{16}$			
7	4				$\frac{31}{32}$	$\frac{5}{32}$	$-\frac{5}{16}$	$\frac{5}{16}$	$-\frac{5}{32}$	$\frac{1}{32}$
8	4			$\frac{1}{32}$	$\frac{27}{32}$	$\frac{5}{16}$	$-\frac{5}{16}$	$\frac{5}{32}$	$-\frac{1}{32}$	
9	4		$-\frac{1}{32}$	$\frac{5}{32}$	$\frac{11}{16}$	$\frac{5}{16}$	$-\frac{5}{32}$	$\frac{1}{32}$		
10	5	$\frac{1}{64}$	$-\frac{3}{32}$	$\frac{15}{64}$	$\frac{11}{16}$	$\frac{15}{64}$	$-\frac{3}{32}$	$\frac{1}{64}$		

TABLE 1. The values of the weight factors and the number of vanishing moments for different minimally constrained discrete filters.

A desirable constraint on a filter is that its Fourier transform be zero at the cut-off frequency, *i.e.* $\hat{G}(\pi/\Delta) = 0$. The mathematical equivalent of this requirement is given by

$$\sum_{l=-K_j}^{L_j} (-1)^l w_l^j = 0. \tag{16}$$

Condition (14) and (16) represent the minimum number of constraints which should be imposed on the filter. Examples of weights for minimally constrained discrete filters are given in Table 1 and associated Fourier transforms for some of these filters are presented in Figs. 2-4. Examples of the Fourier transforms of minimally constrained symmetric filters with one, three, and five vanishing moments are presented
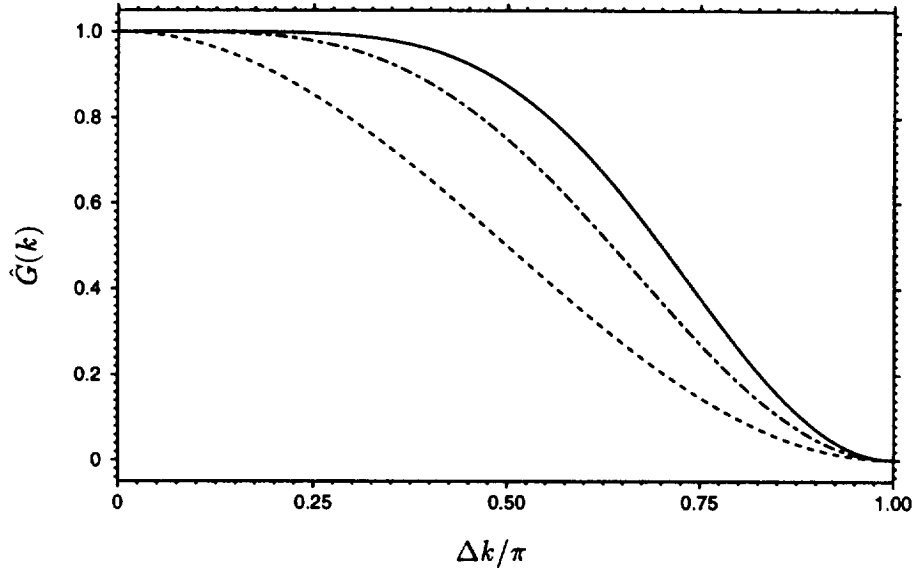
FIGURE 2.   Fourier transform $\hat{G}(k)$ of the symmetric minimally constrained discrete filters with one (-----), three (— · —), and five (———) vanishing moments corresponding respectively to cases 1, 6, and 10 given in Table I.

in Fig. 2. These filters correspond respectively to cases 1, 6, and 10 presented in Table 1. We see that increasing the number of vanishing moments yields a better approximation to the sharp cutoff filter, which is more appealing from a physical point of view. It also can be observed that filters shown in Fig. 2 have different effective cut-off frequencies. Thus, in order to control the effective cut-off frequency, additional constraints should be introduced. The Fourier transform of asymmetric filters with four vanishing moments corresponding to cases 8 and 9 presented in Table 1 are shown in Figs. 3 and 4 correspondingly. Note that the asymmetric filters introduce phase shifts due to their non-zero imaginary parts. The imaginary part should be minimized by introducing additional constraints. Also notice the overshoot in the real part and absolute value of the filter shown in Fig. 3. In general, an overshoot is not desirable since it may lead to non-physical growth of energy. Additional constraints are necessary in order to reduce or remove overshoot.

In the interior of the domain, in order to eliminate the phase shift, the filter should be symmetric, i.e. the following relation should be satisfied

$$w_l^j = w_{-l}^j, \quad l = 1, \ldots, L, \qquad (17a)$$

$$L_j = K_j = L. \qquad (17b)$$

In this case the filter only adjusts the amplitude of a given wavenumber component of the solution and leaves its phase unchanged. Near the boundaries, however,

FIGURE 3. Real $\Re\{\hat{G}(k)\}$ (— · —), imaginary $\Im\{\hat{G}(k)\}$ (----), and absolute value $\left|\hat{G}(k)\right|$ (———) of Fourier transform $\hat{G}(k)$ of the asymmetric discrete filter with four vanishing moments corresponding to case 8 given in Table I.
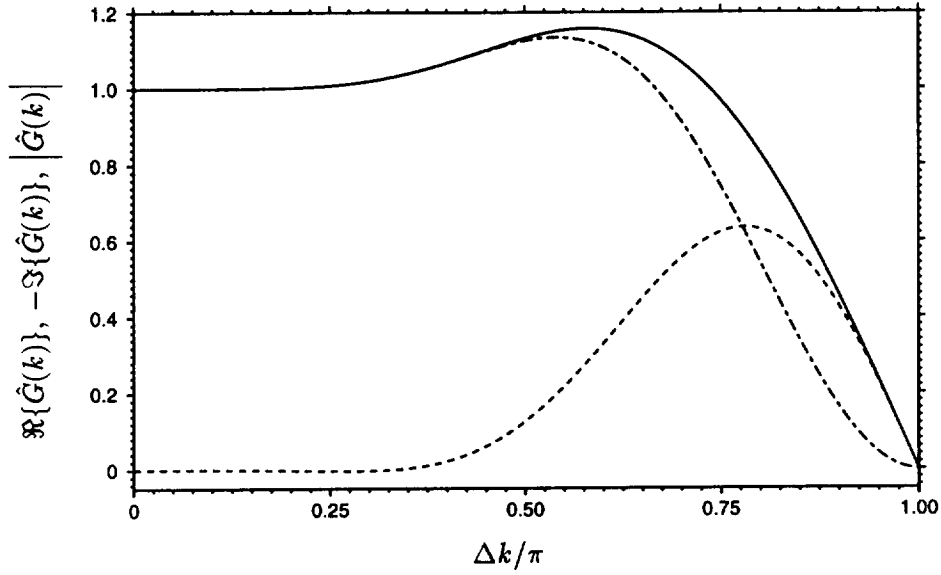

FIGURE 4. Real $\Re\{\hat{G}(k)\}$ (— · —), imaginary $\Im\{\hat{G}(k)\}$ (----), and absolute value $\left|\hat{G}(k)\right|$ (———) of Fourier transform $\hat{G}(k)$ of the asymmetric discrete filter with four vanishing moments corresponding to case 9 given in Table I.
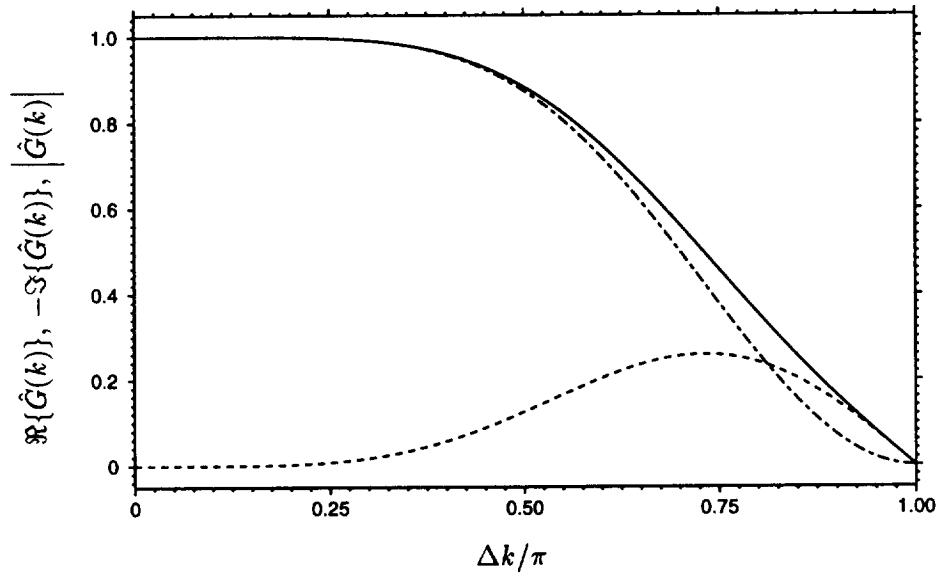
case	number of vanishing moments	additional constraints	w_0	$w_{\pm 1}$	$w_{\pm 2}$	$w_{\pm 3}$	$w_{\pm 4}$	$w_{\pm 5}$
1	3	$\hat{G}(\Delta\pi/3) = 1/2$ $\hat{G}^{(m)}(\Delta\pi) = 0, m = 0, \ldots, 5$	$\frac{373}{1152}$	$\frac{911}{3456}$	$\frac{203}{1728}$	$-\frac{11}{2304}$	$-\frac{203}{6912}$	$-\frac{61}{6912}$
2	3	$\hat{G}(\Delta\pi/2) = 1/2$ $\hat{G}^{(m)}(\Delta\pi) = 0, m = 0, \ldots, 1$	$\frac{1}{2}$	$\frac{9}{32}$	0	$-\frac{1}{32}$		
3	3	$\hat{G}(2\Delta\pi/3) = 1/2$ $\hat{G}^{(m)}(\Delta\pi) = 0, m = 0, \ldots, 1$	$\frac{47}{72}$	$\frac{35}{144}$	$-\frac{11}{144}$	$\frac{1}{144}$		

TABLE 2. The values of the weight factors and the number of vanishing moments for different linearly constrained discrete filters.

it may be necessary to make the filter asymmetric. In this case a phase shift is introduced and one is interested in minimizing this effect.

Examples shown in Figs. 2-4 demonstrate the necessity of the introduction of additional constraints which ensure that the resulting filter has all the desired properties. One way to constrain the filter is to specify either its value or the value of its derivative for a given frequency k_s. Examples of weights for filters with three vanishing moments and different linear constraints are given in Table 2 and associated Fourier transforms for these filters are presented in Fig. 5. These filters are constrained in such a way that the effective filter widths are 3Δ, 2Δ, and $3/2\Delta$ (corresponding to characteristic wavenumbers $\Delta k_s/\pi = 1/3, 1/2, 2/3$). We observed that for the filters with relatively small characteristic wavenumbers, the number of zero derivatives at $k = \pi/\Delta$ should be considerably larger than for filters with characteristic wavenumbers close to π/Δ. If we chose this number small enough, then the value of the Fourier transform of the filter for frequencies larger then characteristic wavenumber may reach a large amplitude. Thus setting the large number of derivatives at $k = \pi/\Delta$ forces the filter to have the desired shape.

2.2.2 Alternative construction of filters with desired properties

Linear constraints are often enough to obtain the desired filter. However, there are situations, especially for non-symmetric filters, where it is difficult to choose a limited number of constraints such that the filter is close to the desired shape. It is much more desirable to specify the target filter function $\hat{G}_t(k)$ and to construct a filter which will be close to it. One way of doing so is to find the set of filter weights which satisfy all linear constraints and minimize a following functional

$$\int_0^{\pi/\Delta} \left(< \left\{ \hat{G}(k) - \hat{G}_t(k) \right\} \right)^2 dk + \int_0^{\pi/\Delta} \left(\Im \left\{ \hat{G}(k) - \hat{G}_t(k) \right\} \right)^2 dk, \quad (18)$$

where $< \{z\}$ and $\Im \{z\}$ denote correspondingly real and imaginary parts of a complex number z. Note that integral ranges as well as relative weights for real and imaginary contributions to the functional can be arbitrarily set depending on the
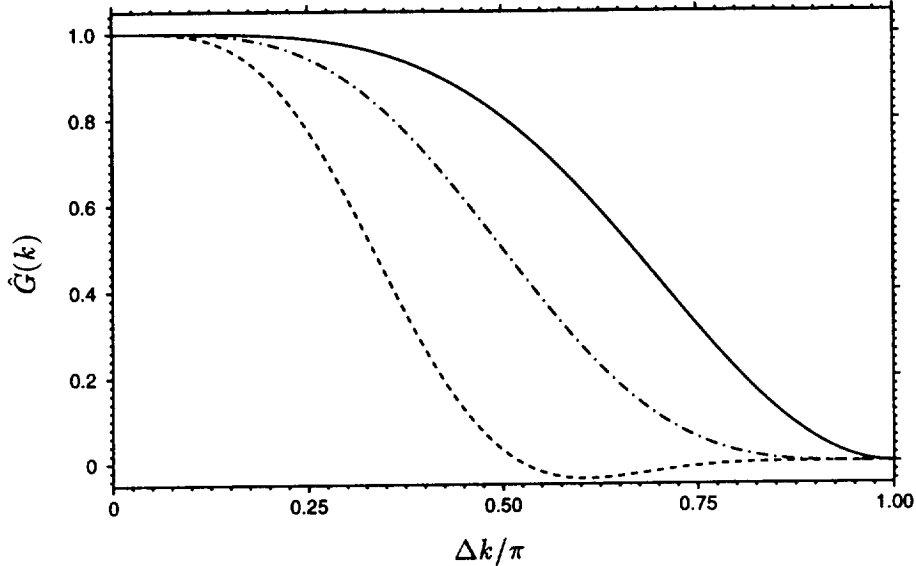
FIGURE 5. Fourier transform $\hat{G}(k)$ of the symmetric discrete filters with different additional linear constraints corresponding to cases 1 (----), 2 (— · —), and 3 (———) given in Table II.

filter function $\hat{G}_t(k)$. The mathematical details of the minimization are given in VLM. Figure 6(a) shows an example of an asymmetric filter with eight point stencil, ($K = 2$ and $L = 5$). The real part of the filter is constrained to be $1/2$ at $\Delta k/\pi = 1/2$. The filter value and its first two derivatives are constrained to be zero at $k = \pi/\Delta$. In order to improve the filter's characteristics, the minimization was performed, where requirements for two derivatives at $k = \pi/\Delta$ were relaxed and quadratic minimization as described in VLM was used instead. The resulting filter is shown in Fig. 6(b). Comparing both filters we can see that the filter presented in Fig. 6(b) has better characteristics. We found that, in general, minimization procedure gives better filters than the ones obtained using only linear constraints.

2.2.3 Pade filters

Discrete filters with vanishing moments are not limited to the simple weighted average form of (13). Pade-type filters are described in this subsection as an example of an alternative formulation. Other discrete filtering approaches can be utilized as well but they will not be discussed here. A Pade filter is defined as

$$\sum_{m=-M_j}^{N_j} v_m^j \overline{\phi}_{j+m} = \sum_{l=-K_j}^{L_j} w_l^j \phi_{j+l}, \tag{19}$$

and requires the solution of linear systems of equations. The Fourier transform
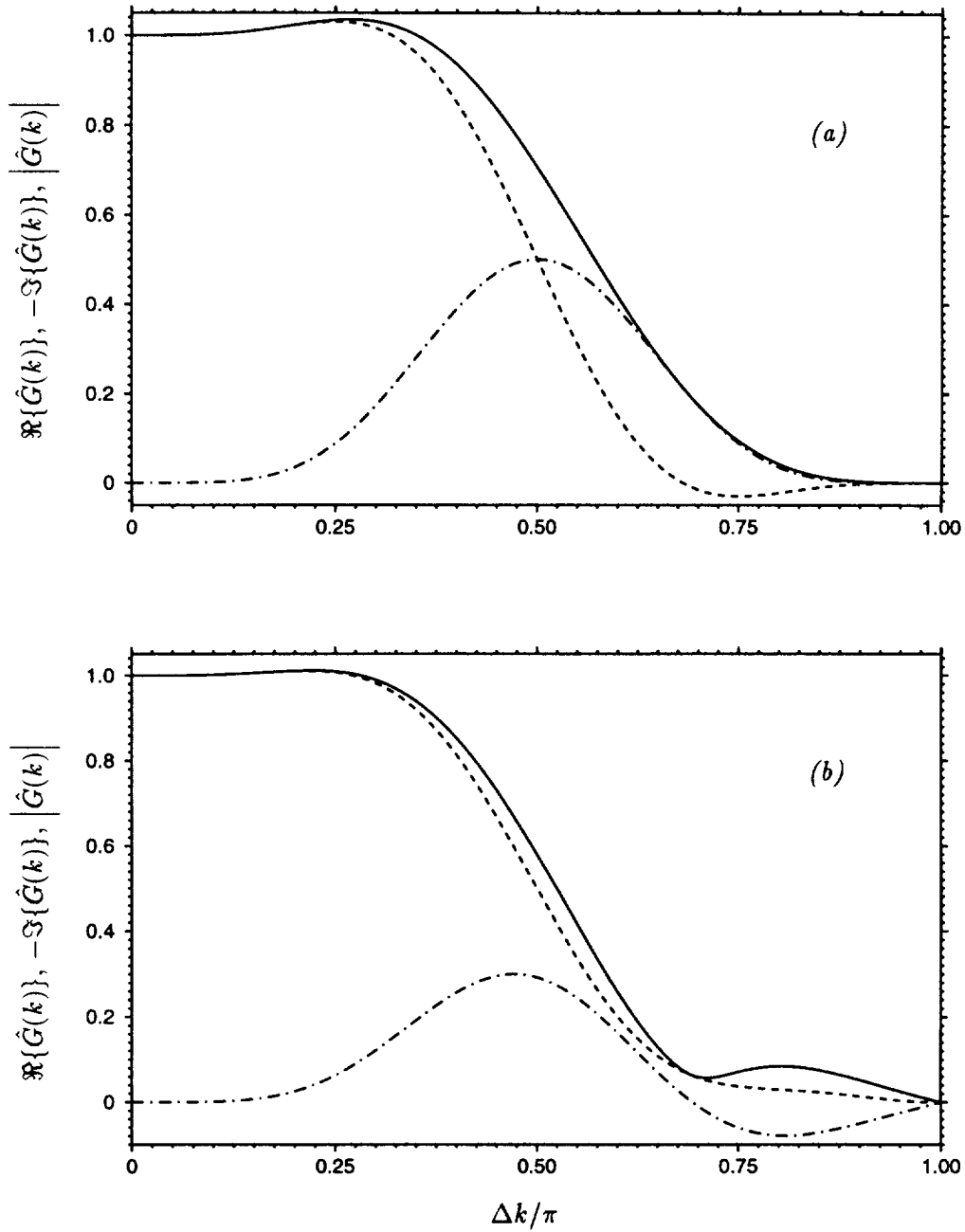
FIGURE 6.   Real $\Re\{\hat{G}(k)\}$ (— $\cdot$ —), imaginary $\Im\{\hat{G}(k)\}$ (- - - -), and absolute value $\left|\hat{G}(k)\right|$ (———) of Fourier transform $\hat{G}(k)$ of the asymmetric discrete filter with three vanishing moments obtained using only linear constraints (a) and quadratic minimization (b).

case	additional constraints	v_0	$v_{\pm1}$	$v_{\pm2}$	$v_{\pm3}$	w_0	$w_{\pm1}$	$w_{\pm2}$	$w_{\pm3}$	$w_{\pm4}$	$w_{\pm5}$
1	$\hat{G}(\Delta\pi/3) = 1/2$ $\hat{G}^{(m)}(\Delta\pi) = 0, m = 0,\ldots,9$	$\frac{543}{128}$	$-\frac{1405}{512}$	$\frac{313}{256}$	$-\frac{51}{512}$	$\frac{63}{256}$	$\frac{105}{512}$	$\frac{15}{128}$	$\frac{45}{1024}$	$\frac{5}{512}$	$\frac{1}{1024}$
2	$\hat{G}(\Delta\pi/2) = 1/2$ $\hat{G}^{(m)}(\Delta\pi) = 0, m = 0,\ldots,7$	$\frac{7}{12}$	0	$\frac{5}{24}$		$\frac{7}{24}$	$\frac{175}{768}$	$\frac{5}{48}$	$\frac{35}{1536}$	0	$-\frac{1}{1536}$
3	$\hat{G}(2\Delta\pi/3) = 1/2$ $\hat{G}^{(m)}(\Delta\pi) = 0, m = 0,\ldots,3$	$\frac{49}{120}$	$\frac{13}{60}$	$\frac{19}{240}$		$\frac{11}{30}$	$\frac{119}{480}$	$\frac{1}{15}$	$\frac{1}{480}$		

TABLE 3. The values of the weight factors for different linearly constrained symmetric Pade filters with five vanishing moments.

$\hat{G}(k)$ associated with Pade-type filters is given by

$$\hat{G}(k) = \frac{\sum_{l=-K_j}^{L_j} w_l^j e^{-i\Delta kl}}{\sum_{m=-M_j}^{N_j} v_m^j e^{-i\Delta km}}. \tag{20}$$

In the case of Pade filters conditions (14) can be rewritten as

$$\sum_{l=-K_j}^{L_j} w_l^j = 1, \tag{21a}$$

$$\sum_{m=-M_j}^{N_j} v_m^j = 1, \tag{21b}$$

$$\sum_{m=-M_j}^{N_j} m^i v_m^j = \sum_{l=-K_j}^{L_j} l^i w_l^j, \quad i = 1,\ldots n-1. \tag{21c}$$

It is straightforward to constrain Pade filters to a specific value at specific frequency. Nevertheless linear constraining of filter derivatives $\hat{G}^{(m)}(k)$ at certain frequency requires additional specification of filter value as well as all previous derivatives. For more details on Pade filters we refer to (Lele, 1992).

The use of Pade-type filters gives more flexibility in constructing filters which are closer to spectral cut-off filters. Examples of weights for symmetric ($M_j = N_j$ and $K_j = L_j$) Pade filters with five vanishing moments and different linear constraints are given in Table 3 and associated Fourier transforms are presented in Fig. 7. Comparing Figs. 5 and 7 it can be seen that Pade filters are considerably better approximations of sharp cut-off filters.

2.2.4 Commutation error of discrete filtering and differentiation

In Section 2.1 we demonstrated that the commutation error of continuous filtering and differentiation operators is determined by the number of vanishing moments
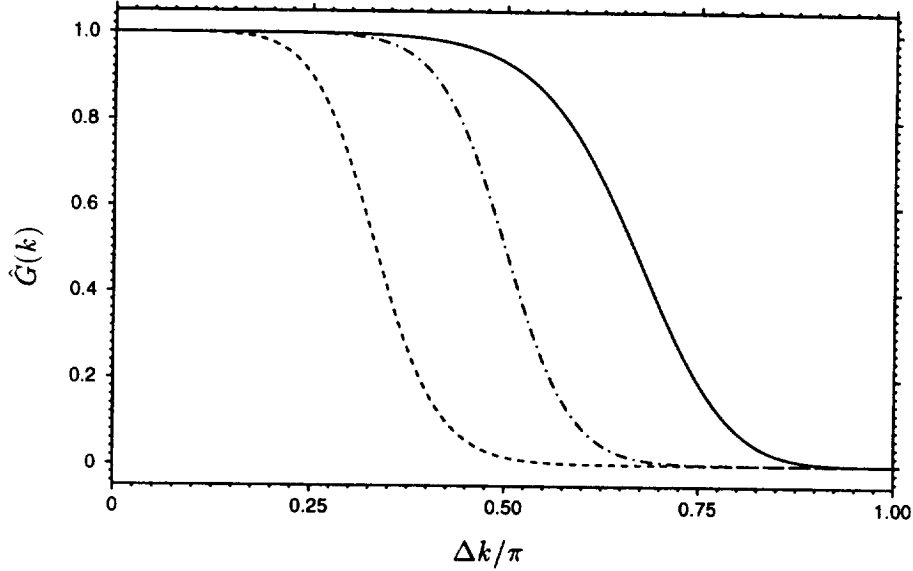
FIGURE 7.   Fourier transform $\hat{G}(k)$ of the symmetric Pade filters with different additional linear constraints corresponding to cases 1 (-----), 2 (—·—), and 3 (——) given in Table III.

of the continuous filter. As it was mentioned earlier in this section the same conclusion is valid for discrete filters. In order to validate that discrete filtering and differentiation commute up to the same order, we perform a numerical test in which we differentiate numerically the Chebyshev polynomial of the 16-th order and determine the commutation error of discrete filtering and differentiation operators. Since the derivative of the Chebyshev polynomial can be calculated exactly, we can calculate the truncation error of the numerical differentiation as well. We choose the nonuniform computational mesh to be given by

$$x_j = -\frac{\tanh\left(\gamma\left(1 - \frac{2j}{N_s}\right)\right)}{\tanh\left(\gamma\right)}, \tag{22}$$

where N_g is the total number of grid points and γ is the stretching parameter. The choice for the hyperbolic grid stretching is motivated by its frequent use in both DNS and LES simulations of wall-bounded flows. For the hyperbolic tangent grid the ratio of largest to smallest grid size is a function of stretching parameter γ and is given by $\cosh^3\gamma/\sinh\gamma$. In this test we choose $\gamma = 2.75$, which makes this ratio approximately 62. The differentiation operator is chosen to be fourth order accurate on the non-uniform grid. Figure 8 shows the truncation error of finite difference scheme and commutation errors as a function of the total number of grid points for filters with different number of zero moments. The results presented on Fig. 8 confirm that the discrete filtering and differentiation operators commute up to the n-th order, provided that discrete filter has $n - 1$ vanishing moments.
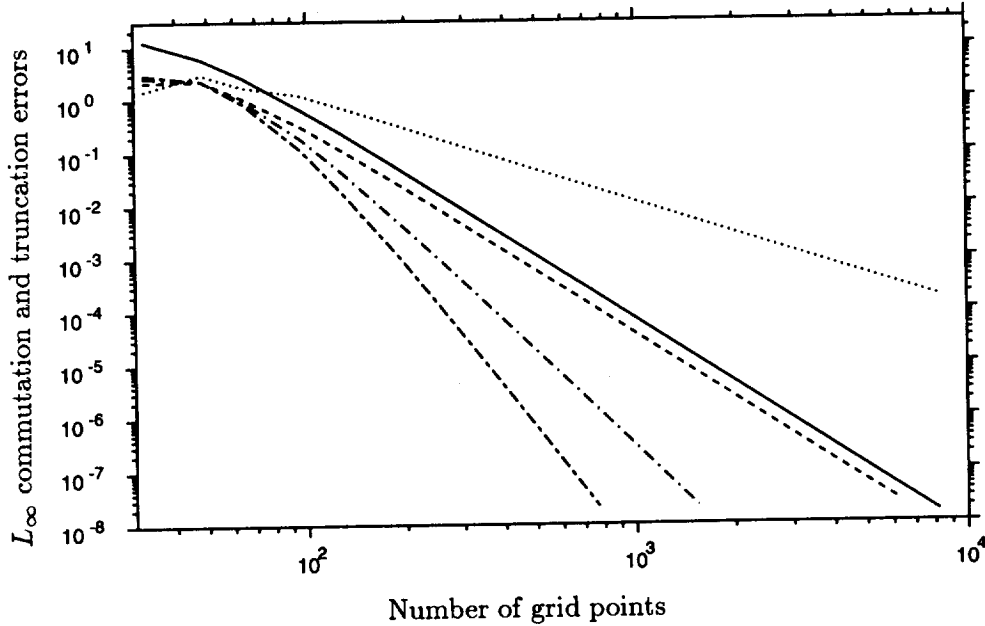
FIGURE 8. Truncation error (———) of the differentiation operator and commutation error for discrete filtering and differentiation operations for the filters with one (········), three (– – – –), five (— · —), and seven (— - —) vanishing moments.

2.3 Conclusions

We have formulated general requirements for a filter having a non-uniform filter width which ensure that the differentiation and filtering operations commute to any desired order. Minimization of the commutation error is achieved by requiring that the filter has a number of vanishing moments. Application of this filter to the Navier-Stokes equations results in the standard LES equations which can be solved on a non-uniform computational grid. The commutation error can be neglected provided that the filter has $n - 1$ vanishing moments, where n is the order of the numerical discretization scheme used to solve the LES equations. A general set of rules for constructing discrete filters in complex geometries is provided. The use of these filters ensures consistent derivation of discrete LES equations. The resulting discrete filtering operation is very simple and efficient.

3. Future plans

The commutative discrete filters presented in this report enable us to perform consistent large eddy simulations of inhomogeneous turbulent flows. The first step in this direction is to study the effect of explicit filtering in LES of turbulent channel flow. For that purpose we are planning to use the fourth-order scheme described in (Morinishi *et al.*, 1997). A discrete filter with a number of vanishing moments will be applied to the incremental field at the conclusion of each time step. This procedure guarantees that no high frequency signal is added to the field from the

previous time step. The dynamic procedure should be modified due to explicit filtering of nonlinear terms. As more experience is gained with the explicit filtering, it will be determined whether explicit filtering is a cost-effective means of improving simulation results. If so, explicit filtering will be applied to more complicated problems.

REFERENCES

BEYLKIN, G. 1992 On the representation of operators in bases of compactly supported wavelets. *SIAM J. Numer. Anal.* **29**, 1716-1740.

BEYLKIN, G. & SAITO, N. 1993 Wavelets, their autocorrelation functions, and multiresolution representation of signals. In *Proceedings of SPIE*, **LB26**, 39-50.

GERMANO, M., PIOMELLI, U., MOIN, P. & CABOT, W. H. 1991 A dynamic subgrid-scale eddy viscosity model. *Phys. Fluids A.* **3**, 1760-1765.

GHOSAL, S., LUND, T. S., MOIN, P., & AKSELVOLL, K. 1995 A dynamic localization model for large-eddy simulation of turbulent flows. *J. Fluid Mech.* **286**, 229-255.

GHOSAL S. & MOIN P. 1995 The basic equations of the large eddy simulation of turbulent flows in complex geometry. *J. Comp. Phys.* **118**, 24-37.

LELE, S. K. 1992 Compact finite difference schemes with spectral-like resolution. *J. Comp. Phys.* **103**, 16-42.

LEONARD, A. 1974 Energy cascade in large-eddy simulations of turbulent fluid flows. *Adv. Geophys.* **18**, 237-248.

LUND, T. S. & KALTENBACH, H.-J. 1995 Experiments with explicit filtering for LES using a finite-difference method. In *Annual Research Briefs*, Center for Turbulence Research, NASA Ames/Stanford Univ., 91-105.

MORINISHI, Y., LUND, T. S., VASILYEV, O. V., & MOIN, P 1997 Fully Conservative Higher Order Finite Difference Schemes for Incompressible Flow. *Submitted to J. Comp. Phys.*

VAN DER VEN, H. 1995 A family of large eddy simulation (LES) filters with nonuniform filter widths. *Phys. Fluids.* **7**, 1171-1172.

VASILYEV, O. V., LUND, T. S., & MOIN, P. 1997 A General Class of Commutative Filters for LES in Complex Geometries. *Submitted to J. Comp. Phys.*

On the use of discrete filters
for large eddy simulation

By T. S. Lund[1]

1. Motivation and objectives

The equations for large eddy simulation (LES) are derived formally by applying a low pass-filter to the Navier-Stokes equations. This filtering must be repeated at each time step in the solution procedure since the non-linear terms continually generate frequencies higher than the assumed cutoff. In spite of this requirement, an explicit filtering operation has rarely been performed in practice. There are a few good reasons for this discrepancy, and perhaps the most compelling of these is the prior lack of filter operators that commute with differentiation. Without commuting operators, the act of filtering alters the Navier-Stokes equations through the addition of 'commutation error terms' (see Ghosal and Moin, 1995). Fortunately the commutation issue has recently been resolved by Vasilyev and Lund (this volume) who constructed filters that commute with differentiation to any specified order of accuracy for arbitrary boundary conditions.

The use of explicit filters opens the possibility to improve the fidelity and consistency of the LES procedure. By removing (or strongly damping) a band of the highest frequencies allowed by the mesh, it is possible to reduce truncation and aliasing errors. The filter is also well defined, which facilitates a comparison with (filtered) experimental data. In order to realize these benefits, however, the filtering process must be implemented correctly, and the filter itself should have satisfied a few constraints in addition to those required by commutation. The purpose of this paper is to outline the general procedure for explicit filtering and to specify the constraints on the filter shape. A second objective of this paper is to revisit some of the issues related to filtering in the dynamic model calculation and to propose a general method of estimating the test filter width.

2. Accomplishments

2.1 Explicit filtering procedure

Application of a commuting filter to the Navier-stokes equations leads to

$$\frac{\partial \bar{u}_i}{\partial x_i} = 0, \tag{1}$$

$$\frac{\partial \bar{u}_i}{\partial t} + \frac{\partial \overline{u_i u_j}}{\partial x_j} = -\frac{\partial \bar{p}}{\partial x_i} + \frac{1}{Re}\frac{\partial^2 \bar{u}_i}{\partial x_j \partial x_j}. \tag{2}$$

1 Present address: University of Texas at Arlington, Department of Mechanical and Aerospace Engineering, Box 19018, Arlington, TX 76019-0018.

The correlation $\overline{u_i u_j}$ is unknown in LES and is typically treated by computing the product of the filtered velocities and modeling the remainder, i.e.

$$\overline{u_i u_j} = \bar{u}_i \bar{u}_j + \underbrace{\left(\overline{u_i u_j} - \bar{u}_i \bar{u}_j\right)}_{\tau_{ij}}. \tag{3}$$

If this decomposition is substituted into the filtered momentum equation, a closed equation for $\bar{u}_i$ is obtained provided a model for τ_{ij} is supplied. This equation can be advanced in time from an initial $\bar{u}_i$ field, *and no explicit filtering operation is required during the solution process*. While this observation seems a bit unsettling, it is often argued that the wavenumber-dependent characteristic of finite-differencing errors act as an effective 'implicit filter'. This argument is based on the following equivalence between a finite difference and the exact derivative of a filtered variable (See Rogallo & Moin, 1984)

$$\left.\frac{\delta u}{\delta x}\right|_i = \frac{u_{i+1} - u_{i-1}}{2\Delta x} = \frac{d}{dx}\int_{x_{i-1}}^{x_{i+1}} u\,dx = \left.\frac{d\bar{u}}{dx}\right|_i. \tag{4}$$

While this equivalence is undoubtedly genuine, there are two significant problems with extending the above observation to filtering as it applies to the solution of the LES equations. First, the equivalence requires a connection between the exact derivative of the filtered variable and the finite difference of the *unfiltered variable*. Thus a strict application of this law to the filtered Navier-Stokes equations would require that the original filterings be removed when the finite difference approximation is made. In order to avoid this problem, one can consider applying a second filter to the Navier-Stokes equations and allow this one to be removed when the finite differences are taken. As we shall see, this argument can not be made rigorous, either, due to the second complication that has to do with the multi-dimensionality associated with the Navier-Stokes equations. The filter used to derive the LES equations must be a three-dimensional operation that represents averaging the velocity field over a small volume in space. The filter implied by the finite difference operator, on the other hand, represents an average in a single coordinate direction. Thus each term in the LES equations is effectively acted on by a different one-dimensional filter when finite differences are used. In particular, the actual equation being solved is

$$\frac{\partial \bar{u}_i}{\partial t} + \frac{\partial \widetilde{\overline{u_i u_1}}^{x_1}}{\partial x_1} + \frac{\partial \widetilde{\overline{u_i u_2}}^{x_2}}{\partial x_2} + \frac{\partial \widetilde{\overline{u_i u_3}}^{x_3}}{\partial x_3} = -\frac{\partial \widetilde{\bar{p}}^{x_i}}{\partial x_i} - \frac{\partial \widetilde{\tau_{i1}}^{x_1}}{\partial x_1} - \frac{\partial \widetilde{\tau_{i2}}^{x_2}}{\partial x_2} - \frac{\partial \widetilde{\tau_{i3}}^{x_3}}{\partial x_3} +$$
$$\frac{1}{Re}\left[\frac{\partial^2 \widehat{\bar{u}_i}^{x_1}}{\partial^2 x_1} + \frac{\partial^2 \widehat{\bar{u}_i}^{x_2}}{\partial^2 x_2} + \frac{\partial^2 \widehat{\bar{u}_i}^{x_3}}{\partial^2 x_3}\right], \tag{5}$$

where $\widetilde{()}^{x_i}$ and $\widehat{()}^{x_i}$ are the effective one-dimensional filters associated with the first and second difference approximations respectively. It should be clear that the above equation can not be derived from the Navier-Stokes equations since the various

effective filters are not distributed uniformly. We conclude that although there is an inherent filtering operation associated with finite-difference approximations, their use does not lead to a well-defined effective three-dimensional filter.

With the issues associated with finite differences aside, there is another difficulty associated with the use of the decomposition given in Eq. (3). The problem with this formulation is that the non-linear product $\bar{u}_i\bar{u}_j$ generates frequencies beyond the characteristic frequency that defines $\bar{u}_i$. These high frequencies alias back as resolved ones and therefore act as fictitious stresses. In principle the subgrid-scale model, τ_{ij}, could exactly cancel this effect, but it is unlikely that such a model could be arranged. The obvious way to control the frequency content of the non-linear terms is to filter them. This strategy would result in the following alternative decomposition:

$$\overline{u_i u_j} = \overline{\bar{u}_i \bar{u}_j} + \underbrace{\left(\overline{u_i u_j} - \overline{\bar{u}_i \bar{u}_j}\right)}_{\tau'_{ij}}. \tag{6}$$

If this relation together with a subgrid-scale model for τ'_{ij} is substituted into Eq. (2), one again obtains a closed equation for $\bar{u}_i$, but this time with an additional *explicit filtering* operation applied to the non-linear term. We now see that the implicit filtering implied by the finite-difference operators shown in Eq. (5) is similar, although the one-dimensional filterings are not nearly as effective at controlling the frequency content of the solution.

While the decomposition of Eq. (6) has several advantageous properties from the point of view of explicit filtering, there is one significant side effect that should be mentioned. It can be shown that if Eq. (6) is substituted into Eq. (2), the resulting equation is in general not Galilean invariant. The residual takes the form $c_j d(\bar{\bar{u}}_i - \bar{u}_i)/dx_j$, where c_j is the uniform translation velocity. The error is seen to be proportional to the difference between the singly and doubly filtered velocity. This difference will be zero for a Fourier cutoff filter, but will not vanish in the general case. The spectral content of the error is proportional to $G(k)(1 - G(k))$ where $G(k)$ is the filter transfer function. This fact implies that error is only generated in the wavenumber band where $G(k)$ differs significantly from 0 or 1. It is also clear that the error is maximized at 25%. Thus it is possible to minimize the error by constructing the explicit filter to be as close as possible to a Fourier cutoff. It is also possible to eliminate the Galilean invariance error all together by switching to yet another alternative decomposition. This step amounts to adding a scale-similarity like term to the filtered Navier-Stokes equations. The difficulty in this approach is that the scale-similarity term generates higher frequencies and thus spoils the explicit filtering procedure. Clearly this issue will require further study. At the present time it appears best to continue with Eq. (6) but to use a filter that is as close as possible to a Fourier cutoff. We shall see that there are other compelling reasons to use this type of filter, and thus its use would be natural in practice.

In order to illustrate the explicit filtering procedure further, consider an Euler

time stepping method applied to the LES equations:

$$\bar{u}_i^{n+1} = \bar{u}_i^n + \Delta t \left[-\frac{\partial \overline{\overline{\bar{u}_i \bar{u}_j}}}{\partial x_j} - \frac{\partial \bar{p}}{\partial x_i} - \frac{\partial \tau'_{ij}}{\partial x_j} + \frac{1}{Re} \frac{\partial^2 \bar{u}_i}{\partial x_j \partial x_j} \right]^n \tag{7}$$

Note that the frequency content of each term on the right-hand side is limited to the bar level (provided the subgrid-scale model is properly constructed). Thus in advancing from time level n to $n+1$, the frequency content of the solution is not altered. This fact implies that the additional filtering of the non-linear term (plus and analogous treatment of the subgrid-scale model) is sufficient to achieve an explicit filtering of the velocity field for all time. It is also important to note that the procedure outlined above is in general different from the 'filtering of the velocity field after each time step' procedure that has been alluded to in the literature, i.e.

$$\bar{u}_i^{\bullet n+1} = \bar{u}_i^n + \Delta t \left[-\frac{\partial \bar{u}_i \bar{u}_j}{\partial x_j} - \frac{\partial \bar{p}}{\partial x_i} - \frac{\partial \tau_{ij}}{\partial x_j} + \frac{1}{Re} \frac{\partial^2 \bar{u}_i}{\partial x_j \partial x_j} \right]^n ,$$

$$\bar{u}_i^{n+1} = \overline{\bar{u}_i^{\bullet n+1}} .$$

While this approach results in the correct treatment for the non-linear term, it is incorrect since the remaining terms are filtered twice. In particular, the additional filtering of the solution at the previous time level, $\overline{\bar{u}_i^n}$ is particularly harmful since the cumulative effect over several time steps implies multiple filterings of the velocity field, i.e.

$$\bar{u}_i^{n+1} = \overline{\overline{\bar{u}_i^{n-1}}} + \Delta t \overline{\overline{\bar{R}^{n-1}}} + \Delta t \overline{\bar{R}^n} .$$

In general, repeated application of the same filter implies a filter with increased width, and thus the procedure of filtering the velocity field after each time step results in a severe loss in spectral information [1].

With the correct explicit filtering procedure established (i.e. Eq. (7)), we are now in a position to address some of the more subtle issues involved, the first of which is commutivity. As discussed above, the issue of commutation between the filter and derivative operators arises mainly in deriving the LES equations from the Navier-Stokes system. Explicit filtering, on the other hand, involves the decomposition of Eq. (6) where the filtered product, $\overline{u_i u_j}$, is replaced with $\overline{\bar{u}_i \bar{u}_j} + \tau'_{ij}$. As we have seen this decomposition is not unique, and the decision to add the second bar to the non-linear term is not required in the basic derivation of the LES system, but rather is used simply as a convenient means to control the frequency content of the solution. Furthermore, Eq. (6) is a substitution for $\overline{u_i u_j}$, which appears inside the divergence operator. Thus, perhaps surprisingly, there does not appear to be any direct commutation requirement on the second filter. Of course, there is an indirect

---

[1] It is important to note that the above argument does not apply to the Fourier cutoff filter where repeated application has no cumulative effect. In this special case, filtering the velocity field at each time step is permissible and is equivalent to the general procedure listed in Eq. (7).

requirement if one requires the first and second bar filters to be identical (since the former was used in the derivation of the LES system). It is not clear whether consistency in this regard is really required in practice, however, and is appears possible to use the second alternative decomposition

$$\overline{u_i u_j} = \widetilde{\overline{u}_i \overline{u}_j} + \underbrace{(\overline{u_i u_j} - \widetilde{\overline{u}_i \overline{u}_j})}_{\tau''_{ij}}, \tag{8}$$

where $\widetilde{()} \simeq \overline{()}$ is a (perhaps non-commuting) approximation to the primary filter[2].

A second subtle issue concerning explicit filtering has to do with an associated false dissipation. The non-linear term in the classical LES decomposition (Eq. (3)) is energy conserving since $\bar{u}_i d(\bar{u}_i \bar{u}_j)/dx_j = d(\bar{u}_j 1/2 \bar{u}_i \bar{u}_i)/dx_j$, and thus an integral over the volume collapses to the surface fluxes via Gauss' theorem. Unfortunately this situation is changed when an explicit filter is applied to the non-linear term. The second filter on the non-linear product prohibits the redistribution of velocity components used to obtain a divergence form and one is left with $\bar{u}_i d(\overline{\bar{u}_i \bar{u}_j})/dx_j = d(\bar{u}_i \overline{\bar{u}_i \bar{u}_j})/dx_j - (d\bar{u}_i/dx_j)\overline{\bar{u}_i \bar{u}_j}$. The second term on the right-hand side does not vanish in general when integrated over the volume and in fact bears some resemblance to the turbulent production. More quantitative information regarding the false dissipation can be obtained by looking at the Fourier-space energy equation for isotropic turbulence which reads

$$\frac{dE(k)}{dt} = \underbrace{\langle -ik\hat{u}_m^* P_{mi} G(k) \sum_{\substack{p \quad q \\ k = p + q}} \hat{u}_i(p)\hat{u}_j(q) \rangle}_{T(k)} - \frac{2}{Re} k^2 E(k),$$

where $E(k) = 1/2\langle \hat{u}_i^* \hat{u}_i \rangle$ is the spectral energy density, $\hat{u}_i$ is the Fourier transform of the velocity (bar omitted for simplicity), P_{li} is the divergence-free projection operator, $G(k)$ is the transfer function associated with the explicit filter, $()^*$ denotes complex conjugate, and $\langle \rangle$ is a shell average. It is clear that the explicit filter affects only the non-linear transfer term, $T(k)$. This term will be conservative if its integral vanishes, i.e. $\int_0^\infty T(k)dk = 0$. It can be shown that the integral will indeed vanish if the filter function $G(k)$ is a Fourier cutoff that passes frequencies up to some limit k_{max} and if the velocity field is truncated at this level before the transfer term is constructed (Kraichnan, 1976). For non-sharp filters the transfer will not integrate to zero since the weighting introduced by a smoothly-varying $G(k)$ destroys the symmetries required to achieve complete cancellation. Further analysis reveals that the residual transfer arises only out of interactions with wavenumber components where $G \neq 1$. The sign of this residual transfer is not fixed kinematically but is constrained to be negative for developed turbulence with a normal down-scale

---

[2] The formulation with an approximate second filter is probably always required in practice since even 'commuting' filters only do so to a specified order of accuracy (see Vasilyev and Lund, this volume)

energy cascade. Thus non-sharp filters lead to a false dissipation that is proportional to the degree to which the filter departs from a sharp-cutoff. For this reason, it is important to use filters that are close approximations to a Fourier cutoff.

It is worthwhile to note that the approximately-commuting filters developed by Vasilyev and Lund (this volume) become increasingly better approximations to a Fourier cutoff as the commutation error is reduced. Thus use of these filters will allow for a consistent explicit filtering scheme (first and second filters the same) and will introduce only a small amount of false dissipation.

2.2 Accurate estimation of discrete filter width

The previous discussion was concerned with explicit filtering of the non-linear terms as a means to improve the fidelity of the LES approach. In this subsection we consider a rather distinct filtering operation that is used in the dynamic modeling procedure. In order to estimate subgrid-scale model coefficients, the dynamic model uses a 'test filtering' operation to isolate the stresses produced by a band of the smallest resolved motions. Fitting model expressions to these stresses then provides a mechanism to determine any unknown model coefficients. The only parameter in the dynamic procedure is the ratio of the test to primary filter width, α, which is usually taken to be $\alpha = 2.0$ (there is very little sensitivity to this parameter). It goes without saying that the numerical value of the filter width ratio used in the dynamic procedure must match the properties of the test filter actually used in the calculation. While this seems like a trivial point, there can be some ambiguity in determining the test filter width. Any errors in this regard will have a negative effect on the solution and should be avoided. There has also been some discussion in the literature regarding the importance of the test filter shape. While the dynamic model derivation presupposes that the test filter is similar in form to the primary filter, there have been several attempts to improve on matters by 'optimizing' the test filter shape (Najjar and Tafti, 1996, Spyropoulos and Blaisdell, 1993). As we shall see most of these latter attempts involve fortuitous results that arise from use of an inconsistent filter width. In order to assess the effect of test filter shape, a numerical experiment was designed to investigate this issue. The isotropic decay experiment of Comte-Bellot and Corrsin (1971) was simulated using LES on a 32^3 mesh. The pseudo-spectral code of Rogallo (1981) was used with the volume-averaged form of the dynamic Smagorinsky model forming the closure. The test filter type was varied and the resulting kinetic energy decay histories compared with the (filtered) experimental data. The kinetic energy history provides a good measure of the accuracy of the subgrid-scale model since the model provides the bulk of the dissipation at this coarse resolution. The test results are shown in Fig. 1. It is clear that the filter type has almost no effect on the results. This fact is reassuring since it provides additional evidence on the robustness of the dynamic model. It also raises an interesting point that, although the derivation would suggest otherwise, there does not seem to be any practical requirement for the test and primary filters to be of the same form (Fourier cutoff in this case).

As mentioned above, most of the perceived sensitivity to test filter type noted in the literature has to do with the use of an incorrect value for the filter width
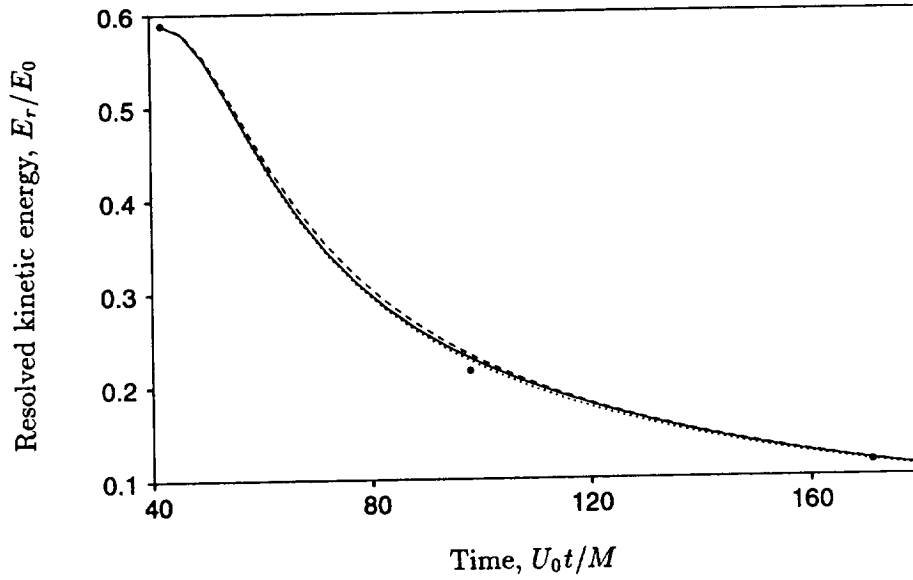
FIGURE 1.   Resolved kinetic energy decay history computed with the dynamic model using various test filter types: ———— , Fourier cutoff; – – – – , Gaussian; ········ , physical space top-hat; ● , experimental of Comte-Bellot and Corrsin (1971).

ratio. This difficulty is usually associated with the inability to estimate the test filter width properly. These difficulties can be avoided by following the procedures listed below.

The width of a positive-definite filter is described best in terms of its standard deviation (Leonard, 1973):

$$\Delta_f = \sqrt{12 \int_{-\infty}^{\infty} x^2 G(x)dx},$$ (9)

where the factor of 12 assures that the width of a physical-space top-hat filter is equal to the interval over which the filter kernel is non-zero. While this formula has been available for quite some time, it does not seem to have been transferred to the realm of discrete filters, which are much more common in practice. The general discrete filter

$$\bar{u}_i = \sum_{j=-(N-1)/2}^{(N-1)/2} W_j u_{i+j}$$ (10)

has an associated kernel that can be written as

$$G(x - x') = \sum_{j=-(N-1)/2}^{(N-1)/2} W_j \delta(x - x' + j\Delta).$$ (11)

When this expression is substituted into Eq. (9) and the integral performed, we arrive at the following discrete analog

$$\alpha \equiv \Delta_f/\Delta = \sqrt{12 \sum_{j=-(N-1)/2}^{(N-1)/2} j^2 W_j}, \tag{12}$$

where Δ is the computational grid spacing.

In order to illustrate the importance of an accurate estimation of the test filter width, we shall consider two different discrete approximations to a physical space top-hat filter of width 2Δ,

$$\bar{u}(x) = \frac{1}{2\Delta x} \int_{x-\Delta x}^{x+\Delta x} u\, dx. \tag{13}$$

In a discrete system we consider $\bar{u}(x_j) \equiv \bar{u}_j$ where j is the mesh index. The integral is evaluated over the interval from x_{j-1} to x_{j+1} where only the three discrete values u_{j-1}, u_j, and u_{j+1} are available. If Simpson's rule is used to perform the quadrature, we obtain the sequence of weights $(W_{-1}, W_0, W_1) = (1/6, 2/3, 1/6)$. If these values are substituted in Eq. (12), we find $\Delta_f/\Delta = 2$ as expected. If the trapezoidal rule is used to evaluate the integral, however, we obtain $(W_{-1}, W_0, W_1) = (1/4, 1/2, 1/4)$ which, according to Eq. (12), have a width $\Delta_f/\Delta = \sqrt{6}$. Thus, perhaps surprisingly, the details of the discrete quadrature can affect the filter width. This is a subtle point that has been overlooked in several previous dynamic model simulations. If the weights associated with the Trapezoidal rule are used but the inconsistent value of the filter width ratio 2.0 is used, the dynamic modeling procedure will loose accuracy. Figure 2 illustrates this effect where kinetic energy decay histories are shown for three cases: (1) Simpson's rule, $\alpha = 2$; (2) Trapezoidal rule, $\alpha = 2$; and (3) Trapezoidal rule, $\alpha = \sqrt{6}$. The first and third cases use consistent values of the filter width ratio and are seen to lead to nearly identical results that are in good agreement with the experimental data. Case (2), on the other hand, uses an inconsistent value of the filter width ratio, and the results are clearly incorrect. If the subtle details of how to compute the filter width ratio correctly were not known, one might mistakenly attribute the poor performance of case (2) to the filter type itself. Unfortunately this type of confusion has appeared in the literature, and there are papers that recommend one filter over another (Najjar and Tafti, 1996, Spyropoulos and Blaisdell, 1993).

The foregoing discussion regarding discrete filters assumes that the discrete second moment used in Eq. (12) is non-zero. There are an important class of filters where this is not the case, however. In particular, Vasilyev and Lund (this volume) show that a filter with $n-1$ vanishing moments will commute to with differentiation to order n. Since the nth filter moment is directly related to the nth derivative of the filter transfer function at zero wavenumber, a filter with n vanishing moments also has n vanishing derivatives at the origin in wavenumber space. Thus by Taylor series, the transfer function remains very close to unity for sizable displacements in
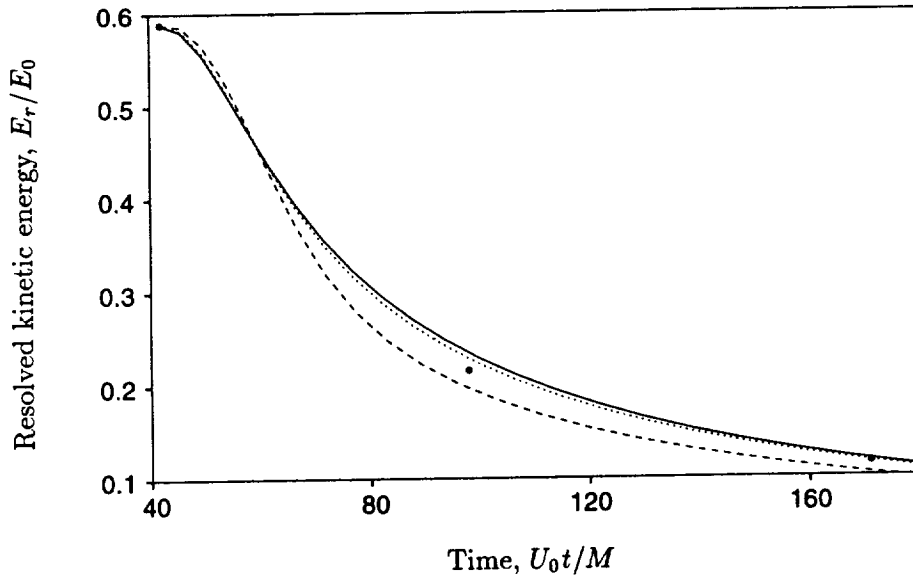
FIGURE 2.   Effect of a mismatch between the true test filter width and the value used in the dynamic model calculation. ——— , Simpson's rule, $\alpha = 2.00$; ———— , Trapezoidal rule, $\alpha = 2.00$; ········ , Trapezoidal rule, $\alpha = \sqrt{6}$; • , experimental of Comte-Bellot and Corrsin (1971).

wavenumber, making these filters good approximations to a Fourier cutoff (at least for low to moderate wavenumbers).

The use of filters with vanishing moments presents a problem since the width can not be based on the second moment *a la* Eq. (12). While a similar expression based on a higher moment could be used, one would eventually encounter a filter where even this moment vanishes. Several more robust definitions of the filter width were investigated and these will be discussed below.

In order to facilitate the discussion, it will be convenient to consider the filter transfer function, which is obtained by taking the Fourier transform of Eq. (11), *viz.*

$$G(k) = \sum_{j=-(N-1)/2}^{(N-1)/2} W_j \cos(jk\Delta). \tag{14}$$

In deriving this result the weights are assumed to be symmetric with respect to j.

The first alternative method of determining the filter width takes advantage of the fact that some of the weights must be negative in order for the sum in Eq. (12) to vanish. More specifically, if a trigonometric interpolant is fit through the weights as a function of their index, an oscillatory distribution similar to the $\sin(\pi x/\Delta_f)/(\pi x)$ function characteristic of a Fourier cutoff is obtained. The position of the first zero crossing can then be used as an estimate of the filter width. The interpolating series

is

$$W(x) = \frac{1}{N} \sum_{j=-(N-1)/2}^{(N-1)/2} G_j \exp\left(i2\pi \frac{j}{N}\frac{x}{\Delta}\right), \tag{15}$$

where the G_j are the discrete values of the filter transfer function:

$$G_j = G\left(\frac{2\pi j}{N\Delta}\right) = \sum_{l=-(N-1)/2}^{(N-1)/2} W_l \cos\left(l\frac{2\pi j}{N}\right). \tag{16}$$

Note that the interpolant is purely real since the G_j must be symmetric with respect to j.

The second alternative strategy works directly with the filter transfer function. In this case the filter width is taken to be proportional to the inverse wavenumber where the filter transfer function falls to 0.5. This rule gives $\alpha = \pi/(k_f\Delta)$.

The third alternative is to base the filter width on the second moment of the *filter transfer function* rather than on the second moment of the filter kernel. Defining the second moment as

$$M^2 = \int_0^{\pi/\Delta} k^2 G(k)dk \tag{17}$$

we may estimate the filter width from

$$\alpha = \left[\frac{\pi^3}{3M^2\Delta^3}\right]^{\frac{1}{3}}. \tag{18}$$

The constants in this formula were chosen so that it predicts the correct width in the case of an exact Fourier cutoff. The second moment for a discrete filter is found by substituting Eq. (14) into Eq. (17) and performing the integration. These operations lead to

$$M^2 = \frac{1}{\Delta^3}\left[\frac{\pi^3}{3}W_0 + 4\pi \sum_{j=1}^{(N-1)/2} \frac{(-1)^j}{j^2}W_j\right], \tag{19}$$

where weights are assumed to be symmetric with respect to j. Combining Eqs. (18) and (19) we obtain the final result

$$\alpha = \left[W_0 + \frac{12}{\pi^2}\sum_{j=1}^{(N-1)/2} \frac{(-1)^j}{j^2}W_j\right]^{-\frac{1}{3}}. \tag{20}$$

As an illustration of a filter that has a vanishing second moment in physical space, consider filter C discussed by Najjar and Tafti (1996). The stencil contains 7 points, and the weights are (1/256)(1, -18, 63, 164, 63, -18, 1). The interpolating function
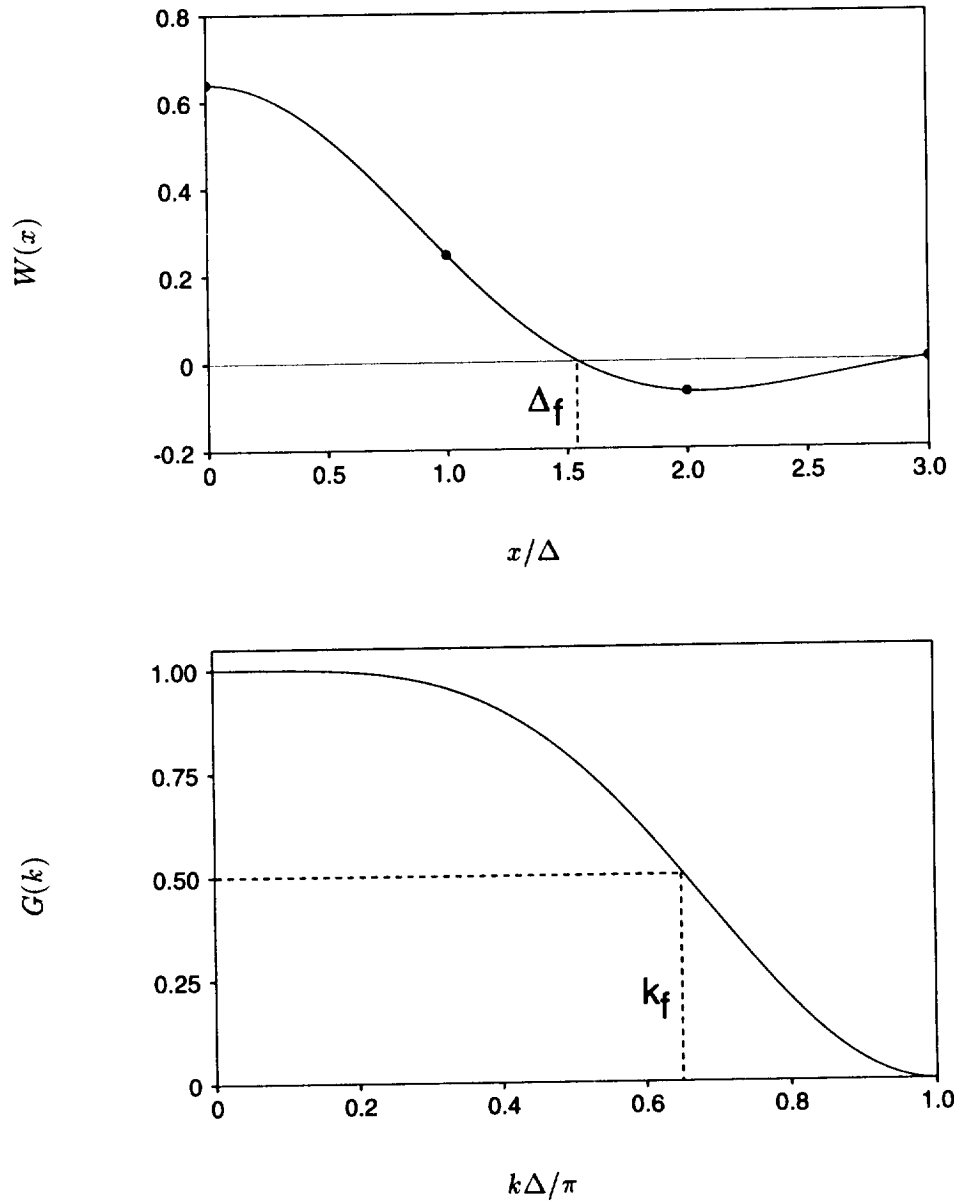
FIGURE 3.   Filter weights and associated transfer function for filter C of Najjar and Tafti (1996).

for the weights as well as the filter transfer function are shown in Fig. 3. The position of the first zero-crossing in physical space gives the estimate $\alpha \simeq 1.55$, the location of the $G = 0.5$ point gives $\alpha \simeq 1.53$, and the second moment of the transfer function gives $\alpha \simeq 1.46$. While the three methods give nearly the same result, we shall see that there is a slight advantage to width predicted by the second moment. Other
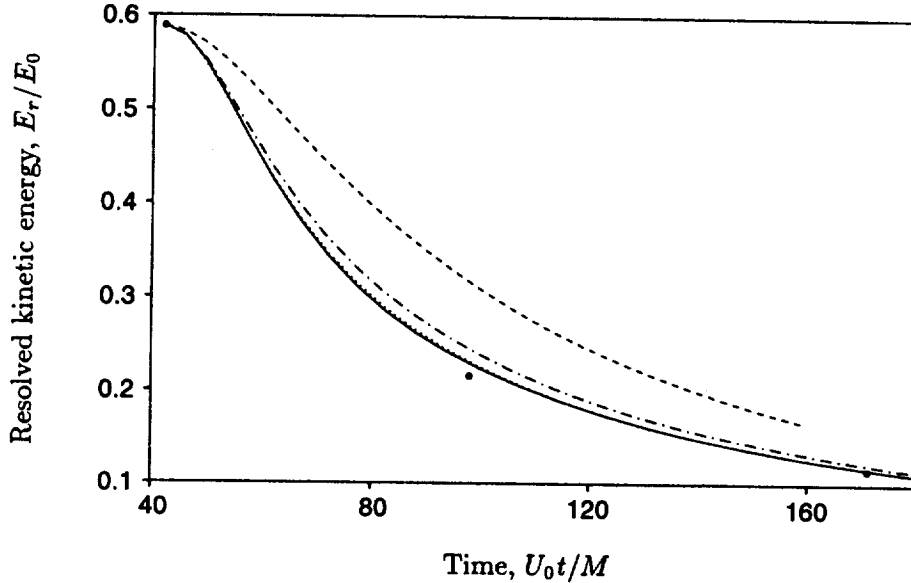
FIGURE 4.   Results for a filter with a vanishing second moment in physical space.
———— , Fourier cutoff; — — — — filter C, $\alpha = 2.00$; —·— , filter C, $\alpha = 1.55$; ········ ,
filter C, $\alpha = 1.46$. Filter C has weights $(1/256)(1, -18, 63, 164, 63, -18, 1)$ and is
described in Najjar and Tafti (1996).

filters were investigated where differences among the three estimates of the width
were greater, and in each case the second moment rule predicted the width most
accurately. The Najjar and Tafti filter was chosen for the purpose of illustration
since these authors incorrectly assigned a value of $\alpha = 2.0$ to this filter. The effect
of this mismatch is shown in Fig. 4 where the kinetic energy decay history is plotted
for the Najjar and Tafti filter using several different values of α. The value $\alpha = 2.0$
is clearly incorrect while the estimate $\alpha \simeq 1.46$ given by the second moment of
the transfer function is the most accurate. While Najjar and Tafti observed some
improvement in their computational results when filter C was used with $\alpha = 2$, this
was most likely a fortuitous effect brought on by a cancellation of errors. Chances
are that, if $\alpha = 1.46$ were used instead, the results would have been nearly identical
to their other cases where the value of α was consistent with the filter used.

3. Conclusions and future plans

Explicit filtering can be used in the LES solution procedure as a means of reducing
truncation and aliasing errors. The required operation involves only filtering the
non-linear terms and amounts to a slightly different definition of subgrid-scale stress.
The procedure is in general different from filtering the entire velocity field at each
time step, which could lead to a severe damping of even the largest scales. The
explicit filter must commute with differentiation only if one insists that the primary
and secondary filters be identical. If strict consistency in this regard is not required,

more general filters can be considered, and the use of approximately commuting filters can be justified on a higher level.

The dynamic modeling procedure was shown to be extremely robust with respect to the test filter type but quite sensitive to mismatches between the true filter width ratio and the value used in the calculation of the model coefficient. Much of the apparent sensitivity to test filter type reported in the literature is related to inaccurate estimates for the test filter width and not to the shape of the filter itself. General rules were developed for accurate estimation of test filter width, and these are related to the second moments of either the filter kernel or its associated transfer function.

Future work will focus on the use of explicit filters in actual large eddy simulations. This work is in progress, and some preliminary results for three-dimensional explicit filtering in turbulent channel flow simulations have been obtained. The indication from these tests is that, while explicit filtering definitely improves the solution, some issues have arisen regarding the required reformulation of the dynamic model as well as the smearing effect of filtering in the inhomogeneous wall-normal direction. Current work is focusing on resolving these issues and in assessing the overall effectiveness of the explicit filtering strategy.

REFERENCES

COMTE-BELLOT & CORRSIN 1971 Simple Eulerian time correlation of full and narrow-band velocity signals in grid-generated isotropic turbulence. *J. Fluid Mech.* **48**, 273-337.

GHOSAL, S. & MOIN, P. 1995 The basic equations of large eddy simulation of turbulent flows in complex geometry. *J. Comp. Phys.* **118**, 24-37.

KRAICHNAN, R.H./1976//EDDY VISCOSITY IN TWO AND THREE DIMENSIONS J. Atmos. Sci//33//1521-1536.

LEONARD, A. 1973 On the energy cascade in large-eddy simulations of turbulent fluid flows, Rep. TF-1, Thermosciences Div., Dept. Mech. Eng., Stanford University, Stanford, CA 94305.

NAJJAR, F.M. & TAFTI, D.K. 1996 Study of discrete test filters and finite difference approximations for the dynamic subgrid-stress model. *Phys. Fluids.* **8**, 1076-88.

ROGALLO, R.S. 1981 Numerical experiments in homogeneous turbulence, NASA Tech. Mem. 81315, Ames Research Center, Moffett Field, CA 94035.

ROGALLO, R.S. & MOIN, P. 1984 Numerical simulation of turbulent flow. *Ann. Rev. Fluid Mech.* **16**, 99-137.

SPYROPOULOS, E.T. & BLAISDELL, G.A. 1993 Evaluation of Inhomogeneous Formulations of the Dynamics Subgrid-Scale Model, in *Transition, Turbulence, and Combustion*, Vol. II, (eds. M. Y. Hussaini, T. B. Gatski, and T. L. Jackson) Kluwer Academic Publishers, pp. 51-60.

Wall models in large eddy simulation of separated flow

By W. Cabot

1. Motivation and objectives

The desire to perform large eddy simulation (LES) of wall-bounded turbulent flows at relatively high Reynolds numbers is typically confounded by the severe resolution requirements near the walls. The structure of the turbulent flow in a boundary layer can become very fine in the near-wall region, scaling as the distance from the wall, and the numerical grid required to resolve it, therefore increases dramatically with Reynolds number. In channel flow LES at moderate Reynolds number, for instance, about half of the grid points must be dedicated to the near-wall flow when it is resolved on a stretched mesh, and the time step is severely reduced by the CFL condition for the fine near-wall scales. The situation becomes even worse at higher Reynolds numbers. The finer near-wall scales also require the subgrid-scale (SGS) model in the LES to describe a larger share of the Reynolds stress than in the core of the flow; this may lead to substantial inaccuracies when standard SGS models based on isotropic models, like the popular Smagorinsky model, are employed in the near-wall region.

To perform LES of high Reynolds numbers, wall-bounded turbulent flow, one needs to remove the requirement of resolving the near-wall region by (a) simulating only the core region of the flow with approximate boundary conditions applied on the boundaries, or (b) simulating the entire domain, including the walls, with the near-wall forces appropriately modeled. Approach (a) has much in common with domain decomposition methods (see Baggett in this volume). Approach (b) has been employed by Deardorff (1970), Schumann (1975), Grötzbach (1987), Piomelli *et al.* (1989), and others (see reviews by Piomelli *et al.*, 1989; Bagwell *et al.*, 1993), who supplied boundary conditions for the flow components tangential to the walls in a channel based on the logarithmic law of the wall. Balaras *et al.* (1996) and Cabot (1995, 1996) also employed thin boundary layer equations to predict wall stress boundary conditions in attached channel and duct flow and in separated flow behind a step. While this strategy works adequately in predicting accurate mean flow statistics in attached flow, it fares more poorly in separating, reattaching, and recovering flow, in part because the assumptions used in modeling the wall (near-wall equilibrium conditions that give rise to the log law, or thin boundary layer approximations) break down.

The broad objective of this work is to develop a procedure, or set of procedures, for modeling the near-wall region in LES such that the numerical grids can be chosen independent of Reynolds number Re, based instead on the outer scales (determined, e.g., boundary layer thickness and flow geometry) or on the core turbulent integral length scales, which remain finite as $Re \rightarrow \infty$. This procedure should be general
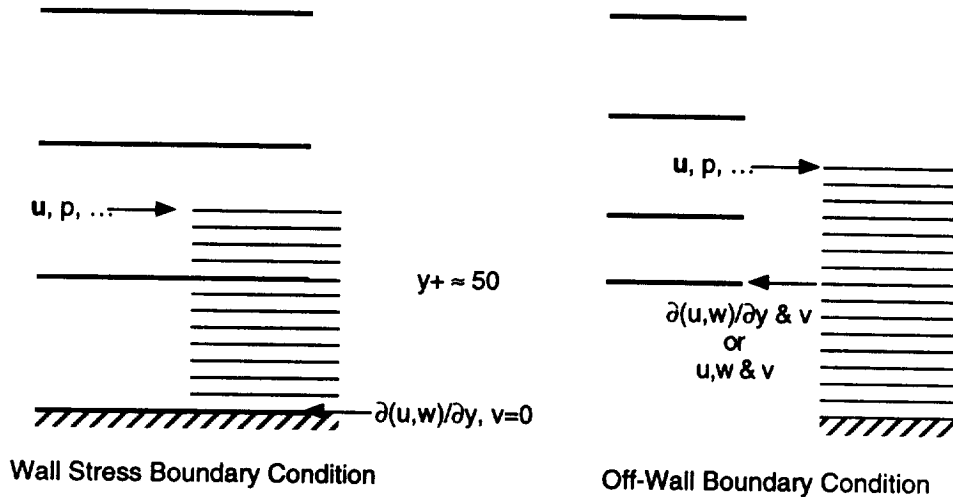
FIGURE 1.   Wall stress boundary conditions are applied at the physical wall location, while off-wall boundary conditions are applied at a location away from the wall. Heavy lines represent the core flow's mesh, while the fine lines represent a fine near-wall grid which may be used by the wall model to generate boundary conditions (algebraic relations may also be used). The wall model extracts flow information from the core flow at an interior point and returns boundary conditions at the core flow's boundary. The distance between arrows illustrates the amount of overlap between the matching conditions.

enough to give accurate LES results in both attached and separated flow cases, and it should be substantially cheaper to use than LES with well resolved walls. There are several (interrelated) issues that need to be addressed on the way to developing successful wall modeling procedures. First, one needs to decide how accurate the LES results for the core flow need to be to deem the procedure a success. This is clearly subjective and depends on the tolerance of the particular flow problem, but at minimum it would be desirable to be able to predict mean flow speeds or mass flow to a few percent and other first-order wall quantities such as skin friction and pressure coefficient. The other physical and numerical issues concern making accurate (enough) wall models, patching together the near-wall and core flow solutions, and constructing consistent SGS models in the wall regions of flows:

(1) Is it more advantageous to apply wall boundary conditions (a) off of the wall, completely removing the wall from the LES, or (b) at the wall, keeping the wall in the LES? The difference between these types of boundary conditions is illustrated in Fig. 1. Numerical issues about gridding and stability arise in this case as well as the accuracy of the wall model used to supply the boundary conditions.

(2) What physical quantities need to be specified in the boundary conditions for

the core flow, and how accurate do they need to be? Velocity or velocity-gradient boundary conditions will be considered here since the velocity is the primitive variable in the simulation codes.

(3) What is the best near-wall model, or set of models, in terms of accuracy and cost, needed to describe a wide variety of physical flow conditions? Some form of the law of the wall may apply for attached boundary layers, but more general models are required, e.g., for separated flow. Thin boundary layer equations are inappropriate near flow separation and reattachment, and the cost of computing them is also generally Reynolds number dependent, which will become prohibitively expensive in many practical flows.

(4) What physical information from the core flow is needed for a particular wall model to specify accurate wall stress or off-wall boundary conditions? The location in the core flow where information is extracted can be a issue for stability and accuracy if it is too close to the numerical boundary and leads to spurious feedback effects.

(5) What modifications are needed in the SGS model of residual Reynolds stresses in the near-wall regions? The standard Smagorinsky SGS model, even when used with the dynamic procedure (Germano *et al.*, 1991), may predict inaccurate Reynolds stresses in the near-wall region, especially on very coarse meshes that effectively filter over large wall-normal variations in the flow. At what resolution does the SGS model give reliable results, and in turn, how close to the wall can one get with the LES? And how does one perform filtering near walls on coarse meshes, or alternatively, how does one model the implicit effects of this filtering properly?

The immediate goal of recent work (also see Baggett and Jiménez & Baggett in this volume) is to provide answers primarily to issues involving the proper type of boundary condition to supply the core flow and how to fit them consistently with the SGS model used in the LES. Here results from wall modeling experiments in two types of separated flows are discussed in relation to these issues. The shortcomings of wall stress models in the separated flow behind a backward-facing step (Akselvoll & Moin, 1995) noted by Cabot (1996) is reexamined briefly. Because one difficulty in this flow was the treatment of the corner behind the step, separated flow on a flat plate due to an induced adverse pressure gradient (Na & Moin, 1996) is being developed as a test bed for wall modeling without the geometric complications of the step.

2. Accomplishments

2.1 Near-wall momentum balance in the flow behind a step

Various models based on the law of the wall, using either instantaneous log laws or boundary layer equations, were employed by Cabot (1996) to provide wall stress boundary conditions on the coarsely resolved bottom wall behind the backward-facing step. In all instances, including the use of no model at all (in which the wall stress in underpredicted by a factor of 2–3), the main separation bubble is observed to accelerate in a deeper pressure low than observed in the LES with resolved walls

(Akselvoll & Moin, 1995). The backward flow penetrates all the way to the step, washing out secondary recirculation features in the corner. On the other hand, the reattachment length and the wall stresses for the attached flow at the outlet were generally well predicted. It was noted that the backward flow has a jet-like structure near the wall, which is unresolved on the coarse mesh, making models based on the law of the wall particularly suspect.

To test the hypothesis that it was the poorly predicted wall stress that caused the aberrant flow behavior, the correct mean wall stress was supplied from Akselvoll & Moin's LES, with the instantaneous values made proportional to the tangential velocity above the wall sublayer (similar to the way Schumann, 1975, and Grötzbach, 1987, applied wall stresses in channel flow). This had surprisingly little effect on the flow development of the separation bubble compared with other wall models. In a related test, the "exact" wall stresses were recorded for a (step-to-outlet) flow-through time using Akselvoll & Moin's code and were fed as wall boundary conditions to the poorly resolved case using the same initial field. Again, an acceleration of the separation bubble toward the step was noted. Note that extending this test to longer times may not be very meaningful because the flow structure in the poorly resolved case may deviate significantly from the resolved case and the wall stresses can no longer be considered exact. Both of these tests suggest that other factors than poor wall stress models are at play here since the anomalous flow behavior occurs even when "good" wall stresses are applied.

One possibility is that the Reynolds stresses being predicted by the SGS model are too inaccurate on the coarse grid near the wall. In this LES, only horizontal (plane) filtering is used in the dynamic procedure with an isotropic (Smagorinsky) base model. Because the grid is very coarse in the wall-normal direction ($\Delta y^+ \approx 40$ at the outlet), the implied grid filter spans large variations in the variables, making the SGS model responsible for a larger fraction of the Reynolds stresses. The mean correction to the streamwise advection term due to wall-normal filtering from the wall at $y = 0$ to $y = y_\ell$,

$$-\frac{\partial}{\partial x_j} \left(\frac{1}{y_\ell} \int_0^{y_\ell} u_j u \, dy - \frac{1}{y_\ell} \int_0^{y_\ell} u_j \, dy \, \frac{1}{y_\ell} \int_0^{y_\ell} u \, dy \right) , \qquad (1)$$

averaged over a flow-through time, is shown in Fig. 2 in comparison with the correction to the wall friction. The advection correction is comparable to the friction correction in the separated region ($x/h \approx 2$–7), but it becomes more negligible downstream in the attached region ($x/h > 7$). The similarity in shape of the two terms is interesting and suggests that there may be fairly simple ways to model the correction to the advection term. When both of these forcings were applied in the wall cells of the coarsely resolved LES, the separation bubble accelerated less toward the step, but the trend was still evident. Perhaps the flow readjusted itself to a different state with this forcing, or other errors due to the low order of the numerical scheme cause substantial differences for on the coarse mesh. In any case, the general conclusion that can be drawn from Fig. 2 is that wall-normal filtering must be taken into account on coarse near-wall grids either through explicit
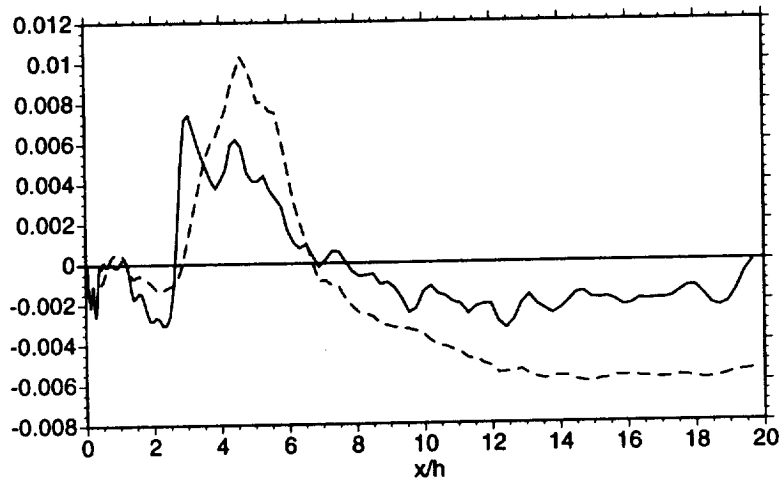
FIGURE 2. The mean correction to the advection term (————) in the streamwise momentum equation due to wall-normal filtering (eq. [1]), and the mean correction to the molecular friction (– – – –) due to underresolution of the wall gradient in the flow along the wall behind a step, computed from a well resolved LES and averaged over span and a flow-through time.

test-filtering in the dynamic procedure or by explicitly modeling the effect of the near-wall inhomogeneity with additional stress or forcing terms. Filtering normal to boundaries is difficult to apply in concept and in practice, and it is unlikely to provide a reliable estimate of near-wall stresses anyway if the models are based on isotropic turbulence. More general SGS models are probably needed in wall regions, e.g., based on Reynolds-averaged Navier-Stokes (RANS) models (Bradshaw, personal communication).

2.2 Separated flow in an adverse pressure gradient

Weak separation in this boundary layer flow over a flat plate is produced by an adverse pressure gradient induced with strong blowing and sucking on the top boundary (Na & Moin, 1996). The inlet boundary layer flow has a Reynolds number of 300 based in momentum thickness and 500 based on displacement thickness (δ). The DNS computes the $357 \times 64 \times 50\delta$ (streamwise, wall-normal, spanwise) domain on a $512 \times 192 \times 128$ mesh stretched in the wall-normal direction. The simulation code uses second-order central finite differences on a staggered grid with third-order Runge-Kutta time advancement and a fractional step method for the pressure.

Preliminary tests of off-wall boundary conditions were performed with the core DNS flow by removing the mesh below $y/\delta \approx 2$; this corresponds to $y^+ \approx 50$ at the inlet, or 1/3 of the total mesh points, and it cuts through the middle of the separation bubble. Simulations were limited to about a quarter of a flow-through time because of their great expense. Horizontal velocities or their wall-normal gradients were specified at the new lower boundary. The wall-normal velocity needed

to be specified (rather than its gradient) in order to fix the global mass balance in the numerical scheme. A simple stress balance model with a mixing length eddy viscosity was used to represent the horizontal velocity components in the near-wall sublayer at each horizontal position on the lower boundary:

$$\frac{\partial u_\ell}{\partial t} = \frac{\partial}{\partial y}(\nu + \nu_T)\frac{\partial u_\ell}{\partial y} \ , \quad \nu_T = \kappa y u_r D^2 \ , \quad D = 1 - \exp(-y u_r/\nu A_+) \ , \quad (2)$$

for $\ell = 1, 3$, where ν and ν_T are the molecular and eddy viscosity, κ is the von Kármán constant, y is the distance from the wall, u_r is the friction velocity, and D is a wall damping function using the constant $A_+ = 17$. This model gives a meld between a log law and a viscous law, which works adequately for attached flow. The wall-normal velocity is given by continuity:

$$u_2 = -\int_0^y \left(\frac{\partial u_1}{\partial x} + \frac{\partial u_3}{\partial z}\right) dy' \ . \quad (3a)$$

The horizontal velocity in the sublayer is set to zero at the wall and is matched to the core flow at a height somewhat above the lower boundary of the core flow (as in Fig. 1) at $y_m/\delta \approx 3$ ($y_m^+ \approx 75$ at the inlet). This overlap was found to be necessary to avoid an unstable feedback between the boundary and matching conditions; a more precise description is needed for the minimum amount of overlap required. Even this overlap was not sufficient when the wall-normal velocity was computed by integrating down from the matching point:

$$u_2 = v(y_m) + \int_y^{y_m} \left(\frac{\partial u_1}{\partial x} + \frac{\partial u_3}{\partial z}\right) dy' \ . \quad (3b)$$

There was no substantial difference using the horizontal velocity or its gradient as the boundary condition for the core flow. The largest effect was due to the low Reynolds stress at the boundary when Eq. (3a) was used instead of (3b); this led to a noticeable acceleration of the flow over short runs. The use of (3b), however, led to long-term instabilities at the boundary. Equation (3b) also generally yields non-zero wall transpiration. The magnitude of the wall stress in the separated region is very small both in the DNS and the wall model case, and the backflow there did not change appreciably. Sufficiently accurate Reynolds stresses at off-wall boundaries appear to be needed to obtain good core flow results. We are currently investigating how much structural information is actually required by the core flow.

Because the DNS runs are very expensive to perform on vector supercomputers, a less expensive LES version is currently being evaluated on grids with 7 and 20 times fewer grid points than in the DNS; this code will also eventually be converted to a parallel architecture. The stability of this simulation has been found to be sensitive to grid spacing and stretching in the region where the blowing from the top meets the stream as it rides over the separation bubble. Without SGS or wall models, the flow is found to separate noticeably farther downstream than in the DNS, but

reattachment is at approximately the same location. The LES being tested uses the dynamic procedure with explicit spatial volume filtering and a mixed base model for the residual Reynolds stress (inspired by Bardina *et al.*, 1980, and Piomelli *et al.*, 1988) comprising a "scale-similar" or "Leonard term", which effectively deconvolves the low wavenumber part of the field for broad filters, and the usual dissipative Smagorinsky part:

$$\tau \sim \overline{\overline{u}\,\overline{u}} - \overline{\overline{u}}\,\overline{\overline{u}} - 2\nu_t \overline{S} , \qquad (4)$$

where the overbar denotes the volume filter for the resolved field and ν_t is the eddy viscosity determined by the dynamic procedure. The dynamic procedure formulation of Vreman *et al.* (1994) is used, although other formulations are possible (e.g., Zang *et al.*, 1993). The mixed model has the nice property of accounting for the large scale features of the flow in the residual stress (in this case, the blowing and sucking at the top boundary) that otherwise would lead to erroneous estimates of the eddy viscosity, which is only meant to account for small-scale energy transfer. (Alternatively, one could apply the high-order accurate filters developed by Vasilyev in this volume to avoid the spurious residuals.)

Both wall stress and off-wall boundary conditions have been implemented in the LES code and will be tested in the future. A matter of particular concern is performing explicit filtering near boundaries. The problem is that one can only resolve a boundary to within the filter width, which can span several grid points with test filtering in the dynamic procedure. This is not so critical for the top (blowing and sucking), inlet, and outlet boundaries, where one can extrapolate values from the interior without doing much damage. The main concern is near the lower boundary on coarse meshes. When the flow is resolved near the wall, wall-normal filtering has little effect, and one can appeal in any case to known asymptotic behavior. It may also be possible to extrapolate values near the off-wall boundary with sufficient accuracy, but this will need to be carefully tested. When the coarse LES mesh extends all the way to wall, it becomes very difficult to estimate the near-wall SGS residual stresses through test filtering, and no simple extrapolation or interpolation may work. In this case, a new or supplemental near-wall model for the residual Reynolds stress may be required. Another possibility would be to contract the wall-normal test filter toward the grid filter level as one approaches the wall; however, it is not known how badly the test signal will degrade near the wall or if there are other significant commutation errors introduced by such a procedure.

3. Future plans

Large eddy simulations of the separated boundary layer on a flat plate will be performed on meshes with coarse and fine near-wall meshes; we will then try to reproduce the statistics of the LES in which the wall is well resolved using both off-wall models and wall stress models. The main focus will be in the following areas: (1) SGS modeling: An accurate way will be developed to predict residual Reynolds stresses from the SGS model on coarse near-wall meshes, which will be implemented in the separated boundary layer simulations and perhaps in the simulation of flow over a step. As a guide DNS fields for these flows (Na & Moin, 1996; Le *et al.*, 1997)
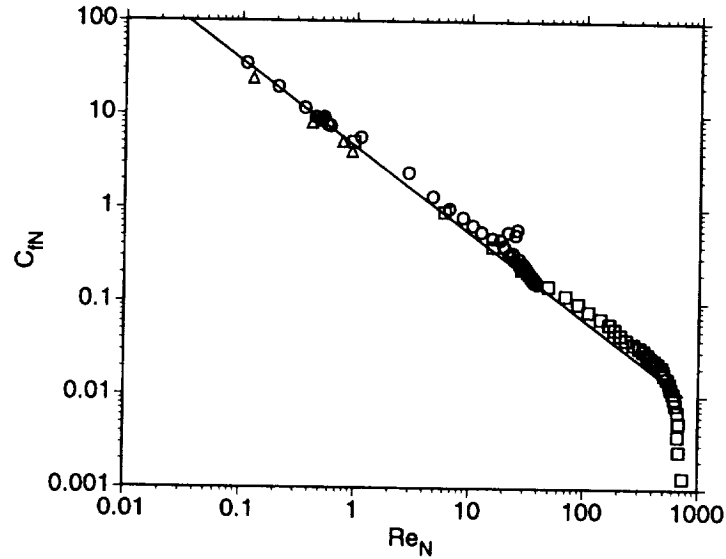
FIGURE 3.   Scaling of the magnitude of the skin friction with backflow Reynolds number (see Eq. [5]) in recirculating regions behind a step in Akselvoll & Moin's (1995) Re_h = 28000 LES: □ primary, o secondary, and △ tertiary recirculation regions; —— Le *et al.'s* (1997) fit from a DNS at Re_h = 5100. The fall-off at the lower right occurs for points near the head of the main separation bubble at $x/h \approx 2$.

will be filtered to give residual stresses. (2) Wall modeling: General wall stress and off-wall boundary conditions will be developed for a variety of flow conditions. One approach will be to attempt to merge various scalings that have been developed for different flows, such as wall jets and reattachment points as well as attached flow, into a useful package. For instance, a scaling of the skin friction in separated regions based on the peak backflow speed U_N and its distance from the wall N (Le *et al.*, 1997),

$$C_{fN} = 2|\tau_w|/U_N^2 \approx 4.5 Re_N^{-0.92} , \quad Re_N = U_N N/\nu , \tag{5}$$

holds roughly in the LES of flow behind a step (§2.1), as shown in Fig. 3. Part of the problem will be devising criteria to sense what flow regime needs to be treated from conditions in the turbulent core flow. It is not yet clear if we must resort to this cataloging approach for each type of flow (with some sort of continuous patching), or if it is possible that the solution of a RANS-like set of differential equations with sufficient physical input from the core flow will prove effective. The best RANS model to consider is probably Durbin's *V2F* model (Durbin, 1991; Parneix in this volume), which does not require ad hoc wall damping functions. We will address the issue of interfacing this model with the LES of the core flow (cf. Carati in this volume) and perform tests with it to determine the performance and cost effectiveness of the approach. (3) Implementation: The degree of overlap in the

patching procedure needs to be quantified into a useful prescription (for a given wall model) such that the distance of overlap allows time for the signal at the boundary to become sufficiently decorrelated with the input signal to the wall model to avoid excessive feedback. Through an examination of DNS databases we also intend to determine the proper grid spacing and location of the wall boundaries for which LES can be expected to perform accurately.

REFERENCES

AKSELVOLL, K., & MOIN, P. 1995 Large eddy simulation of turbulent confined coannular jets and turbulent flow over a backward facing step. Dept. Mech. Eng. Rep. **TF-63**, Stanford Univ.

BAGWELL, T. G., ADRIAN, R. J., MOSER, R. D., & KIM, J. 1993 Improved approximation of wall stress boundary conditions for large eddy simulation, in *Near-wall Turbulent Flows*, ed. R.M.C. So, C.B. Speziale & B.E. Launder (Elsevier Science Pub.), pp. 265-275.

BALARAS, E., BENOCCI, C., & PIOMELLI, U. 1996 Two-layer approximate boundary conditions for large-eddy simulations. *AIAA J.* **34**, 1111-1119.

BARDINA, J., FERZIGER, J. H., & REYNOLDS, W. C. 1980 Improved subgrid scale models for large eddy simulation. *AIAA Paper 80-1357.*

CABOT, W. 1995 Large-eddy simulations with wall models. *Annual Research Briefs 1995*, Center for Turbulence Research, NASA Ames/Stanford Univ. 41-50.

CABOT, W. 1996 Near-wall models in large eddy simulations of flow behind a backward-facing step. *Annual Research Briefs 1996*, Center for Turbulence Research, NASA Ames/Stanford Univ. 199-210.

DEARDORFF, J. W. 1970 The numerical study of three-dimensional turbulent channel flow at large Reynolds numbers. *J. Fluid Mech.* **41**, 453-480.

DURBIN, P. A. 1991 Near wall turbulence closure modeling without "damping functions". *Theor. Comput. Fluid Dyn.* **3**, 1-13.

GERMANO, M., PIOMELLI, U., MOIN, P., CABOT, W. H. 1991 A dynamic subgrid-scale eddy viscosity model. *Phys. Fluids A.* **3**, 1760-1765. Erratum: *Phys. Fluids A* **3**, 3128.

GRÖTZBACH, G. 1987 Direct numerical and large-eddy simulation of turbulent channel flows, in *Encyclopedia of Fluid Mechanics*, vol. 6, ed. N.P. Cheremisinoff (Gulf Pub. Co., Houston), chap. 34, pp. 1337-1391.

LE, H., MOIN, P., & KIM, J. 1997 Direct numerical simulation of turbulent flow over a backward-facing step. *J. Fluid Mech.* **330**, 349-374.

NA, Y., & MOIN, P. 1996 Direct numerical simulation of turbulent boundary layers with adverse pressure gradient and separation. Dept. Mech. Eng. Rep. **TF-68**, Stanford Univ.

PIOMELLI, U., FERZIGER, J., MOIN, P., & KIM, J. 1989 New approximate boundary conditions for large eddy simulations of wall-bounded flows. *Phys. Fluids A.* **1**, 1061-1068.

PIOMELLI, U., MOIN, P., & FERZIGER, J. H. 1988 Model consistency in large eddy simulation of turbulent channel flows. *Phys. Fluids.* **31**, 1884-1891.

SCHUMANN, U. 1975 Subgrid scale model for finite difference simulations of turbulent flows in plane channels and annuli. *J. Comp. Phys.* **18**, 376-404.

VREMAN, B., GEURTS, B., & KUERTEN, H. 1994 On the formulation of the dynamic mixed subgrid-scale model. *Phys. Fluids.* **6**, 4057-4059.

ZANG., Y., STREET, R. L., & KOSEFF, J. R. 1993 A dynamic mixed subgrid-scale model and its application to turbulent recirculating flows. *Phys. Fluids A.* **5**, 3186-3196.

Perspectives for ensemble average LES

By D. Carati[1]

1. Motivation and objectives

With the emergence of parallel computing, running several LES's simultaneously for the same turbulent flow becomes realistic, at least for a rather coarse resolution. We have already investigated this possibility and promising results have been obtained (Carati *et al*, 1996). In this report, we present several new approaches for subgrid scale modeling that can be developed when an ensemble of LES's is known.

1.1 Coupling between LES and RANS

First, we remark that the ensemble of LES's shares some properties with the RANS approach. Indeed, the ensemble average of quantities described by the LES's is equivalent to the large scale property of the same quantities obtained through the RANS. It is thus natural to investigate the possibility of coupling these methods. One interesting procedure that has been considered in a different context (Cabot, 1996) amounts to decomposing the domain into different regions. In some of these sub-domains, a RANS can be used if LES is too expensive. For example, the RANS can be used in the near wall region while the ensemble of LES's would be used for the region away from the wall (outer region). Matching conditions for the RANS quantities are easily accessible from averages of the realizations in the outer region. The main theoretical and practical difficulty is then to supply each LES realization with boundary information generated from the single RANS. This task is difficult since these boundary values are an artifact of the domain decomposition and thus do not reflect any physical or mathematical constraints. Boundary conditions for the LES can only be imposed through physically plausible assumptions that must be considered as part of the modeling effort needed in the LES context.

Using RANS models in wall region has a double advantage. First, RANS are much cheaper than LES, which are strongly limited by the problem of resolution close to solid boundaries. Second, RANS represents ensemble average information and thus requires a single simulation independent of the number of realizations in the outer region. The hope in the proposed approach is that (i) the RANS will be improved by the ensemble of LES's through the information passed at the boundary between the sub-domains, and (ii) the ensemble of LES will be much faster because they will not have to resolve the wall region. This approach has the very reasonable property of letting the LES's focus on the outer region in which the statistical theories that form the basis of subgrid scale modeling are believed to apply.

1 Université Libre de Bruxelles, Belgium

1.2 New models using the ensemble of LES's

To date, the ensemble of LES's has been used only in the determination of the model coefficient in the context of the ensemble averaged dynamic model. However, knowledge of an ensemble of realizations for the same flow can be used in a much more general manner. In particular, most of the concepts used in subgrid scale modeling originate from statistical theories of turbulence (Leslie and Quarini, 1979). With the approach we plan to develop, the link between LES and these theories becomes natural. In Section 2 we present some interesting uses of the ensemble of LES's for subgrid scale modeling purposes.

2. Accomplishments

2.1 The ensemble averaged dynamic model

In a study initiated during the 1996 Center for Turbulence Research Summer Program, we have shown that a collection of LES's can be used to develop new versions of the dynamic model based on the ensemble average. Indeed, the model coefficient is often seen as a "universal function" that can depend on space when the flow is not homogeneous but that should be independent of a particular realization. In an ensemble of LES's this is easily achieved. Moreover, the classical dynamic procedure relies on the existence of directions of homogeneity. When the flow is fully inhomogeneous, the dynamic procedure can be applied, but the coefficient evaluation then requires the solution of an integral equation (Ghosal *et al*, 1995). With the *ensemble averaged dynamic model*, it has been shown that the model coefficient can be obtained simply even for fully inhomogeneous flows. Some preliminary tests of the ensemble averaged dynamic model have been performed and show good agreement with experimental data. Assuming that the Smagorinsky coefficient is independent of the realization for statistically equivalent flows results in the following model:

$$\tau_{ij}^r - \frac{1}{3}\tau_{kk}^r\delta_{ij} \approx -2C\Delta^2|S^r|S_{ij}^r, \tag{1}$$

where C is independent of the realization index r. Here, S_{ij} represents the resolved strain tensor. The dynamic procedure can be used to determine C if the usual average over homogeneous directions is replaced by an average over the ensemble. The error caused by using models for the subgrid scale stresses now depends on the realization. By assuming that *for large ensembles, the Smagorinsky coefficient is essentially constant over the scale of the test filter*, we have been able to derive an analogous expression for C as in the spatially averaged version of the dynamic procedure:

$$C = \frac{\langle L_{ij}M_{ij}\rangle}{\langle M_{ij}M_{ij}\rangle}, \tag{2}$$

where the brackets now represent an ensemble average. The Leonard tensor is given[a] by $L_{ij} = \widehat{u_iu_j} - \widehat{u}_i\widehat{u}_j$ and $M_{ij} = 2\Delta|\widehat{S^r}|S_{ij}^r - 2\widehat{\Delta}|\widehat{S}^r|\widehat{S}_{ij}^r$. Of course, the latter

---

[a] The overline notation $\overline{\cdots}$ will be used for RANS quantities and not for LES variables. In this report, u_i represents the resolved field in the LES and $\widehat{u}_i$ the test field in the dynamic procedure.

assumption has to be verified *a posteriori*. The first conclusion we have reached is quite encouraging. Indeed, it appears that with only 16 simultaneous LES's, the ensemble averaged dynamic model performs as well as the volume averaged model. Moreover, the spatial variability of C decreases drastically when the number of realizations R increases. The comparison between a 512^3 decaying isotropic turbulence DNS and a 32^3 dynamic model LES have shown good agreement both for the total resolved energy and for the spectra (Carati *et al*, 1996).

2.2 Matching conditions for RANS and LES's

When a RANS is used in some sub-domains and LES's in others, new boundary conditions are needed. These conditions are not imposed by the physics of the flow but only by the domain decomposition adopted in the numerical integration. There is thus some arbitrariness in their choice. The first and simplest question is *how can the LES's feed the RANS?* Clearly, the number of boundary conditions will depend on the RANS model and more specifically on the number of variables predicted by the RANS. The natural assumption is then to impose equality between the RANS quantities and the corresponding ensemble averaged LES quantities. This leads to the following type of equalities:

$$\overline{u}_i = \langle u_i^r \rangle, \tag{3a}$$

$$\overline{u_i'^2} = \langle (u_i^r)^2 \rangle - \langle u_i^r \rangle^2. \tag{3b}$$

A much more difficult problem is to determine how one single RANS can be used to derive boundary conditions for an ensemble of LES's. Indeed, $3R$ boundary conditions are needed for the u_i^r, $r = 1 \ldots R$, $i = 1 \ldots 3$. In principle, $3R$ RANS quantities can be matched. In practice, however, only a few RANS quantities are available. Typically, $\overline{u}_i$ plus (maybe) $\overline{k}$, $\overline{\epsilon}$, $\overline{u'^2}$, $\overline{v'^2}$, $\overline{w'^2}$, $\overline{u'v'}$. The minimal condition is of course:

$$\langle u_i^r \rangle = \overline{u}_i. \tag{4}$$

However, the simplest choice of imposing $u_i^r = \overline{u}_i \forall r$ appears to be a very poor solution. Indeed, for a stationary channel flow, $\overline{u}_i$ is likely to be zero in the spanwise and wall-normal directions while it should be constant in the streamwise direction. The LES's for the core flow then reduce to a thinner channel with moving planes which is not realistic. Hence, it can be concluded that the fluctuations should be involved in the boundary conditions for the LES's. The solution we investigated was obtained by matching both the average velocity and the turbulence intensities. Of course, there is an infinity of solutions for these conditions. They can be written as[b]:

$$u_\alpha^r = \overline{u}_\alpha + \frac{h_\alpha^r - \langle h_\alpha^r \rangle}{\langle u_\alpha^r (h_\alpha^r - \langle h_\alpha^r \rangle) \rangle} \overline{u_\alpha'^2}, \tag{5a}$$

---

[b] We adopt the convention of implicit summation over repeated Latin indices. No summation is implied on Greek indices.

where the quantity h_α^r is arbitrary and has to be determined as part of the modeling effort needed in LES. An equivalent formulation has also been considered:

$$u_\alpha^r = \bar{u}_\alpha + \frac{g_\alpha^r - \langle g_\alpha^r \rangle}{\langle (g_\alpha^r - \langle g_\alpha^r \rangle)^2 \rangle^{1/2}} \overline{u_\alpha'^2}^{1/2}, \tag{5b}$$

where g_α^r is now the arbitrary quantity. Both formulations imply $\langle u_\alpha^r \rangle = \bar{u}_\alpha$ and $\langle (\delta u_\alpha^r)^2 \rangle = \overline{u_\alpha'^2}$ (here $\delta u_\alpha^r = u_\alpha^r - \langle u_\alpha^r \rangle$). By coupling RANS for the wall region and an ensemble of LES's for the core flow, the LES model has to deal with both the subgrid scale stress and the boundary conditions. In general, h_i^r is a function of the velocity field and of all its derivatives $h_i^r = h_i^r(u_i, \partial_i u_j, \ldots)$. A promising choice for h_i^r has been considered. First, we note that the existence of a continuous boundary provides an unambiguous decomposition of the velocity into a part normal to the boundary $u_\perp$ and a part parallel to the boundary $\vec{u}_\parallel$ (which is a 2D vector). The choice considered so far consists in imposing the following boundary conditions for the parallel part of the velocity:

$$\vec{h}_\parallel^r = \partial_\perp \vec{u}_\parallel^r \tag{6}$$

and using continuity:

$$\partial_\perp u_\perp^r = -\vec{\nabla}_\parallel \vec{u}_\parallel^r \tag{7}$$

as a boundary condition for $u_\perp^r$. With this choice, the boundary condition for the components of the parallel velocity reduces to:

$$\delta u_{\parallel\alpha}^r = 2 \frac{\partial_\perp \delta u_{\parallel\alpha}^r}{\partial_\perp \langle (\delta u_{\parallel\alpha}^r)^2 \rangle} \overline{u_{\parallel\alpha}'^2}. \tag{8}$$

The set of boundary conditions (5,7-8) must now be tested in simple cases.

2.3 Proposals for new subgrid scale models

As already discussed, the additional information provided by the ensemble of LES can be used for constructing new eddy viscosity models. However, it is known that the eddy viscosity gives a very simplified picture of the subgrid scale stress. For that reason, it is also interesting to investigate the possibility of modifying the structure of the subgrid scale model by using some quantities that are directly accessible from the ensemble of LES's.

2.3.1 Model based on the fluctuating strain tensor

The first model we propose is obtained by subtracting the mean strain:

$$\tau_{ij}^r = -\nu_T^r (S_{ij}^r - \langle S_{ij}^r \rangle) \equiv -\nu_T^r \, \delta S_{ij}^r. \tag{9}$$

This formulation has some nice properties. The average dissipation is given by

$$\mathcal{E} = \langle \nu_T \delta S_{ij}^r \delta S_{ij}^r \rangle + \nu_0 \langle S_{ij}^r S_{ij}^r \rangle, \tag{10}$$

and thus the turbulent dissipation only originates from the fluctuating part of the strain tensor. The mean part only contributes to the molecular dissipation. This property ensures that the model will not produce dissipation in a laminar region. In addition, while this model is dissipative on average (provided the eddy viscosity is positive), individual realizations can have negative dissipation thus representing the inverse transfers of energy from the small unresolved scales to the large ones (backscatter). It is generally believed that backscatter originates from fluctuation phenomena an the subgrid scale, and representation of this effect through fluctuations in the strain tensor is thus very reasonable.

2.3.2 Anisotropic model

Although isotropic turbulence has been studied in great detail for many years, the presence of some anisotropy is almost universal in practical instances of turbulent flow. However, anisotropy usually originates from complex interactions between flow direction, solid boundaries, and external constraints like pressure gradient or global rotation. It is thus quite difficult to predict *a priori* the main direction of anisotropy. In the context of statistical averaged LES, we have access at any instant to mean quantities that will display the anisotropic structure of the turbulence. On the contrary, when only one single LES is accessible, the direction of anisotropy can only be discovered after some averaging in time if there is no direction of homogeneity. A model that would directly take advantage of the ensemble of LES could be:

$$\tau_{ij}^r \approx -\mu \gamma_{ik} \gamma_{jl} S_{kl}^r, \tag{11}$$

where the factor μ plays the role of an eddy viscosity but through an anisotropic relation between the subgrid scale stress and the strain tensor. The tensor γ_{ij} should be a measure of the anisotropy. It can be constructed with the velocity fluctuations:

$$\gamma_{ij} = 3 \frac{\langle \delta u_i^r \, \delta u_j^r \rangle}{\langle \delta u_k^r \, \delta u_k^r \rangle}. \tag{12}$$

This model reduces to the classical eddy viscosity model for isotropic turbulence ($\gamma_{ij} = \delta_{ij}$). Moreover, the sign of the dissipation depends only on the sign of μ since the product of τ_{ij}^r and the strain tensor is given by

$$-\tau_{ij} S_{ij} = \mu S_{ij} \gamma_{ik} \gamma_{jl} S_{kl} \tag{13}$$

whose sign only depends on the sign of μ. Moreover, if there is no turbulence in one direction ($\delta u_a = 0$), the model has the property that the component $\tau_{ia} = \tau_{aj} = 0$. This is an expected property that is missed by the Smagorinsky model, which dissipates even in the laminar regime.

3. Conclusions and future work

We conclude by stressing that the use of an ensemble of LES's is not *per se* much more expensive than the use of a single realization. Indeed, let us consider a

stationary LES and denote by t_t the transient period between the beginning of the simulation and the time at which the turbulence becomes fully developed. Let us also denote by t_s the time (beyond t_t) required to converge the statistics. Then, the CPU time required for obtaining converged statistics with a single LES is $t_t + t_s$. With an ensemble of realizations, statistics are accumulated over both the ensemble and time. Thus, for equivalent sample, the ensemble only needs to be advanced in time by the amount t_s/R. The total CPU cost for the ensemble is thus $R(t_t + t_s/R)$, which amounts in an overhead of $(R - 1)t_t$ over a single realization. If the ratio between the transient phase and the time needed to converge statistics is small, then the additional cost will be acceptable. Moreover, if the LES is not stationary and if there are no homogeneous directions, the ensemble average approach would seem to be the only way to obtain statistics. Finally, a wall model using RANS concepts would greatly reduce the cost of each LES in the ensemble.

Future work must now be devoted to the numerical implementation of the idea developed in this report. A first and very simple test of the matching conditions can be obtained by running an LES in the core flow of a channel with the boundary conditions described in section 2.2 in which the quantities $\overline{u_i'^2}$ are obtained from experimental data. In that case, the LES is fed with "exact" RANS quantities, and the test will clearly determine if the boundary conditions performs reasonably well. The channel flow can also be used for testing the new models proposed in section 2.3.

REFERENCES

CABOT, W. 1996 Near-wall models in large eddy simulations of flow behind a backward-facing step. in *Annual Research Briefs 1996*, Center for Turbulence Research, NASA Ames/Stanford Univ. 199.

CARATI, D., WRAY, A., AND CABOT, W. 1996 Ensemble averaged dynamic modeling. *Proc. 1996 Summer Program*, Center for Turbulence Research, NASA Ames/Stanford Univ. 237.

LESLIE, D. C., AND QUARINI, G. L. 1977 The application of turbulence theory to the formulation of subgrid modeling procedure. *J. Fluid Mech.* **91**, 65.

GHOSAL, S., LUND, T. S., MOIN, P. AND AKSELVOLL, K. 1995 A dynamic localization model for large-eddy simulation of turbulent flows. *J. Fluid Mech.* **286**, 229.

$\mathcal{S}9\text{-}34$

Anisotropic grid-based formulas for subgrid-scale models

By G.-H. Cottet[1] AND A. A. Wray

1. Motivations and objectives

Anisotropic subgrid-scale models have long been recognized as a natural alternative to the isotropic Smagorinsky model. *A priori* tests, based either on experiments (Liu *et al.* 1994) or on DNS data have often shown that these models have much better correlations than the Smagorinsky model. However their efficacy in large eddy simulations has so far been limited by two factors. First, these models are in general viewed, through Taylor expansions, as a way to compute the subgrid-scale contribution of the Leonard term. They are used with the coefficient values which result from these Taylor expansions and thus depend on the form of the filter function. Secondly, anisotropic models are based on tensor forms of the turbulent viscosity and therefore may produce backscatter as well as dissipation. The clipping techniques, which are proposed (Liu *et al.* 1994, Vreman *et al.* 1997) to overcome the destabilizing effects of backscatter, are based on energy balances but ignore that dissipation and backscatter in general coexist at every point along different strain directions of the flow. They thus lead to models which are not dissipative enough, which explains why they are often complemented by Smagorinsky terms in so-called *mixed* models. These formulations, however, are not able to retain the potential gain offered by the anisotropy of the original model, in particular in laminar or wall-bounded flows.

Our goal here is twofold. We first derive formulas based on the quantities computed on the grid that facilitate the implementation of the anistropic model in any code. By distinguishing between backscatter and dissipation directions in the flow, we also present strictly dissipative formulas which lead to stable and truly anisotropic schemes.

2. Accomplishments

2.1 The model

Our starting point will be the following model for the residual shear stresses, sometimes referred to as the self-similarity model (Liu *et al.* 1994) or the gradient model (Vreman *et al.* 1997):

$$\tau_{ij} \simeq C\Delta^2 D_{ik}\overline{u}D_{jk}\overline{u} \tag{1}$$

where $D_{ik}\overline{u} = \frac{\partial \overline{u}_i}{\partial x_k}$ and Δ is the filter width. Throughout the paper, we will use the convention of summation of repeated indices.

1 Permanent address: LMC-IMAG, Université Joseph Fourier, BP 53 Grenoble Cédex 9, France

2.1.1 Integral approximation and grid formulas

Our derivation is based on a numerical filter function ζ satisfying the following moment conditions:

$$\int x_k x_l \zeta(\mathbf{x}) \, d\mathbf{x} = \delta_{kl} \, , \quad k, l = 1, 2, 3 \tag{2}$$

where x_k denote the components of $\mathbf{x}$ and δ_{kl} is the Kronecker symbol. Such a filter can be easily constructed by proper rescaling of any positive function satisfying symmetry properties (e.g. functions with spherical symmetry or functions constructed through tensor product of one-dimensional even functions).

We first write (here and in the sequel we drop the overbar notation for the resolved fields)

$$\Delta^2 D_{ik} \mathbf{u}(\mathbf{x}) D_{jk} \mathbf{u}(\mathbf{x}) = \Delta^{-3} \int D_{ik} \mathbf{u}(\mathbf{x}) D_{jl} \mathbf{u}(\mathbf{x})(y_k - x_k)(y_l - x_l) \zeta(\frac{\mathbf{y} - \mathbf{x}}{\Delta}) \, d\mathbf{y} \tag{3}$$

where we recall that the summation of repeated indices is implied. In the above formula, Δ is the filter width, which for the time being is assumed to be constant. By Taylor expansions of u_i and u_j around $\mathbf{x}$, this yields

$$\Delta^2 D_{ik} \mathbf{u}(\mathbf{x}) D_{jk} \mathbf{u}(\mathbf{x}) =$$
$$\Delta^{-3} \left\{ \int [u_j(\mathbf{y}) - u_j(\mathbf{x})][u_i(\mathbf{y}) - u_i(\mathbf{x})] \zeta(\frac{\mathbf{y} - \mathbf{x}}{\Delta}) \, d\mathbf{y} + O(\Delta^2) \right\}. \tag{4}$$

Since ultimately it is the divergence of τ_{ij} that we need to model in order to solve the filtered Navier-Stokes equations, we take the divergence of (4) to obtain, after cancellation of the term involving the divergence of $\mathbf{u}$:

$$\partial_j [D_{ik} \mathbf{u}(\mathbf{x}) D_{jk} \mathbf{u}(\mathbf{x})] \simeq A_i + B_i$$

where we used the notation ∂_j for $\partial/\partial x_j$ and

$$A_i = -\Delta^{-3} \int [u_j(\mathbf{y}) - u_j(\mathbf{x})] \partial_j u_i(\mathbf{x}) \zeta(\frac{\mathbf{y} - \mathbf{x}}{\Delta}) \, d\mathbf{y}$$

$$B_i = -\Delta^{-4} \int [u_j(\mathbf{y}) - u_j(\mathbf{x})][u_i(\mathbf{y}) - u_i(\mathbf{x})] \partial_j \zeta(\frac{\mathbf{y} - \mathbf{x}}{\Delta}) \, d\mathbf{y}$$

It is readily seen that A_i are convective terms: if one sets $\lambda = \int \zeta(\mathbf{y}) \, d\mathbf{y}$ and

$$\hat{\mathbf{u}}(\mathbf{x}) = \frac{1}{\lambda \Delta^3} \int \mathbf{u}(\mathbf{y}) \zeta(\frac{\mathbf{y} - \mathbf{x}}{\Delta}) \, d\mathbf{y}$$

then A_i can be rewritten as $(\hat{\mathbf{u}} - \mathbf{u}) \nabla u_i$. It thus does not contribute to the energy balance. Since the goal of SGS models is to model the transfer of energy between

large and small scales, we will only be interested in B_i. Hence the SGS model can be expressed as

$$\partial_j \tau_{ij} \simeq -C\Delta^{-4} \int [u_j(\mathbf{y}) - u_j(\mathbf{x})][u_i(\mathbf{y}) - u_i(\mathbf{x})]\partial_j \zeta(\frac{\mathbf{y} - \mathbf{x}}{\Delta})\, d\mathbf{y} \qquad (5)$$

2.1.2 Viscous scales and grid refinement

The above derivation assumes an isotropic filter ζ. In practice, it is natural to use a function which matches the computational grid. For a variable grid such as those generally used for wall-bounded flows, one can then expect that grid refinement in specific directions will translate into variable viscous length scales in the subgrid-scale model. To be more specific let us assume that the filter ζ is built from a unique one-dimensional shape ρ in all 3 directions and that $\Delta_1(x_1), \Delta_2(x_2), \Delta_3(x_3)$ are the local grid sizes in the 3 directions. The natural generalization of formulas (4) and (5) to this case is given by

$$\tau_{ij}(\mathbf{x}) \simeq \frac{C}{\omega(\mathbf{x})} \int [u_j(\mathbf{y}) - u_j(\mathbf{x})][u_i(\mathbf{y}) - u_i(\mathbf{x})]\zeta(\mathbf{x}, \mathbf{y})\, d\mathbf{y}$$

$$\partial_j \tau_{ij}(\mathbf{x}) \simeq \frac{C}{\omega(\mathbf{x})} \frac{1}{\Delta_j(x_j)} \int [u_j(\mathbf{y}) - u_j(\mathbf{x})][u_i(\mathbf{y}) - u_i(\mathbf{x})]\lambda_j(\mathbf{x}, \mathbf{y})\, d\mathbf{y}$$

where $\omega(\mathbf{x}) = \Delta_1(x_1)\Delta_2(x_2)\Delta_3(x_3)$ is the volume of the cell centered at $\mathbf{x}$ and

$$\zeta(\mathbf{x}, \mathbf{y}) = \rho(\frac{x_1 - y_1}{\Delta_1(\mathbf{x})})\rho(\frac{x_2 - y_2}{\Delta_2(\mathbf{x})})\rho(\frac{x_3 - y_3}{\Delta_3(\mathbf{x})})$$

$$\lambda_1(\mathbf{x}, \mathbf{y}) = \rho'(\frac{x_1 - y_1}{\Delta_1(\mathbf{x})})\rho(\frac{x_2 - y_2}{\Delta_2(\mathbf{x})})\rho(\frac{x_3 - y_3}{\Delta_3(\mathbf{x})}).$$

and similar formulas for λ_2, λ_3. It can be shown (see Cottet 1997 for details) by using a coordinate mapping between the mesh and a uniform isotropic grid that these formulas correspond to the differential subgrid-scale model

$$\tau_{ij} \simeq \Delta_k(\mathbf{x})^2 D_{ik}\mathbf{u}D_{jk}\mathbf{u}$$

In other words, the eddy-viscosity length scale is given by the grid spacing in the corresponding direction. In near wall regions, when grid refinement is used, this produces an additional damping in the SGS dissipation which we believe is desirable. Note that the traditional derivation of subgrid-scale models does not apply to varying size filters, making the use of (1) questionable.

2.1.3 Anisotropic clipping

The total subgrid-scale dissipation $\mathcal{D}$ associated to the model (5) is obtained by multiplying this formula by $\mathbf{u}(\mathbf{x})$ and integrating over $\mathbf{x}$. Writing $\mathbf{u}(\mathbf{x}) = \frac{1}{2}[\mathbf{u}(\mathbf{x}) + \mathbf{u}(\mathbf{y})] + \frac{1}{2}[\mathbf{u}(\mathbf{x}) - \mathbf{u}(\mathbf{y})]$ and using the symmetry of ζ, we are left with

$$\mathcal{D} = \frac{C}{2}\Delta^{-4} \int [\mathbf{u}(\mathbf{y}) - \mathbf{u}(\mathbf{x})] \cdot \nabla\zeta(\frac{\mathbf{y} - \mathbf{x}}{\Delta})|\mathbf{u}(\mathbf{y}) - \mathbf{u}(\mathbf{x})|^2\, d\mathbf{x}\, d\mathbf{y}$$
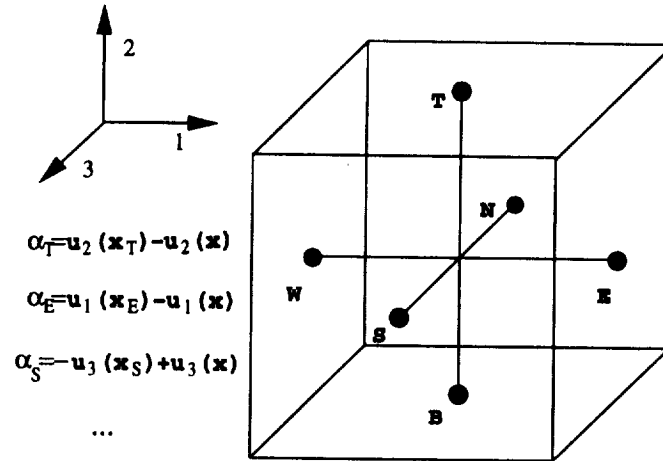
FIGURE 1.   Finite-difference stencil of the subgrid-scale model in the case of a uniform grid with a radial hat filter. $\alpha_T/\Delta, \alpha_E/\Delta, \cdots$ denote the weights of the corresponding grid points.

This formula gives a way to measure the local dissipation at a given point $\mathbf{x}$ as well by restricting the integral over $\mathbf{y}$ only. It also enables us to formulate a strictly dissipative model as follows

$$\partial_j \tau_{ij}(\mathbf{x}) \simeq \Delta^{-4} \int \left\{ [\mathbf{u}(\mathbf{x}) - \mathbf{u}(\mathbf{y})] \cdot \nabla\zeta(\frac{\mathbf{x} - \mathbf{y}}{\Delta}) \right\}_+ [\mathbf{u}(\mathbf{x}) - \mathbf{u}(\mathbf{y})] \, d\mathbf{y} \qquad (6)$$

where $a_+ = \max(0, a)$. Unlike the traditional clipping strategies, which would consist in replacing $\partial_j \tau_{ij}$ by zero whenever the global energy budget would have the wrong sign, this technique respects the anisotropy of the original formula in the sense that it allows to dissipate in one or more directions while controlling the backscatter which would arise in the other directions. A clipping technique can be written along the same lines to make sure that when combining the subgrid-scale model with the effect of the molecular viscosity the method is strictly dissipative.

2.2 Large eddy simulations

2.2.1 Isotropic turbulence

We first examine the validity of our model in simulations of decaying isotropic turbulence. All calculations were done with a spectral code in a periodic box with full dealiasing. The subgrid-scale models is therefore implemented on a uniform grid on which velocity values are classically obtained through FFT.

We have considered two possible choices for the numerical filter ζ: a radial function $\zeta_1(\mathbf{x}) = \alpha f(|\mathbf{x}|)$ and a tensor product function $\zeta_2(\mathbf{x}) = \beta f(x_1)f(x_2)f(x_3)$. The function f is a piecewise quadratic spline with support in $[-1.5, +1.5]$, and α, β
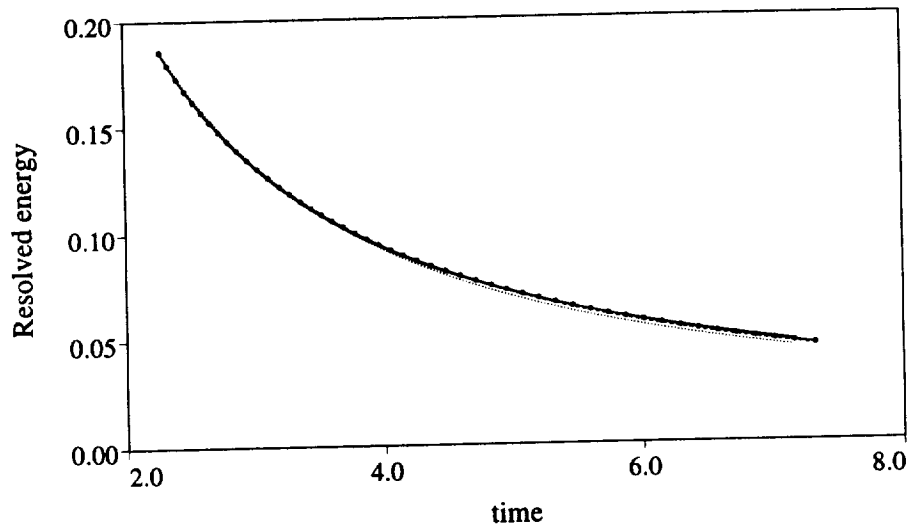
FIGURE 2. Energy decay for DNS and LES with Smagorinsky and anisotropic models. o : DNS results ——— : Smagorinsky model ········ : Anisotropic model with 27 points filter ---- : Anisotropic model with 7 points filter.
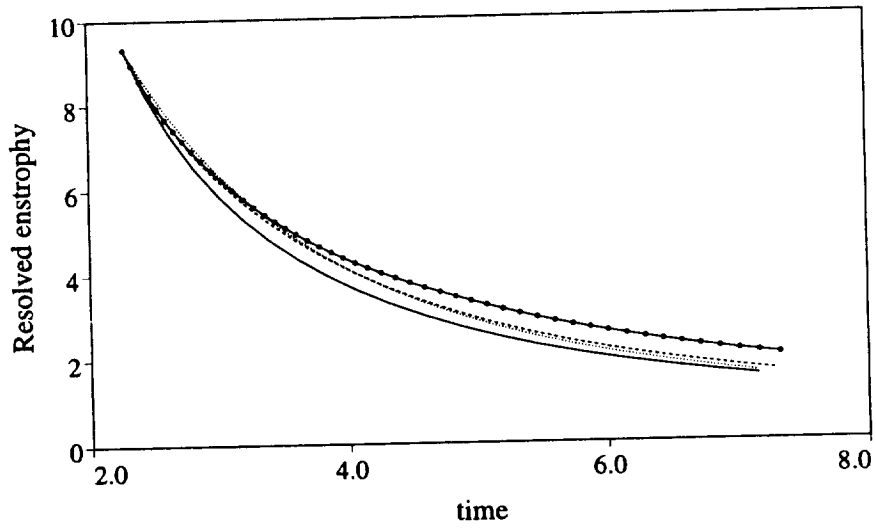

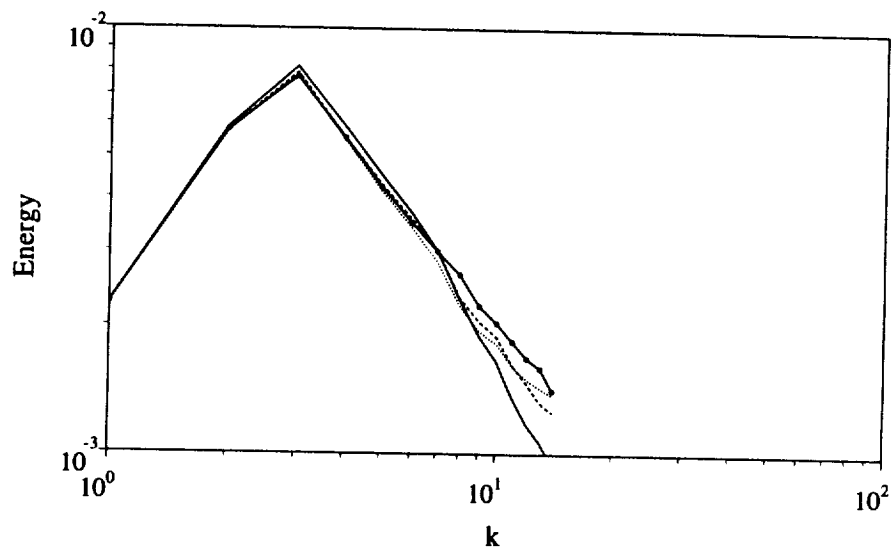FIGURE 3. Enstrophy decay for DNS and LES with Smagorinsky and anisotropic models. See Fig. 2 for symbol legend.

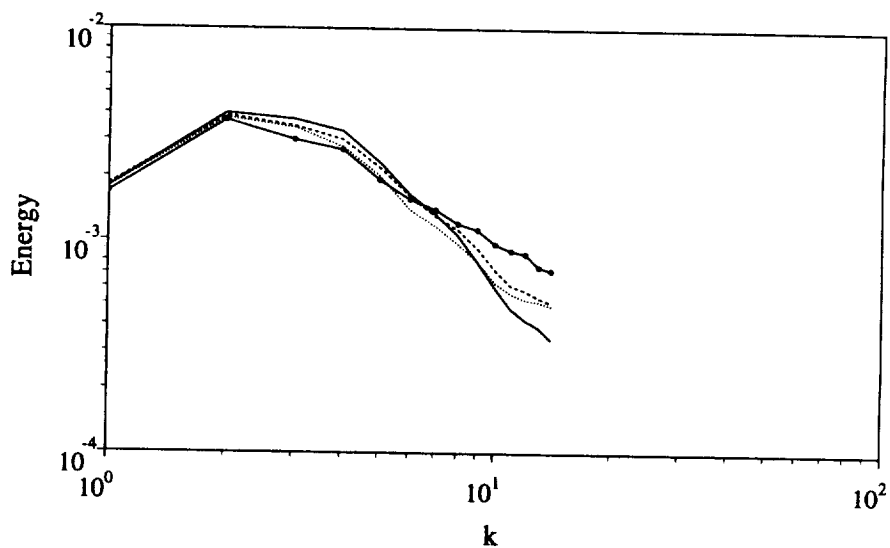FIGURE 4.   Energy spectra at $t = 4$. for DNS and LES. See Fig. 2 for symbol legend.

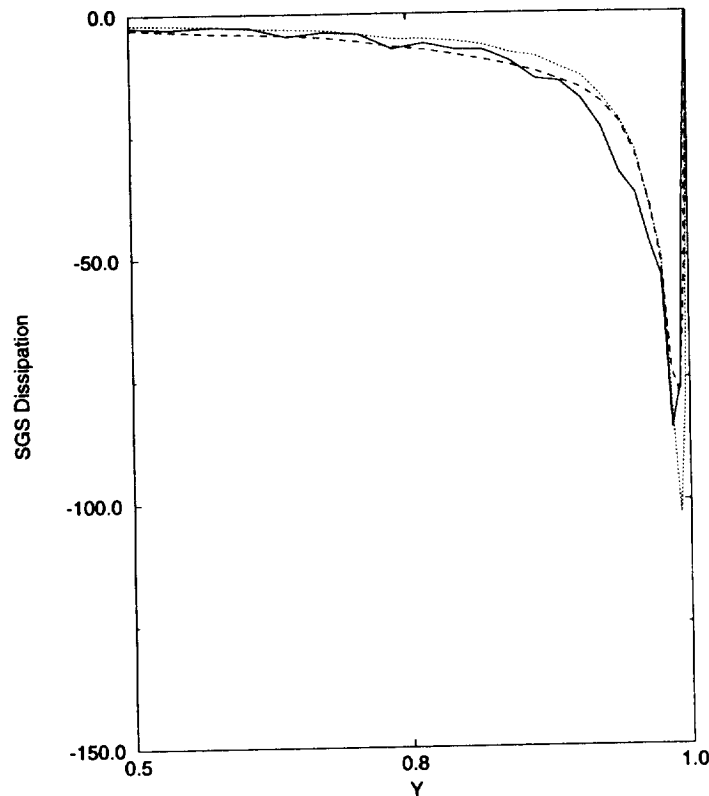FIGURE 5.   Energy spectra at $t = 7$. See Fig. 2 for symbol legend.

FIGURE 6. Subgrid-scale dissipation for the dynamic model and anistropic models.
——— : Dynamic model; ········ : Unclipped C=.25; ---- : Clipped C=.075.

are 2 normalization constants needed to enforce (2). As a result, the stencil corresponding to the implementation of (5) involves 7 points in the first case and 27 in the second one. Figure 1 sketches the particular form of the stencil in the first case.

We have compared the results of LES on a 32^3 grid using the clipped anisotropic model (6), as well as the Smagorinsky model, with a 512^3 DNS. The coefficients of the various models have all been tuned to yield an energy decay which matches the DNS results (Fig. 2). The enstrophy decay curves in Fig. 3 show that the anisotropic models behave better than the Smagorinsky model up to time $T \sim 5$. This is confirmed by the energy spectra showed in Fig. 4. Past this time, all models are too dissipative in the high modes, with slightly better results for the anisotropic model (Fig. 5). The particular implementation chosen for the anisotropic model (isotropic vs tensor-product filter form) does not seem to significantly affect the results.

2.2.2 Channel calculations

This case is more challenging as it is well known that the Smagorinsky model is unable in this geometry to give good results in the absence of *ad hoc* damping at the walls or dynamic coefficient calculation.

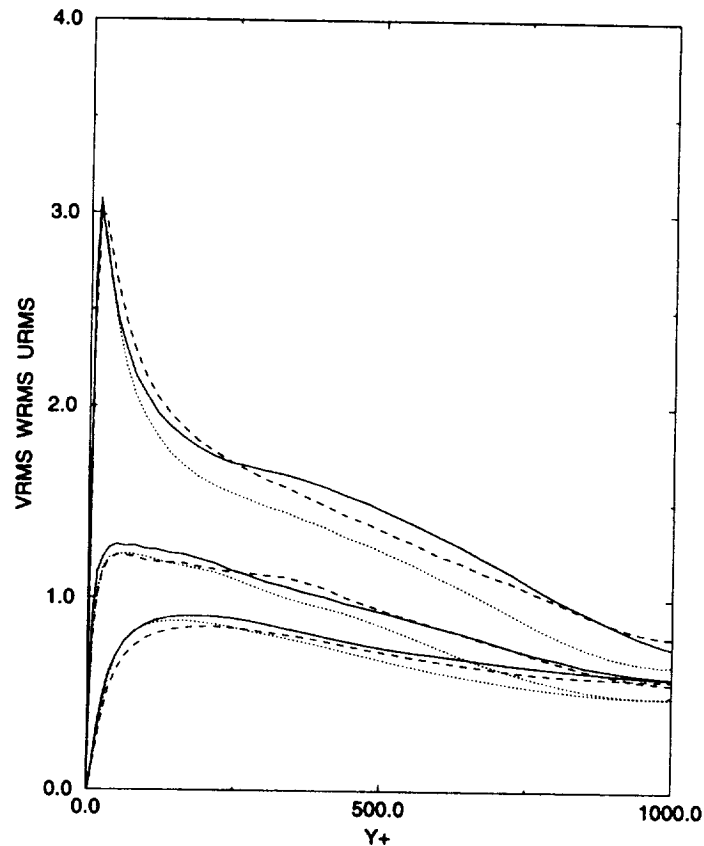We show comparisons between the anisotropic model and the so-called global

FIGURE 7.   Turbulence intensities in wall coordinates; top curves: streamwise velocity, middle curves: normal velocity, bottom curves: spanwise velocity. Symbols same as Fig. 6.

dynamic model (Germano *et al.* 1991), which can considered as the best available model for this geometry. Our tests are done in the context of a Tchebytchev-Fourier collocation code (Kim *et al.* 1987). In this numerical scheme, the Crank-Nicolson time-advancing scheme is used for diffusion in the wall normal direction together with a third order Runge-Kutta method to advance the nonlinear convection and SGS terms. Periodic boundary conditions are assumed in the streamwise and spanwise directions and no-slip conditions at the walls located at $y = \pm 1$. Dealiasing is performed in the periodic directions, and the pressure is updated at each iteration to maintain a constant momentum throughout the calculation. We have focused on the case of a Reynolds number of $Re_\tau = 1,030$ based on the shear velocity, which corresponds to a Reynolds number of about $25,000$ based on the centerline velocity and the channel half-width.

The anistropic model has been implemented with the tensor-product filter ζ_2. Note that the grid refinement given by the Tchebytchev collocation points in the wall normal direction implies a variable eddy-viscosity length scale in this direction as explained in 2.1.2. Two cases have been considered: in the first one the method
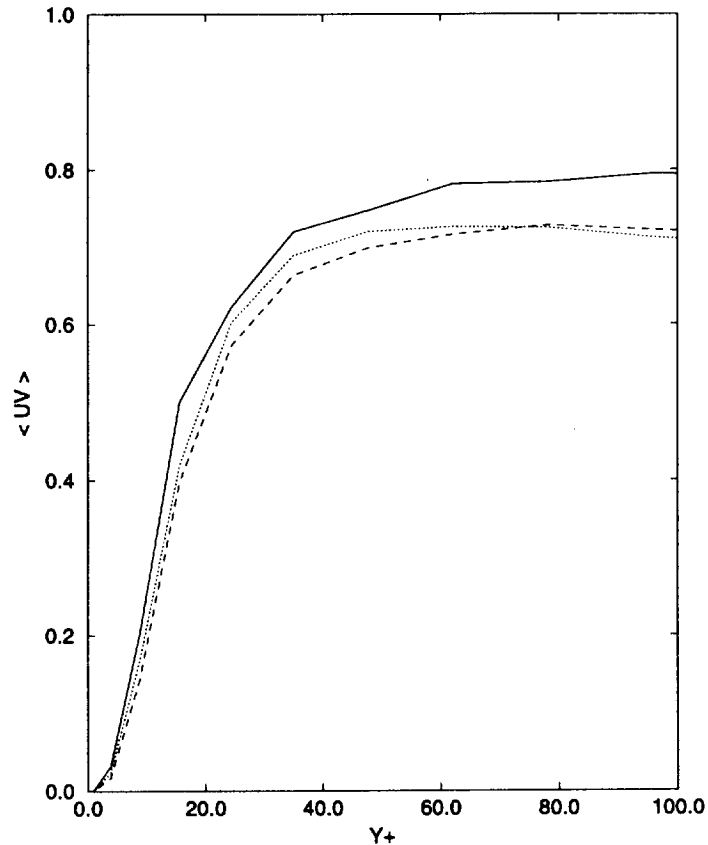
FIGURE 8. Large scale shear stress in wall coordinates. Symbls same as Fig. 6.

(5) is used without any clipping and a coefficient $C = 0.25$, while in the second a method similar to (6) is used in order to prevent the backscatter from overwhelming the molecular dissipation. In this latter case, a smaller value of the coefficient was chosen ($C = 0.075$). Figure 6 shows the subgrid-scale dissipation averaged on planes parallel to the walls. The similarity of the profiles obtained by the anisotropic models and the dynamic model is striking and confirms that the anisotropic model has a much better behavior in near wall regions than the Smagorinsky model. This observation is confirmed by the results obtained for the velocity fluctuations in Fig. 7 and the shear stresses in Fig. 8. We refer to (Cottet 1997) for more numerical results for this case.

3. Future plans

Tests of the anisotropic model have shown the superiority of this model over the Smagorinsky model. This superiority, which can be expected from the *a priori* tests that can be found in the literature, has been confirmed in LES using the present method. The efficacy of the model has gained from its ability to incorporate a truly anistropic backscatter control. The performance of the model both in isotropic and wall-bounded flows encourage trying it for other flows such as shear layers or jets.

Another direction of research is the implementation of a dynamic procedure to compute the model coefficient, along the lines suggested by Cottet (1997). On the basis of the present results, one can expect that this technique should not produce highly oscillatory values for the coefficient. In other words, the anisotropic model should be better conditioned than the Smagorinsky model for a dynamic procedure, in particular when no averaging over homogeneous directions can be used to stabilize it.

REFERENCES

COTTET, G. H. 1997 Anisotropic subgrid-scale models for Large Eddy Simulations of turbulent flows. *submitted.*

GERMANO, M., PIOMELLI, U., MOIN, P. & CABOT, W. H. 1991 A dynamic subgrid-scale eddy viscosity model. *Phys. Fluids A.* **3**, 1760-1765.

KIM, J., MOIN, P. &MOSER, R. 1987 Turbulence statistics in fully developed channel flow at low Reynolds number. *J. Fluid Mech.* **177**, 133-166.

LIU, S., MENEVEAU, C. & KATZ, J. 1994 The property of similarity subgrid-scale models. *J. Fluid Mech.* **275**, 83-119.

VREMAN, V., GEURTS, B. & KUERTEN, H. 1997 Large-eddy simulations of the turbulent mixing layer. *J. Fluid Mech.* **339**, 357-390.

Some modeling requirements for
wall models in large eddy simulation

By Jeffrey S. Baggett

1. Motivation and objectives

Large eddy simulation (LES) works when the energy-containing eddies of the flow are representable on the numerical grid. Unfortunately, in turbulent wall-bounded flows, outside the viscous sub-layer, these eddies can scale as the distance from the wall. As the Reynolds number increases and the viscous sub-layer shrinks, the number of grid points required to resolve the near-wall eddies increases dramatically. This near-wall resolution requirement is currently the severest bottleneck in applying LES to flows of practical interest (Chapman 1979, see also Baggett, Jiménez, and Kravchenko in this volume).

Deardorff (1970), in the first simulation of turbulent channel flow, was the first to use a wall model to avoid resolving the near-wall region in an LES. Computational resources were limited, 6720 grid points were the maximum number that would fit in core memory, and the first near-wall grid point had to be located well outside the viscous sub-layer, thus rendering the computed wall shear stresses highly inaccurate. To remedy this deficiency Deardorff constrained the wall-normal second derivatives of the horizontal velocities at the first off-wall grid point in such a way that the logarithmic law of the wall was satisfied in the mean. Effectively, an instantaneous logarithmic law was used to parameterize the wall shear stresses in terms of the horizontal velocities at the first off-wall grid point.

Since 1970, a number of other wall models have been proposed for use in LES of attached flows. Nearly all of them estimate the wall shear stresses which are used as boundary conditions for the core flow LES (along with zero wall-normal velocity at the wall). As of this writing, there are essentially three kinds of wall models that have been employed in LES.

The first and most widely used kind of wall model is an equilibrium stress model. The logarithmic law of the wall is applied locally to relate the horizontal velocities at some point above the wall to the wall shear stresses. As originally proposed by Schumann (1975), deviations from the mean wall shear stress are assumed to be linearly correlated to deviations from the mean horizontal velocities. This assumption yields an algebraic, possibly nonlinear, relation between the instantaneous wall shear stress and the off-wall horizontal velocity. A number of variations and improvements on this scheme have been proposed (see Piomelli, *et al.* 1989 for a review), but they are all based on an equilibrium stress assumption and their range is, therefore, limited.

A second kind of model, which has much in common with domain decomposition techniques, uses the three-dimensional boundary layer equations with a wall-damped eddy viscosity to represent the near wall region (Cabot 1995, Balaras *et*

al. 1996). The standard LES equations are solved on a coarse grid, with the first off-wall grid point located outside the buffer layer, using wall shear stress and zero transpiration boundary conditions. The wall shear stresses are provided by integrating the three-dimensional boundary layer equations on a grid embedded between the wall and the first off-wall LES grid point. The boundary conditions used for the boundary layer equations are no-slip at the wall, and the velocities are matched to the LES velocities at the first LES off-wall grid point. While the boundary layer equations are cheaper to solve numerically than the LES equations, this approach is still expensive since the grid required in the near-wall region for the boundary layer equations is similar to that required if the original LES were simply to resolve the near-wall region. Furthermore, this approach does not make sense in flows which do not exhibit boundary layers, e.g. separated flows. However, the general idea of applying a domain decomposition strategy and using different constitutive equations in near-wall domains may prove valuable for the general wall modeling problem.

The two kinds of wall models mentioned above apply to a limited class of flows; however, a third approach has been developed which, in principle, can be applied to develop wall models for arbitrary flows. In this approach linear stochastic estimation is used to find the best least squares estimate of the wall stresses given the LES velocities on some plane, or planes, parallel to the wall (Bagwell 1993, Bagwell 1994). Again, the estimated wall shear stresses are used as boundary conditions for the LES. Bagwell successfully employed the resulting wall model in LES of channel flow at $Re_\tau = 180$, but attempts to re-scale the wall model to apply it in an LES of channel flow at $Re_\tau = 640$ met with limited success. While this approach is a general mathematical approach and does not rely on the underlying physics, the two-point correlation tensor of the flow must be known to form the linear stochastic estimation coefficients.

None of the existing wall models seems to be a great candidate for use in LES of complex flows (see Cabot in this volume). Algebraic wall models based on equilibrium conditions are too simple to deal with complex flows, and solving three-dimensional boundary layer equations is expensive and also not easily extended to non-attached flows. One of the goals of the current study is to determine what information is needed from the near-wall region for accurate LES of the core flow. In other words, we would like to establish a target for the further development of wall models. Once a well-defined target is established, it will be the object of further studies to inquire as to whether or not simpler (than full Navier–Stokes or other three-dimensional PDE's) systems, such as low-dimensional dynamical systems, are capable of producing the necessary near-wall information.

In this preliminary study we seek to answer the following question: What information does the core flow need from the near-wall region; that is, what does a wall model have to provide?

2. Accomplishments

To gain some insight into the questions asked above we have conducted some experiments using a coarse grid direct numerical simulation (DNS) of turbulent

channel flow. The DNS was performed using a second order finite difference code (Morinishi 1995). The grid is staggered and stretched in the wall-normal direction using a hyperbolic tangent mapping. Time is advanced using a three-stage Runge Kutta, fractional step scheme in which the wall-normal viscous terms are treated implicitly. The flow domain is 2π, $2\pi/3$, and 2 in the streamwise (x), spanwise (z), and wall-normal (y) directions, respectively. The domain is discretized by 32,32, and 33 grid volumes in the streamwise, spanwise, and wall-normal directions. The Reynolds number, Re_τ, based on the channel half-width, h, and the friction velocity, u_τ, is 200. Unless otherwise noted, all simulations were performed with a constant pressure gradient in the streamwise direction.

Our experimental strategy will begin with a fully developed field as an initial condition and then do a simulation while saving the velocity and/or velocity gradient data on some parallel planes above the wall. The time series of boundary data, or modifications of the time series, is then used to provide boundary conditions to conduct simulations of the flow between the designated boundary plane and the far wall. By making selective modifications to the the time series of boundary data, we can gain insight into what information the near-wall flow must provide for accurate simulation of the core flow.

A possible objection to this study is that a simulation of turbulent channel flow at $Re_\tau = 200$ using only 32^3 grid points is hardly a DNS, and since we have not included an SGS model it is not properly an LES either. However, the resolution is similar to that employed in an LES, and the numerical scheme has enough artificial dissipation that the reference simulation gives remarkably good results. Our goal is simply to achieve the same core flow results with the modified boundary data simulations as in the reference simulation. An SGS model will have to be included in further studies, but for this preliminary study we chose to eliminate that possible source of uncertainty.

2.1 Choice of off-wall boundary conditions

There are many possible choices for supplying boundary conditions to the simulation at some height above the wall. Two possibilities are:

(1) **Dirichlet:** velocities are specified where they are demanded on the staggered grid. In our case, we specify

$$u(x, y^+ \approx 25, z, t), v(x, y^+ \approx 30, z, t), w(x, y^+ \approx 25, z, t),$$

from the reference time series. This fixes the transpiration velocity at the computational boundary and also guarantees the right correlations between u and v at the computational boundary. Note that this does not fix the value of $\langle u'v' \rangle$ at the computational boundary since that is determined by interpolating values of u and v on the staggered grid, and only half of those interpolated values of u are fixed by the boundary condition.

(2) **Mixed:** transpiration velocity and wall-normal gradients of the horizontal velocities are specified on the plane $y^+ \approx 30$:

$$\frac{\partial u}{\partial y}(x, y^+ \approx 30, z, t), v(x, y^+ \approx 30, z, t), \frac{\partial w}{\partial y}(x, y^+ \approx 30, z, t).$$

This fixes the viscous stresses and the transpiration velocity at the plane $y^+ \approx 30$.

Morinishi's DNS code was modified to take either form of boundary condition, and a reference time series of 12,000 time steps, corresponding to $60h/u_\tau$ time units, of boundary data was saved by integrating a fully developed field. As in all the subsequent simulations, the boundary data time series was used to provide boundary conditions for a simulation with one wall removed from the computation. All of the simulations with off-wall boundary data are integrated for the length of the time series, $60h/u_\tau$, with statistics collected over the last $30h/u_\tau$ time units.

First, to test the application of the two types of off-wall boundary conditions, simulations were conducted using the same initial condition as used to generate the time series. The simulation employing the Dirichlet off-wall boundary conditions produced mean flow and second order statistics which were indistinguishable from the reference simulation. This is hardly surprising since no changes were made to the numerical scheme to accommodate the Dirichlet boundary conditions. Any differences in the simulated flow with off-wall boundary conditions and the reference simulations, when using the same initial condition, should be due to round-off errors.

The mixed off-wall boundary conditions did not work as well. The wall-normal gradients of the horizontal velocities are fixed at the computational boundary, $y^+ \approx 30$, but the horizontal velocities themselves are not fixed. Eventually the streamwise velocity, u, "slips" and is no longer correlated properly with the wall-normal velocity, v, which is fixed by the time series. This leads to an under-prediction of the turbulent stresses near the computational boundary, which in turn causes the mean flow to accelerate. Shown in Fig. 1 are statistics accumulated over the last $30h/u_\tau$ time units of a simulation with mixed off-wall boundary conditions conducted over the length of the time series, $60h/u_\tau$ time units. Bagwell (1994) had similar difficulties in attempting to use a wall model to provide the same off-wall mixed boundary conditions in turbulent channel flow.

The Dirichlet off-wall boundary conditions appear to work better. To test their robustness, another simulation was performed with the same time series, but using an initial field completely different than the one used to generate the time series. Initially, the boundary data and the start field are incompatible, and this leads to an under-prediction of the turbulent stresses near the computational boundary. In the absence of enough opposing force, due to the constant pressure gradient, the flow accelerates initially and then slowly, over viscous time scales, settles to the expected mean flow. To accelerate convergence of the statistics, a pressure gradient control scheme was used in the initial $30h/u_\tau$ time units to drive the flow towards one with the expected mass flux. This control scheme was then turned off, and the statistics, shown in Fig. 2, are accumulated over the last $30h/u_\tau$ time units. There are some small discrepancies in the second order statistics which may be statistical.

The fact that the simulation, with Dirichlet off-wall boundary conditions and an inconsistent start field, converges at all suggests that the core flow is responding passively to events in the near-wall region. Perhaps this is not surprising since the main region of turbulent production occurs below the point where the off-wall boundary condition is supplied to the flow. The core flow may be able to be
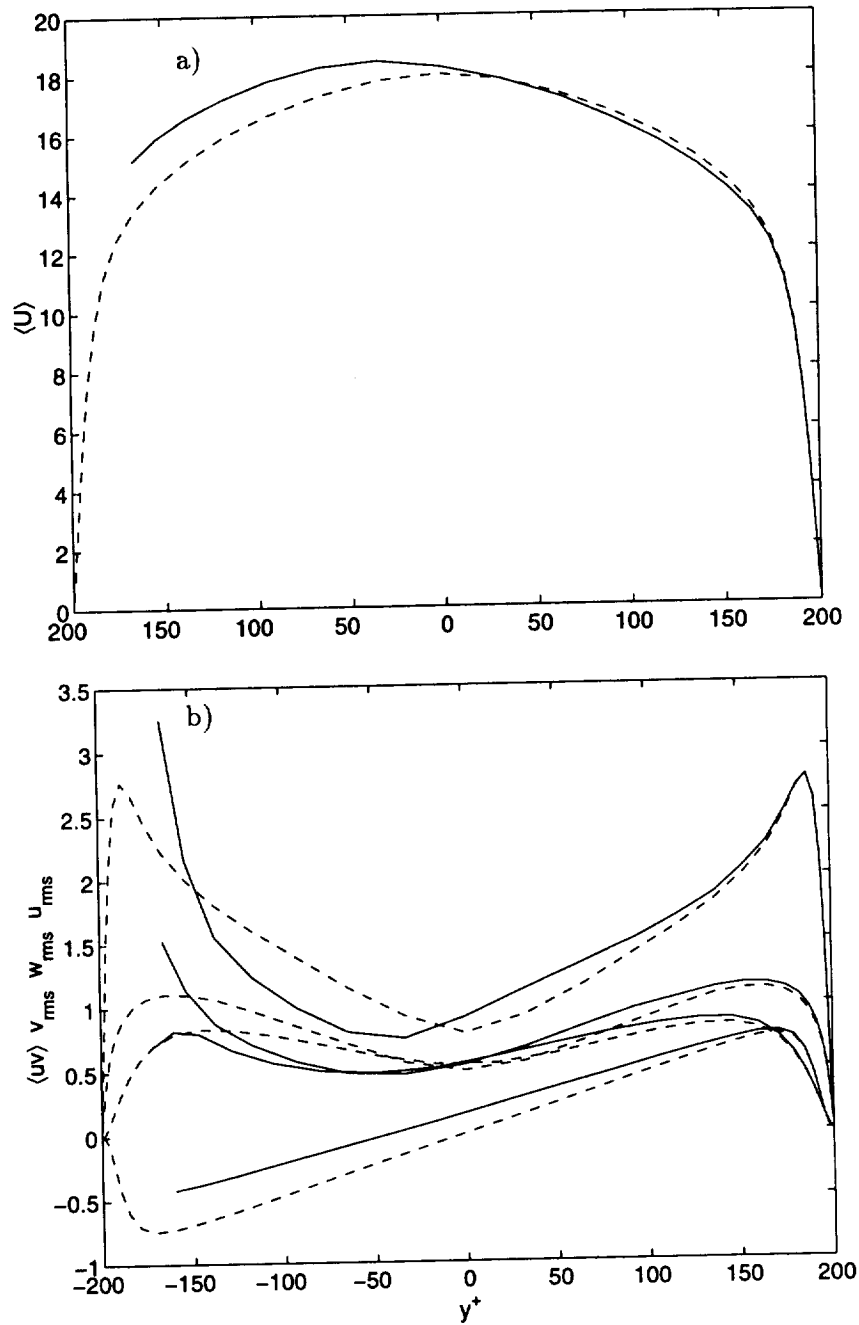
FIGURE 1. Mixed off-wall boundary conditions. Dashed lines show the statistics from the reference simulation used to generate the time series. Solid lines show the statistics from the simulation with mixed off-wall boundary conditions provided at $y^+ \approx 30$ from the time series. Plot a) shows the mean flow, and plot b) shows the r.m.s. velocities and the Reynolds shear stress. The four sets of curves, from top to bottom on the left hand side, correspond, in order, to $u_{rms}, w_{rms}, v_{rms}$, and $\langle u'v' \rangle$.
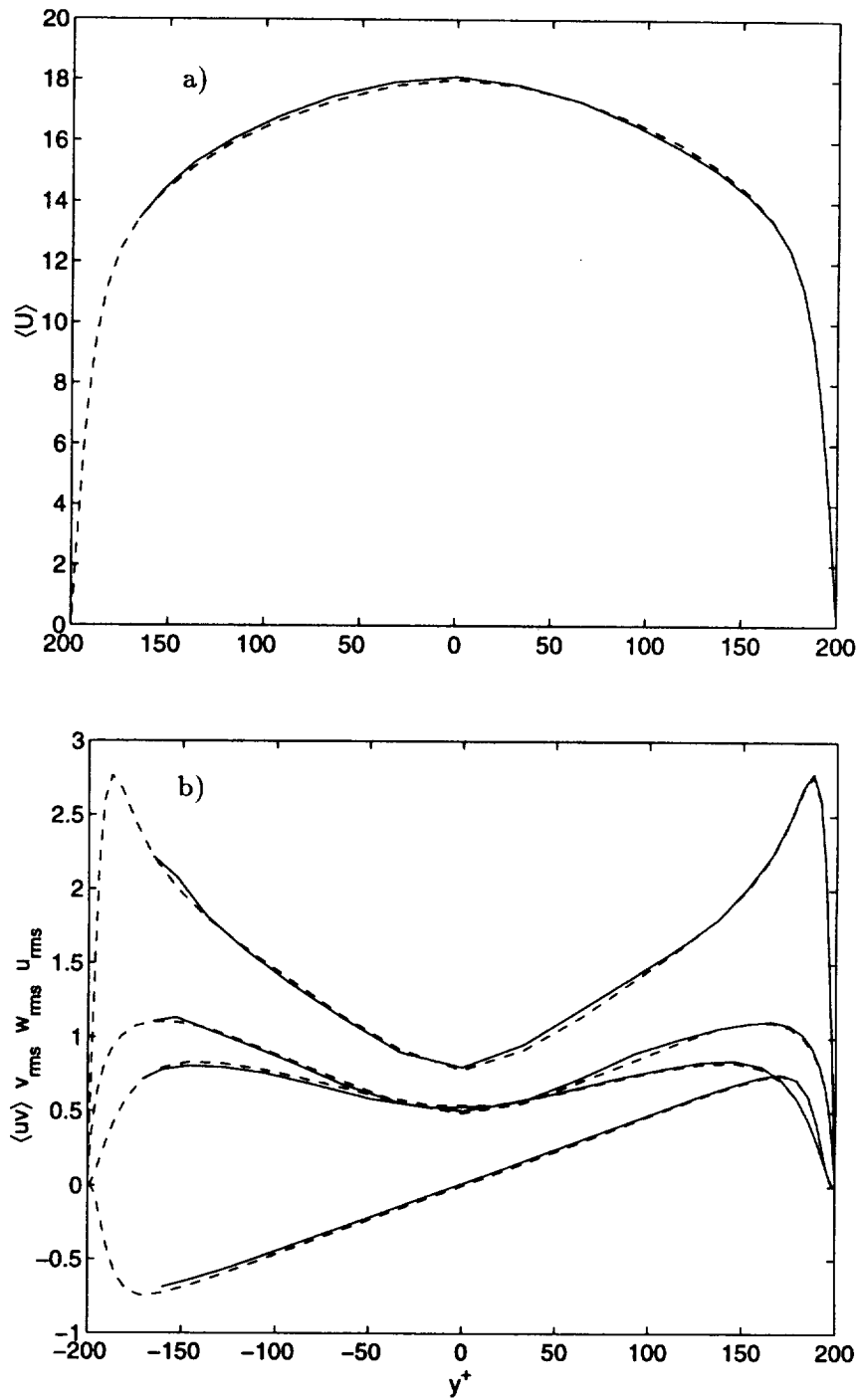
FIGURE 2.   Dirichlet off-wall boundary conditions with inconsistent start field.
As in Fig. 1 the dashed and solid lines show the reference and off-wall boundary
condition simulations, respectively. Plots a) and b) show the same quantities as in
Fig. 1.

simulated by providing a time series of good turbulence data on some plane between the core flow and the region of turbulence production, but it remains to be seen if this boundary data can be provided by a cheap wall model. In any case, the Dirichlet off-wall boundary condition is extremely robust, and we will use it below to study the information flux from near-wall region to the core flow.

2.2 Mildly scrambled Dirichlet data

Providing a good time series of velocity boundary data to the core flow is sufficient to conduct an accurate simulation of just the core flow region. To begin to understand just what structural information has to be incorporated into the velocity boundary data, we make various modifications to the boundary data in this section and the next.

One particularly gentle way to perturb the structure of the boundary data is to randomize the phases of the Fourier components. If the same random phase angle is applied to all three velocity components for each wavenumber vector, then the horizontal spectra and cospectra are not perturbed. The transformation is

$$(\hat{u}_j^s(y), \hat{v}_j^s(y), \hat{w}_j^s(y)) = e^{i\theta_j}(\hat{u}_j(y), \hat{v}_j(y), \hat{w}_j(y)),$$

where $\hat{u}$ and $\hat{u}^s$ denote the Fourier coefficients of the original and scrambled data, respectively. θ_j is a random phase angle chosen uniformly from the interval $[-\pi, \pi)$. Since the boundary data is real, the relation $\theta_j = -\theta_{-j}$ must be satisfied. This transformation has the further advantage that the continuity relation is not affected:

$$k_x \hat{u}_j^s(y) + \frac{\partial}{\partial y}\hat{v}_j^s(y) + k_z \hat{w}_j^s(y) = 0.$$

Thus the horizontal spectra of $\partial v/\partial y$ are not effected at the computational boundary, that is, the mass flux through the boundary plane maintains much of its original structure. Furthermore, the random phase angles are constant with respect to time, so the boundary data maintains its original time scales. Even though the original structure of the Dirichlet boundary is lost, in particular all of the moments of order greater than two are perturbed, the core flow is still simulated well (see Fig. 3).

This result suggests that the core flow can be simulated without complete structural information from the near-wall region. However, as we shall see in the next section, some structural information is necessary.

2.3 Severely scrambled Dirichlet data

We have just shown that the core flow simulation can tolerate some loss of structural information from the near-wall region. Here, we will check to see if it is sufficient to supply boundary data information which has the correct second order statistics and time scales, but for which the turbulence structure is severely perturbed.

One way to achieve such an effect is to randomize the phases of the Fourier components, but, as opposed to the method applied in the previous section, the
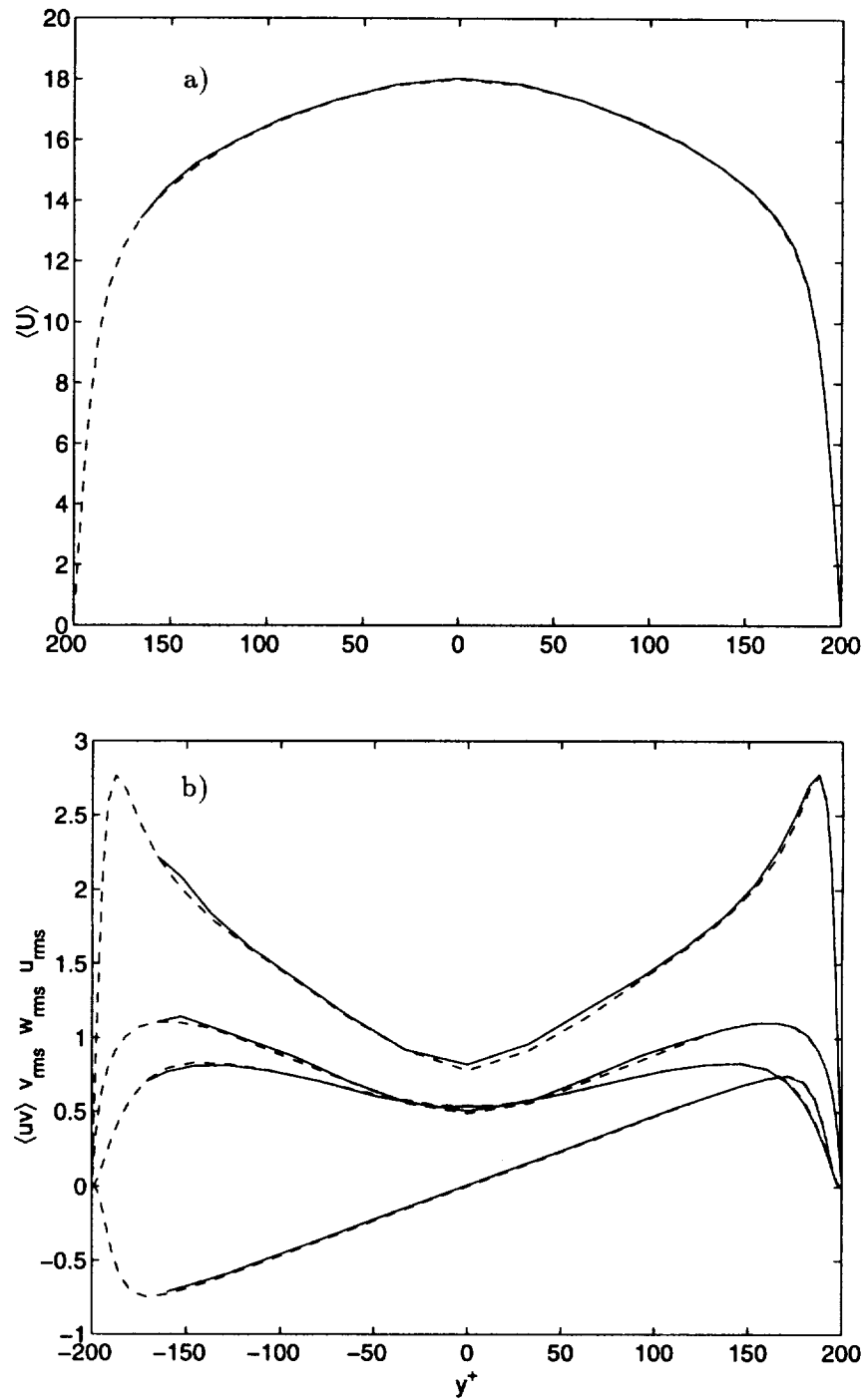
FIGURE 3. Mildly scrambled off-wall Dirichlet boundary conditions. As in Fig. 1
the dashed and solid lines show the reference and off-wall boundary condition sim-
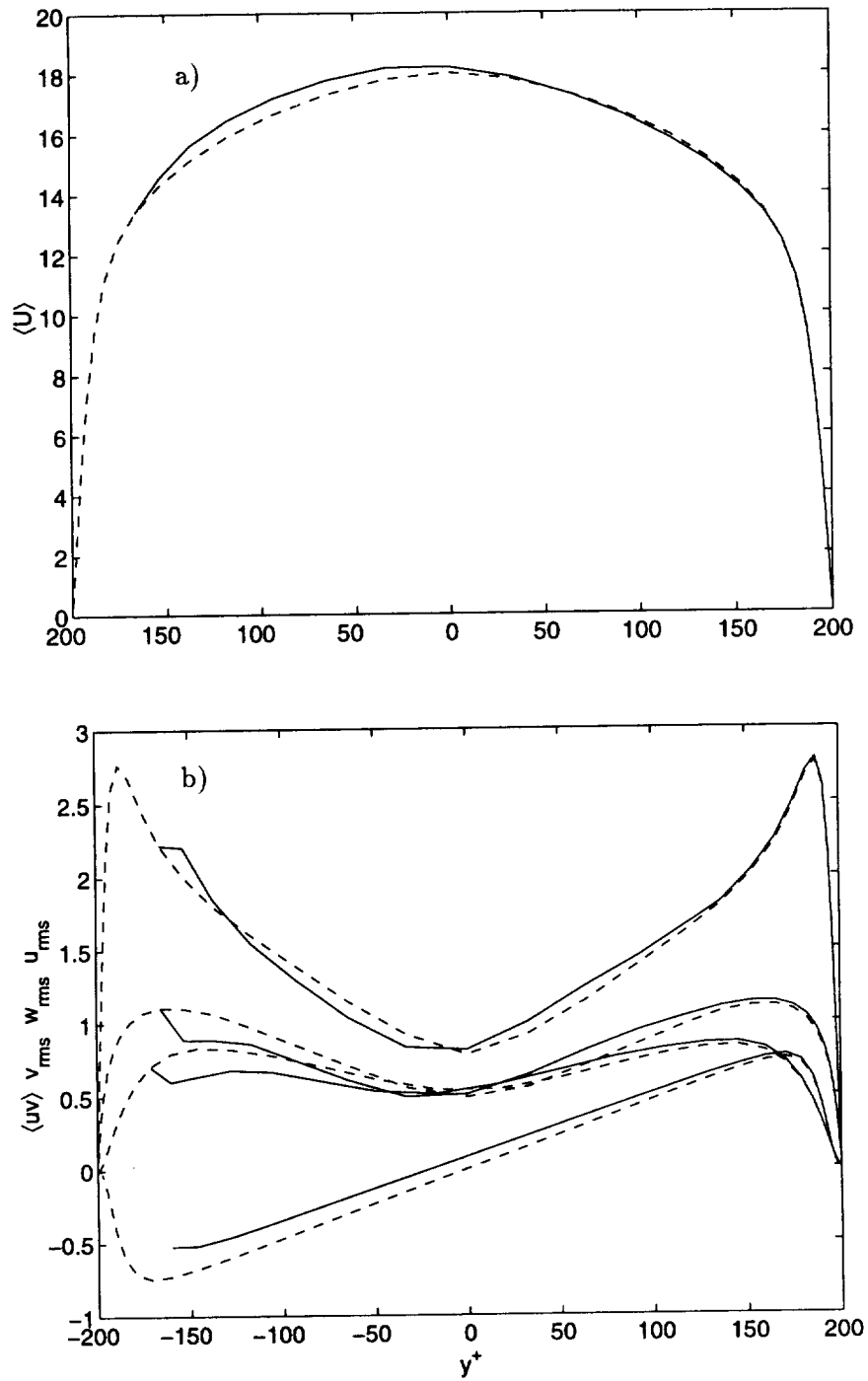ulations, respectively. Plots a) and b) show the same quantities as in Fig. 1.

FIGURE 4.   Severely scrambled off-wall Dirichlet boundary conditions. As in Fig. 1 the dashed and solid lines show the reference and off-wall boundary condition simulations, respectively. Plots a) and b) show the same quantities as in Fig. 1.

random phase angle is chosen independently for each of the velocity components for each wavenumber vector. That is,

$$(\hat{u}_j^r(y), \hat{v}_j^r(y), \hat{w}_j^r(y)) = (e^{i\theta_j^1}\hat{u}_j(y), e^{i\theta_j^2}\hat{v}_j(y), e^{i\theta_j^3}\hat{w}_j(y)).$$

The Fourier coefficients $\hat{u}_j$ are those of the original boundary data, and $\hat{u}_j^r$ are the those of an intermediate set of boundary data. The phase angles $\theta_j^i, i = 1, 2, 3$ are chosen uniformly and independently from the interval $[-\pi, \pi)$, and $\theta_j^i = -\theta_{-j}^i$ so that the boundary data remains real. The relative phase angles between the Fourier coefficients for the u^r and v^r boundary data are changed by this transformation so that $\langle(u^r - \langle u^r\rangle)v^r\rangle$ is also changed. But, by following the technique used by Lee *et al.* (1992) to generate random inflow data for a turbulent simulation, we can rotate the principal axes of u^r and v^r to obtain the correct correlation for the scrambled boundary data. Finally, the scrambled boundary data are given by:

$$u^s = \cos(\psi)u^r + \sin(\psi)v^r,$$

$$v^s = -\sin(\psi)u^r + \cos(\psi)v^r,$$

and

$$w^s = w^r.$$

Details on solving for the rotation angle ψ are given in (Lee *et al.* 1992).

The scrambled boundary data have the correct mean values and second order statistics, but the spectra and cospectra are perturbed. Furthermore the structure of $\partial v/\partial y$ is strongly perturbed through the continuity relation mentioned in the previous section. The random phase angles are constant with respect to time, so the scrambled boundary data still has the correct time scales, but the boundary data are effectively random numbers with the correct second order statistics. w^s has the same horizontal spectra as the original boundary data, but the spectra of u^s and v^s are modified by rotation of their principal axes as are the cospectra.

Again, the simulation was run over $60h/u_\tau$ time units with statistics accumulated over the last $30h/u_\tau$ time units. As can be seen in Fig. 4, the mean flow and second order statistics develop a boundary layer type character near the computational boundary. This indicates that simply providing a time series of boundary data with the correct second order statistics, approximately the correct spectra, and the correct time scales is insufficient for the accurate simulation of the core flow.

3. Conclusions

Off-wall boundary conditions can be used for simulation of just the core region of a turbulent channel flow. Our results indicate that supplying velocity boundary data may be more robust than attempting to fix the wall-normal gradients of the horizontal velocities as well as the transpiration velocity through the computational boundary plane. This may not be surprising since outside of the near-wall viscous sub-layer the total stress is dominated by the contribution from the turbulent stresses. The off-wall Dirichlet boundary conditions fix the correlation between

u and v at the boundary, whereas the mixed off-wall boundary conditions fix only the viscous stresses at the computational boundary.

These preliminary results also suggest that the off-wall velocity boundary conditions must contain at least some turbulence structure. In particular, the simulations performed with the "mildly" scrambled velocity boundary conditions suggests that boundary data with the correct spectra and cospectra may be sufficient for accurate simulation of the core flow. Correct estimation of moments greater than second order is probably not necessary. However, simply supplying the correct statistics, up to second order, is not sufficient — some further structural information is necessary. Thus, even if the second order statistics of the near-wall region are known, it may be difficult to use this information to extrapolate boundary conditions from the core flow as suggested by Carati (in this volume).

On a final note, to see what may happen if structural information about the near-wall region is not incorporated into the wall model, consider the large-eddy simulations of Mason and Callen (1986). They attempted to simulate high Reynolds number turbulent channel flow by forcing the flow to fit a local logarithmic law at the wall along with zero wall-normal transpiration. Their boundary condition guarantees the right total stress in the mean but is incapable of carrying the right turbulence structure. Effectively, they completely excised the region of turbulence production from their computation and used a wall model without any capacity to correct this deficiency. They found that they were unable to simulate an effective logarithmic region in their calculations. This problem was later rectified by Mason and Thomson (1992) by including a stochastic backscatter term which probably helped compensate for the missing production mechanism. It is clear that the core flow needs to see at least some of the turbulence structure produced in the near-wall region. It remains to be seen if cheap wall models can provide the necessary turbulence structure to the core flow.

REFERENCES

BAGWELL, T. G., ADRIAN, R. J., MOSER, R. D. & KIM, J. 1993 Improved approximation of wall shear stress boundary conditions for large eddy simulation, in *Near-Wall Turbulent Flows*, eds. R. M. C. So, C. B. Speziale, & B. E. Launder (Elsevier Science Publishers).

BAGWELL, T. G. 1994 Stochastic Estimation of near wall closure in turbulence models, Ph.D. thesis, Univ. Illinois Urbana-Champaign.

BALARAS, E., BENOCCI, C. & PIOMELLI, U. Two-layer approximate boundary conditions for large-eddy simulations AIAA J. *34*. 1111-1119.

CABOT, W. 1995 Large-eddy simulations with wall models. *CTR Research Briefs* Center for Turbulence Research, NASA Ames/Stanford Univ., 41-50.

CHAPMAN, D. R. 1979 Computational aerodynamics development and outlook. *AIAA J.* **17**, 1293-1313.

DEARDORFF, J. W. 1970 A numerical study of three-dimensional turbulent channel flow. *J. Fluid Mech.* **41**, 453-480.

LEE, S., LELE, S. K. & MOIN, P. 1992 Simulation of spatially evolving turbulence and the applicability of Taylor's hypothesis in compressible flow. *Phys. Fluids A.* **4**, 1521-1530.

MASON, P. J. & CALLEN, N. S. 1986 On the magnitude of the subgrid-scale eddy coefficient in large-eddy simulations of turbulent channel flow. *J. Fluid Mech.* **162**, 439-462.

MASON, P. J. & THOMSON, D. J. 1992 Stochastic backscatter in large-eddy simulations of boundary layers. *J. Fluid Mech.* **242**, 51-78.

MORINISHI, Y. 1995 Conservative properties of finite difference schemes for incompressible flow. *CTR Research Briefs* Center for Turbulence Research, NASA Ames/Stanford Univ., 121-132.

PIOMELLI, U., FERZIGER, J., MOIN, P. & KIM, J. 1989 New approximate boundary conditions for large eddy simulations of wall-bounded flows. *Phys. Fluids.* **1**, 1061-1068.

SCHUMANN, U. 1975 Subgrid scale model for finite difference simulations of turbulent flows in plane channels and annuli. *J. Comp. Phys.* **18**, 376-404.

Numerical simulation of 3D turbulent boundary layers using the V2F model

By S. Parneix AND P. Durbin

1. Motivation and objectives

A 3-D turbulent boundary layer (3DTBL) is usually generated by a change in the geometry, e.g. by a turning channel or an appendage mounted on a channel wall. The resulting spanwise pressure gradient, $\partial p / \partial z$, skews the incoming 2-D boundary layer $U(y)$, creating an extra strain rate $\partial W / \partial y$. The near-wall part of the mean flow, with low momentum, is expected to respond more rapidly to this new pressure gradient than the high momentum free-stream flow. Consequently, variation of the flow turning angle in the normal direction y is expected.

Experimental databases (e.g. Ölcmen & Simpson 1995, Webster *et al.* 1996) have been used to evaluate the ability of classical linear eddy viscosity models to reproduce a 3DTBL. In all cases, it was observed that a non-zero angle can exist between the direction of the flow gradient and of the shear-stress while, with the isotropic eddy viscosity hypothesis, this angle is exactly zero. This has led to a sentiment that more sophisticated turbulence models (Second Moment Closure, non-linear eddy viscosity) are needed to better predict 3-D 'complex' configurations. However, the error associated with prescribing identical directions of Reynolds stress and mean rate of strain may be not crucial in the prediction of the mean flow: at an operational level, the Reynolds stresses are not used, only the eddy-viscosity. In fact, turbulent shear stresses have been found to be smaller than pressure forces in the outer part of the 3-D boundary layer (Johnston & Flack 1996). Moreover, the inner layer of a 3DTBL is a collateral region, i.e. the velocity vectors are coplanar with the wall shear stress direction (Goldberg & Reshotko 1984). If a suitable near-wall turbulence model is being used, these observations give hope that accurate predictions of 3-D turbulent flows can be obtained while keeping the numerically amenable, isotropic eddy viscosity hypothesis.

The *V2F* model was introduced by Durbin (1991) as a restriction of a full Second Moment Closure model (Durbin 1993). It is able to reproduce both the damping of turbulence transport near solid boundaries and the well-known near-wall non-local effects of pressure-deformation fluctuations. Its main advantage is its validity and accuracy up to the wall without using either wall functions or damping functions. This model has been implemented in NASA's INS3D (Rogers & Kwak 1990) and used herein for computing two 3-D flows. The first is the flow over a swept bump mounted on the floor of a wind tunnel (Webster *et al.* 1996). This case involves both curvature and cross-flow effects. For this case, a new coefficient in the ε-model equation, which gets rid of the impractical and 'ill-behaved' wall distance, has been compared with the initial version (Durbin 1995) and with the experiment. Then, the model has been directly applied to the more complex, 3-D flow around

a wall-mounted appendage (Devenport & Simpson 1990, Ölcmen & Simpson 1995, Ölcmen & Simpson 1997). This well-documented flow involves a 3DTBL, massive separation, and secondary flow with a horseshoe vortex around the appendage.

2. Accomplishments

2.1 Flow over a swept bump

2.1.1 Configuration

The experimental configuration is presented in Fig. 1. The bump consists of a short concave section, a longer convex section, and another short concave section. The Reynolds number based on the maximum inlet velocity and the bump chord c (cf. Fig. 1) is about 323,000. The upstream boundary layer begins at a swept suction slot. It is a fully developed boundary layer with a momentum thickness Reynolds number of 3,800 at one-half chord upstream of the onset of curvature. Since channel side wall effects are negligible in the experiment, the flow is homogeneous in the direction parallel to the line of the bump. This allows a 2-dimensional, 3-component computation to be done. In a frame with the $\tilde{x}$-axis perpendicular to the bump and the $\tilde{z}$-axis parallel to it, the $\tilde{z}$-momentum equation is simply the convection diffusion equation:

$$D_t \tilde{W} = \nabla \cdot \left((\nu + \nu_t) \nabla \tilde{W} \right) \tag{1}$$

The inlet condition is $\tilde{W} = U \sin 45°$, $\tilde{U} = U \cos 45°$. The experimental and computational results are presented in the wind-tunnel $x - y$ frame. In this frame, W is equal to 0 at the inlet.
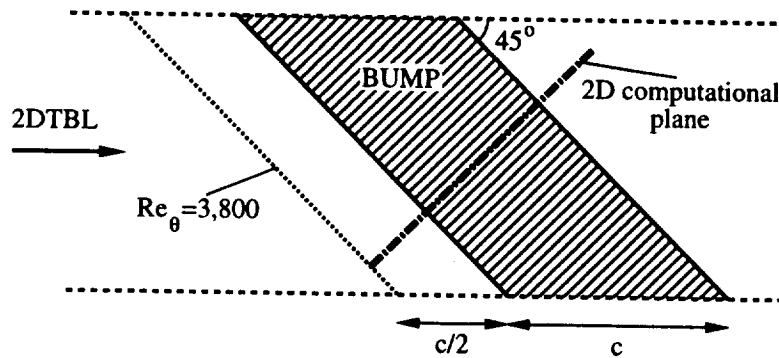

FIGURE 1. Top view of the wall mounted bump.

Inlet profiles of k, $\overline{v^2}$, and ε were obtained from a separate computation of a flat plate boundary layer. The entire channel height is taken into account in all the simulations. These were performed using a general geometry, finite-difference code developed by Rogers & Kwak (1990) to which the V2F model has been added. The spatial discretization scheme is third-order, upwind biased for convection terms

and second-order, central for diffusion terms. A fine stretched, curvilinear grid of 150×120 nodes was used with a high resolution near solid boundaries and around the bump onset and exit. A mesh independency study was performed by dividing the mesh by a factor of 2 in all directions; the results on both mean velocity and skin friction were little changed.

2.1.2 Results

Although the minimum distance to the wall, d, was not used for evaluating the damping of the normal velocity fluctuations at the wall, it was present as an interpolation parameter in Durbin (1995). The motivation was simply to obtain suitable values of C'_{ε_1} in the ε-equation for both turbulent boundary layers ($C'_{\varepsilon_1} = 1.55$) and plane mixing layers ($C'_{\varepsilon_1} = 1.3$): to this end, the formula $C'_{\varepsilon_1} = 1.3 + 0.25/[1 + (d/2\ell)^2]^4$ was used. Here ℓ is a turbulent length scale (see Durbin 1995). The distance to the wall is often criticized for being 'ill-behaved' in complex, 3-D geometries. It is also impractical to use in multizone computations or in unsteady calculations with moving surfaces. In the present formulation, d is replaced by the structural parameter $k/\overline{v^2}$, which has similar properties; in particular, it provides a means to increase the production of ε near solid boundaries. It does this by the physically attractive route of relating C_{ε_1} to the anisotropy of the turbulent velocity fluctuations. The specific formula is $C'_{\varepsilon_1} = C_{\varepsilon_1}(1 + a_1\sqrt{k/\overline{v^2}})$. This is the only change in the equations from those in Durbin (1995). Since this one formula is different, the value of the empirical coefficients had to be recalibrated. For this purpose, the same test-cases as for the initial version were used (a zero-pressure gradient 2DTBL and a low-Reynolds number fully-developed channel flow). The differences between the two versions are indicated below:

- For the initial version (Durbin 1995): $C'_{\varepsilon_1} = 1.3 + 0.25/[1 + (d/2\ell)^2]^4$

$$C_\mu = 0.19, C_L = 0.3, C_\eta = 70.0 \tag{2}$$

- For the present version: $C'_{\varepsilon_1} = 1.4(1 + 0.045\sqrt{k/\overline{v^2}})$

$$C_\mu = 0.22, C_L = 0.25, C_\eta = 85.0 \tag{3}$$

The length scale formula actually involves the product $C_L C_\eta$, which is 21 in both (2) and (3). So the recalibration is relatively minor.

These two versions have been compared on the configuration of the swept bump. The pressure and friction coefficients (Figs. 2 and 3) as well as mean flow profiles (not shown here) obtained by both versions are very similar to each other. It should be added that the new version, i.e. with $k/\overline{v^2}$, has been checked to give similar results, without affecting the numerical stability, in most of the previous two-dimensional test-cases performed with the first version, including adverse pressure gradient boundary layers and recirculating or impinging flows. The two formulas for $C'_{\varepsilon 1}$, having very similar behaviors, are viable alternatives. The present formulation
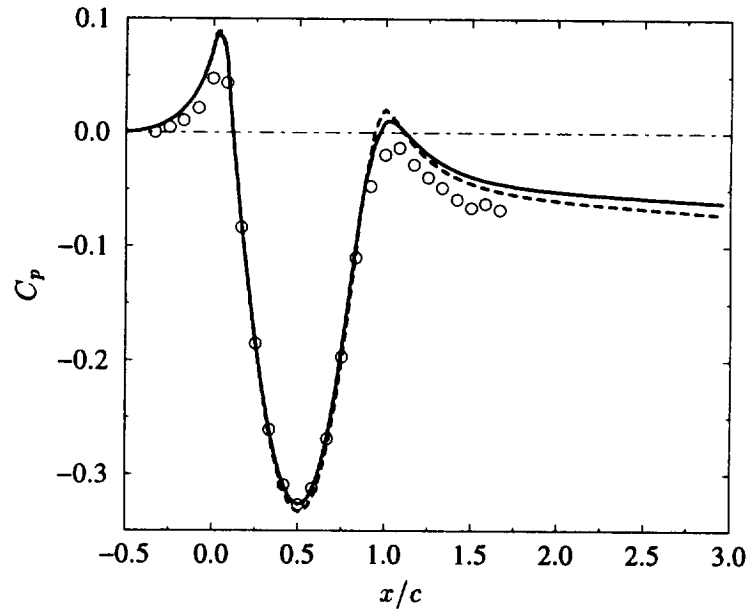
FIGURE 2. Pressure coefficient, ———— : V2F with d (Durbin 1995), ———— : V2F without any reference to d, o : Webster et al. experiment (1996).

has the advantage of not involving the distance to the wall, which may be crucial in 3-D multizone complex configurations.

The results of the V2F model are now compared with the Webster et al. experiment (1996). The discussion will be valid for both versions. For all the following figures, x is taken as the streamwise axis of the wind tunnel, y is the normal axis, z will be the spanwise axis, across the wind tunnel. The homogeneous direction is 45° to the x-axis. All the profiles will be presented with length normalized by c, the chord of the bump in the wind-tunnel cross sectional plane. The scaled height of the wind tunnel is then 1/2. The origin of the x-axis is at the onset of the bump, so the bump ends at $x = 1$.

Figure 2 shows the pressure coefficient along the wall. The presence of the bump first creates a mild adverse streamwise pressure gradient upstream. At the onset of the bump, the regime becomes a strong favorable pressure gradient. The rear of the bump is a region of strong adverse pressure gradient, and the boundary layer recovers in a zero pressure gradient, after a mild favorable pressure gradient region, downstream. One can see that the V2F model reproduces these trends quite well, both qualitatively and quantitatively. Perhaps the downstream recovery is a bit less rapid than in the experiment.

The bump is low enough that separation does not occur in its lee side. This made the maintenance of an infinitely swept condition easier in the experiment. The V2F predictions of the spanwise skin friction coefficient, which characterizes the three-dimensionality of the flow, are in excellent agreement with the experimental data (see Fig. 3). As indicated above, the flow is skewed several times by the spanwise

pressure gradient. The changes in sign of the spanwise friction coefficient, C_f^z, are accurately reproduced by the *V2F* model. The most notable discrepancy is in the level of the streamwise skin friction coefficient, C_f^x, over the bump. This problem also appears in the 2-D case (Wu & Squires 1997a), so it is not related to the three-dimensionality of the flow. There is a possibility that the flow is close to relaminarizing due to the strong favorable pressure gradient on the windward side of the bump.
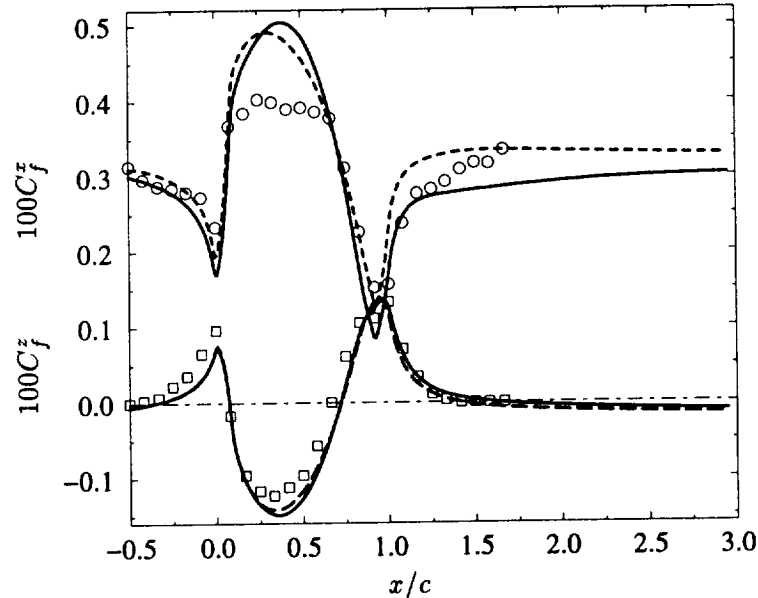

FIGURE 3.   Streamwise and spanwise friction coefficient, ——— :   *V2F* with d (Durbin 1995); ---- :   *V2F* without any reference to d; o : $100C_f^x$, Webster *et al.* experiment (1996); □ : $100C_f^z$, Webster *et al.* experiment (1996).

2.2 Flow around an appendage-body junction

2.2.1 Configuration

Since both versions of the *V2F* model gave very similar results, the computations presented in this section were done only with the present one, which gets rid of the distance to the wall. The studied configuration concerns the turbulent flow around an appendage mounted on a flat plate. The obstacle consists of a 3:2 elliptical nose and a NACA 0020 tail joined at the maximum thickness t (Fig. 4). There are neither sweep nor incidence angles; the flow is symmetric and only half of the domain was actually computed. The incoming boundary layer was tripped in the experiment so that inlet conditions are clean and well defined: at 0.75 chord upstream of the nose, the zero pressure gradient 2DTBL has a momentum thickness Reynolds number of $Re_\theta = 5,940$. The Reynolds number based on the chord length c of the obstacle and the maximum velocity of the incoming 2DTBL, U_0, is about 4.4×10^5. The experimental database used for comparisons consists of a set of

several well documented experiments conducted at Virginia Polytechnic Institute
(Devenport & Simpson 1990, Ölcmen & Simpson 1995, Ölcmen & Simpson 1997).
This test-case is much more complicated than the swept bump since a fully 3-D
computation is required. The presence of the appendage does create a 3DTBL,
but other complex phenomena such as curvature of the obstacle, 3-D separation,
and a horseshoe vortex are also involved. Indeed, the lower wall boundary layer is
both skewed by the presence of the obstacle and also experiences an adverse pressure
gradient in front of the nose of the obstacle that causes the flow to separate upstream
of the leading edge. A recirculation is created in the symmetry plane. This vortical
structure is stretched around the junction, and its direction is reoriented along the
appendage. Although the geometry is fairly simple, the flow is very complex and
is a challenging test-case for turbulence models. Note that accurate predictions of
the horseshoe vortex may be of industrial importance, e.g. heat transfer is strongly
enhanced by the presence of this kind of secondary flow structure [Spencer *et al.*
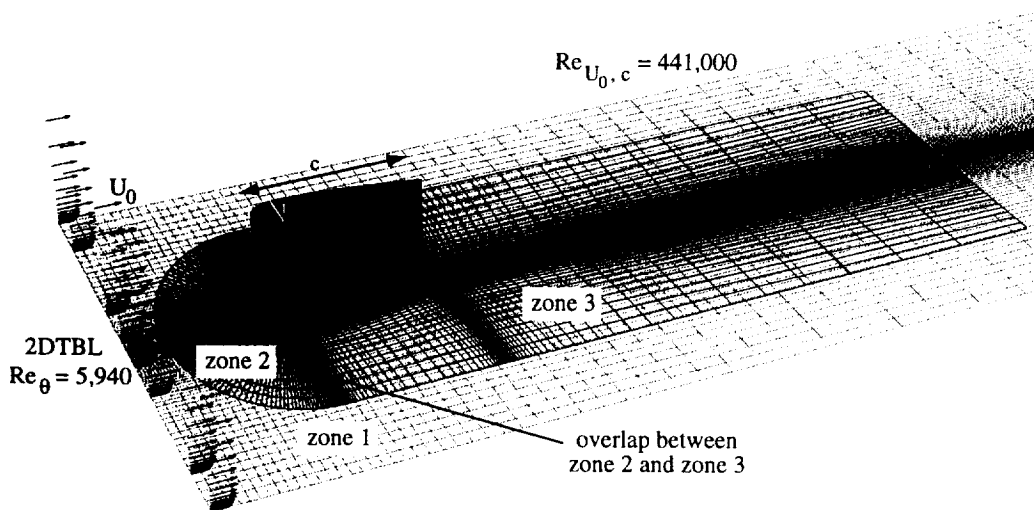1996, Praisner *et al.* 1997].

FIGURE 4.   The geometry and flow conditions of the turbulent flow around a
wall-mounted appendage.

A multizone grid was used with a high resolution near solid boundaries; basically,
the distance between any boundary node and the closest computational point was
less than $y^+ = 5$ in wall units. This assures an accurate resolution of the viscous
layer. The first zone is gridding the experimental channel: it is Cartesian and
allows imposition of the right spanwise blockage ratio and inlet conditions. In the
experiment, inserts for the wind-tunnel side-walls were constructed to minimize
blockage-induced pressure gradients around the obstacle (Devenport & Simpson
1990): these are not modeled in our computations, instead slip conditions have
been imposed. The influence of these boundary conditions has been checked to

be negligible by increasing the channel width by a factor of 2 without any major modification of the results. The two other zones are curvilinear and adapt to the obstacle. The first (zone 2) is restricted to the nose, where separation and the horseshoe vortex arise; the second (zone 3) is discretizing the tail and the wake. The link between each zone is performed by Chimera interpolation stencils (Benek *et al.* 1985, Benek *et al.* 1987). This technique has been applied with success for a long time to CFD. It is considered to be very efficient if there are no sharp gradients normal to the inter-zonal boundaries — which is the case in our computations. The results presented in this section have been performed with a three-zone grid of 210,000, 231,000, and 231,000 nodes, respectively: i.e., 672,000 discretization points in total.

2.2.2 Results

Figure 5 shows a comparison between an oil-flow visualization performed on the experimental test wall by Ölcmen & Simpson (1995) and a set of wall-streamlines from the computation (trajectories of particles released at the first computational point above the flat plate). A line of separation wrapped around the obstacle shows the position of the horseshoe vortex, denoted 'H'. One sees good qualitative agreement between the *V2F* model and experiment. Predictions of the location and the extent of the separation line are very similar to the oil-flow visualizations. The wake seems also to be well estimated. The experiment shows evidence of the existence of a recirculation near the trailing edge, denoted 'T', also predicted by the *V2F* simulation. No specific data are available for this latter phenomenon. Nevertheless, a large database will be used for quantitative comparisons; it concerns the development of the 3DTBL outside of the separation line (stations 1 to 7 in Fig. 5), the recirculation in the symmetry plane upstream of the appendage's leading edge (measurement points are indicated on the figure), and the horseshoe vortex secondary flow (with measurements in the plane perpendicular to the flat plate and to the obstacle, passing through station 5).

Since the simulation of a 3DTBL was the first topic of this study, some comparisons of the spanwise velocity profiles measured at several locations (stations 1 to 7, see Fig. 5) outside of the separation line are presented in Fig. 6. These locations correspond to LDV and hot-wire experimental measurements (Ölcmen & Simpson 1995). Note that the y-axis is in a logarithmic scale; this exaggerates the near-wall region. As expected, the most important effect of the spanwise pressure-gradient is seen close to the wall. The maximum amount of cross-flow increases continuously until stations 4 and 5 (up to 20% of the reference velocity U_0) and then decreases again. The location of these maxima shifts to a higher y-location at each successive location. The agreement between the *V2F* model and the experiment is excellent both qualitatively and quantitatively. This computation confirms the results obtained for the swept bump, where the 3DTBL is very well represented by the simulations, even though the linear eddy viscosity hypothesis is being used.

Devenport and Simpson (1990) reported some LDV measurements in the symmetry plane upstream of the nose of the appendage. They characterized the action of the adverse pressure-gradient on the flow with a separation and a recirculation
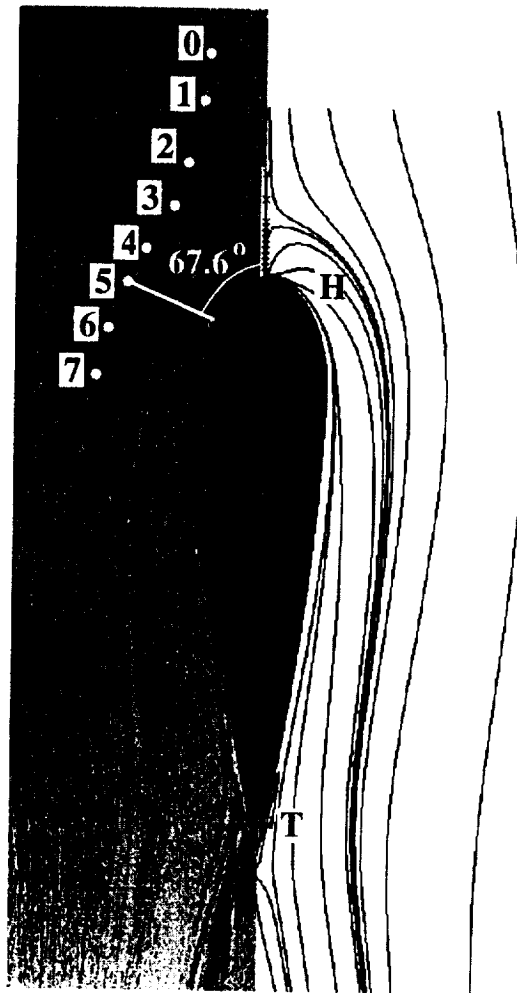
FIGURE 5.   Ölcmen & Simpson (1995) experimental oil-flow visualization (on the left) and computational wall-streamlines (on the right).

bubble. They noted the existence of bimodal histograms of velocity fluctuations, associated with very-low frequencies. This kind of feature is radically different from vortex-shedding and cannot be represented by a RANS calculation. Nevertheless, the frequency of this large-scale unsteadiness is much lower than the passage frequency of coherent structures, which may suggest that only a small fraction of the turbulent structures will be influenced by this bimodality. Figure 7 shows the U-profiles in the symmetry plane in front of the obstacle. The experimental streamwise velocity indicates the separation location around $x/t = -0.35$. The $V2F$ computation shows that the flow has just separated at $x/t = -0.35$. Profiles at $x/t = -0.40$ and -0.30 are well-established unseparated and backflow profiles, respectively, which indicates a separation location close to -0.35, in excellent
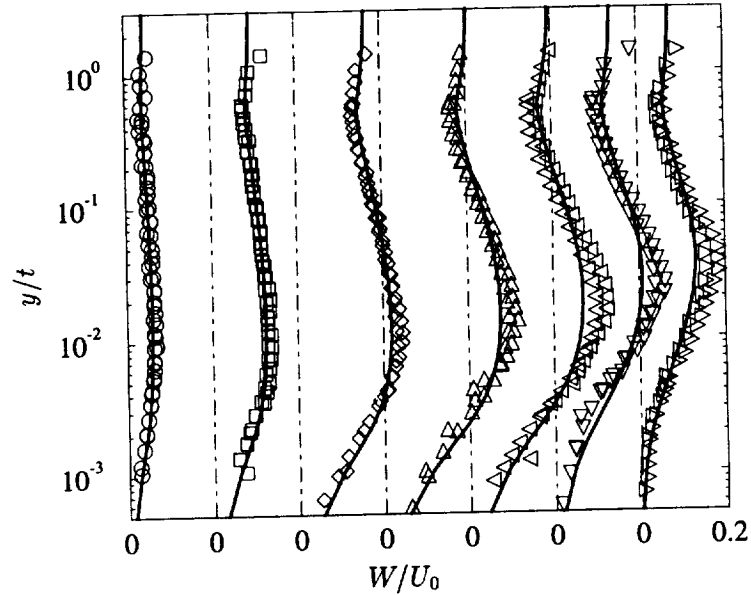
FIGURE 6.   Spanwise velocity profiles of the 3DTBL, symbols: Ölcmen & Simpson experiment (1995) for stations 1 (o), 2 (□), 3 (◇), 4 (△), 5 (◁), 6 (▽) and 7 (▷), ——— : *V2F* model.

agreement with the experiment. The intensity of the backflow is basically well reproduced, even if it is slightly under-predicted in the middle of the recirculation (40% of the nominal velocity instead of 50%). Moreover, in the bubble the extension of the backflow, normal to the plate, seems to be a little more spread out in the experiment. Note also that the model is able to reproduce a kink of U, present at the end of the log-region (around $y/t \simeq 0.5$) in the profiles between $x/t = -0.35$ and -0.20.

Figure 8 shows contours of the turbulent kinetic energy, k, in the symmetry plane. One can observe a strong similarity between the experiment and the *V2F* simulation. As it has been pointed out by Behnia *et al.* (1997), the *V2F* model is able to predict the right damping of turbulent transport near the wall, especially in the impinging region. In this area (along the wing in the symmetry plane), all $k - \varepsilon$ computations reported in the 4th ERCOFTAC/IAHR workshop on refined flow modeling (1995) show a large, spurious production of turbulence, in total disagreement with the experiment. One can also see that the location, shape, and size of the region where high levels of turbulence exist is very well reproduced by the *V2F* model. This is a notable improvement over the $k - \varepsilon$ simulations. Quantitatively, the maxima measured levels of k are about 30% higher than those predicted by the computation (see Fig. 8). A good agreement is obtained outside of the recirculation zone (both for the 2-D adverse pressure-gradient flow and in the vicinity of the appendage), but a strong under-prediction does exist inside the vortex. Devenport & Simpson (1990) noticed that high values of production of k are present in the region where the flow is bimodal (basically in the middle of the recirculation) and concluded that this strong
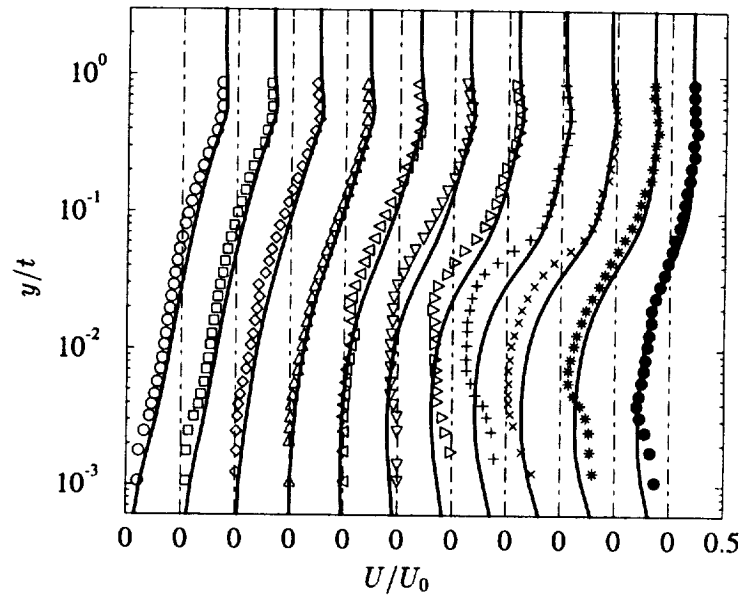
FIGURE 7.   Streamwise velocity profiles in the symmetry plane upstream of the appendage's nose, symbols: Devenport & Simpson experiment (1990), for x/t = -0.86 (○), -0.65 (□), -0.46 (◇), -0.40 (△), -0.35 (◁), -0.30 (▽), -0.25 (◁), -0.20 (+), -0.15 (×), -0.10 (∗), -0.05 (●), ——— : $V2F$ model.

turbulence production was a result of stochastic large-scale unsteadiness rather than conventional shear layer-mechanisms. Based on the present computational results, we may conclude that turbulent quantities seem to be affected by this bistable feature, which cannot be captured by any Reynolds-average turbulence model, but the influence on the mean flow is rather small.

Since the intensity and location of the base of the horseshoe vortex is well predicted (in the symmetry plane), it is interesting to see whether the model is able to reproduce the development around the appendage of the secondary flow associated with this structure. Ölcmen & Simpson (1997) recently reported some flow measurements in a plane normal to the obstacle and the surface. This plane passes through station 5 (see Fig. 5). In this plane, the horseshoe vortex has already turned an angle of 67.6° around the appendage.

Secondary flow streamlines are presented in the background of Fig. 9. These represent particles trajectories in the measurement plane. In this figure, the reference frame has changed: y is still the coordinate normal to the flat plate and s is the coordinate in the plane, normal to the obstacle, denoted as the radial coordinate. Positive values of the flow angle point in the inward direction. A log-scale has been used to focus on the near wall flow and to see the real accuracy of the predictions. The horseshoe vortex is clearly present. A large rotational region shapes the structure of the whole appendage-body junction flow. In this plane, the vortex center is located at about $\log_{10}(y/t) \simeq -1.1$ and $s/t \simeq 0.32$ in the experiment.
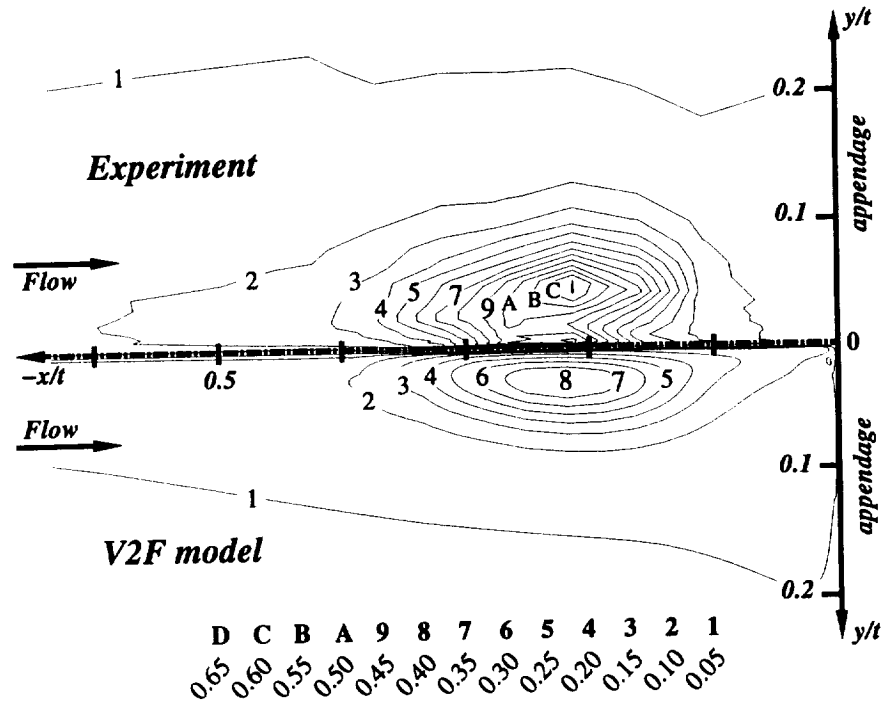
FIGURE 8.   2D-contours of turbulent kinetic energy in the symmetry plane upstream of the appendage's nose.

The simulated secondary flow shows strong similarities with the experiment. The free-stream fluid is directed towards the appendage and rolls around the center of the vortex. Its location is predicted at $\log_{10}(y/t) \simeq 1.1$ and $s/t \simeq 0.28$. One can observe a line of 0 radial velocity with outward flow on one side and inward flow on the other side. The location of this line at the lower wall shows the location of the 3-D separation line seen in Fig. 5. At $y/t \simeq 10^{-3}$, which is very close to the wall, the model is in excellent agreement with the experiment, showing a separation line location of about $s/t \simeq 0.5$. The *V2F* computations predict a tiny, secondary, counter-rotating structure very close to the appendage that is also present in the experiment. Figure 9 also shows contours of the flow angle, relative to the measurement plane, computed as $\arctan(W/U)$, U being the tangential velocity component (normal to the measurement plane) and W being the radial velocity component (normal to the obstacle). The flow is deflected up to 12° towards the appendage and up to 24° away from it. Even if the levels are slightly under-estimated, one can see that the model is able to predict successfully the whole qualitative and quantitative distribution of the turning angle in this cutting plane.

3. Conclusion

A modification of the ε model equation, which allows the *V2F* model to be free of any reference to the distance to the wall, has been presented. The modification
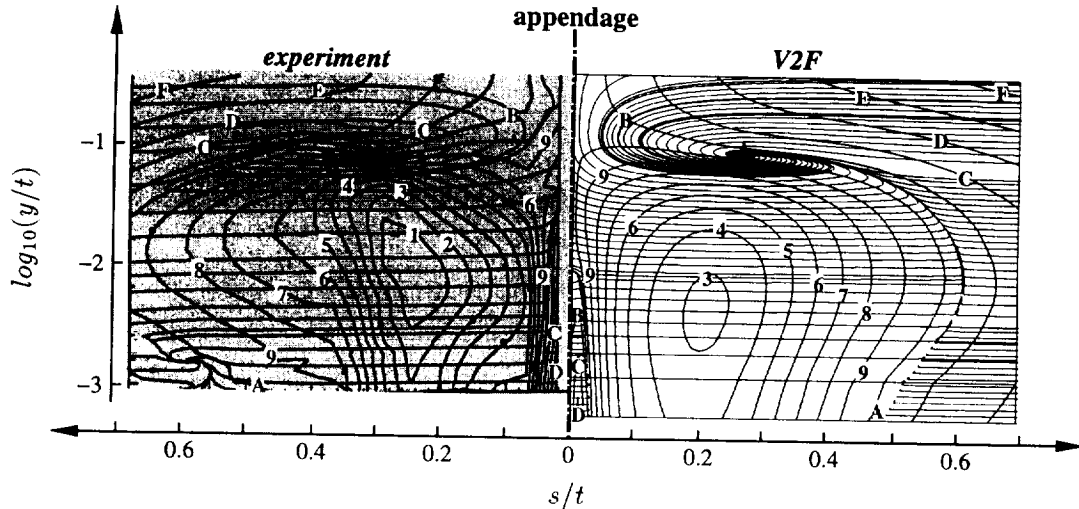
FIGURE 9.   Flow angle—arctan(W/U)—contours and secondary streamlines in background, in the plane normal to the obstacle and to the surface passing through station 5 (see Fig. 5); levels of flow angle: $-24.1°$ (1), $-21.6°$ (2), $-19.0°$ (3), $-16.4°$ (4), $-13.9°$ (5), $-11.3°$ (6), $-8.7°$ (7), $-6.1°$ (8), $-3.5°$ (9), $-1.0°$ (A), $1.6°$ (B), $4.2°$ (C), $6.7°$ (D), $9.3°$ (E), $11.9°$ (F).

makes use of the measure of anisotropy, $\overline{v^2}/k$, provided by the model. This version gives very similar results (in terms of accuracy and stability) to the original one, but it is more suitable for computations in 3-D, complex, multizone configurations.

After the implementation of the *V2F* model in NASA's CFD code, INS3D, computations of three-dimensional turbulent boundary layers have been performed. Despite the linear eddy viscosity hypothesis, the model is able to reproduce the main features of the mean quantities. The secondary flow and the turning angle are predicted correctly both qualitatively and quantitatively in both cases of a swept bump and an appendage mounted on a flat plate. The latter presents a fairly complex 3-D flow including separation and a horseshoe vortex. It is a challenging test-case for turbulence models; *V2F* computations agree very well with the experiment. The description of the horseshoe vortex is reproduced accurately in terms of its location and intensity, even if the secondary flow is slightly under-estimated. The position of the 3-D separation line is correctly simulated and a counter-rotating horseshoe vortex has even been found close to the appendage-body corner, in agreement with the experiment.

In the future, the V2F model needs to be applied to flows getting closer to the configurations met in industry. In particular, we plan to study the effects of rotation, heat transfer, or compressibility associated with some more 3-D complex geometries.

REFERENCES

BEHNIA, M., PARNEIX, S. & DURBIN, P., 1997 Accurate predictions of jet impingement heat transfer. *HTD-Vol. 343 Nat. Heat Transfer Conf., Book No*

H0190. **5,** 111-118.

BENEK, J.A., BUNNING, P.G. & STEGER, P.G., 1985 Chimera: a gridembedding technique. *AIAA paper No. 85-1523.*

BENEK, J.A., DONEGAN, T.L. & SUHS, J.L., 1987 Extended Chimera grid-embedding scheme with applications to viscous flows. *AIAA paper No. 87-1126.*

CHEN, H.C., 1995 Assessment of a Reynolds stress closure model for appendage-hull junction flows. *J. of Fluid Eng.* **117,** 557-563.

DEVENPORT, W. & SIMPSON, R., 1990 Time-dependent and time-averaged turbulence structure near the nose of a wing-body junction. *J. of Fluid Mech.* **210,** 23-55.

DURBIN, P., 1991 Near-wall turbulence closure modeling without "damping functions". *Theoret. Comput. Fluid Dynamics.* **3,** 1-13.

DURBIN, P., 1993 A Reynolds-stress model for near-wall turbulence. *J. of Fluid Mech.* **249,** 465-498.

DURBIN, P., 1995 Separated flow computations with the $k - \varepsilon - \overline{v^2}$ model. *AIAA Journal.* **33** No.4, 659-664.

ERCOFTAC/IAHR, 1995 4th ERCOFTAC/IAHR Workshop on refined flow modeling.

GOLDBERG, U. & RESHOTKO, E., 1984 Scaling and modeling of three-dimensional, pressure-driven turbulent boundary layers. *AIAA Journal.* **22,** 914-920.

JOHNSTON, J.P. & FLACK, K.A., 1996 Review – Advances in three-dimensional turbulent boundary layers with emphasis on the wall-layer regions. *J. of Fluid Eng.* **118,** 219-232.

MOIN, P., SHIH, T.H., DRIVER, D.M & MANSOUR, N.M., 1995 Direct numerical simulation of a three-dimensional turbulent boundary layer. *Physics of Fluids A.* **2,** 601-639.

OLCMEN, S. & SIMPSON, R., 1995 An experimental study of a three-dimensional pressure-driven turbulent boundary layer. *J. of Fluid Mech.* **290,** 225-262.

OLCMEN, S. & SIMPSON, R., 1997 Some features of a turbulent wing-body junction vortical flow. *AIAA paper No. 97-0651.*

PRAISNER, T.J., SEAL, C.V., TAKMAZ, L. & SMITH, C.R., 1997 Spatial-temporal turbulent flow-field and heat transfer behavior in end-wall junctions. *Int. J. of Heat and Fluid Flow.* **18,** 142-151.

ROGERS, S. E. & KWAK, D., 1990 Upwind differencing scheme for the time-accurate incompressible Navier-Stokes equations. *AIAA Journal.* **28,** 253-262.

SPENCER, M.C., JONES, T.V. & LOCK, G.D., 1996 Endwall heat transfer measurements in an annular cascade of nozzle guide vanes at engine representative Reynolds and Mach numbers. *Int. J. of Heat and Fluid Flow.* **17,** 139-147.

SUNG, C.H. & YANG, C.I., 1988 Validation of turbulent horseshoe vortex flows. *17th Symposium on Naval Hydrodynamics, La Hague.*

WEBSTER, D.R., DEGRAAFF, D.B. & EATON, J.K., 1996 Turbulence characteristics of a boundary layer over a swept bump. *J. of Fluid Mech.* **1996,** 323, 1-22.

WU, X. & SQUIRES, K.D., 1997a Nonequilibrium turbulent flow over a bump: a comparison of LES and RANS with experiments. *Submitted to AIAA Journal.*

WU, X. & SQUIRES, K.D., 1997b Prediction of the three-dimensional turbulent boundary layer over a swept bump. *Submitted to AIAA Journal.*

Accurate modeling of impinging jet heat transfer

By M. Behnia, S. Parneix AND P. Durbin

1. Motivation and objectives

In the last two decades, jet impingement heat transfer has received considerable attention because of its many applications for high heat flux cooling or heating. There are numerous papers dealing with this problem both numerically and experimentally. Some reviews have also appeared, amongst which some of the most recent are Jambunathan *et al.* (1992), Viskanta (1993), and Webb & Ma (1995).

There are a number of parameters which can affect the heat transfer rate in a jet impingement configuration. For instance, the jet-to-target distance not only affects the heat transfer rate, but also can have a significant effect on the local heat transfer coefficient distribution (Baughn & Shimizu, 1989). For the design and optimization of jet impingement cooling or heating systems, it is essential that the effect of these parameters of importance be characterized. In some of the previous studies, these effects have been addressed, and results of the experiments performed by different investigators have sometimes been contradictory due to the differences in the experimental conditions. In their review, Jambunathan *et al.* (1992) clearly pointed out this problem and noted that, for a better understanding of the jet impingement heat transfer process, the details of the flow, geometry, and turbulence conditions are required so that a comparison between different experimental data can be made.

Due to the difficulties in performing and comparing experiments, a numerical simulation of the problem would have been an ideal candidate for quantifying the effect of the parameters of interest. However, turbulent impinging jets have complex features due to entrainment, stagnation, and high streamline curvature. These features prove to be incompatible with most existing turbulence models, which are essentially developed and tested for flows parallel to a wall. For instance, Craft *et al.* (1993) have demonstrated some of the problems in these turbulence models, namely a substantial over-prediction of heat transfer in the stagnation region by the widely used $k - \varepsilon$ turbulence model. In fact, the complexity of this flow has led to it being chosen as an excellent and challenging test-case (see ERCOFTAC database at http://fluindigo.mech.surrey.ac.uk) for the validation of turbulence models. A number of investigators have gauged the success of their models based on this flow. However, turbulence modelers encounter numerous difficulties due to the fact that the details of the experimental data are often not known or that the flow conditions and geometry are not well posed.

For validation purposes, we chose the data sets obtained in a fully-developed impinging jet configuration (i.e. Baughn & Shimizu 1987, Baughn *et al.* 1989, Lytle & Webb 1995, Yan 1993 and Mesbah 1996). Some computations with the flat plate configuration (Fig. 1) at a single Reynolds number have been reported in the 1996

CTR Annual Research Briefs (Behnia *et al.* 1996). It has been shown that the *V2F* model successfully and economically predicted the rate of heat transfer. Subsequent simulations are presented in this report to determine the effects of important parameters such as jet-to-target distance, geometry, and Reynolds number, as well as jet confinement.
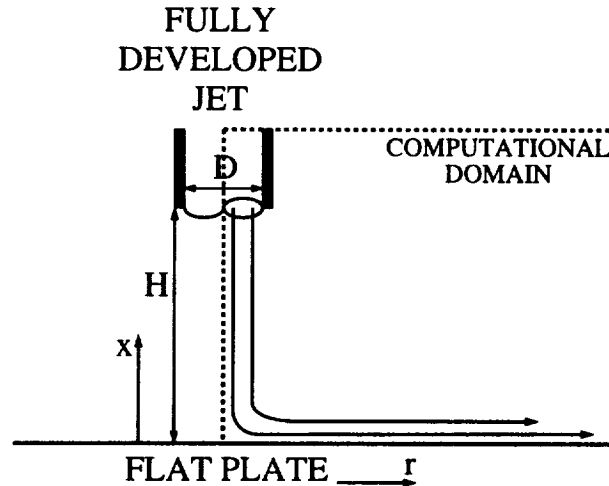

FIGURE 1. Configuration of the jet impinging on a flat plate.

2. Accomplishments

2.1 Background

2.1.1 Simulation techniques

Most predictions of jet impingement heat transfer in industry involve the use of standard or modified versions of the $k - \varepsilon$ turbulence model, available in all existing CFD packages. These models have usually been developed, calibrated, and validated using flows parallel to the wall. Physical phenomena involved in impinging flows on a solid surface are substantially different and have been considered as highly challenging test-cases for the validation of turbulence models. For example, simulations from Craft *et al.* (1993) of a non-confined impinging jet cooling a heated flat plate, using a $k - \varepsilon$ type model, showed dramatically poor results for wall heat transfer coefficients (e.g. more than 100% over-prediction in the stagnation region).

The *V2F* turbulence model, introduced by Durbin (1991, 1993b), could be thought of as a restriction of a full Second Moment Closure model developed subsequently (Durbin 1993a). It has the advantage of keeping an eddy viscosity, which avoids some computational stability problems encountered with Reynolds-stress closure models. It is a general geometry turbulence model, valid right up to the solid wall. It does not need wall functions, whose universality is increasingly being called into question, especially in impinging regions. The alternative is the introduction of damping functions, which are tuned to mimic the near-wall effects. But all these

models use a single-point approach that cannot represent the well-known, non-local effects of pressure-reflection that occur near solid boundaries. Moreover, these damping functions often involve an ill-defined normal distance to the wall, which cannot be used in complex configurations. They are also highly non-linear and sometimes introduce numerical stiffness.

The $V2F$ model brings more physics in its body. First, it introduces a new velocity scale, $\overline{v^2}$, used for the evaluation of the turbulent viscosity, instead of k; $\overline{v^2}$ might be regarded in some cases as the velocity fluctuation normal to the streamlines. It is equivalent to the turbulent kinetic energy, k, far from any solid walls; in the near-wall region, it becomes the velocity fluctuation normal to the solid surface, irrespective of the orientation of the surface relative to the flow. Theoretically, k is unable to represent the damping of turbulent transport close to the wall, whereas normal velocity fluctuations provide the right scaling (Behnia *et al.* 1997). Following the full Reynolds stress analysis (Durbin 1993a), in order to model non-local characteristics of the near-wall turbulence and to avoid the use of two-point correlations, which are not viable for non-homogeneous turbulence, the $V2F$ model uses an elliptic operator to compute a term analogous to the pressure-strain correlation. Ellipticity is introduced by a modified Helmholtz operator, which is amenable to numerical computations and which introduces wall effects by a linear equation, taking care of the transition between the near-wall region and regions far from solid boundaries. Finally, some physical constraints have been added in order to prevent non-realizability of the solution, especially in the stagnation region (Durbin 1996).

The temperature field is computed through a standard eddy diffusivity approximation. Concerning the turbulent Prandtl number, Pr_t, the Kays and Crawford formulation (1993) was chosen for all of the following computations, including those with $k - \varepsilon$, since it gave a more physical representation near the wall (Pr_t increases from 0.85 in the far-field to about 1.7 in the near wall-region) and yielded somewhat better agreement in the impingement region. Nevertheless, the improvement over using a constant value is of the order of 10% (Behnia *et al.* 1997), which cannot explain the 100% error of the $k - \varepsilon$ model. The flow and the turbulent fields have to be accurately resolved for obtaining good heat transfer predictions. The basis and equations of the complete $V2F$ model can be found in Behnia *et al.* (1996).

All computations were performed with INS2D, a general geometry, finite difference code developed by Rogers and Kwak (1990). The spatial discretization of convective terms was via a third order, upwind biased scheme; diffusion terms were central differenced. Fine, non-uniform, orthogonal, cylindrical grids were used, with a high resolution near all solid boundaries. A mesh sensitivity was carried out by dividing each mesh by 2 in the axial and radial directions. This changed the impingement region Nusselt number by less than 1%; therefore, the present solutions are considered grid-independent.

The flow conditions at the nozzle exit may affect the computed flow field. Therefore, for validation purposes, we chose the case of a jet coming from a long pipe so that nozzle-exit conditions are fully turbulent and well defined. A fully-developed

turbulent pipe flow was first computed in a preliminary computation and then interpolated onto the grid to provide the inlet condition of the jet. The flow domain began approximately 2 pipe diameters upstream of the jet exit so that the pipe profiles may evolve in the nozzle as the flow approaches the nozzle outlet. It is noted that prescribing the inlet conditions upstream of singularities is also a requirement in other types of flows, e.g. the backward-facing step. Further, in the unconfined case, this allows the upper computational boundary to be a sufficient distance from the wall that it does not affect the flow near the impingement surface.

2.1.2 The impinging jet on a flat plate

Some computations of jet impingement heat transfer have been reported in the 1996 CTR Annual Research Briefs (Behnia *et al.* 1996). The main conclusions of that paper are summarized on Figs. 2a and 2b. Computational results are presented for the widely-used test-case of an unconfined impinging jet on a flat plat at $Re =$ 23,000 and for a nozzle-to-plate distance of 6 jet diameters. One can see that the experimental results are fairly well reproduced by the *V2F* model; in fact, the simulation falls into the range of available experimental data sets, represented by the gray zone of Fig. 2a. In comparison, the $k - \varepsilon$ model strongly over-predicts the heat transfer rates in the stagnation region (by about 100%). This over-estimation extends up to $2 - 3$ jet diameters away from the stagnation point, although the flow has already been parallel to the surface at this location. This indicates that the quantitative misbehavior spreads up in the region surrounding the impinging area and may influence the whole distribution of heat transfer, even qualitatively.

The excellent *V2F* results have been confirmed by studying the influence of the nozzle-to-target spacing, H/D, on the stagnation Nusselt number. Experimental data of Baughn & Shimizu (1989), Baughn *et al.* (1991), Yan (1993), and Lytle & Webb (1995) are plotted on the same graph, and a line of best fit has been evaluated for comparison purposes. A set of 15 simulations has been performed for each model and plotted against the available experimental data sets (Fig. 2b). The *V2F* model is in very good agreement with the experimental curve of best fit, with an optimal stagnation heat transfer rate at $H/D = 6 - 7$. Note that this optimal value has already been reported in numerous experimental studies (e.g. Martin 1977, Baughn & Shimizu 1989, Webb & Ma 1995). The quantitative over-prediction of the $k - \varepsilon$ model is present for all nozzle-to-plate spacings. If one wants to use this model for design purposes, the efficiency of the cooling system would be over-estimated; however, more dramatically, its optimization would also fail completely. For instance, the $k - \varepsilon$ model predicts 2 optimal nozzle-to-plate distances of 2.5 and 5 diameters, in total disagreement with the experiments.

2.2 Influence of Reynolds number

Turbulence models are sometimes fitted for a given test-case, at a given Reynolds number and might give much worse results when flow conditions are changed. Thus, it is essential to check the range of validity of the results obtained by the *V2F* model in the 1996 report for $Re = 23,000$. The dependence on the nozzle-to-plate distance has already been shown to be well captured by the model.
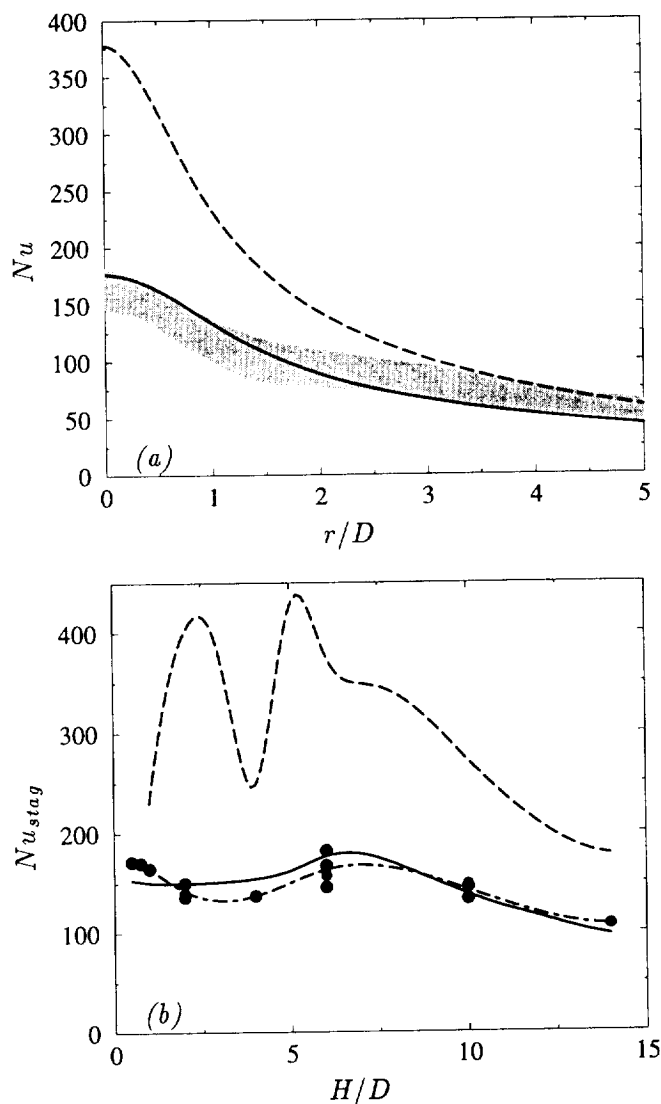
FIGURE 2. Impinging jet on a flat plate, $Re = 23,000$ (a) Local distribution of wall heat transfer for $H/D = 6$, (b) Dependence of stagnation wall heat transfer on H/D, ———— $V2F$, - - - - : $k - \varepsilon$, gray zone and ● : experiments, —·— : line of best fit of experimental data.

The evolution of the local Nusselt number on the flat plate with increasing Reynolds number is presented for $H/D = 2$ (Fig. 3). Comparisons are with Yan's (1993) experimental data. One can observe an augmentation with Re of the relative height of the secondary peak in the Nu distribution. The model is qualitatively consistent with the experiment. As for the lower Reynolds number, this peak is less pronounced in the computations, but its location is very well predicted (around $r/D = 2$). Recall that a 20% scatter existed in the experimental data at
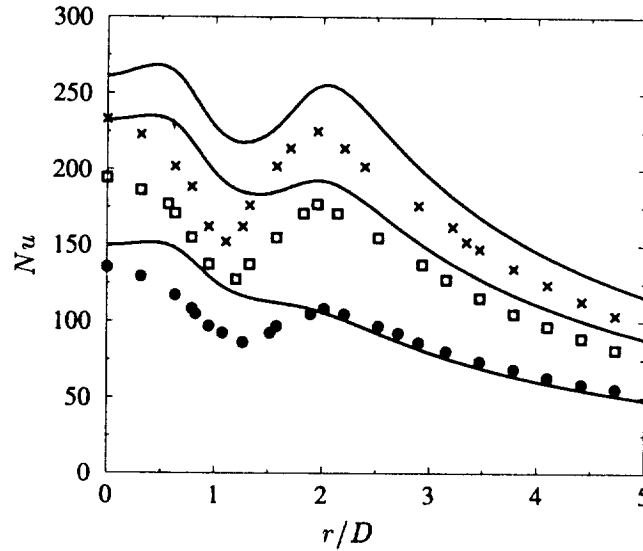
FIGURE 3.   Influence of Reynolds number on the local distribution of wall heat transfer at $H/D = 2$, ——— : *V2F*, symbols: experiments (● : $Re = 23,000$, □ : $Re = 50,000$, × : $Re = 70,000$).

$Re = 23,000$ and that Yan's data were systematically close to the lowest quantitative bound on the whole set of available data. In light of this, the *V2F* results may be considered quite good.

Figure 4 presents the stagnation Nusselt number obtained for different flow rates at $H/D = 6$. The experimental data from Lytle & Webb (1995) and Yan (1993) are plotted on the same graph and a line of best fit has been evaluated for comparison purposes. One can see that the dependence on Reynolds number, predicted by the *V2F* model, is in excellent agreement with the experimental data. In particular, the quasi-laminar correlation $Nu_{stag} \propto Re^{0.5}$ has been obtained accurately. Of course, the Re number is high enough to assure a turbulent regime; for instance, Viskanta (1993) noted that heat transfer rates are $1.4 - 2.2$ times as high as the laminar rates. Moreover, a *V2F* correlation, showing the Nusselt number evaluated at 6 jet diameters away from the stagnation point, for different jet-to-plate distances, has been added to Fig. 4. Here, a dependence on $Re^{0.77}$ is predicted by the *V2F* model, in good agreement with previous experiments, which have established a dependence on $Re^{0.7-0.85}$ (see Jambunathan *et al.* 1992, Viskanta 1993).

2.3 Influence of the impinging surface's geometry

Very little experimental and computational work has been done on impinging flows in geometries other than flat plates. The objective of the work in this section has been to accurately compute the flow and thermal fields in an axisymmetric isothermal fully developed jet perpendicular to a heated pedestal mounted on a flat plate (Fig. 5). The geometry resembles that of an electronic component. Recently, Mesbah (1996) has measured the local heat transfer coefficient in this configuration.
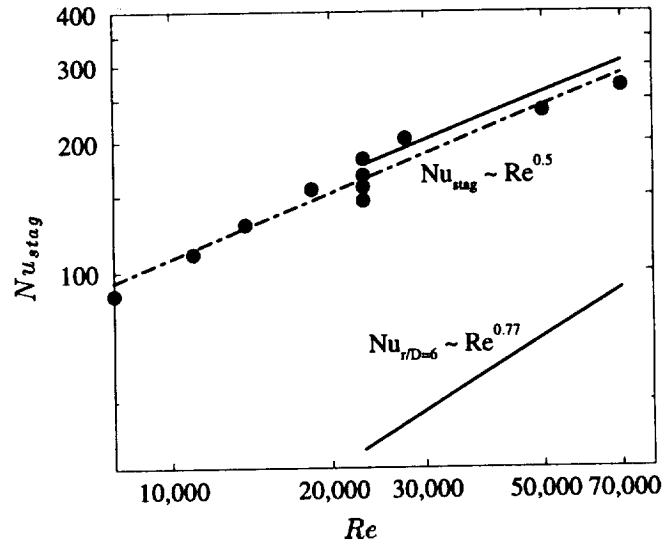
FIGURE 4. Influence of Reynolds number on the wall heat transfer coefficient for $H/D = 6$, at the stagnation point $(r/d = 0)$ and at $r/D = 6$, —— : $V2F$, • : experiments $(r/D = 0)$, —·— : line of best fit of the stagnation experimental data.

He used the preheated-wall transient technique in conjunction with surfaces coated by thermochromic liquid crystals. For comparison purposes, we adopted the same geometry. In addition, computations were also performed using the widely used standard $k - \varepsilon$ turbulence model.
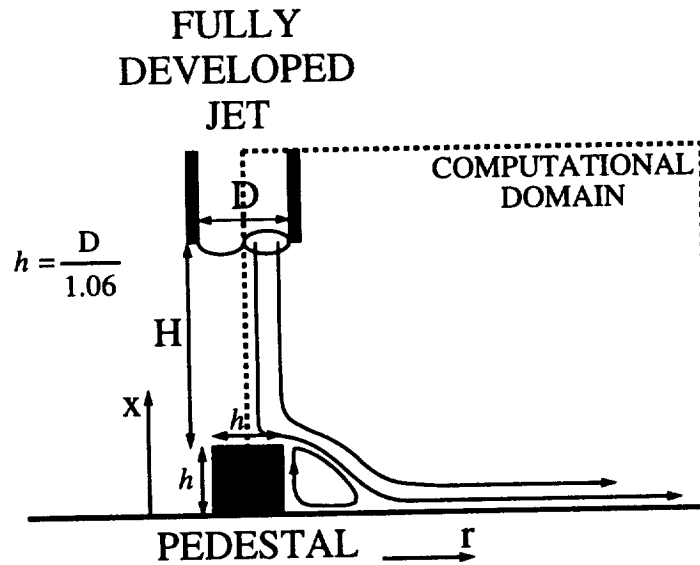

FIGURE 5. Configuration of the jet impinging on a wall-mounted pedestal.

Contours of Stokes streamlines are shown in Fig.6 for $H/D = 6$. Only a qualitative analysis will be done since no flow measurements are available. The flow, parallel to the jet axis at the nozzle exit, develops into a free jet before decelerating in the axial direction on top of the pedestal. Then, it turns sharply and starts to form a radial wall jet along the upper surface of the pedestal. At the corner, the flow separates and re-attaches downstream on the plate. This creates a recirculation which has a significant effect on the wall heat transfer. This bubble is much shorter than that found downstream of a backward-facing step (recirculation lengths between 5 and 8 times the step height); the rather short length is due to the strong influence of the outer region of the impinging jet and to the choice of an axisymmetric configuration. After reattachment, the flow develops into a wall jet along the plate. The ambient fluid outside the jet is entrained into the core with a developing shear layer separating the core and the ambient fluid. This entrainment is shown by the curvature of the streamlines outside the pipe towards the symmetry axis and leads to a small recirculation zone in the vicinity of the exit pipe-wall. This feature and the presence of a secondary recirculation near the bottom of the pedestal indicate a sufficient grid resolution around the exit of the nozzle and next to the pedestal.
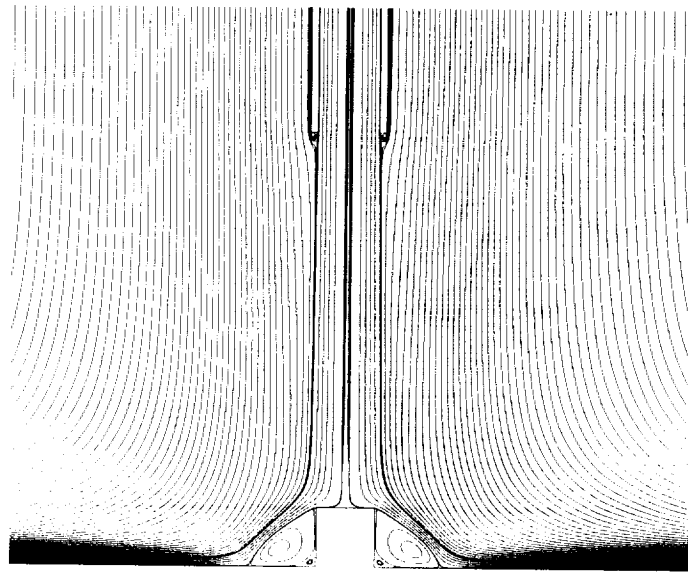

FIGURE 6. Streamlines for $H/D = 6$ computed with the *V2F* model.

We evaluated the temperature distribution for $H/D = 6$ using an isothermal boundary condition along the upper surface of the pedestal and downstream of it, on the plate (Fig. 7). The local wall heat transfer coefficient has a local minimum on the stagnation line on top of the pedestal. The Nu number is nearly constant in the vicinity of the stagnation point and then increases sharply as the corner is approached. The value of stagnation Nusselt number is similar to that of a jet

impinging on a flat plate. However, the local Nusselt number distribution is radically different from the flat plate configuration since, in that case, the stagnation Nusselt number is a local maximum. Hence, the flat plate results may not be suitable for complex geometries that can be found in some industrial applications. Figure 7 shows that the *V2F* model reproduces this behavior in the vicinity of the symmetry line, whereas the $k - \varepsilon$ predictions show a local maximum and a sharp decrease of Nu. Quantitatively, $k - \varepsilon$ predictions over-estimate the wall heat transfer above the whole pedestal upper surface by more than 150%. This over-prediction is believed to be due to the over-prediction of turbulent kinetic energy in that region (note the dark gray zone in Fig. 8). The use of $\overline{v^2}$ as the velocity scale instead of k for computing ν_t is essential here (Behnia *et al.* 1997), and therefore the *V2F* computations are much more realistic with only 5 to 15% of over-prediction. It is recalled that, for the impinging jet on a flat plate, the set of available experiments shows a 20% data scatter (Behnia *et al.* 1996). Moreover, Mesbah (1996) used the transient technique which gave results in the lower band of this experimental data set in the stagnation region. With this in mind, one can say that the *V2F* predictions are excellent.
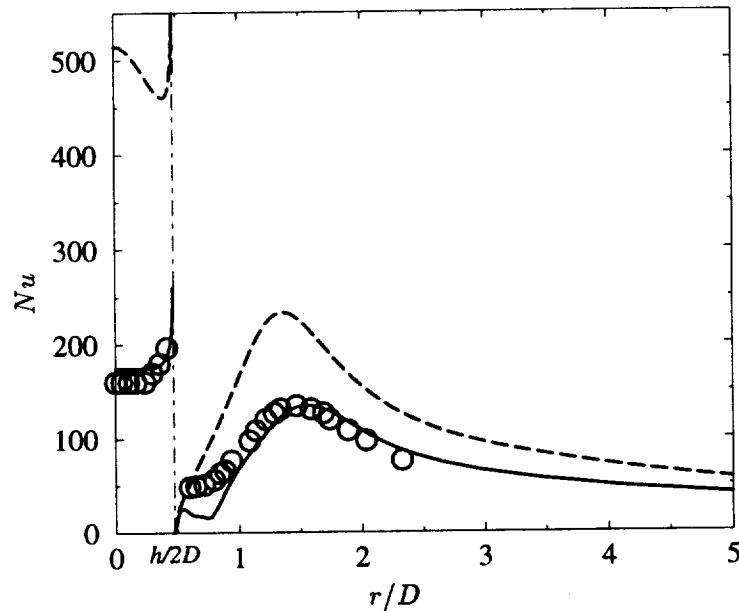

FIGURE 7. Local wall heat transfer coefficient for $H/D = 6$ and $Re = 23,000$ on top of the pedestal (left of —·—) and downstream of it on the flat plate (right of —·—), ——— : *V2F*, ———— : $k - \varepsilon$, o : Mesbah's experiment (1996).

Along the plate, a local maximum wall heat transfer point is created in the reattachment region, about one diameter downstream of pedestal and slightly upstream of the reattachment point, as might be expected from the backward-facing step results (see Vogel & Eaton 1985). The *V2F* model predicts both the location and

magnitude of this peak accurately; $k - \varepsilon$ predictions still show almost 100% over-prediction, which may be more due to the diffusion of the dramatic heat transfer over-prediction on top of the pedestal rather than to an over-prediction of turbulence production in the reattachment area. The angle of impingement is much smaller (between 30° and 40°) in the reattachment region than around the symmetry axis. Finally, the *V2F* simulations show a plateau with a secondary peak at the foot of the pedestal. This phenomenon is believed to be due to the existence of a secondary recirculation. The plateau is present in the experiment, but without any secondary maximum. We suspect that in the experiment, longitudinal heat transfer in the solid near the corners of the pedestal occurs. Also, the longer times required for measurements in this region make the underlying assumption of the measurement technique questionable (Mesbah, 1996). Therefore, a constant temperature or constant heat flux assumption would not be accurate any more, which may explain the discrepancy.
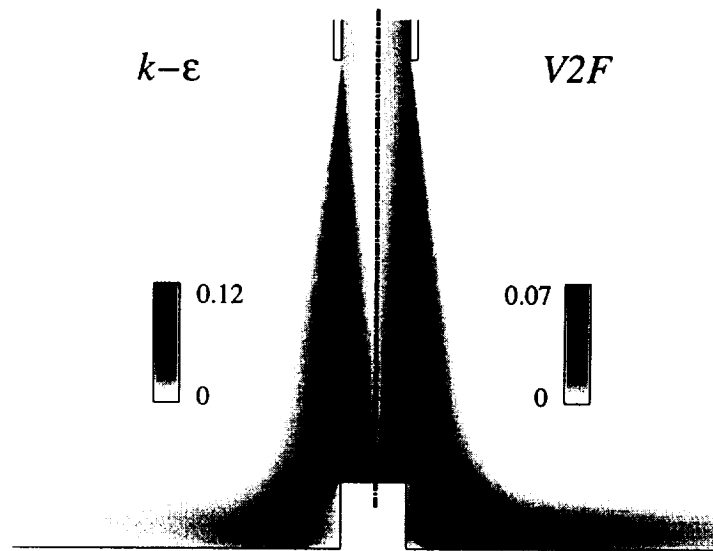

FIGURE 8.   Contours of turbulent kinetic energy for $H/D = 6$. Overprediction of turbulent kinetic energy is reflected in the darkest gray area on top of the pedestal.

Simulations have been carried out for a fixed Reynolds number ($Re = 23,000$) and a wide range of aspect ratios ($1 \leq H/D \leq 8$) to determine the dependence on H/D of the stagnation Nusselt number on top of the pedestal and the local maximum Nusselt number on the plate. The behavior of Nusselt number variation with the jet-to-pedestal distance needs to be known for the design and optimization of impingement cooling or heating systems. Figures 9a and 9b show the corresponding values computed with both the *V2F* and $k - \varepsilon$ models. The *V2F* computations show very good agreement with Mesbah's experiment. As indicated before, the transient technique yielded results in the lower band of the flat plate experimental data set, so the 5 to 15% over-prediction is remarkable. Moreover, it is noted that

this over-prediction is almost constant; the dependence of stagnation Nusselt number on H/D is very well reproduced. Note also that the *V2F* computations show the existence of a maximum of stagnation heat transfer in the range $6 < H/D < 7.5$. This cannot be compared to Mesbah's experiment, since $H/D = 6$ was the highest aspect ratio studied, but this is consistent with previous flat plate results (Martin 1977, Baughn & Shimizu 1989, Behnia *et al.* 1996). The $k - \varepsilon$ model fails to reproduce the experimental trends, not only quantitatively (150% of over-prediction) but also qualitatively, which is even more critical from a practical point of view. Regarding the maximum Nusselt number downstream of the pedestal along the plate, both models reproduce a constant decrease with H/D. The $k - \varepsilon$ computations yield almost 100% over-estimated values, whereas *V2F* simulations are very close to the experiment. The only disagreement is for $H/D = 4$ where the experimental maximum Nusselt number is higher than for $H/D = 1$ and 2. Perhaps more experimental data points should be obtained to assess this non-monotonic behavior.

2.4 Effect of confinement

All the previous computations have been performed for an unconfined geometry. However, industrial applications, especially in electronic cooling, require the impinging jet to be confined with a solid boundary at the level of the nozzle exit. Numerous experiments have been conducted in order to study the effect of confinement on jet impingement heat transfer. The aim was mainly to know whether the physics and correlations involved in unconfined geometries could be applied in a confined context. Obot *et al.* (1982) concluded there was a reduction in the average heat transfer rate from 5 to 10% when confinement was added. Again, comparisons are difficult to establish from different experiments when jet outlet profiles or experimental conditions are different. Moreover, to our knowledge, no experimental data are available for a fully-developed jet coming from a long pipe. Since *V2F* simulations gave satisfactory results in the unconfined geometry, we assume that the model is accurate enough to undertake a numerical comparison study.
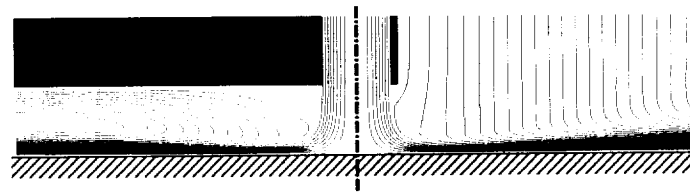

FIGURE 10.   Streamlines for $H/D = 1$ and $Re = 23,000$ computed with the *V2F* model for the confined (left) and unconfined (right) configurations.

Several computations have been performed by adding a wall at the nozzle exit (Fig. 10). We varied the nozzle-to-plate distance, and the local heat transfer rates are compared to the results obtained with an unconfined geometry. Figure 11 shows the Nusselt number distribution for different H/D. One can see that, for a high enough jet-to-plate spacing, the confinement has no effect on the heat transfer rate. The presence of a top wall creates a recirculation (Fig. 10), but its influence
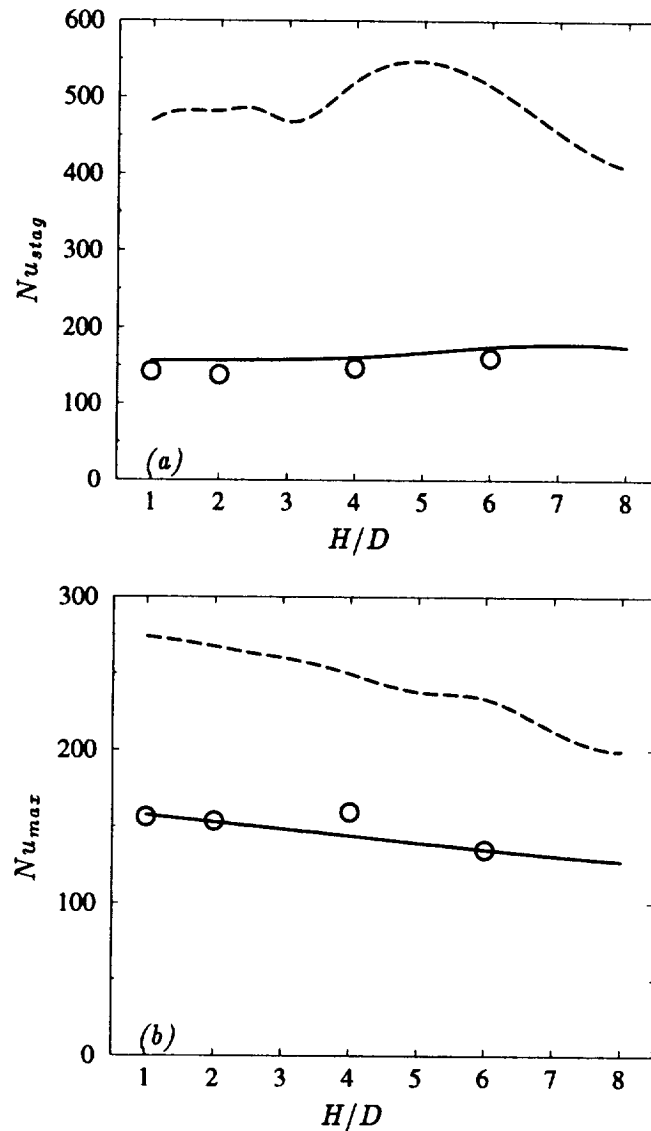
FIGURE 9.   Impinging jet on a pedestal at $Re = 23,000$, influence of nozzle-to-plate distance on (a) the stagnation heat transfer coefficient on top of the pedestal and (b) the maximum heat transfer coefficient downstream of the pedestal along the plate, ——— : $V2F$, ———— : $k - \varepsilon$, o : Mesbah's experiment (1996).

is rather small. Indeed, for $H/D > 1$, no significant difference in the wall heat transfer distribution has been observed. For $H/D < 0.5$, the Nusselt distributions start to diverge. As it has been found in experiments, the average heat transfer rate is slightly lower for the unconfined case. It can be explained by the fact that the top wall introduces a resistance to the flow; the entrainment of the external fluid by the jet is less important, decreasing the global efficiency of the impinging

FIGURE 11. Local wall heat transfer, simulated by the *V2F* model, for the jet impinging on the flat plate at $Re = 23,000$ and different nozzle-to-plate distances $(H/D = 2, 0.5, 0.25,$ and $0.1)$ ——— : confined, ---- : unconfined.
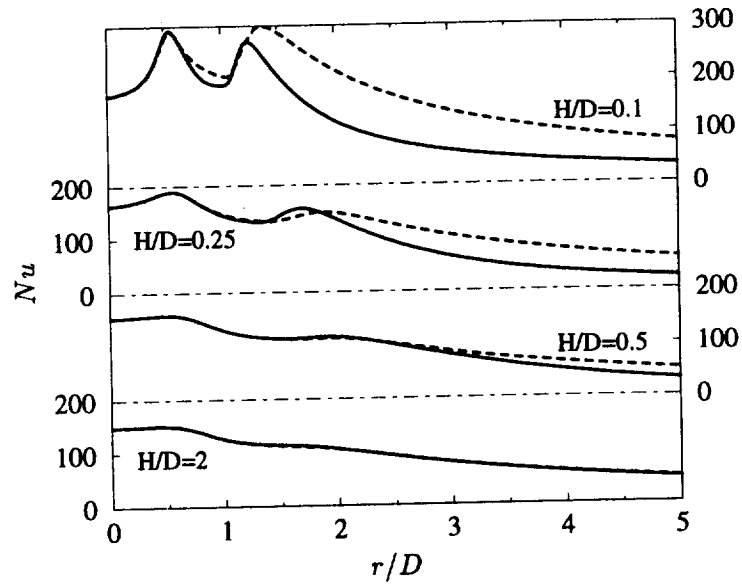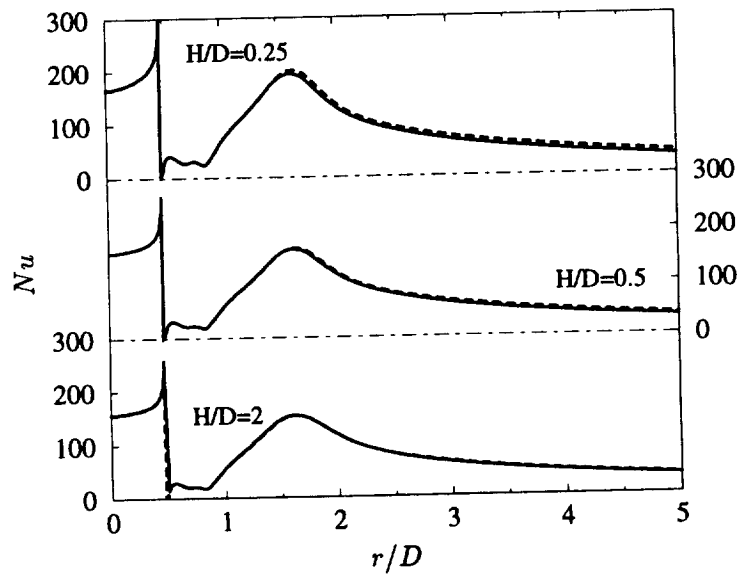

FIGURE 12. Local wall heat transfer, simulated by the *V2F* model, for the jet impinging on the pedestal at $Re = 23,000$ and different nozzle-to-plate distances $(H/D = 2, 0.5,$ and $0.25)$ ——— : confined, ---- : unconfined.

jet heat transfer. In the case of a smaller nozzle-to-plate distance (not shown here), the recirculation is more confined and active; it is located closer to the target plate and then has a stronger influence on the wall heat transfer coefficient. Nevertheless, even for a very low H/D (as low as 0.1), the stagnation heat transfer rates are not noticeably influenced by the presence of confinement. Up to a radial distance of 0.5 jet diameters away from the stagnation point, the Nu distributions stay unchanged whether the jet is confined or not. This is partially confirmed by Garimella & Rice (1995) who noted that, for $H/D > 2$, confinement had little effect on heat transfer at stagnation point. A primary peak is created at $r/D \simeq 0.5$ as H/D decreases. This peak corresponds to the acceleration of the local velocity, which occurs for $H/D < 0.25$. Its location is fixed, in good agreement with Colucci & Viskanta experiment (1996). A secondary peak is also created, but this time, its location is moving toward the axis of symmetry when the nozzle-to-plate distance is decreased. Again, such a behavior has been found to be in good qualitative agreement with Colucci & Viskanta experiment (1996). Similar computations have been performed for the case of the wall-mounted heated pedestal. One can see in Fig 12 that the influence of confinement is much less effective than for the flat plate configuration. Even for $H/D = 0.25$, heat transfer rates stay unchanged. First, the diameter of the pedestal is slightly smaller than the jet diameter. Thus, through the analysis of the previous results for the flat plate, no confinement effect was expected on top of the pedestal ($r/D < 0.5$). Downstream of it, on the plate, the top wall is then at a normalized distance of more than one jet diameter ($H/D + 1/1.06$); this distance is too high to expect any significant change in the heat transfer rate. Moreover, the recirculation, which strongly acts on the Nusselt distribution, is driven by the jet itself and is less subject to be affected by the confinement.

In conclusion, the confinement, present in most industrial applications, does not have a significant impact on the wall heat transfer coefficient unless the jet-to-target spacing is considerably reduced ($H/D < 0.25$). The average Nusselt number decreases with confinement, but the local heat transfer distribution in the stagnation region ($r/D < 0.5$) is not modified; unconfined impinging jet stagnation Nusselt number correlations can thus be used.

3. Future plans

The main aim of this research has been to assess the ability of computational fluid dynamics to accurately and economically predict the heat transfer rate in an impinging jet situation, strongly relevant to industrial applications, e.g. in electronic cooling. The computations carried out herein show that predictions by the normal-velocity relaxation model ($V2F$ model) agree very well with the experiments. The influence of parameters of interest such as nozzle-to-plate distance, Reynolds number, geometry of the impingement surface, or confinement has been shown to be well captured. In comparison, the widely-used $k - \varepsilon$ model does not properly represent the flow features, highly over-predicts the rate of heat transfer, and yields physically unrealistic behavior.

It is planned to perform additional computations to cover a wider range of parameters (e.g. 3D configurations and a range of Prandtl numbers). In particular,

for electronic cooling applications, dielectric liquids in a confined jet geometry and multiple jets configurations need to be explored.

REFERENCES

BAUGHN, J., HECHANOVA, A. & YAN, X. 1991 An experimental study of entrainment effects on the heat transfer from a flat surface to a heated circular impinging jet. *J. Heat Transfer.* **113**, 1023-1025.

BAUGHN, J. & SHIMIZU, S. 1989 Heat transfer measurements from a surface with uniform heat flux and an impinging jet. *J. Heat Transfer.* **111**, 1096-1098.

BEHNIA, M., PARNEIX, S. & DURBIN, P., 1996 Simulation of jet impingement heat transfer with the $k - \varepsilon - \overline{v^2}$ model. *Annual Research Briefs*, Center for Turbulence Research, NASA Ames/Stanford Univ., 3-16.

BEHNIA, M., PARNEIX, S. & DURBIN, P., 1997 Accurate predictions of jet impingement heat transfer. *HTD-Vol. 343 National Heat Transfer Conference.* **5**, Book No H0190, 111-118.

COLUCCI, D. & VISKANTA, R. 1996 Effect of nozzle geometry on local convective heat transfer to a confined impinging air jet. *Experimental Thermal and Fluid Science.* **13**, 71-80.

CRAFT, T., GRAHAM, L. & LAUNDER, B. 1993 Impinging jet studies for turbulence model assessment-II. An examination of the performance of four turbulence models. *Int. J. Heat Mass Transfer.* **36**(10), 2685-2697.

DURBIN, P. 1991 Near-wall turbulence closure without damping functions. *Theoretical and Computational Fluid Dynamics.* **3**(1), 1-13.

DURBIN, P. 1993a A Reynolds-stress model for near-wall turbulence. *J. Fluid Mech.* **249**, 465-498.

DURBIN, P. 1993b Application of a near-wall turbulence model to boundary layers and heat transfer. *Int. J. Heat and Fluid Flow.* **14**(4), 316-323.

DURBIN, P. 1995 Separated flow computations with the $k - \varepsilon - \overline{v^2}$ model. *AIAA J.* **33**(4), 659-664.

DURBIN, P. 1996 On the $k - \varepsilon$ stagnation point anomaly. *Int. J. Heat and Fluid Flow.* **17**, 89-90.

GARIMELLA, S. & RICE, R. 1995 Confined and submerged liquid jet impingement heat transfer. *J. Heat Transfer.* **117**, 871-877.

JAMBUNATHAN, K., LAI, E., MOSS, M. & BUTTON, B. 1992 A review of heat transfer data for single circular jet impingement. *Int. J. Heat and Fluid Flow.* **13**(2), 106-115.

KAYS, W. M.& CRAWFORD, M. E. 1993 Convective heat and mass transfer. Third Edition, McGraw-Hill.

LYTLE, D. & WEBB, B. 1994 Air jet impingement heat transfer at low nozzle-plate spacings. *Int. J. Heat Mass Transfer.* **37**, 1687-1697.

MARTIN, H. 1977 Heat and mass transfer between impinging gas jets and solid surfaces. *Advances in Heat Transfer.* **13**, 1-60.

MESBAH, M. 1996 An experimental study of local heat transfer to an impinging jet on non-flat surfaces: a cylindrical pedestal and a hemispherically concave surface. *PhD Thesis,* University of California, Davis.

OBOT, N., MUJUMDAR, A. & DOUGLAS, W. 1982 Effect of semi-confinement on impinging heat transfer. *Proc. 7th Int. Heat Transfer Conf.* **3**, 395-400.

ROGERS, S. & KWAK, D. 1990 Upwind differencing scheme for the time-accurate incompressible Navier-Stokes equations. *AIAA J.* **28**, 253-262.

VISKANTA, R. 1993 Heat transfer to impinging isothermal gas and flame jets. *Exp. Thermal Fluid Sci.* **6**, 111-134.

VOGEL, J.C. & EATON, J.K. 1985 Combined heat transfer and fluid dynamic measurements downstream of a backward-facing step. *J. Heat Transfer.* **107**, 922-929.

WEBB, B. & MA, C.-F. 1995 Single-phase liquid jet impingement heat transfer. *Advances in heat transfer.* **26**, 105-217.

YAN, X. 1993 A preheated-wall transient method using liquid crystals for the measurement of heat transfer on external surfaces and in ducts. *PhD Thesis,* University of California, Davis.

Application of turbulence
models to high-lift airfoils

By Georgi Kalitzin

1. Motivation and objectives

Accurate prediction of the flow over an airfoil at high lift condition is a very challenging problem. Even for single element geometries under subsonic conditions, complicated flow structures appear with increasing angle of attack. For a sufficiently high Reynolds number, the flow undergoes a transition from laminar to turbulent. Depending on the flow conditions and the shape of the airfoil, a laminar separation bubble may appear on the upper surface upstream of transition. The laminar flow separates, transitions into turbulent flow, and reattaches again. A turbulent separation bubble may occur further downstream near the trailing edge for higher angles of attack. The pressure reaches its lowest value at the suction peak, and the lift generated by the airfoil achieves its maximum value for the considered Reynolds and Mach number. A further increase in the angle of attack leads to stall conditions. The lift drops as a consequence of complete separation of the flow.

Consideration of multi-element airfoils further complicates the problem. The wake of upstream element interacts with newly forming turbulent boundary layers or wakes of downstream elements. This requires from a turbulence model an accurate prediction capability for turbulent wall bounded flows, for free shear layers, and for flow separation.

Although algebraic models are still widely, and often quite successfully, used in the aircraft industry, there is an increasing interest in transport models. This is partly due to limitations of algebraic models in flows around multi-element airfoils and in three-dimensional flows. Additionally, the way in which these models are implemented in a CFD code may strongly influence the results of a computation (Haase *et al.*, 1997). Second moment closure transport models are often very stiff and too expensive due to the high number of strongly coupled Reynolds stress equations. This report concentrates on the application of one- to three-equation eddy-viscosity models and, in particular, of the V2F model.

The accuracy of the results depends on the turbulence model as well as the underlying numerical flow solver. Some of the difficulties encountered in our computations could be traced back to the artificial viscosity added by the numerical scheme. Particular flow features, such as transition, seem to require a locally very fine mesh or a refinement of the numerical scheme.

2. Accomplishments

2.1 Numerical method

An extended version of the code INS2D developed by Rogers and Kwak (1991) has been used to solve the two-dimensional incompressible Reynolds-averaged Navier-Stokes equations and the particular turbulence model. The underlying numerical method is based on the artificial compressibility method suggested by Chorin (1967). The code uses a finite difference scheme for structured grids with third order upwind discretization of the convective terms and a second order discretization for the diffusion terms. The time integration is implicit. The Generalized Minimum Residual (GMRES) method (Saad, 1986) is used to minimize the residual. The turbulence equations are solved separately from the mean flow. The mean flow is solved as a 3 × 3 coupled system.

2.2 V2F turbulence model

The V2F model introduced by Durbin (1995) consists of three transport equations for the turbulence variables. The first two have the form of the standard k-ϵ equations:

$$\frac{\partial k}{\partial t} + \frac{\partial(u_j k)}{\partial x_j} = P_k \mathcal{T} - \epsilon + \frac{\partial}{\partial x_j}\left[(\nu + \frac{\nu_t}{\sigma_k})\frac{\partial k}{\partial x_j}\right],$$

$$\frac{\partial \epsilon}{\partial t} + \frac{\partial(u_j \epsilon)}{\partial x_j} = \frac{C'_{\epsilon 1} P_k \mathcal{T} - C_{\epsilon 2}\epsilon}{\mathcal{T}} + \frac{\partial}{\partial x_j}\left[(\nu + \frac{\nu_t}{\sigma_\epsilon})\frac{\partial \epsilon}{\partial x_j}\right].$$

The third equation describes the transport of the turbulent intensity normal to the streamlines and models the anisotropy of the Reynolds stresses caused by near-wall effects:

$$\frac{\partial \overline{v^2}}{\partial t} + \frac{\partial(u_j \overline{v^2})}{\partial x_j} = kf - \overline{v^2}\frac{\epsilon}{k} + \frac{\partial}{\partial x_j}\left[(\nu + \nu_t)\frac{\partial \overline{v^2}}{\partial x_j}\right].$$

The production of $\overline{v^2}$ is modeled by means of an elliptic relaxation equation:

$$L^2 \frac{\partial^2 f}{\partial x_j \partial x_j} - f = \frac{1}{\mathcal{T}}(C_1 - 1)\left[\frac{\overline{v^2}}{k} - \frac{2}{3}\right] - C_2 \frac{P_k}{k}\mathcal{T}.$$

In these equations the time and length scales are computed as

$$\mathcal{T}' = \max\left[\frac{k}{\epsilon}, 6\sqrt{\frac{\nu}{\epsilon}}\right], \quad L' = C_L \max\left[\frac{k^{3/2}}{\epsilon}, C_\eta(\frac{\nu^3}{\epsilon})^{1/4}\right].$$

An upper bound is imposed on the time and length scales for fully turbulent calculations to suppress the spurious production of eddy-viscosity in the stagnation region (Durbin, 1996):

$$\mathcal{T} = \min\left(\mathcal{T}', \frac{\alpha k}{\sqrt{3}C_\mu \overline{v^2}\sqrt{2S_{ij}S_{ij}}}\right) \tag{1}$$

and

$$L = \min(L', \frac{k^{3/2}}{\sqrt{3}C_\mu \overline{v^2}\sqrt{2S_{ij}S_{ij}}})$$

where $S_{ij} = 0.5(\partial u_i/\partial x_j + \partial u_j/\partial x_i)$ represents the strain tensor. The eddy-viscosity is given by

$$\nu_t = C_\mu \overline{v^2} T,$$

and the model's constants are:

$$C_\mu = 0.19, \ \sigma_k = 1, \ \sigma_\epsilon = 1.3, \ C_{\epsilon 2} = 1.9,$$

$$C_1 = 1.4, \ C_2 = 0.3, \ C_L = 0.3, \ C_\eta = 70, \ \alpha = 0.6.$$

$C'_{\epsilon 1}$ is here a function of the distance to the closest wall d:

$$C'_{\epsilon 1} = 1.3 + 0.25/(1 + (d/2l)^2)^4$$

with $l = L/C_L$. Work is under way (Parneix & Durbin, 1997) to substitute the wall distance with the ratio of $\overline{v^2}$ over k.

The wall boundary conditions for the turbulent quantities are derived from the asymptotic behavior of k and $\overline{v^2}$ as $y \to 0$.

$$k_0 = 0, \ \overline{v_0^2} = 0, \ \epsilon_0 = \frac{2\nu k_1}{y_1^2}, \ f_0 = -\frac{20\nu^2 \overline{v_1^2}}{y_1^4 \epsilon_0}. \tag{2}$$

The indices 0 and 1 label the wall and the first point away from the wall, respectively.

The k and ϵ equations as well as the $\overline{v^2}$ and f equations are solved pairwise simultaneously. The size of the first cells at the wall is for the calculated airfoils of the order of 10^{-6} times the airfoils cord to ensure y^+ values of about 1 for the considered Reynolds numbers. This leads to very large factors in the ϵ and f wall boundary conditions. Very small time steps (on the order of 10^{-4}) were required at the beginning to prevent a divergence of the solution.

Relaxing these boundary conditions, for example by multiplying the latter two equations in (2) by

$$\frac{\min(n, n_a)}{n_a},$$

where n is the iteration counter and n_a is set to a value between 20 and 100, significantly improves the convergence. Keeping the dissipation of the turbulent kinetic energy ϵ small at the wall during the first iterations ensures a rapid grow of the turbulent boundary layer.

Transition is modeled by switching off various source terms by means of an array T, which is set to zero in the laminar part of the flow and 1 elsewhere, with a linear gradual change in the transition region. To ensure a laminar flow upstream of transition, the eddy-viscosity has been multiplied by T in the mean flow equations.

Due to convergence problems, first order upwind discretization of the convective terms for the k, ϵ, and $\overline{v^2}$ transport equations has been employed. Although a higher order discretization of these terms is desired, it is not expected that this significantly influences the prediction accuracy of wall bounded flows in which the dominant terms are the source and diffusion terms. It might, however, influence the wake of particular elements of the airfoil and areas with massive separation.

2.3 The artificial compressibility constant

As mentioned, the code INS2D uses the artificial compressibility method in which a time derivative of pressure is added to the continuity equation

$$\frac{\partial p}{\partial t} + \beta \frac{\partial u_j}{\partial x_j} = 0$$

to couple it with the momentum equation

$$\frac{\partial u_k}{\partial t} + \frac{\partial(u_j u_k)}{\partial x_j} = -\frac{\partial p}{\partial x_k} + \frac{\partial \tau_{jk}}{\partial x_j}.$$

The parameter β is the artificial compressibility constant which seems to be arbitrary since, approaching the steady state, the time derivative of the pressure tends to zero and the momentum equation decouples from the continuity equation. However, as pointed out by Pan and Chakravarthy (1989) *'this is true only in the differential equation level, or in the difference equation level when central difference is used ... In upwind schemes, the upwind difference is directly related to the eigensystem of the problem and is strongly affected by the choice of β. Even in the steady-state solution, the continuity and the momentum equations are still coupled by β, and hence its choice will affect the final solution.'* To see this, let's consider the first order upwind flux between two nodes of the mesh:

$$E_{i+1/2} = \frac{1}{2}(E_{i+1} + E_i) + \frac{1}{2}(\Delta E^-_{i+1/2} - \Delta E^+_{i+1/2}).$$

A first order correction of flux differences is added here to the simple average of the fluxes of the nearby nodes. The flux differences are computed over the Jacobian of the system:

$$\Delta E^\pm_{i+1/2} = \frac{\partial E^\pm}{\partial D} \Delta D_{i+1/2},$$

Following definitions for 2-d curvilinear coordinates have been made:

$$D = \left\{ \begin{array}{c} p \\ u_1 \\ u_2 \end{array} \right\}, \quad E = \left\{ \begin{array}{c} \beta Q \\ u_1 Q + k_1 p \\ u_2 Q + k_2 p \end{array} \right\}, \quad \frac{\partial E}{\partial D} = \begin{pmatrix} 0 & k_1 \beta & k_2 \beta \\ k_1 & k_1 u_1 + Q & k_2 u_1 \\ k_2 & k_1 u_2 & k_2 u_2 + Q \end{pmatrix}, \quad (2)$$

with k_j representing the metric of the computational domain and $Q = k_1 u_1 + k_2 u_2$ the projection of the velocity on the direction of the grid lines. The Jacobian matrices for the positive and negative traveling waves have been derived (Rogers *et al.*, 1991) by splitting the Jacobian of the whole system with a set of right and left eigenvectors:

$$\frac{\partial E^\pm}{\partial D} = R\Lambda^\pm R^{-1}$$

Fine mesh (80000 cells): $\beta = 1$ $\beta = 100$
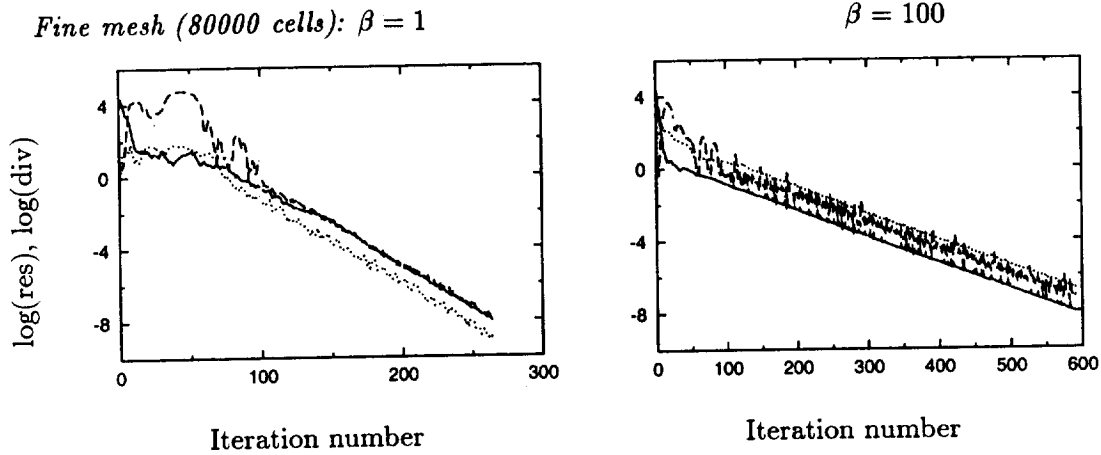

FIGURE 1. Convergence plots for NLR7301, Spalart-Allmaras model, fully turbulent, $\Delta t_{mean\ flow} = \Delta t_{turb.\ model} = 10^{12}$, ——— max. divergence, — — — max. mean flow residual, ········ max. residual of the turbulent kinetic energy.

with

$$R = \frac{1}{2\beta c^2}\begin{pmatrix} 0 & c\beta & -c\beta \\ -2\beta k_2 & u_1(Q+c)+\beta k_1 & u_1(Q-c)+\beta k_1 \\ 2\beta k_1 & u_2(Q+c)+\beta k_2 & u_2(Q-c)+\beta k_2 \end{pmatrix}$$

and

$$R^{-1} = \begin{pmatrix} k_2 u_1 - k_1 u_2 & -Qu_2 - \beta k_2 & Qu_1 + \beta k_1 \\ c - Q & \beta k_1 & \beta k_2 \\ -c - Q & \beta k_1 & \beta k_2 \end{pmatrix},$$

The positive and negative eigenvalue matrices are

$$\Lambda^+ = \begin{pmatrix} \frac{Q+|Q|}{2} & 0 & 0 \\ 0 & Q+c & 0 \\ 0 & 0 & 0 \end{pmatrix}, \quad \Lambda^- = \begin{pmatrix} \frac{Q-|Q|}{2} & 0 & 0 \\ 0 & 0 & 0 \\ 0 & 0 & Q-c \end{pmatrix}.$$

The artificial speed of sound $c = \sqrt{Q^2 + \beta(k_1^2 + k_2^2)}$, which appears by calculating the eigenvalues, is proportional to $\sqrt{\beta}$. While β influences only two elements in the Jacobian matrix (2), it affects almost every element of R and R^{-1}. The first order upwind corrections of the fluxes appear as dissipation terms in the momentum equation of the form $c\Delta u_j$. For a higher order upwind scheme, these dissipation terms are proportional to $c\Delta_{x_k x_k} u_j$, where the operator $\Delta_{x_k x_k}$ consists of higher order differences. In areas of the flow where sudden changes appear, these dissipation terms are non-zero and grow as β increases. Additionally, the artificial speed of sound, and hence β, appears in the far-field boundary condition.

Without specifying transition, the flow around the NLR7301 airfoil has been computed with the one-equation Spalart-Allmaras model (Spalart, 1992) for a wide range of β. The computations have been fully converged until the maximum divergence of the velocity field was below 10^{-8}. Convergence plots of the maximum
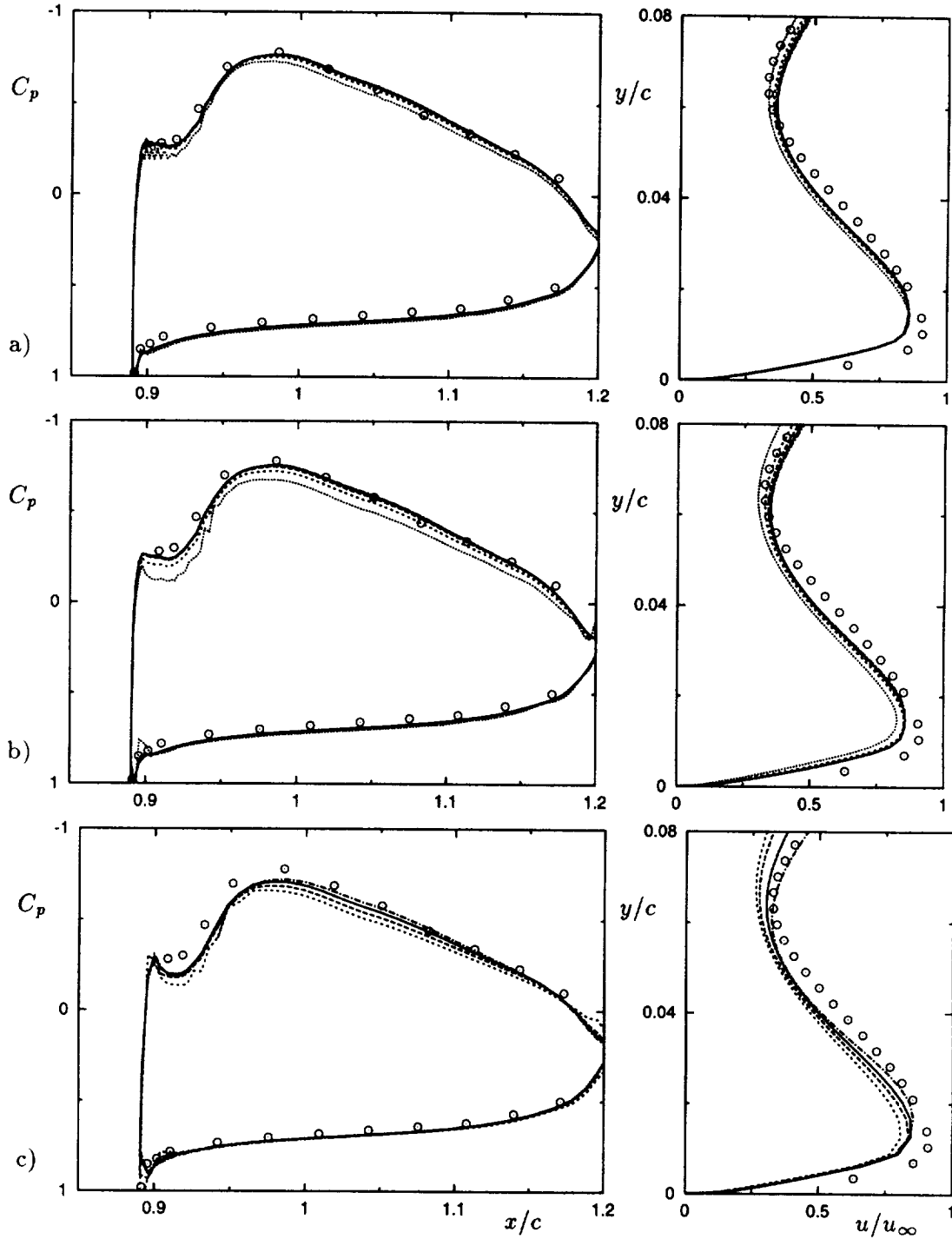
FIGURE 2.   Pressure distribution on flap & velocity profile near trailing edge of flap for NLR7301, 2.6% gap, $\alpha = 13.1^o$, $Re = 2.51 \times 10^6$, Spalart-Allmaras model, fully turbulent; $\beta = 0.1$:———— , 1:———— , 10:———— , 100: ———— , 1000: ········ , o : Experiment. Mesh: a) Fine (80000 cells), b) Medium (40000 cells), c) Coarse (10000 cells).
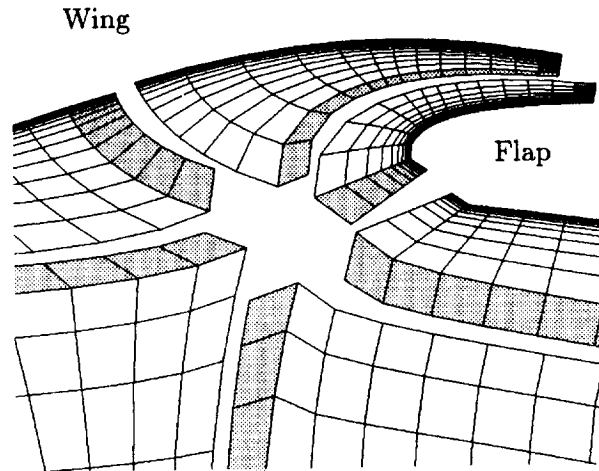
Wing

FIGURE 3.   Multizone mesh with overlapping cells (shaded) for NLR7301.

residual of the mean flow, the maximum residual of the turbulent kinetic energy, and the maximum divergence of the velocity field are shown in Fig. 1. The effect of the input parameter β on the pressure distribution and the velocity profiles, here for station 14 which is normal to the upper surface near the trailing edge of the flap, is shown on Fig. 2. Pressure oscillations and a too high pressure on the upper surface of the flap occur for very large values of β. The plots show that refining the mesh reduces the influence of β. However, it generally also impedes convergence.

2.4 NLR7301 wing-flap airfoil

The flow around the two-element NLR7301-airfoil (Van den Berg, 1979) with 2.6% gap has been computed for the flow condition: $Re = 2.51 \times 10^6$ and angle of attack $\alpha = 13.1°$. The flow is laminar over most of the lower surface of the wing and over the entire lower surface of the flap, while pressure gradients along the upper surface of the flap lead to transition after halfway on the flap. Transition occurs on the upper surface of the wing at $2.4 \dots 3.5\%$, on the lower surface at $71 \dots 74\%$, and on the upper surface of the flap at $106.5 \dots 108\%$ of the cord c. The cord c is here defined slightly larger than the cord of the wing. A laminar separation bubble occurs on the upper surface of the wing upstream of transition. The flow remains fully attached on the trailing edge of the wing and on the flap.

This test case has been extensively investigated during the ECARP project (Haase *et al.*, 1996). The mandatory mesh of this project has been adopted here. The mesh has been split into 12 zones. The zones have been extended with one row of neighboring cells to overlap with each other, enabling communication between the zones. A close-up of the mesh between the wing and the flap is shown in Fig. 3. One can see that one node requires special treatment as it is shared by more than four cells. Here it is treated as a boundary point. The flow variables at this point have been set after every iteration to an average value calculated from the surrounding
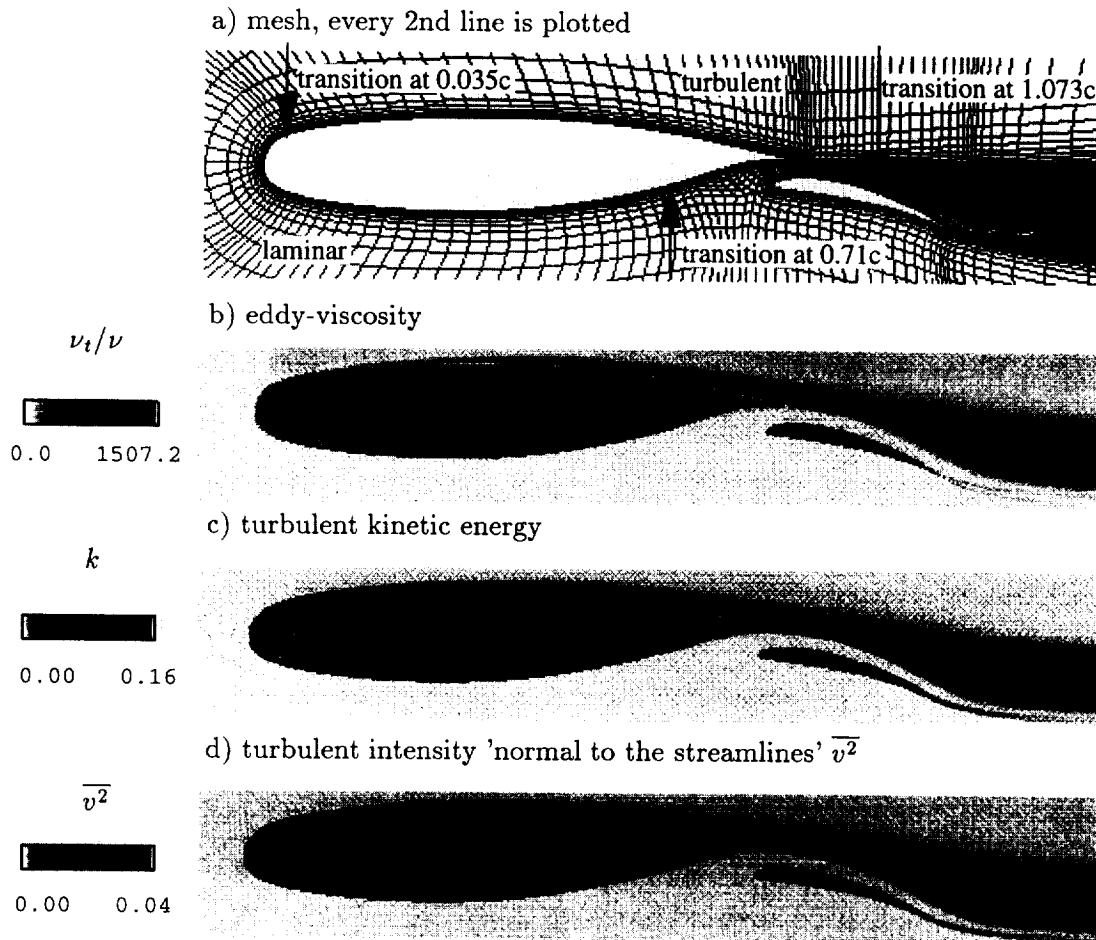
a) mesh, every 2nd line is plotted

b) eddy-viscosity

ν_t/ν

0.0   1507.2

c) turbulent kinetic energy

k

0.00   0.16

d) turbulent intensity 'normal to the streamlines' $\overline{v^2}$

$\overline{v^2}$

0.00   0.04

FIGURE 4.   NLR 7301 with 2.6% gap, $Re = 2.51 \times 10^{-6}$, $\alpha = 13.1°$, 40000 cells.

nodes. Note, that this point is outside of a boundary layer and the turbulent region.

The computational mesh consisting of 40000 cells is shown in Fig. 4a. The laminar and turbulent areas are distinguished with two different grey tones. The location of transition used for the presented results is given on the grid plot. Qualitative results calculated with the V2F model in the form of shaded contour lines for the eddy-viscosity, turbulent kinetic energy, and turbulent intensity normal to the streamlines are shown in the same figure. One can clearly see the different behavior of the turbulent kinetic energy k and the variable $\overline{v^2}$, the maximum value of which is about 4 times smaller than of k. While the eddy-viscosity changes in the transition region relatively smoothly, the largest values of k appear right after transition on the upper surface of the wing, which corresponds to the sharp rise in skin friction shown in Fig. 5. The skin friction plot shows clearly the laminar separation bubble and the transition on the lower surface of the wing. To achieve convergence a large value of β has been employed. Consequently, pressure oscillations on the flap have
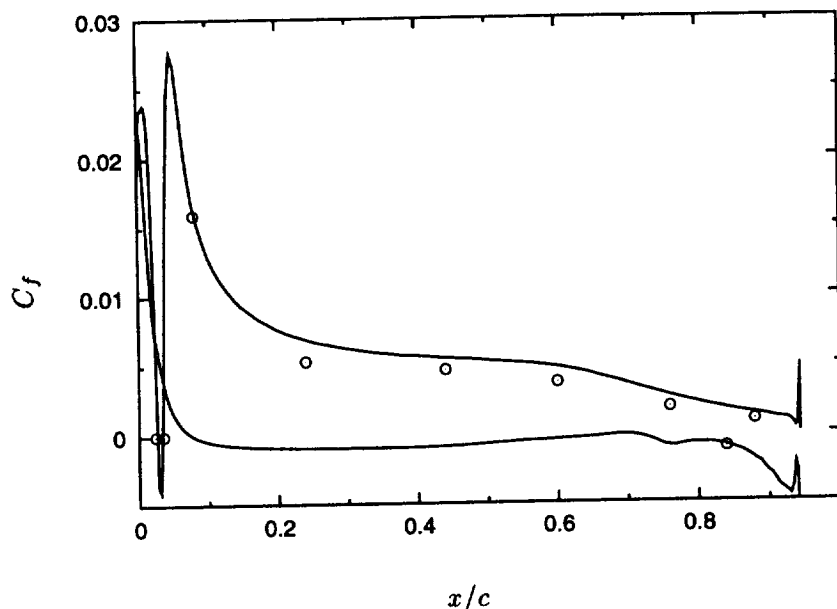
FIGURE 5. Skin friction on wing, NLR7301 with 2.6% gap, $Re = 2.51 \times 10^6$, $\alpha = 13.1^\circ$, 40000 cells, with transition, $\beta = 1400$; ———— : V2F model, o : Experiment.

been obtained similar to the ones described in section 2.3 for the Spalart-Allmaras model.

The laminar separation bubble could not be predicted for the NLR7301 airfoil with the Spalart-Allmaras model. Similar skin friction plots have been obtained for computations with fixed transition and treating the flow fully turbulent. This might be a consequence of the way transition is implemented in INS2D for this model or because of fundamental differences of the one-equation model.

2.5 Collaboration with Boeing

In a cooperative study with Boeing-ISDS, St. Louis, (1997), a three element airfoil, known as the MDA Three-Element High-Lift System (Fig. 6, Valarezo *et al.*, 1991), has been computed for the free stream condition: $M = 0.2$, $Re = 9 \times 10^6$ and angle of attack $\alpha = 19^\circ$. The flow has been computed as a fully turbulent flow.

The mesh, shown in Fig. 7, has been generated by Boeing-ISDS and consists of about 135000 cells. It is split in 4 overlapping zones. The singular mesh points are treated here as internal points. Each of the cells surrounding these nodes overlaps with more than one cell from the neighboring mesh. These sources of errors, however, are kept small by using a very fine mesh and locating these nodes outside of boundaries layers.

Computations have been carried out with two flow solvers: INS2D and the Boeing-ISDS NASTD code, and two turbulence models: the V2F and the Spalart-Allmaras model. First results of these computations are shown in Fig. 8 for the
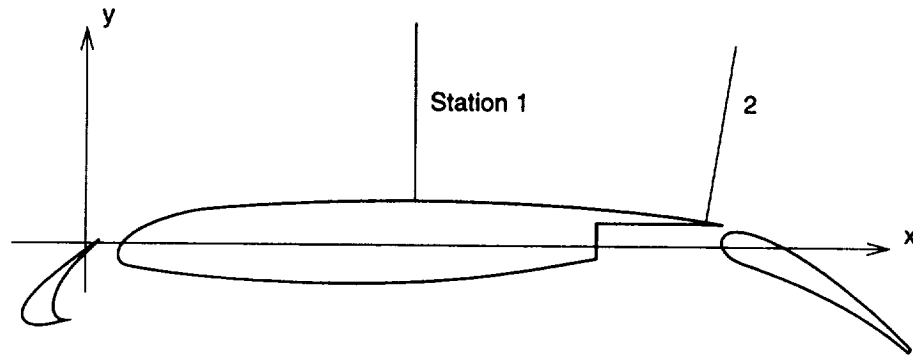
FIGURE 6.   Geometry of the MDA three-element high lift system and velocity survey station locations.
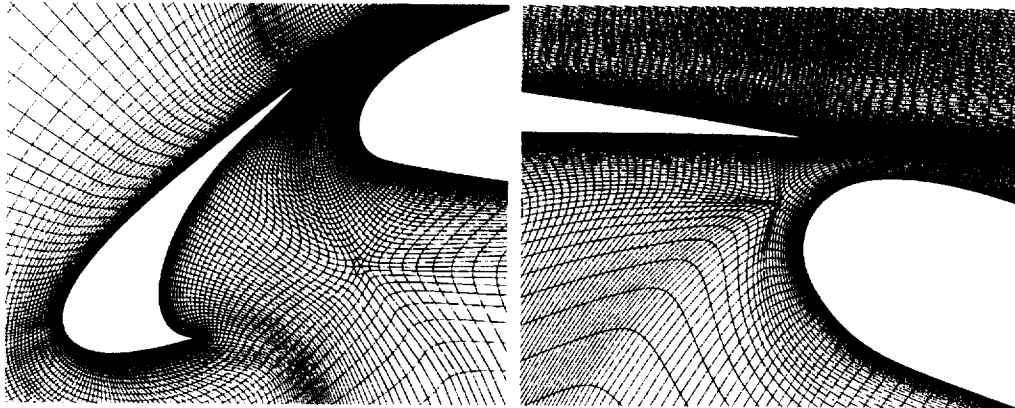

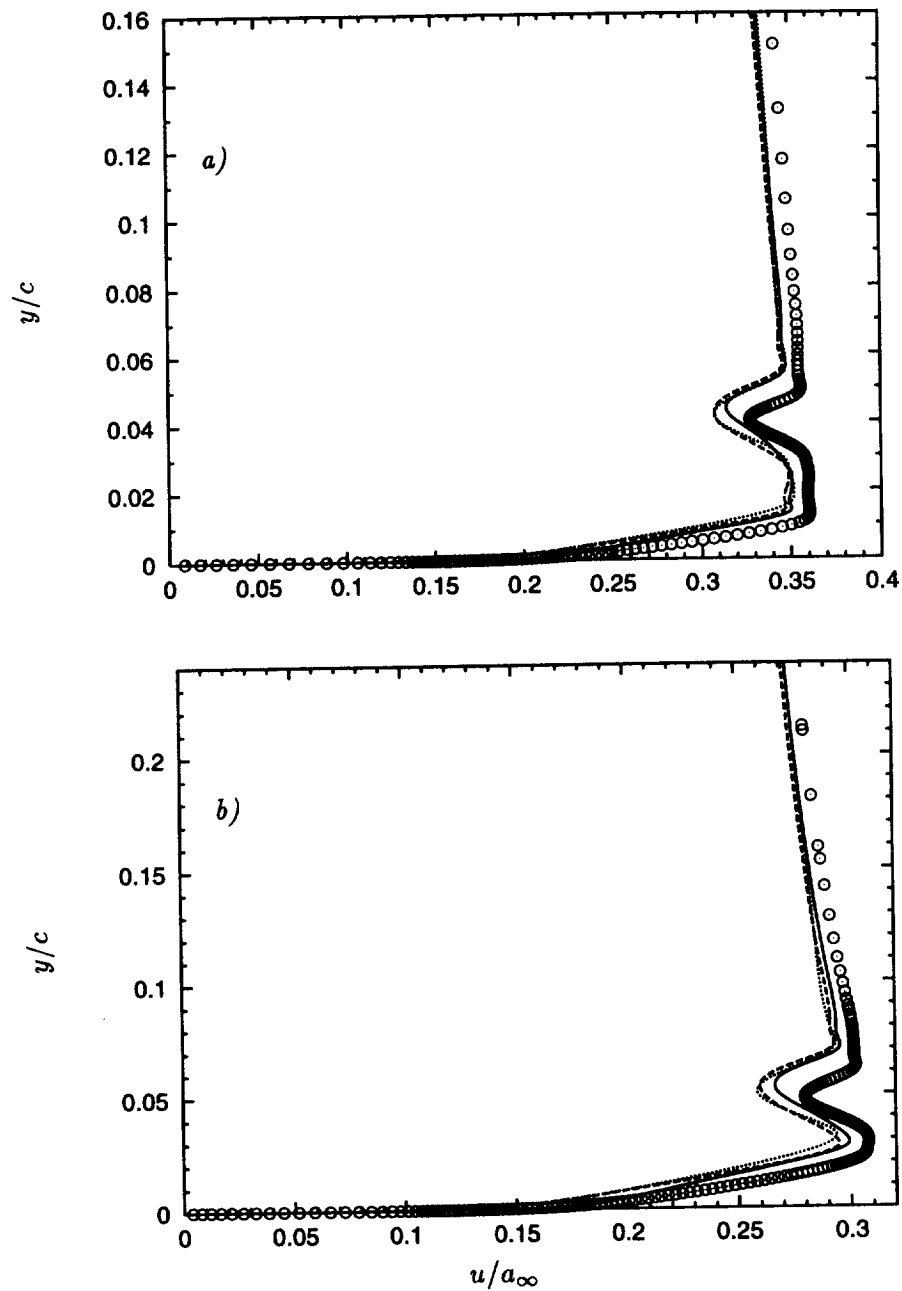FIGURE 7.   Mesh around the slat and between wing and flap of the MDA high lift system.

FIGURE 8.   Velocity profiles on upper surface of the wing of the MDA high-lift system; fully turbulent; ———— : V2F and INS2D, - - - - : Spalart-Allmaras and INS2D, ········ : Spalart-Allmaras and NASTD, o : Experiment. *a) station 1*, $x/c = 0.45$; *b) station 2*, $x/c = 0.85$.

velocity magnitude on station 1 and 2 with $x/c = 0.45$ and $x/c = 0.85$ respectively. The flow is fully attached at these stations. The predictions accuracy at these stations significantly influences separation downstream on the flap.

All three computations predict the velocity at these stations quite well. Major differences can be observed in the velocity gradients near the wall and in the wake of the lower boundary layer of the slat. Increasing the influence of the upper bound on the time scale in the V2F computation by decreasing the coefficient α in Eq. (1) from 1 to 0.6 slightly improved the velocity gradient in the wake of the slat. Computations are under way with fixed transition. This will avoid the need of an upper bound for the time scale.

3. Future plans

The local refinement of the mesh for the NLR7301 airfoil in the region of the laminar separation bubble and transition or the implementation of a suitable TVD scheme into INS2D are expected to allow the use of smaller values for the compressibility constant β to avoid scaling errors introduced by the numerical dissipation.

The capability of the V2F model will be studied in further computations of the MDA high lift system and in comprehensive comparison of results with experimental data and computations with other models.

We plan to implement the V2F model into the NASA Ames OVERFLOW code and to carry out computations of compressible flows. We also intend to work on numerical issues for a stable implementation of the model in explicit Runge-Kutta time-stepping schemes with multigrid techniques (Jameson et al., 1981).

<div align="center">REFERENCES</div>

VAN DEN BERG, B. 1979 Boundary layer measurements on a two-dimensional wing with flap. *NLR TR 79009 U.*

BOEING-ISDS 1997 *Investigation of Incompressible Three-equation Turbulence Models of Durbin for High-Lift Applications.* Informal memorandum and private communications.

CHORIN, A. J. 1967 A Numerical Method for Solving Incompressible Viscous Flow Problems. *Journal of Computational Physics.* **2**, 12-26.

DURBIN, P. 1995 Separated flow computations with the $k - \epsilon - \overline{v^2}$ model. *AIAA J.* **33**, 659-664.

DURBIN, P. 1996 On the k-ϵ stagnation point anomaly. *Int. J. Heat and Fluid Flow.* **17**, 89-90.

HAASE, W. , CHAPUT, E., ELSHOLZ, E., LESCHZINER, M. & MÜLLER, U., R. 1997 *ECARP - European Computational Aerodynamics Research Project: Validation of CFD Codes and Assessment of Turbulence Models.* Vol. 58, Vieweg.

JAMESON, A., SCHMIDT, W. & TURKEL, E. 1981 Numerical solutions of the Euler equations by finite volume methods using Runge-Kutta time-stepping schemes. *AIAA paper.* **81-1259.**

PAN, D. & CHAKRAVARTHY, S. R. 1989 Unified Formulation for Incompressible Flows. *AIAA paper.* **89-0122.**

PARNEIX, S. & DURBIN, P. 1997 Numerical simulation of 3D turbulent boundary layers using the V2F model. *CTR Annual Research Briefs, Center for Turbulence Research.*

ROGERS, S. E., KWAK, D. & KIRIS C. 1991 Numerical solution of the incompressible Navier-Stokes equations for steady-state and time dependent problems. *AIAA J.* **29,** 603-610.

SAAD, Y. & SCHULTZ M. H. 1986 GMRES: a generalized minimal residual algorithm for solving nonsymmetric linear systems. *SIAM J. Sci. Stat. Comp.* **7,** 856-869.

SPALART, P. R. & ALLMARAS, S. R. 1992 A one-equation turbulence model for aerodynamic flows. *AIAA paper.* **92-439.**

VALAREZO, W. O., DOMINIK, C. J., McGHEE, R. J., GOODMAN, W. L. & PASCHAL, K. B. 1991 Multi-Element Airfoil Optimization for Maximum Lift at High Reynolds Numbers. *AIAA paper.* **91-3332.**

Advances in structure-based turbulence modeling

By S. C. Kassinos AND W. C. Reynolds

1. Motivation and objectives

Turbulent flows of importance in aircraft and propulsion system design involve complex three-dimensional time-dependent mean flow, where the turbulence is often subjected to very rapid deformation and strong mean rotation or curvature effects. In these flows the structure of the turbulence plays an important role in determining the transport of the Reynolds stresses, and because the turbulence structure takes some time to respond to the imposed deformation, an eddy-viscosity representation is not appropriate. The ability of aerospace engineers to predict these complex flows is limited by the current state-of-the-art in one-point turbulence modeling, which invariably relies on an eddy-viscosity approach.

The response of turbulence to the kind of deformation that is often encountered in engineering applications (rapid rates and/or strong rotation) is described well by Rapid Distortion Theory (RDT). RDT is a closed two-point theory, but engineering models require one-point formulation. Therefore, what is needed is a one-point model that matches eddy viscosity models for weak deformation rates and RDT for rapid deformations.

The weakness of standard models is due to incomplete information and is particularly troublesome in flows with strong mean rotation. We have shown that it is impossible to model the effects of strong mean rotation or curvature using only the information found in the turbulent stresses themselves. The critical information that must be added relates to the dimensionality of the turbulence structure (see Kassinos & Reynolds 1994). We have introduced a number of one-point turbulent structure tensors that carry this additional information and have derived their exact transport equations (Kassinos & Reynolds 1994). These tensors include the second-rank structure *dimensionality* D_{ij} and structure *circulicity* F_{ij}, and the third-rank, fully symmetric, structure *stropholysis* Q^*_{ijk}. A detailed account of the role of these tensors is given in Kassinos & Reynolds (1994) and Reynolds & Kassinos (1995).

We have completed the formulation of a successful particle representation model (Kassinos and Reynolds 1996) which has the correct viscoelastic character. This model, which we have termed the Interacting Particle Representation Model (IPRM), is a non-local method that can handle remarkably well almost any mean deformation of homogeneous turbulence. The IPRM is exact in the limit of RDT, which it matches with no modeling. With relatively simple structure-based modeling of the non-linear interactions, the IPRM is able to match eddy-viscosity theory for weak deformations and to provide a reasonable blend between eddy-viscosity and RDT for conditions that fall between the two limits. More details on the IPRM formulation are given in Kassinos & Reynolds (1996).

The IPRM is a non-local model, but for engineering use we need one-point formulation. More recently our efforts have been focused on the development of a

one-point structure-based model using the IPRM as the starting point. The present study outlines the formulation for these more recent developments and gives representative results where appropriate. An in-depth discussion of the IPRM and the corresponding one-point model is given in a separate manuscript under preparation.

2. Accomplishments

In Section 2.1 we introduce notation and review the basic formulation of the IPRM. Then in Section 2.2, we present the formulation of a one-point model that follows directly from the IPRM. The IPRM emulates RDT exactly because the non-local rapid pressure fluctuations can be evaluated exactly. This is not the case for the one-point model, which requires additional modeling to deal with the non-locality of the pressure fluctuations. Section 2.2 includes a discussion of this additional modeling. In Section 2.3 we evaluate the one-point model for a number of representative flows.

2.1 An Interacting Particle Representation Model (IPRM)

In a particle representation method, a number of key properties and their evolution equations are assigned to hypothetical particles. The idea is to follow an ensemble of "particles", determine the statistics of the ensemble, and use those as the representation for the one-point statistics of the corresponding field. It is important to appreciate that these particles do not have to be physical elements of fluid. The idea of representing the turbulent flow by a large number of particles, each having its own set of properties, has been used over the past ten years by the combustion community in the form of Lagrangian PDF methods (for example see Pope 1994). In these traditional approaches a stochastic model is used, which can be chosen so that upon taking moments of the governing stochastic evolution equations one recovers one of the standard Reynolds stress transport (RST) models. This approach, however, uses modeling where it is not required, *i.e.* in emulating RDT. A more detailed discussion of the rapid PRM can be found in Kassinos & Reynolds (1994); Vanslooten & Pope (1997) have recently used the ideas given there to construct a PDF model that is consistent with RDT.

2.1.1 Particle properties

We start with a discussion of the properties assigned to each of the hypothetical particles. The assigned properties are:

- **V** velocity vector
- **W** vorticity vector
- **S** stream function vector
- **N** gradient vector
- *P* pressure.

Here we consider a representation method using non-physical "particles" that correspond most closely to a vortex sheet (or 1D-1C flow). The only axis of dependence lies normal to the vortex sheet and parallel to the N_i vector, which provides a measure of gradients normal to the plane. The remaining vectors lie in the plane of independence.

2.1.2 Representations for one-point statistics

The Reynolds stress $R_{ij} = \overline{u_i' u_j'}$ is represented as

$$R_{ij} = \langle V_i V_j \rangle = \langle V^2 v_i v_j \rangle,\tag{1}$$

where the angle brackets denote averaging over an ensemble of particles and $v_i = V_i/\sqrt{V_k V_k}$. Two one-point turbulent tensors that carry useful structure information are the structure *dimensionality* and *circulicity*, defined by

$$D_{ij} = \overline{\Psi_{n,i}' \Psi_{n,j}'} \qquad F_{ij} = \overline{\Psi_{i,n}' \Psi_{j,n}'}.\tag{2}$$

Here Ψ_i' is the turbulent stream function vector, which satisfies

$$u_i' = \epsilon_{its} \Psi_{s,t}' \qquad \Psi_{i,i}' = 0 \qquad \Psi_{i,nn}' = -\omega_i'\tag{3}$$

and ω_i' is the fluctuation vorticity. In the IPRM formulation the structure tensors are represented as

$$D_{ij} = \langle S_n S_n N_i N_j \rangle = \langle V^2 n_i n_j \rangle\tag{4}$$

$$F_{ij} = \langle N_n N_n S_i S_j \rangle = \langle V^2 s_i s_j \rangle\tag{5}$$

where $n_i = N_i/\sqrt{N_k N_k}$ and $s_i = S_i/\sqrt{S_k S_k}$. A consequence of the orthogonality of the three vectors n_i, v_i, and s_i is that, for homogeneous turbulence, the three second-rank tensors satisfy the constitutive equation

$$R_{ij} + D_{ij} + F_{ij} = q^2 \delta_{ij}.\tag{6}$$

Here $q^2 = 2k = R_{ii}$. For homogeneous turbulence $D_{ii} = F_{ii} = q^2$, and it is possible to normalize (6) so that

$$r_{ij} + d_{ij} + f_{ij} = \delta_{ij}\tag{7}$$

where

$$r_{ij} = R_{ij}/q^2 \qquad d_{ij} = D_{ij}/q^2 \qquad f_{ij} = F_{ij}/q^2.\tag{8}$$

The tensor anisotropies $\tilde{r}_{ij} = r_{ij} - \frac{1}{3}\delta_{ij}$, $\tilde{d}_{ij} = d_{ij} - \frac{1}{3}\delta_{ij}$, and $\tilde{f}_{ij} = f_{ij} - \frac{1}{3}\delta_{ij}$ satisfy

$$\tilde{r}_{ij} + \tilde{d}_{ij} + \tilde{f}_{ij} = 0.\tag{9}$$

In the inhomogeneous case additional terms appear in (6) and (9) (see Kassinos & Reynolds 1994).

2.2.3 Emulation of the Rapid Distortion Theory

The evolution of the vector properties assigned to each particle are governed by ordinary differential equations based on the Navier-Stokes equations. For example, a kinematic analysis leads to the RDT evolution equation for **N**

$$\dot{N}_i = -G_{ki} N_k,\tag{10}$$

which shows that **N** plays a role similar to that of the wavenumber vector **k**. Here $G_{ij} = U_{i,j}$ is the mean velocity gradient tensor. The unit vector $n_i = N_i/\sqrt{N_k N_k}$ satisfies

$$\dot{n}_i = -G_{ki} n_k + G_{km} n_k n_m n_i. \tag{11}$$

The PRM evolution equation for **V** is

$$\dot{V}_i = -G_{ik} V_k + 2G_{km} \frac{V_m N_k N_i}{N^2}. \tag{12}$$

The familiar Poisson equation for the rapid pressure is the basis for the analogous definition

$$P = -2G_{km} \frac{V_m N_k}{N^2}. \tag{13}$$

Using (12) and (13), one obtains

$$\dot{V}_i = -G_{ik} V_k - P N_i \tag{14}$$

by analogy to the fluctuation momentum equation under RDT.

2.1.4   Cluster-averaged equations

The cluster-averaged implementation of the PRM offers a better computational efficiency. The idea is to do the averaging in two steps, the first step being done analytically. First, an averaging is done over particles that have the same $n(t)$, followed by an averaging over all particles with different $n(t)$. The one-point statistics resulting from the first (cluster) averaging are conditional moments, which will be denoted by

$$R_{ij}^{|n} \equiv \langle V_i V_j | \mathbf{n} \rangle \qquad D_{ij}^{|n} \equiv \langle V^2 n_i n_j | \mathbf{n} \rangle = \langle V^2 | \mathbf{n} \rangle n_i n_j$$

and

$$F_{ij}^{|n} \equiv \langle V^2 s_i s_j | \mathbf{n} \rangle. \tag{15}$$

The conditionally-averaged stress evolution equation

$$\dot{R}_{ij}^{|n} = -G_{ik} R_{kj}^{|n} - G_{jk} R_{ki}^{|n} + 2G_{km}(R_{im}^{|n} n_k n_j + R_{jm}^{|n} n_k n_i) \tag{16}$$

is obtained by using the definition (15) along with (12). Note that (11) and (16) are *closed* for the conditional stress tensor $R_{ij}^{|n}$ and n_i. That is, they can be solved without reference to the other conditioned moments.

2.1.5   Formulation of the nonlinear model

Whenever the time scale of the mean deformation is large compared to that of the turbulence, the nonlinear turbulence-turbulence interactions become important in the governing field equations. In the context of the Interacting Particle Representation Model (IPRM), these nonlinear processes are represented by a model for the particle-particle interactions.

Direct numerical simulations (Lee & Reynolds 1985) show that under weak strain the structure dimensionality D_{ij} remains considerably more isotropic than does the Reynolds stress R_{ij}. This leads to counter-intuitive R_{ij} behavior in axisymmetric expansion flows (see Section 2.3.1), supported by experiments (Choi 1983). Hence we modify the basic evolution equations (11) and (16) to account for these effects. The resulting cluster-averaged evolution equations are

$$\dot{n}_i = -G_{ki}^n n_k + G_{kr}^n n_k n_r n_i \tag{17}$$

$$\dot{R}_{ij}^{|n} = -G_{ik}^v R_{kj}^{|n} - G_{jk}^v R_{ki}^{|n} - C_r[2R_{ij}^{|n} - R_{kk}^{|n}(\delta_{ij} - n_i n_j)]$$
$$+ [G_{km}^n + G_{km}^v](R_{im}^{|n} n_k n_j + R_{jm}^{|n} n_k n_i). \tag{18}$$

Note that the mean velocity gradient tensor G_{ij} that appeared in (11) and (16) has been replaced by the *effective* gradient tensors G_{ij}^v and G_{ij}^n. These are defined by

$$G_{ij}^n = G_{ij} + \frac{C_n}{\tau} r_{ik} d_{kj} \qquad G_{ij}^v = G_{ij} + \frac{C_v}{\tau} r_{ik} d_{kj}. \tag{19}$$

Here $r_{ij} = R_{ij}/q^2$ and $d_{ij} = D_{ij}/q^2$ where $q^2 = 2k = R_{ii}$. The two constants are taken to be $C_n = 2.2 C_v = 2.2$. The different values for these two constants account for the different rates of return to isotropy of **D** and **R**. The time scale of the turbulence τ is evaluated so that the dissipation rate in the IPRM

$$\epsilon^{\text{PRM}} = q^2 \frac{C^v}{\tau} r_{ik} d_{km} r_{mi} \tag{20}$$

matches that obtained from a modified model equation for the dissipation rate,

$$\dot{\epsilon} = -C_0(\epsilon^2/q^2) - C_s S_{pq} r_{pq} \epsilon - C_\Omega \sqrt{\Omega_n \Omega_m d_{nm}} \, \epsilon. \tag{21}$$

The last term in (21) accounts for the suppression of ϵ by mean rotation. Here Ω_i is the mean vorticity vector, and the constants are taken to be

$$C_0 = 3.67 \qquad C_s = 3.0 \qquad \text{and} \qquad C_\Omega = 0.01. \tag{22}$$

Mean rotation acting on the particles tends to produce rotational randomization of the **V** vectors around the **n** vectors (Mansour *et al.* 1991, Kassinos & Reynolds 1994). The third (bracketed) term on the RHS of (18), is the *slow rotational random-ization model*, which assumes that the effective rotation due to nonlinear particle-particle interactions, $\Omega_i^* = \epsilon_{ipq} r_{qk} d_{kp}$, should induce a similar randomization effect while leaving the conditional energy unmodified. Based on dimensional considera-tions and requirements for material indifference to rotation (Speziale 1981, 1985), we take

$$C_r = \frac{8.5}{\tau} \Omega^* f_{pq} n_p n_q, \quad \Omega^* = \sqrt{\Omega_k^* \Omega_k^*}, \quad \Omega_i^* = \epsilon_{ipq} r_{qk} d_{kp}. \tag{23}$$

The rotational randomization coefficient C_r is sensitized to the orientation of the n vector so that the slow rotational randomization vanishes whenever the large-scale circulation is confined in the plane normal to n.

The pressure P is determined by the requirement that $R_{ik}^{|n}n_k = 0$ is maintained by (17) and (18). This determines the effects of the slow pressure strain—rate-term without the need for further modeling assumptions

$$P = \underbrace{-2G_{mk}\frac{V_k N_m}{N^2}}_{\text{rapid}} - \underbrace{\frac{(C^v + C^n)}{\tau}r_{ml}d_{tk}\frac{V_k N_m}{N^2}}_{\text{slow}}. \tag{24}$$

2.2 A one-point R-D model

A one-point structure-based model for the deformation of homogeneous turbulence can be derived directly from the IPRM formulation. At the one-point level, additional modeling assumptions must be introduced in order to deal with the non-locality of the pressure fluctuations. Here we restrict the formulation of the one-point model to the case of irrotational deformation of homogeneous turbulence and discuss briefly the more general case.

As a result of the constitutive equation (6), a *structure-based* one-point model must carry the transport equations for only two of the three second-rank tensors. Here we propose a model based on the R_{ij} and D_{ij} equations, which are the one-point analogs of (17) and (18). Using the definitions (1) and (2) and the evolution equations (17) and (18), and averaging over all clusters, one obtains

$$\dot{D}_{ij} = -D_{ik}G_{kj}^n - D_{jk}G_{ki}^n + 2q^2 G_{km}^n Z_{kmij}^d - 2G_{km}^v M_{mkij} \tag{25}$$

and

$$\begin{aligned}
\dot{R}_{ij} &= -G_{ik}^v R_{kj} - G_{jk}^v R_{ki} \\
&\quad - \hat{C}_r f_{pq}[2M_{ijpq} - (\delta_{ij}D_{pq} - q^2 Z_{ijpq}^d)] \\
&\quad + [G_{km}^n + G_{km}^v](M_{imkj} + M_{jmki}).
\end{aligned} \tag{26}$$

Here G_{ij}^n and G_{ij}^v are as defined for the IPRM in (19), and $\hat{C}_r = 8.5\Omega^*/\tau$ where Ω^* is given in (23). The fourth-rank tensors

$$Z_{ijkm}^d = \langle V^2 n_i n_j n_k n_m \rangle/q^2 \quad \text{and} \quad M_{ijpq} = \langle V^2 v_i v_j n_p n_q \rangle \tag{27}$$

must be modeled. Note that Z is the fully symmetric, energy-weighted fourth moment of a single vector, for which we have been able to construct a good model. What is more, one can use an exact decomposition based on group theory (see Kassinos & Reynolds 1994) to express M_{ijpq} in terms of fourth moments of a single vector and the second-rank tensors R_{ij} and D_{ij}:

$$\begin{aligned}
M_{ipqj} &= \tfrac{1}{2}q^2(Z_{ipqj}^f - Z_{ipqj}^r - Z_{ipqj}^d) + \frac{1}{6}\big[- 3\delta_{ip}\delta_{qj}q^2 \\
&\quad + 4(\delta_{qj}R_{ip} + \delta_{ip}D_{qj}) + 2(\delta_{qj}D_{ip} + \delta_{ip}R_{qj})\big].
\end{aligned} \tag{28}$$

Note that in the presence of mean rotation (28) involves additional terms that require modeling of the *stropholysis* effects (see section 3). Here

$$Z^r_{ijpq} = \langle V^2 v_i v_j v_p v_q \rangle / q^2 \quad \text{and} \quad Z^f_{ijpq} = \langle V^2 s_i s_j s_p s_q \rangle / q^2 .\tag{29}$$

Substituting (28) in (25) and (26) and using the definitions (8), one obtains

$$\begin{aligned}
\dot{d}_{ij} = & -d_{jk}G^n_{ki} - d_{ik}G^n_{kj} + 2G^v_{km}r_{km}(d_{ij} - \tfrac{2}{3}\delta_{ij}) \\
& - \tfrac{2}{3}G^v_{km}d_{mk}\delta_{ij} + G^v_{kk}(\delta_{ij} - \tfrac{4}{3}d_{ij} - \tfrac{2}{3}r_{ij}) \\
& + (2G^n_{km} + G^v_{km})Z^d_{kmij} + G^v_{km}Z^r_{mkij} - G^v_{km}Z^f_{mkij}
\end{aligned}\tag{30}$$

and

$$\begin{aligned}
\dot{r}_{ij} = & \tfrac{1}{3}(G^v_{mj} + G^n_{mj})(2d_{mi} + r_{mi}) \\
& + \tfrac{1}{3}(G^v_{mi} + G^n_{mi})(2d_{mj} + r_{mj}) \\
& + \tfrac{1}{3}G^v_{jm}(d_{mi} - r_{mi}) + \tfrac{1}{3}G^v_{im}(d_{mj} - r_{mj}) \\
& + \tfrac{1}{3}G^n_{jm}(d_{mi} + 2r_{mi}) + \tfrac{1}{3}G^n_{im}(d_{mj} + 2r_{mj}) \\
& + 2G^v_{km}r_{km}r_{ij} - \tfrac{1}{2}(G^v_{ij} + G^v_{ji} + G^n_{ij} + G^n_{ji}) \\
& + (G^v_{mk} + G^n_{mk})(Z^f_{ikmj} - Z^r_{ikmj} - Z^d_{ikmj}) \\
& - \hat{C}_r f_{pq}[Z^f_{ijpq} - Z^r_{ijpq} + \tfrac{2}{3}\delta_{pq}(r_{ij} - f_{ij}) \\
& + \tfrac{1}{3}\delta_{ij}(r_{pq} - f_{pq})] .
\end{aligned}\tag{31}$$

Closure of (30) and (31) in the irrotational case requires a consistent model for the fully symmetric tensors Z^n_{ijpq}, Z^r_{ijpq}, and Z^f_{ijpq}. We have constructed a model for the energy-weighted fourth moment of any vector t_i in terms of its second moment t_{ij} that allows the successful closure of (30) and (31) while maintaining *full realizability*. The same model can be used for each of the three vectors v_i, n_i, and s_i and their moments and has the general form

$$\begin{aligned}
Z^t_{ijpq} = & \langle V^2 t_i t_j t_p t_q \rangle / q^2 = C_1 \, \mathbf{i} \circ \mathbf{i} + C_2 \, \mathbf{i} \circ \mathbf{t} \\
& + C_3 \, \mathbf{t} \circ \mathbf{t} + C_4 \, \mathbf{i} \circ \mathbf{t}^2 + C_5 \, \mathbf{t} \circ \mathbf{t}^2 + C_6 \, \mathbf{t}^2 \circ \mathbf{t}^2 .
\end{aligned}\tag{32}$$

Here $\mathbf{i}$ and $\mathbf{t}$ stand for δ_{ij} and $t_{ij} = \langle V^2 t_i t_j \rangle / q^2$ respectively. Extended tensor notation is used in (32), where the fully symmetric product of two second-rank tensors **a** and **b** is denoted by

$$\mathbf{a} \circ \mathbf{b} \equiv a_{ij}b_{pq} + a_{ip}b_{jq} + a_{jp}b_{iq} + a_{iq}b_{jp} + a_{jq}b_{ip} + a_{pq}b_{ij} .\tag{33}$$

The coefficients C_1-C_6 are functions of the invariants of t_{ij} and determined by enforcing the trace condition $Z^t_{ijkk} = t_{ij}$, 2D realizability conditions for the case when the vectors t_i lie in a plane, and an important identity,

$$\mathbf{Z}^a = \tfrac{1}{16} \mathbf{i} \circ \mathbf{i} - \tfrac{1}{8} \mathbf{i} \circ \mathbf{b} + \tfrac{3}{8} \mathbf{Z}^b ,\tag{34}$$

which applies between the fourth moments of two vectors a_i and b_i when a_i is randomly distributed about b_i. Kassinos & Reynolds (1994) gave an earlier Z model that does not exactly satisfy (34). The new coefficients will be published separately.

Next, we consider the performance of the Interacting Particle Representation Model (IPRM) and the one-point R-D model for three cases of irrotational mean deformation.

2.3 Evaluation of the R-D model for irrotational flows

In this section, the IPRM based on (17), (28), (21), and (29) and the one-point model based on (21), (25), (26), and (32) are evaluated for several cases of irrotational deformation of homogeneous turbulence. The examples considered here show that, even with a relatively simple closure for nonlinearity, both models achieve remarkably accurate predictions. Additional examples of the IPRM performance are also given in Kassinos & Reynolds (1994) for RDT (large Sk/ϵ), and in Kassinos & Reynolds (1996) for the general deformation of homogeneous turbulence. The evaluation of the complete R-D model (for combinations of mean strain and mean rotation) will be given separately.

2.3.1 Irrotational axisymmetric strain

First we consider the performance of the IPRM and the R-D model for the case of homogeneous, initially isotropic turbulence subjected to irrotational axisymmetric mean deformation. The mean velocity gradient tensor is given by

$$S_{ij} = \begin{pmatrix} S & 0 & 0 \\ 0 & -S/2 & 0 \\ 0 & 0 & -S/2 \end{pmatrix} \tag{35}$$

with $S > 0$ for contraction (nozzle flow) and $S < 0$ for expansion (diffuser flow). In all the cases considered here, the axis of symmetry is taken to be x_1 and the evolution histories are plotted against

$$C = \exp\left(\int_0^t |S_{\max}(t')| \, dt'\right),$$

where $S_{\max}$ is the largest principal value of the mean strain tensor.

Axisymmetric Contraction

A first case of slow irrotational axisymmetric deformation of homogeneous, initially isotropic turbulence is considered in Fig. 1. The initial parameters in this axisymmetric contraction flow $(Sq_0^2/\epsilon_0 = 1.1)$ correspond to the slowest run in the 1985 simulations of Lee & Reynolds. The anisotropy evolution histories for $\tilde{r}$, $\tilde{d}$, and $\tilde{f}$ predicted by the non-local IPRM (solid lines) and the one-point r-d model (dashed lines) are in satisfactory agreement with simulation results (symbols). Both models predict decay of the turbulent kinetic energy k and dissipation rate ϵ at the correct rates (see Fig. 1d).

A case of rapid axisymmetric contraction flow $(Sq_0^2/\epsilon_0 = 110.0)$ is shown in Fig. 2. Comparison of the models is again made with results from the simulations of Lee &
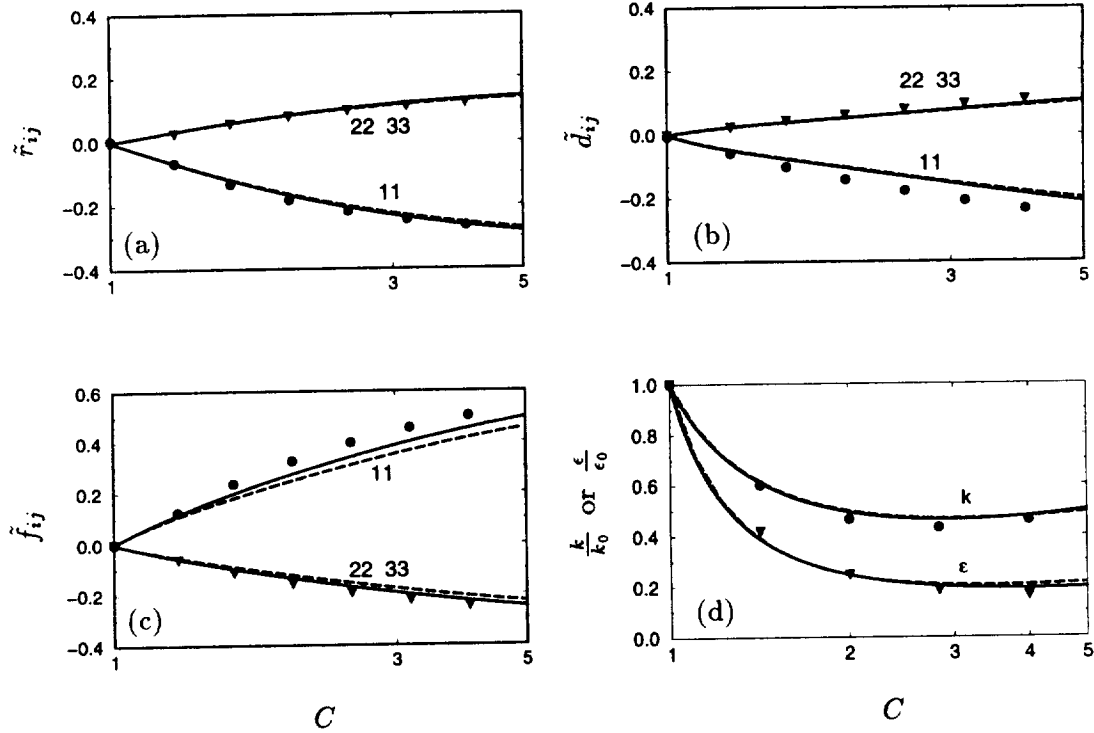
FIGURE 1. Comparison of the one-point model predictions (dashed lines) with the IPRM results (solid lines) and the 1985 DNS of Lee & Reynolds (symbols) for axisymmetric expansion case AXK ($Sq_0^2/\epsilon_0 = 1.1$). (a)-(c) evolution of the the Reynolds stress, dimensionality, and circulicity anisotropies; 11 component ($\bullet$), 22 and 33 components ($\blacktriangledown$). (d) evolution of the normalized turbulent kinetic energy ($\bullet$) and dissipation rate ($\blacktriangledown$).

Reynolds (shown as symbols). Note the excellent agreement of both the IPRM and the one-point model with the simulation results. Rapid Distortion Theory (RDT) predicts that under irrotational deformation $r_{ij} = d_{ij} = \frac{1}{2}(\delta_{ij} - f_{ij})$, and this result is captured by both models.

Axisymmetric Expansion

Results for the case of irrotational axisymmetric expansion flow with an initial $Sq_0^2/\epsilon_0 = 0.82$ are shown in Fig. 2. The predictions of the IPRM (solid lines) and those of the one-point model (dashed lines) are compared with the direct numerical simulation (DNS) of Lee & Reynolds (1985), shown as symbols.

As discussed in Kassinos & Reynolds (1995), the axisymmetric expansion flows exhibit counter-intuitive behavior, where a weaker mean deformation rate produces a level of stress anisotropy r_{ij} that exceeds the one produced under RDT. This effect, which is also supported by the experiments of Choi (1983), is triggered by
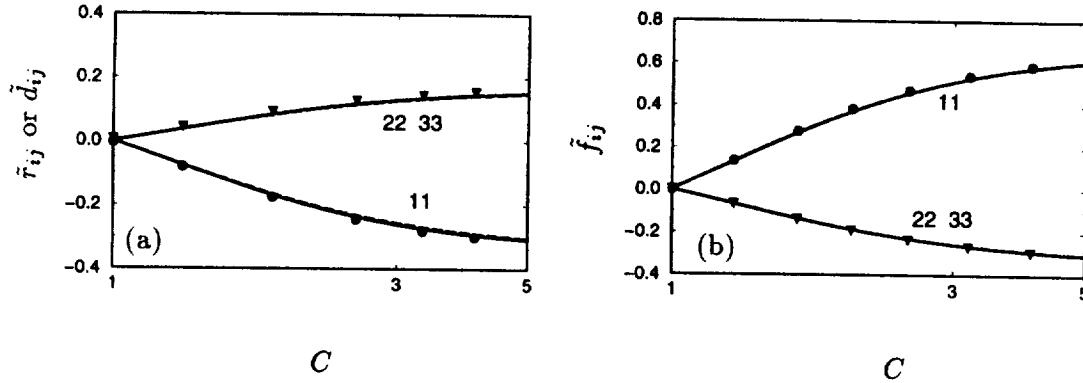
FIGURE 2.   Comparison of the one-point model predictions (dashed lines) with the IPRM results (solid lines) and the 1985 DNS of Lee & Reynolds (symbols) for axisymmetric expansion case AXM $(Sq_0^2/\epsilon_0 = 110.0)$. (a) evolution of the Reynolds stress and dimensionality anisotropies and (b) evolution of the circulicity anisotropy;   11 component ($\bullet$), 22 and 33 components ($\blacktriangledown$).

the different rates of return to isotropy in the $\mathbf{r}$ and $\mathbf{d}$ equations, but it is dynamically controlled by the rapid terms. The net effect is a growth of $\tilde{r}_{ij}$ in expense of $\tilde{d}_{ij}$, which is strongly suppressed. As shown in Fig. 2, the predictions of the IPRM and one-point models are almost indistinguishable from each other, and both are able to capture these intriguing effects quite accurately. The predictions of both models for the evolution of the normalized turbulent kinetic energy and dissipation rate are also in good agreement with the DNS.

The case of irrotational axisymmetric expansion flow with rapid strain $(Sq_0^2/\epsilon_0 = 82.0)$ is considered in Fig. 4. The agreement between the predictions of the IPRM (solid lines) and those of the one-point (dashed lines) with the simulation results (symbols) is excellent. Also note the drastic difference in the anisotropy evolution histories for $\tilde{r}_{ij}$ and $\tilde{d}_{ij}$ between the slow case (Fig. 3) and the rapid case (Fig. 4) and how these effects are captured by both models.

Plane Strain

A third case of irrotational deformation is considered in Fig. 5, where we show results for initially isotropic homogeneous turbulence subjected to plane strain. The mean deformation is in the x_2-x_3 plane according to

$$S_{ij} = \begin{pmatrix} 0 & 0 & 0 \\ 0 & -S & 0 \\ 0 & 0 & S \end{pmatrix} . \tag{36}$$

Fig. 5 shows evolution histories for the three tensor anisotropies, and for k and ϵ, for a case of weak irrotational plane strain $(Sq_0^2/\epsilon_0 = 1.0)$. Again, the IPRM predictions are shown as solid lines and those of the one-point model as dashed
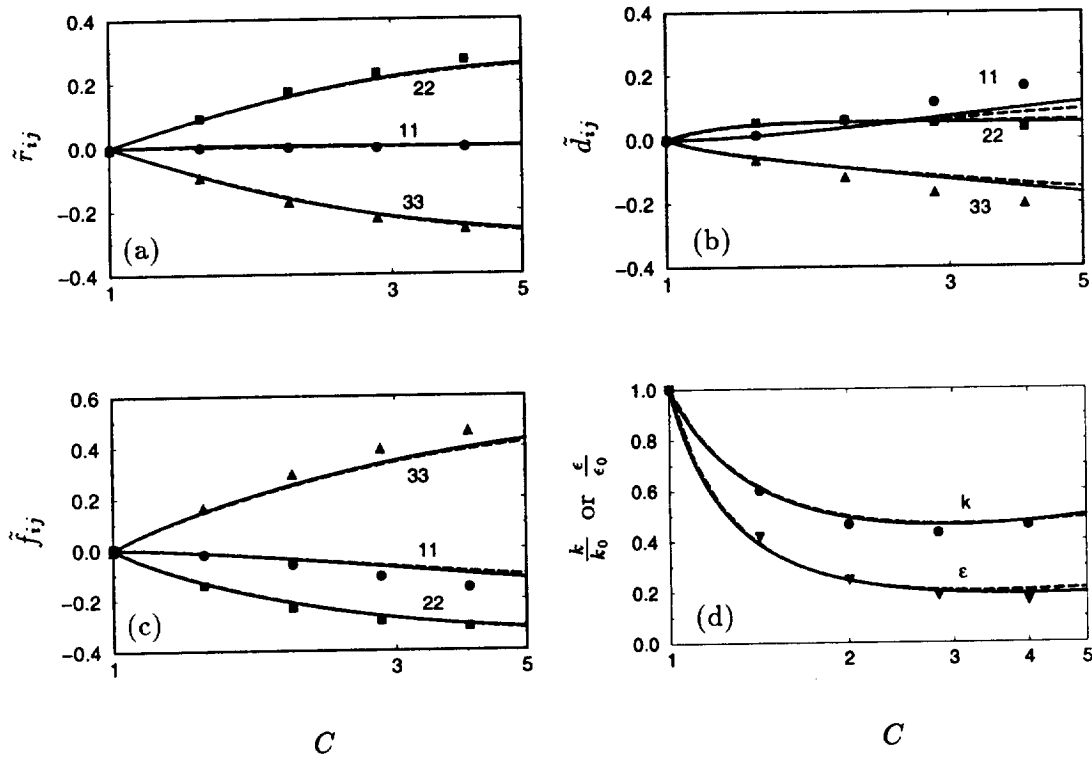
FIGURE 3. Comparison of the one-point model predictions (dashed lines) with the IPRM results (solid lines) and the 1985 DNS of Lee & Reynolds (symbols) for axisymmetric expansion case EXO ($Sq_0^2/\epsilon_0 = 0.82$). (a)-(c) evolution of the the Reynolds stress, dimensionality, and circulicity anisotropies; 11 component ($\bullet$), 22 and 33 components ($\blacktriangledown$). (d) evolution of the normalized turbulent kinetic energy ($\bullet$) and dissipation rate ($\blacktriangledown$).

lines. Comparison is made with the 1985 DNS of Lee & Reynolds (symbols). Note how the predictions of the one-point model are practically indistinguishable from those of the IPRM and how both models are in excellent agreement with the DNS results for all predictions.

The case of homogeneous, initially isotropic turbulence subjected to rapid irrotational plane ($Sq_0^2/\epsilon_0 = 154.0$) is shown in Fig. 6. Comparison is made with case PXF from the DNS of Lee & Reynolds (1985). Both models are in excellent agreement with the simulation results (symbols). A comparison of the rapid plane strain case (Fig. 6) to the slow plane strain case (Fig. 5) shows that, as in the axisymmetric expansion flow, the rate of straining has a strong effect in the evolution of $\tilde{r}_{ij}$ and $\tilde{d}_{ij}$, and the models are able to capture this.

FIGURE 4.   Comparison of the one-point model predictions (dashed lines) with the IPRM results (solid lines) and the 1985 DNS of Lee & Reynolds (symbols) for axisymmetric expansion case EXQ ($Sq_0^2/\epsilon_0 = 82$). (a) evolution of the Reynolds stress and dimensionality anisotropies, (b) evolution of the circulicity anisotropy; 11 component (●), 22 and 33 components (▼).
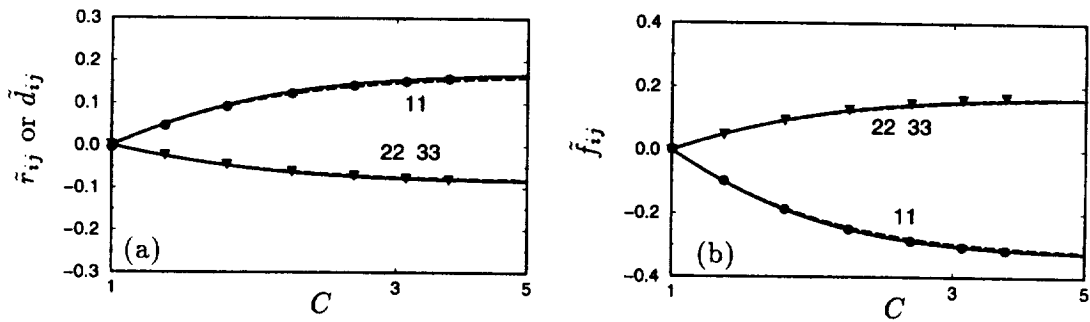

FIGURE 5.   Comparison of the one-point model predictions (dashed lines) with the IPRM results (solid lines) and the 1985 DNS of Lee & Reynolds (symbols) for plane strain case PXA ($Sq_0^2/\epsilon_0 = 1.0$). (a)-(c) evolution of the the Reynolds stress, dimensionality, and circulicity anisotropies;   11 component (●), 22 component (■), and 33 component (▼). (d) evolution of the normalized turbulent kinetic energy (●) and dissipation rate (▼).
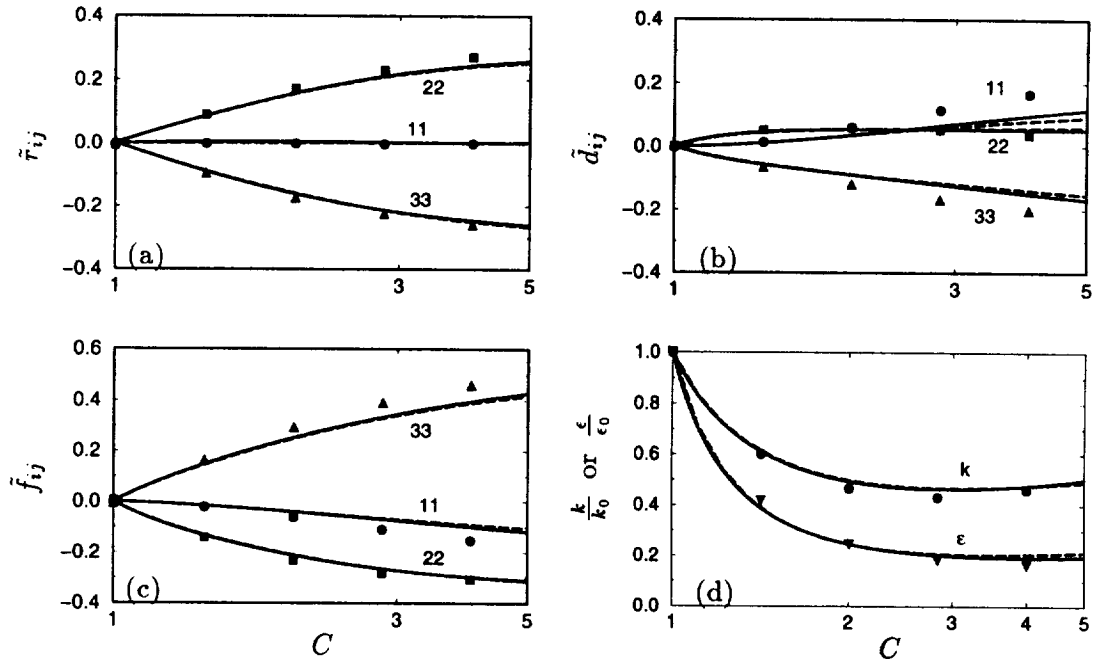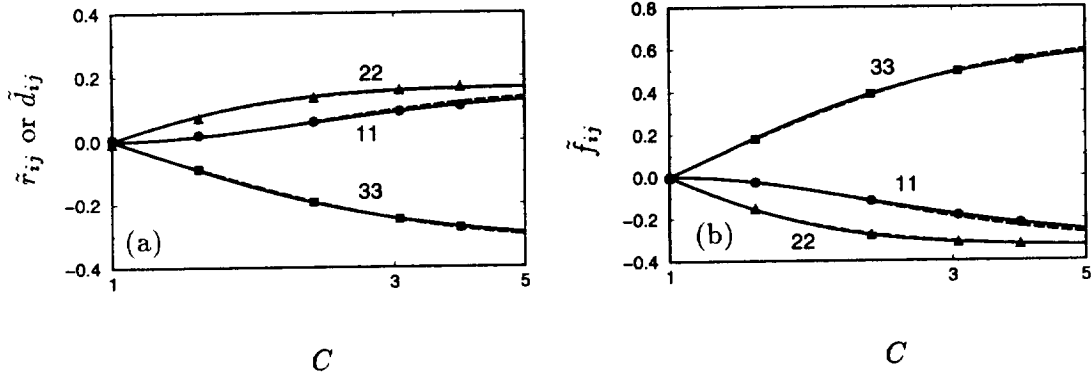
FIGURE 6. Comparison of the one-point model predictions (dashed lines) with the IPRM results (solid lines) and the 1985 DNS of Lee & Reynolds (symbols) for plane strain case PXA $(Sq_0^2/\epsilon_0 = 154.0)$. (a) evolution of the Reynolds stress and dimensionality anisotropies, (b) evolution of the circulicity anisotropy 11 component ($\bullet$), 22 component ($\blacksquare$), and 33 component ($\blacktriangledown$).

3. Remaining issues and future plans

The decomposition given in (28) is valid only under irrotational mean deformations. Under more general modes of deformation, which include combinations of mean strain and mean rotation, reflectional symmetry is broken and stropholysis effects must be included in (28). The exact form of this decomposition under these more general conditions is given by

$$M_{ijpq} = \tfrac{1}{2}(Z_{ijpq}^f - Z_{ijpq}^r - Z_{ijpq}^d) + \frac{1}{2}[\epsilon_{zpj}Q_{ziq}^* - \epsilon_{ziq}Q_{zpj}^*]$$
$$+ \frac{1}{6}\left[- 3\delta_{ij}\delta_{pq}q^2 + 4(\delta_{pq}R_{ij} + \delta_{ij}D_{pq}) + 2(\delta_{pq}D_{ij} + \delta_{ij}R_{pq})\right]. \tag{37}$$

The stropholysis Q_{ijk}^* is defined by (see Kassinos & Reynolds 1994)

$$Q_{ijk}^* = \tfrac{1}{6}[Q_{ijk} + Q_{jki} + Q_{kij} + Q_{ikj} + Q_{jik} + Q_{kji}] \tag{38}$$

where

$$Q_{ijk} \equiv \overline{-u_j' \Psi_{i,k}'}. \tag{39}$$

The IPRM representation of Q_{ijk} is given by

$$Q_{ijk} = \langle V^2 s_i v_j n_k \rangle. \tag{40}$$

A stropholysis model must satisfy some important constraints. The obvious ones are the requirements that Q_{ijk}^* vanishes under the contraction of any two of its indices, that it is fully symmetric, and that it vanishes whenever any two of the three vectors in the basic triad ($\mathbf{v}$, $\mathbf{n}$, $\mathbf{s}$) are randomly distributed around the third (for example,

in irrotational deformations). In addition, when any of the three tensors **r**, **d**, or **f** is two-component (2C), the stropholysis must reduce to a special form (see Kassinos & Reynolds 1994). This last of the three constraints is the most challenging to satisfy. What complicates the issue of stropholysis modeling is the fact that whenever any of the three tensors becomes 2C, the three energy-weighted fourth moments (Z^r_{ijpq}, Z^d_{ijpq}, and Z^f_{ijpq}) must also reduce to special forms. To maintain realizability the **Z** models must not only reduce to the correct 2C forms, they must also do so at the correct rate in conjunction with the **Q*** model. It seems then that the stropholysis and fourth-moment models cannot be constructed completely independently from each other. This fact is the single most complicating issue in the context of an **R-D** model.

We are currently focusing on the construction of a consistent **Z** and **Q*** models that will allow closure of the one-point **R** -**D** model for the general case, while maintaining full realizability. At the same time we are investigating extensions of the IPRM and one-point models for inhomogeneous flows.

REFERENCES

BARDINA, J, FERZIGER, J. H., & REYNOLDS, W. C. 1983 *Improved turbulence models based on large eddy simulation of homogeneous, incompressible, turbulent flows*. Report TF-19, Thermosciences Division, Department of Mechanical Engineering, Stanford University.

CHOI, KWING-SO. 1983 *A study of the return to isotropy of homogeneous turbulence*, Technical Report, Sibley school of Mechanical and Aerospace Engineering, Cornell University, New York.

KASSINOS, S. C. AND REYNOLDS, W. C. 1994 *A structure-based model for the rapid distortion of homogeneous turbulence*. Report TF-61, Thermosciences Division, Department of Mechanical Engineering, Stanford University.

KASSINOS, S. C. AND REYNOLDS, W. C. 1995 An extended structure-based model based on a stochastic eddy-axis evolution equation. *Annual Research Briefs 1995*, Center for Turbulence Research, NASA Ames/Stanford Univ. 133-148.

KASSINOS, S. C. AND REYNOLDS, W. C. 1996 An Interacting Particle Representation Model for the Deformation of Homogeneous Turbulence. *Annual Research Briefs 1996*, Center for Turbulence Research, NASA Ames/Stanford Univ. 31-53.

REYNOLDS, W. C. AND KASSINOS, S. C. 1995 A one-point model for the evolution of the Reynolds stress and structure tensors in rapidly deformed homogeneous turbulence. *Proc. Roy. Soc. London A.* **451**(1941), 87-104.

LEE, M. J. & REYNOLDS, W. C. 1985 *Numerical experiments on the structure of homogeneous turbulence "*. Report TF-24, Thermosciences Division, Department of Mechanical Engineering, Stanford University.

MANSOUR, N. N., SHIH, T.-H., & REYNOLDS, W. C. 1991 The effects of rotation on initially anisotropic homogeneous flows. *Phys. Fluids A.* **3**, 2421–2425.

POPE, S. B. 1994 On the relationship between stochastic Lagrangian models of turbulence and second-moment closures. *Phys. Fluids.* **6**, 973–985.

SPEZIALE, C. G. 1981 Some interesting properties of two-dimensional turbulence. *Phys. Fluids.* **24**(8), 1425-1427.

SPEZIALE, C. G. 1985 Modeling the pressure-velocity correlation of turbulence. *Phys. Fluids.* **28**(8), 69-71.

VANSLOOTEN, P. R. & POPE, S. B. 1997 Pdf modeling for inhomogeneous turbulence with exact representation of rapid distortions. *Phys. Fluids.* **9**(4), 1085-1105.

Incorporating realistic chemistry into direct numerical simulations of turbulent non-premixed combustion

By W. K. Bushe, R. W. Bilger[1] AND G. R. Ruetsch

1. Motivation and objectives

Combustion is an important phenomenon in many engineering applications. Combustion of hydrocarbons is still by far the most common source of energy in the world. In many devices of interest—such as in furnaces, diesel engines and gas turbines—the combustion takes place in what is known as the "non-premixed" regime. The fuel and oxidizer are initially unmixed, and in order for chemical reaction to take place, they must first mix together. In this regime, the rate at which fuel and oxidizer are consumed and at which heat and product species are produced is, therefore, to a large extent controlled by mixing.

In virtually all engineering applications of combustion processes, the flow in which the combustion takes place is turbulent. Furthermore, the combustion process itself is usually described by a very large system of elementary chemical reactions. These chemical kinetic mechanisms are usually extremely stiff and involve, for longer chain hydrocarbon species, hundreds of chemical species. The governing equations describing the chemical composition are closely coupled to those describing the turbulent transport. Also, the chemical reaction rates are non-linear and strongly depend on the instantaneous composition and temperature.

1.1 Modeling turbulent combustion

In order to model turbulent combustion, one must circumvent what is known as the "chemical closure problem". The chemical source term in the Reynolds averaged species transport equation must be modeled. Several models have been proposed to achieve chemical closure, but many of these are only applicable to limited flow or chemistry regimes. For example, in the fast chemistry limit, the chemistry is assumed to be infinitely fast in comparison to the turbulent mixing process (Bilger, 1980), which completely neglects the influence of finite rate chemistry on the combustion process. Laminar flamelet models (Peters, 1984) are only applicable in what is known as the "flamelet regime", where the chemical reactions take place along an interface which is thinner than the smallest turbulent length scale. The PDF model (Pope, 1985), where the transport equation for the joint probability density function of the composition vector is solved, is only practical for systems with very simple chemical kinetic mechanisms—such as reduced chemical kinetic mechanisms.

1 The University of Sydney, Australia

A new method for closing the chemical source term was recently proposed independently by Klimenko (1990) and Bilger (1993a, 1993b). In the Conditional Moment Closure (CMC) method, the transport equations are conditionally averaged, with the condition being some variable on which the chemical reaction rates are known to depend. For non-premixed combustion, an appropriate conditioning variable is the "mixture fraction". This is a conserved scalar, suitably defined to have a value of zero in pure oxidizer and unity in pure fuel.

The average of the mass fraction Y_I of a particular species I, conditional on the mixture fraction Z having some value η, is

$$Q_I(x_k, t; \eta) \equiv \langle Y_I(x_k, t) | Z(x_k, t) = \eta \rangle. \tag{1}$$

For a flow in which the velocity and mixture fraction fields are both isotropic and homogeneous, the conditionally averaged transport equation for Y_I becomes (Smith, 1995)

$$\frac{\partial Q_I}{\partial t}(\eta) = \langle \dot{\omega}_I | Z = \eta \rangle + \frac{\partial^2 Q_I}{\partial \eta^2} \langle \mathcal{D} \frac{\partial Z}{\partial x_i} \frac{\partial Z}{\partial x_i} | Z = \eta \rangle, \tag{2}$$

the right-hand side of which has two unclosed terms: the conditionally averaged reaction rate and a mixing term in which appears the conditionally averaged scalar dissipation, $\langle \mathcal{D} \frac{\partial Z}{\partial x_i} \frac{\partial Z}{\partial x_i} | Z = \eta \rangle$.

There are several models available for the scalar dissipation, such as presumed PDF models (Mell, *et al.*, 1994), and mapping closure models (Bushe, 1996). Closure of the reaction term can be achieved through the first order CMC hypothesis: that the conditional average of the chemical source term of some species I, which is a function of the composition vector Y_J and the temperature T, can be modeled by evaluating the chemical reaction rates using the conditional averages of the composition vector Q_J and temperature $\langle T | Z = \eta \rangle$. Thus,

$$\langle \dot{\omega}(Y_J, T)_I | Z = \eta \rangle \approx \dot{\omega}_I(Q_J, \langle T | Z = \eta \rangle). \tag{3}$$

Various refinements to the closure hypothesis for the chemical reaction term have been proposed, using either a second conditioning variable (Bilger, 1991; Bushe 1996) or a second moment (Li & Bilger, 1993; Smith 1996), which are intended to extend the validity of the closure hypothesis to account for ignition and extinction phenomenon and to improve the performance of the model for chemical reactions where the activation energies are very large.

1.2 Validation of turbulent combustion models

Work attempting to improve and validate models for turbulent combustion has been hampered by a lack of adequate experimental results. Only recently have experimental techniques been devised which might provide the necessary insight; these experiments methods are still quite limited in the information they provide and are also extremely expensive and difficult to perform.

As an alternative to experiments, Direct Numerical Simulation (DNS) of the governing equations can be performed; however, to date such simulations have been

limited by available computer resources—and by the complexity and stiffness of the associated equations—to simple chemical kinetic models (Vervisch, 1994).

With the advent of new techniques for the systematic reduction of chemical kinetic mechanisms, new reduced kinetic mechanisms are now available which are still relatively simple, but which retain sufficient complexity from the original mechanism to provide good predictions of flame structure and reaction rates. In a previous study which implements such a reduced mechanism in DNS (Swaminathan and Bilger, 1997a & 1997b), the flow was assumed to be incompressible, so that effects of heat release on the flow were neglected. While the results of this study have been encouraging, validation of the CMC method against this constant property DNS data is not completely convincing. There is clearly a need to obtain DNS data using realistic chemical kinetics in turbulence where effects of the heat release on the flow are included.

In the present study, a reduced kinetic mechanism has been incorporated into a fully compressible DNS code. The results of the simulations will be used for the validation and, hopefully, improvement of current combustion models such as the CMC model described above.

2. Accomplishments

2.1 Chemistry

2.1.1 Original kinetic mechanism

The chemical kinetic mechanism that was used in the simulations is one representative of the oxidation of a methane/nitrogen mixture by an oxygen/nitrogen mixture. There are three reactions in the mechanism; the first two represent the oxidation of the methane (Williams, 1991), and the third represents the formation of nitric oxide. The reactions are:

$$Fuel + Oxi \rightarrow Int + Prod \tag{I}$$

$$Int + Oxi \rightarrow 2Prod \tag{II}$$

$$N_2 + Oxi \rightarrow 2NO \tag{III}$$

where $Fuel$ is CH_4, Oxi is O_2, Int is $(\frac{4}{3}H_2 + \frac{2}{3}CO)$, and $Prod$ is $(\frac{2}{3}H_2O + \frac{1}{3}CO_2)$.

Rates for reactions (I) and (II), expressed in terms of mass fractions, are given by:

$$\dot{\omega}_I = 1375 \frac{mol \cdot cm^3}{g^2 \cdot s \cdot K^3} \rho \, T^3 \exp\left(-\frac{4404K}{T}\right) Y_{Fuel}Y_H \tag{4}$$

and

$$\dot{\omega}_{II} = 7.19 \times 10^{16} \frac{K^{0.8} \cdot cm^6}{g^2 s^2} \rho^2 \, T^{-0.8} Y_{Oxi} Y_H \Gamma_M. \tag{5}$$

The mass fraction of Hydrogen, which appears in the both of these reaction rate expressions, is given by the steady state approximation:

$$Y_H = 0.136 \, e^{\left(\frac{3045K}{T}\right)} \Theta \left[1 - \exp\left(-10^{-15}K^{-5} \, T^5\right)\right] \frac{\left(Y_{Oxi}Y_{Int}^3\right)^{1/2}}{Y_{Prod}} \tag{6}$$
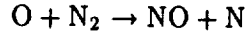
with

$$\Theta = \exp\left\{-4.26 \times 10^{-10} K^{-3}\ T^3\ \frac{Y_{Fuel}}{Y_{Oxi}} \exp\left(\frac{4051K}{T}\right)\right\}. \tag{7}$$

The influence of the enhanced third body M, appearing in the rate expression for reaction II, is

$$\Gamma_M = 0.014 + 0.392 Y_{Fuel} - 0.002 Y_{Oxi} + 0.072 Y_{Int} + 0.167 Y_{Prod}. \tag{8}$$

The rate expression for reaction III is obtained by placing the oxygen free radical in the simple Zel'dovich mechanism

$$O + N_2 \rightarrow NO + N$$

$$N + O_2 \rightarrow NO + O$$

in steady state. The concentration of the oxygen free radical is estimated by assuming it is in partial equilibrium with the hydrogen and hydroxyl free radicals. The resulting rate expression is

$$\dot\omega_{III} = 5.60 \times 10^{11}\ \frac{mol \cdot cm^3}{g \cdot s}\ \rho\ \exp\left(-\frac{45060K}{T}\right) \frac{Y_{Prod} Y_H^2 Y_{N_2}}{Y_{Int}^2}. \tag{9}$$

The rate expressions in Eqs. (4), (5) and (9), each give the reaction rates in units of $mol/g_{mixture}/s$. The rates of change of mass fractions can be calculated by multiplying the reaction rates by each participating species molecular weight,

$$\dot\omega_{Fuel} = -16\ g/mol\ \dot\omega_I$$

$$\dot\omega_{Oxi} = -32\ g/mol\ (\dot\omega_I + \dot\omega_{II} + \dot\omega_{III})$$

$$\dot\omega_{Int} = \frac{64}{3}\ g/mol\ (\dot\omega_I - \dot\omega_{II})$$

$$\dot\omega_{Prod} = \frac{80}{3}\ g/mol\ (\dot\omega_I + 2\dot\omega_{II})$$

$$\dot\omega_{NO} = 30\ g/mol\ (2\dot\omega_{III}).$$

The rate of change of energy due to chemical reaction is calculated by multiplying the reaction rates by each reaction's enthalpy of formation,

$$\dot\omega_e = -291\ kJ/mol\ \dot\omega_I - 511\ kJ/mol\ \dot\omega_{II} + 181\ kJ/mol\ \dot\omega_{III}.$$

2.1.2 Simplifying the mechanism

In order to reduce computational costs and to make the mechanism more tractable for modeling purposes, the reaction rate expressions were simplified.

The equation for Θ, Eq. (7), contains the function

$$f(T) = 4.26 \times 10^{-10} \; T^3 \exp\left(\frac{4051}{T}\right) \qquad (10)$$

which, over a temperature range from 1200 to 2000 K, is well approximated as being constant—as seen in Fig. 1(a). This was taken to be 22.1, which, over that temperature range, predicts Eq. (10) within 15%.

The expression for reaction I, Eq. (4), contains the function

$$g(T) = 1375 \; T^3 \exp\left(-\frac{4404}{T}\right). \qquad (11)$$

This function can be approximated by

$$g(T) \approx 1.57 \times 10^{14} \exp\left(-\frac{9624}{T}\right), \qquad (12)$$

as shown in Fig. 1(b), also to within 15% over the range of 1200–2000K.

The expression for the hydrogen free-radical mass fraction becomes

$$Y_{\mathrm{H}} = 0.136 \; \exp\left(\frac{3045K}{T} - 22.1 \frac{Y_{Fuel}}{Y_{Oxi}}\right)$$
$$\cdot \left[1 - \exp\left(-10^{-15}K^{-5} \; T^5\right)\right] \frac{\left(Y_{Oxi}Y_{Int}^3\right)^{1/2}}{Y_{Prod}} \qquad (13)$$

and the expression for the reaction rate of reaction I becomes

$$\dot{\omega}_{\mathrm{I}} = 1.57 \times 10^{14} \; \frac{mol \cdot cm^3}{g^2 \cdot s} \; \rho \; \exp\left(-\frac{9624K}{T}\right) Y_{Fuel}Y_{\mathrm{H}} \qquad (14).$$

2.1.3 Non-dimensionalizing the mechanism

The DNS code for which the mechanism was being modified uses the constant pressure specific heat C_p, the ratio of specific heats γ, and the speed of sound to non-dimensionalize the governing equations. Thus, C_p and γ are implicitly assumed to be constant. It is also implicitly assumed that the molecular weights of the fuel and oxidizer streams are equal.

In order to remain consistent with previous implementations of this mechanism (Swaminathan & Bilger, 1997a & 1997b), it was decided that the fuel stream would consist of 15% methane (by mass), balance nitrogen, and the oxidizer stream would consist of 30% oxygen, balance nitrogen. These mixtures have molecular weights of 26.2 g/mol and 29.2 g/mol, respectively. The constant molecular weight of both streams, for the purposes of the DNS code's calculations, was taken to be 28 g/mol. The initial temperature of both streams was taken to be 300K.
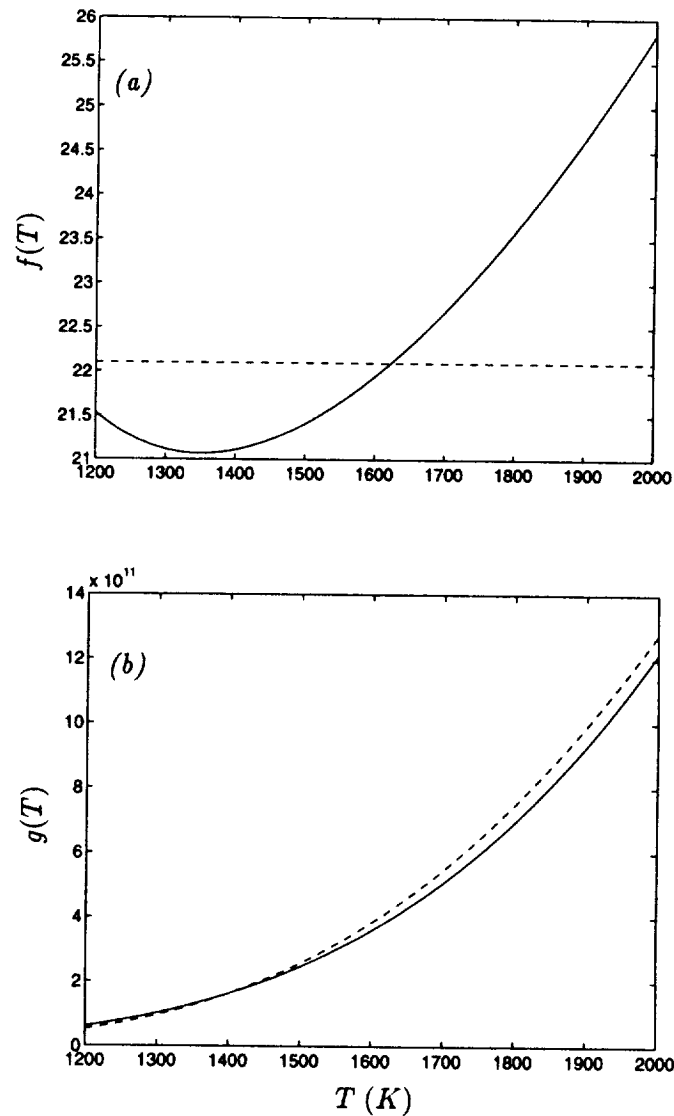
FIGURE 1. Comparison of simplified functions in kinetic mechanism:

(a) ———— , $f(T) = 4.26 \times 10^{-10} \; T^3 \exp\left(\frac{4051}{T}\right)$; ———— , $f(T) \approx 22.1$

(b) ———— , $g(T) = 1375 \; T^3 \exp\left(-\frac{4404}{T}\right)$; ———— , $g(T) \approx 1.57 \times 10^{14} \exp\left(-\frac{9624}{T}\right)$.

In choosing a constant value for the specific heat, care had to be taken to ensure that the maximum temperature would be appropriate for the flame being modeled. The adiabatic flame temperature for a stoichiometric mixture of the two streams described would be 2049K. However, the specific heat is an increasing function with increasing temperature, and in a non-premixed flame, the maximum temperature is limited by the diffusion of heat away from the reaction zone. Thus, choosing a

constant C_p such that the adiabatic flame temperature would be matched would result in an under-prediction of the maximum flame temperature in the non-premixed flame. A value for C_p of 1.30 $J/(g \cdot K)$ was chosen, which yields an adiabatic flame temperature of 2228K. With the ideal gas constant,

$$R = \frac{8.314 \ J/(mol \cdot K)}{28 \ g/mol} = 0.297 \ J/(g \cdot K),$$

this gives $\gamma = 1.3$. Choosing an initial temperature and a value for the specific heat fixes the reference temperature, density, and speed of sound which are used to non-dimensionalize the quantities in the reaction rate expressions.

2.2 One-dimensional simulations

The chemical kinetic mechanism described above was incorporated into a DNS code which solves the governing equations for fully compressible turbulent flow (Ruetsch, 1995), based on the algorithms of Lele (1992) and Poinsot and Lele (1992). In order to test the implementation of the mechanism and to provide initial conditions for simulations with turbulent flow fields, the code was run for a simple, one-dimensional problem.

2.2.1 Initial and boundary conditions

In order to ensure that the pressure in the domain remains constant, fluid must be allowed to leave the domain. An additional constraint is that the reaction rates at the boundaries must be zero; otherwise, the boundary conditions are ill-posed. Also, because the chemical kinetic rates depend on the hydrogen free radical concentration, the mechanism cannot auto-ignite; if the flow is initially unreactive, it will remain so; therefore, the fields must be initialized such that at least some chemical reaction is already underway.

Partially non-reflecting outflow boundary conditions (Poinsot & Lele, 1992) were chosen for both boundaries in the one-dimensional simulations.

The species mass fractions were initialized by first defining the mixture fraction as a linear combination of mass fractions such that the chemical source term in its transport equation is zero:

$$Z = \frac{60Y_{Fuel} - 60Y_{Oxi} - 36Y_{Prod} - 32Y_{NO} + 18}{27}. \tag{15}$$

The mixture fraction was initialized with the analytical solution to the diffusion equation for a semi-infinite slab of fuel mixing with a semi-infinite slab of oxidizer,

$$Z(x,t) = \text{erf}\left(\frac{x}{\sqrt{4\mathcal{D}t}}\right), \tag{16}$$

at an arbitrary time, chosen such that the reaction zone would be sufficiently resolved with the available number of grid points. Mass fractions for each species were then calculated by assuming that an arbitrary fraction of moles for each of

reaction I and II had reacted to completion. This assumption also allowed for the calculation of the heat released as a function of mixture fraction, from which the temperature field can be calculated. The initial pressure was assumed constant at 1 *atm.*—which corresponds to 0.796 non-dimensional pressure units—from which the density could be calculated. The initial velocity was zero.

2.2.2 Broadening the reaction zone

The region in which the chemical reactions are significant—referred to as the "reaction zone"—for the mechanism describe above was found to be very narrow. In order to make the reaction zone broader, reaction rate I and the exponent in Θ of Eq. (7) are divided by a constant of 22.8. This has been shown in previous studies (Swaminathan & Bilger, 1997a & 1997b) to broaden the reaction zone sufficiently to allow the reactions to be easily resolved by DNS without substantially altering the structure of the flame. This is shown in Fig. 2, where the results of a very well resolved simulation *without* the broadened reaction zone are compared to those from a simulation *with* the broadened reaction zone. The two simulations had the same initial conditions and were each run for 100 non-dimensional time units.

Despite the changes to the mechanism, it can be seen in Figs. 2(a) and (b) that the profiles of the mass fractions of the Fuel, Intermediate, and Product are only slightly modified from those given by the original mechanism. Only the fraction of Oxidizer that leaks through the reaction zone to the rich side of the flame is significantly altered by the modification. Figure 2(c) compares the estimated hydrogen radical concentrations. It is clear that, without the modifications to the mechanism, it would be very difficult to resolve the sharp drop in Hydrogen radical mass fraction at the stoichiometric mixture fraction of 1/3. However, *with* the modifications, that sharp drop disappears, and the hydrogen free radical mass fraction can be resolved with far fewer points. The significant difference in magnitude of the reaction rate for reaction I, shown in Fig. 2(d) is almost entirely attributable to that reaction having been slowed by a factor of 22.8. It should be noted that this reaction, as with the hydrogen free radical mass fraction, would severely constrain the resolution of the flame if the modifications were not included—so much so that DNS including turbulence would hardly seem possible without using the modifications. The influence of the modifications on the reaction rates of reactions II and III, shown in Figs. 1(e) and (f), is primarily to also broaden the region of mixture fraction in which they are significant, and they also seem to ease resolution constraints by making the rates more smooth functions of mixture fraction.

2.3 Two-dimensional simulations

Once tests of the newly implemented kinetic mechanism had been completed, the addition of turbulence in two-dimensions was undertaken. This was seen primarily as being a means of establishing what turbulence parameters would be appropriate to provide adequate *three*-dimensional simulation results for modeling purposes; however, it was anticipated that these two-dimensional tests would also provide results from which direct insight could be gained.
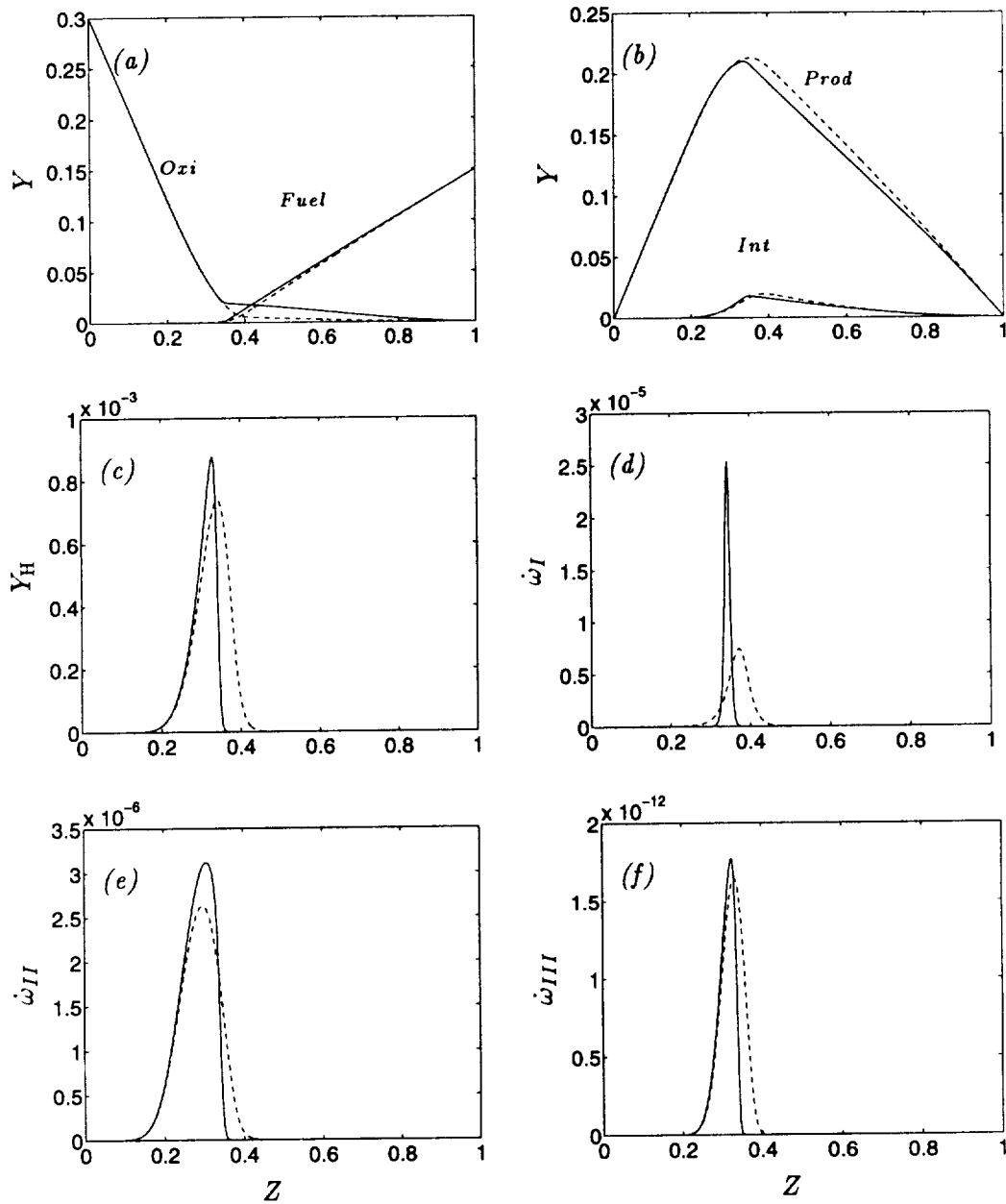
FIGURE 2. Comparison of original mechanism to modified mechanism. (a) Fuel and oxidizer mass fractions; (b) Intermediate and product mass fractions; (c) Hydrogen free radical mass fraction; (d) Rate of reaction I; (e) Rate of reaction II; (f) Rate of reaction III; —————, original mechanism; - - - - , modified mechanism).

2.3.1 Initial and boundary conditions

The same constraints on the initial and boundary conditions described for a one-dimensional domain in Section 2.2.1 apply to two- and three-dimensional domains. This means that at least one of the boundaries in a two- or three-dimensional domain must allow for outflow. Also, the reaction rate at an outflow boundary must be zero.

The mass fraction, temperature, density, and velocity fields were initialized by using the stabilized one-dimensional flame solution described in Section 2.2. By placing a stable flame in the middle of the two-dimensional domain, the time until the reaction zone (the region of the flow in which chemical reaction takes place) reached a boundary could hopefully be maximized.

Initial turbulent velocity fluctuations were obtained by using a pseudo-spectral code to solve the governing equations for incompressible flow and forcing a periodic, three-dimensional flow field on a 120^3 grid from quiescence until its statistics became stationary (Ruetsch & Ferziger, 1997). For the two-dimensional simulations, a slice of the three-dimensional flow was extracted and the components of the velocity that did not satisfy continuity were discarded. Two identical slices were placed next to each other to fill out the 120×240 domain. At the boundaries, the turbulent fluctuations were filtered to zero to avoid potential generation of unphysical vorticity at the boundaries. The turbulent fluctuations were divided by the density so as to satisfy

$$\frac{\partial(\rho u_i)}{\partial x_i} = 0,$$

This rescaling of the turbulent fluctuations was performed to avoid the generation of large, unphysical pressure waves in the flame. It should be noted that this means the vorticity inside the flame is initially much higher than elsewhere; however, since the viscosity in that region is also much higher, the vorticity inside the flame decays very quickly. The resulting turbulent velocity field was added to the one-dimensional flame velocity field.

The initial, cold velocity field had a Taylor Reynolds number of 35. The dissipation length scale was 0.133 box lengths and the dissipation Reynolds number was 107. In order to avoid forcing the turbulence through the reaction zone, the turbulence was allowed to decay.

2.3.2 Results

In extracting statistics such as PDFs or ensemble averages from DNS results, it is usually necessary to make use of isotropy in the turbulence. In an isotropic flow, ensemble statistics can be approximated by averaging points along directions of isotropy. For the results that follow, it was necessary to neglect the effect that the anisotropy in the mixture fraction field might have in order to obtain converged statistics. Previous DNS (Mell *et al.*, 1994) and experimental (Bilger, 1993b) studies of mixing layer flows, such as the one used in this study, have shown that the inhomogeneity in the mixture fraction has only a slight effect on conditional statistics.

The evolution of the Probability Density Function (PDF) of the mixture fraction as a function of (non-dimensional) time is shown in Fig. 3. The PDF represents
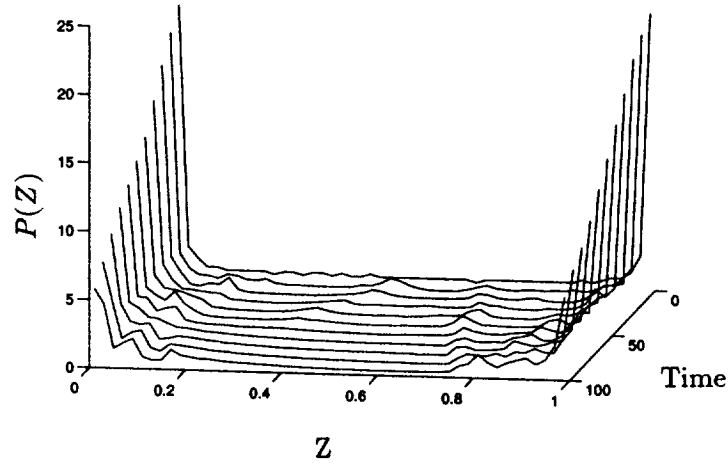
FIGURE 3. Evolution of $P(Z)$ in time.

the entire flow field. The delta functions at $Z = 1$ and $Z = 0$ decay with time as one would expect. There is no evidence of a peak in the PDF between the two delta functions at $Z = 1$ and $Z = 0$, as has been seen for similar flows (Broadwell & Mungal, 1991). This is likely because there is no velocity difference between the fuel and oxidizer streams which would lead to coherent structures created by shear between the streams. In the absence of such coherent structures, the effect of turbulence on the mixing process would appear to be essentially random.

In Fig. 4(a), the PDF of mixture fraction at 100 non-dimensional times is compared to the beta PDF (Cook & Riley, 1994), evaluated using the measured mean (0.47) and variance (0.14) of mixture fraction; the beta PDF is

$$P(Z) = Z^{a-1}(1 - Z)^{b-1}\frac{\Gamma(a + b)}{\Gamma(a)\Gamma(b)}, \tag{17}$$

where

$$a = \overline{Z}\left(\frac{\overline{Z}(1 - \overline{Z})}{\overline{Z'^2}} - 1\right), \quad \text{and} \quad b = (a/\overline{Z}) - a.$$

The beta PDF compares well to the PDF measured from the DNS, with two notable exceptions. For $Z < 0.25$ and $Z > 0.75$, there appears to be some kind of structure in the DNS PDF. This could be a result of there being an inadequate number of points in the domain to obtain converged statistics; however, it is curious that these structures appear at *these* values of Z—there are considerably more points with these values of Z than there are for $0.25 > Z > 0.75$, where the DNS PDF doesn't exhibit such structure. The second difference in the two PDFs is more subtle. The PDF given by the DNS seems to decrease from $Z = 0.2$ to $Z = 0.7$. The beta PDF reaches a minimum at $\overline{Z} = 0.47$. This may be indicative of the influence of variable density on the PDF of mixture fraction.
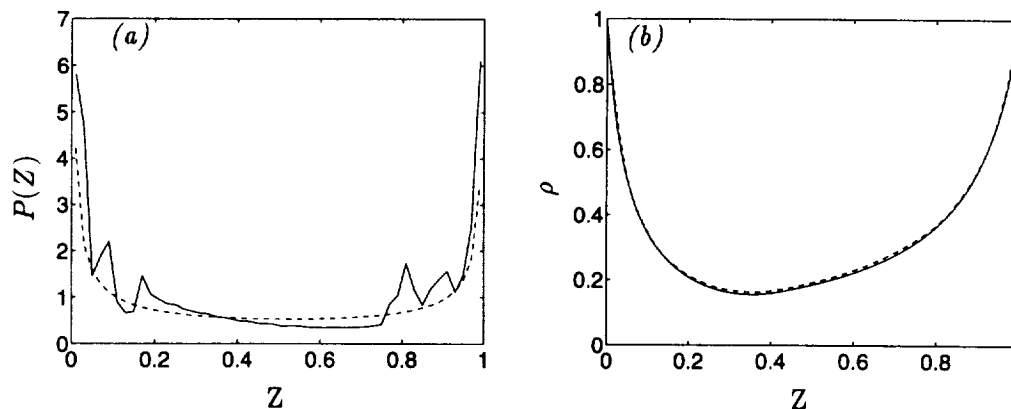
FIGURE 4. (a) Comparison of P(Z) at 100 time units to beta PDF with similar means and variances: ——— , DNS; ———— , beta PDF; (b) Comparison of density profiles between the initial laminar flame and the conditional average in the turbulent flame after 100 time units: ——— , 1D laminar flame; ———— , $\langle \rho | Z = \eta \rangle$ in 2D turbulent flame.

In Fig. 4(b) the conditional average of the density for the entire domain is compared to the density profile (in mixture fraction) of the one-dimensional flame that was used to initialize the two-dimensional simulation. Variations from the conditional average of the density were quite small—the conditional variance of the density was of the order 10^{-4}—nevertheless, there is a discernible difference between the two curves. This is likely caused by the straining of the flame by the velocity field producing regions of local extinction—regions along the flame front where the rate of diffusion of products and heat away from the reaction zone surpasses the reaction rates and the reactions are effectively quenched.

The beta PDF in Fig. 4(a) seems to cross the DNS PDF at a mixture fraction of about 0.35. At about this same value of mixture fraction, the density reaches a minimum. This appears to support the notion that the difference in the two PDFs is attributable to the variation in density.

Scatter plots of the Intermediate, Product, and NO mass fractions as functions of the mixture fraction after 100 time units, are shown in Fig. 5. Also shown is the temperature. Figure 5(a) provides further evidence that the flame has undergone local extinction. Where at a mixture fraction of around 0.4, Y_{Int} has fallen below 0.015, it seems likely that reaction I has essentially stopped providing fresh new Intermediate, and reaction II has then depleted the remaining Intermediate and likely stopped as well. Figures 5(b) and (d) show not only how the temperature is a very strong function of the Product mass fraction for unity Lewis number, but also how the temperature and product mass fractions are affected by the local extinction phenomenon evident in Fig. 5(a). Figure 5(c) reveals just how challenging the chemical closure problem can be when the activation energy of a participating chemical reaction is very large as is the case with reaction III. There is clearly
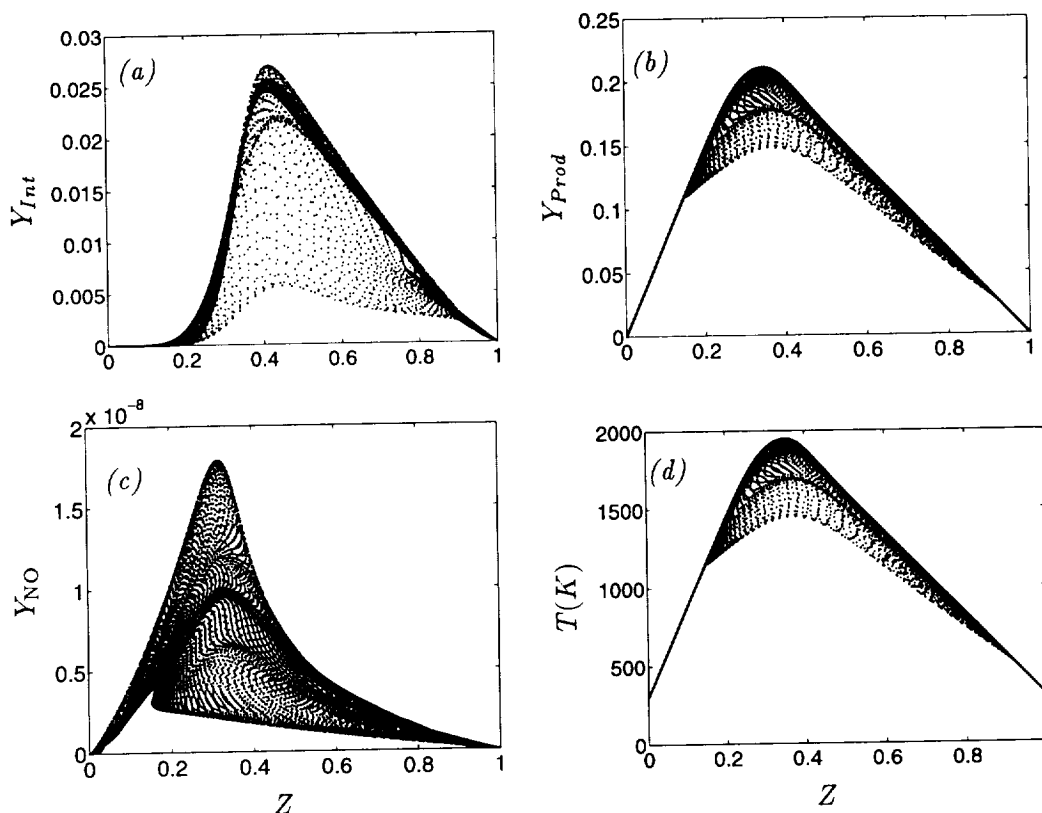
FIGURE 5. Scatter plots of mass fractions and temperature as functions of mixture fraction after 100 time units: (a) mass fraction of Intermediate; (b) mass fraction of Product; (c) mass fraction of NO; (d) temperature.

a great deal of scatter in the NO mass fraction around its conditional average—considerably more than in the temperature—so that the single conditional average would be a poor approximation for the NO mass fraction.

Contour plots of the three reaction rates are shown in Fig. 6. At this time, a region of local extinction is just being re-ignited, with reactions I and II having peaks at $(x, y) = (10, 4)$ and $(9, 4)$. Reaction III, in the region that has been extinguished, has essentially stopped. This is a result of the strong temperature dependence of the reaction rate.

In Fig. 7, the conditionally averaged reaction rates are compared to those predicted by evaluating the reaction rates with the conditionally averaged mass fractions, temperature, and density. This is a test of the validity of first order CMC hypothesis, given by Eq. (3). The reaction rates for reactions I and III are predicted to within 20%, and that for reaction II is predicted to within 10%. It would appear that first order closure would be adequate for predicting the mean reaction rates. This is especially surprising in the case of reaction III, which has an extremely large activation energy and would be expected to require some correction for fluctuations in the temperature around its conditional average.
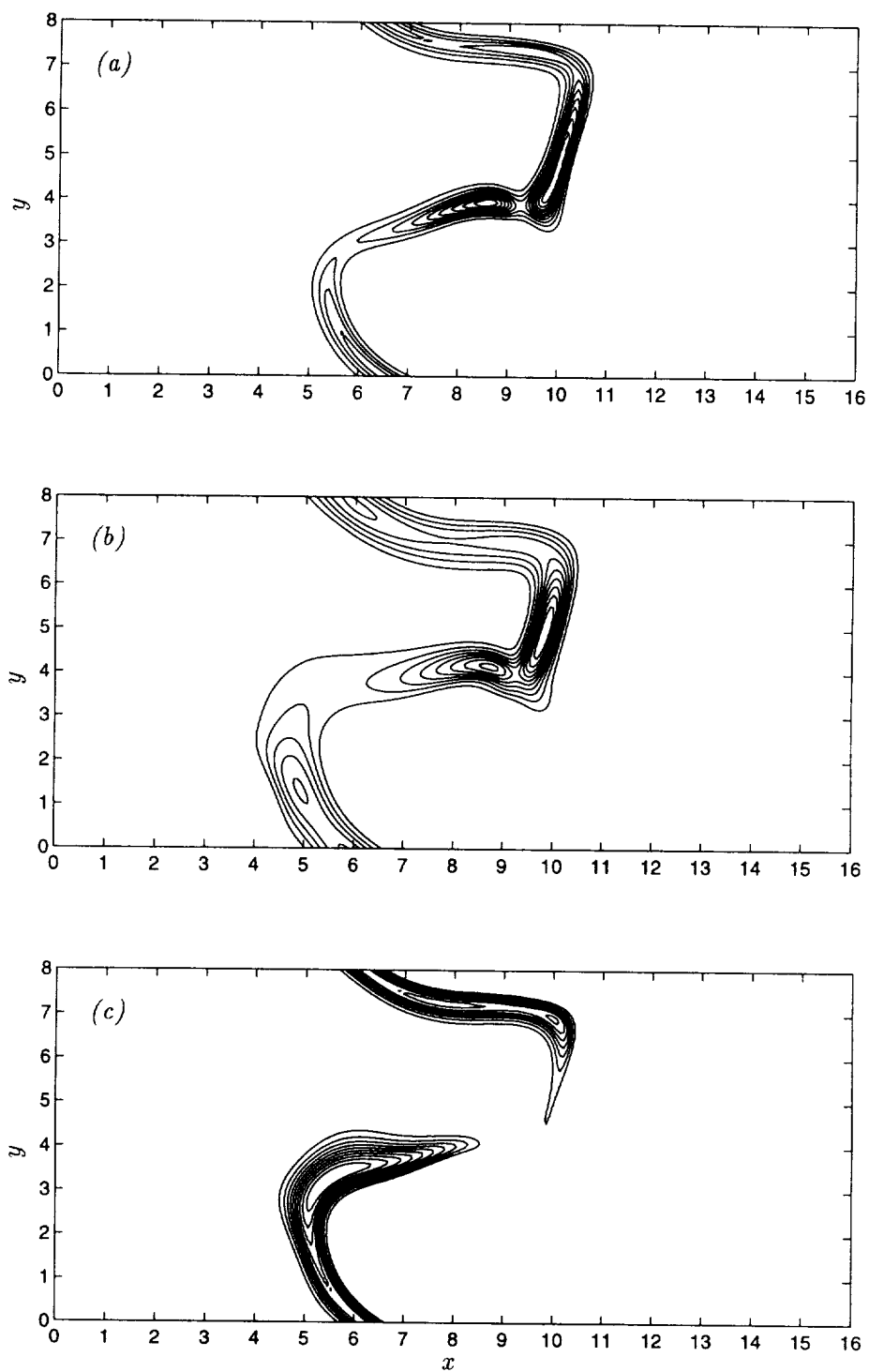
FIGURE 6. Contour plots of reaction rates at 100 time units: (a) reaction I; (b) reaction II; (c) reaction III.
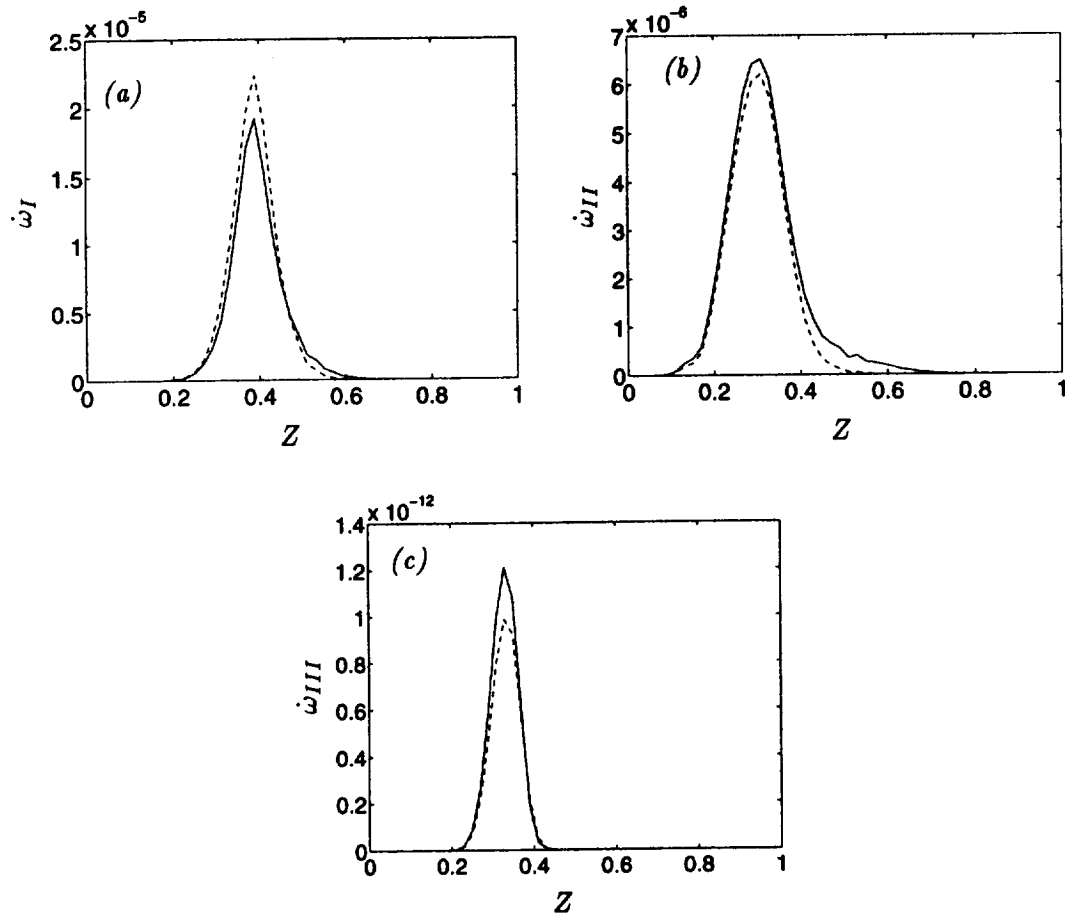
FIGURE 7. Comparison of conditionally averaged reaction rates to reaction rates predicted using the first order CMC approximation at 100 time units:

(a) ———— , $\langle\dot{\omega}_I(Y_J,T)|Z = \eta\rangle$; - - - - , $\dot{\omega}_I(Q_J,\langle T|Z = \eta\rangle)$;

(b) ———— , $\langle\dot{\omega}_{II}(Y_J,T)|Z = \eta\rangle$; - - - - , $\dot{\omega}_{II}(Q_J,\langle T|Z = \eta\rangle)$;

(c) ———— , $\langle\dot{\omega}_{III}(Y_J,T)|Z = \eta\rangle$; - - - - , $\dot{\omega}_{III}(Q_J,\langle T|Z = \eta\rangle)$.

3. Future work

The simulation results presented in Section 2 appear to indicate that the implementation of the chemical kinetic mechanism has been successful. Unfortunately, the conditional statistics extracted from the small two-dimensional domain are inadequately converged to be of significant use in the validation of the CMC model. It has become clear that results in the full, three-dimensional domain will have to be obtained.

The effect of heat release from a premixed flame on a turbulent flow is more significant than in a non-premixed flame since the heat is released in a thin front, which propagates through the fluid. The use of constant property DNS for validation of models of premixed combustion is thus even more questionable than for models

of non-premixed combustion. For this reason, a new project will also be undertaken in which simulations of a *premixed* flame will be performed, using the same code, for the purpose of providing validation for models of premixed turbulent combustion.

Acknowledgments

The authors would like to thank J. Ferziger, K. Mahesh, N. Swaminathan, and T. Poinsot for helpful discussions and suggestions. R. W. B. gratefully acknowledges the financial support of the Australian Research Council. The simulations were performed at the NAS facility of the NASA Ames Research Center.

REFERENCES

BILGER, R. W. 1980 Nonpremixed turbulent reacting flows. *Topics in Applied Physics.* **44**, Springer-Verlag, 65.

BILGER, R. W. 1993a Conditional moment closure for turbulent reacting flow. *Phys. Fluids A.* **5**(2), 436.

BILGER, R. W. 1993b Conditional moment closure modeling and advanced laser measurements. In *Turbulence and Molecular Processes in Combustion*, T. Takeno (Ed), Elsevier, 267.

BROADWELL, J. E. AND MUNGAL, M. G. 1991 Large-scale structures and molecular mixing. *Phys. Fluids A.* **3**, 1193.

BUSHE, W. K. 1996 *Conditional Moment Closure Methods for Autoignition Problems.* PhD thesis, Cambridge University.

COOK, A. W. AND RILEY, J. J. 1994 A subgrid model for equilibrium chemistry in turbulent flows. *Phys. Fluids.* **6**, 2868.

KLIMENKO, A. Y. 1990 Multicomponent diffusion of various admixtures in turbulent flow. *Fluid Dynamics.* **25**, 327.

LELE, S. 1992 Compact finite difference schemes with spectral-like resolution. *J. Comp. Phys.* **103**, 16.

LI, J. D. AND BILGER, R. W. 1993 Measurement and prediction of the conditional variance in a turbulent reactive-scalar mixing layer. *Phys. Fluids A.* **5**, 12, 3255.

MELL, W. E., NILSEN, V., KOSALY, G., AND RILEY, J. J. 1994 Investigation of closure models for nonpremixed turbulent reacting flows. *Phys. Fluids.* **6**(3), 1331.

PETERS, N. 1984 Laminar diffusion flamelet models. *Prog. Energy Combust. Sci.* **10**, 319.

POINSOT, T., AND LELE, S. 1992 Boundary conditions for direct simulations of compressible viscous flows. *J. Comp. Phys.* **101**, 104.

POPE, S. B. 1985 PDF methods for turbulent reactive flows. *Prog. Energy Combust. Sci.* **11**, 119.

RUETSCH, G. R., VERVISCH, L., AND LIÑÁN, A. 1995 Effects of heat release on triple flames. *Phys. Fluids.* **7**, 1447.

RUETSCH, G. R. AND FERZIGER, J. H. 1997 Effects of small-scale structure on turbulent mixing. Submitted to Phys. Fluids.

SMITH, N. A. S. 1995 Modeling complex chemical effects in turbulent nonpremixed combustion. *Annual Research Briefs*, Center for Turbulence Research, NASA Ames/Stanford Univ., 301.

SMITH, N. A. S. 1996 Conditional moment closure of mixing and reaction in turbulent nonpremixed combustion. *Annual Research Briefs*, Center for Turbulence Research, NASA Ames/Stanford Univ., 85.

SWAMINATHAN, N. AND BILGER, R. W. 1997a Direct numerical simulation of turbulent nonpremixed hydrocarbon reaction zones using a two-step reduced mechanism. To appear in *Combust. Sci. and Tech.*

SWAMINATHAN, N. AND BILGER, R. W. 1997b Assessment of combustion sub-models for turbulent nonpremixed hydrocarbon flames. Submitted to Combust. & Flame.

VERVISCH, L. 1992 Study and modeling of finite rate chemistry effects in turbulent non-premixed flames. *Annual Research Briefs*, Center for Turbulence Research, NASA Ames/Stanford Univ., 411.

WILLIAMS, F. A. 1991 in *Reduced Kinetic Mechanism and Asymptotic Approximations for Methane-Air Flames*, Springer-Verlag, New York, 68.

Effects of small-scale structure
on turbulent mixing

By G. R. Ruetsch AND J. H. Ferziger

1. Motivation and objectives

Mixing at small scales in turbulent flows is a process that is important to many applications, including geophysical flows, pollutant dispersion, and reacting flows. In reacting cases, mixing by small scales plays a crucial role in bringing fuel and oxidizer species together, thus affecting the global burning rate.

In 1949, Batchelor and Townsend (1949) examined the phenomenon of intermittency in turbulence, showing that the energy associated with the small scales of turbulence occurs in isolated regions. Kuo and Corrsin (1971, 1972) further investigated the nature of small-scale turbulence and suggested that the small-scale vorticity structure is cylindrical rather than sheet-like as suggested by Betchov (1956) and observed by Schwarz (1990). Through the use of direct numerical simulations, many of the questions regarding the nature of the small-scale structures have been answered. The simulations of Siggia (1981), Kerr (1990), and Vincent and Meneguzzi (1991), among others, indicate that the intense regions of vorticity do occur in cylindrical or tube-like structures. This result seemed counterintuitive as the predominance of points in the flow exhibit two positive principal rates of strain, as indicated by Betchov. The simulations of Ashurst *et al.* (1987) further confirmed this tendency; it was observed that vortex tubes tend to align with the positive intermediate principal rate of strain. Small-scale vortex structures resembling sheets can be found in these simulations if one considers less intense regions of vorticity (She and Jackson 1990, Ruetsch and Maxey 1991). It was further determined that the intense vortex tubes and relatively moderate sheets are not unrelated: the vortex tubes are generated by roll-up of the less intense vortex sheets (Ruetsch and Maxey 1992, Vincent and Meneguzzi 1994).

In addition to the small-scale features of the velocity field, passive scalars also exhibit localized regions of intense gradients, which form due to the alignment with the most compressive principal rate of strain (Kerr 1990, Ashurst *et al.* 1987). A configuration which has received recent attention is that of a uniform temperature gradient, which Corrsin (1952) suggested would be maintained in stationary isotropic turbulence. Such a configuration is attractive for numerical simulations as it can provide ample data for statistical analyses. Simulations concerning the structure and evolution of a small-scale passive scalar field have been performed during the evolutionary phase (Ruetsch and Maxey 1991, Ruetsch and Maxey 1992), and the probability density functions of various quantities related to the passive scalar have also been examined (Pumir 1994a and 1994b, Holzer and Siggia 1994, Overholt and Pope 1996, Jaberi *et al.* 1996). Recent experimental studies of the uniform temperature gradient configuration have also been performed providing probability

density functions and related statistics (Tong and Warhaft 1994), and an asymptotic self-similar solution for the one-point probability density function equation has been presented (Cai *et al.* 1996).

While there have been many investigations regarding small-scale structure and dynamics, the contribution of the small-scale *structure* to global turbulent properties has not been established. There have been several investigations regarding the contribution of the energy associated with small scales to global budgets: the dissipation at and around the vortex tubes has been examined (Ruetsch and Maxey 1991), and by selectively filtering Fourier coefficients of the turbulent velocity field, the contribution of various scales to various statistics has been determined (She *et al.* 1988). However, these studies address the energy content of the small scales. In the present study we wish to address a more subtle issue, that of how the *structure* of the small scales affects the flow, most importantly its mixing characteristics. In other words, we ask how removing the structure from the small scales while maintaining the energy content affects turbulent mixing.

Aside from the fundamental aspects of understanding the importance of small-scale structure to turbulent flows, there are direct applications for the results of such a study. One such area, which motivates this study, regards the fields used to initialize simulations of turbulent combustion (Trouvé and Poinsot 1994, Vervisch 1992). In such simulations, the initial conditions are generally generated by assuming the spectrum and arbitrarily assigning the phases. While providing the correct energy content, this procedure eliminates the structure of the turbulence, and a period of time is required for the flow to recover from the initial conditions. In reacting flow simulations in which the turbulence is decaying, an adjustment time is quite undesirable. For the case of partially premixed and nonpremixed combustion, the problem is compounded by the fact that both the velocity and scalar fluctuating fields must be specified. In this case, not only are there recovery periods for each field, but also for the correlation between the fields.

The outline of this study is as follows. We briefly describe the direct numerical simulation methodology used in this study, including the procedure for removing the small-scale structure while maintaining the energy content. The conditions under which the data can be interpreted in the context of nonpremixed combustion are then given, where additional quantities of interest in reacting flows are presented. The unmodified and structureless data are compared in terms of the vorticity and scalar gradient variables along with terms in their transport equations. In addition to examining the vorticity and scalar gradient field individually, their correlated behavior, represented by the scalar product of the vorticity and scalar gradient, is also examined. After the effect of removing the small-scale structure on these variables has been assessed, the ability of various fields to recover from the removal of the turbulent structure is assessed.

1.1 Numerical simulation

The simulations used to investigate the effects of small scale structure on mixing are described in detail in Ruetsch and Maxey (1991, 1992); a brief review is given here. The simulation is based on a pseudospectral method in a cube of side $L = 2\pi$

with 120 grid points in each direction. The flow field is periodic in all three directions and governed by the rotational form of the incompressible Navier-Stokes equations:

$$\frac{\partial u_i}{\partial t} + \epsilon_{ijk}\omega_j u_k = -\frac{\partial}{\partial x_i}\left(P + \frac{1}{2}u_j u_j\right) + \frac{\partial^2 u_i}{\partial x_j \partial x_j}$$

along with the incompressibility condition

$$\frac{\partial u_i}{\partial x_i} = 0.$$

Here u_i and ω_i are the components of the velocity and vorticity fields in the x_i direction, P is the pressure, and ϵ_{ijk} is the Levi-Civita pseudotensor. The simulations begin with the velocity field at rest, $u_i = 0$, and the turbulence is generated by a source term added to the Navier-Stokes equations, which is itself a solution to the Langevin equation as described in Eswaran and Pope (1988a, 1988b). When the velocity field has reached stationary conditions, the scalar field is introduced.

The initial scalar field configuration has a uniform gradient in the x_3−direction with no fluctuations. The scalar field, Z, is governed by the convective-diffusive equation:

$$\frac{\partial Z}{\partial t} + u_i\frac{\partial Z}{\partial x_i} = \mathcal{D}\frac{\partial^2 Z}{\partial x_i \partial x_i}. \tag{1}$$

To account for the nonperiodic scalar field in the periodic domain, the scalar field Z is decomposed into the mean and fluctuating components:

$$Z = \beta x_3 + \theta \tag{2}$$

where β is the uniform gradient and θ is the periodic fluctuating field used in the computations. Substituting Eq. 2 into Eq. 1 we obtain the governing equation for the fluctuations of θ:

$$\frac{\partial \theta}{\partial t} + u_i\frac{\partial \theta}{\partial x_i} + \beta u_3 = \mathcal{D}\frac{\partial^2 \theta}{\partial x_i \partial x_i}.$$

After the introduction of the scalar field, the simulation is run for more than ten large-eddy turnover times, resulting in stationary scalar and velocity fields. The microscale Reynolds number for the simulations is $Re_\lambda = 59$, the dissipation length scale to Taylor microscale ratio is $l/\lambda = 4.0$, the Taylor microscale to Kolmogorov microscale ratio is $\lambda/\eta = 15.1$, the Schmidt number is unity, and the uniform gradient, β, is $1/(2\pi)$. These fields are then used as the "initial conditions" for the rest of the study. Before continuing the simulations, however, a method of removing the small-scale structure must be applied to this data.

1.2 Removal of the small-scale structure

In this section we describe the method used to remove the small-scale structure. We do not wish to remove the energy associated with the small scales, just the organized structure. Removal of both the small scale structure and the energy

has been examined in other studies (She *et al.* 1988). As mentioned previously, structureless fields are often used to initialize turbulence simulations. We can mimic this procedure by manipulating the phase information in our simulation data.

The algorithm for the removal of organized structure is simply phase scrambling. More precisely, the Fourier coefficients of the velocity and scalar fields from the simulation data, $\hat{u}_i$ and $\hat{\theta}$ respectively, are modified in the following manner:

$$\tilde{u}_i = \hat{u}_i e^{\imath \phi_1}; \qquad \tilde{\theta} = \hat{\theta} e^{\imath \phi_2}.$$

where the phase angles, ϕ_1 and ϕ_2, are random numbers between zero and 2π. This process leaves the energy of each mode the same, $\tilde{\theta}\tilde{\theta}^* = \hat{\theta}\hat{\theta}^*$. While this scrambling is sufficient for the scalar data, the resulting velocity field does not satisfy continuity. To correct this, the filter

$$\bar{u}_i = S(k_1, k_2, k_3) \left(\delta_{ij} - \frac{k_i k_j}{k^2} \right) \tilde{u}_j$$

is used to remove the dilatational component from $\tilde{u}_i$, producing the incompressible field $\bar{u}_i$. Here k_i is the wavenumber component, and δ_{ij} is the Kronecker delta function. The scaling parameter $S(k_1, k_2, k_3)$ rescales the velocity so that $\bar{u}_i \bar{u}_i^* = \hat{u}_i \hat{u}_i^*$, thus the kinetic energy at a particular wavenumber remains unchanged. (One could scramble the data using phase angles that are constrained by the condition $k_i \tilde{u}_i = 0$.)

Phase scrambling is performed only once but is applied at all wavenumbers. Therefore, the scrambling removes the structure from all scales, not just the small scales. However, we will see that for the vorticity and scalar gradient, it is primarily the small scales that are affected.

1.3 Relation to nonpremixed flames

Before we begin the analysis of the simulation data, we describe how the data can be interpreted in terms of the topic that motivated this study, that of nonpremixed combustion, and under what conditions this interpretation is valid. Although the uniform scalar gradient may correspond to several physical quantities such as temperature or salinity, the motivation for this study is reacting flows, so we interpret the scalar in terms of species concentrations. For a one-step chemical scheme where fuel and oxidizer react to form a product,

$$F + rO \longrightarrow (1 + r)P$$
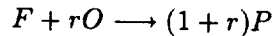
we can define the mixture fraction as

$$Z = \frac{1 + rY_F - Y_O}{1 + r}$$

where r is the mass-based stoichiometric coefficient and Y_F and Y_O are the fuel and oxidizer mass fractions. In the limit of zero heat release and fast chemistry,

the passive scalar field with a uniform gradient can be considered a simulation of nonpremixed combustion where the mixture fraction is governed by Eq. 1. Under these assumptions, the flame will be located on the stoichiometric surface

$$Z_{st} = \frac{1}{1+r}.$$

One of the main issues in turbulent combustion is how flame surface area is increased by turbulent fluctuations, thus increasing the amount of fuel and oxidizer in contact and the global burning rate. By considering all possible values of Z_{st} by specifying different values of r in these passive simulations, the entire flow field can be considered to be an ensemble of flames used to generate well-converged statistics of flame surface area growth. In contrast, cases which account for heat release have a single fixed stoichiometric value, and therefore only a portion of the computational domain lies within the flame.

The average flame surface area over all possible values of Z_{st} in the computational domain can be determined from the techniques developed for calculating the propagation speed of turbulent premixed flames using the G-equation (Kerstein and Ashurst 1988). As a consequence of their initial condition for the scalar field of $G(x_i, t = 0) = x_1$, the turbulent to laminar flame surface area ratio was determined to be $\langle |\nabla G| \rangle$. For our case with an initial condition of $Z(x_i, t = 0) = \beta x_3$, the turbulent to laminar flame surface area ratio is:

$$\frac{A_T}{A_L} = \frac{\langle |\nabla Z| \rangle}{\beta}.$$

With an expression for the average flame surface area in our computational domain, we can now turn our attention to the results on how the removal of small-scale structure affects mixing and the production of flame surface area.

2. Accomplishments

The results from this study are presented in two parts. The effect of the removal of the turbulent structure from the velocity and scalar fields on the vorticity and scalar gradient, and the correlation between these fields, is explored first. Once the effect of removing the structure from these fields has been established, the unmodified and scrambled fields are used as initial conditions in further simulations in the second part. The recovery of the scrambled fields is then evaluated along with the consequences of this recovery for turbulent mixing.

2.1. Comparison of the initial fields

Before we compare the differences between the unmodified and scrambled data sets, we should review their similarities. The magnitude of the Fourier coefficients remains unchanged so that the energy and dissipation spectra for the two fields are the same. In addition, any quantities that can be derived from the spectra are also identical. For example, the two-point correlations, being the Fourier transform of the energy spectra, are unaffected by the scrambling process. Mean quantities
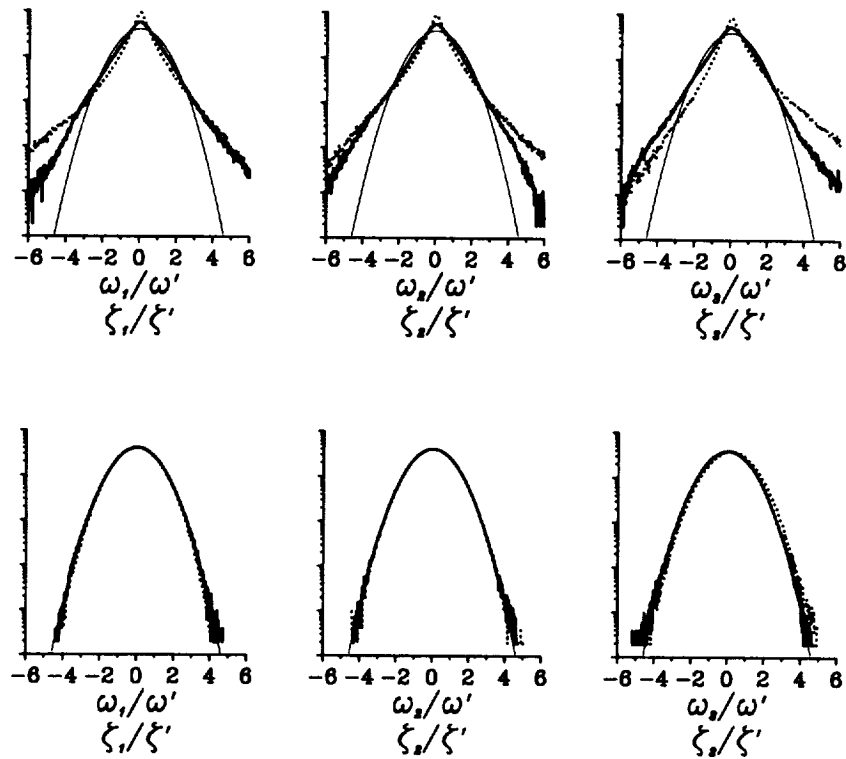
FIGURE 1. Probability density functions for the vorticity (——) and scalar gradient ($\cdots$) components. The unscrambled data (top) exhibit exponential tails while the scrambled data (bottom) show Gaussian distributions. (A Gaussian distribution is shown by the thin solid line in each plot.)

associated with the spectra such as the mean kinetic energy, enstrophy, and square of the scalar gradient are also invariant with respect to the scrambling operation.

Although phase scrambling produces fields with some global parameters unchanged, many properties of the two fields change drastically when the phase information is modified. These features deal with the localized structures in isotropic turbulence, and the aim of this paper is to determine how these small scales differ and what the consequences of the differences are.

We use gradients of the scalar and velocity fields to examine the small scales. The velocity gradient tensor yields the vorticity, ω_i, and the rate of strain tensor, $S_{ij} = 1/2(\partial u_i/\partial x_j + \partial u_j/\partial x_i)$. We also consider the scalar quantities associated with these variables such as the local enstrophy, $\omega_i\omega_i$, and the kinematic part of the kinetic energy dissipation, $S_{ij}S_{ij}$. The gradient of the scalar field is denoted by $\zeta_i = \partial Z/\partial x_i$.

We begin the comparison between unmodified and scrambled data by examining the probability distributions of the vorticity and scalar gradient fields. It is
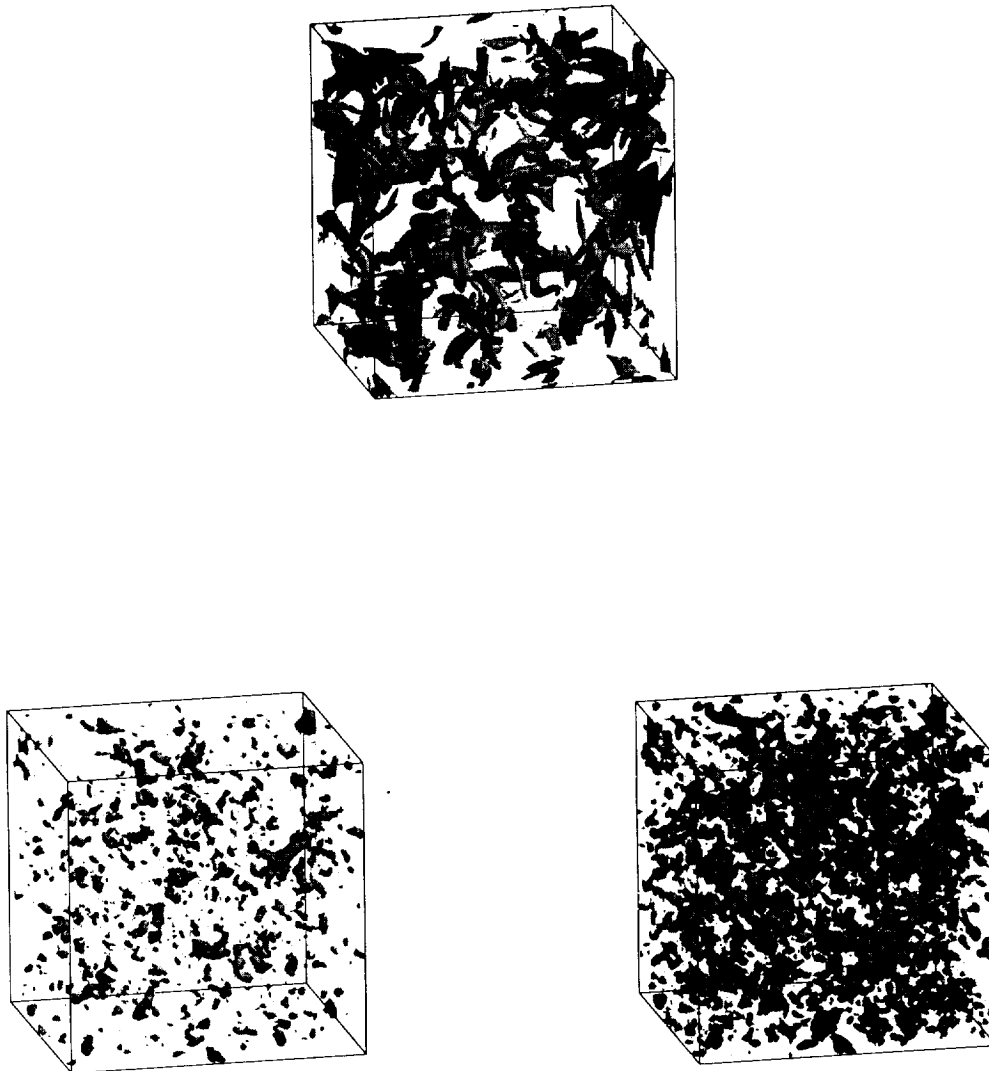
FIGURE 2. Local enstrophy fields before and after the phase information is scrambled. The local enstrophy prior to scrambling is shown on the top with a threshold of $4\langle\omega_i\omega_i\rangle$, containing 3.8% of the total volume. The local enstrophy after phase scrambling with a threshold of $4\langle\omega_i\omega_i\rangle$ is shown on the bottom left, which contains 0.2% of the volume. The local enstrophy after phase scrambling with a threshold in local enstrophy of $2.86\langle\omega_i\omega_i\rangle$, which contains the same volume as the figure of unscrambled data on the top, is shown bottom right.

well known that velocity derivative statistics of isotropic turbulence exhibit non-Gaussian tails in their probability distributions (Batchelor and Townsend 1949, Kuo and Corrsin 1971). Bershadskii *et al.* (1993) found a universal value for the slopes of these exponential tails from various experiments, which agrees well with the results in Fig. 1. The scalar gradient also exhibits this non-Gaussianity, only to a greater extent as seen in Fig. 1.

In addition to the difference in the statistical distributions between the original and scrambled datasets, their spatial distributions also differ. The small-scale structure of the local enstrophy fields in Fig. 2 show that the vortex tubes ("worms") observed in the unmodified data disappear as a result of phase scrambling. This apparent lack of structure in the scrambled data is not a result of the smaller volume taken obtained in thresholding by the local enstrophy. Even when this threshold for the scrambled data is reduced so that the same volume is occupied in both the scrambled and unmodified cases, (top and bottom right images in Fig. 2), we observe no coherent structures in the scrambled case.

The scalar gradient field also shows large variations in structure between the unmodified and scrambled cases. The original $\zeta_i \zeta_i$ field shows sheet-like structures at the small scales as depicted in Fig. 3. As with the scrambled enstrophy fields, the scrambled scalar gradient field shows an absence of these structures regardless of the value of the threshold. These effects are exactly what one would expect. The existence of coherent structures implies coherence in phase among components at different wavenumbers. Obviously phase scrambling destroys that coherence.

Another effect of scrambling concerns the ability of the vorticity and scalar gradient fields to recover from scrambled conditions. While this recovery is examined in detail later, the mechanisms involved in the recovery are discussed here. These are apparent in the transport equations for the local enstrophy and square of the scalar gradient. The local enstrophy transport equation is:

$$\frac{D\omega_i\omega_i}{Dt} = 2\omega_i\omega_j S_{ij} + \nu \left\{ \frac{\partial^2 \omega_i\omega_i}{\partial x_j \partial x_j} - 2\frac{\partial \omega_i}{\partial x_j}\frac{\partial \omega_i}{\partial x_j} \right\}. \tag{3}$$

Analogously, the transport equation for the square of the scalar gradient is:

$$\frac{D\zeta_i\zeta_i}{Dt} = -2\zeta_i\zeta_j S_{ij} + \mathcal{D} \left\{ \frac{\partial^2 \zeta_i\zeta_i}{\partial x_j \partial x_j} - 2\frac{\partial \zeta_i}{\partial x_j}\frac{\partial \zeta_i}{\partial x_j} \right\}. \tag{4}$$

These transport equations contain production, diffusion, and dissipation terms on their right-hand sides. The production of local enstrophy and scalar gradient squared, through vortex stretching and scalar gradient compression, results from the preferential alignment of the vorticity and scalar gradient vectors with the axes of the principal rates of strain. The phase scrambling procedure affects these production terms. The probability distributions of the production terms displayed in Fig. 4 indicate that the exponential tails in the unmodified case are removed by phase scrambling. In addition, the probability distributions of the production terms in the unmodified flow are asymmetric as they yield net positive production of local enstrophy and square of the scalar gradient.
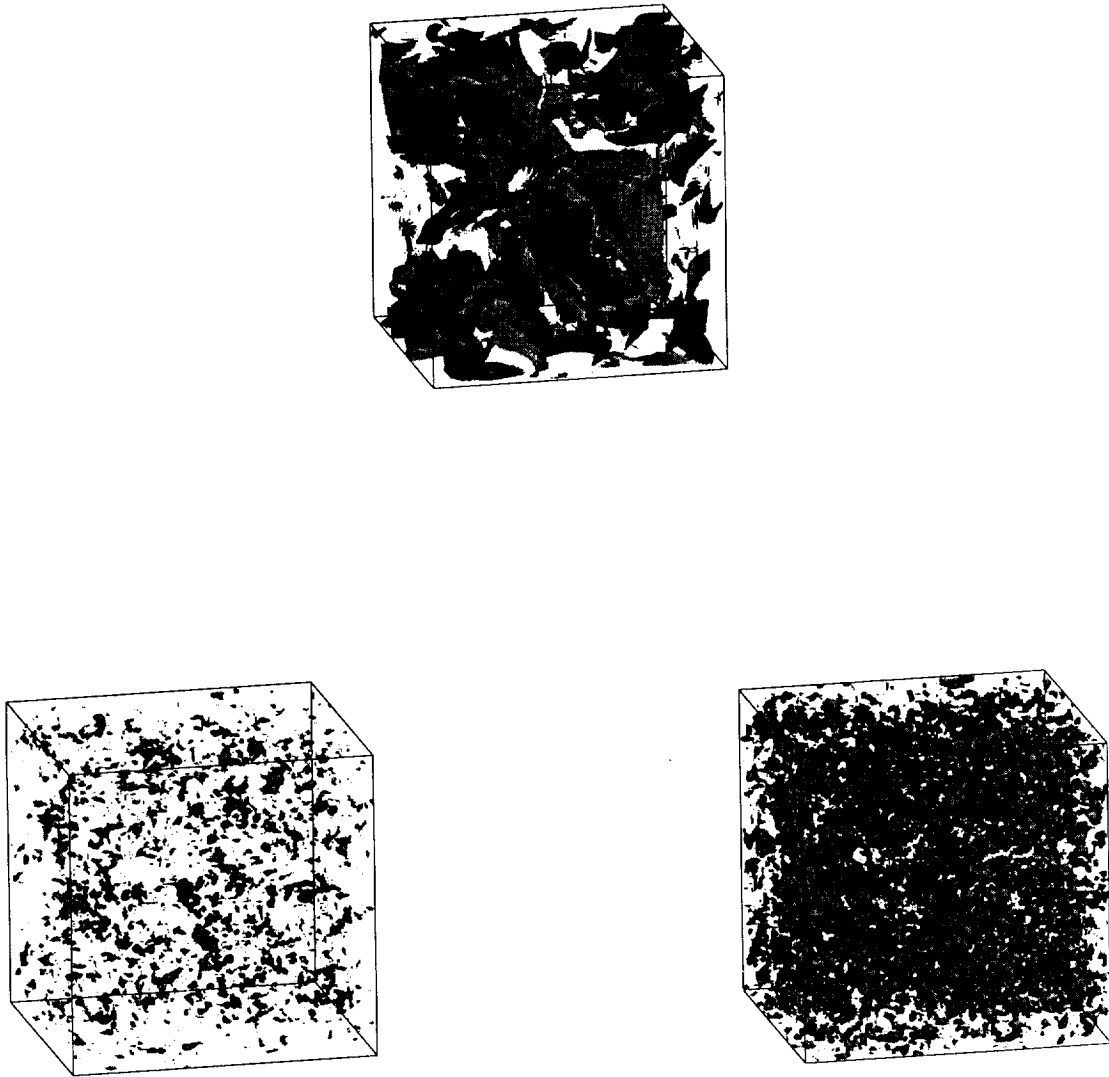
FIGURE 3. Square of the scalar gradient before and after the phase information is scrambled. The square of the scalar gradient prior to scrambling is shown on the top with a threshold of $4\langle\zeta_i\zeta_i\rangle$, containing 4.1% of the total volume. The data after phase scrambling with a threshold of $4\langle\zeta_i\zeta_i\rangle$ is shown bottom left which contains 0.2% of the volume. The data after phase scrambling with a threshold of $2.55\langle\zeta_i\zeta_i\rangle$, which contains the same volume as the figure of unscrambled data on the top, is shown bottom right.
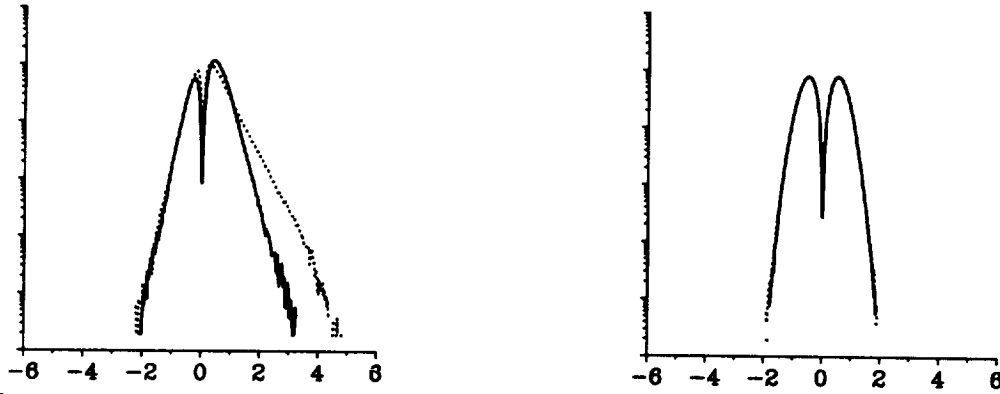
FIGURE 4. Probability distributions for the normalized production terms for local enstrophy, $(\omega_i\omega_j S_{ij})^{1/3}/(\omega'^2 S')^{1/3}$ (——), and square of the scalar gradient, $(-\zeta_i\zeta_j S_{ij})^{1/3}/(\zeta'^2 S')^{1/3}$ ($\cdots$), for the unmodified data (left) and scrambled data (right). The asymmetry of the curves indicates the overall positive production that occurs in turbulent flows, with the greater asymmetry occurring in the scalar field.

While the distribution functions for both local enstrophy and scalar gradient squared production show skewness towards positive production, this skewness is greater for the scalar gradient squared production. This difference in production results in the scalar gradient being large relative to the vorticity (Fig. 1). For the case of unity Schmidt number this difference is not intuitive, but it can be explained by the two-way coupling between the vorticity and strain fields, whereas the passive scalar field has no effect on the strain field. The effect of the strain rate on the vorticity is apparent in Eq. 3. The inverse coupling, that of the vorticity on the strain rate, can be observed in the transport equation for $S_{ij}S_{ij}$, which in incompressible flows is:

$$\frac{DS_{ij}S_{ij}}{Dt} = - 2S_{ij}S_{jk}S_{ki} - \frac{1}{2}\omega_i\omega_j S_{ij}$$
$$- 2S_{ij}\frac{\partial^2 P}{\partial x_i \partial x_j} + \nu\left\{\frac{\partial^2 S_{ij}S_{ij}}{\partial x_k \partial x_k} - 2\frac{\partial S_{ij}}{\partial x_k}\frac{\partial S_{ij}}{\partial x_k}\right\} \tag{5}$$

When $\omega_i\omega_j S_{ij} > 0$, positive production of enstrophy occurs as seen from Eq. 3. This situation, however, results in negative production of strain as is apparent from the second term on the right-hand side of Eq. 5. In terms of the evolution of these fields, an intense localized strain field may create a patch of strong vorticity, but at its own expense. A strong patch of scalar gradient can be created, however, with no adverse effect on the local strain that produced it. Due to these differences in vorticity-strain and scalar gradient-strain couplings, one would expect to observe stronger tails in the (positive) scalar gradient production PDF and scalar gradient PDF than in their vorticity-based counterparts. It is interesting to note that the tails for negative production of both scalar gradient squared and local enstrophy coincide.

Up to this point we have discussed the vorticity and scalar gradient fields, and the effect of phase scrambling on these fields, independently. We now turn our attention
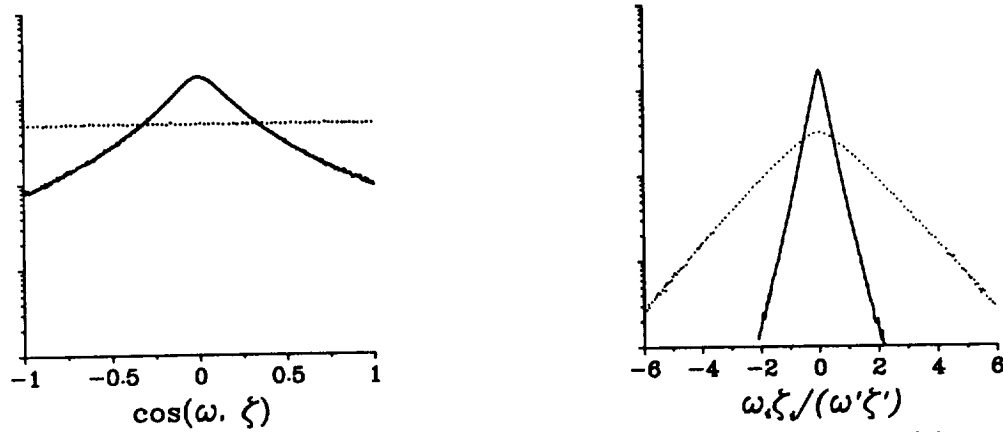
FIGURE 5. Probability distributions of the alignment between the vorticity and scalar gradient vectors (left) and $\omega_i \zeta_i$ (right) for the unmodified data (———) and scrambled data ($\cdots$).

to the correlation between these fields. Two measures of this correlation are the scalar product of the vorticity and the scalar gradient, $\omega_i \zeta_i$, and the alignment between these vectors, $\cos(\omega, \zeta)$. The term $\omega_i \zeta_i$ has contributions from both the alignment of the vectors and their magnitudes, whereas $\cos(\omega, \zeta)$ contains only information on their alignment. The probability distributions of these quantities indicate that the scrambling process has a large effect on the correlation between the velocity and scalar fields. The PDF of the alignment between the vorticity and scalar gradient vectors in Fig. 5 shows a peak when these vectors are orthogonal. Figure 5 also shows an even stronger peak in $\omega_i \zeta_i$, indicating that the large magnitude events in vorticity and strain tend to occur when the two vectors are orthogonal. So, while the intense small scales are represented by the tails in the vorticity and scalar gradient PDFs, they appear in the peaks of the $\omega_i \zeta_i$ and $\cos(\omega, \zeta)$ PDFs.

As with the vorticity and scalar gradient variables, some light can be shed on the dynamics of $\omega_i \zeta_i$ by its transport equation:

$$\frac{D}{Dt}(\omega_i \zeta_i) = \mathcal{D}\left\{ \frac{\partial^2 \omega_i \zeta_i}{\partial x_j \partial x_j} + (Sc - 1)\frac{\partial}{\partial x_j}\left(\zeta_i \frac{\partial \omega_i}{\partial x_j}\right) - (Sc + 1)\frac{\partial \omega_i}{\partial x_j}\frac{\partial \zeta_i}{\partial x_j} \right\}. \qquad (6)$$

The strain rate does not enter this equation explicitly, so there is no production term. In fact, under inviscid and nondiffusive conditions, $\omega_i \zeta_i$ is conserved:

$$\frac{D}{Dt}(\omega_i \zeta_i) = 0.$$

Since modifications to $\omega_i \zeta_i$ occur on a diffusive time scale, in high Reynolds number or large Peclet number flows we expect a slower recovery of this field relative to the recovery of the vorticity and scalar gradient fields, which are affected by inviscid production terms.

The last fields we compare between the scrambled and unmodified data are the flame surfaces. The turbulent to laminar flame surface area for the unmodified
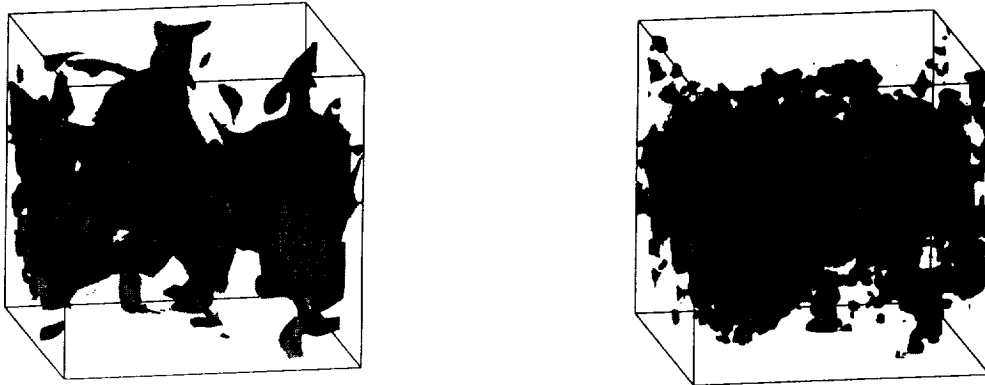
FIGURE 6.   Flame surface area ($Z_{ST} = 0.5$) for the initial fields of the unmodified (left) and scrambled (right) data. The surface area of the scrambled field is larger due to the large number of pockets relative to the more connected unmodified surface.

scalar field, averaging over all stoichiometric surfaces, is $A_T/A_L = 6.93$. Phase scrambling increases this value to $A_T/A_L = 8.71$. In this sense, for a given scalar fluctuation spectrum, turbulence does not produce the maximum flame surface area. The elevated flame surface area after scrambling can be seen in Fig. 6 where we observe a highly disconnected flame surface in the scrambled field; conversely, the flame surface of the unmodified scalar field shows a few pockets, but is relatively coherent and connected. In order to have a distorted but connected flame surface, phase coherence is important. When the phase information is randomized, scalar deviations occur in small disconnected pockets which have a large flame surface area.

2.2 Evolution of the scrambled fields

Having described the difference between the original and scrambled initial conditions, we now turn our attention to the evolution of the velocity and scalar fields and, in particular, to how the modified fields recover from their scrambled states.

Before phase scrambling, the simulations were run with the velocity forced until both scalar and velocity fields reached stationary conditions. Therefore, we expect the simulations using the unmodified data as initial conditions to maintain their stationary states with small fluctuations due to the stochastic forcing of the velocity field. By comparing the simulations using scrambled and unmodified fields as initial conditions, the influence of phase scrambling becomes apparent. For example, the skewness and kurtosis time series of a longitudinal velocity derivative are shown in
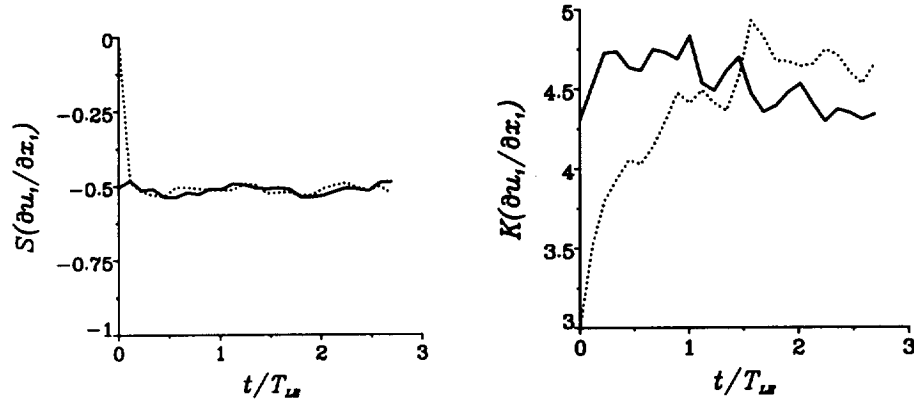
FIGURE 7. Skewness (left) and kurtosis (right) time series of the normal velocity derivative for the simulation with unmodified (———) and scrambled ($\cdots$) initial conditions. The skewness for the scrambled case recovers quickly to the stationary value, while the kurtosis requires on the order of one large-eddy turnover time to recover.

Fig. 7. The velocity derivative skewness for the unmodified data is roughly constant at a value of -0.5, whereas the scrambled initial data have zero velocity derivative skewness but recover to the unmodified case value very quickly, in a fraction of an eddy turnover time. The velocity derivative kurtosis for the unmodified case fluctuates about a mean value of 4.5, while the scrambled initial data have a kurtosis of 3 which recovers relatively slowly, taking about one large-eddy turnover time to reach the unmodified value.

The rapid adjustment of the velocity derivative skewness in Fig. 7 has strong implications for the enstrophy evolution. The velocity derivative skewness can be expressed in terms of the vorticity and strain-rate tensor (Rotta 1972) as:

$$\left\langle \left(\frac{\partial u_1}{\partial x_1}\right)^3 \right\rangle = -\frac{2}{35} \langle \omega_i \omega_j S_{ij} \rangle .$$

The term in brackets on the right-hand side is simply the volume average enstrophy production that occurs in Eq. 3. As the velocity derivative skewness, which is related to enstrophy production, quickly recovers from the scrambled initial conditions, one would expect the local enstrophy itself to recover quickly. From the time sequences of PDFs in Fig. 8, we see that this is the case. These time sequences show that the adjustment from the Gaussian tails of the scrambled initial condition to the exponential tails of the unmodified data occurs in less than $0.5 T_{LE}$ for both vorticity and scalar fields. One also observes that the vorticity and scalar gradient structures recover quickly; see Figs. 9 and 10, respectively.

While the structure and intensity of the vorticity and scalar gradient fields recover within a large-eddy turnover time, the correlation between them does not recover as quickly. As stated previously, while the local enstrophy and square of the scalar gradient equations contain inviscid or nondiffusive production terms, the transport
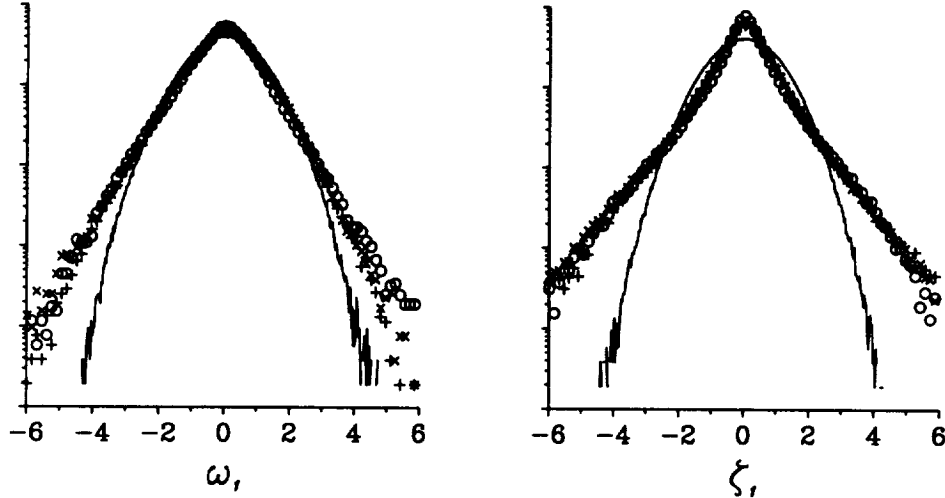
FIGURE 8.   PDF time series of the x_1-component of the vorticity (left) and scalar gradient (right) of the scrambled simulations at times $t/T_{LE} = 0$ (———), $t/T_{LE} = 0.25$ (+), $t/T_L E = 0.5$ (×), and $t/T_{LE} = 1$ (o). The adjustment of the tails from Gaussian to exponential form occurs within $0.5T_{LE}$ for both vorticity and scalar gradient fields.

equation for $\omega_i\zeta_i$ has no such term. Its recovery from the initial conditions occurs only through diffusive processes. The slower recovery is clear in the $\omega_i\zeta_i$-PDF time sequence in Fig. 11.

In addition to the lack of an inviscid/nondiffusive production term, there is another reason for the slower recovery of the $\omega_i\zeta_i$ PDF. The scrambling process affects the $\omega_i\zeta_i$ PDF more than either the vorticity or scalar gradient PDFs. The $\omega_i\zeta_i$-PDF of the unmodified data has a strong peak while the same PDF after scrambling is relatively flat. The scrambling process affects the tails of the vorticity and scalar gradient PDFs.

We now turn our attention to the effect of scrambling on turbulent mixing. In particular, we wish to assess how the flame surface area is affected by scrambling. Flame surface area production depends strongly on the correlation between the flow and scalar fields. The fractional change in flame surface area is given by the flame stretch (Candel and Poinsot 1990), which for a nonpropagating, nondiffusive surface in an incompressible flow is:

$$K = \frac{1}{A}\frac{dA}{dt} = -n_i n_j S_{ij} \qquad (7)$$

where A represents the surface area and the normal to the flame surface is given by $n_i = -\zeta_i/\sqrt{\zeta_j\zeta_j}$. Therefore, flame surface area production is closely related to the scalar gradient production term, $-\zeta_i\zeta_j S_{ij}$. The recovery of the scalar gradient production from scrambled initial conditions could be examined from its transport

FIGURE 9.   Time sequence of the evolution of the local enstrophy field from the scrambled simulations. Surfaces of $\omega_i\omega_i > 4\langle\omega_i\omega_i\rangle$ are shown at times $t/T_{LE} = 0$ (top left), $t/T_{LE} = 0.25$ (top right), $t/T_{LE} = 0.5$ (bottom left), $t/T_{LE} = 1.0$ (bottom right).
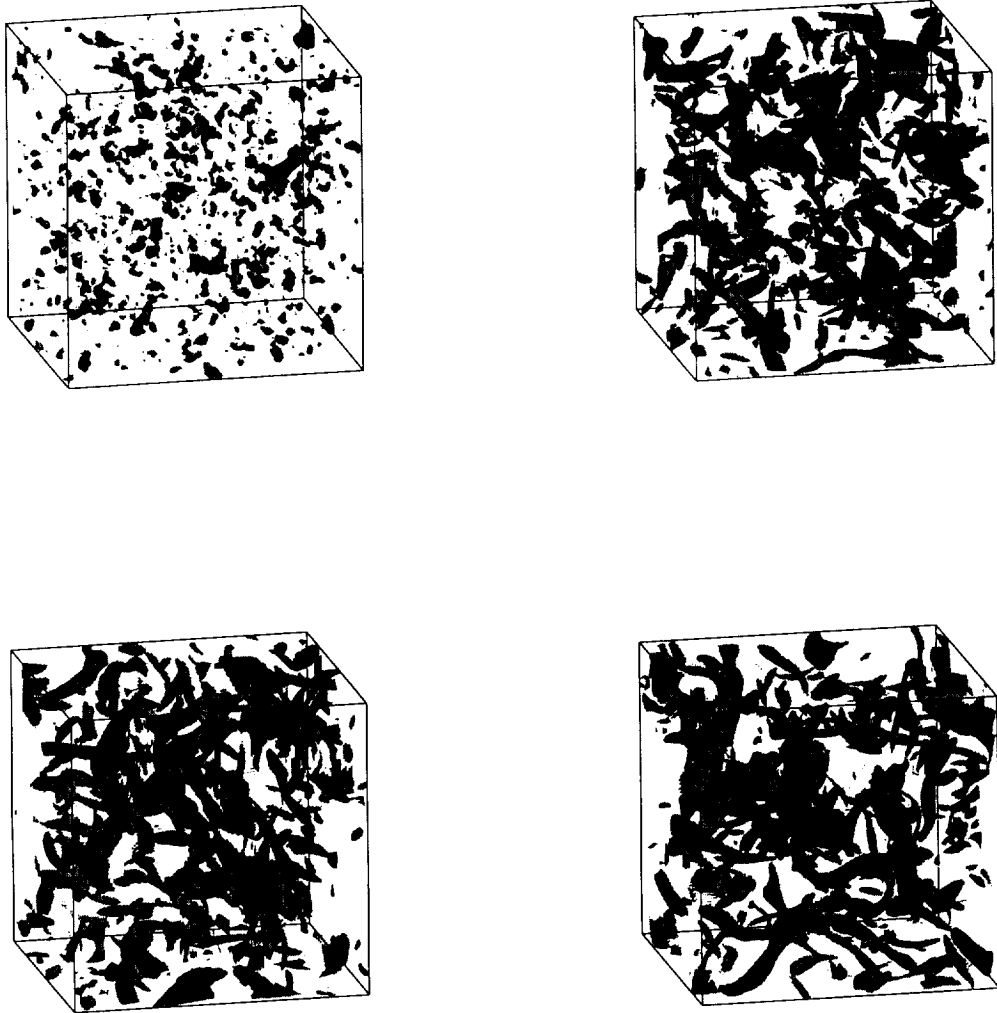
FIGURE 10.   Time sequence of the evolution of the scalar dissipation field from the scrambled simulations. Surfaces of $\zeta_i\zeta_i > 4\langle\zeta_i\zeta_i\rangle$ are shown at times $t/T_{LE} = 0$ (top left), $t/T_{LE} = 0.25$ (top right), $t/T_{LE} = 0.5$ (bottom left), $t/T_{LE} = 1.0$ (bottom right).
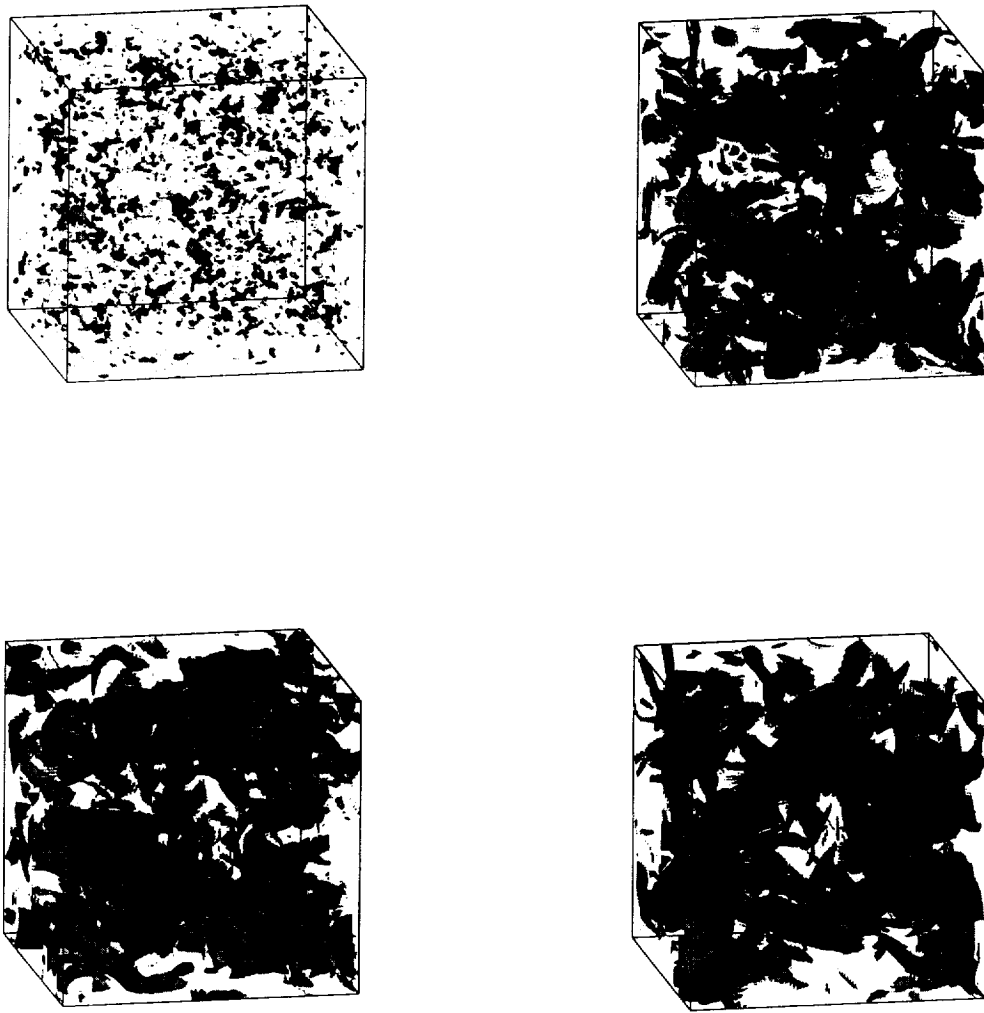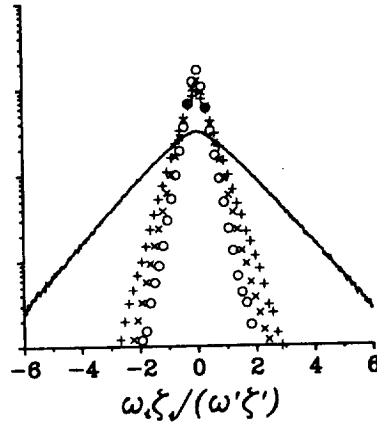
FIGURE 11. PDF time sequence of $\omega_i \zeta_i$ for the scrambled simulations at times $t/T_{LE} = 0$ (———), $t/T_{LE} = 0.25$ (+), $t/T_{LE} = 0.5$ (×), and $t/T_{LE} = 1$ (o).

equation,

$$\frac{D}{Dt}\left(-\zeta_i\zeta_j S_{ij}\right) = 2\frac{\partial u_k}{\partial x_i}\zeta_j\zeta_k S_{ij} + S_{ik}S_{kj}\zeta_i\zeta_j + \frac{1}{4}\left\{(\omega_i\zeta_i)^2 - \omega_i\omega_i\zeta_j\zeta_j\right\}$$
$$+ \zeta_i\zeta_j\frac{\partial^2 P}{\partial x_i\partial x_j} + \mathcal{D}\left\{2\zeta_i S_{ij}\frac{\partial^2 \zeta_j}{\partial x_k\partial x_k} - Sc\,\zeta_i\zeta_j\frac{\partial^2 S_{ij}}{\partial x_k\partial x_k}\right\}$$

however, we shall take a different approach. Rather than use the correlation between the strain and scalar gradient, we shall use the correlation between the vorticity and scalar gradient, $\zeta_i\omega_i$, along with their alignment, $\cos(\zeta_i,\omega_i)$. Although the connection between $-\zeta_i\zeta_j S_{ij}$ and flame surface area production is obvious from Eq. 7, the connection between $\zeta_i\omega_i$ and flame surface area production is not as apparent. This connection is demonstrated in Fig. 12 where two cases of a vortex tube interacting with a flame are portrayed, one with the scalar gradient and vorticity orthogonal, $\omega_i\zeta_i = 0$, and the other with these vectors colinear. When the vorticity and mixture fraction gradient are colinear, the motion induced by the vortex convects material elements within the flame surface, and no increase in flame surface area results. When the vorticity is orthogonal to the mixture fraction gradient, the motion induced by the vortex is perpendicular to the flame surface, and the flame "wraps" or is stretched around the vortex. Although this process does not produce flame surface area, it indicates the presence of flame surface area production elsewhere in the flow. This is seen in the schematic diagram of Fig. 13, which - although representing a simplified two-dimensional view of turbulence - demonstrates the balance between the (net) flame surface area generation through strain and folding and wrapping of the flame by vorticity. Flame surface area is also destroyed by diffusion in the vortex core, but this occurs after the wrapping by the vortex.

Having established a mechanism for flame surface area production in terms of $\omega_i\zeta_i$, we can now return to the PDF in Fig. 11 and relate the effects of scrambling on the generation of flame surface area. Flame surface area generation is greatest when there is a strong peak in the $\omega_i\zeta_i$-PDF at the origin. The scrambled initial
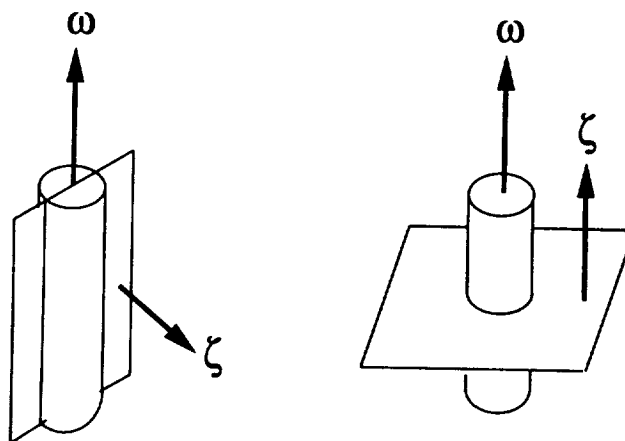
FIGURE 12.   A vortex tube and flame surface (mixture fraction isopleth) interaction. When the vorticity and scalar gradient are orthogonal to each other ($\omega_i \zeta_i = 0$), as in the case on the left, the flame is wrapped around the vortex, increasing the flame surface area. When these two vectors are parallel (right), transport occurs within flame and no increase in area occurs.

condition has a relatively weak peak. Furthermore, the recovery to a strong peak proceeds slowly as we have discussed. Therefore, we expect that the scrambled initial condition will produce a flow with a deficit in flame surface area production relative to the unmodified flow. From examining time series of the flame surface area in Fig. 14, we see that these predicted trends do occur. In this figure, the evolution of the flame surface area is shown for the following initial conditions: unmodified flow, flow with the velocity and scalar fields scrambled, and flow with only the scalar field scrambled. Despite the elevated initial value, the flame surface area quickly drops well below the value in the unmodified case within a large-eddy turnover time for both scrambled cases as the reduced flame surface area production is insufficient to balance the diffusive effects. When only the scalar field is scrambled, the flame surface area recovers after approximately three large-eddy turnover times. For the case in which both the velocity and scalar fields are scrambled, the flame surface area has not recovered even after three large-eddy turnover times. The evolution of the scrambled flame surface during the first large-eddy turnover time is shown in Fig. 15. The destruction of the small detached pockets of the scrambled flame surface within the first quarter large-eddy turnover time corresponds to the rapid decrease in flame area observed in Fig. 14. The absence of intense flame "wrapping" results in this smaller flame area, relative to the unmodified case, for a substantial period of time.

**Flame surface production
via strain,** $-\zeta_i \zeta_j S_{ij} > 0$

**Flame surface accumulation
via vorticity,** $\zeta_i \omega_i \sim 0$
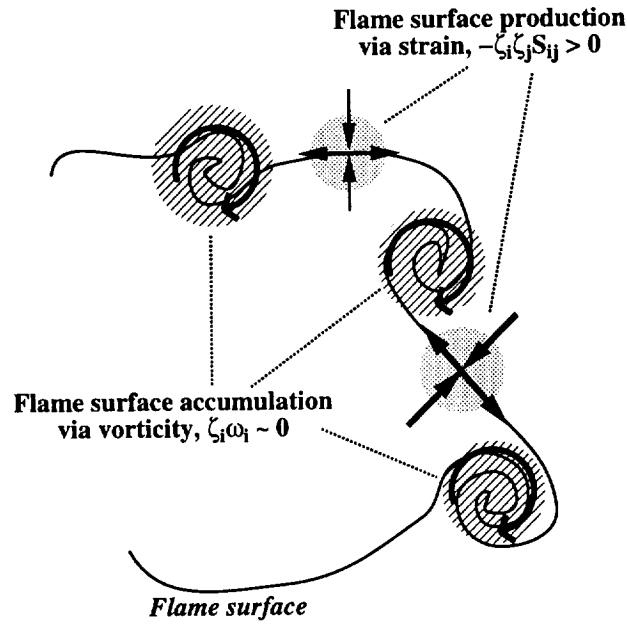
Flame surface

FIGURE 13. A depiction of a flame surface being stretched by strain and folded and wrapped by vorticity. Both processes require correlated velocity and scalar fields and must coexist in order to conserve flame surface area.
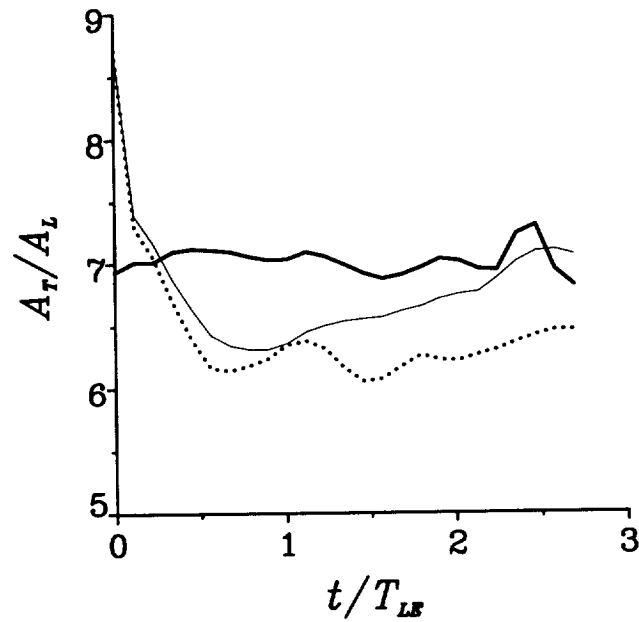
FIGURE 14. Time series of turbulent to laminar flame surface area, A_T/A_L, for simulations with original (———), scrambled scalar (———), and both scrambled scalar and velocity fields ($\cdots$).
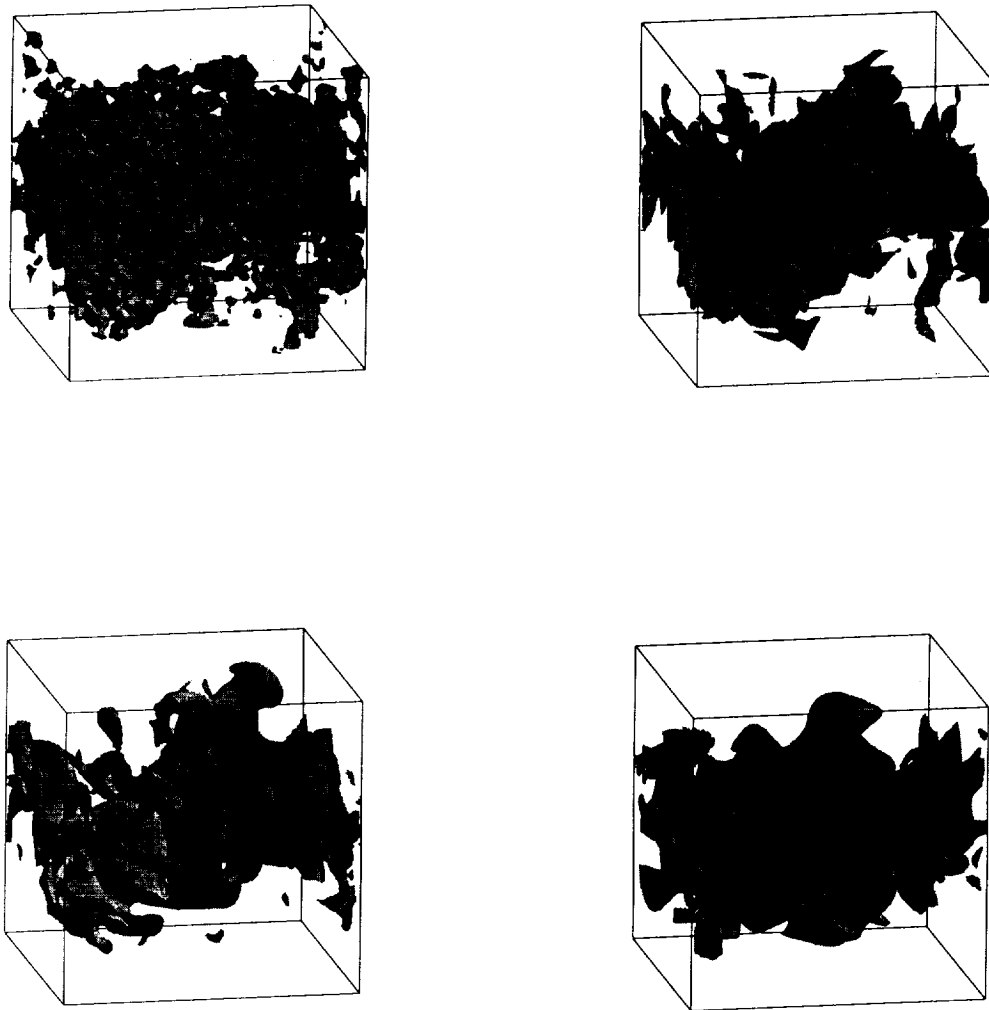
FIGURE 15. Time sequence of the evolution of the flame surface for $Z_{ST} = 0.5$ at times $t/T_{LE} = 0$ (top left), $t/T_{LE} = 0.25$ (top right), $t/T_{LE} = 0.5$ (bottom left), and $t/T_{LE} = 1.0$ (bottom right).

3. Conclusions and future work

The effect of using turbulent fields with arbitrary phase information as initial conditions for numerical simulations has been explored in this paper. The fields with arbitrary phase information show Gaussian rather than exponential tails in the

vorticity and scalar gradient PDFs. In addition to the decreased volume of regions with intense vorticity and scalar gradient, they also show a lack of structure.

Through the use of numerical simulations and analysis of the transport equations for the vorticity and scalar gradient, the recovery from the scrambled initial conditions was found to proceed quickly for the vorticity and scalar gradient fields, whereas the correlation between these fields, $\omega_i \zeta_i$, recovers more slowly. The main reason for the slower recovery is that strain has no direct effect on the evolution of $\omega_i \zeta_i$. This correlation plays a role in flame surface area production; scrambling of phase information results in decreased flame surface area production for a prolonged time.

As expressed in the introduction, the motivation for this work was to determine how using initial fields with arbitrary phases affects the results of simulations of reacting flows. For simulations of premixed combustion where a planar flame can propagate into a turbulent region, the only relevant fluctuating fields initially are the velocity field and its derivatives. (The flame's propagation provides a nondiffusive mechanism for $\omega_i \zeta_i$ recovery.) Therefore, the use of scrambled initial velocity data should not cause problems provided enough time (one large-eddy turnover time) is allowed for the velocity field to recover. However, this adjustment period is undesirable, especially when the turbulence field is not stationary but decaying as is the case in codes which use a compressible formulation of the equations. In such simulations, it would be beneficial to use initial velocity fields taken from incompressible simulations combined with the perturbation procedure of Ristorcelli and Blaisdell (1997), which relaxes these incompressible fields to those of weakly compressible turbulence.

For nonpremixed and partially premixed combustion, the use of initial fields with arbitrary phase information is more problematic. Although the vorticity and scalar gradient fields recover their phase information in approximately a large-eddy turnover time, their correlated behavior recovers much more slowly. This correlated behavior is important as it provides flame surface area production. For simulations of nonpremixed or partially premixed combustion with a decaying velocity field, there is little hope that any turbulence will be left by the time the correlated behavior re-establishes itself. For such cases it is necessary to use initial conditions with proper phase information. Such initial fields can be generated from incompressible simulations with mean scalar profiles and then modified using Ristorcelli and Blaisdell's technique.

REFERENCES

ASHURST, WM. T., KERSTEIN, A. R., KERR, R. M., AND GIBSON, C. H. 1987 Alignment of vorticity and scalar gradient with strain rate in simulated Navier-Stokes turbulence. *Phys. Fluids.* **30**, 2343.

BATCHELOR, G. K., AND TOWNSEND, A. A. 1949 The nature of turbulent motion at large wavenumbers. *Proc. R. Soc. London Ser. A.* **199**, 238.

BERSHADSKII, A., KIT, E., AND TSINOBER, A. 1993 On universality of geometrical invariants in turbulence - Experimental results. *Phys. Fluids.* **5**, 1523.

BETCHOV, R. 1956 An inequality concerning the production of vorticity in isotropic turbulence. *J. Fluid Mech.* **1**, 497.

CAI, X. D., O'BRIEN, E. E., AND LADIENDE, F. 1996 Uniform mean scalar gradient in grid turbulence: Asymptotic distribution of a passive scalar. *Phys. Fluids.* **8**, 2555.

CANDEL, S. M., AND POINSOT, T. J. 1990 Flame stretch and the balance equation for the flame area. *Comb. Sci. and Tech.* **70**, 1.

CORRSIN, S. 1952 Heat transfer in isotropic turbulence. *J. Appl. Physics.* **23**, 113.

ESWARAN, V., AND S. B. POPE, S. B. 1988 An examination of forcing in direct numerical simulations of turbulence. *Comput. Fluids.* **16**, 257.

ESWARAN, V. AND S. B. POPE, S. B. 1988 Direct numerical simulations of the turbulent mixing of a passive scalar. *Phys. Fluids.* **31**, 506.

HOLZER, M., AND SIGGIA, E. D. Turbulent mixing of a passive scalar. Phys. Fluids. *6*. **1820.**

JABERI, F. A., AND MILLER, R. S., MADINA, C. K., AND GIVI, P. 1996 Non-gaussian scalar statistics in homogeneous turbulence. *J. Fluid Mech.* **313**, 241.

KERR, R. M. 1985 Higher-order derivative correlations and the alignment of small-scale structures in isotropic numerical turbulence. *J. Fluid Mech.* **153**, 31.

KERR, R. M. 1990 Velocity, scalar, and transfer spectra in numerical turbulence. *J. Fluid Mech.* **211**, 309.

KUO, A. Y.-S., AND CORRSIN, S. 1971 Experiments on internal intermittency and fine-structure distribution functions in fully turbulent fluid. *J. Fluid Mech.* **50**, 285.

KUO, A. Y.-S., AND CORRSIN, S. 1972 Experiments on the geometry of fine-structure regions in turbulent fluid. *J. Fluid Mech.* **56**, 447.

OVERHOLT, M. R., AND POPE, S. B. 1996 Direct numerical simulation of a passive scalar with imposed mean gradient in isotropic turbulence. *Phys. Fluids.* **8**, 3128.

PUMIR, A. 1994a A numerical study of the mixing of a passive scalar in three dimensions in the presence of a mean gradient. *Phys. Fluids.* **6**, 2118.

PUMIR, A. 1994b Small-scale properties of scalar and velocity differences in three-dimensional turbulence. *Phys. Fluids.* **6**, 3974.

RISTORCELLI, J. R., AND BLAISDELL, G. A. 1997 Consistent initial conditions for the DNS of compressible turbulence. *Phys. Fluids.* **9**, 4.

ROTTA, J. C. 1972 *Turbulente Strömungen*, B. G. Teubner, Stuttgart.

RUETSCH, G. R., AND MAXEY, M. R. 1991 Small-scale features of the vorticity and passive scalar fields in homogeneous isotropic turbulence. *Phys. Fluids A.* **3**, 1587.

RUETSCH, G. R., AND MAXEY, M. R. 1992 The evolution of small-scale structures in homogeneous isotropic turbulence. *Phys. Fluids A.* **4**, 2747.

SCHWARZ, K. W. 1990 Evidence for organized small-scale structure in fully developed turbulence. *Phys. Rev. Lett.* **64**, 415.

SHE, Z.-S., AND JACKSON, E., AND ORSZAG, S. A. 1988 Scale-dependent intermittency and coherence in turbulence. *J. Sci. Comput.* **3**, 407.

SHE, Z.-S., AND JACKSON, E., AND ORSZAG, S. A. 1990 Intermittent vortex structures in homogeneous isotropic turbulence. *Nature.* **344**, 226.

SIGGIA, E. D. 1981 Numerical study of small-scale intermittency in three-dimensional turbulence. *J. Fluid Mech.* **107**, 375.

TONG, C., AND WARHAFT, Z. 1994 On passive scalar derivative statistics in grid turbulence. *Phys. Fluids.* **6**, 2165.

TROUVÉ, A., AND POINSOT, T. 1994 The evolution equation for the flame surface density in turbulent premixed combustion. *J. Fluid Mech.* **278**, 1.

VERVISCH, L. 1992 Study and modeling of finite rate chemistry effects in turbulent non-premixed flames. *Annual Research Briefs,* Center for Turbulence Research, Stanford Univ./NASA Ames, 411.

VINCENT, A., AND MENEGUZZI, M. 1991 The spatial structure and statistical properties of homogeneous isotropic turbulence. *J. Fluid Mech.* **225**, 1.

VINCENT, A., AND MENEGUZZI, M. 1994 The dynamics of vorticity tubes in homogeneous turbulence. *J. Fluid Mech.* **258**, 245.

Turbulent premixed combustion in the laminar flamelet and the thin reaction zone regime

By H. Wenzel[1]

1. Motivations and objectives

1.1 Definition of the thin reaction zone regime

Turbulent premixed combustion is a complex and important process in many engineering applications. The two-way coupling between the turbulent flow and the chemical kinetics produces an intractable problem in its entirety, and simplifications to either the fluid dynamical or chemical components must be made.

Simplifications to the turbulent premixed combustion problems can be made by restricting the conditions under which flames are studied. One method of classifying premixed flame is demonstrated by the plot in Fig. 1. Here the flame is categorized according to two ratios of turbulent flow and flame scales: (1) the velocity ratio u'/s_L, where u' is the root mean square velocity fluctuation and s_L is the laminar burning velocity, and (2) ℓ/ℓ_F, where ℓ is the integral length scale of the turbulence and ℓ_F is the flame thickness. We can subdivide this domain into several regimes. For values of $u'/s_L < 1$ one speaks of the wrinkled flame regime. As the turbulence intensity increases, flames enter the corrugated flame regime. This regime exists as one increases turbulence intensity until the Karlovitz number, defined as

$$\text{Ka} = t_F/t_\eta = \ell_F^2/\eta^2 \, , \tag{1}$$

reaches unity. The Karlovitz number is the ratio of the flame to Kolmogorov time scales, where $t_F = \ell_F/s_L$, and the Kolmogorov length and times scales are $\eta = (\nu^3/\epsilon)^{1/4}$ and $t_\eta = (\nu/\epsilon)^{1/4}$. As seen in Eq. 1, unity Ka also implies unity $\ell_F/\eta = 1$ (for cases with unity Schmidt number Sc = 1).

One can also define a Karlovitz number in terms of the reaction zone thickness. This is advantageous when one considers large activation energy asymptotics (e.g. Peters 1992a), where the flame structure of a one-step chemical mechanism consists of a chemically inert preheat zone and a reaction zone, (Fig. 2). The thickness of the reaction zone δ is typically one order of magnitude smaller than the preheat zone. This gives rise to the definition of a Karlovitz number based on the reaction zone thickness:

$$\text{Ka}_\delta = \delta^2/\eta^2 = \text{Ka} \, \delta^2/\ell_F^2 \, . \tag{2}$$

From this expression, one can derive relations between the turbulence intensity u'/s_L and the length scale ratio ℓ/ℓ_F, again under the assumption of Sc = 1:

$$u'/s_L = \text{Re} \, (\ell/\ell_F)^{-1} = \text{Ka}^{2/3}(\ell/\ell_F)^{1/3} \, . \tag{3}$$

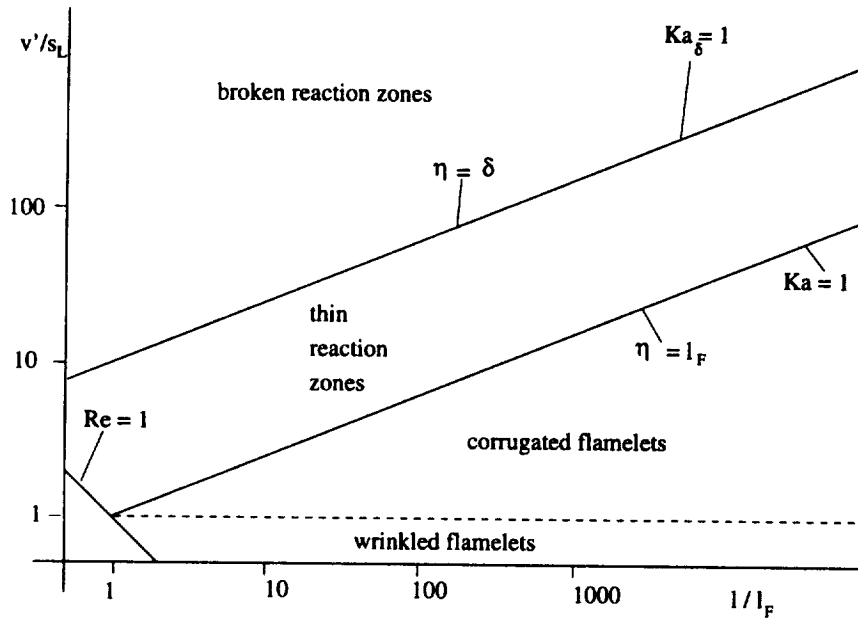1 Institut für Technische Mechanik, RWTH Aachen, Germany

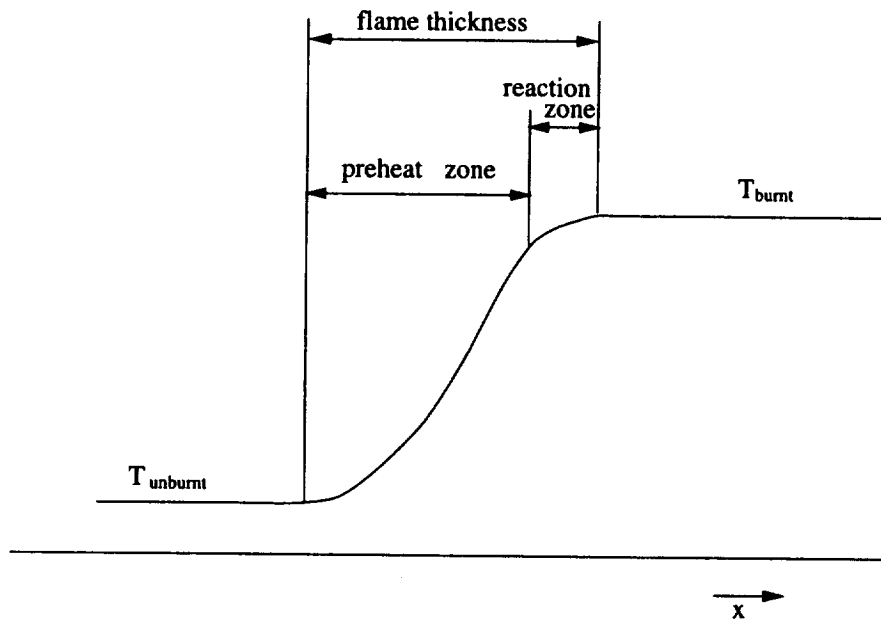FIGURE 1. Regime diagram for premixed turbulent combustion.

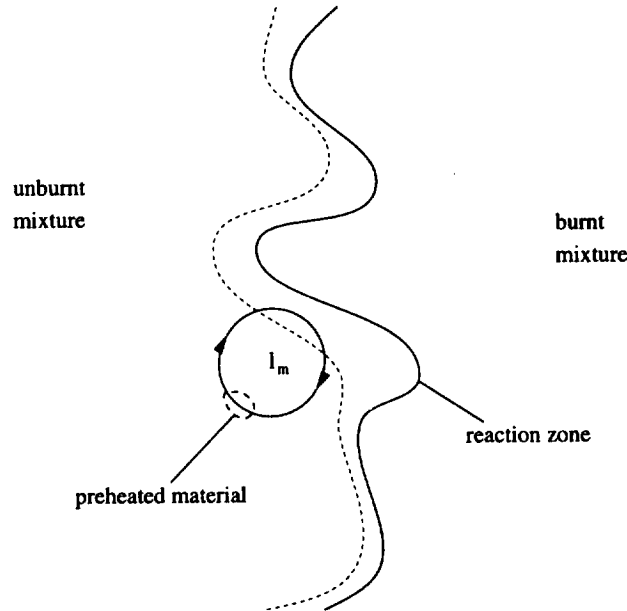FIGURE 2. Asymptotic structure of a premixed laminar flame.

FIGURE 3. Interaction between an eddy of the size l_m and a turbulent flame front.

The line where $Ka_\delta = 1$, or $\eta = \delta$, depicts the separation between the thin and broken reaction zones.

The broken reaction zone regime is not accessible with the methods to be used in this study, and the corrugated and wrinkled flamelet regimes have been examined earlier (Peters 1992b). Therefore, the focus of this work is turned to the only recently described thin reaction zone regime (Peters 1997). In this regime the Kolmogorov length is less than the flame thickness but larger than the reaction zone thickness, so that the smallest turbulent eddies may penetrate the preheat zone but not the reaction zone. The characteristic length scale for this regime is defined as the size of an eddy in the inertial range which has a turnover time t_m equal to the flame time t_F:

$$l_m = (\varepsilon t_F^3)^{1/2} , \qquad (4)$$

where ε is the turbulent dissipation u'^3/ℓ. If one interprets the flame time as the time needed to diffuse heat or chemical species over the flame thickness, $t_F = l_F^2/D$, then the physical meaning of l_m becomes clear as the maximum distance that preheated fluid can be transported away from the reaction zone by turbulent eddies, as illustrated in Fig. 3.

1.2 Derivation of a G-equation for the thin reaction zone regime

In the following, an equation for the displacement of the reaction zone is derived which is very similar to the G-equation for the flamelet regime. Because the turbulence now controls mixing in the preheat zone, the propagation velocity is no longer determined by the mixture alone, but by diffusion and transport effects within the preheat zone as well. We take a similar approach to Ruetsch & Broadwell 1995 and

Vervisch 1995, and start from a diffusive-reactive equation for the deficient species of a one-step chemical reaction:

$$\rho\left(\frac{\partial Y}{\partial t} + \mathbf{v}\cdot\nabla Y\right) = \nabla\cdot(\rho D\nabla Y) + \dot{\omega}\,. \tag{5}$$

Here Y is the mass fraction, $\mathbf{v}$ the fluid velocity, ρ the density, and $\dot{\omega}$ the chemical source term. We can define an isoscalar surface $Y(\mathbf{x},t) = Y_0$ that marks the instantaneous position of the reaction zone. Its substantial derivative, $DY/Dt|_{Y=Y_0}$, vanishes everywhere and it therefore satisfies the equation:

$$\frac{\partial Y}{\partial t} + \nabla Y\cdot\left.\frac{d\mathbf{x}}{dt}\right|_{Y=Y_0} = 0\,. \tag{6}$$

The normal vector on this isosurface which points into the unburnt region, $\mathbf{n} = \nabla Y/|\nabla Y|$, can be used to combine Eqs. 5 and 6 to derive an expression for the displacement speed of the reaction zone:

$$\left.\frac{d\mathbf{x}}{dt}\right|_{Y=Y_0} = \mathbf{v} - \left[\frac{\nabla\cdot(\rho D\nabla Y) + \dot{\omega}}{\rho|\nabla Y|}\right]\mathbf{n}\,. \tag{7}$$

We now want to make the formal connection with the G equation derived by Kerstein *et al.* 1988. We introduce a scalar G so that the isosurface $G = G_0$ is identical to the isosurface $Y = Y_0$ and $G < G_0$ corresponds to the unburnt region. A similar equation to Eq. 6 can be written in terms of G:

$$\frac{\partial G}{\partial t} + \nabla G\cdot\left.\frac{d\mathbf{x}}{dt}\right|_{G=G_0} = 0\,. \tag{8}$$

Eq. 7 may be introduced into Eq. 8 if we realize that the displacement speed and the normal vector are identical for both fields:

$$\frac{\partial G}{\partial t} + \mathbf{v}\cdot\nabla G = -\left[\frac{\nabla\cdot(\rho D\nabla Y) + \dot{\omega}}{\rho|\nabla Y|}\right]|\nabla G|\,, \tag{9}$$

The diffusive term on the right hand side can be split into a curvature term and a term representing diffusion along the normal:

$$\frac{\partial G}{\partial t} + \mathbf{v}\cdot\nabla G = -D\,\kappa|\nabla G| - \left[\frac{\mathbf{n}\cdot\nabla(\rho D\,\mathbf{n}\cdot\nabla Y) + \dot{\omega}}{\rho|\nabla Y|}\right]|\nabla G|\,. \tag{10}$$

where κ denotes the curvature $\kappa = \nabla\cdot\mathbf{n}$ and the normal vector is now given by the G field, $\mathbf{n} = -\nabla G/|\nabla G|$.

The expression in square brackets has the dimension of a velocity. In a steady, laminar, unstrained, planar flame it would be equal to the laminar burning velocity s_L^0, but here the propagation speed of the thin reaction zone can no longer be

prescribed due to the dependence on fluctuating quantities in the preheat zone upstream. It is reasonable, however, to expect it to be of the same order of magnitude as s_L^0. If this hypothesis holds, normalizing Eq. 10 with the Kolmogorov length and time scale shows each term of the order of unity, except for the last one, which is of the order of Ka^{-2} and therefore small in the thin reaction zone regime (Peters 1997). This assumption is supported by an earlier direct numerical simulation of the G-equation (Wenzel & Peters 1997). These simulations contained a laminar burning velocity that depended linearly on strain and curvature and showed a similar behavior of the eikonal propagation term becoming less important when the thin reaction zone regime is reached. In order to analyze Eq. 10, we use the statistical mean value for the expression in the square brackets, which is called $-s_L^*$, and the model G-equation for the thin reaction zone regime can be written:

$$\frac{\partial G}{\partial t} + \mathbf{v} \cdot \nabla G = -D\,\kappa|\nabla G| + s_L^*|\nabla G| \, . \tag{11}$$

The similarity to the G-equation for the laminar flamelet regime becomes apparent when we present the equation we are going to use for the direct numerical simulations in that regime:

$$\frac{\partial G}{\partial t} + \mathbf{v} \cdot \nabla G = -D_{\mathcal{L}}\,\kappa|\nabla G| + s_L^0|\nabla G| \, , \tag{12}$$

where $D_{\mathcal{L}} = s_L^0 \mathcal{L}$ is the Markstein diffusivity taken with the Markstein length $\mathcal{L}$. This equation comes from an asymptotic analysis of the response of the flame speed on curvature and stretch (Clavin & Williams 1982) where the influence of the stretch has been neglected.

Both Eqs. 11 and 12 show exactly the same structure; the only differences are the replacement of the Markstein diffusivity $D_{\mathcal{L}}$ by the mass diffusivity D and the laminar burning velocity s_L^0, which is determined only through chemistry, by the propagation velocity of the reaction layer s_L^*, which is influenced by an interaction between the chemistry and the flow field. Another distinction between these equations should be noted. In the laminar flamelet regime the propagation term $s_L^0|\nabla G|$ plays the most prominent role, whereas in the thin reaction zone regime the evolution of G is primarily influenced by the curvature term $-D\,\kappa|\nabla G|$

1.3 The equation for $\overline{|\nabla G|}$ for the laminar flamelet and the thin reaction zone regime

In modeling turbulent premixed combustion the determination of the ratio of the turbulent to the laminar burning velocity plays an important role. Kerstein *et al.* 1988 could show that this quantity is, under some restrictions, equal to the absolute value of the gradient of G, which is called $\bar{\sigma} \equiv \overline{|\nabla G|}$ in the subsequent part of this work.

Although an exact formulation for $\bar{\sigma}$ can be derived directly from Eqs. 11 and 12 by applying the operator $-(\mathbf{n} \cdot \nabla)$ and then averaging (Wenzel & Peters 1997,

Keller 1996), the resultant expression is intractable, and therefore a model equation for $\overline{\sigma}$ which is valid for both regimes was proposed by Peters 1997:

$$\frac{\partial\overline{\sigma}}{\partial t} + \overline{v}\cdot\nabla\overline{\sigma} = -D_t\overline{\kappa}(\overline{\sigma})|\nabla\overline{\sigma}| + c_0\frac{-\overline{v'_\alpha v'_\beta}}{\overline{k}}\frac{\partial\overline{v_\alpha}}{\partial x_\beta}\overline{\sigma} + c_1\frac{D_t(\nabla\overline{G})^2}{\overline{G'^2}}\overline{\sigma} - c_2\frac{s_L^0\overline{\sigma}^2}{\overline{G'^2}^{1/2}} - c_3\frac{D\overline{\sigma}^3}{\overline{G'^2}}.$$
(13)

The terms on the left-hand side are the unsteady change and the convection of the mean value, the first term on the right-hand side is the turbulent transport, the second the production by mean velocity gradients, and the third the production by turbulent fluctuations of the velocity field. The remaining two terms are sink terms; the one proportional to $\overline{\sigma}^2$ due to flame propagation is of most importance in the flamelet regime. The last one comes from the curvature term in the G-equation and is most active in the thin reaction zone regime. For a further details regarding this equation the readers are referred to Peters (1997).

In the following sections of this study we will carry out a direct numerical simulation for turbulent premixed combustion both in the laminar flamelet and in the thin reaction zone regime by solving Eqs. 11 and 12 numerically for the case of homogeneous, isotropic turbulence. The objective is to gain insight into the physical interaction of a propagating scalar with the flow field and to check the assumptions that had to be made in the process of deriving the equation for the mean value of σ, Eq. 13. Furthermore, we want to determine the model constants that appear in that equation.

This aim puts some severe demands on the numerical scheme to be used: (1) it has to be highly accurate to avoid numerical diffusion contaminating the solution, and (2) it has to be stable for a wide range of the two parameters: the burning velocity and diffusivity. The first goal was achieved by using a pseudo-spectral code. To accomplish the second goal a new numerical scheme had to be developed that allows for the formation of cusps in a iso-G front.

2. Accomplishments

As mentioned above, we want to solve the G-equation subjected to homogeneous, isotropic turbulence. The underlying turbulent flow field was calculated using a pseudo-spectral code developed and described in Ruetsch 1992. This code is able to compute the development of a dissipative scalar in addition to the flow field. This feature was used to solve the complete left-hand side of the G-equation and the diffusive term on the right-hand side. The main part of the following section focuses on the incorporation of the eikonal propagation term $s_L|\nabla G|$ into the computer code and the evaluation of the numerical scheme by comparing it to an analytical solution of the G-equation.

2.1 A numerical scheme for the G-equation

To make the following part as clear as possible, we turn attention now solely towards the propagation term of the G-equation; convection and diffusion are not taken into account. The equation we want to solve then is:

$$\frac{\partial G}{\partial t} = s_L|\nabla G|,$$
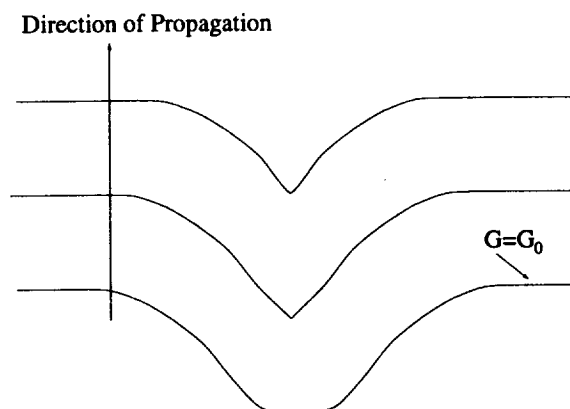(14)

Direction of Propagation

FIGURE 4.   Formation of cusps.

where s_L is a prescribed constant propagation velocity.

It is well known (e.g. Kerstein *et al.* 1988, Sethian 1996) that this equation governs the motion of a front due to Huygen's principle through a quiescent medium. One feature of this type of propagation is the formation of cusps from an initially smooth front. This is illustrated in Fig. 4. At the location of these cusps, the derivative of G undergoes a jump, which makes the numerical treatment of Eq. 14 quite difficult. Some previous studies (e.g. Im *et al.* 1996) therefore tried to suppress the formation of cusps by choosing the diffusivity in the G-equation (Eqs. 11 and 12) large enough so the sharp gradients did not occur. This way of circumventing this difficulty is no longer applicable if we want to analyze these equations in the zero diffusivity limit.

We will use a numerical scheme that was originally developed for a scalar hyperbolic conservation law and was applied to this class of level-set equations by Sethian (1996). It has previously been used on this particular problem by Wenzel & Peters (1997) in the framework of a second-order finite-difference method.

To see the connection between the G-equation and a hyperbolic equation we rewrite Eq. 14 for the one dimensional case:

$$\frac{\partial G}{\partial t} - s_L |\nabla G| = \frac{\partial G}{\partial t} - s_L \frac{\partial G/\partial x}{|\partial G/\partial x|} \frac{\partial G}{\partial x} = \frac{\partial G}{\partial t} \pm s_L \frac{\partial G}{\partial x} = 0 \ . \qquad (15)$$

This is actually a hyperbolic conservation equation for G with $\pm s_L$ as the signal velocity.

If we adopt this interpretation of the G-equation, we may use an upwind-scheme for the numerical calculation of this equation. To do so we follow the procedure outlined in Sethian (1996) and transform Eq. 15 again, into an equivalent Hamiltonian formulation:

$$\frac{\partial G}{\partial t} + H\left(\frac{\partial G}{\partial x}\right) = 0 \ , \qquad (16)$$

with the Hamiltonian H defined as:

$$H\left(\frac{\partial G}{\partial x}\right) = -s_L \frac{\partial G/\partial x}{|\partial G/\partial x|} \frac{\partial G}{\partial x} \ . \tag{17}$$

A numerical approximation of this expression might be given in terms of derivatives of the G-field to the left and right of the point x_i where we want to compute the Hamiltonian:

$$H\left(\frac{\partial G}{\partial x}\right)\Bigg|_{x_i} \approx h(D^l G|_{x_i}, D^r G|_{x_i}) \ . \tag{18}$$

The numerical Hamiltonian $h(D^l G|_{x_i}, D^r G|_{x_i})$ is evaluated like the flux function of a Godunov Scheme for a scalar hyperbolic conservation law. Sethian (1996) uses the Enquist-Osher scheme in his work to calculate this quantity, but this scheme suffers from the implicit addition of diffusivity by replacing a compression shock by a compression wave in the corresponding Riemann problem. We therefore use an exact formulation that was given in Hirsch (1990):

$$h(D^l G|_{x_i}, D^r G|_{x_i}) =$$
$$\begin{cases}
min(H(D^l G|_{x_i}), H(D^r G|_{x_i})) & \text{if} \quad D^l G|_{x_i} \leq D^r G|_{x_i} \\
max(H(D^l G|_{x_i}), H(D^r G|_{x_i})) & \text{if} \quad D^l G|_{x_i} > D^r G|_{x_i} \\
max(H(D^l G|_{x_i}), H(D^r G|_{x_i}), H(0)) & \text{if} \quad D^l G|_{x_i} > D^r G|_{x_i} \\
& \quad \wedge D^l G|_{x_i} \cdot D^r G|_{x_i} < 0
\end{cases} \ . \tag{19}$$

Exact in this context means that in the Riemann problem all characteristics retain their nature and no shock is replaced by a fan or vice versa.

The evaluation of Eq. 19 needs the calculation of the spatial derivatives $D^{r/l} G|_{x_i}$ of the G-field. They are computed at points $x_{i\pm1/2} = x_i \pm \Delta x/2$ using a spectral method.

The entire numerical procedure above could only be extended from a finite-difference framework to this pseudo-spectral framework because we followed a view on pseudo-spectral methods that Fornberg (1996) developed. He interprets them as a high-accuracy limit of finite-difference methods, so that the upwind scheme presented here becomes applicable.

To integrate these formulas into the computer code, they need an extension from one to three dimensions. This, fortunately, is quite straightforward. Either in the simplified G-equation Eq. 14 or in Eqs. 11 and 12, the eikonal term $s_L|\nabla G|$ can be computed by the sum of the numerical Hamiltonians h in the $x-$, $y-$, and $z-$directions:

$$s_L|\nabla G| \approx -\left(h(D^l G|_{x_i}, D^r G|_{x_i}) + h(D^l G|_{y_i}, D^r G|_{y_i}) + h(D^l G|_{z_i}, D^r G|_{z_i}) \right) \ . \tag{20}$$
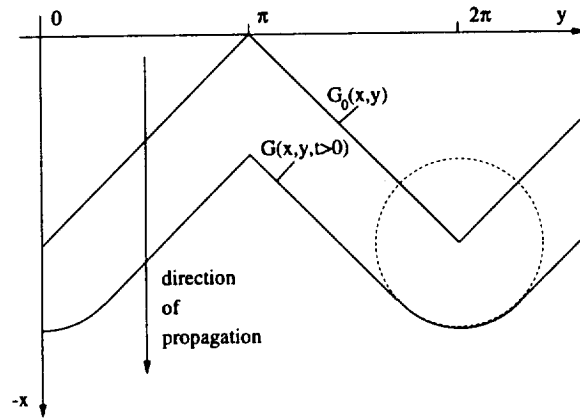
FIGURE 5. Propagation of an iso-G front according to the Huyghen's principle.

The three-dimensional Hamiltonian H which is needed in the evaluation of Eq. 20 is defined as:

$$H\left(\frac{\partial G}{\partial x_\alpha}\right) = -s_L \frac{\partial G/\partial x_\alpha}{\sqrt{(\partial G/\partial x_k)(\partial G/\partial x_k)}} \frac{\partial G}{\partial x_\alpha}, \tag{21}$$

where Einstein's summation convention is only applied to the index k and not to the index α.

2.2 Validation of the numerical scheme for the G-equation

Spectral methods are known to perform quite poorly when discontinuities are present in the solution (Canuto *et al.* 1988). For that reason the numerical scheme developed in this work needs to be validated. To that end we will construct an analytical solution for a two-dimensional version of Eq. 14 with a specific initial condition and check that against the numerical solution with the new scheme.

The derivation of the analytical solution is given first. On a 2π periodic grid, the G-field is initialized as a sawtooth function:

$$G_0(x,y) = \begin{cases} x - y & \text{for} \quad 0 \le y < \pi \\ x + y - 2\pi & \text{for} \quad \pi \le y < 2\pi \end{cases}. \tag{22}$$

Each iso-G front propagates according to the Huyghen's principle, as shown in Fig. 5. The solution for $G(x,y,t)$ can be constructed by geometrical considerations. Only the region $0 \le y < \pi$ is taken into account. The equation for the region $y \le \pi < 2\pi$ immediately follows from symmetry.

The general procedure is to divide the domain into a subdomain which is not influenced by the rarefaction fan that develops at the leading edge of the G-front, and a subdomain which is influenced by it. Within each subdomain the spatial derivatives can be formulated and and then fed into the two-dimensional G-equation, so that the time integration is possible. The outermost point influenced by the
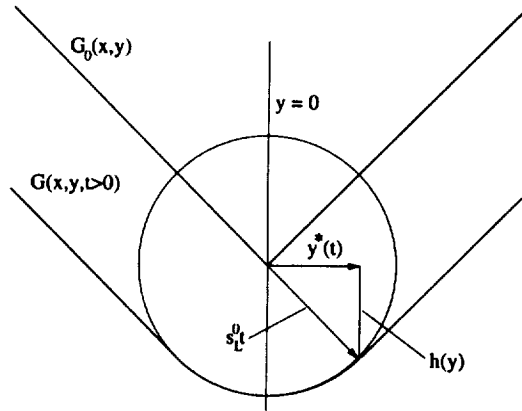
FIGURE 6.   Detail of the the Huyghen's propagation.

rarefaction fan, y^*, travels in y-direction with a constant speed of $s_L/\sqrt{2}$, see Fig. 6. Inside the rarefaction fan the following relation holds:

$$h(y) = \sqrt{(s_L t)^2 - y^2} \Rightarrow \frac{\partial h}{\partial y} \equiv \frac{\partial G}{\partial y} = -\frac{y}{\sqrt{(s_L t)^2 - y^2}} \, . \tag{23}$$

Since all the spatial partial differentials in the G-equation are known, the time integration can be carried out:

$$\frac{\partial G}{\partial t} = s_L \sqrt{\frac{\partial G^2}{\partial x} + \frac{\partial G^2}{\partial y}} = \begin{cases} s_L \sqrt{1 + \dfrac{y^2}{(s_L t)^2 - y^2}} & \text{for} \quad 0 \le y < \dfrac{s_L t}{\sqrt{2}} \\[2em] s_L \sqrt{2} & \text{for} \quad \dfrac{s_L t}{\sqrt{2}} \le y < \pi \end{cases} \, . \tag{24}$$

Defining the time $t^* = \sqrt{2}y/s_L$, when the rarefaction fan reaches a point on the y-axis, one obtains the following analytical equation for $G(x, y, t)$:

$$G(x, y, t) = \begin{cases} G_0(x, y) + \sqrt{2} s_L t & \text{for} \quad t \le t^* \\[1em] G(x, y, t^*) + s_L \displaystyle\int_{t^*}^{t} \sqrt{1 + \dfrac{y^2}{(s_L \tilde{t})^2 - y^2}} d\tilde{t} = & \text{for} \quad t > t^* \\[1em] G_0(x, y) + 2y + \sqrt{(s_L t)^2 - y^2} - \sqrt{(s_L t^*)^2 - y^2} \end{cases} \, . \tag{25}$$

The numerical solution for that problem has to capture the two basic features of a propagating scalar according to the Huyghen's principle (see Fig. 5): (1) the cusps at the back of the front must retain their shape, and (2) circular rarefaction waves must develop at the leading edge. To confirm the reproduction of these feature by the numerical solution, the results of both numerical integration of this problem and the analytical solution from Eq. 25 for two different grid resolutions are presented
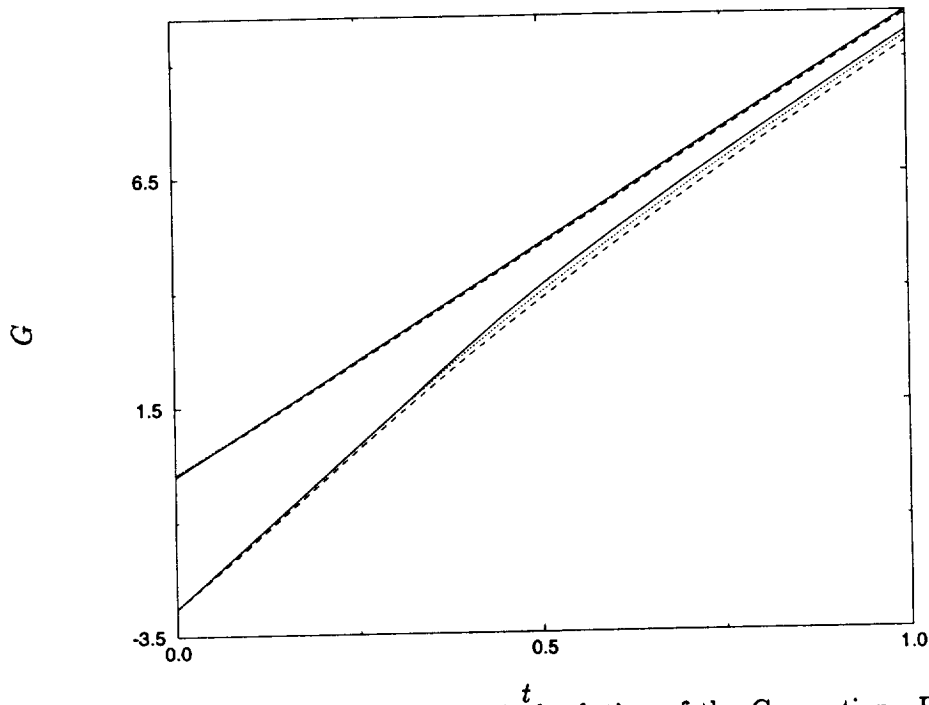
FIGURE 7. Analytical versus numerical solution of the G-equation. Results for two values of y are plotted. $y = 0$ corresponds to the upper set of lines, $y = 2.9$ to the lower set. ———— : analytical solution, – – – – : 32-point grid, ········ : 64-point grid.

in Fig. 7. This plot shows the time evolution for two points on the y-axis, $y = 0$ and $y = 2.9$. The first location was chosen because it is the leading edge of the propagating front, and any violation of feature (2) would become apparent. The ability of the scheme to capture feature (1) is proven with the time evolution at $y = 2.9$. This point lies very close to the the back of the front, and any problems in dealing with the cusp at that location should become apparent there.

The stability of the scheme is demonstrated in Fig 8 where the partial derivative $\partial G / \partial y$ for a typical case during the numerical calculation is shown. There are some overshoots in the vicinity of the cusp at $y = \pi$, but they are not amplified, and they actually become smaller because the jump in the derivatives gets smaller once the rarefaction fan reaches this position. Any disturbances introduced by the discontinuity in the gradient of G smooth out immediately by the variation-diminishing nature of the G-equation, if, in an explicit code, the CFL-condition formulated with the laminar burning velocity is obeyed.

The excellent agreement of the numerical scheme with the closed solution for this test case and its remarkable stability encourage its use in direct numerical simulations of the G-equation for turbulent flow.
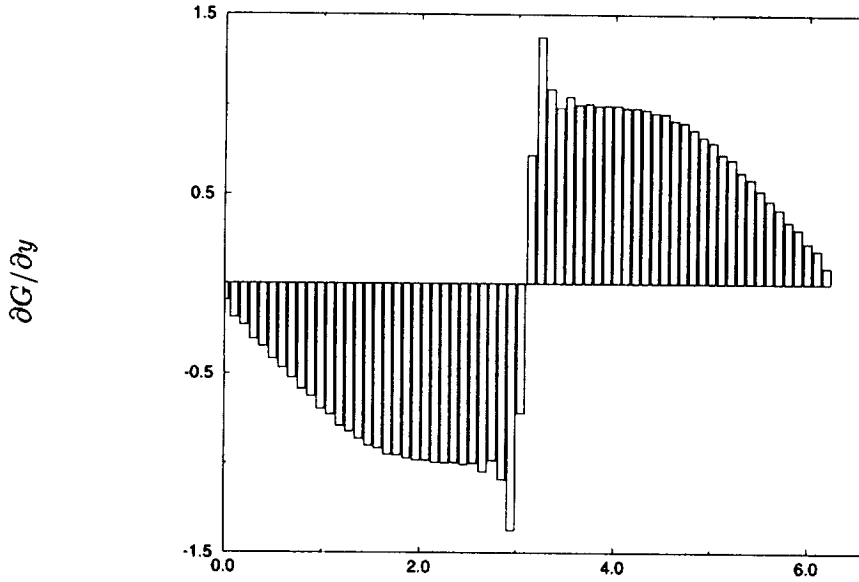
FIGURE 8.   Partial y-derivative of the G-field at $t = 0.1755$.

2.3 The treatment of the curvature term $\kappa|\nabla G|$

The curvature term $\kappa|\nabla G|$ which appears in Eqs. 11 and 12 is basically diffusive in its nature and, therefore, much easier to incorporate into a pseudo-spectral code than the propagation term $s_L|\nabla G|$. However, it is highly nonlinear, and some caution has to be taken to minimize aliasing errors. To achieve this we express the curvature κ as:

$$\kappa = \nabla \cdot \mathbf{n} = \nabla \cdot \left(-\frac{\nabla G}{|\nabla G|}\right) = -\left(\frac{\nabla^2 G|\nabla G| - \nabla G \cdot \nabla|\nabla G|}{|\nabla G|^2}\right) \qquad (26)$$

Using this relation, we can split $\kappa|\nabla G|$ into a linear diffusive term that can be treated very efficiently with a spectral method in Fourier space, and a nonlinear term:

$$-\kappa|\nabla G| = \nabla^2 G - \frac{\nabla G \cdot \nabla|\nabla G|}{|\nabla G|} = \nabla^2 G - \nabla G \cdot \nabla \ln(|\nabla G|) . \qquad (27)$$

The nonlinear product $\nabla G \cdot \nabla \ln(|\nabla G|)$ is computed in physical space. It only contains a double product as opposed to a triple product that occurs in a direct evaluation of Eq. 24 and thus the aliasing error is much smaller.

2.4 Results

The DNS for Eqs. 11 and 12 were made on a 64^3-grid and statistical data was dumped every 50 time steps. Typical time series for $\bar{\sigma}$ are plotted in Fig. 9 for three different sets of the parameters burning velocity and diffusivity.

Saturation of $\bar{\sigma}$ was reached at approximately $t_0 = 0.85$. The computation was carried further until $t_1 = 2.5$; the difference is about 15 integral time scales of the
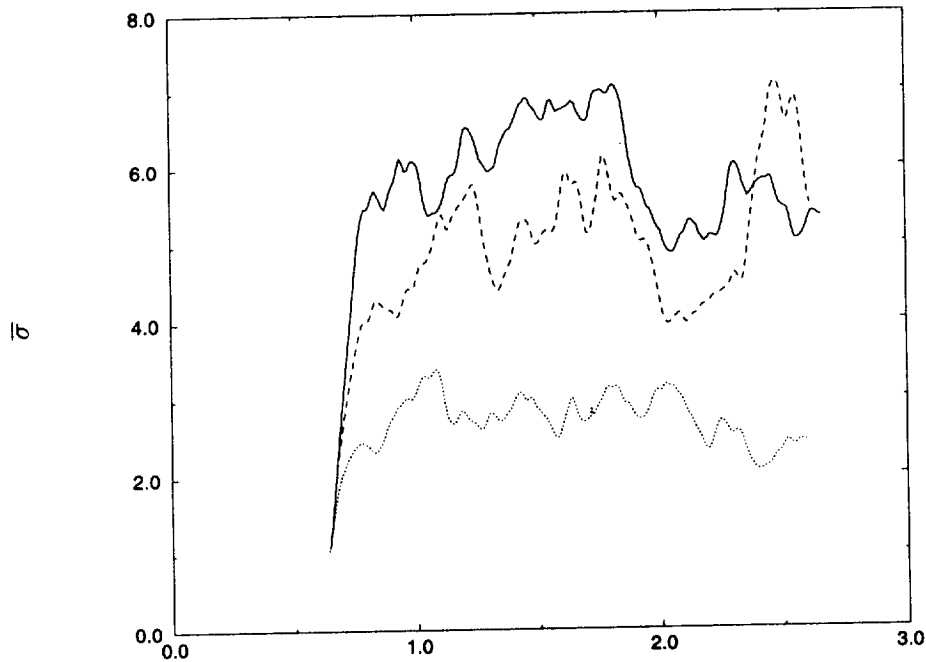
FIGURE 9. Time series of $\bar{\sigma}$. ——— : $s_L^0 = 1.0, D = 0.48$; ---- : $s_L^0 = 8.0, D_{\mathcal{L}} = 0.0$; ⋯⋯⋯ : $s_L^0 = 16.0, D_{\mathcal{L}} = 0.0$.

flow, so that stable statistically stationary results can be expected. In that time interval the mean values of $\bar{\sigma}, u'$ and ℓ were time averaged. The results are given in the following table:

u'/s_L^0	ℓ/ℓ_F	$\bar{\sigma}$ (DNS-results)	$\bar{\sigma}$ (Eq. 28)
1.47	19.2	2.83	2.78
1.47	38.5	3.02	3.15
1.11	-	2.78	-
17.7	1.59	5.53	5.04
17.8	3.16	6.0	6.95
4.41	6.07	4.89	4.16
4.41	12.1	5.2	5.37
2.21	-	5.04	-
2.21	12.9	3.86	3.41
2.21	25.8	3.99	4.08

These results may be used to determine two of the constants in Eq. 13. After applying closure assumptions regarding the turbulent diffusivity, it is possible to derive an expression for $\bar{\sigma}$ in terms of the velocity ratio u'/s_L^0 and the length ratio ℓ/ℓ_F for the limit where the turbulent production of $\bar{\sigma}$ is balanced by the two

destruction terms in that equation (Peters 1997):

$$\bar{\sigma} = -\frac{0.39}{2}\frac{\ell}{\ell_F} + \sqrt{\left(\frac{0.39}{2}\frac{\ell}{\ell_F}\right)^2 + 0.78\,\alpha\,\frac{\ell}{\ell_F}\frac{u'}{s_L^0}}\,. \tag{28}$$

The implied assumption for the large scale turbulence limit $\bar{\sigma} = 2.0\,u'/s_L^0$ is fulfilled quite well in the runs with zero Markstein diffusivity. These are marked by a dash in the length ratio column in the table above since the flame thickness vanishes for that case. The constant $\alpha = c_3/c_1$ is then fitted with the results of the other DNS runs to a value of 1.3.

In this section we derived a new numerical scheme for solving the G-equation with a pseudo-spectral code. It was shown to possess the ability to handle the cusps that develop naturally in the propagation of a scalar due to Huyghen's principle. The direct numerical simulations that were carried out with this new scheme proved it to be a valuable tool in understanding premixed turbulent combustion because it can handle all possible sets of parameters that may appear if one analyzes this interesting and complex physical phenomenon in the framework of the G-equation.

3. Future work

In the near future we want to apply the code to gather more statistical data for the G-equation, the $\bar{\sigma}$-equation, and the equation for the variance of G. The latter equation was not presented in this work, but plays an important role in the closure of the turbulent G-equation if we don't retreat to the limiting case of production equals destruction in the model equation for $\bar{\sigma}$. It is then necessary to evaluate every term that appears in these equations, and the simple averaging procedure where the quantities are averaged over the whole box can no longer be used. Instead these quantities have to be conditionally averaged according to their position in the turbulent flame brush. This work was accomplished previously (Wenzel & Peters 1997) with finite-difference methods and has to be reimplemented using spectral methods.

In the formulation of dynamical sub-grid models for the G-equation there still lie some uncertainties (Im *et al.* 1996), which can be tackled using this newly developed numerical scheme because it can handle the interesting limiting case of zero diffusivity. In that context it will be of high interest to compute and compare the spectra of both the flow field and the scalar field. To get meaningful results from that kind of analysis, the resolution should be improved to a 96^3 or 128^3 grid to get a larger inertial range.

The whole study that was presented here dealt only with the passive G-equation. That is, heat release effects were not accounted for. By this heat release the flame can have influence back on the flow field, and some new interesting effects can be seen. In the future these phenomena should be definitively included in a direct numerical simulation of the turbulent G-equation, although it seems clear at this moment that a pseudo-spectral code can no longer be applied to solve that problem and some higher order finite-difference or finite-volume methods will have to be used.

Acknowledgments

REFERENCES

CANUTO, C., HUSSAINI, M.Y., QUARTERONI, A., & ZANG, T.A. 1988 *Spectral Methods in Fluid Dynamics.* Springer-Verlag.

CLAVIN, P. & WILLIAMS, F. 1982 Effects of molecular diffusion and of thermal expansion on the structure and dynamics of premixed flames in turbulent flows of large scale and low intensity. *J. Fluid Mech.* **116**, 251-282.

FORNBERG, B. 1996 *A practical guide to pseudo-spectral methods.* Cambridge Monographs on Applied and Computational Mathematics, Cambridge University Press.

HIRSCH, C. 1990 *Numerical Computation of internal and external flows Vol.2, chapter 20.5.1.* J. Wiley & Sons.

IM, H.G., LUND, T.S., & FERZIGER, J.H. 1996 Dynamic models for LES of turbulent front propagation with a spectral method. *Annual research briefs 1995,* Center for Turbulence Research, NASA Ames/Stanford Univ., 101-113.

KELLER, P. 1996 Berechnung der turbulenten Flammenausbreitung bei der otto-motorischen Verbrennung mit einem Flamelet-Modell. *Ph.D. Thesis.* RWTH Aachen.

KERSTEIN, A., ASHURST, W., & WILLIAMS, F. 1988 Field equation for interface propagation in an unsteady flow field. *Phys. Rev. A.* **37**(7), 2728-2731.

PETERS, N. 1992a Fifteen lectures on laminar and turbulent combustion: Lecture 6 *Ercoftac Summer School 1992.* RWTH Aachen.

PETERS, N. 1992b A spectral closure for premixed turbulent combustion in the flamelet regime. *J. Fluid Mech.* **242**, 611-629.

PETERS, N. 1997 The turbulent burning velocity for large scale and small scale turbulence. Submitted to: *J. Fluid Mech.*

RUETSCH, G.R. 1992 The structure and dynamics of the vorticity and passive scalar fields at small scales in homogeneous isotropic turbulence *Ph.D. Thesis.* Brown University.

RUETSCH, G.R. & BROADWELL, J.E. 1995 Effects of confinement on partially premixed flames. *Annual research briefs 1995,* Center for Turbulence Research, NASA Ames/Stanford Univ., 323-333.

SETHIAN, J.A 1996 A Review of the Theory, Algorithms, and Applications of Level Set Methods for Propagating Interfaces. *Acta Numerica.* Cambridge University Press.

VERVISCH, L. 1995 Probability density functions and dynamics of iso-concentration surfaces in premixed turbulent combustion.*Euroconference on Premixed Turbulent Combustion - Introduction to the State of the Art.* RWTH-Aachen.

WENZEL, H. & PETERS, N. 1997 Direct numerical simulation of premixed turbulent combustion using a flamelet approach. *Notes on Numerical Fluid Mechanics: Computation and Visualization of three-dimensional vortical and turbulent flows.* Viewer Verlag, to appear.

Large eddy simulation of combustion instabilities in turbulent premixed burners

By D. Veynante[1] AND T. Poinsot[2]

1. Motivations and objectives

Large Eddy Simulation (LES) techniques are viewed today as the next step in Computational Fluid Dynamics studies to address classes of problems where classical Reynolds-averaged Navier Stokes approaches (RANS) have proved to lack precision or where the intrinsically unsteady nature of the flow makes RANS clearly inadequate. In the field of combustion, the understanding and the control of combustion instabilities are domains where LES is required and will be applied in practical systems. There are at least two reasons for this:

(1) Reacting flows submitted to instabilities are dominated by very large eddies sweeping the combustion chamber. Such flows are obviously fully unsteady and make RANS approaches difficult to use.

(2) Structures controlling combustion in these flows are large, and LES should be easier in such cases than for turbulent combustion in general where an extended range of eddies has to be resolved to characterize the turbulence/chemistry interaction.

Multiple techniques have been proposed in the past to perform LES of turbulent premixed combustion (Menon and Kerstein 1992, Menon *et al.*1994, Smith and Menon 1996, 1997, Piana *et al.*1996, 1997, Veynante and Poinsot 1997a). Few of them have been used in a realistic configuration (see for example Kailasanath *et al.*1991). In most cases, fundamental studies in simple configurations such as freely propagating flames or stagnation point flames have been performed. In such situations, assumptions are generally made in the fundamental studies (e.g. ignition and quenching mechanisms are ignored) but must be reconsidered in more realistic configurations. Flame stabilization and flame-wall interactions, for example, should be considered in detail and may influence the choice of the LES formulation.

We will briefly recall the basis of LES techniques for combustion and investigate in more detail the performance of one specific method: the Thickened Flame approach, proposed by Butler & O'Rourke (1977). Our objective is to test this method in a configuration where combustion instabilities occur: the flame stabilized behind a backward-facing step. This configuration was chosen since results from many experimental studies are available (Keller *et al.*1981, Poinsot *et al.*1987) and since the configuration contains many features in common with real combustion chambers. Our attention will be also focused on flame stabilization and flame-wall interaction.

1 Laboratoire EM2C, C.N.R.S. and Ecole Centrale Paris, France

2 Institut de Mecanique des Fluides de Toulouse and CERFACS, France

These issues have been addressed previously using DNS and RANS approaches (Poinsot 1996, Poinsot *et al.*1996, Bruneaux *et al.*1996) but have not received much attention in the context of LES. Our first goal is to propose a LES technique which correctly reproduces flame wrinkling, at least when the flow is dominated by large structures, and handles flame-wall interactions and stabilization regions in a physical manner without ad hoc corrections.

The different techniques proposed for LES of premixed combustion will be briefly summarized in Section 2. Our decision to investigate the thickened flame (TF) model, initially proposed by O'Rourke and his coworkers (Butler & O'Rourke 1977, O'Rourke & Bracco 1979), will be explained.

Section 3 will present the configuration studied and Section 4 the numerical code and the boundary conditions. The stabilization studies are described in Section 5, and Section 6 presents flame response to inlet velocity fluctuations. The effect of numerical parameters controlling this response (LES treatment, perturbation amplitude, thermal conditions on inlet sections) is also discussed.

2. LES techniques for turbulent premixed combustion

2.1 LES framework for combustion

Assuming that G is the LES filter and x the location, any filtered quantity $\overline{Q}$ is defined as:

$$\overline{Q}(x,t) = \int_{-\infty}^{+\infty} Q(x,t)\, G(x - x')\, dx' \tag{1}$$

For reacting flows, a Favre filtering is defined as:

$$\overline{\rho}\widetilde{Q} = \overline{\rho Q} = \int_{-\infty}^{+\infty} \rho Q(x,t)\, G(x - x')\, dx' \tag{2}$$

where $\overline{\rho}$ is the filtered density. The previous definition is similar to Favre averaging, widely used in RANS context.

Filtering the conservation equations controlling reacting flows introduces unknown quantities to be modeled: (1) $\widetilde{u_i u_j} - \widetilde{u_i}\widetilde{u_j}$, the unresolved Reynolds stresses, which requires a subgrid scale turbulence model; (2) $\widetilde{u_i Y_k} - \widetilde{u_i}\widetilde{Y_k}$, the unresolved species fluxes, where a simple gradient expression is usually assumed:

$$\widetilde{u_i Y_k} - \widetilde{u_i}\widetilde{Y_k} = -\frac{\nu_T}{S_c}\frac{\partial \widetilde{Y_k}}{\partial x_i} \tag{3}$$

with ν_T the subgrid kinematic turbulent viscosity and S_c the turbulent Schmidt number; (3) $\widetilde{u_i T} - \widetilde{u_i}\widetilde{T}$, the unresolved heat fluxes, also modeled by a gradient expression; (4) $\widetilde{Y_k T} - \widetilde{Y_k}\widetilde{T}$ and $\widetilde{Y_k T^n} - \widetilde{Y_k}\widetilde{T^n}$, the species-temperature correlations, occurring when specific heats C_p are expressed in terms of polynomial approximations of T, which are usually neglected; and (5) the filtered reaction rate $\overline{\dot{\omega}_k}$.

In the following, our attention will be focused on modeling the filtered reaction rate $\overline{\dot{\omega}_k}$. The other terms have been addressed in previous studies. The Reynolds

stresses are generally described using Smagorinsky or Germano dynamic models whereas unresolved turbulent transports are expressed with gradient expressions. No attempt has been yet conducted to take into account counter-gradient transport evidenced by theory (Libby & Bray 1981, Bray *et al.*1989) or DNS (Veynante *et al.*1996, Veynante & Poinsot 1997b) in LES.

One difficulty is encountered for large eddy simulations of premixed flames: the flame thickness δ_l^0 is in the range of approximately 0.1 to 1.0 mm and is generally smaller than the LES mesh size Δ. Accordingly, species mass fraction and temperature profiles are very stiff variables, thus the flame front cannot be resolved on the computational mesh. To overcome this difficulty, two main approaches have been proposed: simulation of an artificially thickened flame (TF) or use of a flame front tracking technique (G-equation).

2.1 Arrhenius law based on filtered quantities (Arrhenius model)

A first simple model is to neglect subgrid scale contributions and to write the reaction rate as an Arrhenius law for filtered quantities:

$$\overline{\dot{\omega}}_F = A\overline{\rho}^2 \widetilde{Y}_F \widetilde{Y}_O \widetilde{T}^b \exp\left(-\frac{T_a}{\widetilde{T}}\right) \qquad (4)$$

Such simple expressions assume perfect mixing at subgrid scales and implicitly assume that turbulent time scales, τ_t, are shorter than chemical time scales, τ_c ($\tau_t \ll \tau_c$). The reaction zone thickness is also assumed sufficiently large to be resolved on the LES mesh size. This formulation is generally used for reacting flows in atmospheric boundary layers (Nieuwstadt, 1997) but is not relevant in most combustion applications. Segregation factors may be also introduced to correct Arrhenius expression to account for unmixedness. Specific Arrhenius-type expressions incorporating combustion delays and changes due to subgrid scale mixing may also be derived in an ad-hoc manner, for example Kailasanath (1985,1991).

2.2 The field equation (G model)

In this approach (Kerstein *et al.*, 1988), the flame surface is described as an infinitely thin propagating surface (i.e. flamelet). In using this approach, one tracks the position of the flame front using a field variable G. The flame surface is associated with a specific isolevel $G = G^*$. The gradients in the G-field can be much smoother than those of the progress variable c to the point where they can be resolved on the LES mesh. Work in progress on the use of G equation has shown the potential but also the difficulties of this approach (see Bourlioux *et al.*1996; Piana *et al.*1996, 1997, Im *et al.*1996, Veynante and Poinsot 1997a).

2.3 Random vortex methods (RVM model)

Random vortex methods are another class of models suitable for LES of premixed combustion. In this grid-free approach, chemistry may be handled in a Lagrangian manner by following flame elements. Examples of such approaches may be found in Ghoniem *et al.*(1988, 1992).

2.4 The thickened flame model (TF model)

The key idea of the thickened flame (TF) model is to consider a flame having the same laminar flame speed s_l but a larger flame thickness than the actual actual flame in order to be resolved on the LES computational grid (Butler and O'Rourke 1977, O'Rourke and Bracco 1979). Following simple theories of laminar premixed flame (Williams 1985, Kuo 1986), the flame speed s_l and the flame thickness δ_l may be expressed as:

$$s_l \propto \sqrt{a\dot{W}} \quad ; \quad \delta_l \propto \frac{a}{s_l}$$

where a is the thermal diffusivity and $\dot{W}$ the total reaction rate. Then, an increase of the flame thickness δ_l^0 by a factor F while maintaining a constant flame speed s_l^0 may be achieved by replacing the thermal diffusivity a by Fa and the reaction rate $\dot{W}$ by $\dot{W}/F$ as summarized in Table I. Numerically, such a transformation is performed simply by dividing the pre-exponential constant and the Prandtl and the Schmidt numbers by the thickening factor F.

Table I: Comparison between normal (superscript 0) and thickened flame (superscript 1). The thickening factor is F.

	Flame speed	Flame thickness	Preexponential Factor	Prandtl	Schmidt
Normal flame	s_l^0	δ_l^0	A^0	P_r^0	S_c^0
Thickened flame	$s_l^1 = s_l^0$	$\delta_l^1 = F\delta_l^0$	$A^1 = A^0/F$	P_r^0/F	S_c^0/F

For sufficiently large values of the factor F, the thickened flame front may be resolved on the LES computational mesh. In practical applications, values of δ_l^0 (estimated by $\delta_l^0 s_L^0/a \simeq 4$) are of the order of 0.2 to 1 mm so that thickening factors F of the order of 3 to 10 should suffice for many practical simulations. Based on Arrhenius law, the TF model has the advantages that it can handle ignition and flame-wall interaction processes without any sub-model.

However, thickening the flame front may have the following two undesired effects. First, the flame propagation may be affected when small scales are present in the flow because these structures could become unable to wrinkle the thickened flame front (Poinsot et al.1991). For combustion instabilities, this drawback may not be crucial because of the large values of the ratio of the vortex size L to the flame thickness δ_l^0. Second, the sensitivity of the flame to stretch is also increased by F because of the transformation. The thickened flame will react to a stretch of κ/F as the actual flame would to a stretch of κ. Many DNS of turbulent premixed combustion have suggested that, in the mean, the effect of stretch on the local flamelets was not strong (Haworth & Poinsot 1992, Baum et al.1994, Trouvé & Poinsot 1994) but increasing this effect by a factor F of the order of 10 may have unexpected effects,

for example on quenching. Note however that this difficulty is also encountered in the G-equation approach where strain effects on the displacement speed have to be introduced in an ad-hoc fashion because the G model is, by construction, insensitive to stretch.

3. Objectives and configuration

Our objective in the present work is to investigate the limits of the TF model for large eddy simulations of combustion instabilities in premixed burners. The issues mentioned before will be analyzed by computing the same flow (prototype of a combustion instability in a premixed burner) with both "normal" and a "thickened" flame descriptions. The normal flame is described using a classical DNS formulation. For thickened flame simulations, no LES model is used for the flow itself: our objective is just to qualify the TF approach independently of the LES turbulence model. Furthermore, for the present two-dimensional simulations, no small-scale turbulence is present. These TF simulations are in fact DNS where the flame characteristics have been changed according to the relations summarized in Table I. For future studies in three-dimensional flows, an additional coupling model between the turbulence LES model and the TF model should be incorporated.
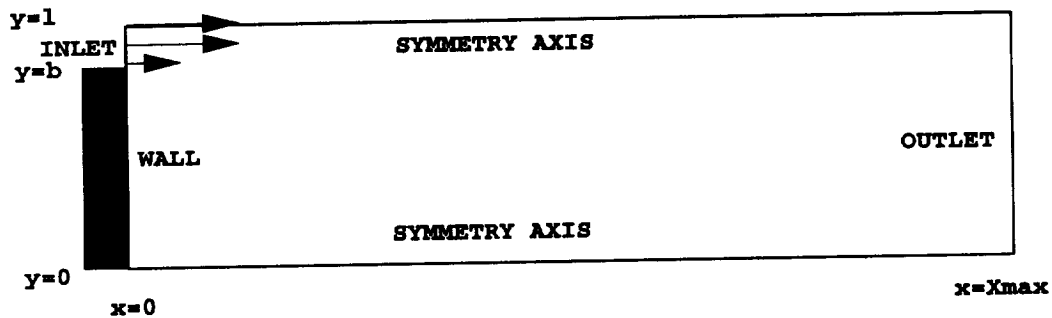

FIGURE 1.   Numerical configuration corresponding to the premixed propane/air burner used by Poinsot *et al.*(1987) to investigate combustion instabilities. The actual burner has five injection slots.

The numerical configuration, displayed in Fig. 1, corresponds to the turbulent premixed propane-air experimental burner of Poinsot *et al.*(1987). This burner is dominated by multiple instability modes corresponding to acoustic eigenmodes of the whole combustion system (including compressor and inlet pipes). Observed frequencies range between 440 Hz and 590 Hz. The strongest mode occurs at 530 Hz for an equivalence ratio ϕ of 0.92 and a total flow rate $\dot{m}$ of 73 g/s (flow conditions are summarized in Table II).

Table II: Flow conditions for the 530 Hz instability mode (Poinsot *et al.*1987). U_0 is the inlet velocity, c_0 the sound speed. ν_0 is the kinematic viscosity of fresh gases. l and b are respectively the burner and the step thickness (see Fig. 1).

ϕ	s_l^0 (m/s)	δ_l^0 (m)	U_0 (m/s)	c_0 (m/s)	$Re = c_0 l/\nu_0$ acoustic	$U_0(l-b)/\nu_0$ inlet	Frequency (Hz)
0.92	0.40	$1.1\ 10^{-4}$	42	345	$2.1\ 10^5$	3950	530

For the flow conditions in Table II, the whole system resonates at a frequency of 530 Hz while mushroom-like vortices are shed at the same frequency from all five injection slots. These structures are not created by hydrodynamic instabilities (which are also observed but at a higher frequency) but are due to strong simultaneous velocity surges in the five injection slots. These vortices grow, are convected, and interact with vortices issued from neighboring slots, leading to small-scale turbulence and intense heat release. The time delay between the velocity surge leading to the formation of these vortices and the peak heat release is an essential parameter for all combustion instability models (see Crocco & Cheng 1956, Crocco 1969, McManus *et al.*1993, Candel *et al.*1996). Estimating this delay does not require one to take into account the whole system and the acoustics which induce the vortex formation itself. A proper strategy is to create a vortex by pulsating the combustion chamber inlet flow field and to study the effect of this vortex on the overall combustion process.

4. Numerical technique and protocol to study flame response

This study is conducted using the NTMIX code, a two-dimensional DNS solver developed by CTR and Ecole Centrale Paris and described in Veynante & Poinsot (1995) or Veynante *et al.*(1996). The full compressible reacting Navier-Stokes equations are solved assuming perfect gases with constant molar mass and a specific heat ratio $\gamma = 1.4$. The thermal conductivity λ and the diffusion coefficient $\mathcal{D}$ are obtained from the dynamic viscosity coefficient μ according to

$$\lambda = \mu C_p / P_r \quad \text{and} \quad \mathcal{D} = \mu / (\rho S_c), \tag{5}$$

where the Prandtl number P_r and the Schmidt number S_c are constant. As a consequence the Lewis number $L_e = S_c/P_r$ is also constant. The viscosity μ is a function of temperature according to $\mu = \mu_u (T/T_u)^n$ where $n = 0.76$.

The computational domain is $L_x \times L_y$ with $N_x \times N_y$ grid points. Boundary conditions (Fig. 1) correspond to a partially blocked inlet (blockage ratio b/l of 85 %) on the left, non-reflecting boundary conditions on the right, and symmetric boundaries on both sides. The velocity profile at the inlet is a *tanh* function with a thickness δ_Y.

An important difficulty in studying combustion delays is that excitation procedures have to be performed on a given baseline flow. Either this baseline flow is

stable and the flame response might not correspond to the one expected for unstable cases, or the baseline flow is unstable and measuring a transfer function becomes extremely difficult because the flow is dominated by its own instability (similar difficulties are encountered for DNS of non-reacting flows in absolutely unstable regimes). Experimentally, the only possible approach is the first solution: Poinsot *et al.*(1986), for example, have measured the reflection coefficient of a premixed flame but only for stable regimes close to instability. Numerically, however, it is possible in certain cases to create a stable baseline flow in a regime which should be unstable by slightly changing the expression of the reaction rate. Indeed, theoretical studies of combustion instabilities indicate that one main factor promoting instabilities is the dependence of the reaction rate on pressure (i.e. on density) as evidenced by the Rayleigh criterion which states that instability occurs when pressure and total heat release oscillate in phase (Crocco 1956, McManus *et al.*1993). Poinsot and Candel (1988), for example, verified numerically that an anchored flame was more likely to become unstable when flame speeds were pressure dependent. This suggests the following approach. Assuming that fuel is the deficient species controlling the reaction rate $\dot{\omega}_F$:

$$\dot{\omega}_F = B\rho Y_F \exp\left(-\frac{T_a}{T}\right) \tag{6}$$

then for the pressure sensitive (PS) case, any pressure increase (corresponding to an increase of the density ρ) will also increase the reaction rate. To inhibit this effect, a second expression called PI (pressure insensitive) is also used:

$$\dot{\omega}_F = B\frac{P_0}{rT}Y_F \exp\left(-\frac{T_a}{T}\right) \tag{7}$$

where P_0 is a constant reference pressure. The PI expression makes the reaction rate insensitive to pressure waves and cuts an important link in the combustion instability loop.

The PS and PI expression will give the same results for a stable flame (for example, an unconfined flame). However, only the PI expression can produce a stable baseline flow in ducted flows.

5. Stabilization and baseline flows for ducted flames

The different runs presented in this report are summarized in Table III. Runs B2, S4, S5 and S7 correspond to DNS (flames with normal thickness δ_l^0) while runs M1, S3, S6, and S9 correspond to thickened flames (by a factor F ranging from 2.5 to 7.5). Runs B2, M1, S6, and S9 correspond to the same physical flow ($Re = 75000$) where the computation is performed with DNS for B2 ($F = 1$) and with various values of the thickening factor F: 2.5 (M1), 5 (S6), and 7.5 (S9). Runs S4, S5, and S7 correspond to DNS with a lower Reynolds number ($Re = 15000$). Two thermal conditions have been tested for the blockage wall lying between $y = 0$ and $y = b$ at the inlet (Fig. 1). This wall may be adiabatic (adiabatic wall, called AW) or cooled

with an imposed temperature $T_w = T_1$ where T_1 is the inlet gases temperature (cooled wall, called CW in Table III).

Table III: Flow conditions for the DNS and LES of ducted flames. For all flows: $U_0/c_0 = 0.1$; the Reynolds number Re is $= c_0 l/\nu_0$; the temperature change through the flame front is $T_2/T_1 = 4$ ($\alpha = (T_2 - T_1)/T_2 = 0.75$); the sound speed in the fresh gas is c_0 (and $2c_0$ in the burnt gas); the activation temperature T_a is such that $\beta = \alpha T_a/T_2 = 7$; the box height is $l/L = 1$; the flame Mach number s_l^0/c_0 is 0.0032; the blockage is 0.85 ($b/l = 0.85$). δ_l^1 is the flame thickness after thickening ($\delta_l^1 = F\delta_l^0$).

RUN	l/δ_l^1	Re	F	RR	Wall cond.	δ_Y/l cond.	$Xmax/l$	N_x	N_y
S3	9.6	75000	5	PS	AW	0.03	9	150	64
S4	9.6	15000	1	PI	CW	0.01	9	150	64
S5	9.6	15000	1	PI	CW	0.01	12	200	64
S6	9.6	75000	5	PI	AW	0.03	9	150	64
S7	9.6	15000	1	PI	AW	0.01	9	150	64
S9	6.4	75000	7.5	PI	AW	0.03	9	150	64
M1	19.2	75000	2.5	PI	AW	0.03	9	300	128
B2	48	75000	1	PI	AW	0.03	9	750	300

These conditions do not correspond exactly to the experiment of Poinsot *et al.*Although the geometry is the same, the Reynolds number of the largest simulation (B2) is only one third of the experiment. Our goal, however, is to validate the TF methodology and, for the moment, no detailed comparisons are performed with the experiment.

5.1 Effects of formulations of $\dot{\omega}$ on stabilization

All computations are initialized with an oblique flame starting behind the step using temperature and fuel mass fraction profiles corresponding to a one-dimensional laminar premixed flame for the same equivalence ratio. Starting from this field, the simulation evolves without external excitation until a steady state is reached or when a well established oscillation is found. Figure 2 compares the temporal evolution of the total reaction rate for PS and PI formulations in cases S3 and S6. The PS formulation leads to oscillations both in transverse ($fl/c_0 \simeq 1$) and longitudinal modes ($fl/c_0 \simeq 18$) of the computational box. On the other hand, the PI formulation leads to a constant reaction rate and a steady flame regime.

5.2 Effect of inlet wall thermal condition

Figure 3 shows velocity vectors and the reaction rate field for run S5 in the vicinity of the injection slots. This flow exhibits a recirculation zone having a length of about 7.7b. The gas temperature inside this recirculation zone controls the anchoring of
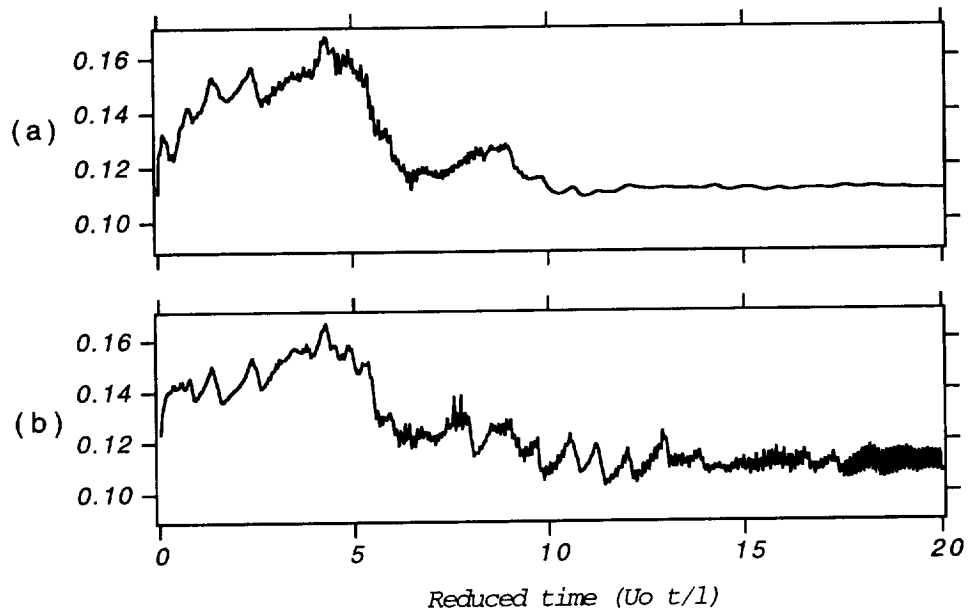
FIGURE 2. Effect of reaction rate formulation on flow stabilization: (a) case S6: pressure insensitive form; (b) case S3: pressure sensitive form. Time evolution of total burning rate (adiabatic walls).
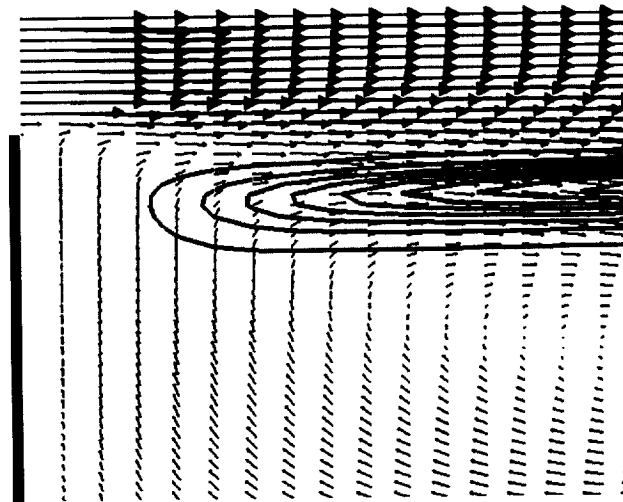

FIGURE 3. Zoom on velocity vectors and reaction rate field in the vicinity of the injection slot (Cold Wall - run S4).
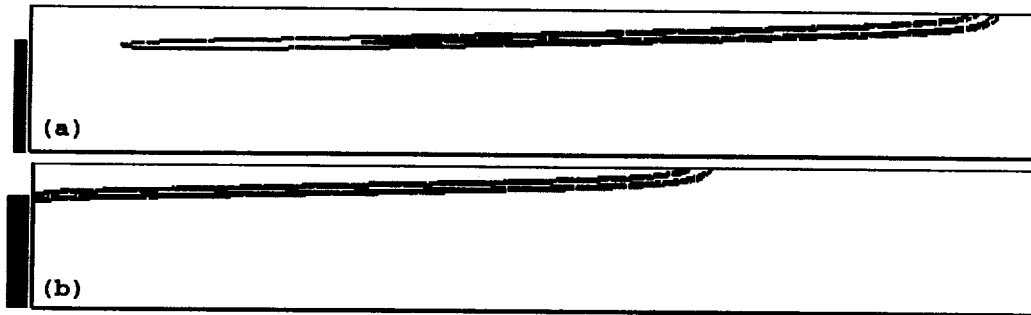
FIGURE 4. Reaction rate field. Effect of wall condition on the flame stabilization: (a) Cold wall (CW, run S4); (b) Adiabatic wall (AW, run S7).

the flame. These hot gases are produced by combustion and recirculated behind the step but may also be cooled by the wall. Therefore the thermal conditions on the wall between $y = 0$ and $y = b$ are important parameters (see Fig. 1).

Any heat losses in the vicinity of the recirculation gas have a strong effect on the steady flame position but also on its response to unsteady pulsations. Two thermal conditions have been tested for this wall. The adiabatic wall (AW) condition (run S7) allows the flame to start on the wall while the cooled wall (CW) condition (run S4) inhibits reaction near the wall and forces the flame to be lifted as shown by the reaction rate fields in Fig. 4. The flame length is also increased and the characteristic flame time is changed (see next Section).

6. Transfer function of premixed ducted flames

6.1 Methodology

Once stable flames are obtained, their transfer function may be studied by injecting acoustic disturbances through the inlet. The inlet velocity profile is modulated here according to the following expression:

$$U(x,y,t) = U_{steady} \left(1 + U_{inc}^+ \exp\left[-\left(\frac{t - t_{trig}}{t_{width}} \right)^2 \right] \right) \tag{8}$$

Examples of a flame excited with $U_{inc}^+ = 1$, $U_0 t_{trig}/l = 0.5$ and $U_0 t_{width}/l = 0.6$ are displayed in Fig. 5 for run S6 (see table III). The formation of a large reacting vortex is observed. The shape of this vortex is similar to the mushroom vortices observed in the experiment of Poinsot *et al.*(1987). Because of the AW condition used for the wall, the flame remains anchored at all times on the wall.

Figure 6 shows that the total heat release lags the inlet flow rate by a delay $\tau \simeq 2.5l/U_0$. This delay directly controls the instability modes since the period T of most combustion instabilities is of the order of 2τ (Crocco & Cheng 1956, Poinsot *et al.*1987). However, the delay obtained through such a simulation must be used with caution because it depends on multiple parameters. In the following, three parameters will be investigated: (1) the thickening parameter F of the TF model,
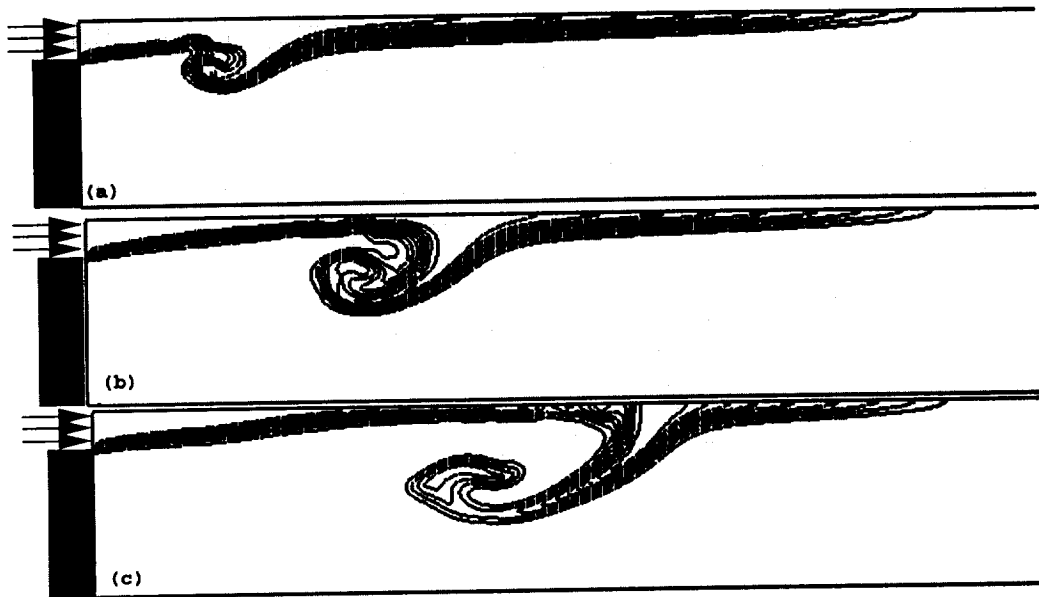
FIGURE 5.   Pulsated premixed flame (S6) computed using the TF model (thickening factor $F = 5$).   Temperature field.   (a) $U_0 t/l = 0.8$, (b) $U_0 t/l = 1.6$, (c) $U_0 t/l = 2.4$.
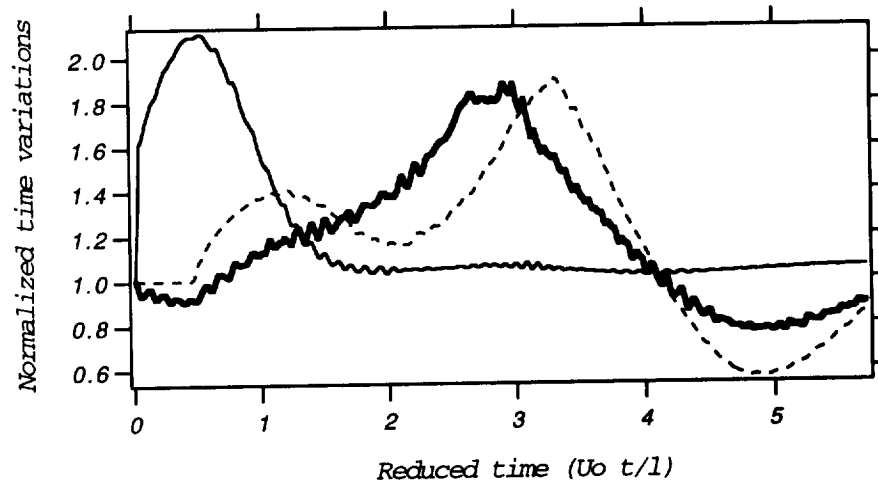

FIGURE 6.   Time evolution of inlet flow rate (————), total reaction rate (━━━━) and outlet flow rate (- - - -).   Run S6 with $F = 5$.

corresponding to the LES treatment of the reaction rate, (2) the wall condition (cold or adiabatic), and (3) the excitation amplitude U_{inc}^+.

6.2 Effects of LES treatment (thickening factor F)

The $Re = 75000$ case was computed with thickening factors $F = 1$ (run B2, 750 × grid 300 points), $F = 2.5$ (M1, 300 × 128 points), $F = 5$ (S6, 150 × 64 points) and $F = 7.5$ (S9, 150 × 64 points). As the flame becomes larger (F is increased), the grid size $N_x \times N_y$ may be reduced, decreasing the computational time. The excitation parameters are $U_{inc}^+ = 1$, $U_0 t_{trig}/l = 0.5$ and $U_0 t_{width}/l = 0.6$. Figure 7 shows the time evolution of the total reaction rate for these four simulations.
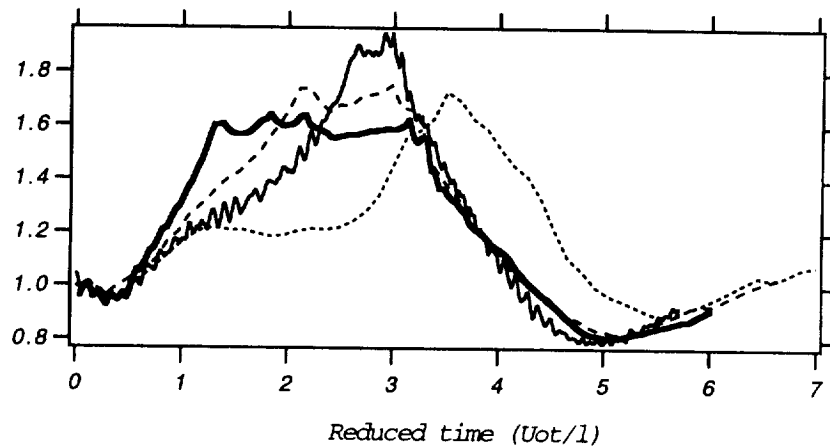

FIGURE 7. Effects of the thickening factor F (LES treatment of the reaction rate). The normalized total burning rate is displayed versus time. Comparison between DNS, $F = 1$ (run B1, ———), LES with $F = 2.5$ (M1, ----), $F = 5$ (S6, ———) and $F = 7.5$ (S9, ········). Excitation parameters are $U_{inc}^+ = 1$, $U_0 t_{trig}/l = 0.5$ and $U_0 t_{width}/l = 0.6$.

The general evolution of all flows is similar: differences of the order of 20% are observed for the total reaction rate. However the shapes of the reaction rate curves are different: the DNS ($F = 1$) burns initially faster than the LES cases but more slowly in the late stages of the interaction. This finding is consistent with the TF formalism: less flame surface is created for LES runs than for DNS, leading to a reduced combustion, because the sensitivity of a thickened flame to a hydrodynamic perturbation is lower than the one of a thin flame as shown by Poinsot *et al.*(1991). Later on, however, the additive reactants injected during the excitation have to burn, leading to a larger combustion rate in the LES computations.

Figures 8 and 9 display fields of instantaneous reaction rates for the four computations at times $U_0 t/l = 1.6$ and $U_0 t/l = 2.8$, respectively. These plots confirm the thickening of the reaction zone when the factor F is increased. This thickening affects flame wrinkling in complex ways: the DNS creates a first pocket of fresh gases

in the burnt products earlier than the three LES runs. More flame surface is also generated. This flame surface is mainly due to small scale wrinkling, which leads to the formation of small pockets. These pockets are burned out rapidly. On the other hand, less small pockets are initially created in the LES cases so that a large pocket of fresh reactants is consumed later. This phenomenon becomes dramatic for the $F = 7.5$ LES run where the evolution of the flow after $U_0 t/l = 1$. differs from the DNS result by 30% because most of the flame wrinkling is missed.
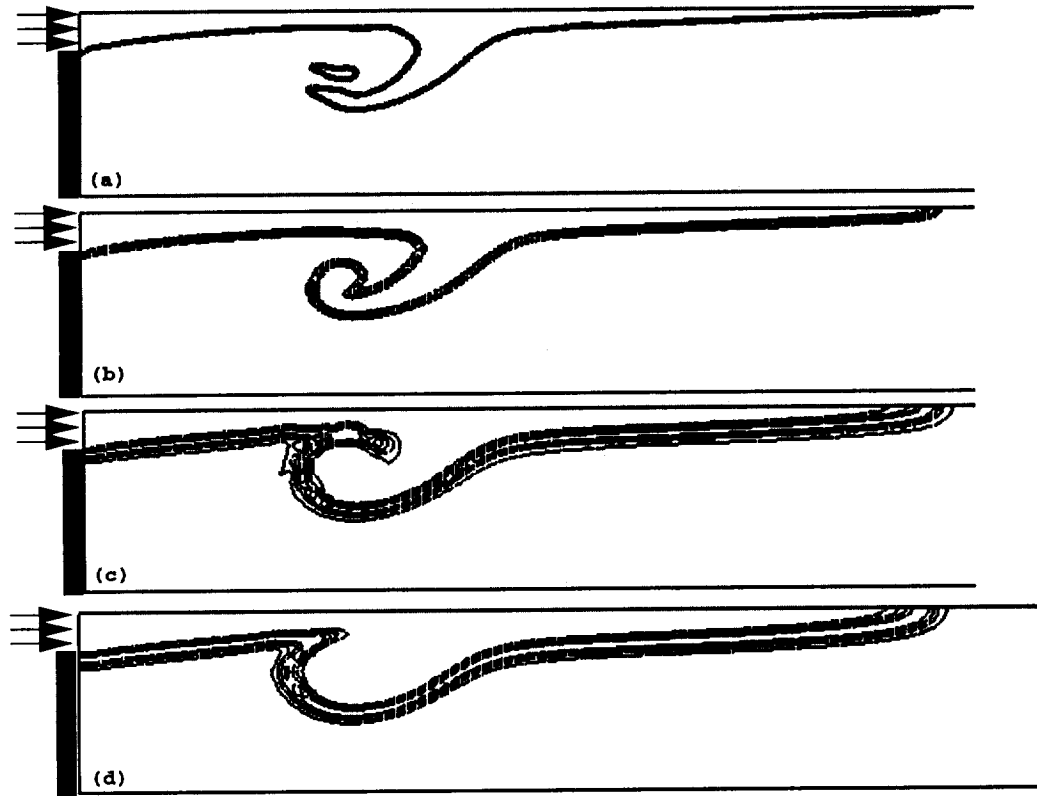

FIGURE 8.   Instantaneous reaction rate fields at time $U_0 t/l = 1.6$. Comparison between DNS (a), LES with $F = 2.5$ (b), LES with $F = 5$ (c) and LES with $F = 7.5$ (d). See caption of Fig. 7 for runs characteristics.

6.3 Effects of inlet wall condition

Figure 10 compares two DNS simulations (runs S5 and S7) for an excitation corresponding to $U^+_{inc} = 1$, $U_0 t_{trig}/l = 1.5$ and $U_0 t_{width}/l = 0.6$. Run S5 is similar to S4 (only the box length is different) and performed with a cold wall (CW) condition on the inlet wall while S7 assumes an adiabatic wall (Reaction rate contours for both flames under steady conditions are displayed on Fig. 4).

Figures 11 and 12 display fields of reaction rates for these two computations at reduced times $U_0 t/l = 2.4$, 3.6, 4.8 and 6. The flame stabilized behind a cold
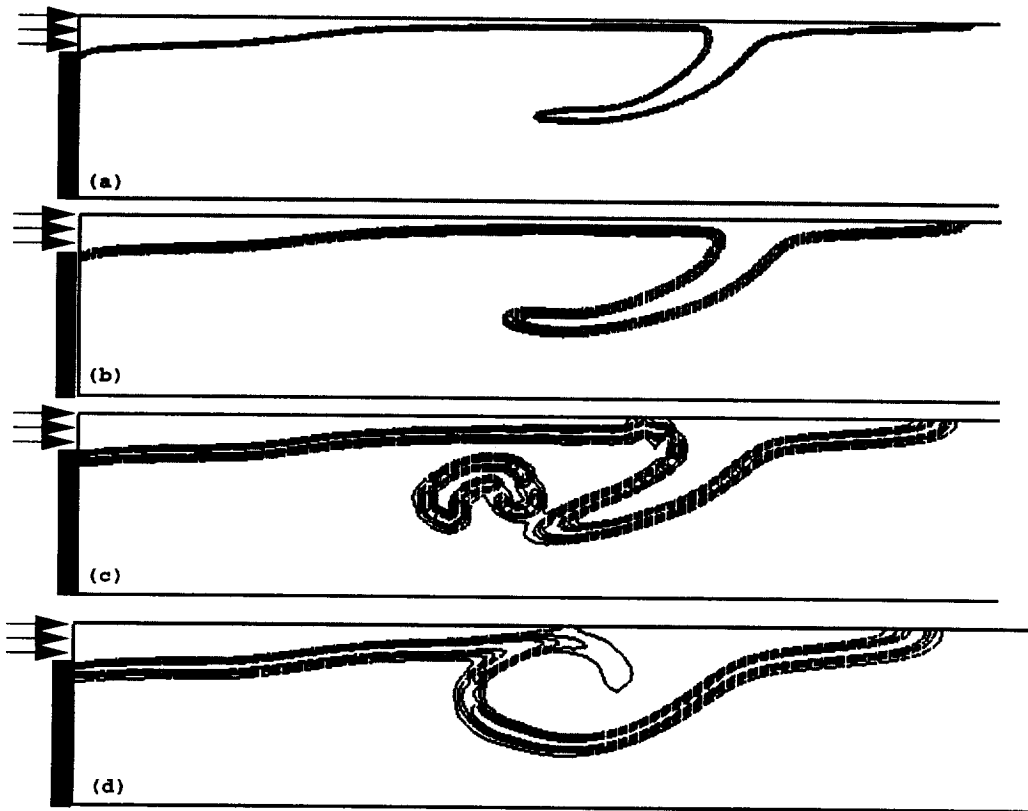
FIGURE 9.   Instantaneous reaction rate fields at time $U_0 t/l = 2.8$. Comparison between DNS (a), LES with $F = 2.5$ (b), LES with $F = 5$ (c) and LES with $F = 7.5$ (d). See caption of Fig. 7 for runs characteristics.

wall (Fig. 12) reacts later to excitation than the adiabatic flame (Fig. 11) but more strongly. Large differences both in delay and amplitude are observed, demonstrating the importance of the condition chosen for the inlet wall. Two factors explain these differences: (1) the CW flame lies closer to the recirculating burnt region than the AW flame and, therefore, 'feels' the vortex with less amplitude and at a later time than the AW flame, and (2) the reaction rate of the CW flame is very small near the injection slot because of heat losses while the AW flame burns everywhere with the laminar flame speed. The resulting pattern of this 'flame-vortex' interaction is, therefore, extremely different. The effects of this boundary condition appear to be as strong as the thickening factor F used in the TF model. This shows that the LES of the purely propagating flame (handled with the TF model) is only one aspect of CFD for combustion instabilities of confined flames and that factors such as boundary conditions and flame stabilization could play a crucial role.

LES with cold wall conditions are not presented here because specific treatments of wall heat fluxes will be required for these cases. Dividing P_r by a factor F thickens the flame but also increases heat transfer to the walls by the same factor
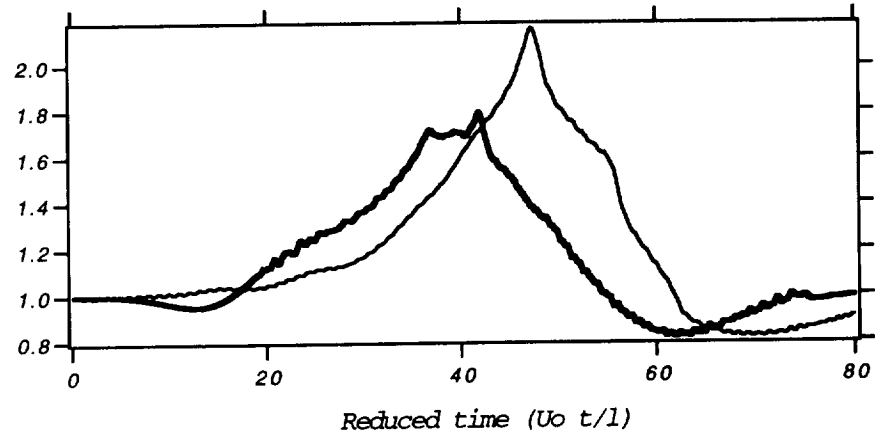
FIGURE 10.   Effects on inlet wall condition. Normalized total burning rate versus time. Comparison between adiabatic wall (AW - S7) (———) and cold wall (CW - S5) (———)
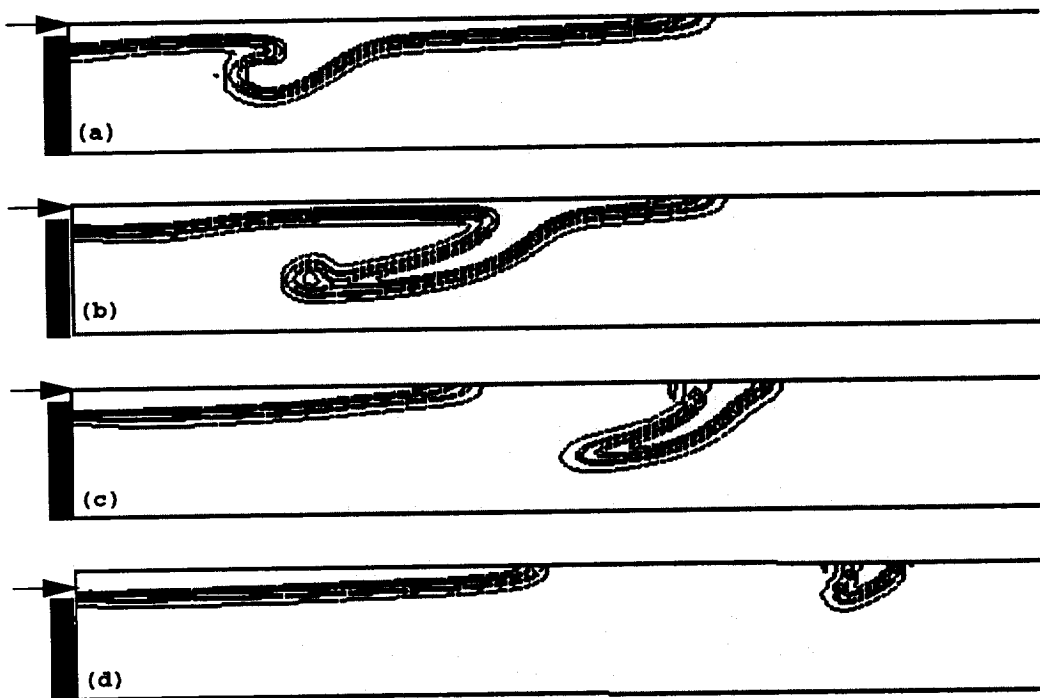

FIGURE 11.   Fields of reaction rate for simulation S7 (DNS, adiabatic wall): (a) $U_0 t/l = 2.4$, (b) $U_0 t/l = 3.6$, (c) $U_0 t/l = 4.8$ and (d) $U_0 t/l = 6$.
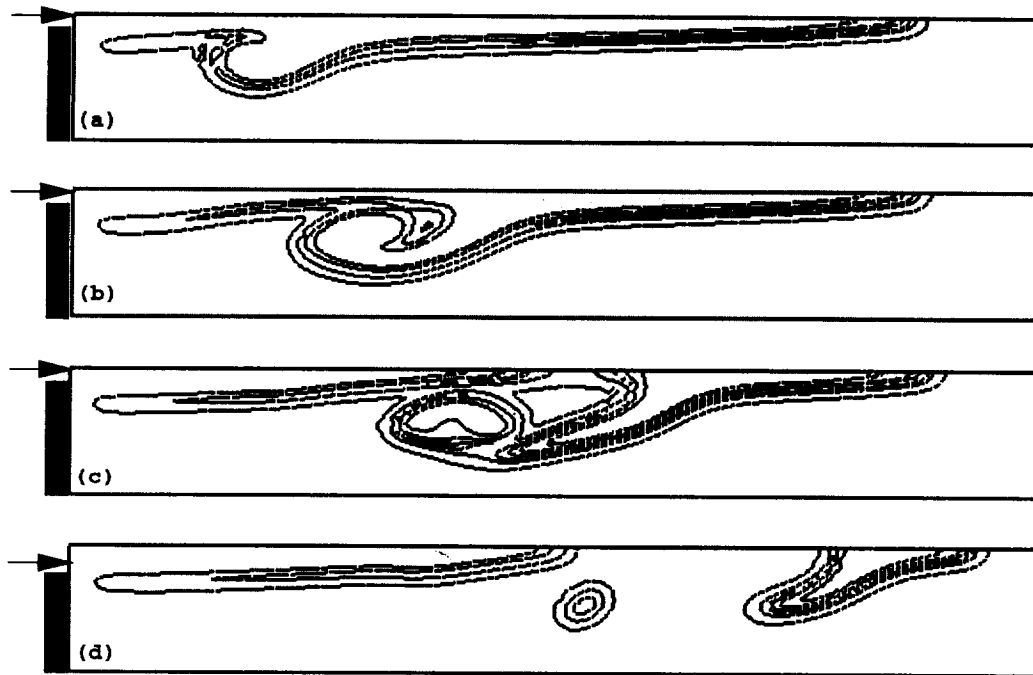
FIGURE 12.   Fields of reaction rate for simulation S5 (DNS, cold wall): (a)
$U_0 t/l = 2.4$, (b) $U_0 t/l = 3.6$, (c) $U_0 t/l = 4.8$ and (d) $U_0 t/l = 6$.

F. This could be avoided by an adequate treatment of wall fluxes but remains to
be investigated.

6.4 Effects of excitation amplitude

Most models for combustion instability are linear. It is, however, well-known
that flame response is strongly non-linear, and the excitation amplitude to pulsate
flames has to be chosen carefully. Figure 13 shows flame response for an LES
run (S6, $F = 5$) for three excitation levels: $U_{inc}^+ = 0.1$, 0.5, and 1. In all cases,
$U_0 t_{trig}/l = 0.5$ and $U_0 t_{width}/l = 0.6$. For low levels of excitation amplitude (10% of
incoming velocity for $U_{inc}^+ = 0.1$), the delay is much longer than it is in cases with
more intense perturbations. Examination of the instantaneous flow fields reveals
that no pocket is formed for case $U_{inc}^+ = 0.1$. Flame wrinkling is higher in the two
other cases where the flame is shred by the vortical field.

6.5 Theoretical analysis of the thickened flame response

The response of a thickened flame to an excitation is now analyzed. Our objective
is to propose a simple model explaining the findings of Fig. 7 and 13. Under the
flamelet assumption, the flame stretch K measures the increase in flame surface
area A (Candel & Poinsot, 1991):

$$K = \frac{1}{A}\frac{dA}{dt} \tag{9}$$
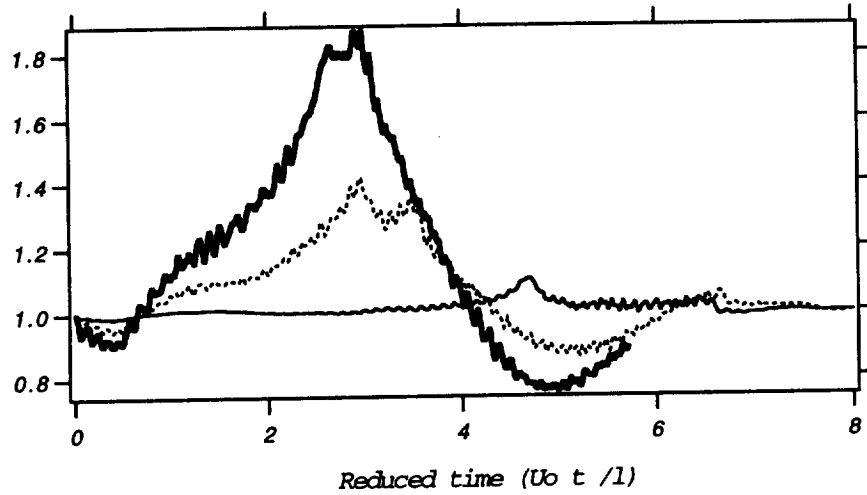
FIGURE 13. Effects of excitation amplitude. Normalized total burning rate versus time for $U_{inc}^+ = 0.1$ (———), $U_{inc}^+ = 0.5$ (- - - -) and $U_{inc}^+ = 1$ (———). Run S6 ($F = 5$).
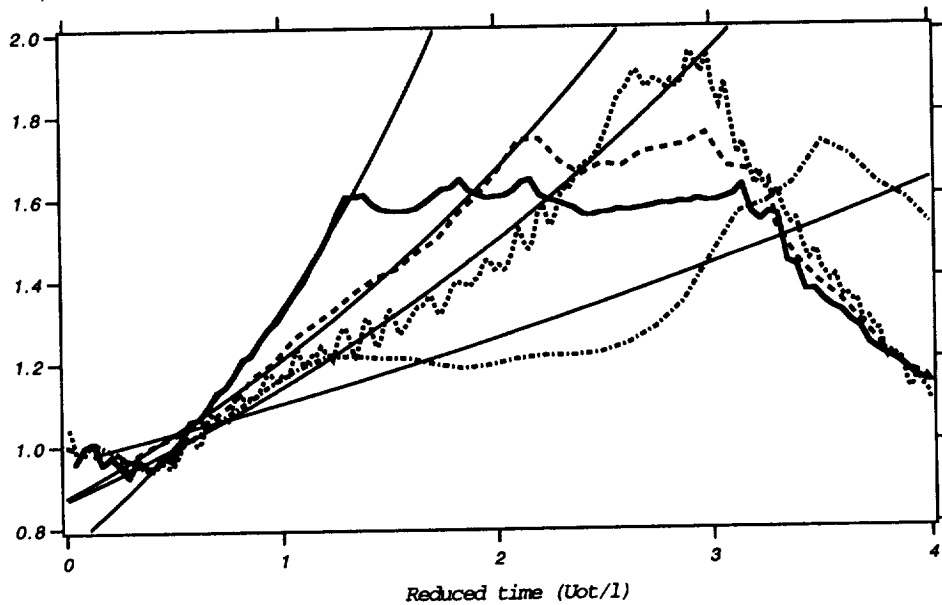
FIGURE 14. Analysis of the initial flame response. The normalized total burning rate is displayed versus time. Bold lines correspond to numerical results (already displayed on Fig. 7), thin lines (———) are fits according to Eq. (10). DNS, $F = 1$ (run B1, ———), LES with $F = 2.5$ (M1, - - - -), $F = 5$ (S6, ·······) and $F = 7.5$ (S9, —·—·—). Excitation parameters are $U_{inc}^+ = 1$, $U_0 t_{trig}/l = 0.5$ and $U_0 t_{width}/l = 0.6$.
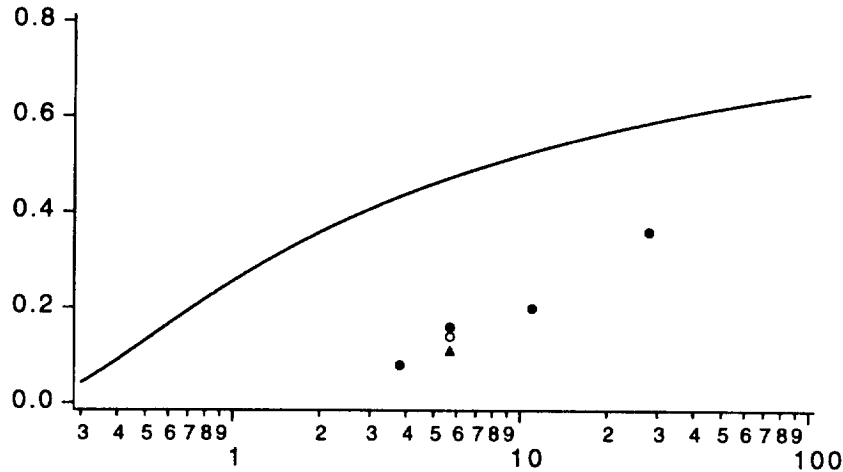
FIGURE 15.   Estimation of the efficiency function C (see Eq. 10) plotted as a function of the length scale ratio r/δ_l^1 between the size of the perturbation and the artificial thickness of the flame. The continuous line (———) corresponds to the efficiency function C_{MP} estimated by Meneveau and Poinsot (1991). Excitation parameters are $U_0 t_{trig}/l = 0.5$, $U_0 t_{width}/l = 0.6$ and $U_{inc}^+ = 1.0$ ($\bullet$), $U_{inc}^+ = 0.5$ ($\circ$) and $U_{inc}^+ = 0.1$ ($\blacktriangle$).

Assuming that the local reaction rate per unit of flame surface area is almost constant along the flame front, the total reaction rate $\dot{W}$ is proportional to the flame area A and depends on the mean stretch in the same way.

In our simulations, the mean stretch is mainly due to the strain κ, which is in turn due to the vortex generated by the inlet velocity perturbation. But, following Meneveau and Poinsot (1990), an efficiency function C depending on the ratio between the vortex size r and the flame thickness δ_l has to be introduced to take into account the reduced ability of small vortices to wrinkle the flame front. Then, integrating Eq. (9) leads to an estimate of the time evolution of the reduced total reaction rate $\dot{W}/\dot{W}_0$, where $\dot{W}_0$ corresponds to the total reaction rate under steady state operation:

$$\frac{\dot{W}}{\dot{W}_0} = \exp\left[C\left(\frac{r}{\delta_l}\right)\kappa\, t\right] \tag{10}$$

Estimates of the vortex size r and the strain rate κ are now required. One may propose:

$$r \approx U_0\, t_{width} \qquad ; \qquad \kappa \approx U_{inc}^+ \frac{U_0}{r} \tag{11}$$

The efficiency function $C(r/\delta_l)$ may now be estimated by fitting the expression (10) on reduced reaction rates displayed on Fig. 7 and 13. Reaction rate fits are displayed against numerical simulations on Fig. 14 (Only the growing phase of the total reaction rate is used here). The agreement is quite satisfactory. On Fig. 15, the efficiency function $C(r/\delta_l)$ is plotted as a function of the length scale ratio r/δ_l^1 and compared to the efficiency function C_{MP} proposed by Meneveau and Poinsot

(1991) and extracted from the flame-vortex interaction DNS conducted by Poinsot *et al.*(1991). As expected, the efficiency function C is found to decrease with the length scale ratio r/δ_l^1 with a shape similar to C_{MP}. The discrepancy between C and C_{MP} is probably due to the difference between present simulations and those of Poinsot *et al.*(two vortices interacting with a normal flame in Poinsot *et al.*DNS, one velocity perturbation interacting with an oblique flame here), leading to differences in the estimation of r and κ. Another point is that, in our simulation, the flame structure is modified by decreasing the pre-exponential factor B and the Schmidt number S_c, keeping the hydrodynamic perturbation constant. In the simulations of Poinsot *et al.*, the flame structure remains unchanged whereas vortex size and strength are modified. Nevertheless, this finding is very interesting because the efficiency function $C(r/\delta_l^1)$, and more generally an ITNFS-like formulation (see Meneveau and Poinsot, 1991), could be implemented in the reaction rate expression to correct the reduced ability of a thickened flame to be wrinkled by small structures. This point could be investigated from DNS of flame-vortex interactions using various values of the thickening factor F.

7. Conclusion

The forced response of a flame stabilized behind a step in a geometry corresponding to the experiment of Poinsot *et al.*(1987) has been studied at different Reynolds numbers using Direct Numerical Simulations and Large Eddy Simulations based on the Thickened Flame model. This model allows the computation of a premixed flame on a coarse grid by increasing its thickness while maintaining its flame speed. The TF model is able to compute the flame response within 20% when thickening factors as large as 5 are used. Even though the TF model modifies the flame response, its influence is smaller than other parameters which are specifically linked to combustion instabilities in dump-stabilized flames: the excitation amplitude and the thermal condition on the wall near the injection slot, for example, are found to have comparable effects on the flame response. An efficiency function, similar to the ITNFS formulation proposed by Meneveau and Poinsot (1991), could be introduced to reduce the modification of the flame response due to the TF model. Accordingly, the thickened flame (TF) approach seems to be a good compromise for large eddy simulations of combustion instability in premixed burners.

REFERENCES

BAUM, M., POINSOT, T., HAWORTH, D. & DARABIHA, N. 1994 Using Direct Numerical Simulations to study $H_2/O_2/N_2$ flames with complex chemistry in turbulent flows. *J. Fluid Mech.* **281**, 1-32.

BOURLIOUX, A., KLEIN, R. & MOSER, V. 1996 Large eddy simulations of turbulent premixed flames using a capturing/tracking hybrid approach. *Sixth International Conference on Numerical Combustion*, New Orleans, Louisiana.

BOURLIOUX, A., IM, H.G. & FERZIGER, J. 1996 A dynamic subgrid scale model for LES of the G-equation. *Proceedings of the CTR Summer Program* Center for Turbulence Research, NASA Ames/Stanford Univ., 137-148.

BRAY, K. N. C., CHAMPION, M. & LIBBY, P. A. 1989 The interaction between turbulence and chemistry in premixed turbulent flames. In *Turbulent Reactive Flows, Lecture Notes in Eng.* **40**, Springer-Verlag.

BRUNEAUX, G., AKSELVOLL, K., POINSOT, T. & FERZIGER, J. 1996 Flame-wall interaction in a turbulent channel flow. *Combust. & Flame.* **107**, 27-44.

BUTLER T.D. & O'ROURKE P.J. 1977 *Sixteenth Symposium (International) on Combustion*, The Combustion Institute, Pittsburgh, 1503-1515.

CANDEL, S. M. & POINSOT, T. 1990 Flame stretch and the balance equation for the flame surface area. *Combust. Sci. Tech.* **70**, 1-15.

CANDEL, S., HUYNH, C. & POINSOT, T. 1996 Unsteady combustion *Nato ASI Series*, Kluwer Academic Publishers, Dordrecht, 83-112.

CROCCO, L. & CHENG, S. I. 1956 *Book Theory of combustion instability in liquid propellant rocket motors.* Butterworths Science.

CROCCO, L. 1969 Research on combustion instability in liquid propellant rockets. *12th Symp. (Int.) on Combustion*, The Combustion Institute, Pittsburgh, 85-99.

GHONIEM, A. & KRISHNAN, A. 1988 Origin and manifestation of flow-combustion interactions in a premixed shear layer. *22nd Symp. (Int.) on Combustion*, The Combustion Institute, Pittsburgh, 665-675.

GHONIEM, A. F., SOTERIOU, M. C. & KNIO, O. M. 1992 Effect of steady and periodic strain on unsteady flamelet combustion. *24th Symp. (Int.) on Combustion*, The Combustion Institute, Pittsburgh, 223-230.

HAWORTH, D. C. & POINSOT, T. J. 1992 Numerical simulations of Lewis number effects in turbulent premixed flames. *J. Fluid Mech.* **244**, 405-436.

IM, H.G., LUND, T. & FERZIGER, J. 1996 Dynamic models for LES of turbulent front propagation with a spectral method. *CTR Annual Research Briefs*, Center for Turbulence Research, NASA Ames/Stanford Univ.,101-115.

KAILASANATH, K., GARDNER, J., BORIS, J. & ORAN, E. 1985 Acoustic vortex interactions in an idealized ramjet combustor. *22nd JANNAF Combustion Meeting.*

KAILASANATH, K., GARDNER, J. H., ORAN, E. S. & BORIS, J. P. 1991 Numerical simulations of unsteady reactive flows in a combustion chamber. *Comb. Flame.* **86**, 115-134.

KELLER, J. O., VANEVELD, L., KORSCHELT, D., HUBBARD, G. L., GHONIEM, A. F., DAILY, J. W. & OPPENHEIM, A. K. 1981 Mechanism of instabilities in turbulent combustion leading to flashback. *AIAA Journal.* **20**, 254-262.

KERSTEIN A.R., ASHURST W.T. AND WILLIAMS F.A. 1988 Field equation for interface propagation in an unsteady homogeneous flow field. *Physical Rev. A.* **37(7)**, 2728-2731.

KUO, K.K. 1986 *Principles of Combustion.* J. Wiley & Sons.

LIBBY, P. A. & BRAY, K. N. C. 1981 Countergradient diffusion in premixed turbulent flames. *AIAA Journal.* **19**, 205-213.

McMANUS, K., POINSOT, T. & CANDEL, S. 1993 A review of active control of combustion instabilities. *Prog. Energy Comb. Sci.* **19**, 1-29.

MENEVEAU, C. & POINSOT, T. 1991 Stretching and quenching of flamelets in premixed turbulent combustion. *Combust. Flame.* **86**, 311-332.

MENON, S. & KERSTEIN A. 1992 Stochastic simulation of the structure and propagation rate of turbulent premixed flames. *Twenty Fourth Symp. (Int.) on Combustion*, The Combustion Institute, Pittsburgh, 443-450.

MENON, S., McMURTHY, P.A., KERSTEIN, A.R. & CHEN, J.Y. 1994 Prediction of NOx production in a turbulent hydrogen-air jet flame. *J. Prop. Power.* **10**, 161-168.

NIEUWSTADT, F.T.M. 1997 The large-eddy simulation of the dispersion of pollutants in the atmospheric boundary layer. *New tools in turbulence modeling*, O. Metais and J. Ferziger Eds, Les Editions de Physique.

O'ROURKE, P.J. & BRACCO, F.V. 1979 Two scaling transformations for the numerical computation of multidimensional unsteady laminar flames. *J. Comp. Physics.* **33**, 2, 185-203.

PIANA, J., VEYNANTE, D., CANDEL, S. & POINSOT, T., 1996 Direct numerical simulation analysis of the G-equation in premixed combustion. *Second ER-COFTAC workshop on Direct and Large Eddy Simulation*, Septembre 16-19, Grenoble, France.

PIANA, J., DUCROS, F. & VEYNANTE, D. 1997 Large eddy simulations of turbulent premixed flames based on the G-equation and a flame front wrinkling description. *11th Symposium on Turbulent Shear Flows*, September 8-10, Grenoble, France.

POINSOT, T., LE CHATELIER, T., CANDEL, S. & ESPOSITO, E. 1986 Experimental determination of the reflection coefficient of a premixed flame in a duct. *J. Sound Vibration.* **107**, 265-278.

POINSOT, T., TROUVÉ, A., VEYNANTE, D., CANDEL, S. & ESPOSITO, E. 1987 Vortex driven acoustically coupled combustion instabilities. *J. Fluid Mech.* **177**, 265-292.

POINSOT, T. & CANDEL, S. 1988 A nonlinear model for ducted flame combustion instabilities. *Comb. Sci. Tech.* **61**, 121-153.

POINSOT, T., VEYNANTE, D. & CANDEL, S. 1991 Quenching processes and premixed turbulent combustion diagrams. *J. Fluid Mech.* **228**, 561-606.

POINSOT, T. 1996 Using direct numerical simulation to understand turbulent premixed combustion. *25th Symposium (Int.) on Combustion*, The Combustion Institute, Pittsburgh.

POINSOT, T., CANDEL, S. & TROUVÉ, A. 1996 Application of Direct Numerical Simulation to premixed turbulent combustion. *Prog. Energy Comb. Sci.* **21**, 531-576.

SMITH, T. & MENON, S., 1996 Model simulations of freely propagating turbulent premixed flames. *Twenty-sixth Symposium International on Combustion*, The Combustion Institute, Pittsburgh.

SMITH, T.M. & MENON, S. 1997 Large Eddy Simulations of turbulent reacting stagnation point flows. *35th Aerospace Sciences Meeting & Exhibit*. Reno, NV.

TROUVÉ, A. & POINSOT, T. 1994 The evolution equation for the flame surface density. *J. Fluid Mech.* **278**, 1-31.

VEYNANTE, D. & POINSOT, T. 1995 Effects of pressure gradients on turbulent premixed flames. *CTR Annual Research Briefs*, Center for Turbulence Research, NASA Ames/Stanford Univ., 273-300.

VEYNANTE, D. & POINSOT, T. 1997a Reynolds-averaged and Large Eddy Simulation modeling for turbulent combustion. *New tools in turbulence modeling*, O. Metais and J. Ferziger Eds, Les Editions de Physique.

VEYNANTE, D. & POINSOT, T. 1997b Effects of pressure gradients on turbulent premixed flames. *J. Fluid Mech.* In press.

VEYNANTE, D., TROUVÉ, A., BRAY, K. N. C. & MANTEL, T. 1996 Gradient and counter-gradient transport in turbulent premixed flames. *J. Fluid Mech.* **332**, 263-293.

WILLIAMS, F. A. 1985 *Combustion theory*. 2nd ed., Addison-Wesley.

On the generation of vorticity at a free-surface

By T. Lundgren[1] AND P. Koumoutsakos

1. Motivations and objectives

In free surface flows there are many situations where vorticity enters a flow in the form of a shear layer. This occurs at regions of high surface curvature and superficially resembles separation of a boundary layer at a solid boundary corner, but in the free surface flow there is very little boundary layer vorticity upstream of the corner, and the vorticity which enters the flow is entirely created at the corner. Rood (1994) has associated the flux of vorticity into the flow with the deceleration of a layer of fluid near the surface. These effects are quite clearly seen in spilling breaker flows studied by Duncan & Philomin (1994), Lin & Rockwell (1995) and Dabiri & Gharib (1997).

In this paper we propose a description of free surface viscous flows in a vortex dynamics formulation. In the vortex dynamics approach to fluid dynamics, the emphasis is on the vorticity vector which is treated as the primary variable; the velocity is expressed as a functional of the vorticity through the Biot-Savart integral. In free surface viscous flows the surface appears as a source or sink of vorticity, and a suitable procedure is required to handle this as a vorticity boundary condition.

As a conceptually attractive by-product of this study we find that vorticity is conserved if one considers the vortex sheet at the free surface to contain "surface vorticity". Vorticity which fluxes out of the fluid and appears to be lost is really gained by the vortex sheet. As an example of the significance of this, consider the the approach of a vortex ring at a shallow angle to a free surface. It has been observed (Bernal & Kwon, 1988; Gharib, 1994) that the vortex disconnects from itself as it approaches the surface and reconnects to the surface in a U-shaped structure with surface dimples at the vortex ends. There is a clear loss of vorticity from the fluid and an acceleration of the surface in the direction of motion of the ring as discussed by Rood (1994). Since vorticity is conserved the missing vorticity has been flattened out into a vortex sheet which connects the vortex ends. In a real water-air interface, the connection is in a thin vortex layer in the air. The completion of vortex lines along the surface allows one to maintain the physical picture of closed vortex tubes.

When vortex dynamics methods are used for viscous flows with solid boundaries, a vorticity boundary condition may be determined by following Lighthill's (1963) discussion of the problem. Lighthill noted that the velocity field induced by the vorticity in the fluid will not in general satisfy the no-slip boundary condition. This spurious slip velocity may be viewed as a vortex sheet on the surface of the body.

1 Permanent address: Dept. of Aerospace Engr. & Mechanics, Univ. of Minnesota, Minneapolis, MN 55455
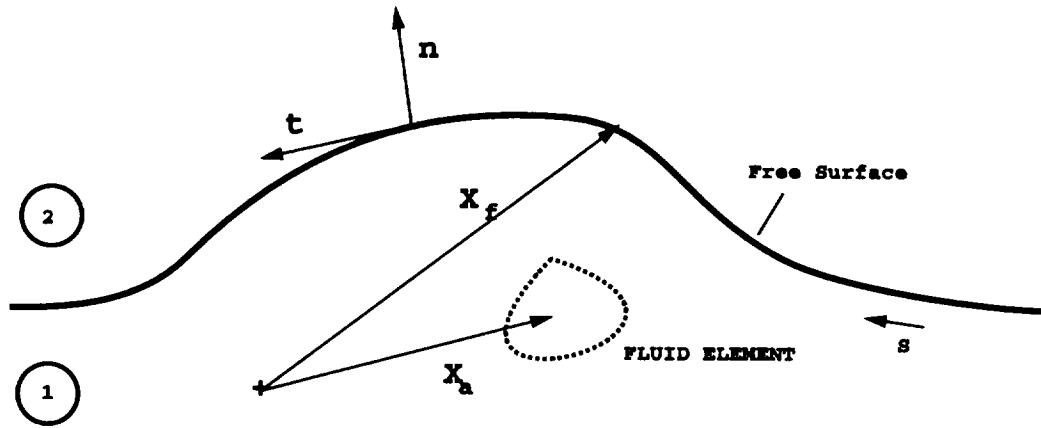
FIGURE 1.   Definition sketch.

In order to enforce the no-slip boundary condition, the vortex sheet is distributed diffusively into the flow, transferring the vortex sheet to an equivalent thin viscous vortex layer by means of a vorticity flux. The vorticity flux is the strength of the spurious vortex sheet divided by the time increment.

For free surface flows a vortex sheet is employed in order to adjust the irrotational part of the flow. Unlike the case of a solid wall this vortex sheet is part of the vorticity field of the flow and is used in order to determine the velocity field. The strength of the vortex sheet is determined by enforcing the boundary conditions resulting from a force balance at the free surface.

The physical character of Lighthill's method has led to its direct formulation and implementation by Kinney and his co-workers (1974, 1977) in the context of finite difference schemes, and by Koumoutsakos, Leonard and Pepin (1994) in order to enforce the no-slip boundary condition in the context of vortex methods. Their method has produced benchmark quality simulations of some unsteady flows (Koumoutsakos and Leonard, 1995). The present strategy can be easily adapted to such a numerical scheme and can lead to improved numerical methods for the simulation of viscous free surface flows.

2. Accomplishments

In order to introduce the vorticity generation mechanism, we consider, without loss of generality, two-dimensional flow of a Newtonian fluid with a free surface (Fig. 1). We consider the stresses in *fluid 2* as negligible, and when not otherwise stated the flow quantities refer to *fluid 1*.

2.1 Mathematical formulation

Two-dimensional incompressible viscous flow may be described by the vorticity transport equation

$$\frac{d\omega}{dt} = \nu \nabla^2 \omega \tag{1}$$

with the Lagrangian derivative defined as

$$\frac{\mathrm{d}}{\mathrm{d}t} = \frac{\partial}{\partial t} + \mathbf{u} \cdot \nabla \ ,$$

where $\mathbf{u}(\mathbf{x}, t)$ is the velocity, $\boldsymbol{\omega} = \omega\hat{k} = \nabla \times \mathbf{u}$ the vorticity, and ν denotes the kinematic viscosity. The flow field evolves by following the trajectories of the vorticity carrying fluid elements $\mathbf{x}_a$ and the free-surface points $\mathbf{x}_f$ based on the following equation:

$$\frac{\mathrm{d}\mathbf{x}_p}{\mathrm{d}t} = \mathbf{u}(\mathbf{x}_p)$$

where $\mathbf{x}_p$ denotes $\mathbf{x}_a$ or $\mathbf{x}_f$.

2.1.1 Boundary conditions

The *boundary conditions* at the free-surface are determined by a force balance calculation. For a Newtonian fluid the stress tensor is expressed as

$$\mathbf{T} = -p\mathbf{I} + 2\mu\mathbf{D} \ . \tag{2}$$

where $\mathbf{D}$ is the symmetric part of the velocity gradient tensor. The local normal and tangential components of the surface traction force are expressed as $\hat{n} \cdot \mathbf{T} \cdot \hat{n}$ and $\hat{n} \cdot \mathbf{T} \cdot \hat{t}$ respectively. Balancing these two force components results in the following two boundary conditions at a free-surface.

1. Zero Shear Stress. Assuming negligible surface tension gradients, balancing the tangential forces at the free-surface results in

$$\hat{t} \cdot \mathbf{D} \cdot \hat{n} = 0 \ .$$

This may be expressed

$$\hat{n} \cdot \nabla\mathbf{u} \cdot \hat{t} + \hat{t} \cdot \nabla\mathbf{u} \cdot \hat{n} = 0 \ . \tag{3}$$

For the purposes of our velocity-vorticity formulation we wish to relate this boundary condition to the vorticity field and to the velocity components at the free-surface.

For a two-dimensional flow, by the definition of vorticity in a local coordinate system, we have

$$\omega = \hat{n} \cdot \nabla\mathbf{u} \cdot \hat{t} - \hat{t} \cdot \nabla\mathbf{u} \cdot \hat{n} \ . \tag{4}$$

Using (3) we may rewrite (4) as

$$\omega = -2\hat{t} \cdot \nabla\mathbf{u} \cdot \hat{n} \ . \tag{5}$$

By some further manipulation the free-surface vorticity may be expressed in terms of the local normal and tangential components of the velocity field;

$$\omega = -2\frac{\partial \mathbf{u}}{\partial s} \cdot \hat{n} \tag{6}$$

$$= -2\frac{\partial \mathbf{u} \cdot \hat{n}}{\partial s} + 2\mathbf{u} \cdot \frac{\partial \hat{n}}{\partial s} \tag{7}$$

$$= -2\frac{\partial \mathbf{u} \cdot \hat{n}}{\partial s} + 2\mathbf{u} \cdot \hat{t}\,\kappa \tag{8}$$

where κ is the curvature of the surface, defined by $\kappa = \hat{t} \cdot \partial \hat{n}/\partial s$. For steady flow, where the free-surface is stationary, $\mathbf{u}_1 \cdot \hat{n}$ is zero and the first term on the right in (8) drops out. The steady version of (8) was given by Lugt (1987) and by Longuet-Higgins (1992), the unsteady form by Wu (1995). A three-dimensional version of (5) was derived by Lundgren (1989).

The sense of (8) is that vorticity develops at the surface whenever there is relative flow along a curved interface. This condition prevents a viscous free-surface flow from being irrotational. Enforcing the vorticity field given by the above equation at the free-surface is equivalent to enforcing the condition of zero shear stress.

2. Pressure Boundary Condition. This is the condition that the jump in normal traction across the free-surface interface is balanced by the surface tension. It is expressed as

$$\|\hat{n} \cdot \mathbf{T} \cdot \hat{n}\| = -T\kappa$$

where T is the surface tension and the vertical braces denote the jump in the quantity. Using (Eq. 2), this becomes

$$-p_1 + \mu\hat{n} \cdot \nabla\mathbf{u} \cdot \hat{n} + p_2 = -T\kappa \;.$$

Using the continuity equation, expressed in local coordinates, we get

$$\hat{n} \cdot \nabla\mathbf{u} \cdot \hat{n} = -\hat{t} \cdot \nabla\mathbf{u} \cdot \hat{t}$$

$$= -\frac{\partial \mathbf{u} \cdot \hat{t}}{\partial s} + \mathbf{u} \cdot \frac{\partial \hat{t}}{\partial s}$$

$$= -\frac{\partial \mathbf{u} \cdot \hat{t}}{\partial s} - \mathbf{u} \cdot \hat{n}\,\kappa \;.$$

Therefore

$$p_1 = p_2 + T\kappa - \rho\nu\left(\frac{\partial \mathbf{u} \cdot \hat{t}}{\partial s} + \mathbf{u} \cdot \hat{n}\,\kappa\right) \tag{9}$$

where p_2 is the constant pressure on the zero density side of the interface.

Since pressure does not occur in the vorticity equation, the pressure condition must be put in a form which accesses the primary variables. From the momentum equation at the free-surface we obtain

$$\hat{t} \cdot \frac{d\mathbf{u}_1}{dt} = -\frac{1}{\rho}\frac{\partial p_1}{\partial s} + \nu\hat{n} \cdot \nabla\omega - g\hat{j} \cdot \hat{t} \tag{10}$$

where g is the gravitational constant; $\hat{j}$ is upward.

For our purposes this equation may be put in a more tractable form by further manipulation. First we observe that

$$\hat{t} \cdot \frac{d\mathbf{u}_1}{dt} = \frac{d\mathbf{u}_1 \cdot \hat{t}}{dt} + \mathbf{u}_1 \cdot \frac{d\hat{t}}{dt}$$

and

$$\mathbf{u}_1 \cdot \frac{d\hat{t}}{dt} = \mathbf{u}_1 \cdot \hat{n} \; \hat{n} \cdot \frac{d\hat{t}}{dt} \;.$$

Then using the fact that the free-surface is a material surface we obtain the kinematic identity

$$\hat{n} \cdot \frac{d\hat{t}}{dt} = \hat{t} \cdot \nabla \mathbf{u} \cdot \hat{n}$$

$$= \frac{\partial \mathbf{u}_1 \cdot \hat{n}}{\partial s} - \mathbf{u}_1 \cdot \hat{t} \; \kappa \;.$$

Using this identity we find

$$\frac{d\mathbf{u}_1 \cdot \hat{t}}{dt} = \mathbf{u}_1 \cdot \hat{n} \; \frac{\partial \mathbf{u}_1 \cdot \hat{n}}{\partial s} - \mathbf{u}_1 \cdot \hat{t} \; \mathbf{u}_1 \cdot \hat{n} \; \kappa - \frac{1}{\rho} \frac{\partial p_1}{\partial s} + \nu \hat{n} \cdot \nabla \omega - g \hat{j} \cdot \hat{t} \;. \qquad (11)$$

We emphasize that the material derivative here is taken following a fluid particle on side 1 of the interface.

With p_1 substituted from (9), this formula may be regarded as equivalent to the pressure boundary condition. Except for the flux term all the terms on the right-hand-side of the equation are quantities defined on the surface and derivatives of these along the surface. We prefer to think of the role of the vorticity flux in this equation as a term which modifies the surface acceleration, rather than consider that the equation determines the flux.

Using a strategy analogous to Lighthill's for a solid wall, we propose a fractional step algorithm that enforces the pressure boundary condition in a vorticity-velocity framework. This strategy allows us to gain insight into the development and generation of vorticity at a viscous free surface and can be used as a building tool for a numerical method.

3. A fractional step algorithm

In order to show that the free-surface boundary conditions are satisfied in a velocity-vorticity formulation, we consider the evolution of the flow field during a single time step. In a manner similar to Lighthill's approach for a solid boundary, a vortex sheet is employed to enforce the boundary conditions. The vortex sheet becomes part of the vorticity field of the flow. The *difference* between the solid wall and the free surface is the role of the surface vortex sheet in adjusting the velocity field of the flow. In the case of the *solid wall*, the vortex sheet is *eliminated* from the boundary (so that the no-slip boundary condition is enforced) and enters the flow diffusively, resulting in the flux of vorticity into the flowfield. In the case of a *free*

surface, the vortex sheet *remains at the surface* to enforce the pressure boundary condition and constitutes a part of the vorticity field of the flow. The task is to determine the strength of the vortex sheet at the free surface so as to satisfy the boundary conditions.

For the purpose of describing this process, we assume that the velocity and the vorticity field are known at time t^n throughout the flow field and at the free surface, and we wish to obtain the flow field at time $t^{n+1} (\equiv t^n + \delta t)$.

Step 1. Given the velocity and vorticity at time t^n we update the positions of the vorticity carrying elements and the surface markers by solving $dx_p/dt = \mathbf{u}(\mathbf{x}_p, t)$;

$$\mathbf{x}_p^{n+1} = \mathbf{x}_p^n + \delta t \mathbf{u}^n(\mathbf{x}_p^n) \ .$$

We update the vorticity field by solving

$$\frac{d\omega}{dt} = \nu \nabla^2 \omega$$

with initial condition $\omega = \omega^n$ at $t = t^n$ and boundary condition $\omega = \omega^n(\mathbf{x}_f)$ at $\mathbf{x} = \mathbf{x}_f$. The solution to this equation, which we denote by $\omega^{n+1/2}$, is still incomplete. It does not satisfy the correct vorticity boundary condition at the end of the time step and must be corrected in step 2. The boundary condition which we have imposed ensures (rather arbitrarily) that the vorticity on the boundary is purely convected. The correction which is needed will be a vortical layer along the free-surface with vorticity of order δt and with thickness of order $(\delta t)^{1/2}$. We reason that the additional *velocity* field induced across this layer can be neglected since its variation is only of order $(\delta t)^{3/2}$.

For an incompressible flow the velocity may be expressed in terms of a stream function ψ by

$$\mathbf{u} = -\hat{k} \times \nabla \psi \tag{12}$$

and the vorticity itself is related to ψ by

$$\omega \equiv \hat{k} \cdot \nabla \times \mathbf{u} = -\nabla^2 \psi. \tag{13}$$

We use the convention that $\hat{n}$ is always outward from the fluid, $\hat{t}$ is the direction of integration along the surface, and $\hat{k} = \hat{n} \times \hat{t}$ is a unit vector out of the page. The solution of this equation gives

$$\psi = \psi_\omega + \psi_\gamma \tag{14}$$

where

$$\psi_\omega(\mathbf{x}) = -\frac{1}{2\pi} \int\limits_{\text{fluid}} \omega(\mathbf{x}_a, t) \ln|\mathbf{x} - \mathbf{x}_a| d\mathbf{x}_a \tag{15}$$

and ψ_γ represents an irrotational flow selected to satisfy boundary conditions. It is consistent with vortex dynamics to take this irrotational part as the flow induced by a vortex sheet along the boundary of the fluid, i.e. by

$$\psi_\gamma(\mathbf{x}, t) = -\frac{1}{2\pi} \int\limits_{\text{intfc}} \gamma(\mathbf{x}_f(s'), t) \ln|\mathbf{x} - \mathbf{x}_f(s')| ds' \ , \tag{16}$$

but it must be shown that this can be done in such a way as to satisfy the boundary conditions. In this formulation the boundary can be either solid or free or a mix of these, but in this paper we are specifically interested in free boundaries which separate an incompressible fluid from a fluid of negligible mass density. The velocity field is obtained by applying (12), giving the Biot-Savart law;

$$\mathbf{u}(\mathbf{x}, t) = \mathbf{u}_\omega(\mathbf{x}, t) + \mathbf{u}_\gamma(\mathbf{x}, t) \tag{17}$$

where

$$\mathbf{u}_\omega(\mathbf{x}) = \frac{1}{2\pi} \int\limits_{\text{fluid}} \omega(\mathbf{x}_a, t)\, \hat{k} \times \nabla \ln |\mathbf{x} - \mathbf{x}_a|\, d\mathbf{x}_a \tag{18}$$

and

$$\mathbf{u}_\gamma(\mathbf{x}) = \frac{1}{2\pi} \int\limits_{\text{intfc}} \gamma(\mathbf{x}_f(s), t)\, \hat{k} \times \nabla \ln |\mathbf{x} - \mathbf{x}_f(s)|\, ds \ . \tag{19}$$

The velocity field is also defined by these integrals for points outside the fluid; $\mathbf{u}_\omega$ is continuous across the interface, and $\mathbf{u}_\gamma$ has a jump discontinuity. As the position vector $\mathbf{x}$ tends to a point on the interface from inside the fluid, which we will indicate with a subscript "1", we get

$$(\mathbf{u}_\gamma \cdot \hat{t})_1 = -\frac{\gamma(s)}{2} - \text{P.V.} \frac{1}{2\pi} \int\limits_{\text{intfc}} \gamma(s', t)\, \hat{n} \cdot \nabla \ln |\mathbf{x}_f(s) - \mathbf{x}_f(s')|\, ds' \tag{20}$$

while as the point is approached from the outside, indicated by "2",

$$(\mathbf{u}_\gamma \cdot \hat{t})_2 = +\frac{\gamma(s)}{2} - \text{P.V.} \frac{1}{2\pi} \int\limits_{\text{intfc}} \gamma(s', t)\, \hat{n} \cdot \nabla \ln |\mathbf{x}_f(s) - \mathbf{x}_f(s')|\, ds' \ . \tag{21}$$

Here P.V. indicates the principal value of these singular integrals. By subtracting these equations it is clear that the vortex sheet strength is the jump in tangential velocity across the interface; since $\mathbf{u}_\omega \cdot \hat{t}$ is continuous, we have

$$\gamma = \mathbf{u}_2 \cdot \hat{t} - \mathbf{u}_1 \cdot \hat{t} \ . \tag{22}$$

By (17) and (20) the tangential component of the surface velocity is

$$-\frac{\gamma(s)}{2} - \text{P.V.} \frac{1}{2\pi} \int\limits_{\text{intfc}} \gamma(s', t)\, \hat{n} \cdot \nabla \ln |\mathbf{x}_f(s) - \mathbf{x}_f(s')|\, ds' = \mathbf{u}_1 \cdot \hat{t} - (\mathbf{u}_\omega \cdot \hat{t})_1 \ . \tag{23}$$

Equation (23) is a Fredholm integral equation of the second kind the solution of which determines the strength (γ) of the free surface vortex sheet when the right-hand side is given. In the case of multiply connected domains the equation needs to be supplemented with m constraints for the strength of the vortex sheet, where $m+1$ is the multiplicity of the domain (Prager, 1928). For example, in the case of a free

surface extending to infinity, no additional constraint needs to be imposed as the problem involves integration over a singly connected domain. However, in the case of a bubble, an additional constraint such as the conservation of total circulation in the domain needs to be imposed in order to obtain a unique solution.

The right-hand side of the equation may be determined from the quantities which have been updated. In particular $\mathbf{u}_\omega$ can be computed via the Biot-Savart integral (18) from the known vorticity field $\omega^{n+1/2}$ with order δt accuracy. The tangential component of the velocity of the free surface can be computed using (11) in the form

$$(\mathbf{u}_1 \cdot \hat{t})^{n+1} = (\mathbf{u}_1 \cdot \hat{t})^n + \delta t Q^n(\mathbf{u}_1, \hat{n}, \hat{t}, \nu\frac{\partial\omega}{\partial n}, p_1)$$

where Q^n signifies the right-hand side of (11) evaluated at time t^n. The pressure boundary condition enters the formulation of the problem at this stage. Upon solving (23) the strength of the vortex sheet is determined such that the pressure boundary condition is satisfied, justifying the previous assertion. We should add that (23) admits more than one solution in multiply connected domains, such as a two-dimensional bubble configuration, but unique solutions may be obtained by using Fredholm's alternative.

Note that the present method of enforcing the pressure boundary condition is equivalent to previous *irrotational* formulations (Lundgren & Mansour, 1988, 1991) which employ a velocity potential.

At the end of this step the points of the free-surface, the velocity field, and the strength of the vortex sheet have been updated ($\mathbf{x}_p{}^{n+1}$, $\mathbf{u}^{n+1}$ and γ^{n+1}). The vorticity field ($\omega^{n+1/2}$) still needs to be corrected near the free surface.

Step 2. At this step we consider generation of vorticity at the free surface. Having determined the strength of the vortex sheet from Step 1, we can compute the normal and tangential components of the velocity field at the free surface in order to determine the free surface vorticity and enforce the zero-shear stress boundary condition.

Using (14,15,16) we can compute an updated value of the stream function on the surface and from this compute $\mathbf{u}_1 \cdot \hat{n} = \partial\psi/\partial s$. Since the surface shape and $\mathbf{u}_1 \cdot \hat{t}$ have already been updated, we have all the ingredients necessary to compute an updated value of ω_1 from (3). The next step in this process is to solve the vorticity transport equation for the vorticity field using ω_1 as boundary condition. For the final partial step we need to solve the heat equation,

$$\frac{\partial\omega}{\partial t} = \nu\nabla^2\omega , \tag{24}$$

with initial condition $\omega = 0$ at $t = t^n$, and with the boundary condition

$$\omega(\mathbf{x}_f) = (\omega_1^{n+1} - \omega_1^n)(t - t^n)/\delta t$$

assuming a linear time variation of the surface vorticity between the two time levels. The solution of this partial step is to be added to $\omega^{n+1/2}$, thus yielding the completely updated vorticity field ω^{n+1}.

An analytical solution for this diffusion equation can be obtained using the method of heat potentials (Friedman, 1964). For a two-dimensional flow the solution to the above equation may be expressed in terms of double-layer heat potentials as

$$\omega(\mathbf{x}, t + \delta t) = \int_t^{t+\delta t} \int_{\text{intfc}} \frac{\partial G}{\partial n'}(\mathbf{x} - \mathbf{x}_f(s'), t - t')\mu(s', t')\, ds'\, dt'$$

where G is the fundamental solution of the heat equation and the function $\mu(s, t)$ is determined by the solution of the following second order Fredholm integral equation:

$$-\frac{1}{2}\mu(s, t) + \int_t^{t+\delta t} \int_{\text{intfc}} \mu(s', t) \frac{\partial G}{\partial n'}(\mathbf{x}_f(s) - \mathbf{x}_f(s'), t - t')\, ds'\, dt' = \omega(\mathbf{x}_f(s), t) \, .$$

Following Greengard and Strain (1990) and Koumoutsakos, Leonard and Pepin (1994), we can obtain asymptotic formulas for the above integrals. Similar formulas could help in the development of a numerical method based on the proposed algorithm.

This update strategy was posed without requiring any particular numerical methods for the computational steps. We have particular methods in mind, however, for using this strategy for future numerical work. We will use a boundary integral method similar to that used by Lundgren & Mansour (1988, 1991) for the surface computations. That work was for irrotational inviscid flow. Instead of the pressure boundary condition in the form of (11), an unsteady Bernoulli equation was used to access the pressure.

For the vortical part of the flow we propose to use the point vortex method employed by Koumoutsakos *et al* (1994, 1995) for viscous flow problems with solid boundaries. In these problems the Lighthill strategy provides a vorticity flux boundary condition for the second step in the vorticity update, a Neuman condition. In the proposed free-surface strategy, a Dirichlet condition is required for the second vorticity step. This modification can be accomplished by using double layer heat potentials (as suggested above) where single layer potentials were used in the solid boundary work.

4. Conservation of vorticity

We will show that vorticity is conserved in two-dimensional free-surface problems; vorticity which flows through the free-surface doesn't disappear, but resides in the vortex sheet along the surface. (This is shown for general three-dimensional flows in the Lundgren and Koumoutsakos (1998).)

In the interior of the fluid it is easy to show from Helmholtz's equation that

$$\frac{d}{dt} \int_{A_1} \omega\, dA = \int_{S_1} \nu \frac{\partial \omega}{\partial n}\, ds \tag{25}$$

where A_1 is a material "volume" and S_1 its "surface", n is outward from the region, and $-\nu\partial\omega/\partial n$ is the vorticity flux in the outward direction. This says that the

vorticity in A_1 increases because of viscous vorticity flux into the region; there are no vorticity sources in the interior of the fluid.

Everything we need to know about the velocity on side 2 is contained in (17,18,19). We will only use the fact that, because the velocity on side 2 is irrotational, there must be a velocity potential($\mathbf{u}_2 = \nabla\Phi$). We use d/dt to mean the material derivative along side 1, and note that $\mathbf{u}_2 - \mathbf{u}_1 = \gamma\hat{t}$, then by some simple manipulations

$$\frac{d\mathbf{u}_2}{dt} = \frac{\partial\mathbf{u}_2}{\partial t} + \mathbf{u}_1 \cdot \nabla\mathbf{u}_2 \tag{26}$$

$$= \nabla\left(\frac{\partial\phi_2}{\partial t} + \frac{1}{2}\mathbf{u}_2 \cdot \mathbf{u}_2\right) - \gamma\hat{t} \cdot \nabla\gamma\hat{t} - \gamma\hat{t} \cdot \nabla\mathbf{u}_1 \ .$$

Then

$$\hat{t} \cdot \frac{d\mathbf{u}_2}{dt} = \frac{\partial}{\partial s}\left(\frac{\partial\phi_2}{\partial t} + \frac{1}{2}\mathbf{u}_2 \cdot \mathbf{u}_2 - \frac{1}{2}\gamma^2\right) - \gamma\hat{t} \cdot \nabla\mathbf{u}_1 \cdot \hat{t} \ . \tag{27}$$

The last term in this equation is the strain-rate of a surface element and may be expressed as

$$\hat{t} \cdot \nabla\mathbf{u}_1 \cdot \hat{t} = \frac{1}{ds}\frac{d}{dt}ds \ , \tag{28}$$

where ds is a material line element on side 1. Subtracting (10) from (27) then gives

$$\frac{d\gamma}{dt} + \frac{\gamma}{ds}\frac{d}{dt}ds = \frac{\partial}{\partial s}\left(\frac{\partial\phi_2}{\partial t} + \frac{1}{2}\mathbf{u}_2 \cdot \mathbf{u}_2 - \frac{1}{2}\gamma^2 + \frac{p_1}{\rho} + gy\right) - \nu\hat{n} \cdot \nabla\omega \ . \tag{29}$$

This may be written

$$\frac{d}{dt}\gamma ds = -\nu\frac{\partial\omega}{\partial n}ds - \frac{\partial\Phi}{\partial s}ds \tag{30}$$

with Φ given by

$$\Phi = -\left[\frac{\partial\phi_2}{\partial t} + \frac{1}{2}\mathbf{u}_2 \cdot \mathbf{u}_2 - \frac{1}{2}\gamma^2 + gy\right] - \frac{p_1}{\rho} \ . \tag{31}$$

If we integrate (30) over a material segment along the interface we obtain

$$\frac{d}{dt}\int_a^b \gamma ds = -\int_a^b \nu\frac{\partial\omega}{\partial n}ds - \int_a^b \frac{\partial\Phi}{\partial s}ds \ . \tag{32}$$

From this form we see that Φ should be interpreted as a surface-vorticity flux. Since γ is a density (circulation density or surface-vorticity density) the last term in (32), which may be written $\Phi_a - \Phi_b$, is the flux of surface-vorticity into the interval at a minus the flux out at b, while the first term on the right is the flux of vorticity into the interval through the surface.

If the interval is extended over the entire interface, by extending it to infinity for an "ocean" or continuing b around to a for a closed interface like a bubble, we get

$$\frac{d}{dt} \int_{\text{intfc}} \gamma ds = - \int_{\text{intfc}} \nu \frac{\partial \omega}{\partial n} ds. \tag{33}$$

Now letting A_1 in (25) be the entire fluid, we get

$$\frac{d}{dt} \int_{\text{fluid}} \omega dA = \int_{\text{intfc}} \nu \frac{\partial \omega}{\partial n} ds \ . \tag{34}$$

Adding (34) and (33) gives

$$\frac{d}{dt} \int_{\text{fluid}} \omega dA + \frac{d}{dt} \int_{\text{intfc}} \gamma ds = 0 \ . \tag{35}$$

It is in this sense that vorticity is conserved.

We began this approach as an attempt to obtain an evolution equation for γ which would eliminate solving an integral equation, (23), to update γ. Equation (29) or (30) might appear to play such a role, but the occurrence of the velocity potential ϕ_2 in the equation makes it unuseable for this purpose. Since ϕ_2 could be expressed by an integration over the surface involving γ, the time derivative of ϕ_2 would involve a surface integral of $d\gamma/dt$ therefore an integral equation for $d\gamma/dt$ would result, defeating the purpose.

A similar result can be shown for the conservation of vorticity in three-dimensional flows (Lundgren and Koumoutsakos, 1998).

4.1 Pedley problem

A problem solved by Pedley (1968) as part of a study on the stability of swirling torroidal bubbles gives an example which illustrates some concepts discussed here. One can describe the flow as a potential vortex of circulation Γ swirling around a bubble cavity of radius R. The flow is induced by a vortex sheet of strength $\gamma_0 = \Gamma/2\pi R$ at the bubble interface. At some initial time one turns on the viscosity and vorticity begins to leak from the vortex sheet into the fluid. The circulation at infinity remains constant; therefore, the strength of the vortex sheet must decrease with time.

We pose this problem in the form described in Section 2. Since the flow is axially symmetric the vorticity satisfies

$$\frac{\partial \omega}{\partial t} = \nu \left(\frac{\partial^2 \omega}{\partial r^2} + \frac{1}{r} \frac{\partial \omega}{\partial r} \right) \ . \tag{36}$$

The vorticity boundary condition (8) is

$$\omega_1 = -2V_1/R \ , \tag{37}$$

where $V_1 = \mathbf{u}_1 \cdot \hat{t}$ is the tangential component of the velocity at the interface (with the tangent convention used earlier V_1 is negative for positive swirl), and R is the constant radius of curvature of the surface. The pressure boundary condition (11) is

$$\frac{\partial V_1}{\partial t} = -\nu \left(\frac{\partial \omega}{\partial r} \right)_1 . \tag{38}$$

The velocity inside the bubble is zero so $\mathbf{u}_2 \cdot \hat{t} = 0$. The strength of the vortex sheet is therefore $\gamma = -V_1$, a positive quantity. The sense of the problem is that since ω_1 is required to be non-zero, a layer of positive vorticity must develop in the fluid. The resulting flux of vorticity out of the interface causes γ to decrease with time.

Equations (37) and (38) may be combined into a single boundary condition

$$\frac{\partial \omega_1}{\partial t} = \frac{2\nu}{R} \left(\frac{\partial \omega}{\partial r} \right)_1 . \tag{39}$$

Therefore, the problem is to solve (36) with this boundary condition and with initial conditions $\omega = 0$ for all $r > R$ and $\omega = 2\gamma_0/R$ for $r = R$. This last condition prevents the trivial solution.

For large $\tau (\equiv \nu t/R^2)$ Pedley gives an approximate solution;

$$\omega = \frac{\pi \gamma_0}{2R\tau} \exp\left(-\frac{r^2}{4R^2 \tau} \right) . \tag{40}$$

This satisfies (36) exactly but has a relative error of order τ^{-1} in the boundary condition. For small τ another approximate similarity solution is

$$\omega = \frac{2\gamma_0}{R} \exp(2x + 4\tau) \, \mathrm{Erfc}\left(\frac{x}{2\sqrt{\tau}} + 2\sqrt{\tau} \right) \tag{41}$$

where $x = (r - R)/R$. This solution satisfies the boundary condition exactly but neglects the last term in (36), requiring that τ be small enough that the vortical layer is thin compared to the radius of the bubble.

Further details of the solution are unimportant here. This problem illustrates both conservation of vorticity and generation of vorticity when there is flow along a curved free-surface.

5. Conclusion

In this paper we have presented a strategy for solving free surface viscous flow problems in a vortex dynamics formulation. This strategy centers on determining suitable boundary conditions for the vorticity in analogy with Lighthill's strategy for solid boundary flows. The two free surface boundary conditions play distinct roles in determining free surface viscous flows. We have shown that the pressure boundary condition determines the strength of a vortex sheet at the free surface, which determines the irrotational part of the flow. The pressure force modifies the surface velocity, from which the vortex sheet strength is found by solving an integral

equation. The zero shear stress boundary condition, on the other hand, determines the *value* of the vorticity at the surface, providing a Dirichlet condition for the vorticity equation.

We have shown that vorticity is conserved for both two- and three-dimensional free surface flows, the vortex sheet being considered part of the vorticity field. It follows that vorticity which might appear to be lost by flux across the free surface now resides in the vortex sheet. It was shown in the appendix that vorticity is conserved for two *viscous* fluids in contact across an interface. It is physically clear that, in the limit as the density and viscosity of one of the fluids tend to zero, the vorticity in that fluid would be confined to a thin surface layer. Vorticity would then be conserved in the remaining fluid plus a contribution in the surface layer. Therefore, the conclusions we draw for free surface flows are physically reasonable for real fluids.

REFERENCES

BERNAL, L. P. & KWON, J. T. 1989 Vortex Ring Dynamics at a Free Surface. *Phys. Fluids A.* **1**, 449-451.

DABIRI, D. & GHARIB, M. 1997 Experimental investigation of the vorticity generation within a spilling water wave. *J. Fluid Mech.* **330**, 113-139.

DUNCAN, J. H., PHILOMIN, V., BEHRES, M. & KIMMEL, J. 1994 The formation of spilling breaking water waves. *Phys. Fluids.* **6**, 2558-2560.

FRIEDMAN, A. 1966 *Partial Differential Equations of Parabolic Type.* Prentice-Hall, Englewood, NJ.

GHARIB, M. 1994 Some Aspects of Near-Surface Vortices. *Appl. Mech. Rev.* **47**, S157-S162.

GREENGUARD, L. & STRAIN, J. 1990 A Fast Algorithm for the evaluation of Heat Potentials. *Comm. Pure Appl. Math.* **43**, 949-963.

KINNEY, R. B. & PAOLINO, M. A. 1974 *ASME J. Appl. Mech.* 41.

KINNEY, R. B. & CIELAK, Z. M. 1977 Analysis of Unsteady Viscous Flow Past an Airfoil: Part I–Theoretical Development. *AIAA J..* **15**, 52-61.

KOUMOUTSAKOS, P., LEONARD, A. & PEPIN, F. 1994 Boundary conditions for viscous vortex methods. *J. Comp. Phys.* **113**, 52-61.

KOUMOUTSAKOS, P. & LEONARD, A. 1995 High-resolution simulations of the flow around an impulsively started cylinder using vortex methods. *J. Fluid Mech.* **296**, 1-38.

LIGHTHILL, M. J. 1963 In *Boundary Layer Theory.* (ed. J.Rosenhead) pp. 54-61. Oxford University Press.

LIN, J. C. & ROCKWELL, D. 1995 Evolution of a quasi-steady breaking wave. *J. Fluid Mech.* **302**, 29-44.

LONGUET-HIGGINS, M. S. 1992 Capillary rollers and bores. *J. Fluid Mech.* **240**, 659-668.

LUGT, H. J. 1987 Local flow properties at a viscous free surface. *Phys. Fluids.* **30**, 3647-3652.

LUNDGREN, T. S. 1989 In Mathematical aspects of vortex dynamics. (ed. R. E. Caflisch), pp. 68-79. SIAM, Philadelphia.

LUNDGREN, T. S & KOUMOUTSAKOS, P. 1998 On the generation of vorticity at a free surface. *Submitted to J. Fluid Mech.*

LUNDGREN, T. S. & MANSOUR, N. N. 1988 Oscillations of drops in zero gravity with weak viscous effects. *J. Fluid Mech.* **194**, 479-510.

LUNDGREN, T. S. & MANSOUR, N. N. 1991 Vortex Ring Bubbles. *J. Fluid Mech.* **224**, 177-196.

PEDLEY, T. J. 1967 The stability of rotating flows with a cylindrical free surface. *J. Fluid Mech.* **30**, 127-147.

PRAGER, W. 1928 Die Druckverteilung an Körpern in ebener Potentialströmung. *Phys. Zeit.* **29**, 865-869.

ROOD, E. P. 1994 Interpreting vortex interactions with a free surface. *J. Fluids Eng.* **116**, 91-94.

TRUESDELL, C. 1953 The Kinematics of Vorticity. Indiana Univ. Press.

WU, J.-Z. 1995 A theory of three-dimensional interfacial vorticity dynamics. *Phys. Fluids.* **7**, 2375-2395.

Active control of turbulent channel flow

By P. Koumoutsakos

1. Motivations and objectives

The active control of turbulent flows is gaining recognition as a possible means for greatly improved performance of aerospace and marine vehicles. While passive devices have been used effectively in the past, active control strategies have the potential of allowing a significant improvement in the performance of future configurations.

Along with small and robust sensors and actuators, simple yet effective control algorithms, which are based on measurable flow quantities, are needed to make active feedback control of turbulence a reality. An algorithm for active feedback turbulent flow control (herein referred to as opposition control) was first introduced by Choi, Moin and Kim (1994). In the opposition control approach, the vertical motion of the turbulent flow near the wall is countered by an opposing blowing/suction distribution of velocity on the wall. Using this technique a 25% drag reduction was obtained by counteracting the velocity field sensed at $y^+ \approx 15$. Though the opposition control algorithm is simple and effective for viscous drag reduction, it has the substantial drawback that it requires measurements inside the flow domain. In order to alleviate this difficulty, Lee *et al.* (1997) employed a neural network to construct a simple feedback control algorithm using information only at the wall. Their methodology was shown to reduce skin friction by about 20%.

We outline here a novel feedback control algorithm using information that can be obtained at the wall. This framework relies on the identification of the near-wall structures via their induced wall vorticity flux. The present control scheme is based on the manipulation of the vorticity flux components, which can be obtained as a function of time by measuring the instantaneous pressure at the wall and calculating its gradient. An algorithm is presented which allows for the explicit calculations of the necessary control strengths. Application of the present control scheme to low Reynolds number turbulent channel flow produced drag reduction of up to 40% using wall information only. Moreover, it appears that using the present methodology open-loop control laws can be devised.

Further details of the present methodology and the results discussed herein can be found in Koumoutsakos (1997,1998) and Koumoutsakos et. al. (1997).

2. Accomplishments

The present scheme (Koumoutsakos, 1997) is based on the manipulation of the vorticity creation at a wall, using wall information only. The pressure field is sensed at the wall and its gradient (the wall vorticity flux) is calculated. Blowing/suction at the wall is the actuating mechanism and its strength is calculated explicitly by formulating the mechanism of vorticity generation at a no-slip wall.

In wall bounded flows, the tangential motion of fluid elements relative to the wall establishes velocity gradients. With the definition of vorticity ($\boldsymbol{\omega}$) as the curl of velocity ($\boldsymbol{\omega} = \nabla \times \mathbf{u}$), this may be equivalently described in terms of the vorticity that is acquired by the fluid elements near the wall. (Lighthill, 1963) envisioned the wall as a system of sources and sinks of vorticity.

We consider a cartesian coordinate system and flow over a flat wall identified with the xz plane, normal to the y-axis. The vorticity flux vector is then expressed as:

$$\sigma = -\left(\nu \frac{\partial \omega}{\partial y} \right)_{w}$$

For an incompressible viscous flow over a stationary wall, the vorticity flux is directly proportional to the pressure gradients, as the momentum equations reduce at the wall to (Panton 1984):

$$\nu \left(\frac{\partial \omega_x}{\partial y} \right)_{w} = \frac{1}{\rho} \left(\frac{\partial P}{\partial z} \right)_{w}, \quad -\nu \left(\frac{\partial \omega_z}{\partial y} \right)_{w} = \frac{1}{\rho} \left(\frac{\partial P}{\partial x} \right)_{w}$$

where P is the pressure and ω_x and ω_z are the streamwise and spanwise vorticity components. Note that the flux of the wall normal vorticity, ω_y, may be determined from the kinematic condition ($\nabla \cdot \boldsymbol{\omega} = 0$).

2.1 Measurements of the wall vorticity flux

In order to assess the practical implications of the proposed algorithm, we outline some research efforts associated with measurements of the vorticity flux. Experimental measurements of the wall vorticity flux in a turbulent flow have been reported by Andreopoulos and Agui (1996). Their measurements demonstrated the significance of vorticity flux in describing near wall processes. They observed that fluid acquires or loses vorticity at the wall during rather violent events followed by periods of small fluctuations. Their experiments demonstrated that the major contributions to the vorticity flux come from the uncorrelated part of the pressure signals, at two adjacent locations, which contain a wide range of vortical scales. As the degree of correlation is smaller between the small scales, their contribution to the vorticity flux is more pronounced. This imposes a severe requirement on the spatial resolution of the pressure gradients/vorticity flux measurements. Practical applications (Moin & Bewley 1995) would require actuators and sensors with sizes in the order of $50\mu m$ and actuator frequencies of 1MHz. Recent advances in micro pressure sensor fabrication technology (Ho & Tai 1996) give us an opportunity to overcome these difficulties. Löfdahl et. al. (1996) presented measurements in a two-dimensional flat plate boundary layer with a resolution of eddies with wave numbers less than ten viscous units using microscopic silicon pressure transducers. It appears that using this new technology one may be able to describe in detail physical processes in terms of the wall vorticity and the wall vorticity flux.

2.2 Vorticity flux induced by blowing and suction at the wall

The role of the vorticity flux from oscillating walls as a mechanism for the control of unsteady separated flows was discussed by Wu *et al.* (1993). They concluded that wall oscillations can produce a mean vorticity flux that is partially responsible for phenomena of vortex flow control by waves. Gad-El-Hak (1990) has shown that the vorticity flux can be affected by wall transpiration as well as by wall-normal variation of the kinematic viscosity (ν) as a result of surface heating, film boiling, cavitation, sublimation, chemical reaction, wall injection of higher/lower viscosity fluid, or in the presence of shear thinning/thickening additive.

However, these works do not provide us with an explicit formulation for the actuator strength necessary to induce a desired vorticity flux at the wall. This may be achieved by considering the generation of vorticity at the wall as a fractional step algorithm (Lighthill 1963).

At each time step (δt) the no-slip boundary condition can be rendered equivalent to a vorticity flux boundary condition (Koumoutsakos, Leonard, & Pepin 1994) which is materialized in successive substeps. During the first substep we consider the inviscid evolution of the vorticity field in the presence of solid boundaries. The no-through flow boundary condition is enforced via the introduction of a vortex sheet $\gamma(\mathbf{s})$ along the surface ($\mathbf{s}$) of the body. The vortex sheet is equivalent to a spurious slip velocity on the boundary that needs to be eliminated in order to enforce the no-slip boundary condition. This is achieved at the next substep of the algorithm as the vortex sheet enters diffusively into the flow field. When γ is eliminated from the body surface in the interval $[t, \, t + \delta t]$, the circulation (Γ) of the flow field would be modified according to:

$$\oint \gamma(s)\, ds \;=\; \int_{t}^{t+\delta t} \frac{d\Gamma}{dt'}\, dt' \tag{1}$$

On the other hand, Kelvin's theorem states that the rate of change of circulation induced to the fluid elements due to the presence of the body is:

$$\frac{d\Gamma}{dt} \;=\; \nu \oint \frac{\partial \omega}{\partial n}(s)\, ds \tag{2}$$

If we consider this vorticity flux to be constant over the small interval of time (δt), we will have:

$$\nu \frac{\partial \omega}{\partial n}(s) \;=\; -\gamma(s)/\delta t \tag{3}$$

This constitutes then a Neumann type vorticity boundary condition for the vorticity field equivalent to the no-slip boundary condition (Koumoutsakos, Leonard, & Pepin 1994).

This formulation helps us determine the vorticity flux induced by a set of actuators such as ideal sources/sinks located at the wall. Without loss of generality we consider a two-dimensional flow over a flat wall and a system of sources/sinks of strength q_j that are distributed uniformly over a panel of size d_j, centered at

locations $x'_j, j = 1, 2, 3, ...N$. When the sources/sinks are switched on, the induced tangential velocity at point x_i on the wall and the corresponding vorticity flux can be determined as:

$$\nu \, \delta t \, \frac{\partial \omega}{\partial y}(x_i) \;=\; \sum_{j=1}^{N} \frac{q_j}{2\pi} \int_{-d_j/2}^{d_j/2} \frac{ds}{x - s} \tag{4}$$

where $x = x_i - x'_j$. The methodology outlined herein may be formulated for a variety of actuators, such as wall acceleration, deformation, etc.

3. An active control strategy

For the purposes of our control scheme we consider a series of vorticity flux (or equivalently pressure gradient) sensors on the wall at locations $x_i, i = 1, 2, 3, ...M$. Using the formulas described above we can explicitly determine the actuator strengths necessary to achieve a desired vorticity flux profile at the wall at a time instant, k, by solving the linear set of equations:

$$B\,u_k + X_{k-1} \;=\; D_k \tag{5}$$

where $D_k = (\frac{\partial \omega^k}{\partial y}(x_1), \frac{\partial \omega^k}{\partial y}(x_2), ..., \frac{\partial \omega^k}{\partial y}(x_M))$ is an $M \times 1$ vector of the *desired* vorticity flux at the sensor locations, $X_{k-1} = (\frac{\partial \omega^{k-1}}{\partial y}(x_1), \frac{\partial \omega^{k-1}}{\partial y}(x_2), ..., \frac{\partial \omega^{k-1}}{\partial y}(x_M))$ is an $M \times 1$ vector of the *measured* vorticity flux at the sensor locations and $u_k = (q_1^k(x'_1), q_2^k(x'_2), ..., q_N^k(x'_N))$ is an $N \times 1$ vector of source strengths at the actuator locations, B is an $M \times N$ matrix whose elements B_{ij} are determined by evaluating the integrals in Eq. 4. The unknown source/sink strengths are determined by solving the system in Eq. 5. If the relative locations of the sensors and actuators remain constant, matrix B need be inverted only once, thus minimizing the computational cost of the method.

We may distinguish between *in-phase* control (implying enhancement of the wall vorticity flux) by selecting $D_k = 2X_{k-1}$ and *out-of-phase* control (implying cancellation of the induced vorticity flux) by selecting $D_k = 0$.

Moreover, the present technique gives us the flexibility to adapt the actuator strengths to specific constraints. In the present calculations the requirement of zero net mass flux

$$\sum_{j=1}^{N} q_j \;=\; 0$$

is easily incorporated in the above scheme by appropriately adjusting matrix B. A square, invertible matrix is always possible by accordingly modifying the number of sensors and actuators. The simplicity of the present scheme allows for a number of different placements of sensors and actuators. Here we chose the locations of sensors and actuators to be collocated. Physically this may be understood as an advantageous situation as the sensors are able to detect the vorticity field induced by the actuators, which allows the control scheme to suitably compensate for it.
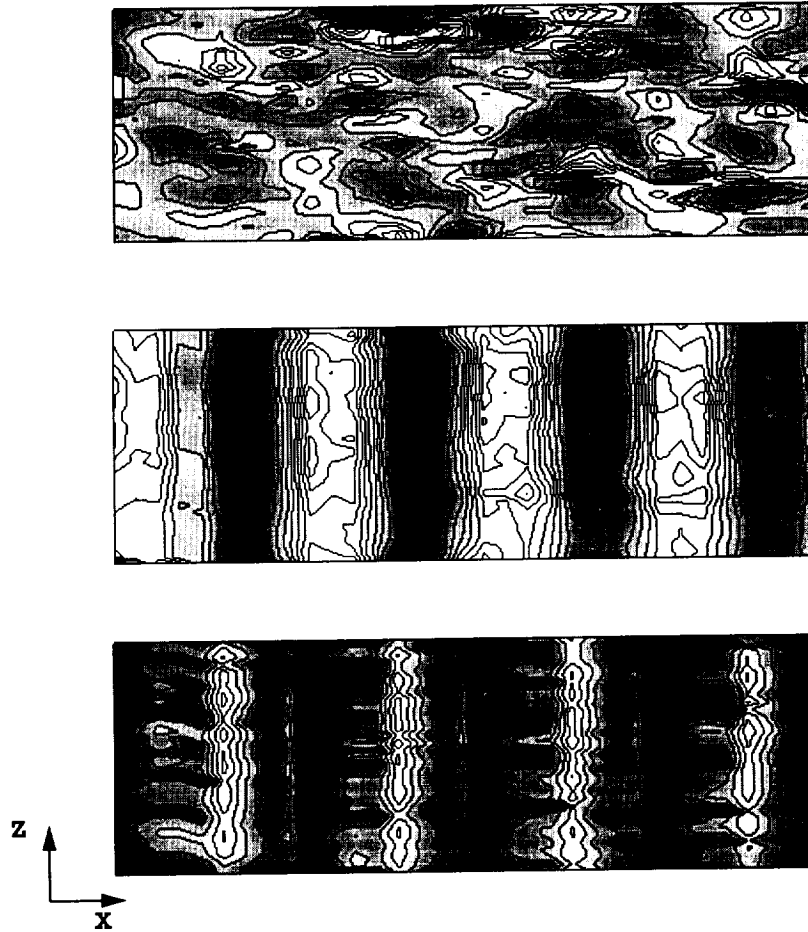
FIGURE 1.   Contour plots of streamwise vorticity flux (top), Spanwise vorticity flux (middle) and shear stresses (bottom) in a *controlled* turbulent channel flow. Black (positive) and white (negative) color coding is used for the plots.

4. Control of turbulent channel flow

Simulations of the model problem of vortex dipole-wall interactions (Koumout-sakos, 1997) have revealed that the present control scheme can alter drastically these interactions. In-phase control results in the "trapping" of the primary vortices by the enhanced secondary vorticity field. The out-of phase control has resulted in the absorption of the impinging dipole and the establishment of small oscillating vortical structures over the wall. These structures are maintained by the present algorithm as the system constantly reacts to the production of the vorticity induced by the actuators.
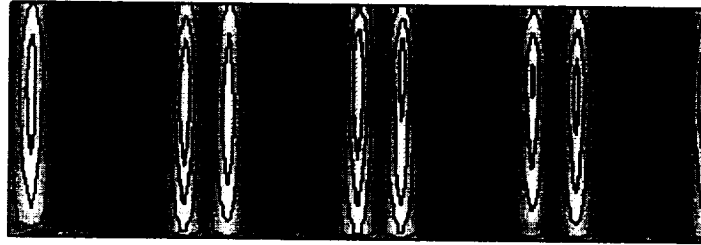
FIGURE 2.   Contour plots of actuator strengths.   Black (blowing) and white (suction) color coding is used for the plots.
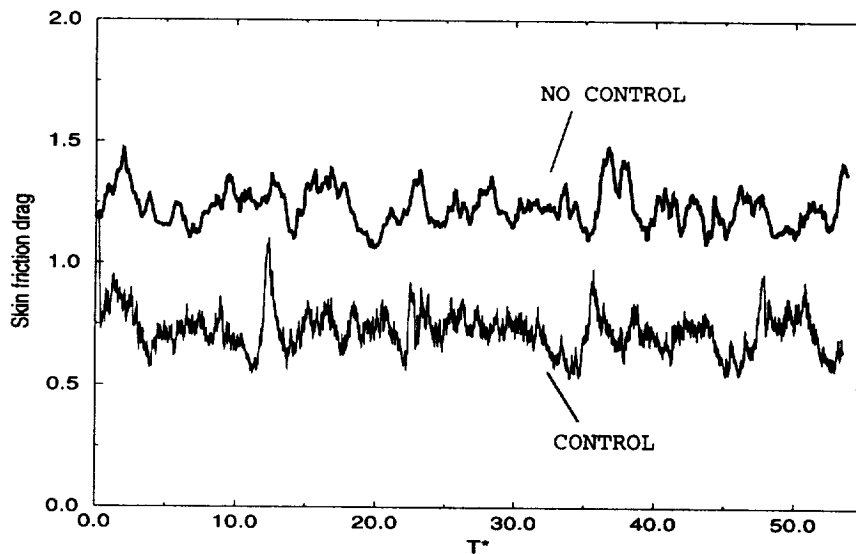

FIGURE 3.   Skin friction drag on the bottom wall of the controlled and uncontrolled flow.

We present here some results from the application of this vorticity-flux control algorithm on a low Reynolds number turbulent channel flow ($Re_\tau = 200$).

The numerical method (Le, Moin and Kim 1997) is a fractional step algorithm in primitive variables ($\mathbf{u} - P$), using central finite differences for spatial discretization and a third order Runge-Kutta time advancement scheme. The channel dimensions

are $2\pi, 2.10, 2.0$ for the streamwise, spanwise, and wall normal direction. Simulations were carried out with a grid resolution of $N_x \times N_z \times N_y = 128 \times 64 \times 128$. A cosine spacing was employed for the grid points in the wall-normal direction. The non-dimensional discretization is:$\Delta x^+ \approx 12$, $\Delta z^+ \approx 8$, $\Delta y^+ \approx 0.1 - 7$.

Control is applied only on the bottom wall with a a collocated arrangement of sensors and actuators. In this arrangement the rows of sensors and actuators are located at alternating streamwise grid locations on the bottom wall. Their strength is determined using a technique similar to the two-dimensional techniques already described.

In the present scheme for three-dimensional flows, the 'desired' and the measured vorticity flux may be related as:

$$
\begin{pmatrix} \nu \frac{\partial \omega_x}{\partial y} \\ \nu \frac{\partial \omega_z}{\partial y} \end{pmatrix}_{control} = \begin{pmatrix} a & b \\ c & d \end{pmatrix} \begin{pmatrix} \nu \frac{\partial \omega_x}{\partial y} \\ \nu \frac{\partial \omega_z}{\partial y} \end{pmatrix}_{measured} \tag{6}
$$

The coefficients a, b, c, d can be chosen *a-priori*, and they may be constant or spatially varying. The parameter space can be optimized for drag reduction/increase.

We have conducted several sets of simulations, varying locally and globally the coefficients a, b, c, d. Most of our simulations have been conducted with the set of parameters $a = b = c = 0$ and $d = \pm 1$, which is equivalent to considering *In/Out* of phase control of the *spanwise* vorticity flux.

In particular, we present here some results from the out-of phase control. After a short transient state a drastic modification of the inner wall structure is observed. The streaks are eliminated, and highly spanwise correlated patterns are established for the spanwise vorticity flux, the shear stresses (Fig. 1), and the actuator strengths (Fig. 2). These structures and further flow visualizations (Koumoutsakos, 1998) suggest the formation of unsteady spanwise vortical "rollers" in the inner layer of the wall. These spanwise vortical rollers result in the formation of positive and negative shear stresses at the wall. The spanwise correlation of the near wall structures persist till about $y^+ = 15$, beyond which the influence of the wall is not discernible in the flow field. Moreover, the regularity in the resulting actuator strengths (Fig. 2) suggest that it is possible to devise open loop control laws using the present methodology (Koumoutsakos, 1998).

The elimination of streaks and the disruption of the near wall processes by the establishment of the particular vortical "rollers" resulted in skin friction drag reduction in the order of 40% (Fig. 3).

5. Conclusions

A new feedback control algorithm (Koumoutsakos, 1997) based on the manipulation of vorticity creation at the wall was outlined. In this scheme the vorticity flux is sensed at the wall via the measurement of wall pressure. A simple control strategy allows calculation of the strength of wall transpiration to achieve a desired wall vorticity flux. Implementation of the vorticity flux feedback control algorithm in the simulation of a low Reynolds number turbulent channel flow shows a drastic modification of the near wall vortical structures and indicates high skin friction drag

reduction ($\approx 40\%$). The results of the present simulations suggest that it is possible to devise open-loop control laws using the present methodology. Work is underway to implement the proposed strategy in the control of unsteady separated bluff body flows.

6. Acknowledgments

REFERENCES

ANDREOPOULOS & AGUI 1996 Wall-vorticity flux dynamics in a two-dimensional turbulent boundary layer. *J. Fluid Mech.* **309**, 45-84.

BEWLEY, T. R. 1997 Optimal and robust control and estimation of transition and turbulence. *Ph.D. dissertation, Stanford University.*

CHOI, H., MOIN, P., & KIM, J. 1994 Active turbulence control for drag reduction in wall-bounded flows. *J. Fluid Mech.* **262**, 75-110.

GAD-EL-HAK, M. 1990 Control of Low-Speed Airfoil Aerodynamics. *AIAA J.* **118**, 1537-1552.

HO, C. & TAI, Y. 1996 Review: MEMS and its applications for flow control. *J. Fluids Eng.* **118**, 437-447.

HORNUNG, H. 1990 *Sources of Vorticity, Ae 232. Class Notes, California Institute of Technology.*

JOHANSSON, A. V., ALFREDSSON, P. H., & HARITONIDIS, J. H. 1987 Evolution and dynamics of shear-layer structures in near-wall turbulence. *J. Fluid Mech.* **224**, 579.

KIM, J., MOIN, P., & MOSER, R. 1987 Turbulence statistics in fully developed channel flow at low Reynolds number. *J. Fluid Mech.* **177**, 133-166.

KOUMOUTSAKOS, P. 1997 Active Control of Vortex-Wall Interactions. *Phys. Fluids.* **9**, 3808-3816.

KOUMOUTSAKOS, P. 1998 A new method for the active control of turbulent channel flow. *Submitted for publication.*

KOUMOUTSAKOS P., BEWLEY T., HAMMOND E. & MOIN, P. 1997 Feedback Algorithms for turbulence control - some recent developments. *AIAA paper No. 97-2008.*

KOUMOUTSAKOS, P., LEONARD, A. & PEPIN, F. 1994 Boundary conditions for viscous vortex methods. *J. Comput. Phys.* **113**, 52.

LE, H., MOIN, P. & KIM, J. 1997 Direct numerical simulation of turbulent flow over a backward-facing step. *J. Fluid Mech.* **330**, 349-374.

LEE, C., KIM, J., BABCOCK, D., & GOODMAN, R. 1997 Application of neural network to turbulence control for drag reduction. *Phys. Fluids A.* **9**, 740-1747.

LIGHTHILL, M. J. 1963 *Introduction. Boundary Layer Theory.* J. Rosenhead (editor) - Oxford University Press, New York, 54-61.

LÖFDAHL, L., KÄLVESTEN, E., & STEMME, G. 1996 Small silicon pressure transducers for space-time correlation measurements in a flat plate boundary layer. *J. Fluids Eng.* **118**, 457-463.

MOIN, P., & BEWLEY, T. R. 1995 Application of control theory to turbulence. *Twelfth Australasian Fluid Mechanics Conference, Dec. 10-15, Sydney,* 109-117.

PANTON, R. L. 1984 *Incompressible Flow. Wiley.*

WU, J. Z., WU, X. H., & WU, J. M. 1993 Streaming Vorticity Flux from Oscillating walls with finite amplitude. *Phys. Fluids A.* **5**, 1933-1938.

A generalized framework for
robust control in fluid mechanics

By T. Bewley, R. Temam AND M. Ziane

1. Motivation and objectives

The application of *optimal* control theory to turbulence has proven to be quite effective when complete state information from high-resolution direct numerical simulations is available (Bewley, Moin, & Temam 1997a). In this approach, an iterative optimization algorithm based on the repeated computation of an adjoint field is used to optimize the controls for a finite-horizon nonlinear flow problem (Abergel & Temam 1990). In order to extend this infinite-dimensional optimization approach to control externally disturbed flows for which the control must be determined based on limited noisy flow measurements alone, it is necessary that the control computed be insensitive to both state disturbances and measurement noise. For this reason, *robust* control theory, a generalization of optimal control theory, is now examined as a technique by which effective control algorithms might be developed for infinite-dimensional laminar (linear) and turbulent (nonlinear) flows subjected to a wide class of external disturbances.

The numerical approach proposed to solve the robust control problem is based on computations of an $O(N)$ adjoint field, where N is the number of grid points used to resolve the continuous PDE for the flow problem. Note that $N \sim O(10^6)$ for problems of engineering interest today and may be expected to increase in the future. Computation of the adjoint field is only as difficult as the computation of the flow itself, and thus is a numerically tractable approach to the control problem whenever the computation of the flow itself is numerically tractable. In contrast, control approaches based on the solution of $O(N^2)$ Riccati equations have not been shown to be numerically tractable for discretizations with $N > O(10^3)$.

In its essence, robust control theory (Doyle *et al.* 1989, Green & Limebeer 1995) boils down to Murphy's Law (Bewley, Moin, & Temam 1997b) taken seriously:

If a worst-case system disturbance can disrupt
a controlled closed-loop system, it will.

When designing a robust controller, therefore, one should *plan* on a finite component of the worst-case disturbance aggravating the system, and design a controller which is suited to handle even this extreme situation. A controller which is designed to work even in the presence of a finite component of the worst-case disturbance will also be robust to a wide class of other possible disturbances which, by definition, are not as detrimental to the control objective as the worst-case disturbance. Thus, the problem of finding a robust control is intimately coupled with the problem of finding the worst-case disturbance, in the spirit of a non-cooperative game.

To summarize the robust control approach briefly, a cost functional $\mathcal{J}$ describing the control problem at hand is defined that weighs together the (distributed) control

ϕ, the (distributed) disturbance w, and the flow perturbation $u(\phi, w)$. The cost functional considered in the present work is of the form

$$\mathcal{J}(\phi, w) = \frac{1}{2} \int_0^T \int_\Omega |\mathcal{C}_1 u|^2 \, dx \, dt + \frac{1}{2} \int_\Omega |\mathcal{C}_2 u(x, T)|^2 \, dx + \int_0^T \int_{\partial\Omega} \mathcal{C}_3 \frac{\partial u}{\partial n} \cdot \vec{r} \, d\sigma \, dt$$

$$+ \frac{1}{2} \int_0^T \int_\Omega \left[\ell^2 |\phi|^2 - \gamma^2 |w|^2 \right] dx \, dt.$$

This cost functional is simultaneously minimized with respect to the control ϕ and maximized with respect to the disturbance w, as illustrated in Fig. 1. The robust control problem is considered to be solved when a saddle point $(\bar{\phi}, \bar{w})$ is reached; note that such a solution, if it exists, is not necessarily unique. Four cases of particular interest are:

a. $\mathcal{C}_1 = d_1 \, I$ and $\mathcal{C}_2 = \mathcal{C}_3 = 0 \Rightarrow$ regulation of the turbulent kinetic energy.

b. $\mathcal{C}_1 = d_2 \, \nabla \times$ and $\mathcal{C}_2 = \mathcal{C}_3 = 0 \Rightarrow$ regulation of the square of the vorticity.

c. $\mathcal{C}_2 = d_3 \, I$ and $\mathcal{C}_1 = \mathcal{C}_3 = 0 \Rightarrow$ terminal control of the turbulent kinetic energy.

d. $\mathcal{C}_3 = d_4 \, \nu \, I$ and $\mathcal{C}_1 = \mathcal{C}_2 = 0 \Rightarrow$ minimization of the average skin-friction in the direction $\vec{r}$ integrated over the boundary of the domain.

All four of these cases, and many others, may be considered in the present framework; the extension to other linear/quadratic interior/boundary regulation/terminal constraints is straightforward. The dimensional constants d_i (which are the appropriate functions of the kinematic viscosity ν, a characteristic length L_0, a characteristic velocity U_0, and the volume V_0 and the surface area S_0 of the domain Ω) are included to make the cost functional dimensionally consistent.

It cannot be assumed at the outset that a solution to the min/max problem described above even exists. However, it is established in the present paper that, for a sufficiently large γ and reasonable requirements on the regularity of the problem (described later in this introduction), a solution to this min/max problem indeed does exist, with the (finite) magnitudes of the disturbance and the control governed by the scalar parameters γ and ℓ. To accomplish this, we will extend the optimal control setting of Abergel & Temam (1990) to analyze the non-cooperative differential game of the robust control setting in which a saddle point $(\bar{\phi}, \bar{w})$ is sought. The analysis will also account for the possibility of corners in the boundary Ω. Our treatment of the presence of corners in the domain avoids "smoothing" out the corners as was done in Abergel & Temam (1990) and thus further extends the optimal control analysis contained therein.

Note that, for simplicity, only the *control* problem is considered; the concomitant *estimation* problem, required to determine the control when only partial flow information is measured, is closely related to the control problem discussed here.

1.1 An intuitive introduction to robust control theory

Consider the present problem as a differential game between a fluid dynamicist seeking the "best" control ϕ which stabilizes the flow perturbation with limited
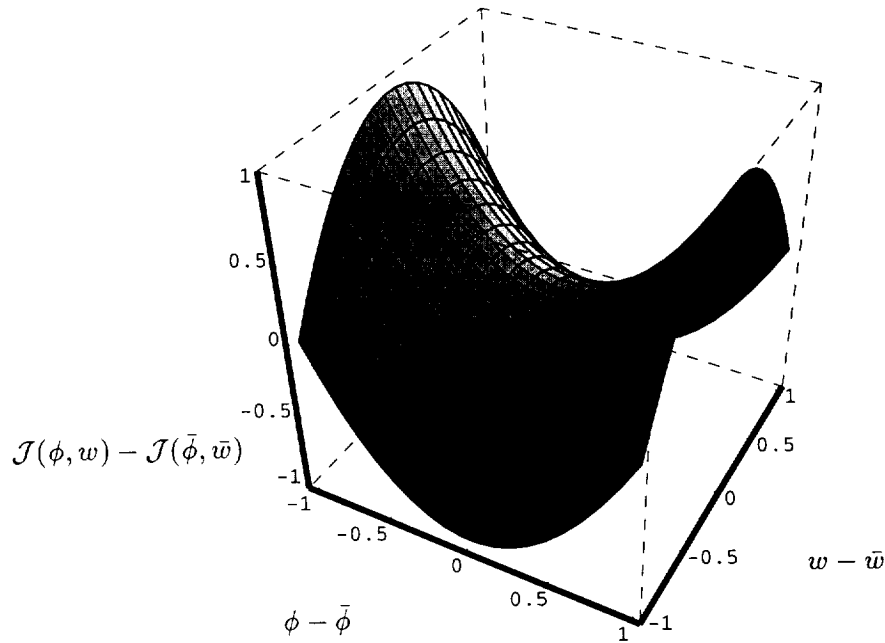
FIGURE 1. Schematic of a saddle point representing the neighborhood of a solution to a robust control problem with one scalar control variable ϕ and one scalar disturbance variable w. When the robust control problem is solved, the cost function $\mathcal{J}$ is simultaneously minimized with respect to ϕ and maximized with respect to w, and a saddle point such as $(\bar{\phi}, \bar{w})$ is reached. The present paper formulates the infinite-dimensional extension of this concept, where the cost $\mathcal{J}$ is related to a distributed control ϕ and a distributed disturbance w through the solution of the Navier-Stokes equation.

control effort and, simultaneously, nature seeking the "maximally malevolent" disturbance w which destabilizes the flow perturbation with limited disturbance magnitude (Green & Limebeer 1995). The parameter γ^2 factors into such a competition as a weighting on the magnitude of the disturbance which nature can afford to offer, in a manner analogous to the parameter ℓ^2, which is a weighting on the magnitude of the control which the fluid dynamicist can afford to offer.

The parameter ℓ^2 may be interpreted as the "price" of the control to the fluid dynamicist. The $\ell \to \infty$ limit corresponds to prohibitively "expensive" control and results in $\phi \to 0$ in the minimization with respect to ϕ for the present problem. Reduced values of ℓ increase the cost functional less upon the application of a control ϕ. A nonzero control results whenever the control ϕ can affect the flow perturbation u in such a way that the net cost functional $\mathcal{J}$ is reduced.

The parameter γ^2 may be interpreted as the "price" of the disturbance to nature. The $\gamma \to \infty$ limit results in $w \to 0$ in the maximization with respect to w, leading to the optimal control formulation of Abergel & Temam (1990) for ϕ alone. Reduced values of γ decrease the cost functional less upon the application of a disturbance w. A nonzero disturbance results whenever the disturbance w can affect the flow

perturbation u in such a way that the net cost functional $\mathcal{J}$ is increased.

Solving for the control ϕ which is effective even in the presence of a disturbance w, which maximally spoils the control objective, is a way of achieving system robustness. As stated earlier, a control which works even in the presence of the malevolent disturbance w will also be robust to a wide class of other possible disturbances.

In the present systems, for $\gamma < \gamma_0$ for some critical value γ_0 (an upper bound of which is established in this paper), the non-cooperative game does not have a finite solution; essentially, the malevolent disturbance wins. The control ϕ corresponding to $\gamma = \gamma_0$ results in a stable system even when nature is on the brink of making the system unstable. However, note that the control determined with $\gamma = \gamma_0$ is not always the most suitable as it may result in a very large control magnitude and may have degraded performance in response to disturbances with structure more benign than the worst-case scenario. In the implementation, variation of ℓ and γ provide the necessary flexibility in the control design to achieve the desired trade-offs between disturbance response and control magnitude required (Bewley & Liu 1997).

1.2 Governing equations

We begin with the Navier-Stokes equation for a flow U in an open domain $\Omega \subset \mathbb{R}^3$ such that, in $\Omega \times (0, \infty)$, we have

$$
\begin{cases}
\dfrac{\partial U}{\partial t} - \nu \Delta U + (U \cdot \nabla)U + \nabla P = F, \\[2mm]
\operatorname{div} U = 0, \\[2mm]
U = 0 \qquad \text{on } \partial\Omega, \\[2mm]
U(0) = U_0 \qquad \text{at } t = 0.
\end{cases}
\tag{1.1}
$$

We focus our attention on the case in which the forcing is applied by way of an interior volume force on the r.h.s. of the momentum equation; the case of boundary forcing (such as wall transpiration) is closely related and will be treated later. A stationary or non-stationary solution $U(x,t)$ to this equation with a corresponding forcing $F(x,t)$ will be referred to as the "target" flow for the control problem. (If no target flow is known or given, U and F are taken as zero.)

We are interested in the robust regulation of the deviation of the flow from the desired target (U, F). In §2, we consider the control of the linearized equation which models small perturbations (u, f) to the target flow (U, F) with Dirichlet boundary conditions and known initial conditions such that, in $\Omega \times (0, \infty)$, we have

$$
\begin{cases}
\dfrac{\partial u}{\partial t} - \nu \Delta u + (u \cdot \nabla)U + (U \cdot \nabla)u + \nabla p = f, \\[2mm]
\operatorname{div} u = 0, \\[2mm]
u = 0 \qquad \text{on } \partial\Omega, \\[2mm]
u(0) = u_0 \qquad \text{at } t = 0.
\end{cases}
\tag{1.2}
$$

In §3, we consider the control of the full nonlinear equation which models large perturbations (u, f) to the target flow (U, F) such that, in $\Omega \times (0, \infty)$, we have

$$
\begin{cases}
\dfrac{\partial u}{\partial t} - \nu \Delta u + (u \cdot \nabla)U + (U \cdot \nabla)u + (u \cdot \nabla)u + \nabla p = f, \\[2mm]
\text{div } u = 0, \\[2mm]
u = 0 \qquad \text{on } \partial\Omega, \\[2mm]
u(0) = u_0 \qquad \text{at } t = 0.
\end{cases}
\tag{1.3}
$$

1.3 Mathematical setting

Let Ω be a bounded open set of $\mathbb{R}^3$ with boundary $\partial\Omega$, and let $\vec{n}$ be the unit outward normal vector to $\partial\Omega$. We denote by $H^s(\Omega)$, $s \in \mathbb{R}$ the Sobolev spaces constructed on $L^2(\Omega)$, and $H_0^s(\Omega)$ the closure of $C_0^\infty(\Omega)$ in $H^s(\Omega)$. Following Temam (1984), we set $X = \left\{ u \in ((C_0^\infty(\Omega))^3; \text{ div } u = 0 \right\}$, and denote by H (resp. V) the closure of X in $(L^2(\Omega))^3$ (resp. $(H^1(\Omega))^3$); we have

$$
H = \left\{ u \in (L^2(\Omega))^3; \text{ div } u = 0 \text{ in } \Omega, \ u \cdot \vec{n} = 0 \text{ on } \partial\Omega \right\}
$$

and

$$
V = \left\{ u \in (H_0^1(\Omega))^3; \text{ div } u = 0 \text{ in } \Omega \right\}.
$$

The scalar product on H is denoted by $(u, v) = \int_\Omega u \cdot v \, dx$, that on V is denoted by $((u, v)) = \int_\Omega \nabla u \cdot \nabla v \, dx$, and the associated norms are denoted by $| \cdot |_{L^2}$ and $\| \cdot \|$ respectively. We denote by A the Stokes operator, defined as an isomorphism from V onto the dual V' of V such that, for $u \in V$, Au is defined by

$$
\forall \, v \in V, \quad \langle Au, v \rangle_{V', V} = ((u, v))
$$

where $\langle \cdot, \cdot \rangle_{V', V}$ is the duality bracket between V' and V. The operator A is extended to H as a linear unbounded operator with domain $D(A) = (H^2(\Omega))^3 \cap V$ when $\partial\Omega$ is a C^2 surface; the case of a domain Ω with corners is treated in §4. We also recall the Leray-Hopf projector $\mathcal{P}$, which is the orthogonal projector of the non-divergence-free space $(L^2(\Omega))^3$ onto the divergence-free space H. The Stokes operator is defined with this projector such that

$$
Au = -\mathcal{P}(\Delta u), \quad \forall \, u \in D(A).
\tag{1.4}
$$

We shall denote by $0 < \lambda_1 \leq \lambda_2 \leq \ldots$ the increasing sequence of the eigenvalues of A. Define the bilinear mapping B by

$$
B(u, v) = \mathcal{P}((u \cdot \nabla)v), \quad \forall \, u, v \in V.
\tag{1.5}
$$

Note that B is a bilinear mapping from V into V'. Define a continuous trilinear form b on V such that, with $u, v, w \in (H^1(\Omega))^3$, we have

$$
b(u, v, w) = \langle B(u, v), w \rangle_{V', V}
$$
$$
= \int_\Omega (u \cdot \nabla)v \cdot w \, dx = \int_\Omega u_i \frac{\partial v_j}{\partial x_i} w_j \, dx,
$$

where Einstein's summation is assumed.

The operators A and B may be used to write the Navier-Stokes equation in the "abstract form" useful for mathematical analysis. By application of the Leray projector to (1.2), noting (1.4), (1.5), and that $\mathcal{P}u = u$ and $\mathcal{P}(\nabla p) = 0$, the linearized Navier-Stokes equation, to be considered in §2, may be written in the form

$$\begin{cases} \dfrac{du}{dt} + \nu A u + B(u, U) + B(U, u) = \mathcal{P}f, \\ u \in V, \\ u(0) = u_0, \end{cases} \qquad (1.6)$$

where the regularity required on f, u_0, and U are

$$\begin{cases} f \in L^2(0, T; L^2), \quad \forall\, T > 0; \\ u_0 \in V; \quad U \in C([0, T], V) \cap L^2(0, T; D(A)). \end{cases} \qquad (1.7)$$

Similarly, application of the Leray projector to the nonlinear form (1.3), to be considered in §3, gives

$$\begin{cases} \dfrac{du}{dt} + \nu A u + B(u, U) + B(U, u) + B(u, u) = \mathcal{P}f, \\ u \in V, \\ u(0) = u_0. \end{cases} \qquad (1.8)$$

1.5 Control framework

In the control framework, the interior forcing f is decomposed into a control $\phi \in L^2(0, T, L^2)$ and a disturbance $w \in L^2(0, T, L^2)$, with $T > 0$, in the spirit of the non-cooperative game discussed in §1.1. Thus, we write f as

$$f = B_1 w + B_2 \phi, \qquad (1.9)$$

where B_1 and B_2 are given bounded operators on $(L^2(\Omega))^3$. Only the divergence free part of the forcing f will affect the evolution of the velocity field u, as seen on the r.h.s. of the governing equations (1.6) and (1.8). Thus, in the remainder of this paper, we consider only the divergence free part of the forcing by writing

$$\begin{aligned} \mathcal{P}f &= \mathcal{P}(B_1 w + B_2 \phi) \\ &= \mathcal{B}_1 w + \mathcal{B}_2 \phi, \end{aligned} \qquad (1.10)$$

where $\mathcal{B}_1 = \mathcal{P}B_1$ and $\mathcal{B}_2 = \mathcal{P}B_2$ are mappings from $(L^2(\Omega))^3$ to H. Note that the difference $f - \mathcal{P}f$ may be written as the gradient of a scalar and thus will only modify the pressure p in (1.2) and (1.3). As the solution to the Navier-Stokes equation in the abstract form is implicitly confined to a divergence-free manifold of $(L^2(\Omega))^3$, the pressure p may be entirely neglected in the mathematical analysis.

1.6 Important identities and inequalities

We now recall some important properties of the nonlinear operator b, which can be found, for instance, in §3 of Temam (1984). First, we have the orthogonality identity

$$b(u, v, v) = 0, \quad \forall\, u, v \in V \tag{1.11}$$

as a consequence of div $u = 0$, as shown by integration by parts. Moreover, the continuity of the nonlinear mapping in various functional spaces are expressed by the following classical inequalities: there exists a constant $C_0(\Omega)$ such that

$$\begin{cases} |b(u,v,w)| \le C_0 \|u\| \|v\|^{1/2} |Av|_{L^2}^{1/2} |w|_{L^2}, & \forall\, u \in V,\ v \in D(A),\ w \in H, \\[2mm] |b(u,v,w)| \le C_0 |u|_{L^2}^{1/4} |Au|_{L^2}^{3/4} \|v\| \|w\|_{L^2}, & \forall\, u \in D(A),\ v \in V,\ w \in H,\ , \\[2mm] |b(u,v,w)| \le C_0 |u|_{L^2}^{1/4} \|u\|^{3/4} \|v\| \|w\|_{L^2}^{1/4} \|w\|^{3/4}, & \forall\, u \in V,\ v \in V,\ w \in V. \end{cases}$$

where C_0 denotes here and throughout this paper a numerical constant whose value may be different in each inequality.

Note that the mapping $u \mapsto B(u) = B(u, u)$ is differentiable from V into V'; its differential is defined by

$$\begin{aligned} B'(u)v &= B(u,v) + B(v,u) \qquad \forall\, v \in V \\ &= \mathcal{P}\big((u \cdot \nabla)v + (v \cdot \nabla)u\big). \end{aligned} \tag{1.12}$$

Let $B'(u)^*$ denote the adjoint of $B'(u)$ for the duality between V and V'; the adjoint operator $B'(u)^*$ is thus defined by

$$\langle v, B'(u)w \rangle_{V,V'} = \langle B'(u)^* v, w \rangle_{V',V}. \tag{1.13}$$

It follows from integration by parts (Abergel & Temam 1990) that

$$\begin{aligned} \langle B'(u)^* v, w \rangle_{V',V} &= \int_\Omega \left(\frac{\partial u_i}{\partial x_j} v_i - \frac{\partial v_j}{\partial x_i} u_i \right) w_j \, dx \\ &= \int_\Omega \left((\nabla u)^T \cdot v - (\nabla v) \cdot u \right) \cdot w \, dx, \end{aligned} \tag{1.14}$$

where, again, Einstein's summation is assumed.

The use of adjoint operators to define an appropriate $O(N)$ adjoint field will be central to the development of an efficient numerical algorithm to solve the robust control problem. For the linear problem described in §2, an appropriately defined adjoint field reveals the solution $\{\bar{\phi}, \bar{w}\}$ of the robust control problem directly, as shown in §2.2. For the nonlinear problem described in §3, a solution $\{\bar{\phi}, \bar{w}\}$ of the robust control must be found by iteration, as discussed in §3.2. At each iteration k, an adjoint field is computed to determine the gradients $\mathcal{D}\mathcal{J}/\mathcal{D}\phi$ and $\mathcal{D}\mathcal{J}/\mathcal{D}w$ in the vicinity of $\{\phi^k, w^k\}$. The control ϕ^k and the disturbance w^k are then updated based on this gradient information and a new adjoint field computed until the iteration in k converges and a saddle point for the full nonlinear problem is reached. Proof of the convergence of such an algorithm is currently under development.

2. Accomplishments

As discussed in the introduction, the objective in the robust control problem is to find the best control ϕ in the presence of the disturbance w which is maximally aggravating to the control objective. The cost functional considered in the present work, in the mathematical setting described in §1.3, is given by

$$
\mathcal{J}(\phi, w) = \frac{1}{2} \int_0^T \left| \mathcal{C}_1 u \right|^2_{L^2(\Omega)} dt + \frac{1}{2} \left| \mathcal{C}_2 u(T) \right|^2_{L^2(\Omega)} + \int_0^T \left(\mathcal{C}_3 \frac{\partial u}{\partial n}, \vec{r} \right)_{L^2(\partial\Omega)} dt
$$
$$
+ \frac{1}{2} \int_0^T \left[\ell^2 \left| \phi \right|^2_{L^2(\Omega)} - \gamma^2 \left| w \right|^2_{L^2(\Omega)} \right] dt. \tag{2.1}
$$

where the scalar control parameters γ and ℓ are given and b is a known vector field on $\partial\Omega$. The operators $\mathcal{C}_1$ and $\mathcal{C}_2$ are unbounded operators on $(L^2(\Omega))^3$ satisfying

$$
|\mathcal{C}_i u|^2_{L^2} \leq \alpha |u|^2_{L^2} + \beta \|u\|^2 \quad \text{for} \quad i = 1, 2, \tag{2.1a}
$$

with $\alpha \geq 0$, $\beta \geq 0$, $\alpha + \beta > 0$, and $\mathcal{C}_3$ is a bounded operator of $(L^2(\partial\Omega))^3$, so that, by the Trace theorem (Lions & Magenes 1972), we have

$$
\left| \left(\mathcal{C}_3 \frac{\partial u}{\partial n}, \vec{r} \right)_{L^2(\partial\Omega)} \right| \leq \kappa \|u\|_{H^{3/2}} \leq \kappa' \|u\|^{1/2} |Au|^{1/2}_{L^2}. \tag{2.1b}
$$

where the constants κ and κ' depend upon $\vec{r}$ and Ω. In this chapter, the flow u is assumed to be related to the control ϕ and the disturbance w through the linearized Navier-Stokes equation

$$
\begin{cases}
\dfrac{du}{dt} + \nu Au + B(u, U) + B(U, u) = \mathcal{B}_1 w + \mathcal{B}_2 \phi, \\
u \in V, \\
u(0) = u_0,
\end{cases} \tag{2.2}
$$

which models small deviations of the flow perturbation u from the desired target flow U. The regularity required is given by

$$
\begin{cases}
\phi, w \in L^2(0, T; L^2); \quad \mathcal{B}_1, \mathcal{B}_2 \in \mathcal{L}(L^2, H); \\
u_0 \in V; \quad U \in \mathcal{C}([0, T], V) \cap L^2(0, T; D(A)),
\end{cases}
$$

and the Stokes operator A, the bilinear mapping B, and other notations are described in §1.3. The robust control problem to be solved is stated precisely as:

Definition 2.1 The control $\bar{\phi} \in L^2(0, T, L^2)$ and disturbance $\bar{w} \in L^2(0, T, L^2)$, and the solution u to (2.2) associated with $\bar{\phi}$ and $\bar{w}$, are said to solve the robust control problem when a saddle point $(\bar{\phi}, \bar{w})$ of the cost functional $\mathcal{J}$ defined in (2.1) is reached such that

$$
\sup_{w \in L^2(0,T,L^2)} \mathcal{J}(\bar{\phi}, w) \leq \mathcal{J}(\bar{\phi}, \bar{w}) \leq \inf_{\phi \in L^2(0,T,L^2)} \mathcal{J}(\phi, \bar{w}). \tag{2.3}
$$

In this chapter, we will establish both existence and uniqueness of the solution to the robust control problem stated in Definition 2.1, and will present an iterative adjoint algorithm to solve a two-point boundary value problem to find this solution.

2.1 Existence of a solution of the robust control problem

The proof of the existence of a solution $(\bar{\phi}, \bar{w})$ to the robust control problem is based on the following existence result:

Proposition 2.1. *Let $\mathcal{J}$ be a functional defined on $X \times Y$, where X and Y are non-empty, closed, convex sets. If $\mathcal{J}$ satisfies*

(a) $\forall\, w \in Y, \quad \phi \mapsto \mathcal{J}(\phi, w)$ *is convex lower semicontinuous,*

(b) $\forall\, \phi \in X, \quad w \mapsto \mathcal{J}(\phi, w)$ *is concave upper semicontinuous,*

(c) $\exists\, w_0 \in Y$ *such that* $\displaystyle\lim_{\|\phi\|_X \to +\infty} \mathcal{J}(\phi, w_0) = +\infty,$

(d) $\exists\, \phi_0 \in X$ *such that* $\displaystyle\lim_{\|w\|_Y \to +\infty} \mathcal{J}(\phi_0, w) = -\infty,$

then the functional $\mathcal{J}$ has at least one saddle point $(\bar{\phi}, \bar{w})$ and

$$\mathcal{J}(\bar{\phi}, \bar{w}) = \operatorname*{Min}_{\phi \in X} \operatorname*{Sup}_{w \in Y} \mathcal{J}(\phi, w) = \operatorname*{Max}_{w \in Y} \operatorname*{Inf}_{\phi \in X} \mathcal{J}(\phi, w).$$

Proof: See §6 of Ekeland & Temam (1974).

In order to establish conditions (a) through (d) of Proposition 2.1 for the present problem, we need to analyze the evolution equation (2.2). It can be proven rigorously that, given $u_0 \in V$, $U \in \mathcal{C}([0,T], V) \cap L^2(0,T; D(A))$, and $\phi, w \in L^2(0,T; L^2)$, there exists a unique solution u of (2.2) such that

$$u \in L^2(0,T; V) \cap L^\infty(0,T,H).$$

The proof is based on the following "*a priori* estimates". Multiplying (2.2) with u, we can write

$$\frac{d}{dt}|u|_{L^2}^2 + \nu\|u\|^2 \leq \frac{1}{\nu\lambda_1} |\mathcal{B}_1 w + \mathcal{B}_2\phi|_{L^2}^2 + 2|b(u, U, u)|$$

$$\leq \frac{1}{\nu\lambda_1} |\mathcal{B}_1 w + \mathcal{B}_2\phi|_{L^2}^2 + C_0\|U\|\,|u|_{L^2}^{1/2}\|u\|^{3/2},$$

Hence,

$$\frac{d}{dt}|u|_{L^2}^2 + \frac{\nu}{2}\|u\|^2 \leq \frac{1}{\nu\lambda_1} |\mathcal{B}_1 w + \mathcal{B}_2\phi|_{L^2}^2 + \frac{C_0}{\nu^6}\|U\|^4|u|_{L^2}^2.$$

Let $M_0 = \dfrac{C_0}{\nu^6} \displaystyle\sup_{0 \leq t \leq T} \|U\|^4(t)$. Then, we have

$$|u|_{L^2}^2(t) \leq |u_0|_{L^2}^2\, e^{M_0 t} + \frac{e^{M_0 t}}{\nu\lambda_1} \int_0^t |\mathcal{B}_1 w + \mathcal{B}_2\phi|_{L^2}^2\, ds \qquad (2.4)$$

and

$$\frac{1}{t}\int_0^t \|u\|^2 ds \leq \frac{2}{\nu^2\lambda_1}\frac{1}{t}\int_0^t |\mathcal{B}_1 w + \mathcal{B}_2\phi|_{L^2}^2\, ds + \frac{2M_0}{\nu t}\int_0^t |u|_{L^2}^2 ds$$

$$\leq \frac{2}{\nu^2\lambda_1 t}\int_0^t |\mathcal{B}_1 w + \mathcal{B}_2\phi|_{L^2}^2\, ds + \frac{2}{\nu}|u_0|_{L^2}^2\, e^{M_0 T} \qquad (2.5)$$

$$+ \frac{2e^{M_0 T}}{\nu^2\lambda_1}\int_0^T |\mathcal{B}_1 w + \mathcal{B}_2\phi|_{L^2}^2\, ds.$$

Similarly, multiplying (2.2) with Au, we can write

$$\frac{d}{dt}\|u\|^2 + \nu|Au|_{L^2}^2 \leq \frac{1}{\nu}|\mathcal{B}_1 w + \mathcal{B}_2\phi|_{L^2}^2 + 2|b(u, U, Au)| + 2|b(U, u, Au)|$$

$$\leq \frac{1}{\nu}|\mathcal{B}_1 w + \mathcal{B}_2\phi|_{L^2}^2 + C_0\|U\|^{1/2}|AU|_{L^2}^{1/2}\|u\||Au|_{L^2}$$

$$+ C_0|U|_{L^2}^{1/4}|AU|_{L^2}^{3/4}\|u\||Au|_{L^2}.$$

Letting

$$M_1(T) = \frac{C_0^2}{2\nu}\sup_{0\leq t\leq T}\left(\|U\|(t) + |AU|_{L^2}(t) + |U(t)|_{L^2}^{1/2}|AU(t)|_{L^2}^{3/2}\right),$$

we have

$$\frac{d}{dt}\|u\|^2 + \frac{\nu}{2}|Au|_{L^2}^2 \leq \frac{1}{\nu}|\mathcal{B}_1 w + \mathcal{B}_2\phi|_{L^2}^2 + M_1\|u\|^2.$$

Therefore

$$\|u\|^2(t) \leq \|u_0\|^2\, e^{M_1 t} + \frac{1}{\nu}e^{M_1 t}\int_0^t |\mathcal{B}_1 w + \mathcal{B}_2\phi|_{L^2}^2\, ds \qquad (2.6)$$

and

$$\frac{1}{t}\int_0^t |Au|_{L^2}^2 ds \leq \frac{2}{\nu^2 t}\int_0^t |\mathcal{B}_1 w + \mathcal{B}_2\phi|_{L^2}^2\, ds + \frac{2M_1}{t}\int_0^t \|u\|^2 ds$$

$$\leq \left(\frac{2}{\nu^2 t} + \frac{4M_1}{\nu\lambda_1} + \frac{2M_1}{\nu\lambda_1}e^{M_0 T}\right)\int_0^t |\mathcal{B}_1 w + \mathcal{B}_2\phi|_{L^2}^2\, ds. \qquad (2.7)$$

The *a priori* estimates (2.4), (2.5), (2.6), and (2.7) allow us to characterize the mapping $(\phi, w) \mapsto u(\phi, w)$. Specifically, we have:

Lemma 2.1. *For* $\phi \in L^2(0, T; L^2)$, *the mapping* $w \mapsto u(\phi, w)$ *from* $L^2(0, T; L^2)$ *into* $L^2(0, T; V)$ *is affine and continuous. Similarly, for* $w \in L^2(0, T; L^2)$ *the mapping* $\phi \mapsto u(\phi, w)$ *from* $L^2(0, T; L^2)$ *into* $L^2(0, T; V)$ *is affine and continuous. For* $\phi \in L^2(0, T; L^2)$, *the mapping* $w \mapsto u(\phi, w)|_T$ *from* $L^2(0, T; L^2)$ *into* V *is affine and continuous. Similarly, for* $w \in L^2(0, T; L^2)$ *the mapping* $\phi \mapsto u(\phi, w)|_T$ *from* $L^2(0, T; L^2)$ *into* V *is affine and continuous. Furthermore, for* $u_0 \in V$ *and*

$w \in L^2(0, T; L^2)$, the mapping $w \mapsto u(\phi, w)$ has a Gâteau derivative $\xi(w_1)$ in every direction $w_1 \in L^2(0, T; L^2)$, and $\xi(w_1)$ is the solution of the linear evolution equation

$$\begin{cases} \dfrac{d\xi}{dt} + \nu A\xi + B(U, \xi) + B(\xi, U) = \mathcal{B}_1 w_1, \\ \xi \in V, \\ \xi(0) = 0, \end{cases} \tag{2.8}$$

and it follows that $\xi \in L^\infty(0, T; V) \cap L^2(0, T; D(A))$.

Proof. The fact that $w \mapsto u(\phi, w)$ and $\phi \mapsto u(\phi, w)$ are affine and continuous follows from the linearity of (2.2) and the *a priori* estimates (2.4), (2.5), (2.6), and (2.7). The existence of the Gâteau derivative as well as its characterization by (2.8) is proved in Abergel & Temam (1990), to which we refer the reader for more details.

Remark 2.1. *The solution ξ of (2.8) can be expressed as a function of w_1 in terms of the Green-Oseen's tensor $G(x, t, x', t')$ (see Ladyzhenskaya 1969); vaguely, we write*

$$\xi(x, t) = \int_0^T \int_\Omega G(x, t, x', t') \, w_1(x', t') \, dx' \, dt' \equiv G \cdot w_1.$$

Notationally, we will denote G by $\mathcal{D}u/\mathcal{D}w$ and $\xi(w_1)$ by $(\mathcal{D}u/\mathcal{D}w) \cdot w_1$. Note that the Green-Oseen's tensor $G = \mathcal{D}u/\mathcal{D}w$ is an infinite-dimensional extrapolation of the Jacobian of a finite-dimensional discretization of u with respect to a finite-dimensional discretization of w, as suggested by this notation. By causality, $G(x, t, x', t') = 0$ for $t' > t$.

With Lemma 2.1 established, we are ready to prove that conditions (a) through (d) of Proposition 2.1 are indeed satisfied for the present robust control problem:

Lemma 2.2. *Let $u_0 \in V$. There exists γ_0 such that, for $\gamma \geq \gamma_0$, we have*

(A) $\forall \, w \in L^2(0, T; L^2)$, $\phi \mapsto \mathcal{J}(\phi, w)$ *is convex lower semicontinuous,*

(B) $\forall \, \phi \in L^2(0, T; L^2)$, $w \mapsto \mathcal{J}(\phi, w)$ *is concave upper semicontinuous,*

(C) $\lim\limits_{|\phi|_{L^2(0,T;L^2)} \to +\infty} \mathcal{J}(\phi, 0) = +\infty$,

(D) $\lim\limits_{|w|_{L^2(0,T;L^2)} \to +\infty} \mathcal{J}(0, w) = -\infty$.

Proof. Condition (A): by Lemma 2.1, the map $\phi \mapsto \mathcal{J}(\phi, w)$ is lower semicontinuous. As $\phi \mapsto u(\phi, w)$ is affine, the convexity of $\phi \mapsto \mathcal{J}(\phi, w)$ follows promptly.

Condition (B): by Lemma 2.1, the map $w \mapsto \mathcal{J}(\phi, w)$ is upper semicontinuous. In order to prove concavity, note that it is sufficient to show that

$$h(\alpha) = \mathcal{J}(\phi, \alpha w_1 + w_2)$$

is concave w.r.t. α, i.e., $h''(\alpha) \leq 0$. To this end, we compute

$$h'(\alpha) = \int_0^T \left(\mathcal{C}_1 u, \mathcal{C}_1 \frac{\mathcal{D}u}{\mathcal{D}w} \cdot w_1 \right)_{L^2(\Omega)} dt + \left(\mathcal{C}_2 u(T), \mathcal{C}_2 \frac{\mathcal{D}u(T)}{\mathcal{D}w} \cdot w_1 \right)_{L^2(\Omega)}$$

$$+ \int_0^T \left(\mathcal{C}_3 \frac{\partial}{\partial w} \frac{\mathcal{D}u}{\mathcal{D}w} \cdot w_1, \vec{r} \right)_{L^2(\partial\Omega)} dt - \gamma^2 \int_0^T \left(\alpha w_1 + w_2, w_1 \right)_{L^2(\Omega)} dt.$$

It is clear that $\xi(w_1) = (\mathcal{D}u/\mathcal{D}w) \cdot w_1$ is independent of α. Therefore,

$$h''(\alpha) = \int_0^T \left| \mathcal{C}_1 \frac{\mathcal{D}u}{\mathcal{D}w} \cdot w_1 \right|_{L^2}^2 dt + \left| \mathcal{C}_2 \frac{\mathcal{D}u(T)}{\mathcal{D}w} \cdot w_1 \right|_{L^2}^2 - \gamma^2 \int_0^T |w_1|_{L^2}^2 \, dt.$$

Note that $\xi(w_1)$ satisfies (2.8) by Lemma 2.1. Hence, using the *a priori* estimates (2.4), (2.5), (2.6), and (2.7), we have

$$\int_0^T \left| \mathcal{C}_1 \frac{\mathcal{D}u}{\mathcal{D}w} \cdot w_1 \right|_{L^2}^2 dt \le \alpha \int_0^T |\xi|_{L^2}^2 dt + \beta \int_0^T \|\xi\|^2 \, dt \le k_1 \int_0^T |\mathcal{B}_1 w_1|_{L^2}^2 \, dt$$

$$\le k_1 |\mathcal{B}_1|_{\mathcal{L}(L^2,H)} \int_0^T |w_1|_{L^2}^2 \, dt,$$

and, similarly,

$$\left| \mathcal{C}_2 \frac{\mathcal{D}u(T)}{\mathcal{D}w} \cdot w_1 \right|_{L^2}^2 \le k_1 |\mathcal{B}_1|_{\mathcal{L}(L^2,H)} \int_0^T |w_1|_{L^2}^2 \, dt.$$

Now under the assumption that

$$\gamma^2 \ge 2k_1 |\mathcal{B}_1|_{\mathcal{L}(L^2,H)},$$

we have $h''(\alpha) \le 0$ for $\alpha \in \mathbb{R}$. Thus the function h is concave, and the concavity of $w \mapsto \mathcal{J}(\phi, w)$ follows immediately.

Condition (C): Using (2.1b), we can write

$$\mathcal{J}(\phi, 0) \ge \frac{\ell^2}{2} |\phi|_{L^2(0,T;L^2)}^2 - \kappa' \int_0^T \|u\|^{1/2} |Au|_{L^2}^{1/2} \, dt,$$

and by the *a priori* inequalities (2.4), (2.5), (2.6), and (2.7), there exists a constant $C_0 = C_0(T, \Omega, \|u_0\|)$ such that

$$\int_0^T \|u\|^{1/2} |Au|_{L^2}^{1/2} \, dt \le C_0 |\phi|_{L^2(0,T;L^2)}.$$

Hence,

$$\mathcal{J}(\phi, 0) \ge \frac{\ell^2}{2} |\phi|_{L^2(0,T;L^2)}^2 - C_0 |\phi|_{L^2(0,T;L^2)},$$

and condition (C) follows promptly.

Condition (D): it follows from (2.4) that

$$\int_0^T |\mathcal{C}_1 u|_{L^2}^2 \, dt \le \int_0^T (\alpha |u|_{L^2}^2 + \beta \|u\|^2) dt \le k_1 \left[|\phi|_{L^2(0,T;L^2)}^2 + |w|_{L^2(0,T;L^2)}^2 \right] + k_2,$$

and, similarly,

$$|\mathcal{C}_2 u(T)|^2_{L^2} \le (\alpha|u(T)|^2_{L^2} + \beta\|u(T)\|^2) \le k_1 \left[|\phi|^2_{L^2(0,T;L^2)} + |w|^2_{L^2(0,T;L^2)}\right] + k_2.$$

Thus, if $\gamma^2 \ge 4(k_1 + k_2)$ and $|w|_{L^2(0,T;L^2)} \ge 1$, we have

$$\mathcal{J}(0, w) = \frac{1}{2}\int_0^T |\mathcal{C}_1 u|^2_{L^2}\, dt + \frac{1}{2}|\mathcal{C}_2 u(T)|^2_{L^2} + \int_0^T \int_{\partial\Omega} \mathcal{C}_3 \frac{\partial u}{\partial n} \cdot \vec{r}\, d\sigma\, dt - \frac{\gamma^2}{2}\int_0^T |w|^2_{L^2} ds$$

$$\le -\frac{\gamma^2}{4}|w|^2_{L^2(0,T;L^2)} + C|w|_{L^2(0,T;L^2)},$$

which implies (D).

Putting the statements of this section together, we have established existence of a solution $(\bar{\phi}, \bar{w})$ to the robust control problem for a sufficiently large γ:

Theorem 2.1. *Assume that γ is sufficiently large so that*

$$\gamma^2 \ge 4(k_1 + k_2) \quad \text{and} \quad \gamma^2 \ge 2k_1 |\mathcal{B}_1|_{\mathcal{L}(L^2,H)},$$

where

$$k_1 = \frac{2}{\nu^2} + \frac{Te^{M_0 T}}{\nu} \quad \text{and} \quad k_2 = \lambda_1 |u_0|^2_{L^2} e^{M_0 T}.$$

Then there exists a saddle point $(\bar{\phi}, \bar{w})$ and $u(\bar{\phi}, \bar{w})$ such that

$$\mathcal{J}(\bar{\phi}, w) \le \mathcal{J}(\bar{\phi}, \bar{w}) \le \mathcal{J}(\phi, \bar{w}), \quad \forall \phi, w \text{ in } L^2(0, T; L^2).$$

Proof. The proof follows promptly from Lemmas 2.1 and 2.2 and Proposition 2.1.

2.2 Identification of the unique solution to the robust control problem

The existence of a saddle point $(\bar{\phi}, \bar{w})$ of the functional $\mathcal{J}$ implies that

$$\frac{\mathcal{D}\mathcal{J}}{\mathcal{D}\phi}(\bar{\phi}, \bar{w}) = 0 \quad \text{and} \quad \frac{\mathcal{D}\mathcal{J}}{\mathcal{D}w}(\bar{\phi}, \bar{w}) = 0. \tag{2.9}$$

Define an adjoint state by the equation

$$\begin{cases} -\dfrac{d\lambda}{dt} + \nu A^* \lambda + B'(U)^* \lambda = \mathcal{C}_1^* \mathcal{C}_1\, u, \\ \lambda \in V_r = \left\{v \in (H^1(\Omega))^3;\ \text{div } v = 0 \text{ in } \Omega,\ v = \mathcal{C}_3^* \vec{r} \text{ on } \partial\Omega\right\}, \\ \lambda(T) = \mathcal{C}_2^* \mathcal{C}_2\, u(T), \end{cases} \tag{2.10}$$

where A^* is defined by

$$\left(u, A^* \lambda\right)_{L^2} = \left(Au, \lambda\right)_{L^2} - \left(\mathcal{C}_3 \frac{\partial u}{\partial n}, \vec{r}\right)_{L^2(\partial\Omega)} \quad \text{for } u \in D(A),\ \text{and } \lambda \in V_r.$$

We have the following:

Lemma 2.3. *Let* $U \in L^\infty(0,T;V) \cap L^2(0,T;D(A))$, *and let* u *be the solution of* (2.2), $\xi_i(h)$, $i = 1,2$, $h \in L^2(0,T;L^2)$ *the solution of*

$$\begin{cases} \dfrac{d\xi_i}{dt} + \nu A\xi_i + B'(U)\xi_i = B_i h & \text{for } i = 1,2, \\[2mm] \xi_i \in V, \\[2mm] \xi_i(0) = 0. \end{cases} \tag{2.11}$$

Then

$$\int_0^T \left(B_i^* \lambda, h\right)_{L^2(\Omega)} dt = \int_0^T \left(C_1^* C_1 u, \xi_i\right)_{L^2(\Omega)} dt + \left(C_2^* C_2 u(T), \xi_i(T)\right)_{L^2(\Omega)} \\ + \int_0^T \left(C_3 \frac{\partial}{\partial n}\xi_i, \vec{r}\right)_{L^2(\partial\Omega)} dt, \tag{2.12}$$

where B_i^* *is the adjoint of* B_i *for* $i = 1,2$.

Proof. The proof follows from integration by parts and the regularity of u, ξ_i and λ:

$$\int_0^T \left(C_1^* C_1 u, \xi_i\right)_{L^2(\Omega)} dt + \left(C_2^* C_2 u(T), \xi_i(T)\right)_{L^2(\Omega)} + \int_0^T \left(C_3 \frac{\partial}{\partial n}\xi_i, \vec{r}\right)_{L^2(\partial\Omega)} dt$$

$$= \int_0^T \left(\left[-\frac{d\lambda}{dt} + \nu A^*\lambda + B'(U)^*\lambda\right], \xi_i\right)_{L^2(\Omega)} dt$$

$$+ \left(\lambda(T), \xi_i(T)\right)_{L^2(\Omega)} + \int_0^T \left(C_3 \frac{\partial}{\partial n}\xi_i, \vec{r}\right)_{L^2(\partial\Omega)} dt$$

$$= \int_0^T \left(\lambda, \frac{d\xi_i}{dt}\right)_{L^2(\Omega)} dt + \int_0^T \left(\lambda, \nu A\xi_i\right)_{L^2(\Omega)} dt + \int_0^T \left(\lambda, B'(U)\xi_i\right)_{L^2(\Omega)} dt$$

$$= \int_0^T \left(\lambda, B_i h\right)_{L^2(\Omega)} dt = \int_0^T \left(B_i^* \lambda, h\right)_{L^2(\Omega)} dt.$$

Now we prove

Theorem 2.2. *Let* $(\bar{\phi}, \bar{w})$ *be a solution of the robust control problem stated in Definition 2.1. Then*

$$\bar{\phi} = -\frac{1}{\ell^2} B_2^* \bar{\lambda} \quad \text{and} \quad \bar{w} = \frac{1}{\gamma^2} B_1^* \bar{\lambda}, \tag{2.13}$$

where $\bar{\lambda}$ *is found from the solution* $(\bar{u}, \bar{\lambda})$ *of the following coupled system:*

$$\begin{cases} \dfrac{d\bar{u}}{dt} + \nu A\bar{u} + B'(U)\bar{u} = \left(\dfrac{1}{\gamma^2} B_1 B_1^* - \dfrac{1}{\ell^2} B_2 B_2^*\right)\bar{\lambda}, \\[2mm] -\dfrac{d\bar{\lambda}}{dt} + \nu A^*\bar{\lambda} + B'(U)^*\bar{\lambda} = C_1^* C_1 \bar{u}, \\[2mm] \bar{u} \in V, \ \bar{\lambda} \in V_r, \\[2mm] \bar{u}(0) = u_0 \ \text{and} \ \bar{\lambda}(T) = C_2^* C_2 \, u(T), \end{cases} \tag{2.14}$$

which admits a unique solution for $\gamma > \gamma_0(|\mathcal{B}_1|_{\mathcal{L}(L^2, H)}, |\mathcal{B}_2|_{\mathcal{L}(L^2, H)}, \ell)$.

Proof. A necessary condition for $(\bar{\phi}, \bar{w})$ to be a saddle point of the functional $\mathcal{J}$ is

$$\frac{\mathcal{D}\mathcal{J}}{\mathcal{D}\phi}(\bar{\phi}, \bar{w}) \cdot h_1 = 0 \quad \text{and} \quad \frac{\mathcal{D}\mathcal{J}}{\mathcal{D}w}(\bar{\phi}, \bar{w}) \cdot h_2 = 0, \quad \forall \, h_1 \in L^2(0, T; H).$$

Thus,

$$\frac{\mathcal{D}\mathcal{J}}{\mathcal{D}w}(\bar{\phi}, \bar{w}) \cdot h_1 = \int_0^T \left(\mathcal{C}_1 u, \mathcal{C}_1 \frac{\mathcal{D}u}{\mathcal{D}w} \cdot h_1 \right)_{L^2(\Omega)} dt + \left(\mathcal{C}_2 u(T), \mathcal{C}_2 \frac{\mathcal{D}u(T)}{\mathcal{D}w} \cdot h_1 \right)_{L^2(\Omega)}$$
$$+ \int_0^T \left(\mathcal{C}_3 \frac{\partial}{\partial n} \frac{\mathcal{D}u}{\mathcal{D}w} \cdot h_1, \bar{r} \right)_{L^2(\partial\Omega)} dt - \gamma^2 \int_0^T \left(\bar{w}, h_1 \right)_{L^2(\Omega)} dt = 0.$$

and

$$\frac{\mathcal{D}\mathcal{J}}{\mathcal{D}\phi}(\bar{\phi}, \bar{w}) \cdot h_2 = \int_0^T \left(\mathcal{C}_1 u, \mathcal{C}_1 \frac{\mathcal{D}u}{\mathcal{D}w} \cdot h_2 \right)_{L^2(\Omega)} dt + \left(\mathcal{C}_2 u(T), \mathcal{C}_2 \frac{\mathcal{D}u(T)}{\mathcal{D}w} \cdot h_2 \right)_{L^2(\Omega)}$$
$$+ \int_0^T \left(\mathcal{C}_3 \frac{\partial}{\partial n} \frac{\mathcal{D}u}{\mathcal{D}w} \cdot h_2, \bar{r} \right)_{L^2(\partial\Omega)} dt + \ell^2 \int_0^T \left(\bar{\phi}, h_2 \right)_{L^2(\Omega)} dt = 0.$$

Hence, by (2.12),

$$\int_0^T \left(\mathcal{B}_1^* \bar{\lambda} - \gamma^2 \bar{w}, h_1 \right)_{L^2(\Omega)} dt = 0, \quad \forall \, h_1 \in L^2(0, T; H)$$

and

$$\int_0^T \left(\mathcal{B}_2^* \bar{\lambda} + \ell^2 \bar{\phi}, h_2 \right)_{L^2(\Omega)} dt = 0, \quad \forall \, h_2 \in L^2(0, T; H),$$

which implies that (2.13) follows from the definition of the coupled system given in (2.14).

The uniqueness of the solution of the coupled system (2.14) is classical. For γ sufficiently large $[\gamma > \gamma_0(|\mathcal{B}_1|_{\mathcal{L}(L^2, H)}, |\mathcal{B}_2|_{\mathcal{L}(L^2, H)}, \ell)]$, we have $\left(\gamma^{-2} \mathcal{B}_1 \mathcal{B}_1^* - \ell^{-2} \mathcal{B}_2 \mathcal{B}_2^* \right)$ is positive definite. The proof of uniqueness then follows by multiplying the $\bar{u}$ equation by $\bar{\lambda}$ and the $\bar{\lambda}$ equation by $\bar{u}$, integrating between 0 and T, and then adding the two resulting equations.

2.3 Generalized framework

We now identify all possible sources of forcing in the two-point boundary-value problem (2.14) and thereby establish a generalized framework for which the approaches discussed herein can be applied to a wide variety of problems in fluid mechanics.
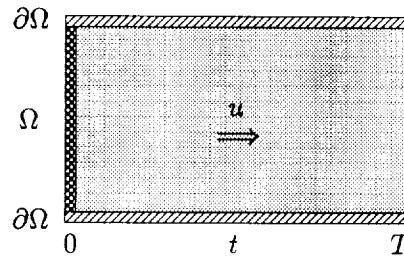
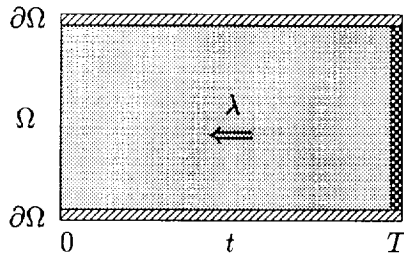FIGURE 2. Schematic representation of the domain over which the flow field u is computed. The arrow indicates the direction in time that the p.d.e. is marched.

The space-time domain over which the flow field u is computed is illustrated in Fig. 2. The possible regions of forcing in this system are:

a. the r.h.s. of the p.d.e., indicated by ▢, representing flow control by interior volume forcing (e.g., externally-applied electromagnetic forcing by wall-mounted magnets and electrodes);

b. the b.c.'s, indicated by ▨, representing flow control by boundary forcing (e.g., wall transpiration);

c. the i.c.'s, indicated by ▦, representing the optimization of the initial state in a data assimilation framework (e.g., the weather forecasting problem).

Only the first of these cases is treated in detail in the present work.

FIGURE 3. Schematic representation of the domain over which the adjoint field λ is computed. The arrow indicates the direction in time that the p.d.e. is marched.

The space-time domain over which the adjoint field λ is computed is illustrated in Fig 3. The possible regions of forcing in this system are:

a. the r.h.s. of the p.d.e., indicated by ▢, representing regulation of an interior quantity (e.g., turbulent kinetic energy);

b. the b.c.'s, indicated by ▨, representing regulation of a boundary quantity (e.g., wall skin-friction);

b. the i.c.'s, indicated by ▦, representing terminal control of an interior flow quantity (e.g., turbulent kinetic energy).

All three possible locations of forcing of the adjoint problem are considered in the present framework. Note that an interesting singularity arises when considering the

terminal control of a boundary quantity such as wall skin-friction. The (inhomogeneous) boundary conditions on the adjoint field for such a case are the same as in the corresponding regulation problem with a delta function applied at time $t = T$.

3. Future work

We are currently repeating the analysis of section 2 for the nonlinear problem. As mentioned in the introduction, this analysis will account for corners in the domain Ω. The analysis of existence of the solution for the nonlinear problem and the characterization of a simple gradient search routine (with fixed step size) to find this solution are both straightforward, though results are only available for a) small initial data, b) small T, or c) a 2D domain. Such a restriction is a direct consequence of the fundamental lack of a complete mathematical characterization currently available for the 3D Navier-Stokes equation, not a shortcoming of the present analysis.

In addition, we are attempting to establish rigorously the convergence of *practical* gradient search algorithms for the iterative solution of the robust control problem. To be practical, such algorithms must have *variable step size*, perhaps updating ϕ to minimize $\mathcal{J}$ in the direction $\mathcal{DJ}/\mathcal{D}\phi$ and/or updating w to maximize $\mathcal{J}$ in the direction $\mathcal{DJ}/\mathcal{D}w$ at each step of the iteration. Further, the initial guess of the solution (ϕ^0, w^0) must, in general, be considered to be "far" from the nearest solution $(\bar{\phi}, \bar{w})$ of the robust control problem. A thorough mathematical understanding of such a search algorithm is *essential* before testing these ideas numerically, as gradient searches for a saddle points even in low dimensional problems may easily get caught in limit cycles or fail altogether unless the optimization problem is thoroughly understood.

REFERENCES

ABERGEL, F., & TEMAM, R. 1990 On some control problems in fluid mechanics. *Theor. and Comp. Fluid Dynamics.* **1**, 303-325.

BEWLEY, T.R., & LIU, S. 1997 Optimal and robust control and estimation of linear paths to transition. *Submitted to J. Fluid Mech.*

BEWLEY, T.R., MOIN, P., & TEMAM, R. 1997a Optimal control of turbulence. *To be submitted to J. Fluid Mech.*

BEWLEY, T.R., MOIN, P., & TEMAM, R. 1997b Optimal and robust approaches for linear and nonlinear regulation problems in fluid mechanics. *AIAA Paper No. 97-1872.*

DOYLE, J.C., GLOVER, K., KHARGONEKAR, P.P., & FRANCIS, B.A. 1989 State-space solutions to standard $\mathcal{H}_2$ and $\mathcal{H}_\infty$ control problems. *IEEE Trans. Auto. Control.* **34**, (8), 831-847.

GREEN, M., & LIMEBEER, D.J.N. 1995 *Linear robust control.* Prentice-Hall.

LADYZHENSKAYA, O. A. 1969 *The mathematical theory of viscous incompressible flow.* Gordon & Breach.

LIONS, J.L., 1969 *Quelques méthodes de résolution des problèmes nonlinéaires.* Gauthier Villars.

TEMAM, R. 1984 *Navier-Stokes equations*, Studies in Mathematics and its Applications 2. North-Holland.

Combined immersed-boundary/B-spline methods for simulations of flow in complex geometries

By J. Mohd-Yusof

1. Motivation and objectives

For fluid dynamics simulations, the primary issues are accuracy, computational efficiency, and the ability to handle complex geometries. Spectral methods offer the highest accuracy but are limited to relatively simple geometries. In order to accommodate more complex geometries, finite-difference or finite-element methods are generally used. However, these methods suffer from relatively low accuracy, requiring fine meshes to obtain good results. Finite element schemes, while able to handle complex geometries, often require significant computational time for grid generation. Spectral element methods can be used for complex geometries, but the grid stretching inherent in these methods leads to timestep limitations and clustering of grid points in an inefficient manner.

In general, any computational scheme which requires re-gridding to accommodate changes in geometry will incur significant penalties in simulating time-varying geometries. For relatively simple motions, it is possible to use grid-stretching techniques, (Carlson *et al.*, 1995), but these are still slow. Vortex element methods for moving bodies (Koumoutsakos, 1995) are presently under development but are also rather slow, especially with respect to calculation of spectra.

To address these problems, we propose a discrete-time immersed boundary method which will allow implementation of complex moving geometries in existing pseudospectral codes. The method does not incur significant additional cost as compared to the base computational scheme, and changes in surface geometry simply require modification of the input files without any further modification of the code itself.

2. Accomplishments

The immersed boundary method has been successfully implemented and tested in the B-spline/Fourier pseudospectral numerical scheme of Kravchenko *el al.* (1996). The interpolation scheme developed for this application makes use of the compact properties of the B-spline transform to maintain the highest possible order at the immersed surface. The combined scheme has been successfully tested on the laminar ribbed channel case of Choi, Moin and Kim (1991) (hereafter CMK).

2.1 Immersed boundary concept

We begin with an examination of the continuous (in time and space) Navier-Stokes equations to demonstrate the principle of the immersed boundary technique. We consider incompressible flows governed by the Navier–Stokes equations, including the body force term:

$$\frac{\partial \mathbf{u}}{\partial t} = -\mathbf{H} - \nabla P + \frac{1}{Re}\nabla^2 \mathbf{u} + \mathbf{f} \tag{1}$$

and the continuity equation:

$$\nabla \cdot \mathbf{u} = 0 \tag{2}$$

where Re is the Reynolds number, $\mathbf{u} = (u, v, w)$ is the velocity vector, $\mathbf{H} = \mathbf{u} \times \omega = (H_u, H_v, H_w)$ is the convective term, and $\mathbf{f} = (f_u, f_v, f_w)$ is the forcing vector .

The full Navier-Stokes equations allow the inclusion of an external body force. In incompressible flows, this force is generally assumed to derive from some potential field (e.g. gravity) which is constant and therefore may be neglected. However, the NS equations themselves allow the force to be a function of both time and space. In that event, the divergence of the force may be non-zero and therefore must be included in the Poisson equation for pressure if that equation is used to solve the system.

The immersed boundary method involves specifying the body force term in such a way as to simulate the presence of a flow boundary within the computational domain without altering the computational grid. The advantage of this is that bodies of almost arbitrary shape can be added without grid restructuring, a procedure which is often time-consuming. Furthermore, multiple bodies may be simulated and relative motion of those bodies may be accomplished at reasonable computational cost.

The concept of the immersed boundary technique has been used for pseudo-spectral simulations of flows in complex geometries (Goldstein *et al.* 1995). However, the timestep restriction imposed by their derivation severely limits the applicability of the method to turbulent and other strongly time-dependent flows. This restriction can be removed by the use of a *discrete-time* derivation of the forcing value (Mohd-Yusof 1996). When combined with appropriate choice of internal boundary conditions, this scheme leads to a forcing scheme which does not require any filtering of the forcing field.

A second issue of importance to the immersed boundary method is the ability of the underlying numerical scheme to place a sufficient number of grid points near the immersed boundary to adequately resolve the flow scales in that region. While the grid geometry may be considerably simplified as compared to a body-fitted grid, there is still a fundamental need to tailor the grid point distribution to the underlying flow scales. To this end, we employ a B-spline formulation, which allows flexibility of grid point distribution, zonal embedded grids, and high accuracy (Kravchenko *et al.* 1996). Coupled with Fourier-pseudo-spectral methods, this yields a numerical scheme which allows simulation of flows in complex geometries on Cartesian grids with near-spectral accuracy.

2.2 Numerical method

We now consider the discrete-time Navier-Stokes equations in general form:

$$\frac{\mathbf{u}^{n+1} - \mathbf{u}^n}{\Delta t} = -\mathbf{H} - \nabla P + \frac{1}{Re}\nabla^2 \mathbf{u} + \mathbf{f} \tag{3}$$

We wish to drive the velocity, $\mathbf{u}$, on some surface, Ω, to some desired value, $\mathbf{v}(\Omega)$. Rearrangement of the discrete NS equation gives us the velocity update equation

which is of the form:

$$\mathbf{u}^{n+1} = \mathbf{u}^n + \Delta t(-\mathbf{H} - \nabla P + \frac{1}{Re}\nabla^2\mathbf{u} + \mathbf{f}) \tag{4}$$

If we know $\mathbf{H}$, ∇P and $\nabla^2\mathbf{u}$ then the forcing term is simply:

$$\mathbf{f} = \begin{cases} \mathbf{H} + \nabla P - \frac{1}{Re}\nabla^2\mathbf{u} + \frac{1}{\Delta t}(\mathbf{v} - \mathbf{u}^n), & \text{on } \Omega; \\ 0 & \text{elsewhere.} \end{cases} \tag{5}$$

Velocity-vorticity formulation

Following the same approach as in Kim *et al.* (1991) one can reduce Eqs. (1) and (2) to a fourth-order equation for v, and a second-order equation for the normal component of vorticity g:

$$\frac{\partial}{\partial t}\nabla^2 v = h_v + \frac{1}{Re}\nabla^4 v + \nabla^2 f_v \tag{6}$$

$$\frac{\partial}{\partial t}g = h_g + \frac{1}{Re}\nabla^2 g + f_g \tag{7}$$

$$p + \frac{\partial v}{\partial y} = 0 \tag{8}$$

where

$$p = \frac{\partial u}{\partial x} + \frac{\partial w}{\partial z}, \quad g = \frac{\partial u}{\partial z} - \frac{\partial w}{\partial x} \quad f_g = \frac{\partial f_u}{\partial z} - \frac{\partial f_w}{\partial x} \tag{9}$$

$$h_v = -\frac{\partial}{\partial y}\left(\frac{\partial H_u}{\partial x} + \frac{\partial H_w}{\partial z}\right) + \left(\frac{\partial^2}{\partial x^2} + \frac{\partial^2}{\partial z^2}\right)H_v \tag{10}$$

$$h_g = \frac{\partial H_u}{\partial z} - \frac{\partial H_w}{\partial x} \tag{11}$$

The numerical approximation of the velocity vector $\mathbf{u}$ is $\tilde{\mathbf{u}} = (\tilde{u}, \tilde{v}, \tilde{w})$. It is written in terms of spectral and B-spline functions:

$$\tilde{v}(x,y,z,t) = \sum_{k_x,j,k_z} \hat{v}_j(k_x,k_z,t)e^{ik_x x}e^{ik_z z}B_j^l(y) \tag{12}$$

$$\begin{pmatrix} \tilde{u} \\ \tilde{w} \end{pmatrix}(x,y,z,t) = \sum_{k_x,j,k_z} \begin{pmatrix} \hat{u}_j(k_x,k_z,t) \\ \hat{w}_j(k_x,k_z,t) \end{pmatrix} e^{ik_x x}e^{ik_z z}B_j^{l-1}(y) \tag{13}$$

where $B_j^l(y)$ is the B-spline of order l. B-spline functions of order l are defined on a set of knot points t_j by the following recursive relationship

$$B_j^l(y) = \frac{(y - t_j)}{(t_{j+l} - t_j)}B_j^{l-1}(y) + \frac{(t_{j+l+1} - y)}{(t_{j+l+1} - t_{j+l})}B_{j+1}^{l-1}(y) \tag{14}$$

where a B-spline of order zero is a top hat function, i.e $B_j^0(y) = 1$ if $t_j \leq y \leq t_{j+1}$ and 0 otherwise. Note that the v-velocity is represented in terms of B-splines which are one order higher than the B-spline expansion functions for u and w. This allows the continuity equation, Eq. (8), to be satisfied exactly by the numerical representation.

Using the method of weighted residuals, we obtain the discrete weak forms of Eqs. (6) and (7):

$$\int_V \xi \frac{\partial}{\partial t} \nabla^2 \tilde{v} dV = \int_V \xi \tilde{h}_v dV + \int_V \xi \frac{1}{Re} \nabla^4 \tilde{v} dV + \int_V \xi \nabla^2 \tilde{f}_v dV \qquad (15)$$

$$\int_V \zeta \frac{\partial}{\partial t} \tilde{g} dV = \int_V \zeta \tilde{h}_g dV + \int_V \zeta \frac{1}{Re} \nabla^2 \tilde{g} dV + \int_V \zeta \tilde{f}_g dV \qquad (16)$$

where ξ and ζ are the weight functions, which we select to be:

$$\xi(x, y, z) = e^{-ik_x' x} e^{-ik_z' z} B_i^l(y)$$

,

$$\zeta(x, y, z) = e^{-ik_x' x} e^{-ik_z' z} B_i^{l-1}(y). \qquad (17)$$

Evaluating the integrals in Eqs. (15) and (16), we obtain two systems of ordinary differential equations for $\hat{v}$ and $\hat{g}$ for each independent Fourier mode (k_x, k_z):

$$\mathbf{M}_v \frac{d\hat{v}}{dt} = \mathbf{D}_v \hat{v} + \mathbf{R}_v(\hat{u}, \hat{v}, \hat{w}) + \mathbf{F}_v \qquad (18)$$

$$\mathbf{M}_g \frac{d\hat{g}}{dt} = \mathbf{D}_g \hat{g} + \mathbf{R}_g(\hat{u}, \hat{v}, \hat{w}) + \mathbf{F}_g \qquad (19)$$

where $\mathbf{R}_v, \mathbf{R}_g$ are the expressions resulting from the nonlinear terms, $\mathbf{F}_v, \mathbf{F}_g$ are the expressions for the forcing terms, and $\mathbf{M}_v, \mathbf{M}_g, \mathbf{D}_v, \mathbf{D}_g$ are banded matrices. The matrix elements of $\mathbf{M}_v, \mathbf{M}_g, \mathbf{D}_v, \mathbf{D}_g$ are given in Kravchenko *et al* (1996).

The time-advancement of Eqs. (18) and (19) is carried out with a semi-implicit scheme that uses Crank-Nicholson for the viscous terms and third order Runge-Kutta for the nonlinear terms *(rk3)*. All time dependent simulations were performed with variable time steps and with the CFL number never exceeding $\sqrt{3}$ to satisfy the stability condition of the third order Runge-Kutta scheme.

In this context, the form of the forcing function becomes:

$$\mathbf{f} = \begin{cases} (\alpha \mathbf{H}^n + \beta \mathbf{H}^{n-1}) + \nabla P - \frac{1}{Re} \nabla^2 \mathbf{u}^n + \frac{1}{\Delta t}(\mathbf{v} - \mathbf{u}^n), & \text{on } \Omega; \\ 0 & \text{elsewhere} \end{cases} \qquad (20)$$

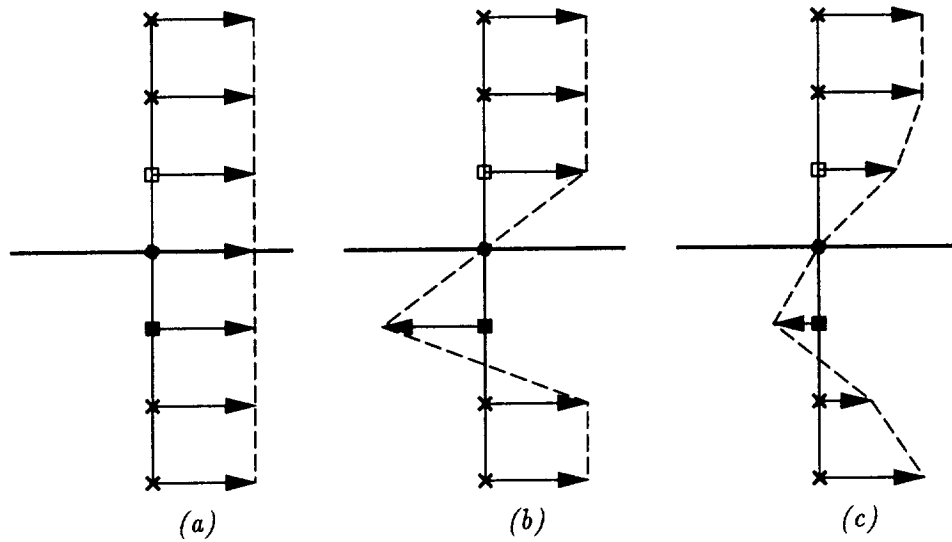where α and β are the Runge-Kutta coefficients.

FIGURE 1. Sketch showing the effect of forcing and of a central difference diffusion operator on the velocity field imposed by the forcing. Forcing is applied at the surface (●) to drive the velocity to zero. The velocity at the point immediately interior to the surface (■) is forced to be the reverse of the velocity at the point immediately exterior to the surface (□). (a) initial velocity field, (b) velocity field imposed by forcing, (c) velocity field after diffusion step.

Generation of no-slip walls

We consider the generation of a no-slip wall, with the objective of obtaining a smooth velocity field.

In order to obtain a smooth velocity field without resorting to smoothing of the forcing function, we apply forcing on a set of points adjacent to the surface and interior to the body. At these points (see Fig. 1), we reverse tangential velocities across the solid surface and preserve normal velocities. This makes the velocity gradients smooth across the boundary, minimizing any error due to the estimation of the diffusion term.

Consider first the velocity component tangential to the surface. If we make the velocity gradient linear across the surface, we will achieve the smoothest local tangential velocity. This is accomplished by simply reversing tangential velocities across the surface. The internal tangential velocity is scaled to produce no-slip at the desired location according to $u_{tan,i} = \xi u_{tan,o}$. The scaling factor is set to $\xi = x_i/x_o$ where x_i and x_o are the distances from the desired surface location to the internal and external flow reversal points, respectively.

Notice that the effect of a second-order diffusion operator on the resulting velocity field (Fig. 1) will be to maintain the desired velocity at the surface. If the initial field is uniform, then the velocity field imposed by the forcing will reverse flow across the boundary. The effect of diffusion will then maintain the no-slip condition at the virtual surface, and vorticity will naturally diffuse into the flow. The effect
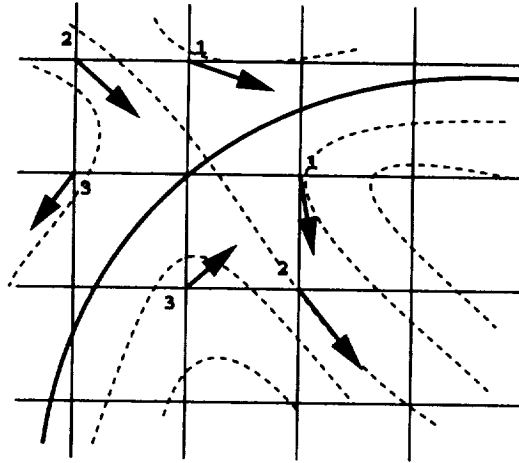
FIGURE 2.   Sketch showing how the simple reversal of tangential component and preservation of normal velocity across the virtual surface leads to the expected stagnation point flow. The numbers indicate pairs of flow-reversal points.

of this operator on the 'external' flow will be identical to that in the presence of a conventional Dirichlet boundary: the vorticity at the surface will be diffused into the flow by the action of viscosity.

Since we attempt to reverse tangential velocities across a solid surface, the resultant velocity gradient normal to the surface is linear, and the velocity gradient tangent to the surface will be zero, by definition. In that case, $\nabla^2 u$ will be zero on the surface, and we have eliminated one of the terms in the error. In fact, since the velocity gradient will never be exactly linear across the boundary, we also include an estimate of the Laplacian in the force term, using the velocity field at the present timestep.

Figure 2 shows how this forcing scheme will naturally reproduce the internal flow corresponding to a stagnation point on a curved surface. The (local) specification of the forcing to preserve normal velocity and reverse normal velocity at the numbered pairs of flow reversal points is sufficient to reproduce the no-slip surface and the internal flow corresponding stagnation point flow.

Note that this is the same boundary condition prescribed by Harlow and Welch (1965) and is divergence free, thus ensuring compatibility with the velocity-vorticity formulation of the velocity field. This choice of forcing may also be viewed as introducing vorticity at the immersed surface to mimic the presence of a solid, no-slip boundary. In this sense the method may be viewed as a grid-based vortex method. However, it is also distinct from most vortex methods since it requires only local information to calculate the value of the force. The effect of the forcing is to generate an internal boundary layer within the body, in the reverse direction to the external flow. One consequence of this method is the generation of internal flow fields which are comparable to the local external velocities. When we deal with three-dimensional bodies with significant surface curvature, this can lead to internal
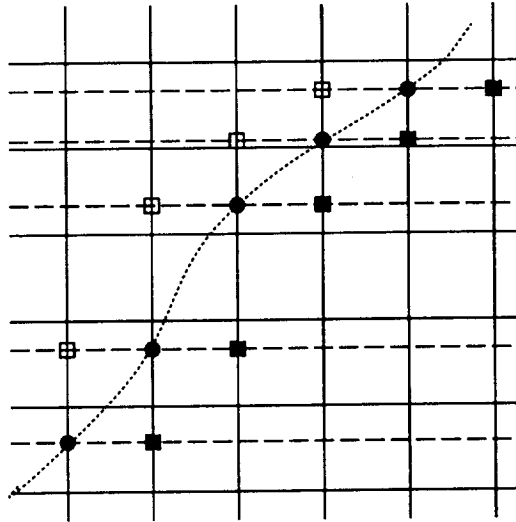
FIGURE 3. Sketch showing the relationship between the desired surface location (········), the base computational grid (———) and the B-spline planes used for force calculation (– – – –). The surface forcing points (●), internal forcing points (■), and external velocity interpolation points (□) are also shown. Note that the force calculation planes need not be evenly spaced.

velocities which exceed the free-stream values. This can present a problem either by causing the timestep to be reduced (in a variable-time-step computational scheme), or by exceeding the CFL number stability limits (in a fixed time-step scheme). In our simulations, the effect on the timestep was not observed.

2.1.1 Floating forcing mesh

To avoid the error incurred by interpolating between grid points in the Fourier directions, we interpolate data across B-spline planes to ensure that the surface sampling points (solid circles in Fig. 3) always coincide with Fourier collocation points. Since the B-splines have compact support in physical space, it is economical to perform the direct inversion of the transform to obtain the velocity field on any desired $x - z$ plane. Note that the planes on which the forcing function is applied (dashed horizontal lines) need not necessarily coincide with the planes on which the flow is computed (solid horizontal lines). The reversal of tangential velocities is accomplished by forcing at points inside the surface (solid squares), where the velocity is forced to be the reverse of the velocity measured at the corresponding points in the external flow (dashed squares).

2.2 Laminar ribbed channel

For a test of the scheme we simulate laminar flow in a ribbed channel. The geometry of the problem is shown in Fig. 4. We consider a flow between two ribbed walls with periodic boundary conditions in the streamwise and spanwise directions. As in the case of CMK, we keep the channel cross-section and pressure gradient
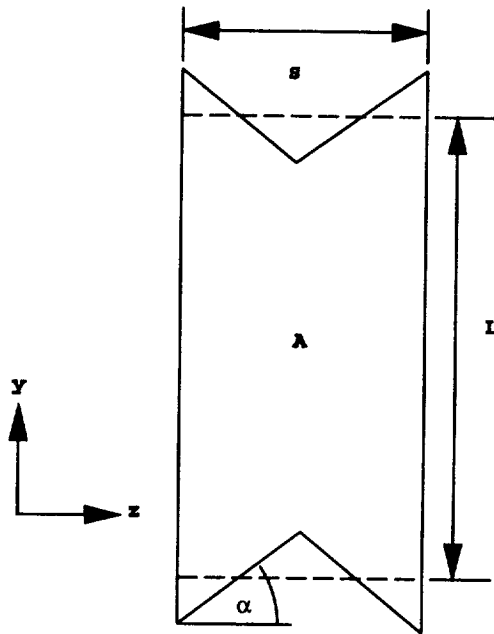
FIGURE 4.   Sketch of the cross-sectional geometry of the channel. The mean channel height L is kept fixed while the riblet angle α is varied.
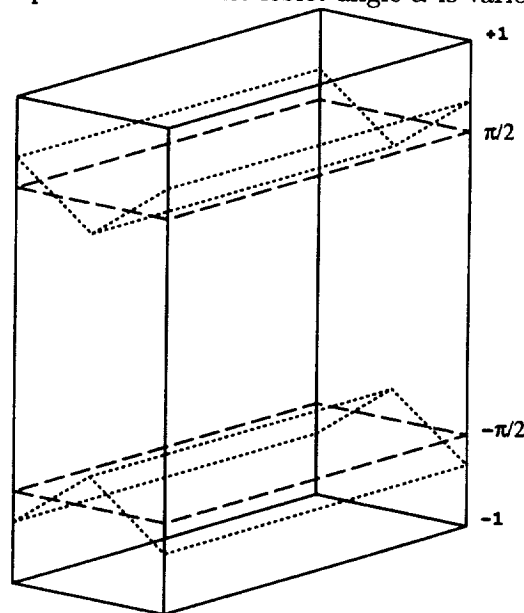

FIGURE 5.   Sketch showing the computational domain (solid lines) and the location of the immersed boundary (dotted line). The mean location of the ribbed wall (corresponding to the flat channel case) is shown by the dashed line.
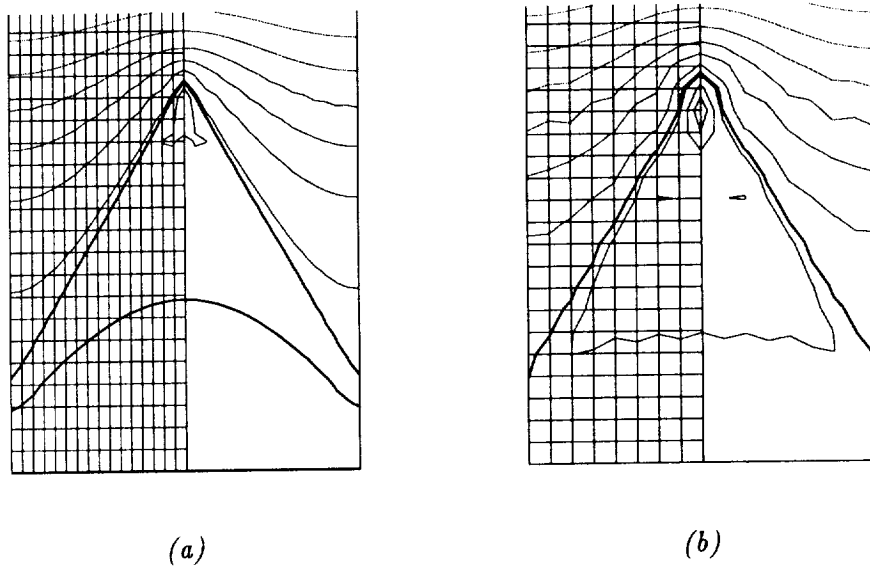
(a) *(b)*

FIGURE 6. Isosurface of zero streamwise velocity and contours of streamwise velocity for the 60° riblet case, using 3rd-order B-splines. (a) 32 spanwise grid points (b) 16 spanwise grid points.
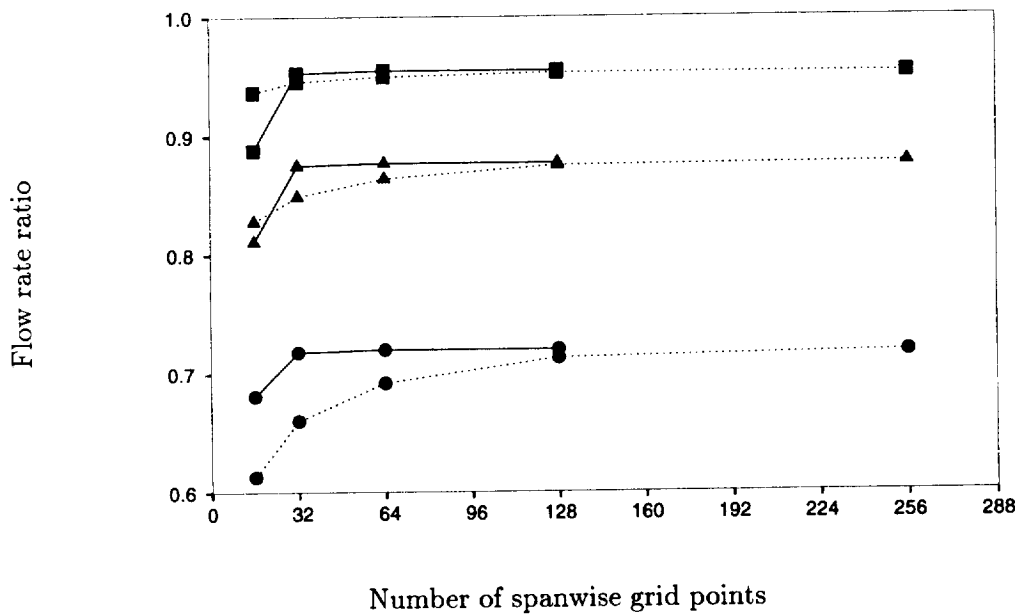

Number of spanwise grid points

FIGURE 7. Variation of ratio of flow rates with riblets to flow rate in flat wall channel as a function of spanwise resolution. $S/L = 0.2$. ——— current scheme ········ CMK results, ■ 30°, ▲ 45°, ● 60° riblets.

constant and monitor the variation of the steady-state flow rate with the riblet geometry. CMK show that in the laminar case, the variation of the flow rate with geometry is independent of the Reynolds number and thus the specific choice of Re does not affect the results.

The computational domain extends from $-1 < y < +1$. No-slip conditions are applied to the computational boundary. The immersed riblet surfaces are centered at $y = \pm\pi/4$. Thus the height of the channel is $\pi/2$. The streamwise extent of the computational domain is fixed at $\pi/2$ for all simulations. A sketch of the computational domain and the location of the immersed boundary is given in Fig. 5.

2.2.1 Results

Figure 6 shows the isosurface of zero streamwise velocity for the case $\theta = 60^\circ$, $S/L_y = 0.2$, using 3rd-order B-splines. Note that the sharp tip of the riblet is well captured, even though only 32 spanwise grid points are used (Fig. 6a). A comparison is also shown with the case using only 16 spanwise modes (Fig. 6b). The rounding of the riblet tip can be seen in this instance and also the oscillations in the velocity contours, due to inadequate spanwise resolution.

Figure 7 shows the comparison of computed flow rate ratios for the 3rd order B-spline results with those of CMK. Note that the current method only requires 32 grid points per riblet in the spanwise directed as compared to 128 for the previous code. Note also that since there is no grid-deformation in the current scheme, the riblet angle does not affect the relative error to a large degree. In contrast, the highly non-orthogonal grids required in the boundary-fitted grid method cause much larger errors for the higher riblet angles.

Future plans

The numerical scheme will be extended to allow moving solid boundaries. Due to the expense of calculating the B-spline coefficients at each timestep, it may be necessary to utilize high order interpolation schemes to obtain field information at points that do not coincide with the solution collocation points. Such methods are readily available and are used in vortex schemes, for example, during remeshing steps. The resulting moving-boundary code will be used to test open and closed-loop control schemes (Koumoutsakos 1996) to minimize wall drag in turbulent flows.

REFERENCES

CARLSON, H. A., BERKOOZ G. & LUMLEY J. L. 1995 Direct numerical simulation of flow in a channel with complex, time-dependent wall geometries: A pseudospectral method. *J. Comp. Phys.* **121**, 155-175.

CHOI, H., MOIN, P., & KIM, J. 1991 On the effect of riblets in fully developed laminar channel flows. *Phys. Fluids A.* **3**, 1892-1896.

GOLDSTEIN, D., HANDLER R. & SIROVICH L. 1993 Modeling a no-slip flow boundary with an external force field. *J. Comp. Phys.* **105**, 354-366.

HARLOW, F. H. AND WELCH, J. E. 1965 Numerical calculation of time-dependent viscous incompressible flow of fluid with a free surface. *Phys. Fluids.* **8**, 2182-2189.

KIM, J., MOIN, P. & MOSER, R. 1987 Turbulence statistics in fully developed channel flow at low Reynolds number. *J. Fluid Mech.* **177**, 133-166.

KOUMOUTSAKOS, P. 1995 Fast multipole methods for three-dimensional N-body problems. *Annual Research Briefs 1995*, Center for Turbulence Research, NASA Ames/Stanford Univ., 377-390.

KOUMOUTSAKOS, P. 1996 A new method for the adaptive control of vortex-wall interactions. *Annual Research Briefs 1996*, Center for Turbulence Research, NASA Ames/Stanford Univ., 165-181.

KRAVCHENKO, A. G., MOIN, P. & MOSER, R. 1996 Zonal embedded grids for numerical simulations of wall-bounded turbulent flows. *J. Comp. Phys.* **127**, 412-423.

MOHD-YUSOF, J. 1996 Interaction of massive particles with turbulence. *PhD thesis*, Cornell University.

DNS of shock boundary-layer interaction – preliminary results for compression ramp flow

By N. A. Adams

Preliminary results of a direct numerical simulation of a turbulent boundary layer along a compression-ramp at $M = 3$ are presented. The evolution of mean-flow profiles and correlations are in accordance with trends in experimental data and theoretical predictions. With the present simulation parameters no large-scale streamwise vortical structures can be found, and there is no upstream-communication across the region of flow separation. Explicit compressibility effects are significant in the region of strong interaction between shock and turbulent boundary layer.

1. Motivation and objectives

In this report we summarize recent accomplishments of an ongoing effort towards direct numerical simulation and large-eddy simulation of shock-turbulence interaction. The main objective is to provide a quantitative assessment of the shock boundary layer interaction. Also, we hope eventually to be able to understand the complex coupling mechanisms in the non-equilibrium area where shock, turbulence, and mean-flow (separation) interact strongly. A goal of this effort is to provide DNS results for the validation of relevant LES simulations.

In this report we want to demonstrate the feasibility of DNS for these kinds of physically complex flows. Preliminary analysis of the generated data-base should indicate trends for turbulence statistics. A subsequent improved simulation which is presently in progress is expected to allow for a conclusive assessment.

2. Accomplishments

We present preliminary results for the flow structure and flow phenomena associated with shock turbulent boundary layer interaction along an $18°$ compression ramp. The flow is at $M = 3$ and $Re = 5000$, based on the free stream velocity and kinematic viscosity and using as a reference length about a fifth of the turbulent boundary-layer thickness at inflow. Well documented experimental data at same Mach number, significantly higher Reynolds number, and a ramp deflection angle of $25°$ are available by Zheltovodov, see Settles *et al.* (1991). The experimental oncoming fluctuation profiles, however, are significantly distorted due to boundary-layer tripping. As the experiment shows, the wall temperature is almost constant before and after the compression. This is consistent with our assumption of an isothermal wall in the present simulation.

The numerical scheme is based on the hybrid compact-upwind ENO schemes as proposed by Adams & Shariff (1996). The numerical method, boundary conditions, implementational issues, and code validation have been reported by Adams (1994, 1995, 1997).
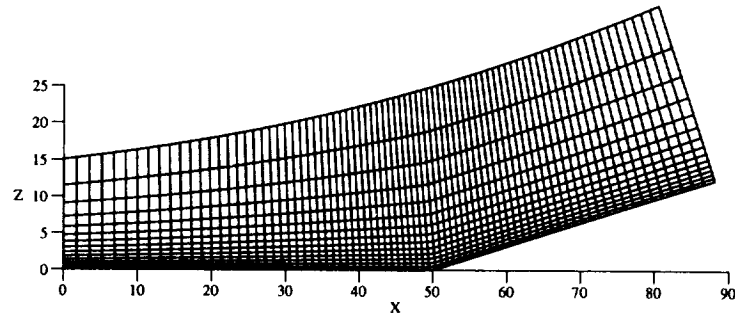
FIGURE 1. Computational mesh (each 10th grid line shown).

Inflow data are taken from a separate DNS of a temporally evolving turbulent flat plate boundary layer. We use one realization, i.e. the streamwise periodic flow field at one time instant, of this DNS which is convected at $0.8U_\infty$ through the inflow-plane of the computational domain. This convection velocity is estimated from the average absolute speed of large-scale structures (Adams and Kleiser 1996). For a recent discussion on turbulent inflow data for DNS see Chung and Sung (1997). Since our main purpose here is to demonstrate the feasibility of supersonic compression ramp DNS, inflow-data deficiencies are considered to be less significant. In a subsequent well-resolved DNS, inflow data are to be taken from a separate spatial boundary-layer DNS. For the present simulation a discretization of 800 cells in the streamwise, 70 the in spanwise, and 140 in the wall-normal direction have been used. The sampling-time was about 515 time-units with 280 data samples, which yields about 90 GWords of stored data. The computing time was about 600 CPU hours on 4 concurrently running CPUs on a NEC SX-4, where the code presently reaches about 3.3 GFLOPs on 4 CPUs (work on further parallel optimization is in progress).

In Fig. 1 we present a side-view of the domain and the mesh discretization, and in Table 1 the start-point coordinates of mesh planes are given along which flow-data have been sampled and evaluated.

TABLE 1. Evaluation mesh-line start-point coordinates.

i	(x,0)	(0,z)
1	25.00	0.00
2	45.04	0.11
3	48.02	1.03
4	51.96	3.00
5	54.95	5.07
6	74.97	7.84

Figures 2 and 3 show visualizations of the instantaneous flow field. In Fig. 2 the gray-scale distribution of the backward plane and the ramp surface corresponds
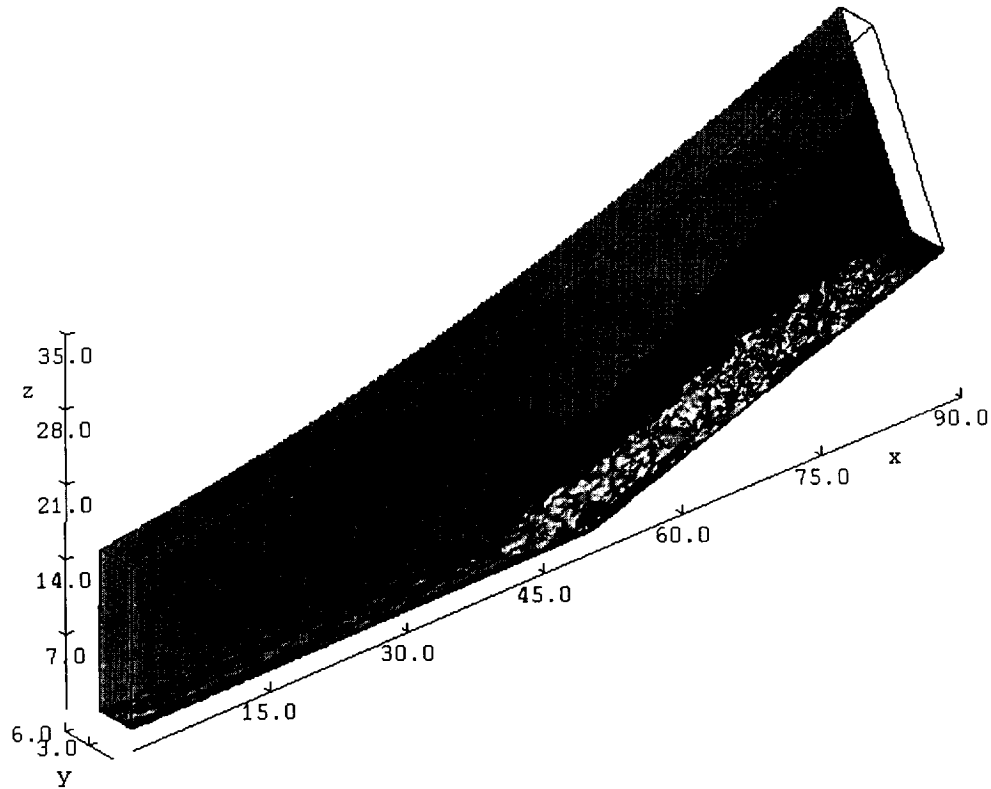
FIGURE 2. Pressure and iso-surface of longitudinal velocity. $u = 0.4, t = 846.96$.

to the local static pressure. The ramp-shock, emerging from the area of separated flow close to the corner, is evident. A surface of streamwise contravariant velocity component $u^c = 0.4U_\infty$ indicates the increased fluctuation level after the compression. In the back-plane pressure distribution, close to the boundary-layer edge, local pressure peaks can be seen. From a time sequence it has been confirmed that these pressure-peaks are generated whenever a violent ejection event occurs. Subsequently, they are convected downstream and their strength decreases. Similar observations, identified as shocklets, have been made experimentally, see Smits and Dussauge (1996). In Fig. 3 the shock, which forms essentially outside of the boundary layer, is visualized by a surface of high negative velocity dilatation ($\text{div}\,u = -0.2$). Essentially, no shock motion can be detected from time sequences of shock surfaces, except for some shock-foot oscillations towards and away from the wall. This behavior is related to the dynamics of the flow near the corner.

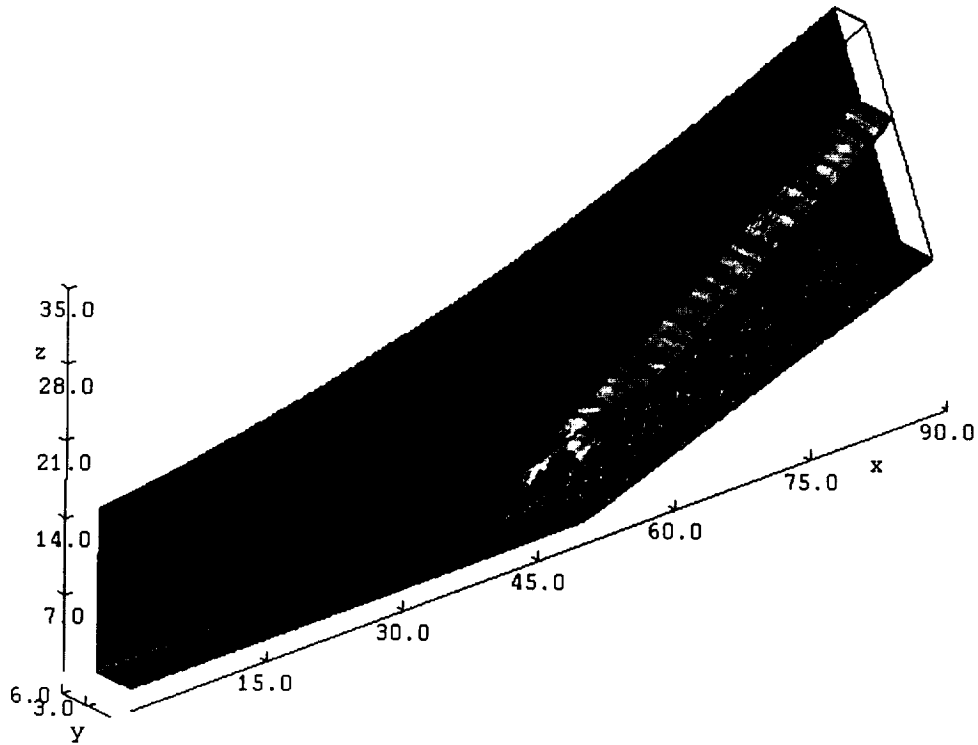Figure 4 shows iso-contours of the instantaneous spanwise vorticity field in a

FIGURE 3.   Density and shock-surface. $div(u) = -0.2, t = 846.96$.

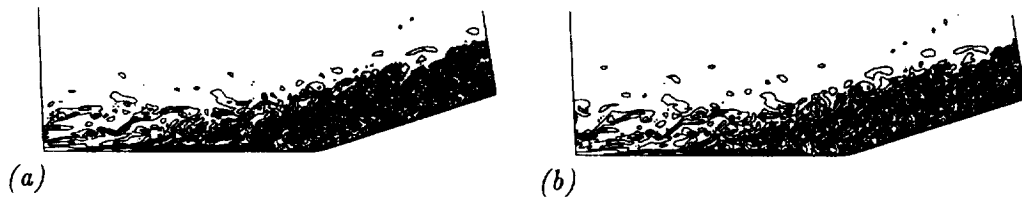*(a)*   *(b)*

FIGURE 4.   Spanwise vorticity at $y = 1.2$, $t = 846.96$, (a), and $t = 848.81$, (b).

cross-plane (truncated to an area close to the corner) at two time instances. The pressure rise in front of the corner causes the near-wall shear layer to separate. There is no indication of large-scale vortical structures, such as Görtler-like vortices, for instance.

Iso-contours of the time-averaged (using 280 samples over about 520 time-units)
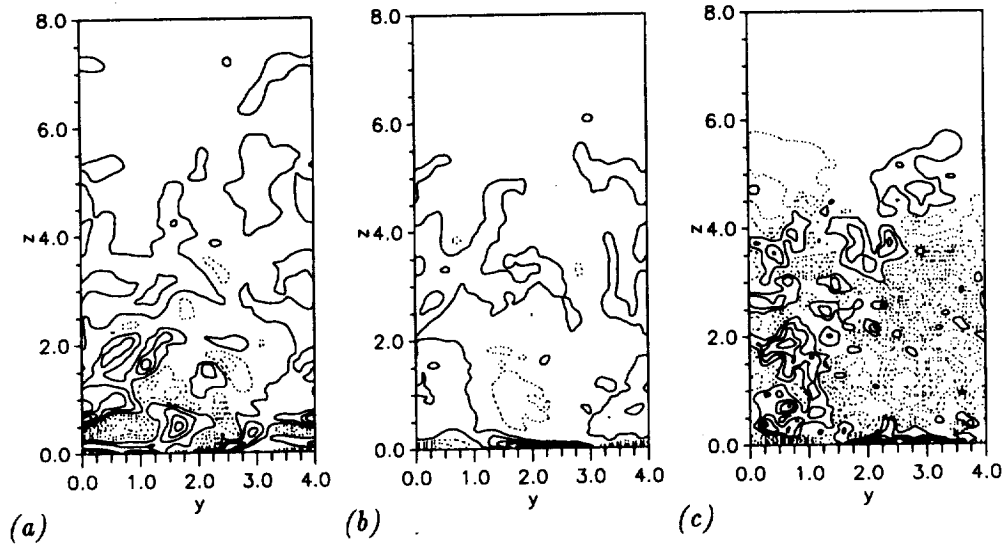
FIGURE 5. Time-averaged streamwise contravariant vorticity at position 2 (a) $-1.54 \leq \overline{\omega^c_x} \leq 2.69$, 4 (b) $-2.58 \leq \overline{\omega^c_x} \leq 3.68$ and 6 (c) $-0.33 \leq \overline{\omega^c_x} \leq 0.42$.

streamwise contravariant (approximately longitudinal) vorticity-field in cross-planes are shown in Fig. 5. Position 2 is in front of the corner, Fig. 5(a), position 4 right after the corner, Fig. 5(b), and position 6 further downstream, Fig. 5(c). These figures confirm the apparent lack of large-scale streamwise vortical motions.

The Görtler number, estimated from streamline curvature of the Favre-averaged velocity-field, does not exceed values of about $G_T = 3$ (for a definition see e.g. Smits and Dussauge (1996), p. 277) so that Görtler instability of the separated flow seems not likely (the critical value for the Görtler number defined with the momentum thickness is about 7). In any case, the spanwise wavelength of a dominant Görtler instability is about $2\delta_0$ (two mean boundary-layer thicknesses), which cannot be represented in our simulation since the spanwise extent of the computational domain is too narrow (somewhat less than one mean boundary-layer thickness). Note that, in a numerical simulation of a supersonic transitional boundary layer along a compression ramp at low Reynolds number by Comte & David (1996), Görtler vortices were present.

Results of rapid distortion theory (RDT) indicate that the strong Reynolds analogy (SRA) is not valid across the interaction region (Mahesh *et al.*, 1996). To address this issue the correlation of u'' and T'' has been time-traced at 6 positions before, within, and after the interaction area (Table 2). Apparently SRA holds within generally accepted accuracy of about 80% correlation before the interaction, collapses within the interaction region, and recovers only slowly further downstream. This fact is of significance for turbulence modeling, where SRA is often employed when incompressible models are extended to compressible flows.

Figure 6(a) shows surface-pressure and skin-friction, averaged over 280 time samples. The ramp corner is at $x = 50$. The skin friction coefficient of the oncoming

TABLE 2. Evaluation mesh-line start-point coordinates.

x	y	z	corr(T"u")
24.95	0.00	1.29	-0.79
24.95	1.07	1.29	-0.80
47.89	0.00	1.65	-0.46
47.89	1.07	1.65	-0.17
54.76	0.00	3.27	-0.68
54.76	1.07	3.27	-0.23

turbulent mean flow is about $C_f = 0.0024$ which corresponds to a Reynolds number about 5 times smaller than in the previously mentioned experiment of Zheltovodov, according to the van Driest C_f-correlation (Schlichting, 1982, p. 734). The Reynolds number, defined with the distance from the leading edge, is approximately $Re_L \simeq 170000$ for the simulation, while for the experiment it is about $Re_L \simeq 876900$. The C_f-distribution downstream of the compression still becomes smoother by adding more samples. The value of the surface pressure p_{surf} after the compression reaches the level predicted by inviscid theory. An inflection point in the p_{surf}-distribution has developed roughly at the corner, indicating incipient separation. Within the sponge layer, between $x = 82$ and the end of the computational domain, the mean-flow profiles are significantly distorted since the turbulent flow is forced towards a thin laminar profile. This is the reason for the strong excursions of C_f in this region. In a subsequent simulation the flow will be forced to a turbulent mean-flow profile instead.

Figure 6(b) shows time-traces of an average "instantaneous" separation location, which we define as the first point where the spanwise averaged skin-friction becomes negative and the average "instantaneous" reattachment location, the last point where the spanwise averaged skin-friction becomes positive again. While the separation line shows a clearly regular oscillation, the reattachment line does not. The Fourier-transform of the separation-point location has a peak at a frequency of about $\omega = 0.11$, which corresponds to the time-scale imposed by the inflow-data. The abovementioned way of imposing inflow-data generates a temporal correlation time scale of size $L_x/0.8$ at inflow ($L_x = 7$ is the streamwise computational box-size of the temporal DNS). The Fourier-transform of the reattachment-point location, however, does not show a similar dominant frequency. It can be concluded that hypotheses about upstream communication effects in a separation bubble (Smits and Dussauge, 1996), are not validated by our simulation since separation and reattachment location are apparently decorrelated.

Profiles at streamwise positions 1 through 6 as given in Table 1 are shown. Figure 7(a) shows a sequence of Favre-averaged temperature profiles, staggered by increments of 0.5 for convenience. A sequence of Favre-averaged contravariant-velocity profiles in Fig. 7(b), staggered by increments of 0.5, shows deformations by regions of retarded flow due to the adverse pressure gradient. From Fig. 6(a) it can be seen
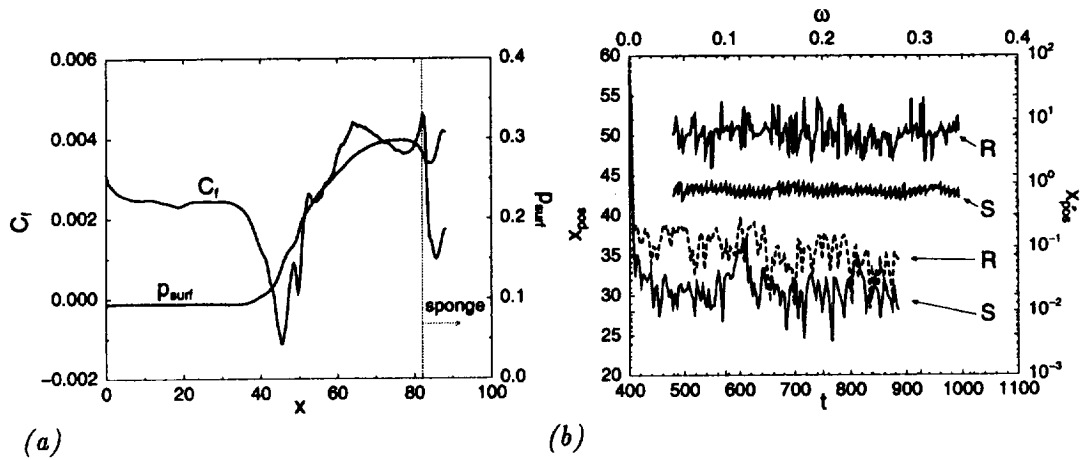
FIGURE 6.   Skin friction and surface pressure, (a). Mean separation (S) and reattachment (R) locations and their Fourier-transforms, displayed over frequency ω, (b).
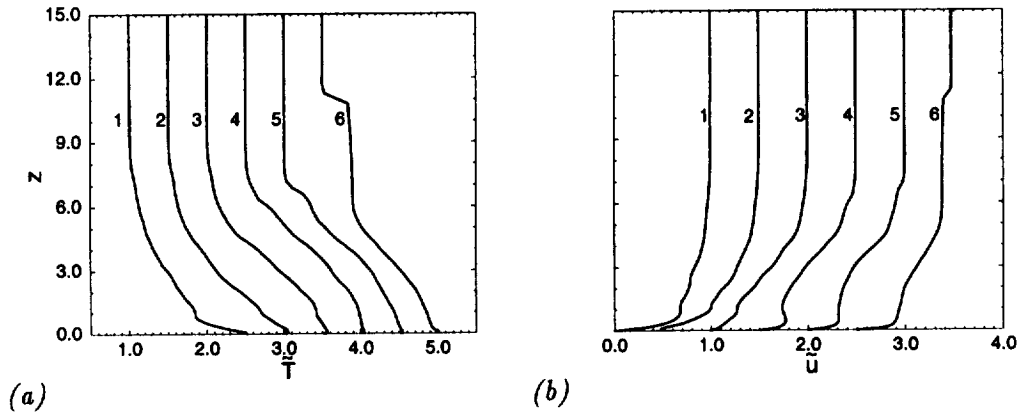

FIGURE 7.   Favre-averaged temperature, (a), and Favre-averaged contravariant velocity profiles, (b).

that the mean flow reattaches just before the corner. This behavior is consistent with experimental results at $M = 2.25$ for an incipient separation at an 18°-ramp (Ardonceau *et al.*, 1979). Note that sampling stations 2 and 3 are just after mean separation and just after mean reattachment, respectively, such that a region of separated flow can only be seen vaguely in profile number 2. Favre-averaged velocity profiles first thicken across the interaction region to become thinner again further downstream, mainly also due to the reduced post-shock boundary layer edge-velocity. The mean velocity profiles recover slowly towards an equilibrium shape.
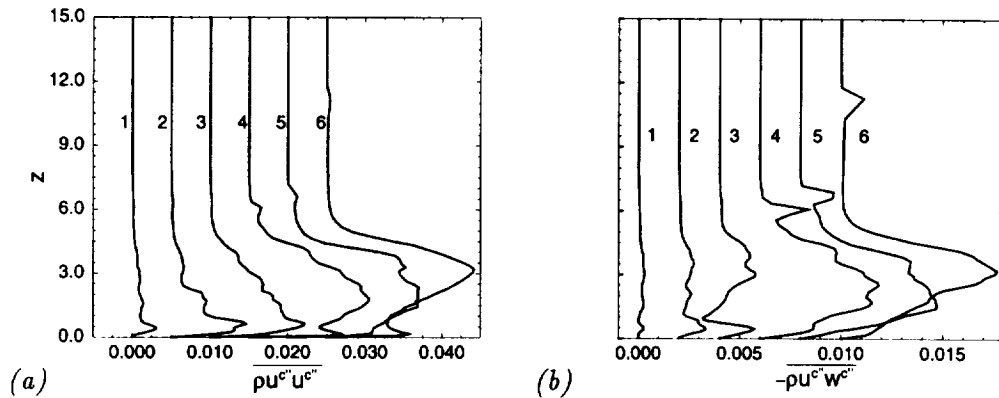
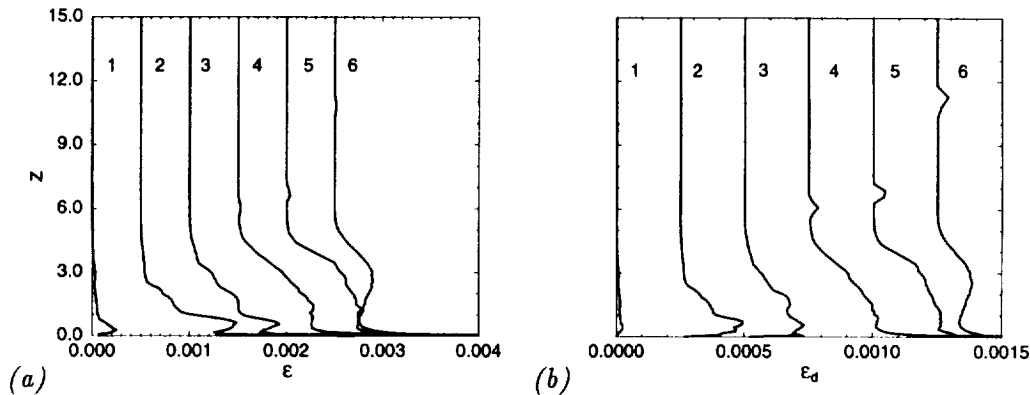FIGURE 8.   Normal Reynolds-stress, (a), and Reynolds shear-stress, (b).

FIGURE 9.   Total dissipation (a), and dilatational dissipation (b).

Profiles of Reynolds-stresses (using contravariant velocities), shown in Fig. 8, staggered by 0.005 and 0.002, respectively, evolve qualitatively essentially as reported in Smits and Muck (1987). The evolution of the normal stresses is characterized by a pronounced peak near the boundary-layer edge, besides the near-wall peak which can be found in any statistically developed turbulent boundary layer, Fig. 8(a). Figure 8(b) shows profiles of the shear-stress profiles at stations 1 through 6. Profiles 2 and 3 show an increased $u''w''$-correlation near the boundary layer edge, which is also typical for a late transitional boundary layer (Adams and Kleiser, 1996), where detached shear-layers in the outer boundary-layer part are generated and break up. The areas of maximum Reynolds shear-stress do not coincide with those of maximum turbulence intensity (those rather follow the Reynolds normal-stress) at these stations. Similar to the normal stresses, the shear-stresses are amplified across the interaction region and show a non-equilibrium profile at station 6. Qualitatively,

the results again agree with experimental data of Smits and Muck (1987).

Well within the boundary layer the normal-stresses are amplified across the interaction region by about one order of magnitude, which corresponds to experimental findings, Smits and Muck (1987). Essentially the same holds for the Reynolds shear-stress. The amplification of the Reynolds shear-stress is consistent with RDT-predictions (Mahesh *et al.*, 1996) for large shock-obliqueness angles,whereas for a normal shock the Reynolds shear-stress would be damped.

The simulation results also indicate that terms appearing explicitly in the compressible form of the turbulent-kinetic-energy equation, such as pressure dilatation and dilatational dissipation, assume an appreciable value of up to 25% of the total dissipation in the interaction region (Fig. 9) whereas they are insignificant in flat plate boundary layers up to $M = 6$ (Guo & Adams, 1994). These results need to be confirmed by higher resolution simulations.

3. Future plans

Well resolved simulations at higher Reynolds number are in progress. Along with the DNS, effort on LES is presently pursued by evaluating modeling strategies with respect to their suitability for compressible boundary layer. To assess the effectiveness of the LES for compression ramp flow we will conduct a priori analyses of the compression ramp DNS data. Implications for turbulence modeling will be addressed.

Acknowledgments

REFERENCES

ADAMS, N. A. 1994 Numerical study of boundary layer interaction with shocks - method and code validation. *CTR Annual Research Briefs 1994*, Center for Turbulence Research, NASA Ames/Stanford Univ., 339-356.

ADAMS, N. A. 1995 Numerical study of boundary layer interaction with shocks - method improvement and test computation. *CTR Annual Research Briefs 1995*, Center for Turbulence Research, NASA Ames/Stanford Univ., 361-376.

ADAMS, N. A. 1997 Direct numerical simulation of turbulent compression ramp flow. Technical report, ETH Zürich, Inst. of Fluid Dynamics, Zürich, Switzerland. Submitted to *Theoretical and Computational Fluid Dynamics*.

ADAMS, N. A. & KLEISER, L. 1996 Subharmonic transition to turbulence in a flat plate boundary layer at Mach number 4.5. *J. Fluid Mech.* **317**, 301-335.

ADAMS, N. A. & AND SHARIFF, K. 1996 A high-resolution hybrid compact-ENO scheme for shock-turbulence interaction problems. *J. Comp. Phys.* **127**, 27-51.

ARDONCEAU, P., LEE D. H., ALIZARY DE ROQUEFORT T. & GOETHALS, R. 1979 Turbulence behavior in a shock wave / boundary layer interaction. In *AGARD CP-271*, pages 8-1-8-14, Neuilly Sur Seine, France. AGARD.

CHUNG Y. M. & SUNG, H.-J. 1997 Comparative study of inflow conditions for spatially evolving simulation. *AIAA Journal.* **35**, 269-274.

COMTE, P. & DAVID, E. 1996 Large-eddy simulation of Görtler vortices in a curved compression ramp. In *Experimentation, modeling and computation in flow, turbulence and combustion*, pages 45-61, Désidéri, J. A., Chetverushkin, B. N., Kuznetsov, Y. A., Périaux & Stoufflet, B. (eds.), John Wiley & Sons, Chichester.

GUO, Y. & ADAMS, N. A. 1994 Numerical investigation of supersonic turbulent boundary layers with high wall temperature. *CTR Proc. 1994 Summer Program*, Center for Turbulence Research, NASA Ames/Stanford Univ. 245-267.

MAHESH, K., MOIN, P. & LELE, S. K. 1996 The interaction of a shock wave with a turbulent shear flow. *Technical Report TF-69*, Department of Mechanical Engineering, Stanford University, Stanford, California.

SCHLICHTING, H. 1982 *Grenzschicht-Theorie*. Verlag G. Braun, Karlsruhe, Germany.

SETTLES, G. S. & DODSON, L. J. 1991 Hypersonic shock/boundary-layer interaction database. *Technical Report NASA CR 177577*, NASA Ames Research Center, Moffett Field, California.

SMITS, A. J. & DUSSAUGE J.-P. 1996 *Turbulent Shear Layers in Supersonic Flow*. AIP Press, Woodbury, New York.

SMITS, A. J. & MUCK, K.-C. 1987 Experimental study of three shock wave / turbulent boundary layer interactions. *J. Fluid Mech.* **182**, 291-314.

Appendix
ROSTER

NAME/TERM		AREA OF RESEARCH
POSTDOCTORAL FELLOWS		
BAGGET, Dr. Jeffrey 9/96-present	(Ph.D. Mathematics, 1996, Cornell)	Turbulence modeling
BASTIN, Dr. Francois 10/95-2/97	(Ph.D. Aeroacoustics, 1995, Ecole Centrale Paris)	Aeroacoustics
BOERSMA, Dr. Bendiks Jan 9/97-present	(Ph.D. Engineering 1997, Delft University of Technology)	Large eddy simulation, Turbulent combustion, Aeroacoustics
BUSHE, Dr. W. Kendal 9/96-present	(Ph.D. Engineering, 1996, Cambridge)	Turbulent combustion
DUBOIS, Dr. Thierry 9/1/97-present	(Ph.D. Mathematics, 1989, University of Paris - Sud)	Incremental unknowns for large eddy simulation
FATICA, Dr. Massimiliano 10/95-present	(Ph.D. Fluid Mechanics, 1995, University of Rome)	Large-eddy simulation
KALITZIN, Dr. Georgi 1/97-present	(Ph.D. Mechanical Engineering, 1991, Technical University, Magdeburg)	Turbulence modeling
KIM, Dr. ChongAm 9/97-present	(Ph.D. Mechanical & Aerospace Engr., 1997, Princeton)	Numerical methods
MOHD. YUSOF, Dr. Jamaludin 9/96-present	(Ph.D. Aerospace Engr., 1996, Cornell)	Numerical methods for complex flows

OBERLACK, Dr. Martin 4/95-4/97	(Ph.D., Technical Mechanics, 1994, RWTH-Aachen)	Turbulence theory
PARNEIX, Dr. Sacha 12/95-present	(Ph.D. Fluid Mechanics, 1995, University of Bordeaux)	Turbulence modeling
SU, Dr. Lester 9/97-present	(Ph.D. Aerospace Engineering, 1995, University of Michigan)	Turbulent combustion
VASILYEV, Dr. Oleg V. 9/96-present	(Ph.D. Aerospace & Mechanical Engineering, 1996, Notre Dame University)	Large-eddy simulation
ZIANE, Dr. Mohammed 6/97-present	(Ph.D. Mathematics, 1997, Indiana Univ., Ph.D. Applied Analysis, 1995, Univ. de Paris, Sud)	Optimal control theory

RESEARCH ASSOCIATES

CABOT, Dr. William H. 3/88-present	(Ph.D. Physics, 1983, University of Rochester)	Large-eddy simulation and convection
KASSINOS, Dr. Stavros 1/95-present	(Ph.D. Mechanical Engineering, 1994, Stanford)	Turbulence modeling
KOUMOUTSAKOS, Dr. Petros 8/94-present	(Ph.D. Aeronautics & Applied Mathematics, 1992, California Institute of Technology)	Turbulence physics Active control
LUND, Dr. Thomas S. 11/90-9/97	(Ph.D. Aero-Astro, 1987, Stanford)	Large-eddy simulation
MAHESH, Dr. Krishnan 6/96-present	(Ph.D., Mechanical Engineering, 1996, Stanford)	High speed flows Plasmas

RUETSCH, Dr. Gregory 9/93-present	(Ph.D. Applied Mathematics, 1991, Brown University)	Turbulent combustion
WANG, Dr. Meng 9/92-present	(Ph.D. Mechanical Engr., 1989, University of Colorado)	Aerodynamic noise

SR. VISITING FELLOWS

ADAMS, Dr. Klaus 8/97	ETH Zentrum, Zurich	Shock boundary-layer interaction
BEHNIA, Prof. Masud 6/96-2/97, 8/97	University of New South Wales	Turbulence modeling
BILGER, Prof. Robert W. 3/97-4/97, 7/97	University of Sydney	Turbulent combustion
CARATI, Prof. Daniele 5/97-6/97	University Libre de Bruxelles	Turbulence modeling
COTTET, Prof. George-Henri 9/96-6/97	Universite Grenoble	Large eddy simulation Vortex dynamics
KALTENBACH, Dr. Hans-Jakob 6/97-7/97	Technical University - Berlin	Large eddy simulation
MARCUS, Prof. Philip 9/96-6/97	UC-Berkeley	Turbulence theory
MITTAL, Prof. Rajat 5/97-6/97	University of Florida	Large-eddy simulation
POINSOT, Dr. Thierry 8/97	CERFACS	Turbulent combustion
STEINER, Dr. Helfried 1/97-present	Technical University - Graz	Turbulent combustion
VEYNANTE, Dr. Denis 8/97	Ecole Centrale Paris	Turbulent combustion

SR. RESEARCH FELLOWS

BROADWELL, Dr. James E.
1/94-present

Turbulent combustion

JIMENEZ, Prof. Javier
1987-present

Small scales in turbulence

YAGLOM, Prof. Akiva
7/95-present

Writing of 2nd edition,
"Statistical Fluid
Mechanics"

GRADUATE STUDENTS

BUICE, Carl
7/95 - 12/97

Measurements in a
symmetric planar diffuser

DAY, Mark
4/97-6/97

Compressible reacting
mixing layer

LUI, Calvin
10/96-9/97

Compressible mixing
layers

WENZEL, Holger
6/97-8/97

(ITM-RWTH Aachen)

Turbulent combustion

1997 ADVISORY COMMITTEE

Prof. Eugene Covert
Massachusetts Institute of Technology

Prof. John L. Lumley (Chairman)
Cornell University

Dr. David E. Crow
United Technologies Pratt & Whitney

Dr. James M. McMichael
Air Force Office of Scientific Research

Prof. Steven Crow
University of Arizona

Prof. Norbert Peters
RWTH - Aachen

Mr. Robert H. Kelly-Wickemeyer
Boeing Commercial Airplane Group

Dr. Dennis M. Bushnell (Ex-officio)
NASA Langley Research Center

Prof. Brian Launder
University of Manchester

Dr. Marvin E. Goldstein (Ex-officio)
NASA Lewis Resesarch Center

Dr. Spiro Lekoudis
Office of Naval Research

Dr. John Howe (Ex-officio)
NASA Ames Research Center

In addition, Dr. L. Patrick Purtell (ONR), Dr. Om Sharma (Pratt & Whitney), and Dr. Mark Glauser (AFOSR) attended the 1997 meeting of the Advisory Committee.

1997 STEERING COMMITTEE

Prof. Paul A. Durbin
Professor, Mechanical Engineering,
Stanford

Prof. Javier Jiménez
Ssenior Research Fellow, Center for
Turbulence Research, and
Professor, University of Madrid

Dr. Nagi N. Mansour
Turbulence Physics Section,
NASA Ames Research Center

Mr. Joseph G. Marvin
Aeronautical Technologies Division,
NASA Ames Research Center

Prof. Parviz Moin
Director, Center for Turbulence Research
Professor, Mechanical Engineering and
Aeronautics & Astronautics, Stanford
Sr. Staff Scientist, NASA Ames Research
Center

Prof. William C. Reynolds
Program Coordinator, Center for Turbulence
Research
Professor, Mechanical Engineering and
Aeronautics & Astronautics, Stanford
Sr. Staff Scientist, NASA Ames Research
Center

Dr. Charles A. Smith
Acting Chief
AeronauticalTechnologies Division
NASA Ames Research Center